Cranfield University

A. Bradshaw

Development of Coatings for Gas Turbines Burning Biomass and Waste-Fuels

School of Applied Sciences

PhD Thesis

Cranfield University

School of Applied Sciences

PhD Thesis

Academic Year 2009-2010

A. Bradshaw

Development of Coatings for Gas Turbines Burning Biomass and Waste-Fuels

Supervisors: Professor J. R. Nicholls
Dr N. J. Simms

November 2009

Abstract

Worldwide, carbon dioxide emission reductions are in progress following the Kyoto Protocol implementation programme to mitigate climate change. More stringent reductions are expected to follow the present programme which ends in 2012. In addition to reducing carbon dioxide emissions, the major climate change mitigation policy is the elimination of waste. This project addresses both aspects, by facilitating the use of biomass and waste fuels in the gas turbines of highly efficient, integrated gasification combined cycle electricity generating units. Gases from the gasification of these fuels contain potentially damaging contaminants which, when combusted in gas turbines, will initiate hot corrosion. To resist hot corrosion, but still maximise gas turbine efficiency, the hot components of gas turbines require protective coatings.

Five activities in this project required original research to meet the objectives. Firstly, to identify potentially damaging species in gasifier gases, which could remain after hot gas cleaning and, following combustion, initiate hot corrosion along the gas path of the gas turbine. Thermodynamic assessments, using MTDATA software, identified cadmium and lead species that could initiate hot corrosion in the gas turbine. The second research activity, involved Type II hot corrosion tests of the identified species on superalloys and typical commercial coatings. These tests simulated the same corrosion environment as in industrial high temperature gas turbine operation. Test results confirmed the thermodynamic assessments, with hot corrosion being initiated on all items tested, and was worse with lead and/or cadmium additions. The third research activity was to develop novel hot corrosion protective coatings. The approach was to develop the most economic coatings, which would provide comparable, or superior, hot corrosion performance to that provided by well proven commercial coatings already used with fossil fuel firing. From previous research at Cranfield, published literature, and after aluminising and silicon modified aluminising CVD trials, single-step silicon modified aluminising was adopted as the basis for novel coating development. The fourth research activity consisted of cyclic oxidation tests and, type II and type I hot corrosion tests, to assess the oxidation and hot corrosion protection provided by the novel coatings on IN738LC and CMSX-4 substrates. Cyclic oxidation tests at 950°C and 1050°C showed the novel coatings produced by CVD, at a soak temperature of 1050°C and soak period of one hour, were superior for both substrates. Microstructurally, TCP phases were formed in CMSX-4 samples which could reduce mechanical strength in service. The TCP phases were observed in the high silicon containing coatings through a reaction with refractory metals diffusing outward from the CMSX-4. This was most noticeable in samples cyclically oxidised at 1050°C for long times. Results of hot corrosion tests undertaken at 700°C (type II) and 900°C (type I) showed novel coatings on IN738LC samples to be more resistant than commercial coatings. Those on CMSX-4 samples had similar hot corrosion resistance to commercial coatings. The novel coatings provided high levels of hot corrosion resistance, which could be enhanced by improvements in deposition. The fifth research activity was to carry out EB-PVD TBC trials on an IN738LC turbine blade, which demonstrated that the novel coating provided an effective bond for the TBC. It is concluded that the novel, single-step silicon-aluminide coatings developed in this project, with identified improvements in quality, will provide effective hot corrosion resistance for gas turbines burning gasified biomass and waste fuels.

Acknowledgements

The creative nature of this project and acquisition of knowledge I have gained, have been most fulfilling, particularly as the overall objective was to assist in making a contribution to sustainability in this field of study. Throughout the period of study I have been helped by all staff at Cranfield. In particular I would like to thank my supervisors, Professor J.R. Nicholls and Dr Nigel Simms, for their guidance in all scientific and technical matters and for their enthusiastic support throughout this project.

Thanks are due to the following Cranfield University staff for their willing and friendly assistance over the few years I spent on the project; Tim Pryor, Tony Gray, Christine Chalk, Kevin Long, Andrew Potter, Tim Rose, Simon Gray, Richard Wellman and Sharon McGuire, from the National High Temperature Surface Engineering Centre.

From the Energy Technology Centre, my thanks are due to Adriana Encinas-Oropesa, Paul Kilgallon, Nigel Legrave and Peter West, and to Andrew Dyer, Matthew Kershaw and Christine Kimpson from the Metallography and Sample Preparation, and Materials Characterisation Laboratories.

My thanks also to the ever pleasant and helpful staff in the Cranfield University Library and the Information Technology Centre.

Contents

List of Figures

List of Tables

Page

1. Introduction

The objective of this project is to develop coatings for gas turbine hot components, to retard oxidation and hot corrosion originated by trace metal species, in gases produced by gasification of biomass and waste fuels.

Today gas turbines are in widespread industrial use, particularly as components in highly efficient integrated combined cycle (ICC) power generating cycles. In such cycles the gas turbine(s) drive their own electricity generator(s) and, by exhausting their gases into steam generators, produce steam to drive steam turbine-generators. The ICC is used in straight power production and in combined heat and power (CHP) or co-generation plants. CHP cycles operate at higher thermal efficiencies than cycles which use only boiler/steam turbine units for power generation. In co-generation, part of the converted thermal energy supplies process steam for industrial processes and/or heat for district heating. The ICC is the basis of the integrated gasification combined cycle (IGCC), which incorporates a gasifier, to gasify solid fuels for supplying fuel gases to the gas turbine(s).

There is an increasing application of biomass and waste fuels in power generation, in both developed and developing countries. This can be a consequence of lower fuel costs from biomass fuels produced in countries having an advantageous climate or to consume waste-fuel, such as sewage sludge or municipal waste. Overall economic drivers for burning biomass and waste fuels also reflect the drive for sustainable energy sources and replacement of fossil-fuels, to reduce the emission of greenhouse gases (GHG) as a consequence of national commitments to the United Nations Framework Convention on Climate Change (UNFCCC) and the Kyoto Protocol. Biomass is also of increasing interest as a fuel, in the face of decreasing reserves of fossil fuel, or where the cost and security of energy supplies are high. International and national global climate change policies increasingly focus on the use of sustainable energy, including biomass and waste fuels. The term “biomass” refers to any plant derived organic matter available on a renewable basis, including dedicated energy crops and trees, agricultural food and feed crops, agricultural crop wastes and residues, wood wastes and residues, aquatic plants, animal wastes, parts of municipal wastes, and other waste materials. Fuels derived from waste are in widespread use, examples include municipal waste, tyres, sewage effluent and animal waste. These fuels can form the feedstock for gasification or for combustion in boilers or for conversion into liquid fuels; ethanol, methanol, biodiesel and gaseous fuels, such as hydrogen and methane.

Gas turbines are commonly fired by fossil-fuels (ie. natural gas, diesel oil and gasified coal) and there is a growing potential for using biomass and waste fuels for use in them. However, it is suspected that the trace elements to be found in biomass- and waste-fuels could have significant, adverse effects on hot corrosion in gas turbines, which is already a major factor in gas turbines burning fossil-fuels. For these fuels, effective coatings which provide hot corrosion protection for gas turbines are available commercially.

The objective of this project is to develop novel coatings which provide hot corrosion protection for gas turbines fuelled by biomass and waste fuels.

The first action was to identify trace elements in gases from the gasification of biomass and waste fuels, which could remain in the gases after hot gas cleaning, and following combustion in the gas turbine, condense in the gas path to initiate hot corrosion on the hot components of the gas turbine(s). For this action, the identification of species of trace elements, that may be present in these fuels and could initiate hot corrosion in the gas turbine(s), was carried out in two stages. In the first stage, thermodynamic assessments were made, using the MULTIPHASE Module of MTDATA, to identify trace species which would remain in gaseous form in the gasifier gases produced from a range of biomass and waste-fuels. The type of gasifier selected for these assessments was of the air-blown circulating fluidised bed design, operating at atmospheric pressure through a temperature range of 300^{o}C to 1200^{o}C. Of the fifteen elements selected, vapour phase species of eight elements remained in the gasifier gases.

Following this activity, two components were involved, the first took into account the hot cleaning and filtration of the gasifier gases that would occur in an IGCC plant cycle. These could remove some or all of the condensed species contained in the gasifier gases, before they passed forward for combustion in the GT. Five of the eight trace elements were eliminated after this component, some because species would have been removed by gas cleaning, others if not removed would remain in the gaseous phase through to the gas turbine exhaust, and could not initiate hot corrosion. Species of three elements remained for further investigation; cadmium, lead and antimony.

The second stage consisted of thermodynamic assessments, again using the MTDATA MULTIPHASE Module, of the three elements contained in the gasifier gases, but using the relevant fuel:air ratio and operating pressure required for combustion in the gas turbine. Three condensed species, with their dew-points, were identified at this stage; cadmium sulphate (700^{o}C), lead sulphate (800^{o}C) and antimony oxide (800^{o}C). As these dew-points occured within the typical gas path temperature range of 1200^{o}C to 540^{o}C at the turbine exhaust, they could form molten deposits on component surfaces and thereby initiate hot corrosion. A series of assessments was also carried out for each of these three species, under the same combustion conditions, but in the presence of low, medium and high contents of chlorine, fluorine and sulphur, found in biomass and waste fuels, to assess the effect of these elements on dew points of these species. In all tests the dew points were within the typical gas turbine gas path temperature range.

Two series of corrosion tests, each of 500 hours duration at 700°C, then confirmed that the hot corrosion predicted by the assessments occurred in typical substrates and commercial coatings. The results of these tests later provided comparisons, of hot corrosion protection provided by novel coatings developed in this project, with the protection provided by commercial coatings.

Development of novel coatings, to provide protection against hot corrosion initiated by gases produced from biomass and waste fuels, had the main objective of forming oxide scale which would grow to maintain the initiation stage for a viable service period. It was also important that inward diffusion of coating elements would not degrade the substrate microstructure sufficiently to impair its mechanical integrity.

The philosophy adopted in coating development, was to optimise material costs, process durations and temperatures, to produce novel coatings providing superior or comparative hot corrosion protection to that provided by proven commercial coatings. The need to coat internal cooling passages of turbine blades and vanes led to chemical deposition being the starting point of novel coating development. Literature reviews and results of previous coating research at Cranfield, led to the selection of single step silicon aluminising CVD, using low activity powder packs, as the basis for the novel coatings. A series of aluminising CVD operations, at a soak temperature of 1050°C, for soak periods of one, two, four and eight hours, were used to calibrate aluminide coating depths against time. Silicon-aluminising trials were carried out to investigate the effects of varying CVD soak periods and soak temperatures on coating depth and phase stability. The first series consisted of one hour CVD soak periods, at 800°C, 850°C and 1050°C, which showed the highest soak temperature produced the most satisfactory coating. The next silicon-aluminising CVD runs, carried out at 1050°C, with CVD soak periods of 15 minutes, 30 minutes and 60 minutes, produced stable silicon aluminide coatings, of varying depths. Two series of cyclic oxidation tests, on IN738LC and CMSX-4 substrates, at 950°C and 1050°C, proved that only the silicon modified aluminised coatings produced by 60 minutes CVD at 1050°C, provided viable oxidation resistance.

The hot corrosion protection provided by these coatings was tested by two series of corrosion tests on the same substrates, both of 500 hours duration, one series at 700°C, the second series at 900°C. The lower temperature (Type II) corrosion tests, with comparable conditions to those carried out on commercial coatings, showed that the novel coatings provided superior or comparable hot corrosion protection to that of the commercial coatings. Results of the high temperature corrosion tests (Type I) on novel coatings were also encouraging. Finally, the ability of the novel coating to directly bond an EB-PVD deposited thermal barrier coating (TBC) to a turbine blade of IN738LC, was investigated. Results showed the thermally grown oxide bonding of the TBC to the silicon-aluminide hot corrosion protective coating to be effective, and provided similar depths and microstructures of both coatings on the blade.

The content of this thesis includes the relevant literature reviews and, describes the equipment and methods used in the five areas of original research required to meet the objective of the project. Also included, are explanations of the steps taken to develop novel coatings, the analyses of oxidation and corrosion test results undertaken to evaluate and compare hot corrosion protection provided by coatings. Finally, results are provided of the trial to assess TBC bonding performance of the single step silicon-aluminide coating.

2. Literature review

2.1. Biomass and waste fuels

There is an increasing application of biomass and waste fuels in gas turbines, particularly for power generation, in both developed and developing countries. This can be a consequence of lower fuel costs from biomass fuels produced in countries having an advantageous climate or to consume waste-fuel, such as sewage sludge or municipal waste, or regulations/subsidiaries encouraging use of biomass. The overall economic drivers for burning biomass and waste fuels also reflect the drive for sustainable energy sources and replacement of fossil-fuels, to reduce the emission of greenhouse gases (GHG) as a consequence of national commitments to the Kyoto Protocol to the United Nations Framework Convention on Climate Change (UNFCCC) [1]. The Kyoto Protocol, which entered into force in 1997, defines GHG as; carbon dioxide (CO_2), methane (CH_4), nitrous oxide (N_2O), hydrofluorocarbons (HFCs), perfluorocarbons (PFCs) and sulphur hexafluoride (SF_6). At that time, carbon dioxide was responsible for over 60% of the "enhanced" greenhouse effect, the annual emissions amounting to over 23 billion tonnes, or almost 1% of the total mass of carbon dioxide in the atmosphere. The Kyoto Protocol explained that, of the many billions of tonnes of carbon exchanged naturally each year, between the almosphere, the oceans and land vegetation, carbon dioxide levels appear to have varied by less than 10% during the 10,000 years before industrialisation. In the 200 years since 1800, however, carbon dioxide levels have risen by over 30%.

Biomass is a major energy provider throughout the world, particularly in the developing countries of Africa, South America and India. With a total population of nearly four billion, the developing countries are estimated to consume rather more than 3Gt of biomass per year. In the industrialised nations the consumption of biomass fuels only represents some 3% of primary energy consumption [2]. Biomass is also of increasing interest as a fuel, in the face of decreasing reserves of fossil fuel, or where the cost and security of energy supplies are high. International and national global climate change policies increasingly focus on the use of sustainable energy, including biomass and waste-fuels [3].

The term "biomass" applies to any plant derived organic matter available on a renewable basis, including dedicated energy crops and trees, agricultural food and feed crops, agricultural crop wastes and residues, wood wastes and residues, aquatic plants, animal wastes, municipal wastes, and other waste materials [4]. Fuels derived from waste are in widespread use, examples include municipal waste, tyres, sewage effluent and animal waste. The motivation for waste conversion to fuel results from the increasing production of waste and increasingly high costs of waste disposal and these combine to increase the economic viability of waste fuel production. These fuels can form the feedstock for gasification, or for combustion in boilers, or for conversion into liquid fuels; ethanol, methanol, biodiesel and gaseous fuels such as hydrogen and methane.

Gas turbines are commonly fired by fossil-fuels; natural gas, diesel oil and more rarely gasified coal. However, with the increasing use of gas turbines for electricity generation, there is a growing potential for using biomass and waste fuels for use in them.

2.1.1 Biomass and waste-fuel energy conversion

2.1.1.1 Biomass

Biomass is defined as any store of energy which is being replenished continually by the sun. The energy stored in plants is recycled naturally through a series of conversions involving chemical and physical processes in the plant, the soil, the atmosphere and other living matter. From this cyclic process, it is possible to capture some of the stored chemical energy in the biomass [4]. Most of the biofuels, derived from living or recently dead biomass contain oxygen and, although their molecules are much larger and more complex than methane (from fossil-fuels) their combustion can be represented by considering their carbohydrates in an example quoted by Boyle [5]. In this case the ratio of constituents is approximately one oxygen and two hydrogens to each carbon, so that one typical carbohydrate sub-unit can be written as CH_2O. Hence the burning process can be written as:

$$(CH_2O) + O_2 \longrightarrow CO_2 + H_2O + \text{energy}$$

The details will be specific to each type of biomass, but the example provides the principle. Boyle also identified the average energy content of biomass-fuels and fossil-fuels, and for comparison purposes, these are shown in Table 2.1.

Fuel	**Energy content** (GJt^{-1})	**Energy content** (GJm^{-3})
Wood (air-dried, 20% moisture)	15.0	10.0
Paper (stacked newspapers)	17.0	9.0
Dung (dried)	16.0	4.0
Straw (baled)	14.0	1.4
Sugar cane (air-dried stalks)	14.0	10.0
Domestic refuse (as collected)	9.0	1.5
Commercial wastes (UK average)	16.0	*
Grass (fresh cut)	4.0	3.0
Oil (petroleum)	42.0	34.0
Coal (UK average)	28.0	50.0
Natural gas (supply pressure)	55.0	0.04
*Note: * wide variation depending on type of material*		

Table 2.1: Average energy content of some biomass and waste-fuels [5]

There are many sources of biomass in countries worldwide, depending on latitude, region and state of national development. In this project, the biomass and waste-fuels considered are those for use in power generation or power/energy cogeneration. Such plants are installed in many regions and countries. It is in this context that the worldwide potential for biomass energy supplies in the year 2050, predicted by Johansson et al [6], is shown in Table 2.2.

Biomass resource	**Pot'l ann'l supply** (*EJ*)
Energy crops	128
Dung	25
Forestry residues	14
Cereal residues	13
Sugar cane residues	12
Existing forests	10
Urban refuse	3
TOTAL	205

Table 2.2: Potential for biomass energy supplies in the year 2050[6]

Methods of extracting energy from biomass, ranging from the very basic to complex processes, include [7,8]:

- Direct combustion of the raw biomass;
- Combustion after simple physical processing, such as sorting, chipping, air-drying and compression;
- Thermochemical processing to upgrade the biofuel, such as pyrolysis, gasification and liquefaction;
- Biological processing by natural means such as anaerobic digestion and fermentation.

2.1.1.2. Waste-Fuels

Waste-fuels range from municipal refuse waste and sewage sludge, to animal wastes such as chicken manure and animal carcases. In Britain much of the municipal waste, deposited in landfill sites, generates methane gas, some of which is used for power generation. With over 25Mt of household waste a year, 90% of which is presently deposited in landfill sites, it is estimated that 5TWh electricity are produced annually [7] from landfill. Abroad, municipal waste is commonly incinerated and used for power generation, despite increasing adverse public opinion, attributed to loss of amenity and fear of pathogens emitted in incinerator flue gases. Sewage sludges are increasingly being considered for producing energy. Where animal wastes are at an economically viable level, they are being used for electricity generation, examples being chicken manure and animal carcasses, the energy being extracted by anaerobic digestion.

Municipal refuse waste consists of many different materials and, prior to processing it requires sorting to remove non combustible matter and then treatment to assist in handling and feed control.

Energy conversion technologies of waste include [7,8]:

- biological processes; landfill gas recovery, in-plant anaerobic digestion and hydrolysis/fermentation;
- refuse-derived fuel (RDF) manufacture and combustion, including the use of fluidised bed systems;
- pyrolysis/gasification

2.2. Gasification and combined cycle electricity generation

The objective of this project is to develop coatings for gas turbines burning biomass and waste-fuels in integrated gasification combined cycles (IGCC). These cycles, when used in power generation, provide high thermal efficiency and flexibility. They are versatile cycles when used in co-generation, where they can produce electricity, heat and/or steam, at various pressures, for example, for industrial estates. The schematic diagram of an IGCC is shown in Figure 2.1.

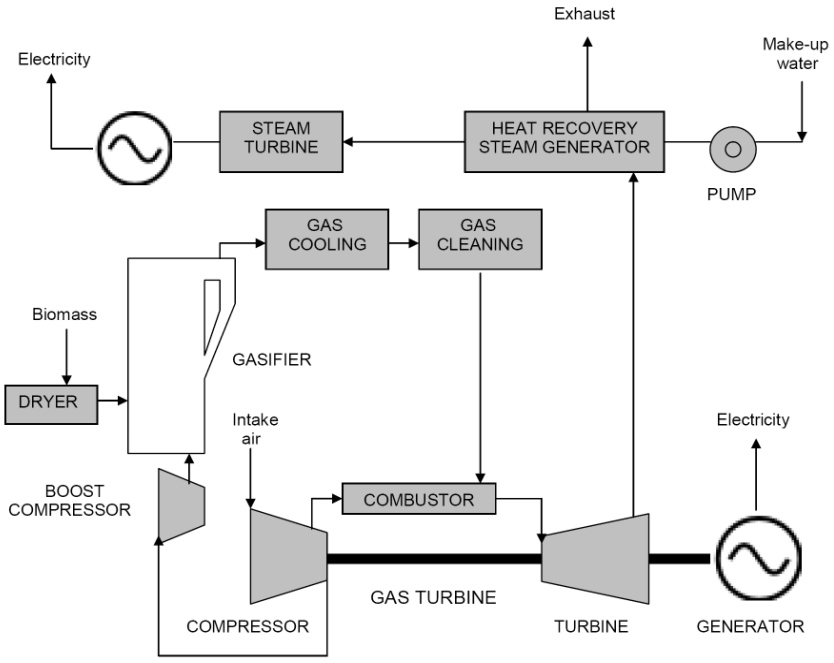

Figure 2.1: Schematic diagram of a biomass-gasifier/gas turbine combined cycle [9]

Gasification is an effective energy conversion technology for both biomass and wasteis appropriate for this project as integrating gasifiers with gas turbines can lead to high efficiencies and low unit capital costs in modest-scale biomass electricity generating plant.

Electricity generated using biomass-integrated gasifier/gas turbine electricity systems can be competitive with electricity produced from coal and nuclear energy under a wide range of circumstances. If future coal fired electricity generating units, using the Rankine cycle (boiler/steam turbine) with supercritical steam conditions and double reheat, are also required to adopt carbon capture facilities, to meet national and international carbon emission limits, the advantages of biomass and waste-fuel may be more clear-cut. However, these cost advantages may be reduced if large capacity fossil fuel fired plants are built, benefiting from the economies of scale, because biomass plants are usually of lesser generating capacity. This often results from the dispersed nature of biomass supplies and their lower heat content/mass ratio [10].

The IGCC combines the advanced Brayton cycle (gas turbine) electricity generation or cogeneration cycles, widely used internationally when fired by natural gas and clean liquid fuels, with a closely coupled biomass and waste-fuel gasifier. The designs of the latter are also based to a great extent on gasifiers already developed in coal fired gas-turbine electricity generating cycles. The disadvantage of biomass electricity generating units using the Rankine cycle is their low operating pressures and temperatures, typically of about 60bar and 480^{o}C, compared with the typical steam pressures of 100bar-300bar and temperatures of 510^{o}C-620^{o}C, in modern large capacity coal fired units. In contrast, the peak cycle temperature for long-life industrial gas turbines is typically 1200^{o}C, providing an inherent thermodynamic advantage [10].

2.2.1 Gasification

Demirbas [11] explains that gasification for power production involves devolatilising and converting biomass in an atmosphere of steam and/or air, to produce a medium or low calorific gas. The gasification medium is an important variable and the air blown gasifiers use an exothermic reaction between oxygen and the organics to provide the heat necessary to devolatilise biomass and to convert residual carbon-rich chars.

A number of gasification systems are available, based on different types of gasification processes, e,g, entrained flow, fixed bed, fluidised bed, originally developed for coal-firing. Of the different gasifier options available, circulating fluidised bed (CFB) gasifiers have been developed more, due to their flexibility and suitability for the scale of available biomass feedstocks [10].

The simplicity of a basic circulating fluidised bed gasifier is shown in Figure 2.2. Biomass is fed into the combustion chamber and mixed with a bed material, such as sand or limestone, where the reduction of sulphurous compounds in the combustion gases is required. Alternatively, limestone may be admitted into the chamber separately. The air input from below the bed fluidises the fuel, ash and bed material, causing them to circulate and rise through the combustion chamber, to enter a separator.

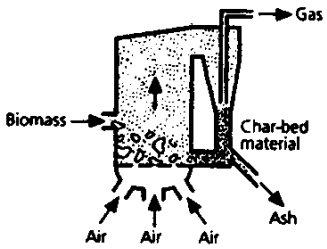

This captures most of the circulating solids, including unburned fuel and returns this material to the combustion chamber through a non mechanical device. Continuous circulation of solids increases fuel residence time to provide efficient fuel combustion. The turbulent environment mixes fuel and limestone to capture >90% of sulphur, as a dry solid, calcium sulphide in the gasifier.

Figure 2.2: CFB gasifier [10]

Gasifiers may be designed to use either oxygen or air as the oxidant in the chamber and conversion of the solid fuel to fuel gas can be controlled, from complete (>99%) to partial (e.g. 75% conversion). Circulating fluidised bed gasifiers may be designed to operate under pressure or at atmospheric pressure. In this project, it is assumed that an air blown gasifier, operating at atmospheric pressure, will be used when carrying out thermodynamic assessments of contaminants.

2.2.2 Gasifier gas cleaning

Of particular importance in relation to a closely coupled gasifier/gas turbine cycle is the cleanliness of gasifier gases. These have to be cooled and cleaned before going forward for combustion in the gas turbine; Figure 2.3 shows a schematic diagram of a gasifier with hot gas cleaning, in an IGCC.

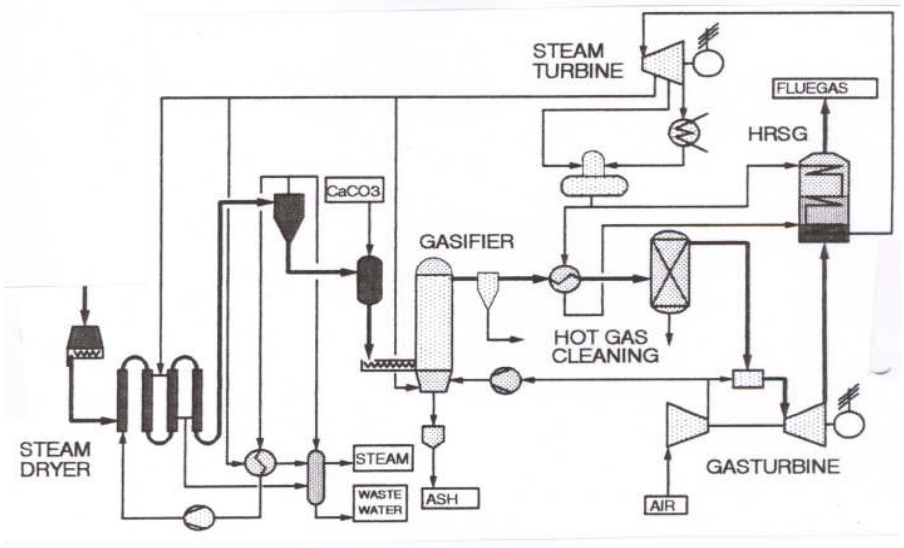

Figure 2.3: Schematic diagram of pressurised gasifier with hot gas cleaning, in an IGCC [12]

The purpose of each gasifier application has a heavy bearing on the degree of cooling and cleaning to be adopted because each has efficiency and plant cost penalties. For example gas cleaning by water scrubbing leads to lower cycle efficiencies and needs scrubbing and waste water treatment facilities, and requires the disposal of liquid waste [10]. Gas turbines in an IGCC plant have stringent gas quality requirements and environmental emission limits, requiring their gas fuel to be cleaned.

In the gasifier, the particles may be vapourised, react with other substances or have no response and hence become ash. Along the path of the gases, the gasified particles, depending on their volatility, will separate into different substances, through entrainment, deposition, as vapours or gases, or be removed as particulates. Kilgallon et al [7] show the fate of these particles diagrammatically in Figure 2.4.

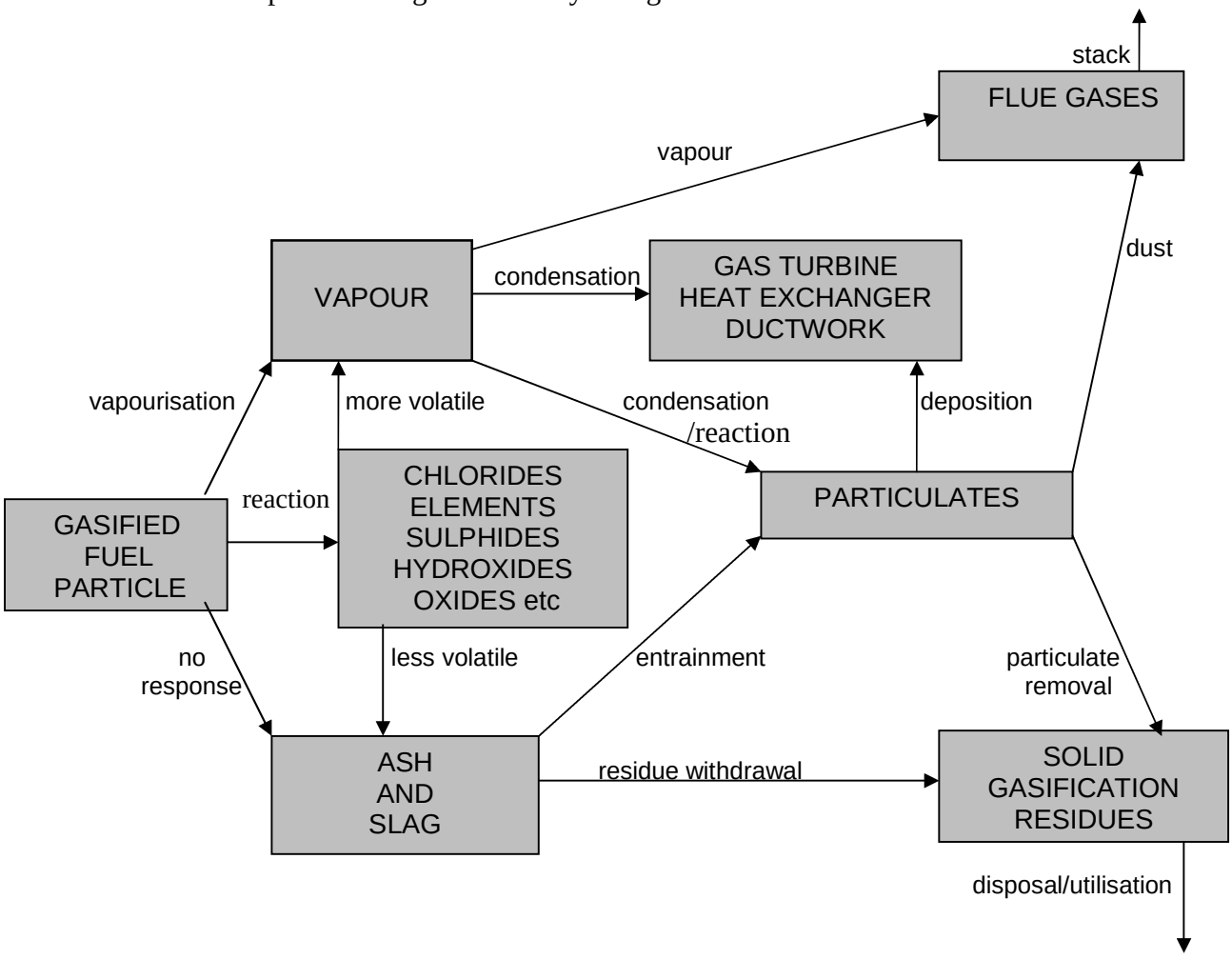

Figure 2.4: Flow diagram of the fates of trace elements of an air blown gasifier showing gas clean-up [7]

Stevens [13] identifies five gas phase contaminants to be taken into account when determining what gas cleaning facilities should be provided for gas turbine fuel gases; particulates, alkali compounds, tars, nitrogen-containing components and sulphur.

2.2.2.1 Particulates

Particulates are defined as solid-phase materials entrained in the raw product gas stream exiting the gasifier and typically include inorganic ash formed from mineral matter in the biomass feedstock, unconverted biomass and material from any gasifier bed.

Bed materials can be entrained as a result of turbulent conditions in a gasifier causing high particulate loadings in the product gas. The initial stage of separation of the bed material is achieved by cyclones included in the fluidized bed gasification system. These remove the bulk of coarse particles, but not the finer fly ash that remains in the gas stream. The mineral matter in the biomass feedstock is a primary source of fly ash particulates and therefore has a major impact on the concentrations of ash in the product gas. Typical mineral concentrations in clean wood are 1%-2%, herbaceous crops contain approximately 10% and crop residues, such as straw or rice husks, typically contain 15%-20% inorganic material. Another source of particulates is char, formed when the biomass feedstock is incompletely gasified, which contains unconverted biomass, contributing to lower conversion efficiencies. The CFB design will also influence to what extent the inorganic matter from the feedstock may be entrained in the gasifier bed or be swept from the reactor.

For gas turbines the particulate level must be reduced to 15 mg/Nm^3 [13]. Various technologies are commonly used including; cyclonic filters, barrier filters, electrostatic precipitators and wet scrubbers. In circulating fluidized bed gasifiers, cyclone filters, often designed as multiple units in series, can remove >90% of particulates above 5 micron at minimum pressure drops of 0.01atm and partial removal of material in the 1-5 micron range is possible. However, cyclone filters become ineffective with sub-micron particles.

Barrier filters contain porous materials that allow gases to pass through but prevent particles passing through. These filters remove particulates from gas streams in the 0.5 µm to 100 µm diameter range and particles in the sub-micron range, but at the expense of high pressure drop across the filter. To reduce particle size, barrier filters are usually placed downstream of cyclones but are only suitable for removing dry particles. Tars cause fouling of the filter surface. Barrier filters suitable for use with biomass systems include; rigid, porous filters or cross-flow filters, constructed of metal or ceramic materials, or bag filters constructed of woven material or packed bed filters. Ceramic and metal candle-filters have been tested in an air-blown pressurized circulating fluidized bed gasifier associated with a 6MW IGCC in Sweden, when the gas had first been cooled to 350^{o}C. Demonstration facilities have proved ceramic filters to be successful, when gas, produced at 980^{o}C, was cooled to about 700^{o}C by water injection and then passed through metal candle-type filters.

As optimum thermal efficiency will be better met by filtering particulates at higher temperatures, for this project it is assumed that ceramic filters could be used for hot-gas cleaning, to avoid cooling the gases to 350^{o}C or even lower, to enable bag-filters to be used.

Electrostatic precipitators have been extensively used for particulate removal over the last sixty years. These work on the principle of passing the product gas past high voltage electrodes that charge the particles which then migrate to collector plates of the opposite polarity, where they deposit on the surface. Both wet and dry methods of removing particulates from the collector plates are effective.

Dry scrubbers, using mechanical periodic mechanical action, for example by rapping or by vibration can operate at 500^{o}C or higher, whereas wet scrubbers, using a thin film of water to remove particulates, are limited to temperatures of about 35^{o}C. Despite electrostatic precipitators being best suited to large scale applications, due to their high cost, systems with generating capacities of 3.5MW and 1.0MW, have been used in Denmark [9]. Wet scrubbers, usually using liquid water sprays, collect particles by collision with water droplets which are then de-trained from the gas stream by a demister. Particulate removal efficiency is proportional to the pressure drop across the venturi, but with a pressure drop of between 2.5-25KPa, the scrubbers can remove 99.9% of the particles.

2.2.2.2 Alkali compounds

Biomass feedstocks may contain significant amounts of alkali salts, which can affect the physical properties of ash, such as the softening-, melting- or vaporisation-points. The problem of alkali vapour formation and deposition is critical for gas turbine systems where the product gas is used at high temperature to maintain the cycle efficiency. Gas turbines require clean fuel gases to reduce the probability of salt deposition causing imbalance at their high rotational speeds, possibly leading to catastrophic failure. Alkali salts can also be corrosive to metal surfaces and also de-activate catalysts in tar cracking and synthesis gas applications. Removal of alkali salts has therefore a high priority.

High alkali content can create gas cleanup challenges, as sodium and potassium salts in ash, for example, vaporize at moderate temperatures, and remain in the product gas at high temperatures. Alkali vapours cannot readily be removed from the hot gas stream by simple filtration [13]. As condensation of particles in the gas stream starts at around 650^{o}C, deposition can occur on cooler surfaces in the system, including heat exchangers and in the gas turbine. Problems arise where alkali vapours pass through gas cleanup systems and deposit at turbine temperatures above 785^{o}C, as a glassy ash material. Despite most biomass feedstocks having low levels of sulphur, naturally occurring concentrations can lead to vapour formation and the resulting eutectic salt can vapourise at modest temperatures of 700^{o}C or above. Although biomass gasification in typically used turbulent flow gasifiers occurs at 900^{o}C, higher than the temperature at which alkali salts vaporize, the vaporized alkali salts may be present in the product gas at the gasifier outlet. Cooling the gas leads to condensation of the vapours into fine solids.

Unless these are removed from the gas stream they may re-volatilise in hot regions, such as gas turbine combustors, downstream of the gasifier. Current gasification systems remove the alkali vapours by cooling the product gas below about 600^{o}C, for the material to condense into solid particles. These are then removed by the particulate filters described in the previous section. For gas turbine fuel gases, the filtration system must account for the small particle size and chemical behaviour of the condensed material. Cyclones will not remove solids of <5μm and a particular alkali may corrode ceramic or metallic barrier filters.

Stevens [13] has identified research into a two stage filter system which removes alkali effectively and, at the same time maintains high gas temperatures. In this system, hot gases at about 825^{o}C from a bench-scale gasifier, were passed through a ceramic filter and then into a packed-bed filter charged with activated bauxite operating at 650-725^{o}C. Comparisons of the measured gas phase concentration of sodium, potassium and chlorine are shown in Table 2.3. Although this system has not been proved in a large-scale plant, the results are encouraging, suggesting that alkali collection by this means is effective and at the same time preserves the heat content of the product.

Alkali	**Measured concentration without Bauxite Filter ppmw**	**Measured concentration with Bauxite Filter ppmw**
Sodium	28	0.07
Potassium	11	0.58

Table 2.3: Alkali filtration results [13]

As alkali salts and other contaminants in gasifier gases have particular relevance in relation to hot corrosion in gas turbines, a critical component of this thesis, they are discussed further in Chapter 5.

2.2.2.3 Tar removal technologies

As described previously, removal of tars from the gas stream is vital to prevent vapourised tars from condensing and clogging up filters and system components. The choice of optimized gasifier design can minimize tar production and matching gasifier performance with end-use application is a first step to preventing problems from tar accumulation.

Raw product gas from a gasifier contains vapourised tars and aerosols of condensed tars, or a combination of the two. The two approaches to tar removal from the product gas stream are:

- Condensed tar droplets are physically removed using technologies applicable for particulate removal such as wet scrubbers or electrostatic precipitators;
- Catalytic and thermal tar reduction methods to convert the tars to permanent gases.

At present tars are commonly removed from the gas stream by cooling the product gas to condense the tars and to form aerosol droplets, which are removed by particulate removal technologies.

However, condensed tars are 'sticky' and can foul or plug gas conditioning equipment. Hence, tars are removed separately from particulates. Wet scrubbers work by impinging tars on water droplets and then separating the bulk tars from the aqueous phase. The disadvantage of water scrubbers when used in the gasification system supplying GTs is that the product gases are generally cooled to around 35-60^{o}C.

However, research projects aimed at large scale biomass gasification have shown that wet scrubber systems, in which the gas is cooled to about 240^{o}C or below and where the particulates are removed prior to tar removal, have the potential to remove tars. Stevens [13] quotes as examples, the Amergas facility in The Netherlands which is in early stages of operation and the ARBRE facility in Britain that has yet to be commissioned. In addition to the provision of wet-scrubbers, this solution for tar removal has to carry the additional cost of the tar and waste treatment/removal/disposal. This solution is not considered further in this project.

Wet electrostatic precipitators, used for tar removal operate on the same principles as those for particulate removal, but for the former, wire and tube designs are preferred to the collector plates used for the latter. The collector surfaces are washed continuously to remove the tar material. This method is efficient for removing tars and can remove 99% of materials under 0.1µm in diameter but their high capital costs are the main barriers to their use for large scale biomass applications.

Various types of barrier filters have been used for tar removal in biomass gasification systems [13]. Tar capture is by impingement of condensed aerosols on the filter surface and tar removal from the surface remains a problem when particulates are present, because the filter cake cannot easily be removed. Fabric filters and rigid hot gas ceramic and metal filters are generally inappropriate for tar removal from biomass gasification systems. Packed bed filters have been used on biomass gasification facilities, using materials such as sawdust, wood chips, cork and sand. However, although these materials remove tars, filter cleaning causes operational difficulties and cost penalties, that are uneconomic for biomass gasification applications.

Cyclone filters, using centrifugal force to separate solids and aerosols, are suitable for removing tars with aerosol diameters larger than 5µm. However, the combination of sticky tars and particulates that form deposits of the material on the cyclone surfaces are difficult to remove.

2.2.2.4. Nitrogen containing contaminants

The primary nitrogen-containing contaminant in raw gas from biomass gasifiers is ammonia (NH_3), formed from the protein and other components. When the gas is burned, ammonia in the gas leads to the formation of NO_x by the reaction of of nitrogen or nitrogen-containing molecules with oxygen, at high temperatures.

When the clean biomass fuel gas is burned in the gas turbine, NO_x will be produced. The use of fuel gases rather than solid biomass provides the opportunity to reduce or control NO_x emissions through modifying burner design or alteration of air distribution to cool the flame.

The reduction of NO_x emissions from gas turbines by improving burner design or by back-end catalytic reactors is common practice and will not have any impact on this project.

2.2.2.5. Sulphur

Biomass has relatively low sulphur compared to coal [14], wood for example typically contains <0.1% of sulphur by weight, whereas refuse-derived fuel (RDF) may contain 1% or more, similar to bituminous coal. Sulphur in biomass feedstock can be converted to hydrogen sulphide in gasification, or SO_2/SO_3 in combustion.

In most applications where biomass feedstocks are used, the removal of sulphur will not be necessary. In this project, to identify potentially damaging contaminants in gasifier gases, low, medium and high levels of sulphur were used in both the thermodynamic assessments of trace elements in fuel gases and to determine dew-points of those condensed species which will remain in the gas turbine combustion gases.

2.2.3 Biomass and waste-fuel gasification – effects on gas turbine components

In all biomass and waste fuel IGCCs, gas turbine performance is vital to their overall efficiency and economic viability. Within the gas turbine, hot corrosion and/or erosion, due to contaminants in the fuel gas, are more life limiting for turbine blades and vanes, than creep and fatigue in the longer term. The hot gas path environment depends on the contaminants in the fuel and air entering the turbine and the operating conditions of temperature, pressure and flow. The effects of contaminants in industrial gas turbines burning fossil fuels, such as natural gas and heavy fuel oils, are well known and solutions have been developed to overcome the associated problems.

Fuel gases derived from biomass and waste-fuels can cause both erosion, depending on particle size and composition, and corrosion damage, from gaseous species that condense on component surfaces. Vapour species well known for their propensity for initiating hot corrosion, in gas turbines burning clean fuels, are the alkalis, predominantly sodium, and sulphur. Vanadium has the same propensity in gas turbines fuelled from heavy fuel oils. Biomass and waste-fuels can contain significant levels of alkali metals, particularly potassium and heavy metals such as lead and zinc [7].

2.2.3.1 Elements in biomass and waste-fuel feedstocks

The identification of trace species contained in gasifier gases, which may be carried through for combustion in the gas turbine, subsequently to initiate hot corrosion, is a key component of this project.

It is opportune here to identify the route by which trace elements become present in biomass derived fuels and to provide examples that cite the content of elements contained in vegetation. The starting point is to identify the origins of elements which are needed to sustain growth of vegetation and a comprehensive list of elements in the Earth's crust, soils and plant tissues is shown in Table 2.4.

Element	Crust (median)	Soil (median)	Plant (range)
Oxygen	474 000	490 000	397 000–440 000
Silicon	227 000	330 000	200–62 000
Aluminium	82 000	71 000	38–530
Calcium	41 000	15 000	400–13 000
Iron	41 000	40 000	2–700
Sodium	23 000	5 000	2–1 500
Magnesium	23 000	5 000	700–9 000
Potassium	21 000	14 000	1 000–68 000
Titanium	5 600	5 000	<0.02–56
Phosphorus	1 000	800	120–10 000
Fluorine	950	200	0.02–24
Manganese	950	1 000	0.3–1 000
Barium	500	500	4.5–150
Carbon	480 (inorganic)	20 000 (organic)	450 000
Strontium	370	250	3–400
Sulphur	260	700	600–8 700
Zirconium	190	400	0.48–2.3
Vanadium	160	90	0.001–2
Rubidium	90	150	0.5–52
Nickel	80	50	0.02–5.3
Zinc	75	90	1.4–400
Cerium	68	50	0.01–16
Copper	50	30	4–20
Neodymium	38	35	0.3–7
Lanthanum	32	40	0.003–15
Nitrogen	25	2 000	12 000–75 000
Cobalt	20	8	0.005–4.6
Lead	14	35	0.2–20
Boron	10	20	8–200

Units – mg/kg

Table 2.4: Elemental composition of the Earth's crust, soils and plant tissue [15]

Jeffrey [15] explains that the general route for elements to enter vegetation, is from its supply of water and mineral ions, via the roots, where their metabolic behaviour depends on the ion content of different elements, some of which act as nutrients. To complete this brief outline of the mineral composition of plants, Figure 2.5 presents data on the element content from grassland sites. In the figure, Group A are those in the highest concentration range, Group B are the trace elements considered to be essential to plants and their symbionts, and Group C are elements commonly found in plant tissues but are not known to be essential for plants. The figure shows that there are a range of values for each

element and when their interaction is taken into account, there may be a great number of variations in the content of trace species when gasified. This is compounded for those IGCCs which are fired with a variety of plant feedstocks.

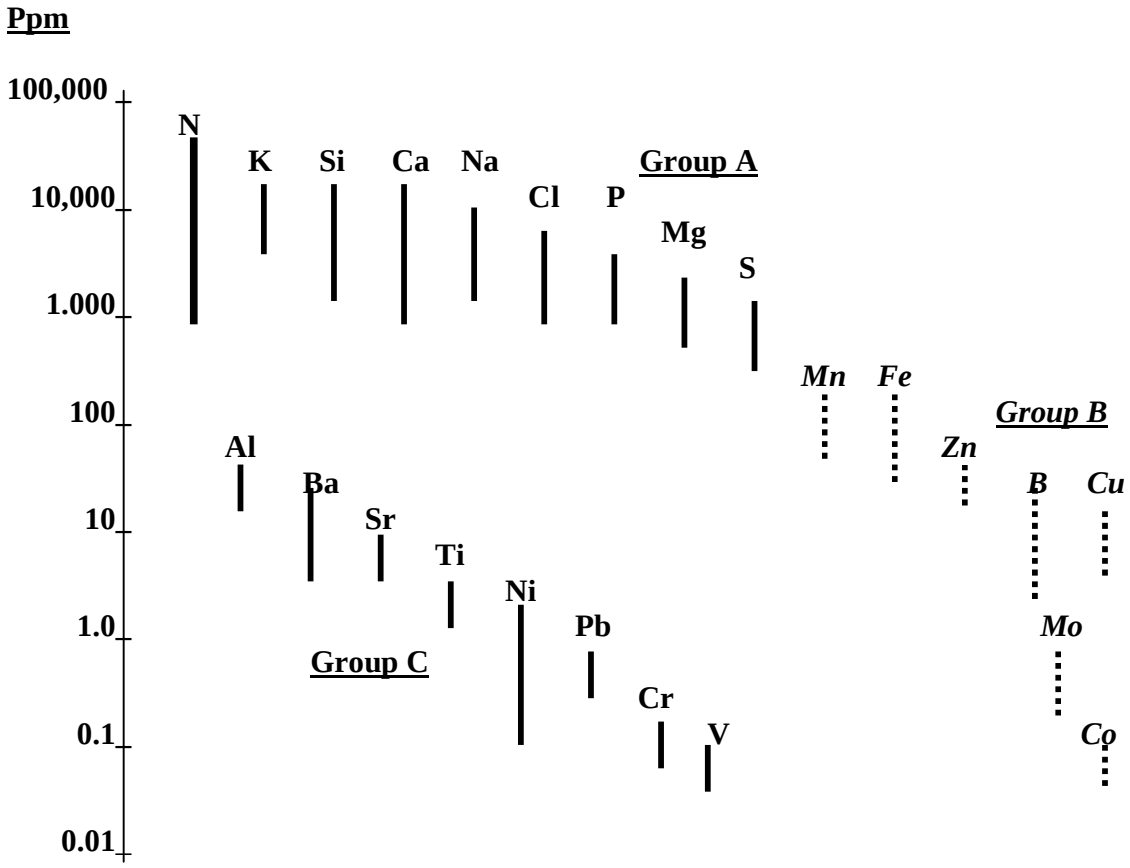

Figure 2.5: Mineral composition of plants from grassland sites[15]

2.2.3.2 Effects of variations of alkali and trace metal species in gasifier gases

Results of thermodynamic studies at Cranfield University [7] to determine which trace elements are more/less likely to enter the hot gas paths of gasification systems showed that some elements can be affected by the inclusion (or omission) of another element. One example quoted was the effect of nickel on the equilibrium diagram for arsenic; as nickel is commonly used in gas turbine gas path components, its influence on other trace elements needs to be considered. Without nickel, arsenic species are gaseous, whereas with nickel present, solid As_2Ni_5 is predicted to be the major species formed up to 1000^oC.

Other significant variables are sulphur and chlorine levels in the fuel gas stream, present mainly as H_2S and HCl. Increased levels of H_2S for example can increase or decrease the dewpoints of zinc, tin or lead.

The main points arising from these studies, which will also be significant in relation to this project are:

- Fuel composition; on a mass basis, contaminant species sulphur, chlorine and alkali and trace metals of many biomasses are similar or lower than coal – exceptions being K and Cl in straw; P, Cd, Pb, Zn, Ba, Cr, Cu, Mn in wood; V, Zn, Cr, Cu Mn, Hg in sewage sludge;
- Fuel gas compositions vary significantly between gasification systems at the trace element level and at the frequently reported bulk gas composition level;
- Most trace and alkali metals are more volatile in gasification systems than in combustion systems
- S and Cl levels, both absolute and relative, as well as operating pressure and gasification process can influence the volatility of trace and alkali metal species;
- Potentially damaging levels of Pb, Zn, Cd and Sn, and V in some systems, can pass through the fuel gas path to the gas turbine, as well as the alkali metals, of which Hg, B, Sb, and Se can also pass through the gas turbine;
- The high levels of trace metals present in gasifier product gases can be reduced by use of low filter operating temperatures, dependent on gasification systems.

Thermodynamic assessments of the element content of gasifier gases, which are applicable to biomass and waste-fuels, to identify potentially damaging species for this project, are dealt with comprehensively in Chapter 5 of this thesis.

2.3 Gas turbines

2.3.1 Introduction

Gas turbines are in widespread use for power generation and for driving compressors and pumps for the oil and gas industry. They provide high efficiency and reliability and can operate on a wide range of gaseous and liquid fuels. Gas turbines for power generation are produced in capacities ranging from 100kW, for small public installations such as hospitals [16], up to around 200MW.

When the exhaust gases are recovered to provide heat, the overall cycle efficiency can rise from the lower end of 36% to in excess of 50% [17]. Earlier industrial gas turbines used for power generation in the UK utilised aero-gas turbines as the gas generator to drive the power turbine, itself coupled via a reduction gearbox to the generator. In some installations where higher power generating capacities were required, two or three aero-gas turbine gas generators would drive the single power turbine to provide generating capacities of 37MWe. Today, with the exceptions of some large capacity gas turbine generators, of around 100MWe, industrial gas turbines are purpose made.

This project concentrates on industrial GTs having capacities in the 5MWe to 15MWe range; comparatively small machines, but considered to be applicable to plants being fuelled by biomass-and waste-fuels. The cross-section of a 5.05MWe GT is shown in Figure 2.6, together with the main operating pressures and temperatures. The most critical components, operating under the most arduous conditions of temperature and stress, with rapid temperature transients at various points during the engine cycle, are the high pressure turbine blades. In addition, the hot gases surrounding the blade are highly oxidising and may contain damaging contaminants and combustion products of solid fuels may cause erosion. However, the onerous conditions under which turbine components operate impose very high mechanical stresses that directly impact on their design and material technology.

2.3.2 Gas turbine hot component materials

Design of a component and the selection of its alloy material must ensure that the component has the required mechanical properties and the capability to retard hot corrosion at the target operating temperature, to meet the specified service life and operating cycles. Bradley [18] lists important mechanical properties that gas turbine substrate materials must have to achieve acceptably long service lives at specific temperatures: tensile strength, yield strength, elongation, creep strength, stress-rupture strength and fatigue strength. For aerofoil applications, the important material properties are creep strength, stress- rupture strength, resistance to thermal fatigue and environmental damage to the rotating blades. Failure by stress-rupture or mechanical fatigue may occur before excessive creep. Hot corrosion, which also may cause aerofoil deterioration, is discussed more fully later in this chapter.

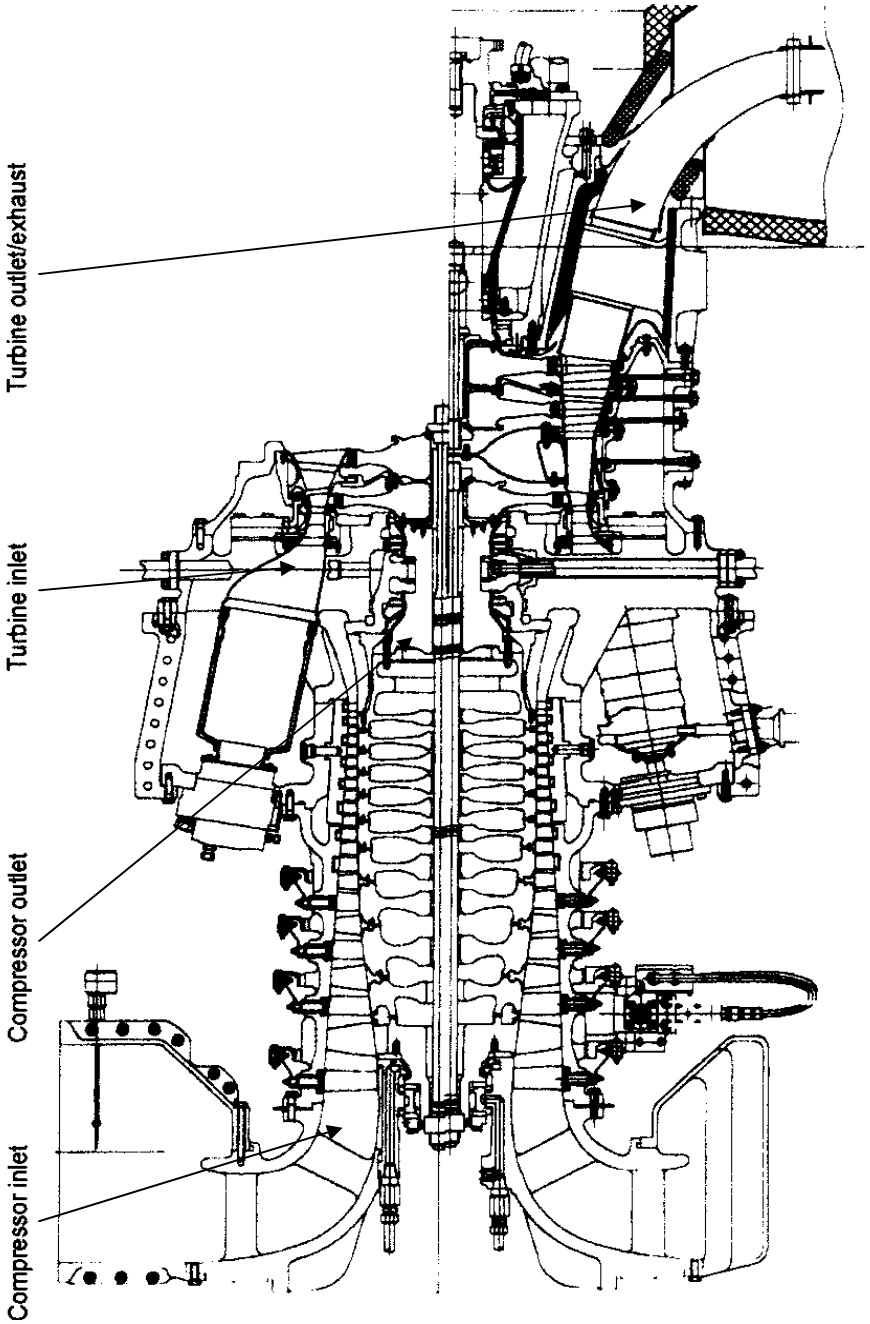

Unit	Compressor inlet (P1)	Compressor outlet (P2)	Turbine inlet	Turbine outlet/ exhaust
Pressure PSIA	14.7	203	195	14.7
Pressure kPa	101.3	1403	1347	101.3
Temp °C	15.0	390	1111	546

Figure 2.6: Cross section through Typhoon 5.05MW industrial gas turbine and operating parameters (*Courtesy of Siemens Power Generation)*

To meet such onerous high temperature and mechanical stressing operating conditions, yet preserving high surface stability, superalloys have been developed. These are generally divided into three classes; nickel-base, cobalt-base and iron-base superalloys. Of these, nickel-base superalloys are used for gas turbine hot components operating in the 650°C-1100°C range. The stress-rupture strengths of selected superalloys, in the range 600°C-1200°C), are shown in Figure 2.7.

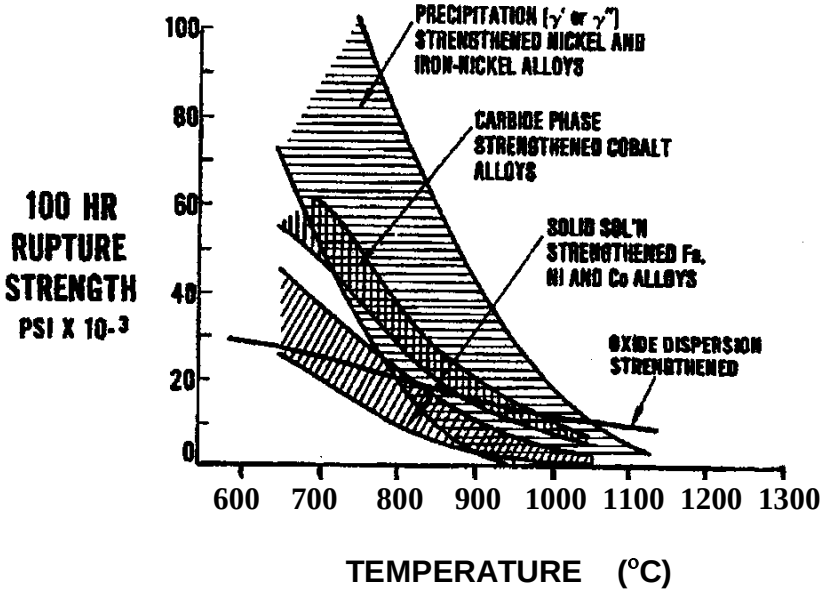

Figure 2.7: Stress-rupture strengths of selected superalloys [18]

2.3.3 Nickel-base superalloys

The properties given the most attention for aircraft engine blades, which are fired by clean fossil fuels and operate in comparatively clean ambient conditions, were high temperature tensile strength, creep rupture strength to 5000h and oxidation resistance, to provide 20,000h-50,000h lives. Industrial gas turbine designers, particularly for IGCC applications, required blade alloys with known longer time, creep rupture properties and good hot corrosion resistance, for lives up to 100,000h [19].

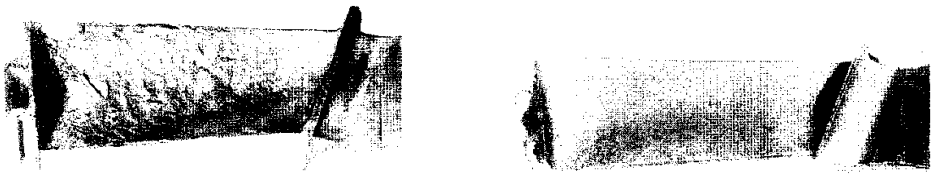

(a) (b)

Figure 2.8: Examples of uncoated (a) and aluminised (b) gas turbine blades after hot corrosion operation *(by courtesy of Rolls-Royce)*

2.3.3.1 Elemental composition of nickel-base superalloys

The composition of nickel-base superalloys includes up to 13 elements, which tend to be grouped with some commonality in the periodic system, as can be seen in Figure 2.9. The first class consists of elements that make up the face-centred cubic (fcc) austenitic (γ) matrix, taken from Groups VIA and VIIIA, and include nickel, cobalt, chromium, molybdenum and tungsten. The second class of elements partition to and make up the γ' precipitate, Ni_3X, and are from groups III, IV and V and include aluminium, titanium, tantalum and hafnium. The third class, are from Groups II, III and IV, are oddly sized in terms of atomic diameter and include boron, carbon and zirconium.

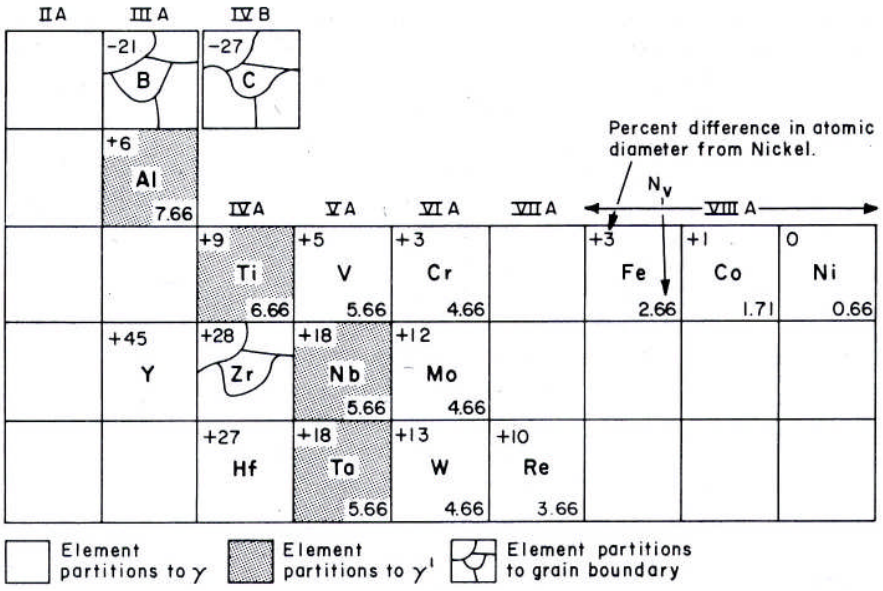

Figure 2.9: Elements important in the constitution of nickel-base superalloys [20]

There are two subclassifications beyond the three mentioned above. The first includes carbide phase formers, which are used in polycrystalline alloys as grain boundary strengtheners along with low levels of zirconium and boron, and include chromium, molybdenum, tungsten, niobium, tantalum and titanium. The second subclassification elements are intended to develop adherent diffusion-resistant oxide scales, to protect the alloys from the environment, and consist of chromium and aluminium oxide formers.

2.3.3.2 Structure and microstructure of nickel-base superalloys

For nickel-base superalloys, Ross & Sims [20] describe the major phases to be:

- Gamma matrix (γ), the continuous matrix is an fcc nickel-base austenitic phase that contains a high percentage of solid-solution elements such as Cr, Mo and W;

- Gamma prime (γ'), where Al and Ti are added in amounts and mutual proportions to precipitate high volume fractions of fcc γ', which precipitate coherently with the austenitic γ matrix;
- Carbide formation, from carbon added at levels of 0.05%-0.2%, combining with reactive and refractory elements, including Ti, Ta and Hf, to form their carbides, tend to populate their grain boundaries;
- Grain boundary γ', to improve rupture properties for the stronger superalloys, by heat treatment and service exposure generating a film of γ' along grain boundaries;
- Borides, occur as infrequent grain boundary particles;
- Topologically close packed type phases, form plate-like phases under certain conditions, such as σ, μ and Laves, form. These may lower rupture strength and ductility [19,20,21,22,23].

The earlier development of nickel superalloys, resulted in increasingly strength over time, but retained usable ductility. This development is shown by the microstructure changes presented in the drafted panoramic sketch (at about 10,000x) shown in Figure 2.10. The upper half of the figure show the improvement, whereas, the lower half shows the phases which were found to cause brittleness, have lower strength or create other problems.

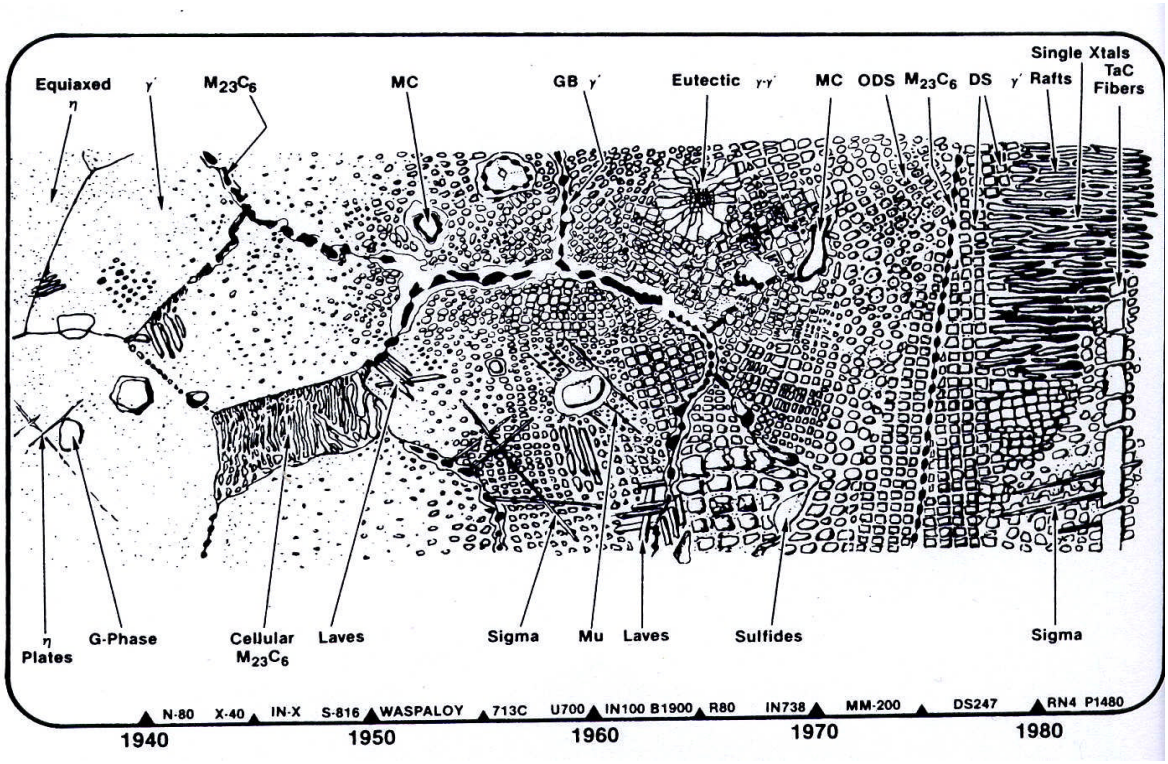

Figure 2.10: Panorama of the development of the nickel superalloy microstructure showing beneficial and deleterious phases [20]

The superalloy microstructures resulting from the major phases, listed above, can be considered in four broad areas; matrix, precipitation strengtheners, secondary phases and carbide formation (described earlier) [19]. The basic fcc γ-phase matrix based on the highly tolerant nickel, with the addition of elements with different atomic sizes, such as Co, Cr, Mo, W, Ta, Re, Al and Ti, create solid solution hardening in the γ-phase. The strain introduced in the γ-lattice by the atomic size differentials inhibits dislocation movement.

Aluminium and titanium also act as precipitate hardeners by forming the γ' precipitation hardening phase. Precipitation hardening strengthens the alloy by forming physical barriers to the glide planes of dislocations, which impede their movement. At the physical barriers, dislocation energy is 'absorbed' as the dislocations are forced to loop, climb or cut through the precipitate. Solid-solution strengthening requires a greater dislocation driving force, compared with precipitate hardening, to overcome the back-pressure created by the strain field induced by the lattice mismatch. The maximum benefit is provided by γ'-precipitates when they are evenly distributed as a fine dispersion with close inter-particle spacing. Similarity of γ and γ' phases provides fine phase separation, attributed to the low mismatch between matrix and precipitate, the degree of mismatch also accounting for the microstructure of the superalloy. The cubic precipitate microstructure seen in modern superalloys, see Figure 2.11, is produced when the mismatch falls between 0.4% to 1%, less than 0.4% mismatch creates a spherical precipitate and a greater than 1% mismatch produces a plate-like microstructure, the latter being considered to be detrimental to the mechanical properties of the superalloy.

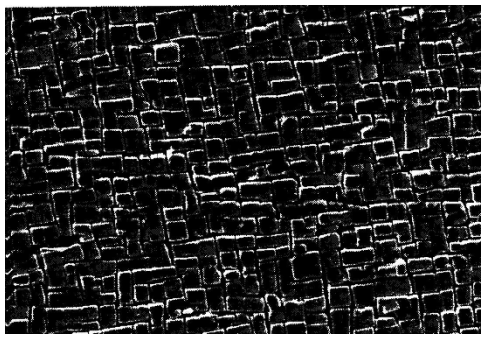

Figure 2.11: Cubic γ/γ' microstructure of a Ni-base superalloy, shown in the etched condition [20]

Secondary phases are generally detrimental to the Superalloy. Development of superalloys with γ contents in excess of 60%, led to alloys with microstructures that changed with time at temperature, which caused the formation of mechanically detrimental phases. Highly alloyed γ' can become metastable and transform to η-Ni_3Ti phase which is hexagonally close packed, the grain boundaries lead to embrittlement [20].
Formation of the η-phase can be reduced by additions of alloying elements such as boron.

Some high-niobium alloys form γ'', a body centred tetragonal phase which is used as a precipitation hardener, although an undesirable form of it may result from the reaction: $\gamma' \longrightarrow \gamma'' \longrightarrow \delta\text{-}Ni_3Nb$(orthorhombic) [20].

The secondary phase having significantly reduced creep-rupture strength and room temperature ductility is sigma phase (σ), see Figure 2.10, in the form $(Cr,Mo)_x(Ni,Co)_y$. The sigma phase, plate-like structure can be generated in a wide variety of superalloys, given the correct conditions of stress and temperature. The likelihood of forming sigma phase or its modification to a less detrimental structure can be achieved by careful control of the heat treatments. R- and μ-phases are also secondary phases and have been identified in platinum aluminide coatings [20].

2.3.3.3 Processing technology

Two technologies applied to the manufacture of modern turbine blades, vacuum melting and directional-solidification, result in strengthened superalloys. Vacuum melting allows better control of compositions and improved removal of detrimental impurities.

Improved ductility and reduction of crack initiation was achieved by removing those grain boundaries which were perpendicular to the load [20]. The resulting directional solidification was obtained in production by careful control of the temperature gradient in the mould. This encouraged the growth of columnar boundaries and near elimination of transverse grain boundaries, thus creating aligned grain structures, aligned grain boundaries, and strengthening filaments, such as TaC, as seen in Figure 2.10. The preferred low-modulus (001) texture, or orientation parallel to the solidification direction, provided by the directional solidification process, improves ductility and results in a significant enhancement in thermo-mechanical fatigue resistance, compared with conventionally cast superalloys. This property is advantageous in high temperature components.

Further advancement in casting technology led to the development of single-crystal alloys and Figure 2.12 shows the difference between a single crystal metal and a polycrystalline metal, noting the distorted boundary between three crystals of the latter.

Manufacture of a single crystal metal is achieved by using seed crystals to reduce the initiation energy required for crystallisation of the alloy, growing a single crystal ahead of the bulk of the melt. The mould physically constrains the solidification front which allows only one grain to enter it, thus ensuring the component solidifies as a single crystal.

Being a single crystal, without grain boundaries, removes the need for the grain boundary strengthening elements, such as carbon, hafnium or boron. As a result, a more uniform γ/γ' structure can be obtained from higher heat treatments, which further improves alloy properties [20].

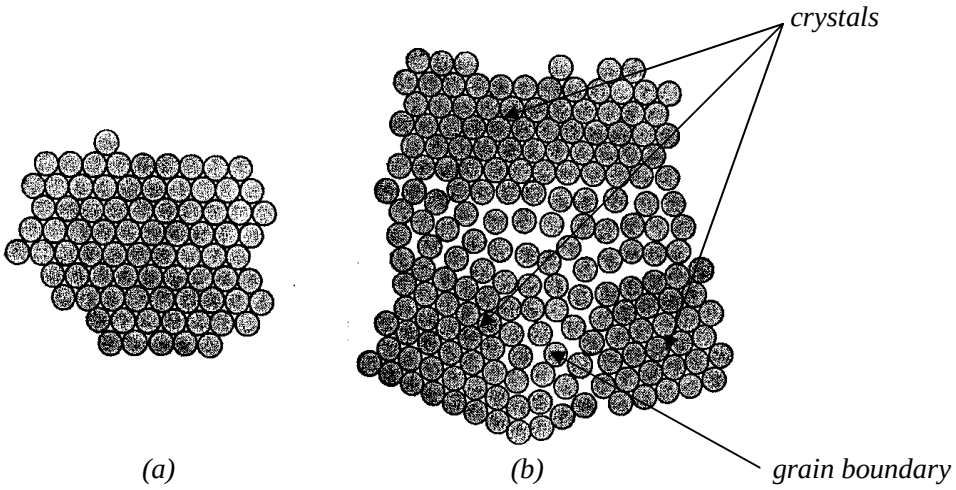

Figure 2.12: Sketch illustrating the difference between (a) single crystal and (b) polycrystalline metal [18]

Elimination of grain boundaries in single crystals removes potential failure initiation sites and enhances high temperature ductility. More recently, transverse plates of γ' have been created in single crystals, (seen in Figure 2.10) by heat treatment, which provide still more alloy strengthening.

2.3.3.4 Effects of alloying elements in superalloys

Additions of various elements are made to assist formation of the superalloy, for example chromium additions decrease the minimum aluminium content required to form a continuous alumina scale [18]. Additions of reactive elements (Y, Hf, Ce, La, etc) and metals, such as Pt, decrease scale growth rate and improve spallation resistance. However, the addition of alloying elements to improve performance in one aspect may cause deterioration in other aspects.

The use of refractory metals (Mo, Ta and W) in nickel-base alloys is one example. They are beneficial as strengtheners, assisting γ' formation, carbide formation and solution effects, and also act as oxygen-getters, which assist in the formation of Al_2O_3 and Cr_2O_3 healing layers. In contrast, these elements decrease the diffusion of aluminium, chromium and silicon in the alloy, thus opposing healing layer formation, although tantalum is less severe in this respect than the others. As the deleterious effects of refractory metals outweigh the benefits they are not added to superalloys to improve oxidation behaviour.

In the NiAl system, the minimum concentration of aluminum at which alumina is the dominant scale is about 35 at%Al, but with the addition of about 5 at%Cr the formation of dominant Al_2O_3 is achieved with 12 at%Al. Thus, chromium influences the selective oxidation of aluminium and formation of continuous Al_2O_3, by internal oxidation of chromium in the early, transient stages by reducing the oxygen flux into the metal.

A sequence proposed by Giggins and Pettit [23], shown in Figure 2.13, explains how the oxidation occurs. The first oxide scale that form on a Ni-Al-Cr alloy will be a mixture, such as NiO-Ni(Cr,Al)$_2$O$_4$, in proportions that reflect the alloy composition.

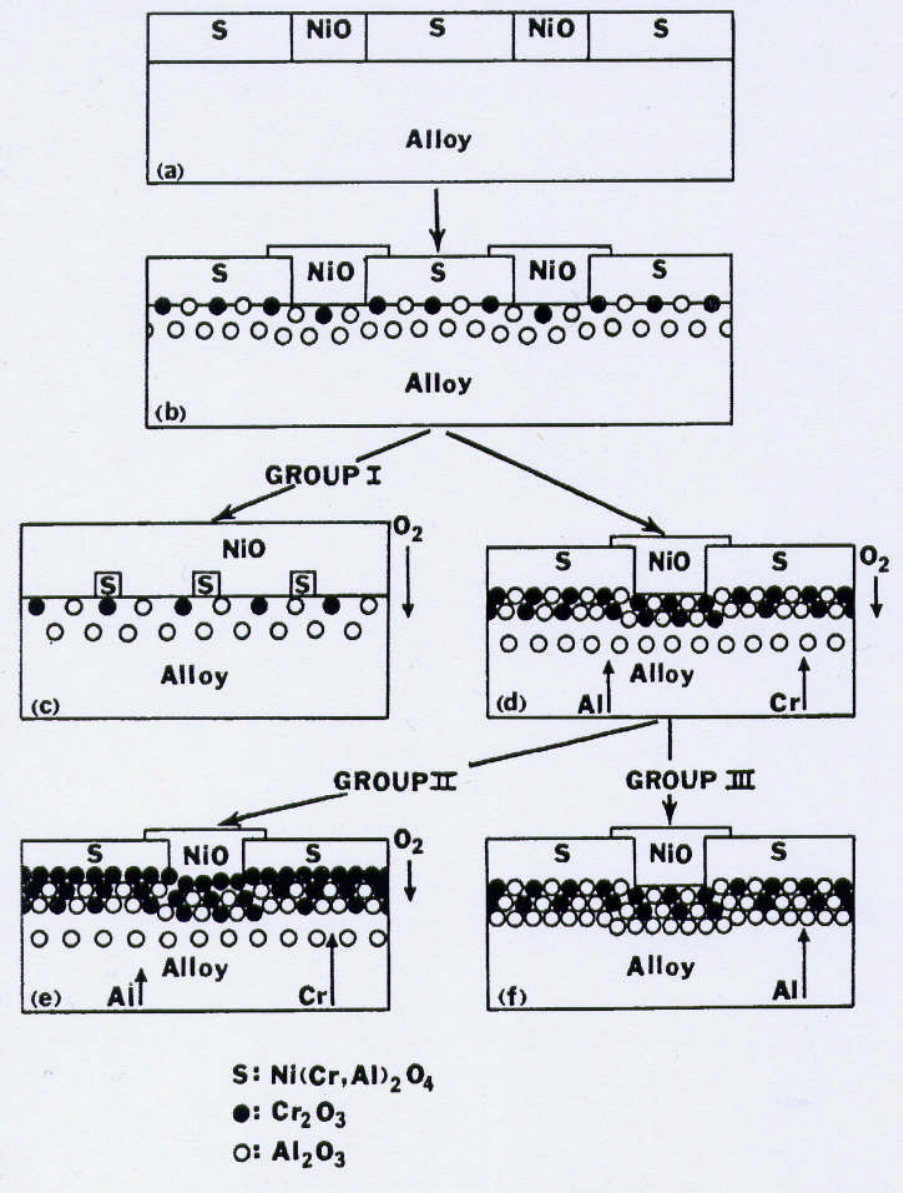

Figure 2.13: Schematic diagram illustrating the oxidation mechanism for Ni-Cr-Al alloys [23]

As Cr_2O_3 is stable at low oxygen partial pressures, it can form below the scale, but Al_2O_3 is even more stable and forms as internal oxide particles, below the Cr_2O_3 grains. If the Al and Cr contents of the alloy are low, NiO will continue to form (Group 1 in Figure 2.13) and no continuous Al_2O_3 or Cr_2O_3 layers build up.

If the Al or Cr contents are higher, a Cr_2O_3 layer forms at the mixed-oxide/alloy interface reducing oxygen diffusion, thus slowing growth of both internal Al_2O_3 grains and the outer NiO-$Ni(Cr,Al)_2O_4$ mixture. If the Al content is high enough, a continuous layer of Al_2O_3 appears which becomes rate determining , and Al_2O_3 formation continues (Group III). A lower content of Al in the alloy will result in the Al_2O_3 remaining but as internal oxide precipitates and the duplex layer will be enriched in Cr (Group II). The continuous Al_2O_3 layer formation (Group III) steady state occurs after about 1h at 1000^{o}C.

In addition to Al and Cr, other common alloying elements are Mn, Ti, Si, Mo, Ta and W. Each element is added to enhance some alloying parameter but may have a deleterious effect on others. An example is titanium which promotes Cr_2O_3 formation on Ni-20Cr and Co-20Cr but does not affect the Cr_2O_3 growth rate. It also slightly increases the growth rate of Al_2O_3 scales on β-NiAl but does not promote exclusive Al_2O_3 formation on γ'-Ni_3Al or γ-Ni(Al) alloys. Titanium also has a deleterious effect on adherence in nickel-base alloys [24].

2.3.3.5 Superalloy production methods

The objective of this project is to develop coatings for biomass and waste-fuel fired gas turbines. These coatings are to be developed for high temperature components, including air cooled turbine blades, which involves casting as the production method. Literature reviews of production methods are not considered to be necessary and will not be included in this chapter.

2.3.3.6 Superalloys – hot corrosion

It will be apparent that addition of alloying elements contributes predominantly to the mechanical integrity of the superalloy, including creep, fatigue etc. These limit the content of elements which enhance the hot protection provided by a superalloy. This is particularly the case in single crystal superalloys, where chromium content, at 6% for CMSX-4, compares with the 16% content of the polycrystalline IN738LC. As a result, hot corrosion protection for gas turbines burning biomass and waste-fuels, the subject of this project, relies on the development of novel protective coatings. Details of the superalloys used in this project, IN939, IN738LC and CMSX-4, are set out in the chapters on corrosion and oxidation tests and in evaluating the performance of novel coatings.

2.4 Degradation mechanisms in hot components

In the previous section it was explained that development of superalloys for gas turbines, had reached the stage where high mechanical integrity, in the high temperature, highly stressed environment in which they operate, had been achieved, but their resistance to hot corrosion was limited. Overcoming this limitation has been achieved by developing coatings to protect the substrate alloy from environmental degradation. This section considers the various degradation mechanisms and their effects on the alloys and coatings.

Oxidation of an alloy or coatings is a primary attack mechanism, involving reaction of the alloy with oxygen to form oxides. The oxides consume the alloy and may reduce the mechanical properties of the substrate. As coatings oxidise they are designed to form a slow growing thin, adherent and compact oxide layer on the surface, e.g. alumina or chromia, significantly reducing oxidation rates compared to Ni and thereby increasing component life.

Interdiffusion is the term given to the mechanism whereby coatings degrade as a result of inward diffusion of coating elements into the substrate and outward diffusion of substrate elements into the coating. Inward diffusion reduces the ability of the coating to replenish the protective scale, whereas outward diffusion reduces the protective performance of the coating structure and, by causing premature spallation, reduces the life of the coating. Outward diffusion of some elements, e.g. titanium, over time can adversely affect the substrate structure and hence its mechanical integrity.

Hot corrosion occurs at high temperature whenever salt or ash deposits accumulate on alloy surfaces, thus altering the environment-alloy reactions that would otherwise have occurred. It is usually a more serious degradation mechanism than oxidation. All hot corrosion mechanisms have two stages of attack, an early stage where the alloy is able to counteract the effect of the salt deposit, known as the initiation period, and the second stage, where the rate of attack is greatly increased and known as propagation phase.

2.4.1 Oxidation

Oxidation occurs when a metal is exposed to air or steam and leads to the formation of oxide layers, with the reaction between the metal and oxygen being expressed by the formula [25]:

$$aM(s) + b/2O_2(g) \longrightarrow M_aO_b(s)$$

Thermodynamic reactions of metal and oxygen initiate corrosion and form scale, with the initial oxidation starting with adsorption, followed by oxygen dissolution then oxide nucleation through to scale growth, or internal oxidation. The oxide layer formed on the surface grows laterally to form a film, which separates the two reactants and further reaction requires transportation of the reacting ions and electrons through the film as shown in Figure 2.14.

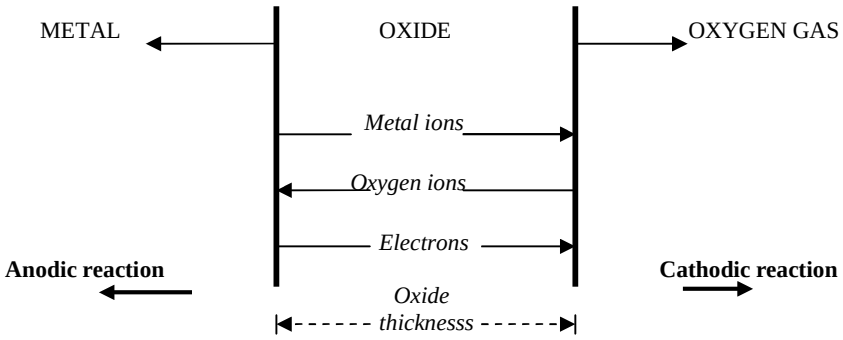

Figure 2.14: Oxidation by diffusion of reactants through a growing scale [25]

The migration of ions and electrons within the scale, driven by the free energy decrease which occurs with the formation of an oxide, was the basis for the classical theory of oxidation proposed by Wagner[26,27]. His was the first comprehensive theory for oxidation of a metalwhich explained why, at a fixed temperature, the oxide scale growth rate is parabolic and of the form:

$$(\text{Rate of oxide growth})^2 = k_p \text{ Time}$$

where k_p is the parabolic rate constant. The rate of oxidation is limited by diffusion processes, the rate of oxide growth depends on temperature, so that at constant ambient oxygen pressures, it obeys the Arrhenius-type equation [40]:

$$k = k_o \, exp(-Q/RT)$$

where Q is the activation energy, R is the universal gas constant and T the absolute temperature. Ionic diffusion via defect sites in the scale will occur if the scale is dense, exhibits electronic conduction and adheres uniformly to the metal substrate. In the absence of these conditions the oxidation rate will be higher. At a critical thickness the oxide will spall and the oxidation process begins again, but involving a slightly different alloy composition, resulting from the earlier consumption of scale forming elements. Thermal expansion mismatches or an over-thick oxide scale cause the oxide spallation. By the formation and reformation of oxides of the superalloy elements, the cross-sectional area of the superalloy and its load-bearing capacity are reduced. Load-bearing capacity is also reduced by internal oxidation and nitridation setting up stress concentrations which create a fatigue deficit. After spallation, an oxide scale is redeveloped from the superalloy which may be less protective, such as $NiCr_2O_4$, and the oxidation rate therefore increases.

The overall driving force for metal-oxygen reactions is the free energy change associated with the formation of the oxide from the reactants. Thermodynamically, the oxide will be formed only if the ambient oxygen pressure is larger than the dissociation pressure of the oxide in equilibrium with the metal. The standard free energies of formation of oxides as a function of temperature and the corresponding dissociation pressures of the oxides can be exhibited in the form of an Ellingham/Richardson diagram shown in Figure 2.15.

The diagram shows the most stable oxides have the largest negative values of ΔG. It can also be seen that, for the oxide systems most applicable to gas turbine technology; Fe_2O_3, CoO, NiO, Cr_2O_3, TiO_2, SiO_2 and Al_2O_3, the stability of the oxides increases from Fe_2O_3 to Al_2O_3 [28,29].

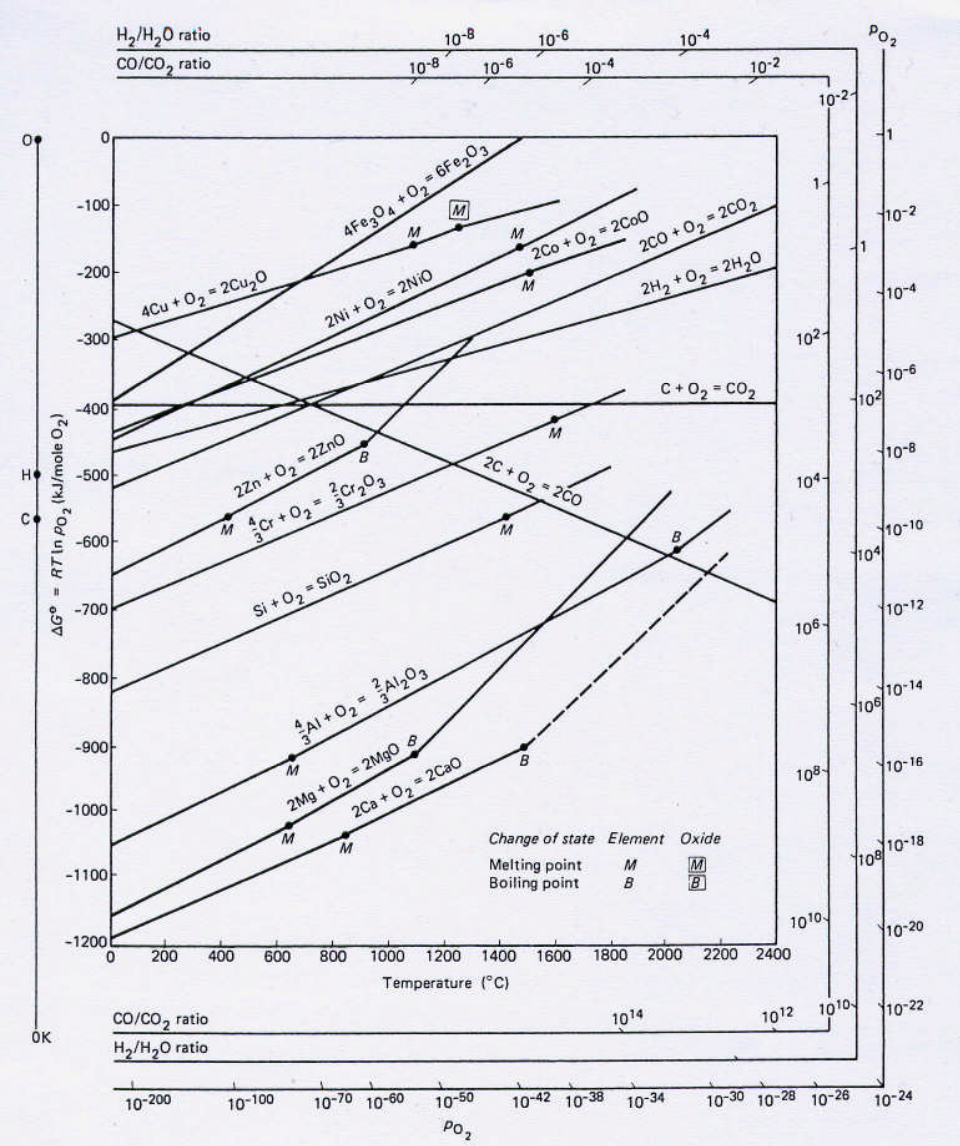

Figure 2.15: Ellingham/Richardson diagram; standard free energy of formation of selected oxides as a function of temperature [28]

Kofstad [25] explains that the kinetics of oxidation, of oxide scale formation and growth, can be divided into the three main stages shown schematically in Figure 2.16. Firstly, the metal-oxygen reaction involves adsorption of gas on the metal surface. Secondly, as the reaction proceeds, oxygen may dissolve into the metal and oxide is formed on the surface.

The surface oxide may form as a film or separate oxide nuclei, which then grows laterally to form a continuous oxide layer covering the whole surface. Simultaneously, the oxidant continues to dissolve in the metal substrate, at a rate depending on its solubility and diffusivity in the metal (diffusion is explained in the next section). The first two stages are functions of crystal defects at the surface, on surface preparation and impurities in both the metal and the gas. In the third stage, as the surface oxide separates the metal from the gas, further growth of the oxide film occurs normal to the surface, by solid-state diffusion of the reactants through the film.

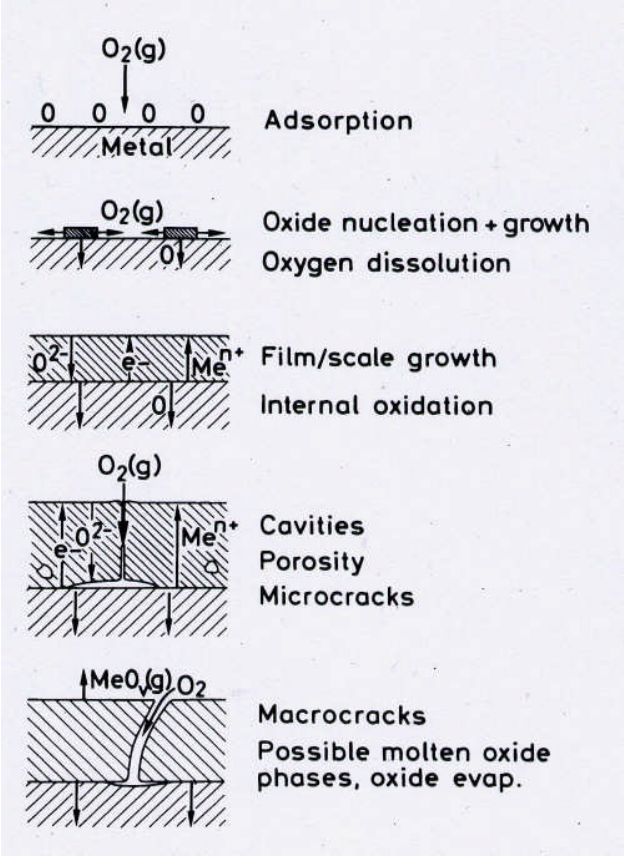

Figure 2.16: Schematic illustration of the main phenomena and part-processes taking place in the reaction of metals with single oxidant gases, e.g. oxygen [25]

A variety of well known factors influence the reaction path and oxidation behaviour of the metal. These include; temperature, thermal cycles, composition and velocity of the gas and alloy composition [25,30,31,32,33,34]. The reaction will continue as long as neutral atoms or ions and electrons migrate across scale oxides which are assumed to be non-stoichiometric compounds. Rate of oxide scale growth varies as a function of time and temperature and in high temperature oxidation may occur in three different ways; parabolic, linear and logarithmic. These are shown schematically in Figure 2.17.

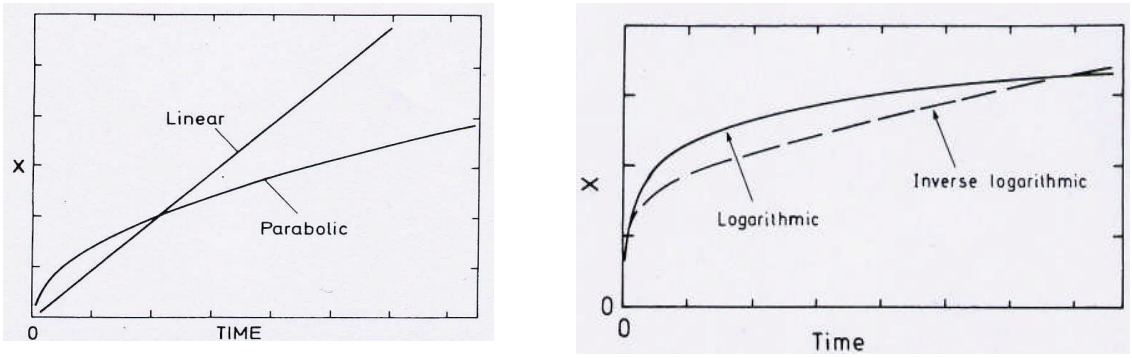

Figure 2.17: Schematic illustration of the variation of oxide thickness (x) with time for parabolic, linear and logarithmic oxidation [30]

At high temperatures, when the layer of reaction products remains dense and continuous, the reactions are controlled by diffusional transport of the reactant and electrons through the layer of reaction products. Diffusion is described more fully in Section 2.4.2. As thin layers grow into thicker scales, the diffusion paths lengthen and the reaction rate decreases with time in a parabolic relationship, described by the following parabolic rate equation:

Differential: $dx/dt = k'_p/x$

Integral: $x^2 = 2k'_p t + C = k_p t + C$

Where k'_p *and* k_p *= the parabolic constant (* $k_p = 2k'_p$ *)*
and C = the integration constant

Stresses may build up in the scales, accompanied by balancing stresses in the underlying metal and these may cause plastic deformation of the metal or lead to cracking of the scale. Repeated cracking will cause the scale to lose its protective capability. Diffusion through a thin reaction product layer, of near constant thickness next to the metal, or by phase boundary reactions, will govern the reactions. Such reactions are described by a linear equation:

Differential: $dx/dt = k_1$

Integral: $x = k_1 t + C$

Where k_1 *= the linear rate constant*
and C = the integration constant

At low temperatures, generally below 400^{o}C, oxide scale growth may for many metals follow the logarithmic type rate equations, which include direct- and indirect-logarithmic rate equations:

Direct logarithmic: $x = k_{log} \cdot \log(t+t_0) + A$

Indirect logarithmic: $1/x = B - k_{il} \log t$

Where x = thickness of the metal oxide, the amount of oxygen consumed per unit surface area of the metal, the amount of metal transformed to oxide.
t = time
k_{log} and k_{il} = rate constants
A and B = constants

Parabolic kinetics are the most common for practical alloys oxidised at high temperatures, having oxides that grow the most slowly, Cr_2O_3, Al_2O_3, SiO_2, being the most desirable, as may be seen in Figure 2.18

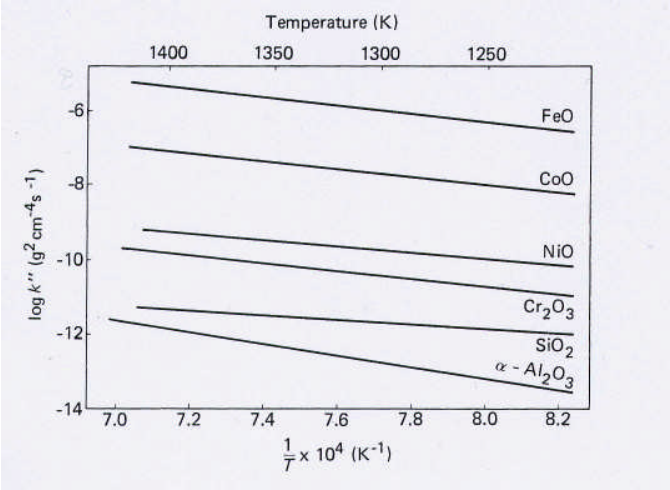

Figure 2.18: Order-of-magnitude parabolic rate constants for the growth of several oxides [34]

Higher oxidation rates may also result where oxide scales, e.g. chromia, react with oxygen to form volatile oxides and thus deplete the alloy of chromium. At temperatures above 1100°C the rate of evaporation of CrO_3 is severe.

High stresses may also cause cavities, cracks or micro cracks in/under the oxide scale, causing it to fail as a protection shield. These may develop during oxidation as part of the growth of the oxide scale or be a result of thermal cycling, the latter due to the thermal expansion mismatch between the oxide scale and the metal. Formation and reformation of oxides from the superalloy elements consume the alloy and thereby decrease the cross-sectional area and hence load-bearing capacity [34]. Internal oxidation and nitridation reduces load-bearing capacity and set up stress concentrations which introduce a fatigue deficit, and an example of internal oxidation can be seen in Figure 2.20. An over-thick oxide scale and/or thermal expansion mismatches, may cause oxide spallation, reducing the protective properties of the remaining scale.

The redeveloped oxide scale, formed from the underlying superalloy, may be a mixed oxide scale such as $NiCr_2O_4$ and $NiTiO_3$ leading to an increased oxidation rate.

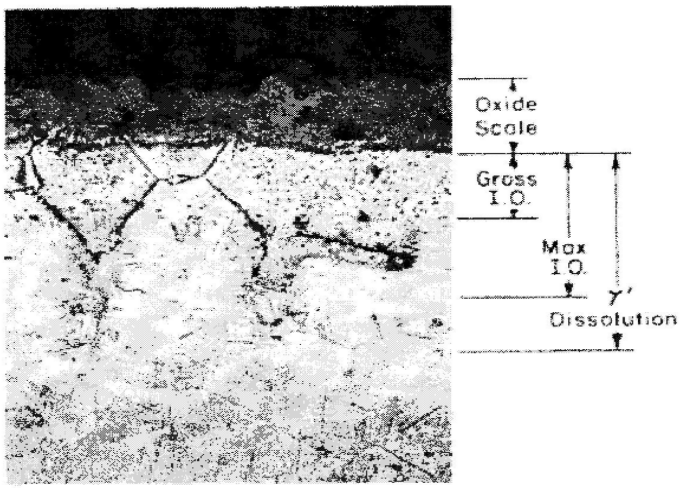

Figure 2.19: Alloy exhibiting internal oxidation and γ' dissolution [30]

2.4.2 Interdiffusion and effect of substrate composition

2.4.2.1 Diffusion

Diffusion is a basic metallurgical process which is the result of more or less random motion of individual atoms. In a metal crystal, because of thermal energy, atoms are in constant motion around their equilibrium sites. Occasionally, resulting from this motion an atom will jump to a neighbouring site.

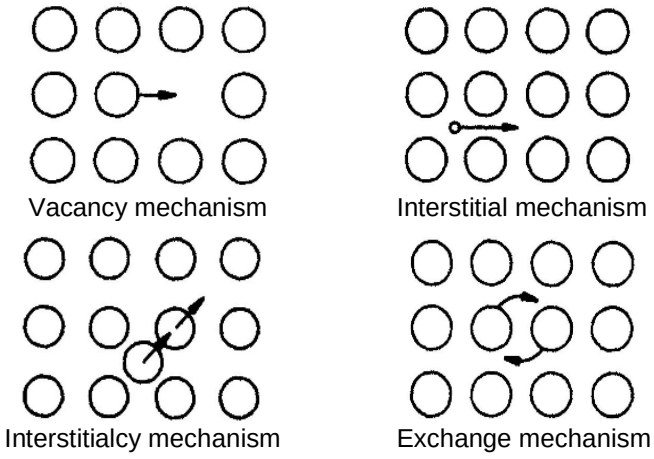

Figure 2.20: Four main types of diffusion mechanism [35]

As temperature rises, atom jump frequencies increase, the net rate of atomic migration eventually becoming large enough to provide readily observable effects. These include transport of atoms over significant distances and appreciable changes in chemical composition or atomic distribution.

Manning [35] identifies four general types of diffusion mechanism which are shown in Figure 2.20. The elementary atom jumps for these mechanisms are:

- vacancy, where any atoms neighbouring on a vacant lattice site, present in a crystal, can diffuse by jumping into the vacancy, interchanging the position of atom and vacancy;
- interstitial, whereby an interstitial atom diffuses by moving directly from one interstitial site to another without causing net motion of any other atom;
- interstitialcy, or indirect interstitial mechanism, a mechanism separate from the interstitial mechanism, whereby an interstitial atom moves by pushing a normal lattice atom into an interstitial site and moving into the lattice site itself. In this way, the location of the interstialcy during the elementary jump may move twice as far as do the individual atoms themselves;
- exchange, whereby the simultaneous motion of two lattice atoms, in a single jump, exchange places with each other. In practice this occurs infrequently.

There are many variations possible in these four basic types, for example, pairs of vacancies, bound together as divacancies cause diffusion to occur in a different manner than do single vacancies diffusing independently. Diffusion is a three dimensional mechanism, which can be influenced by a wide variety of factors such as; lattice composition, pressure and defects, and the various forms of energy required to cause atoms to jump, include temperature gradient, electric field, chemical potential, centrifugal force and stress. These factors also influence the atom jump frequencies as the atom moves through a series of equilibrium lattice positions. The various driving forces involved in diffusion are shown in Table 2.5.

Description of driving forces	**Atomic force F**	**Property of the material which governs the force**
Electric field (E)	$F = qE$	q = effective charge
Temperature gradient ($\delta T/\delta x$)	$F = -\frac{Q^*}{T} \cdot \frac{\delta T}{\delta x}$	Q^* = heat of transport
Non-ideal part of chemical potential gradient ($\delta \mu'/\delta x$)	$F = -kT \cdot \frac{\delta \ln \gamma}{\delta x}$	γ = activity coefficient
Centrifugal force from angular velocity (ω)	$F = M \omega^2 r$	M = effective molecular mass
Stress field	$F = -\frac{\delta U}{\delta x}$	U = interaction energy

Table 2.5: Atomic driving forces in diffusion [35]

From the aforegoing it is implicitly assumed that each atom jump is independent of all previous jumps. This is only true of an isolated interstitial atom moving by the interstitial mechanism and for some cases of diffusion by exchange mechanisms. Otherwise, correlations occur between the directions of successive atom jumps, in which the direction of one jump by an atom, is influenced by the direction of a previous jump taken by it. Correlation effects and the resulting correlation factors depend on crystal structure and the

diffusion mechanism involved. Correlation can also result from what is termed the vacancy wind effect. In this case, when there is a net flux of vacancies in a crystal, vacancies in their first approach to an atom are more likely than random to arrive from the side from which the vacancy flow approaches the atom, than from the opposite side. This effect is illustrated in Figure 2.21.

The diagram in the figure shows that the vacancy flux from right to left brings vacancies up to atom X (which cannot move until a vacancy arrives) more frequently at site A than at site B on the left.

The vacancy wind effect can be important when diffusion occurs in a driving force, such as an electric field.

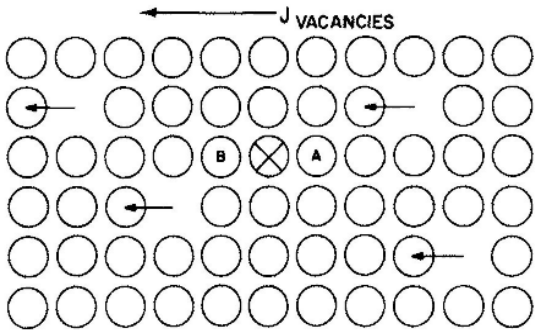

Figure 2.21: Diffusion, vacancy wind effect [35]

As already indicated, diffusion is a very complex series of mechanisms, each of which can influence the others. In this section, only an outline of diffusion has been given and, for more detailed information it is recommended that the reader refers to Manning [35].

2.4.2.2 Interdiffusion

Interdiffusion is a major degradation mechanism of coatings. At high temperature the protective element, usually aluminium, diffuses into the substrate from the coating. This, when coupled with the loss of aluminium from the coating, due to severe oxidation and/or hot corrosion, can deplete aluminium content to a level where a continuous alumina scale can no longer be formed and the coating fails. Interdiffusion relates to both the depletion of the coating reservoir, by diffusion of the protective element into the substrate, and diffusion of elements from the substrate into the coating. The protective scale is thereby weakened causing premature failure of the coating. Interdiffusion can also form mechanically undesirable secondary phases in the interdiffusion zone. As a major coating degradation process, interdiffusion has been extensively studied [36,37,38,39]. Standard aluminide coatings break down into a network of γ'-Ni_3Al precipitates, which penetrate into the β-NiAl coating. A short-circuit corrosion path is opened up when this network reaches the surface, increasing corrosion rates. Platinum additions have been found to stabilise the β-phase reducing the interdiffusion rates into and out of the coating, and the rate of formation of γ'- Ni_3Al leaders is greatly decreased and aluminide purity improved.

Outward diffusion of the various elements present in a superalloy to the protective scale can have differing effects on oxidation performance of the superalloy. Aluminium and chromium are beneficial for the oxidation process, but nickel and cobalt are not, since they oxidise more rapidly and the resulting scales are less-protective [40].

Vanadium is detrimental to coating life and elements such as molybdenum, tungsten and niobium reduce the oxidation performance of a coating/substrate [38]. Rhenium has been found to be beneficial for cyclic oxidation of β-NiAl with σ-Cr particles [41]. Outward diffusion of titanium has been found to decrease coating life of diffusion aluminides [42], platinised CMSX-4 [43]and MCrALY's [44].

2.4.3 Hot corrosion

2.4.3.1 Introduction

Gases from the gasification of biomass and waste-fuel contain aggressive species which, after combustion in the gas turbine, may be deposited on the surfaces of its turbine blades and vanes, as metal sulphates and/or chlorides. When they reach their melting points, these deposits may cause accelerated corrosion and degradation of the underlying metal.

Hot corrosion is a serious problem in gas turbines, necessitating extensive research over the years, to determine the mechanisms by which it takes place and to develop protective coatings [30,45,46,47,48,49,50,57,58,59].

2.4.3.2 Hot corrosion molten surface deposits

Following the formation of deposits on the substrate surface, the extent to which they affect the corrosion resistance of the alloy will depend on whether the deposits melt, how they adhere and the extent to which they wet the surface. Generally, a liquid deposit is necessary to initiate severe hot corrosion [34]. When the alloy-surface has been partially or completely wetted by the molten salt(s), conditions for severe corrosion can develop.

The melting point of salt(s) has a critical effect on the development of hot corrosion. Although the melting point of a single salt may be above the metal temperature of a component surface, in combination with other salts, which is usual in biomass and waste-fuels, the melting point is lowered. A prime example concerns the deposition of sulphates of sodium and potassium, commonly present in gases of these fuels [52].

Pure Na_2SO_4 has a melting point of 884^oC, but in the presence of other dissolved salts such as NaCl or K_2SO_4, the melting point is reduced. Research into the content of fossil fuel, biomass and waste-fuels at Cranfield University, has identified sulphates of sodium and potassium as commonly present in gasifier gases [53,54,55]. The melting point of these sulphates when present in the mol ratio Na_2SO_4(80) and K_2SO_4(20), as seen in Figure 2.22, is 823^oC. Alkali Cl – SO_4 mixes have even lower melting points.

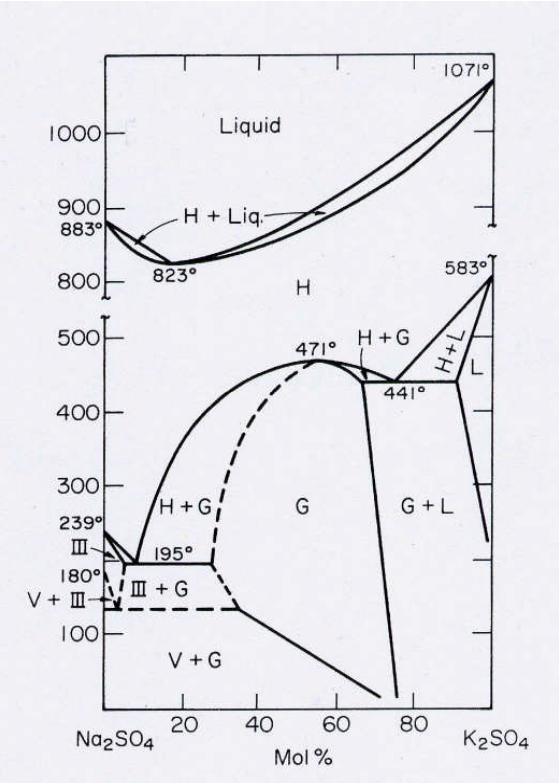

Figure 2.22: Binary equilibrium diagram for system Na_2SO_4- K_2SO_4 [53]

2.4.3.3 Hot corrosion degradation sequence

Giggins and Pettit [57] proposed a "hot corrosion degradation sequence". This stated that mass change data for hot corrosion as a function of time, indicated two stages of attack: an initial stage of initiation or incubation, during which the attack is not too severe and a later stage, propagation, where the attack has considerably increased. During the initiation stage, corresponding to the growth and dissolution of the protective oxide layer, described in section 2.4.1, and formation of the deposits. The reaction rate of the metal surface at this stage is very slow. Propagation occurs when protective oxide scales are no longer formed. It is characterised by a rapid increase in the corrosion rate, associated with significant changes in the morphology of the corrosion layers, after the oxide layer has broken down.

The two stages are illustrated in Figure 2.23 for three types of high temperature oxidation/ corrosion test. It shows that the transition from initiation to propagation is influenced by spalling of the oxide scale (cyclic oxidation) and salt deposition (hot corrosion). During the initiation (incubation) stage, the alloy surface and scale growth are being changed to make the alloy susceptible to rapid attack.

These changes include; depletion of the elements forming the scale (usually Al and Cr), sulphide formation in the alloy as a result of sulphur diffusion through the scale, dissolution of oxides into the salt and development of growth stresses in the scale.

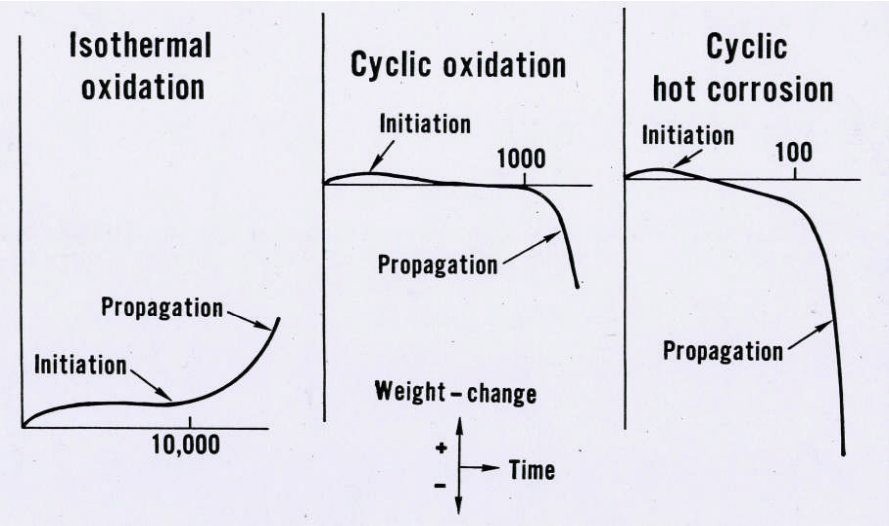

Figure 2.23: Schematic weight changes versus time to illustrate that the degradation of corrosion resistant systems consist of initiation and propagation stages [51]

Twp types of hot corrosion morphology have been identified. These depend on the temperature of the corrosion environment; the degradation rates due to hot corrosion peak at two different temperatures, as shown in Figure 2.24.

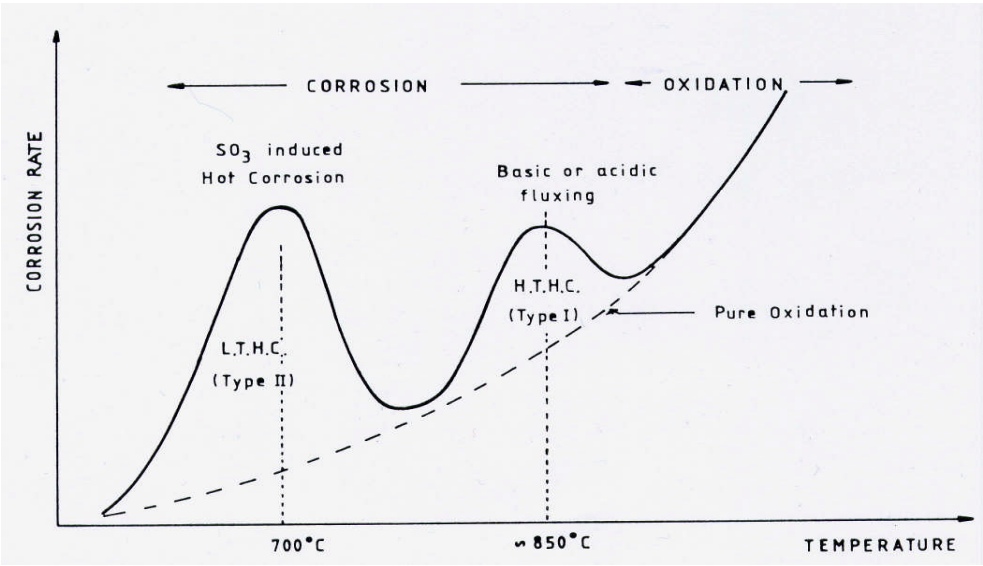

Figure 2.24: Schematic diagram of corrosion rate versus temperature [60]

The first maximum temperature, at around 700^{o}C corresponds to low temperature or Type II hot corrosion and the second maximum temperature, at around 850^{o}C corresponds to high temperature or Type I hot corrosion.

These can be summarised as:

- Type I hot corrosion is caused by the basic fluxing mechanism, alloy induced acidic fluxing or sulphidation and occurs typically at 800°C - 950°C;
- Type II hot corrosion is caused by gas induced acid fluxing or sulphidation and occurs typically at 600°C - 750°C.

2.4.3.4 Type I (High Temperature) hot corrosion

Type I hot corrosion, also known as High Temperature Hot Corrosion (HTHC) and results from sulphidation and a fluxing process (either basic fluxing or alloy-induced acidic fluxing). It is usually present when the temperature is between 800°C and 950°C and operates by dissolving the protective scale by a basic molten deposit, usually Na_2SO_4-based, and was first proposed as the concept of basic fluxing in 1969 [49] by Bornstein and DeCrescente. The basic dissolution of the oxide scale can be described in terms of sulphate ions [61]:

$$Cr_2O_3 + 3/2O_2 + 2SO_4^{2-} = 2CrO_4^{2-} + 2SO_3$$

$$Al_2O_3 + SO_2^{2-} = 2AlO_2^{-} + SO_3$$

This reaction consumes the scale and the substrate can then be attacked by sulphidation. The reaction products frequently have metal deposits dispersed through the oxide deposits. These metal deposits contain little or no aluminium or chromium. The degree of attack on the scale depends on the production of oxide ions in the molten deposit, and a supply of Na_2SO_4 is required to maintain the attack. The higher the temperature, the more severe the degradation, because the ion content available to react with the scale, increases as the temperature increases. Evaporation of the salts limits the temperature of the process [57,62]. The basic fluxing mechanism of Type I hot corrosion is shown schematically in Figure 2.25.

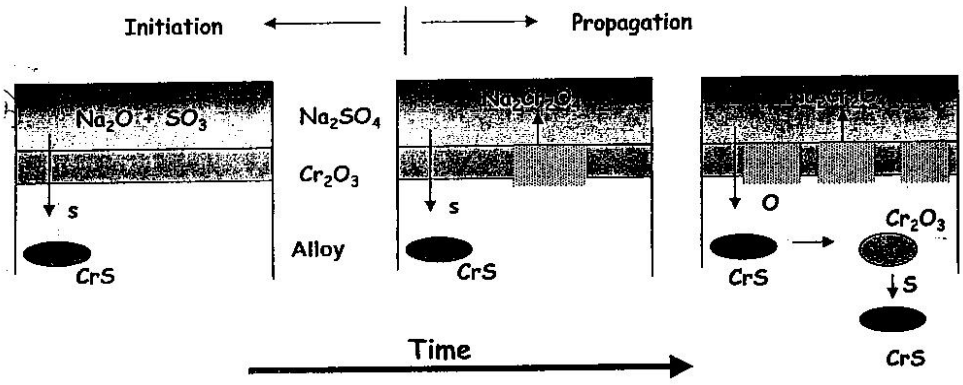

Figure 2.25: Schematic diagram of Type I (high temperature) hot corrosion [61]

The reduced oxygen partial pressure under the melt allows the sulphur to react with substrate elements, notably chromium, to form sulphides within the alloy ahead of the oxide front. These sulphides are characteristic of Type I hot corrosion, hence the term sulphidation for this mechanism. Formation of sulphides occurs more rapidly when SO_2 is present in the atmosphere, but above 850^{o}C sulphidation will occur if SO_2 is not present. The protective scales of alumina and chromia will dissolve in a molten deposit if suitable deposit chemistry is present, however, silica has a lower solubility in molten sodium sulphate at 923^{o}C than the other two protective scales [63].

A schematic diagram illustrating the progression of Type I hot corrosion is shown in Figure 2.26.

If the chromium concentration is high enough to form a protective Cr_2O_3 scale (~15wt%), resistance to Type I hot corrosion is markedly increased. It is believed that chromium is effective in acting against both Type I and Type II hot corrosion because Cr_2O_3 forms an oxide ion activity in Na_2SO_4 that is insufficient to cause basic fluxing and not enough to cause acidic fluxing [34,51].

Aluminium inhibits Type I hot corrosion when the aluminium concentration is high enough to form continuous Al_2O_3 scales. When the alumina concentration is not sufficient to form continuous scales, burner rig conditions, as described by Morrow et al [64] caused rapid degradation of aluminium containing alloys.

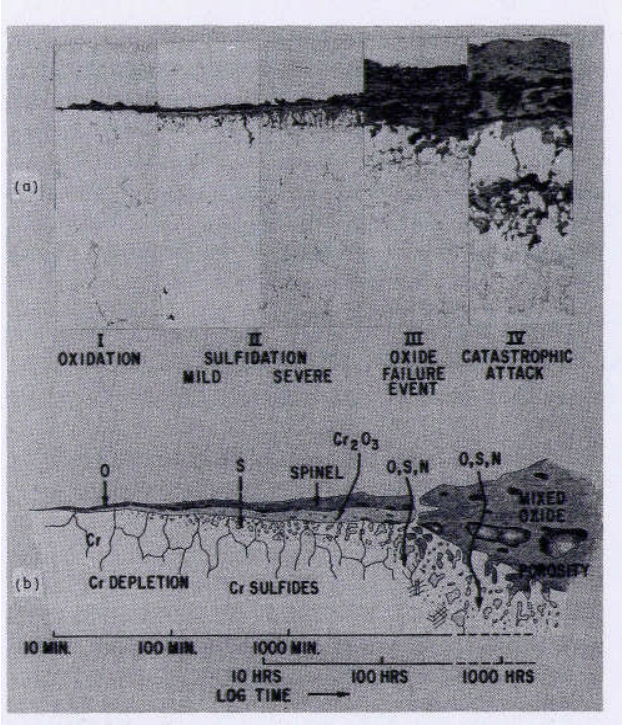

Figure 2.26: Schematic diagram showing the progression of Type I hot corrosion [65]

Long [63] reported that work performed at Rolls-Royce had indicated that silicon-aluminides provide excellent protection against Type 1 hot corrosion; of significance when considering novel coating development in this project.

2.4.3.5 Type II Hot Corrosion

This degradation mechanism is also known as Low Temperature Hot Corrosion (LTHC), with gas induced acidic fluxing the process of dissolving the protective scale. Fluxing is the process whereby the protective scale becomes soluble in the molten deposit, and oxide ions are donated to this deposit by the protective oxide e.g. Al_2O_3 or Cr_2O_3 [63].

The reactions would be:

$$Al_2O_3 \longrightarrow 2Al^{3+} + 3O^{2-}$$

$$Cr_2O_3 \longrightarrow 2Cr^{3+} + 3O^{2-}$$

Acidic conditions can be caused by two processes, the first requires one component of the gas stream to acidify the molten deposit (Type II hot corrosion), the other requires that oxides of the superalloy substrate acidify the molten deposit (Type I hot corrosion by acidic fluxing). For hot corrosion the gas stream is usually a combustion environment, hence the environment will contain various fuel contaminants, most notably acidic SO_3. When this is incorporated into the molten deposit it acidifies the molten deposit [50]. The acid fluxing mechanism is shown schematically in Figure 2.27. The lack of oxide ions in the molten deposit is the driving force for dissolving the protective oxide into the molten deposit.

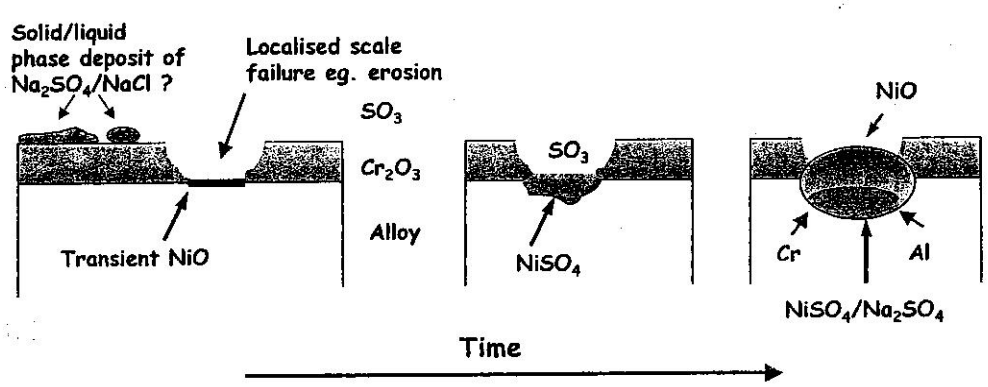

Figure 2.27: Schematic diagram illustrating the acid fluxing mechanism of Type II hot corrosion [61]

Type II hot corrosion has certain distinctive microstructures, depending on the alloy composition and environment. The corroded microstructure exhibits pitting with little depletion of aluminium and chromium and only incidental alloy sulphidation. Attack does not occur when the protective scale is intact, but is rapid on failure of the scale.

The characteristic pattern of attack of Type II hot corrosion consists of:

- Localised attack occurring by gas-induced acidic fluxing or sulphidation;
- Non-uniformly distributed pitting with a lamellar scale rich in sulphur through the progressive fluxing action of the deposits;
- Sulphur concentrated at the pitting/metal interface, not forming internal sulphides in the alloy.

The reaction mechanism of low temperature hot corrosion of Ni-Cr and Co-Cr alloys in SO_3 containing gases is shown in the schematic diagram in Figure 2.28.

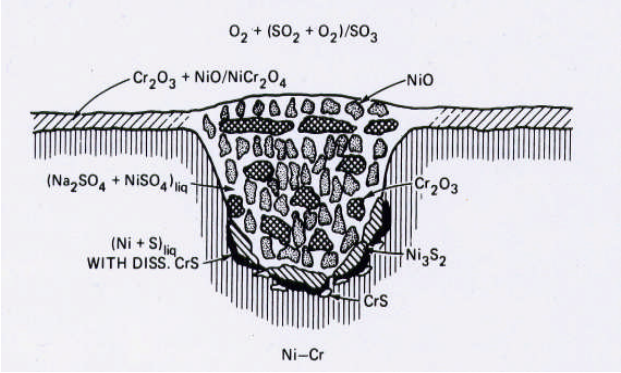

Figure 2.28: Schematic diagram of the reaction mechanism of Type II hot corrosion of Ni-Cr and Co-Cr alloys in SO_3 containing gases [19]

Although most alloys are susceptible to Type II hot corrosion, some alloys will survive it better than others. Luthra and Wood have shown that CoCr coatings with a chromium content above 37.5% provide excellent resistance to this mode of degradation [67].

This was confirmed by Luthra and Shores [66] when they tested Co-Cr and Ni-Cr alloys under Type II hot corrosion conditions. Small additions (~1wt%) of silicon and yttrium were found by Luthra and Wood to improve the resistance of CoCr coatings in a burner rig environment at 870°C, while these additions slightly decreased corrosion resistance of CoCr alloys at 730°C [67].

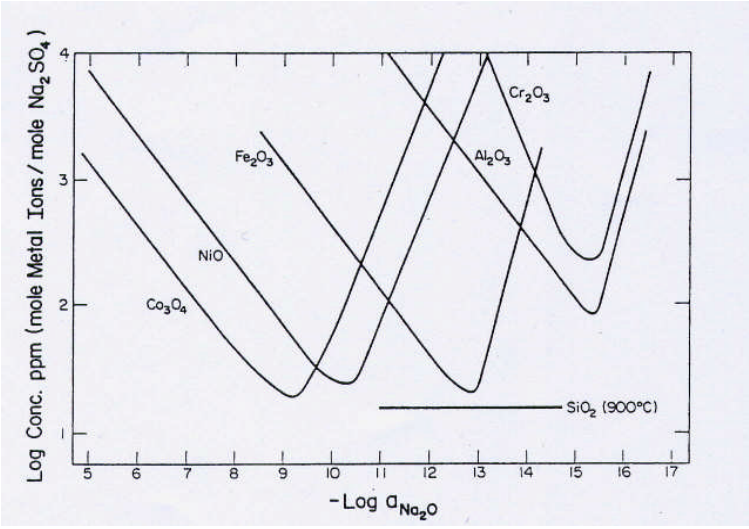

Figure 2.29: Measured oxide solubilities in fused Na_2SO_4 at 927°C and 1atm O_2 [68]

Oxides of active elements such as yttrium can serve as sites where molten scale can penetrate the oxide scale [68]. These reactive element oxides frequently form continuous stringers extending through the alumina scales to react with the acidic molten deposits. This leads to the conclusion that yttrium-modified aluminides may not provide adequate protection against Type II hot corrosion, if such oxide stringers form.

Increasing the chromium content of alloys does not increase the initiation time for acidic fluxing but does decrease the propagation rate [69]. Chromising should provide excellent protection ahainst Type II hot corrosion since NiCr and CoCr coatings are very protective under Type II conditions [46,70]. Increasing the chromium content has a greater effect on alloys and coatings that have a chromium content less than ~20%.

As shown in Figure 2.29, silica has low solubility in acidic molten Na_2SO_4 and is very good against Type II hot corrosion. For this reason Sermaloy J, a slurry-based coating containing silicon and aluminium, produced by Sermatech, is used extensively in the gas turbine industry, as both a full and touch-up coating due to its excellent corrosion resistance [72].

2.4.3.6 Alloy-induced hot corrosion

Alloy-induced hot corrosion exhibits pitting similar to Type II hot corrosion, but is usually observed at the higher temperatures of the Type I hot corrosion regime [46,73], due to the amount of oxidation required to produce sufficient refractory element oxides. Alloy-induced hot corrosion is different to Type II hot corrosion because the alloy-induced hot corrosion is self-sustaining [50,72] and an important mechanism for turbine blade materials due to the quantity of solid-solution strengthening elements present in single crystal alloys. The basic fluxing degradation mode, which is not uncommon, often precedes the alloy-induced hot corrosion by introducing refractory oxides into the molten deposit.

Some elements present in CMSX-4 have been found to be detrimental to corrosion performance, when their oxides acidify the deposit. Elements such as molybdenum, tungsten and vanadium are well known to acidify molten deposits [46], while elements such as tantalum [73-75] and rhenium [41,73,76,77] are believed to benefit corrosion performance.

2.4.3.7 Chloride-accelerated hot corrosion

Chloride-accelerated attack is significant at temperatures as low as 450^{o}C and as high as 1000^{o}C. This mechanism has mainly been observed for marine gas turbines and when present chloride-induced hot corrosion is both a degradation mechanism and a catalyst for other degradation mechanisms. In the marine case sea slat is involved and, as it contains nearly 90% chlorides [79], this mechanism will be present. It has been proposed that failure of the protective scale is caused by mechanical stresses augmented by the presence of chlorine, and when the scale has been cracked, the substrate elements react with chlorine and oxygen to form volatile oxy-chlorides [78,79].

The volatile gases cause voids under the protective scale which accelerate spallation of the oxide, exposing the substrate to attack by chlorides and molten sulphate deposits. High degradation rates occurring on several chromia forming alloys have been reported, when only 5ppm of NaCl was introduced into the gas stream [80]. Other researchers have confirmed that chlorine in the deposit increases the rate of scale cracking in both chromia and alumina, reducing the incubation period of the alloy coating [79,80,82-89].

When the concentration of chlorine in the deposit is above the ppm range, aluminium and chromium are rapidly stripped away from the alloys, the attack becoming more severe as the temperature rises [47]. Chloride attack leaves a pitted microstructure with many pores and channels where chromium and aluminium have been stripped out of the alloy [88].

Totally non-protective oxide scales form on the surface of the alloy and degradation of the alloy is then rapid. Although much of the work on chlorine-accelerated attack has been aimed at marine environments, there can be significant levels of chlorine in biomass and waste-fuels. Their gasification may lead to gases containing hydrogen chloride which interact with sodium and other metallic sulphates to initiate hot corrosion, and therefore chloride influences need to be considered in this project.

2.5 Protective coatings

2.5.1 Introduction

As shown in the previous section, hot corrosion problems, whether Type I, Type II, alloy induced or chlorine accelerated corrosion, result from salt contaminants, including alkali sulphates and chlorides, that in combination produce low melting deposits to dissolve the oxide surface. Degradation occurs in two stages, initiation and propagation. The initiation phase leads to a lower rate of attack due to the low dissolution of the surface oxide. If the surface-oxide can be maintained and extended by the use of effective coating(s) the resistance to hot corrosion attack will be greatly extended.

Although superalloy compositions and microstructures provide optimum mechanical properties for GT hot components they do not provide adequate resistance to hot corrosion. Hence protective coatings are necessary to allow full exploitation of superalloy strength at high temperature by reducing scaling by oxidation and/or the rate of hot corrosion damage. In developing an effective coating it is also important to consider the substrate and surface conditions, so the combination will cause low rates of scale formation, uniform surface attack, a ductile surface scale and efficient bonding. Table 2.6 summarises the surface-coating-substrate related properties and framework around which the design requirements of a coating for good oxidation/corrosion resistance can be formulated.

The surface of the coating should form a stable, slow-growing oxide that forms a barrier between the coating-alloy and environment in which it operates. To sustain formation of the oxide scale requires sufficient content of the components that forms the scale, such as aluminium and chromium.

This action effectively maintains the initiation phase of hot corrosion for as long as the scale forming component lasts, the target being the required life of the particular GT component and thereby preventing propagation.

Superalloy coatings commonly form alumina, as this is slow-growing, adherent, continuous and compact, which combine to minimise oxidation rates. The critical quantity of aluminium in an alloy depends on the concentrations of other alloying elements, particularly of chromium, the physical state of the component, temperature and oxygen partial pressure [36].

Coating Property	Requirement	Coating Surface	Mid Coating	Coating/ substrate interface
Oxidation/ corrosion resistance	• Low rates of scale formation	X	...	...
	• Uniform surface attack	X	...	...
	• A thermodynamically stable surface oxide	X	...	...
	• Ductile surface scales	X	...	...
	• Adherent surface scales	X	...	...
	• High concentration of scale forming element within coating to act as reserve for scale repair	X	X	...
Interface stability	• Low rate of diffusion across the interface at operating temperatures	...	...	X
	• Limited compositional changes across interface	...	...	X
	• Absence of embrittling phase formation during service	...	...	X
Good adhesion	• Matched coating and substrate properties to minimise coating mismatch and stress generation at coating/substrate interface	...	X	X
	• Optimum surface condition before coating	...		X
	• Stresses during coating formation should be minimised	...	X	X
Mechanical strength	• Coating must withstand all stress (creep, fatigue, and impact loading) that is generated at component surface during service	...	X	...
	• Well matched thermal expansion coefficients between coating and substrate to minimise thermal stressing and thermal fatigue	...	X	X

Table 2.6: Desirable features of an oxidation/corrosion resistant coating [36]

In the binary alloy Ni-Al, the critical aluminium concentration is in the range 8-12wt%, but in the ternary M-29%Cr-Al alloys the critical concentration is only 3-4wt%. Alumina has a highly stable phase termed α-Al_2O_3, but also forms several meta-stable phases before the alpha phase is formed [63]. From comparison of growth rates of various alumina scales it was found that the parabolic rate constant k_p at a given temperature, is approximately two orders of magnitude greater for the θ-Al_2O_3 scale than for the α-Al_2O_3 scale, thus the growth of the meta-stable alumina phases in the early stages of oxidation heavily influences the initial oxidation rate and growth of the stable α-Al_2O_3 scale [63].

2.5.2 Types of coatings

Two generic types of coatings provide hot corrosion resistance; diffusion and overlay. A third class of coating, the thermal barrier coating (TBC) is used (in combination with component cooling) where the reduction of substrate surface temperature (typically by up to 150^{o}C) can result in more durable coatings (usually from a mechanical perspective) but may also be economic by retarding corrosion. Diffusion and overlay coatings have been combined to form Smartcoat systems which are 'tailor made' to retard hot corrosion in the most economical manner. These coatings may also support a thermal barrier coating as they are alumina formers [96,97].

2.5.3 Diffusion coatings

Diffusion coating processes are used extensively in aviation gas turbines to enhance resistance to oxidation and corrosion of turbine components. Diffusion coatings are formed by the interaction between constituents of the coating materials, such as aluminium, chromium or silicon, and the substrate alloy. Their properties are determined by the process methodology, the substrate composition and subsequent heat treatment.

Aluminising is the most common diffusion coating used by gas turbine manufacturers [63]. The diffusion coating forms a surface scale of alumina, termed a thermally grown oxide (TGO), which is dense and slow-growing, that prevents oxygen penetrating into the component, thus retarding the oxidation process. Diffusion aluminide coatings are based on the intermetallic compound β-NiAl. An example of a platinum aluminide coating is shown in Figure 2.30.

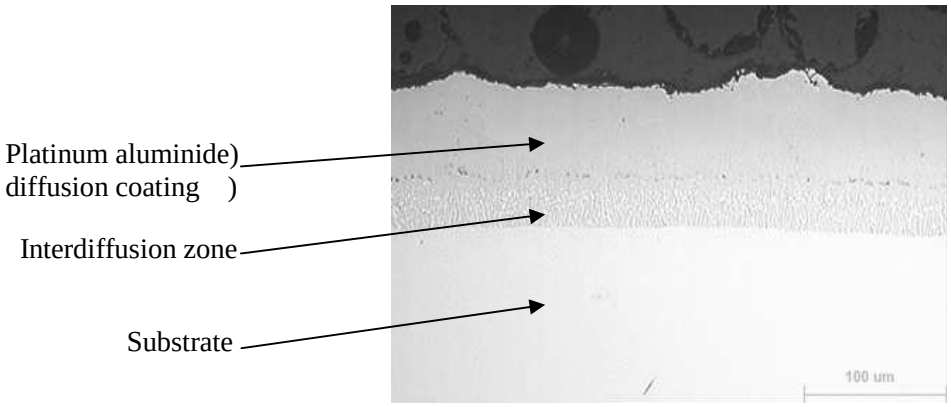

Figure 2.30: Example of platinum-aluminide coating RT-22 deposited on single crystal substrate SC^{2} [19]

Aluminide coatings can be applied by a range of methods such as pack cementation, slurry cementation, chemical vapour deposition (CVD), gas phase CVD, metallising and fluidised-bed technique [36].

However, they offer limited protection under severe corrosion conditions or at temperatures above 1100^{o}C and hence modified aluminide coatings were developed [36]. Chromium, platinum and silicon modified aluminides are the most common, with platinum added for its benefit to high temperature oxidation, and chromium and silicon added to improve hot corrosion resistance. Silicon modified aluminide diffusion coatings are the basis for developing novel coatings in this project and, for more information on diffusion coatings reference can be made to section 8.2.5.

2.5.4 Overlay coatings

Overlay coatings are a family of corrosion-resistant alloys specifically designed for high-temperature surface protection and are referred to as M-Cr-Al-Y coatings where M is the alloy base metal (normally nickel, cobalt or a combination of these two). Chromium provides hot corrosion resistance, but the content is limited by its effect on the substrate and the formation of Cr-rich phases in the coating. The aluminium content, typically 10%-12% by weight, controls the oxidation rate, however, too high an aluminium content significantly reduces ductility. More complex coating systems, involving the addition of other oxygen-active alloy additions, such as hafnium and silicon, have provided higher resistance. These are called M-Cr-Al-X, where X refers to oxygen-active elements other than Yttrium, in which case it becomes M-Cr-Al-X-Y. A typical overlay coating is illustrated in Figure 2.31.

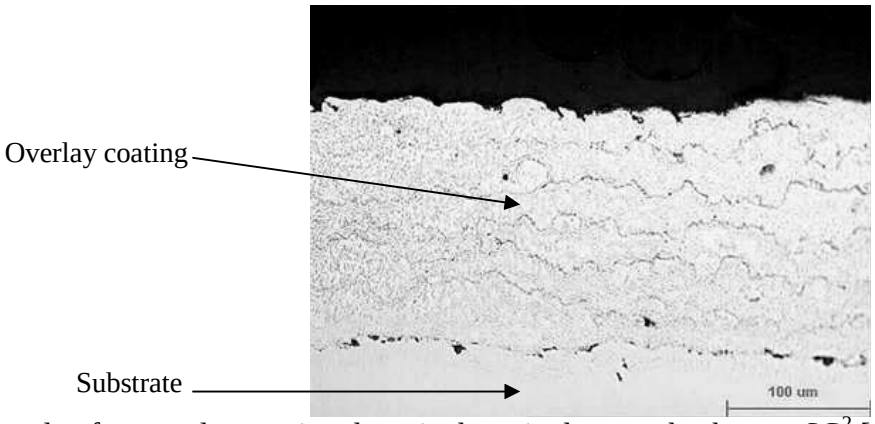

Figure 2.31: Example of an overlay coating deposited on single crystal substrate SC^{2} [19]

MCrAlY coatings have a two-phase microstructure β+γ, with γ increasing the ductility and thereby enhancing thermal fatigue resistance. As with β-NiAl coatings, at high temperatures aluminium is depleted to the thermally grown oxide (TGO). Aluminium is also depleted, by interdiffusion, into the substrate. Therefore, as oxidation/ corrosion increases, the β phase dissolves. This is often described as an aluminium reservoir and the coating life may be measured in terms of the depletion of β [91]. A schematic of the MCrAlY microstructure and a diagram to illustrate the effect of aluminium diffusion to the oxide layer and to the substrate, resulting in depletion of β, are shown in Figure 2.32.

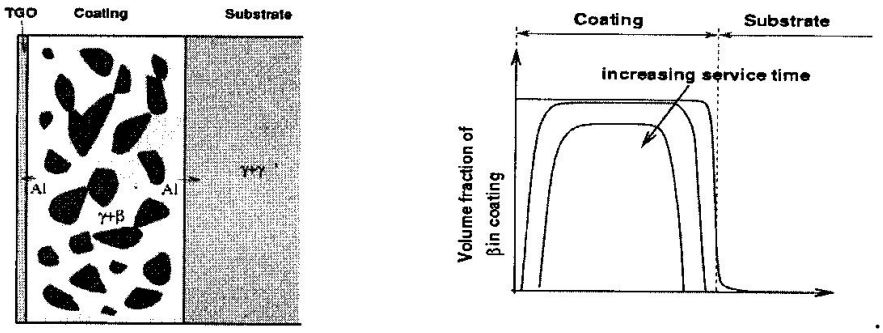

(a) (b)

Figure 2.32: (a) Schematic diagram of the MCrAlY microstructure and (b) aluminium diffusion to oxide layer and substrate [91]

The compositions of overlay systems are selected to provide a good balance between oxidation resistance, corrosion resistance and coating ductility, while the active-element additions improve oxide-scale adhesion and decrease the oxidation rate. Ni-Cr-Al-Y coatings are generally the most oxidation resistant while Co-Cr-Al-Y systems provide good hot corrosion resistance as may be seen in Figure 2.33.

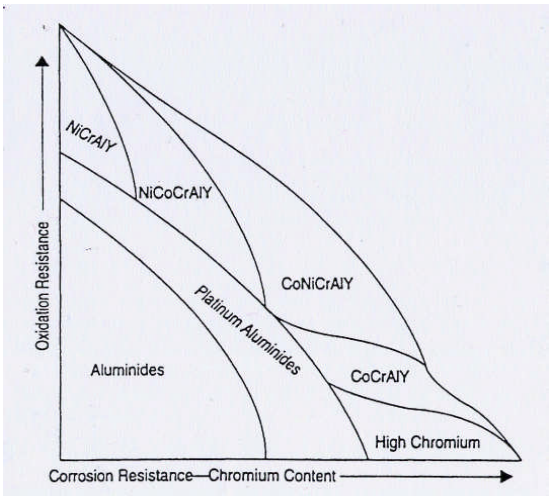

Figure 2.33: Relative oxidation and corrosion resistance of high temperature coating systems [36]

In his review of a range of overlay coatings, Nicholls [98] found the following results:

- Overlay coatings containing chromium (18-22%) and aluminum (8-12%) perform better at high temperatures where oxidation is the predominant failure mode (above 900^{o}C). This results from good adherence of the thin alumina scales, which is assisted by active elements such as yttrium. In high-temperature oxidising conditions, Ni-Cr-Al-Y and Ni-Co-Cr-Al-Y perform better than Co based systems;

- At low temperatures (Type II, 650-800^{o}C), the high chromium content Co-Cr-Al-Y overlay coatings show the best performance, generally outperforming Ni-Cr-Al-Y coatings, whereas corrosion rates for the Ni-Cr-Al-Y and the Ni-Co-Cr-Al-Y overlay coatings can be relatively high.

Improvements to the traditional M-Cr-Al-Y coatings, to increase their hot-corrosion resistance have been investigated, using platinum under-layers and over-layers. Other additions, such as titanium, zirconium, hafnium, silicon and tantallum have also been examined [98].

For this project, as the requirement of novel coatings would be to form coatings that could also be used to coat internal cooling air passages of turbine blades, the decision was made to base the development of novel coatings on diffusion aluminide coatings.

2.5.5 Thermal barrier coatings

Although this project is more directly involved in the development of diffusion and overlay coatings which retard hot corrosion, mention is made of the thermal barrier coating (TBC) and its role in conjunction with corrosion resistant coatings. TBCs offer the potential, in combination with air cooling of hot components, to reduce the oxidation rate. In addition to reducing the oxidation rates by an order of magnitude, reducing the component surface temperature by 150^{o}C will have the added benefit of reducing creep damage to the component and, in itself, increase the operating temperature and hence the gas turbine thermal efficiency.

Two other major benefits can be realised, by using TBCs on highly stressed turbine blades and aerofoils, which will result in lower specific fuel consumption or higher output capacity:

- For the same gas-path operating temperatures, cooling system requirements can be reduced;
- For the same cooling air flow, the hot gas temperature can be raised significantly.

A further benefit, which is often overlooked, is that the ceramic surface temperature remains hot (or is hotter). This means that condensation reactions (deposition of salts) are reduced.

The TBC utilises a ceramic coating, usually yttria partially stabilised zirconia, applied with a bond coat to the substrate material. Deposition processes for TBC systems:

Bond coat	Plasma spraying vacuum/LLPS	
	Physical Vapour Deposition (PVD)	- Electron Beam PVD
		- Plasma assisted PVD
		- Ion plating
		- Sputtering
		- Sputter Ion Plating
	Electroplating	- Occluded plating

Thermal Barrier	Plasma spraying	- air - argon shrouded
	PVD	- E.B.PVD - Plasma assisted PVD - Ion plating

Plasma-sprayed TBCs are well established, having been used since the 1950s [19] to improve component creep lives, particularly in the turbine section. Attention continues to be applied to highly stressed turbine blades and vanes, in particular to these components within commercial gas-turbines. Plasma sprayed TBCs suffer from poor erosion resistance, poor thermal fatigue resistance on small radii and poor surface finish, EB-PVD structures overcome these limitations [93].

Development is in progress at Cranfield University of the next generation EB PVD TBCs, for airfoil applications. This is aimed at producing EB-PVD coating microstructures, which have the same thermal conductivities of the plasma-sprayed coating, yet retaining good thermal shock resistance (strain tolerance) and erosion resistance. Figure 2.34 shows schematically a comparison of plasma sprayed and electron beam–PVD TBCs [93].

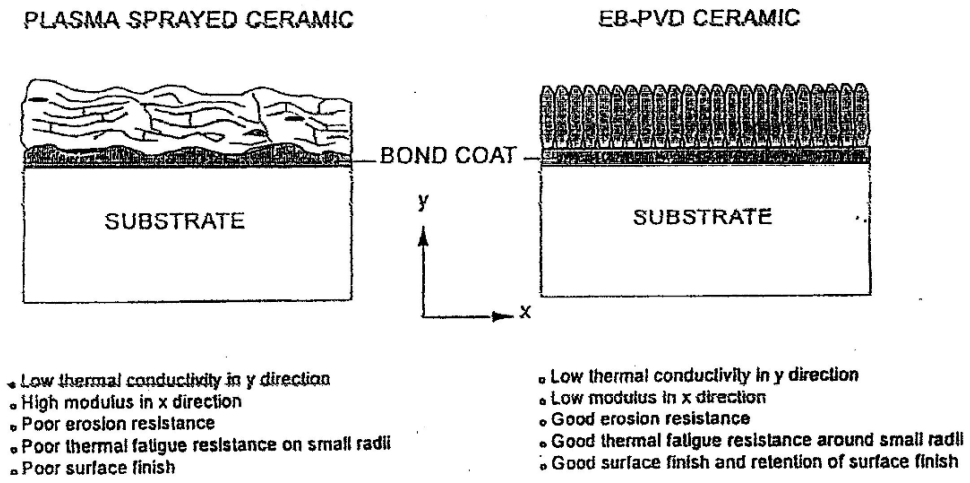

Figure 2.34: Schematic comparison of plasma sprayed and EB-PVD TBCs [36]

The final activity in the development of novel coatings in this project, is to test whether the novel coatings will combine the required corrosion resistance with the facility to bond with TBCs. This is reported in Chapter 11.

2.5.6 Smart coatings

Smart coatings, having several active elements use the concept that, although elements such as chromium and aluminium improve oxidation behaviour, they operate by different mechanisms [100]. By including multiple active elements in one coating, smart coatings provide oxidation-resistance over a wide temperature range. The Smartcoat concept is shown diagrammatically in Figure 2.35, and a micrograph of Smartcoat SmC155 is given in Figure 2.36. The Smart coating aims to improve high-temperature oxidation resistance of overlay coatings by including multiple active elements. Although active elements (yttrium, hafnium, tantalum and silicon) produce similar improvements in oxidising performance, they function by different mechanisms. To protect against hot corrosion a different approach is adopted in the Smart coating. For high-temperature oxidation and Type I hot corrosion resistance, NiCrAlY coatings, which form a stable aluminide scale, offer the best performance, Under Type II hot corrosion conditions, high chromium containing MCrAlY provide better resistance. The Smart coating, developed to resist both forms of attack in a single coating, is a functionally gradient overlay coating produced by using a combination of plasma spray and diffusion techniques [36,100,101,102] .

The addition of TBCs to these combined coatings completes the smart coating, contributing to optimising hot corrosion resistance, oxidation resistance and gas turbine efficiency [100,101,102].

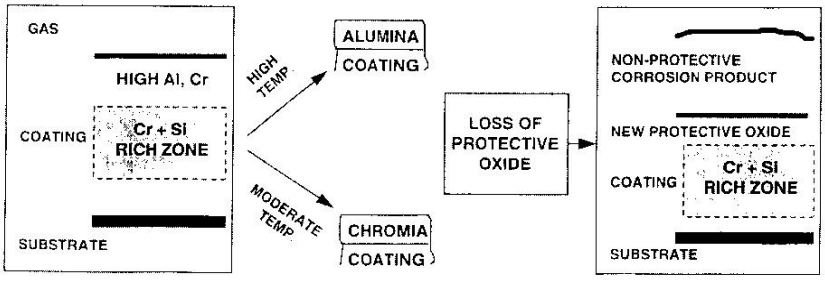

Figure 2.35: Schematic diagram of the smart coating concept [101]

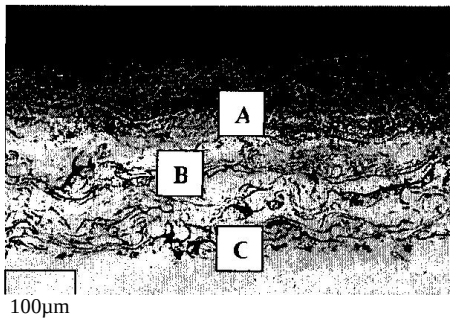

Figure 2.36: Micrograph of Smartcoat SmC155 [100]

Diffusion Coatings	Overlay Coatings	Thermal Barrier Coatings (TBCs)
Formed by surface enrichment of an alloy with : Aluminium (aluminides), Chromium (chromized), Silicon (siliconized). In some systems these are combined, eg chromium-aluminized, silicon-aluminized	Family of corrosion-resistant alloys specially designed for H-T surface protection, (often referred to as M-Cr-Al-Y coatings, where M is the alloy base metal (usually Ni, Co or a combination of these) More recently, other oxygen-active alloying additions to the coating have been used including ; Hf, Si and Y, such that the system is referred to as; M-Cr-Al-X or, M-Cr-Al-X-Y, where X = oxygen-active elements other than yttrium.	TBCs insulate the substrate from the heat of the gas path. A coating system (usually yttria partially stabilised zirconia) usually overlaid on top of an oxidation-resistant bond coat. The bond coat is typically an M-Cr-Al-Y overlay coating or a diffusion aluminide coating.

Table 2.7: Summary of coating types [36]

A summary of coating types is presented in table 2.7. In this project, three typical commercial coatings were used as reference coatings in the corrosion tests, in order to provide comparisons with the hot corrosion resistance of the novel coatings. The commercial coatings which were used in this project, and whose microstructures are shown in Figure 2.37, are:

- GT29+ ; a CoCrAlY overlay plus diffusion aluminide top coat
- RT-22; a platinum-aluminide
- Sermaloy1515; a triple-cycle silicon-aluminide

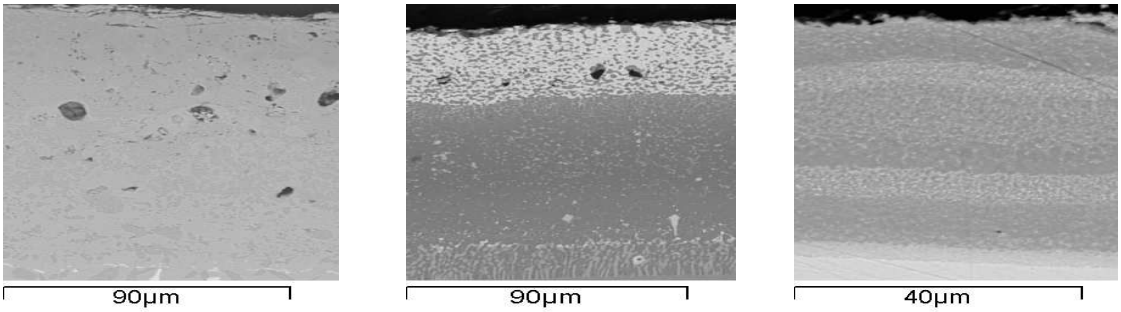

GT29+ RT-22 Sermaloy 1515

Notes: different scales of images

: images produced during the corrosion tests reported in Chapter 7

Figure 2.37: Backscatter (BSE) images of commercial coatings used in this project

2.5.7 Coatings – thermal stability and mechanical properties

In addition to their anti-corrosion properties, coatings must be capable of retaining thermal stability and mechanical properties throughout the required service life of the component. Coatings degrade by losing scale-forming elements to the surface and by interdiffusion with the substrate, which adversely affect their structural stability and protective properties over extended periods of operation at high temperatures. In aluminide coatings, this degradation results in the breakdown of the outer β-NiAl phase by the formation of a γ'-Ni_3Al network. This, after sufficient time, can penetrate through the β-phase. These γ' leaders act as short-circuit paths and cause rapid failure of the coating [95].

2.5.7.1 Thermal stability of coatings

Studies into the thermal stability of a number of diffusion coatings, including pack-aluminide, chromium-aluminide and platinum-aluminide variants showed that the thermal stability of β-NiAl can be improved by the addition of platinum and that the two-layered $PtAl_2$-β structure degrades to single-phased β with no γ' leaders, even after long periods of time [95]. This contributes to the improved corrosion resistance of platinum-aluminide coatings, compared with conventional aluminides.

The diffusion of elements between the substrate and coating can be a major factor for coating performance and, to provide long-term stability at higher temperatures. The development of diffusion-barrier coatings, to minimise the interdiffusion between the coating and the substrate, may be necessary. However, some interdiffusion is required to provide good adhesion and the diffusion barriers should be made to limit the movement of particular problematic elements. If the concept of a diffusion barrier is proven to be effective for giving good interface stability, then substrate compatibility is no longer needed for specifying the overlay coating composition and the overlay coating can be designed for optimised oxidation or corrosion resistance.

Different base-alloy compositions can provide optimum performance, depending on temperature and environment, and in this context, with particular Cr and Al levels, the Ni-Cr-Al-Y systems provide the optimum hot-corrosion-resistant compositions for coatings [36].

2.5.7.2 Mechanical properties of coatings

Resistance of coatings, at high temperature, to cracking by thermally induced stresses and knowledge of the transition from the ductile to brittle condition is critical. Of coating material bases, the ductile-to-brittle transition temperatures (DBTT) of aluminides is higher than that of many of the overlay coatings. As peak tensile surface strains on turbine blades occur at relatively low temperatures the diffusion coatings may have inadequate ductility for relatively high strain applications. Transition from ductile to brittle behaviour as the temperature reduces is significant during gas turbine thermomechanical cycling, during its service lifetime, and may crack the coating through to the substrate interface.

The possibility arises that the crack propagates into the substrate, or may be deflected along the coating/substrate interface, hence reducing component life. The mechanical behaviour of coated components is clearly of major importance in designing protective coatings [36]. Unlike aluminides, the ductile-to-brittle transition of overlay coatings can be modified, by changing the coating composition, as demonstrated in Table 2.8.

Diffusion Coatings	**DBTT (^{o}C)***	**Overlay Coatings**	**DBTT (^{o}C)***
Nickel Alloys		Co-Cr-Al-Y	
LTHA Aluminide	840	18Cr,9Al	235
HTLA Aluminide	600	15Cr,10Al	250
Cobalt Alloys		23Cr,12Al	740
LTHA Aluminide	970	27Cr, 12Al	910
Platinum		Ni-Cr-Al-Y	
Aluminide	>840	38Cr,11Al	430
LTHA	760		
HTLA			

Note : temperature for 1% strain to crack*
Key : LTHA – low temperature high activity, HTLA – high temperature low activity

Table 2.8: Ductile-brittle transition temperatures of diffusion and overlay coatings [95]

2.5.8 Diffusion coating processes

Diffusion processes have been successfully used for many years for improving the environmental resistance of a base alloy, by enriching the surface in chromium, aluminium, or silicon. In this project, as aluminium diffusion was selected as the basis for developing novel coatings; see section 8.3, for explanations on alternative coating processes. Discussions here will be limited to diffusion coatings.

2.5.8.1 Pack-cementation aluminising process

Techniques for applying diffusion coatings to hot gas components include, pack cementation, overpack chemical vapour deposition (CVD), gas phase CVD and metallizing. Fluidized-bed techniques are used for applying diffusion coatings in the laboratory, as it allows the coating of large components with a close tolerance on coating thickness. This results from the uniform temperatures and chemical processes within the fluidized-bed. In the pack-cementation process components for coating are buried in a pack sealed in an aluminizing retort. The retort is heated within a hydrogen- or an inert-gas atmosphere, to prevent oxidation. The required composition and thickness of the coating and subsequent substrate heat treatment determine the actual soaking process cycle, time and temperature. The pack contains:

- A donor alloy that releases solute material at a known rate and thus, determines the pack activity;
- A halide activator, which disassociates during the process cycle and acts to transport solute material from the pack to the component to be coated;
- An inert oxide dilutent to prevent sintering of the pack.

Typical compositions of the pack to produce a range of metallic coatings are shown in Table 2.9. Of the processes shown, those most widely used are aluminizing and chromizing.

Coating	Pack Deposition Composition (wt.%)	Temperature (°C)
Al	Al_2O_3-2.2 Al-1.2NaF	900-1,100
Cr	Al_2O_3-48Cr-4NH_4Cl	850-1,050
Ti	77Ti-3NH_4Cl-bal.TiO_2	850-1,050
Si	Al_2O_3-5Si-3NH_4Cl	850-1,050

Table 2.9: Typical pack compositions and deposition temperatures for halide-activated pack cementation [36]

In this project, the Cranfield University powder pack CVD equipment was used for all coating development and a schematic diagram of the equipment is shown in Figure 8.2. Difficulties in aluminizing the internal passages of turbine blades by in-pack aluminizing led to improved aluminizing diffusion processes being developed [36]. Improved processes included; above-pack aluminizing, vapour aluminizing and true CVD aluminizing.

2.5.8.2 Overpack and gas-phase CVD processes

Both overpack and gas-phase processes yield low-activity coatings, with more ductility and higher purity, thus allowing the coating of internal cooling passages and cooling holes. Interdiffusion between the Al deposit and the substrate alloy causes the formation of the intermetallic coating, either NiAl or CoAl, depending on the alloy base used these coatings may contain most of the elements in the base alloy, either in solution or as dispersed phases.

2.5.8.3 Above-pack aluminising

In this process, the components are suspended above the pack with a carrier gas flowing over the pack to carry the vapour to the component. The diagram of an overpack aluminising or gas-phase CVD retort is shown in Figure 2.38. A further development led to the use of two packs, one piped up the internal passages of the turbine blades and the other leading to the external surfaces of the blades.

Restall et al [103] quoted the major variables of out-of-pack vapour deposition as; process temperature, pack composition, geometric shape of the blades and soak time. Fluoride activators are used to stabilise vapour pressure as they maintain lower pressures than other halides. These include; Na_3AlF_6, (or NaF and AlF_3), NH_4F and AlF_3 [93]. Fluoride activators are also used for low pressure aluminising where the process is under a vacuum of below 100Torr, although pressures as low as 0.1Torr have achieved good results [93].

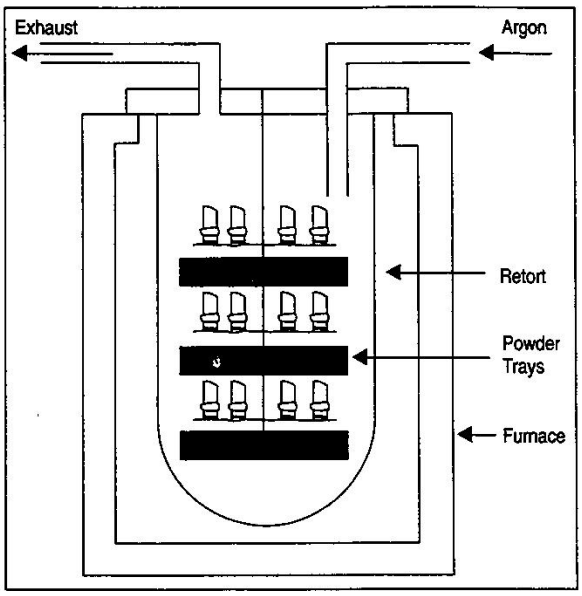

Figure 2.38: Diagram of an overpack aluminising or gas-phase CVD retort [36]

The equilibrium vapour, sublimation or dissociation pressures of various halide activators are presented in Table 2.10. Pressure pulsing has also been used to improve the kinetic pressure of the aluminising vapour giving good results [63].

Activator	Temp ^{o}C	Pressure Torr		Activator	Temp ^{o}C	Pressure Torr
AlF_3	927	1.3		CrF_3	785	0.01
$AlCl_3$	180	760		CrF_2	927	0.001
$AlBr_3$	225	760		$CrCl_2$	927	5.0
NaF	927	0.1		$CrBr_2$	810	0.9
NaCl	927	2.4		CrI_2	793	1.4
NaBr	927	4.8		CoF_2	927	0.05
NaI	927	15.0		FeF_2	927	0.02
KF	927	1.2		$FeCl_2$	934	760
KCl	927	4.0		$FeCl_3$	319	760
F_2	183	760		NH_4Cl	397	760
Cl_2	-34	760		HCl	167	760
Br_2	61	760				

Table 2.10: Equilibrium vapour, sublimation or dissociation pressures of various halide activators [63]

2.5.8.4 Vapour aluminising

Vapour aluminising has many advantages over pack-aluminising if the components can be processed out-of-pack. This process uses an aluminium donor material, usually Al-Cr chips in combination with a suitable activator and enables aluminising vapour to coat a large number of components. Other advantages of vapour aluminising compared with in-pack aluminising are; avoidance of the health and safety issues, disposal problems and expenses of using pack powder, and low thermal inertia means reduced power costs, accurate heating control and reduced cycle times. Improved thermal homogeneity reduces thickness variations in the coatings and improves process control. Other advantages are: reduced post-cleaning operations; the Al-Cr chips can be re-used with screening to remove small chips and easy replenishment between runs; good surface finish; more uniformity of the vapour cloud; and if possible, the facility of switching off the vapour source and of post-heat treatment being carried out in situ.

2.5.8.5 True, gas phase CVD aluminising

In true, gas phase CVD, vapour generators external to the coating chamber supply the vapour for coating the components. In this process, HCl flows through the heated donor material in the external generator at around 300^{o}C, then the vapour is injected into the chamber through piping to coat the components. As the vapour streams can be switched on and off, this process offers better control. Multiple generators may be used that allow highly controlled multiple element deposition. There is also the potential for performing post-heat treatment in-situ thus offering processing stages and complexity. A schematic diagram of the 'true' or gas phase CVD process is shown in Figure 2.39.

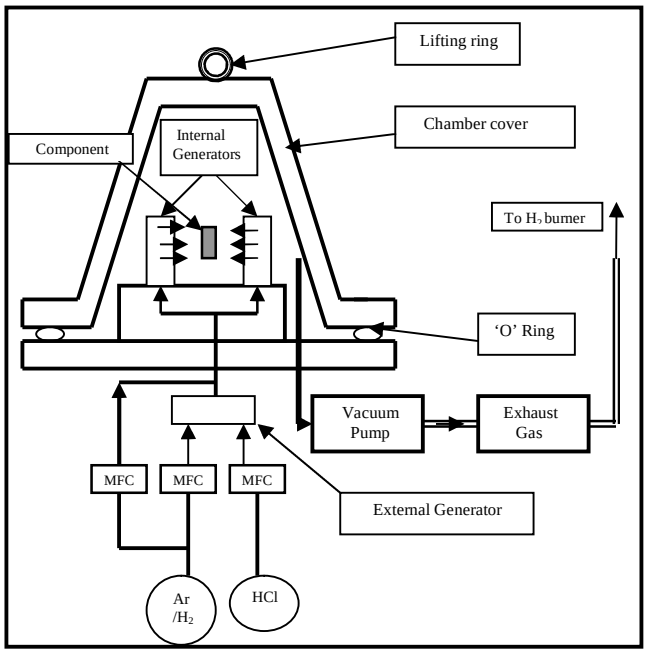

Figure 2.39: Schematic diagram of a 'true' CVD system [63]

The specific arrangement and design of true CVD equipment will depend on the manufacturer. The external generator will contain the source material such as aluminium or silicon pellets. HCl flows through the external generator with the carrier gas, argon or hydrogen, to form aluminium trichloride vapour in the reaction:

$$Al(s) + 3HCl(g) \longrightarrow {}^{3}/_{2}H_2 + AlCl_3(g)$$

From the external generator this vapour is carried into the internal generators which contain more aluminium as Cr-Al alloy chips which react with the $AlCl_3(g)$ to form aluminium subchlorides in the reactions:

$$Al + AlCl_3 \longrightarrow AlCl_n \text{ (where n=1 or 2)}$$

These subchlorides are then directed at the component on the surface of which a further reaction occurs:

$$AlCl_n + Ni \longrightarrow Ni_yAl + AlCl_3$$

The aluminium trichloride is then exhausted to the exhaust cleaning system, if hydrogen is used as the carrier gas it will be burned off in a hydrogen burner prior to being vented. The full potential of gas-phase CVD is realised when multiple elements are involved in the process. A gas-deposition technique to aluminise with yttrium, hafnium, zirconium and silicon additions has been developed. The CVD process can also be used to desulphurise the substrate surface [63] in which case the desulphurisation to 1ppm of sulphur has the same effect as the addition of reactive elements.

2.5.9 Low-activity aluminising

Such aluminide coatings are so called because the aluminium activity in the pack is low, $a_{Al}<1$ [105], the coating phase formed is β-NiAl from the preferential outward diffusion of nickel from the substrate into the coating and an interdiffusion region rich in precipitates is formed between the substrate and coating. These precipitates may be enriched by the refractory elements; Cr, W, Ta, Re, Co and Mo and are secondary phases such as Laves, Sigma, Mu and R-phase. In the low activity/outward diffusion coatings, the alloying elements present in the substrate tend to diffuse into the coating, to a depth depending on their solubility. A schematic illustration of an aluminide coating obtained by low activity pack cementation is shown in Figure 2.40. The external zone is typically Al rich β-NiAl, whereas the internal zone is Ni rich.

The development of novel coatings in this project is based on aluminide diffusion coatings where outward diffusion of nickel from the substrate into the coating is required. The decision to proceed with novel coating development using low-activity aluminising is discussed in more detail in section 8.3.7.

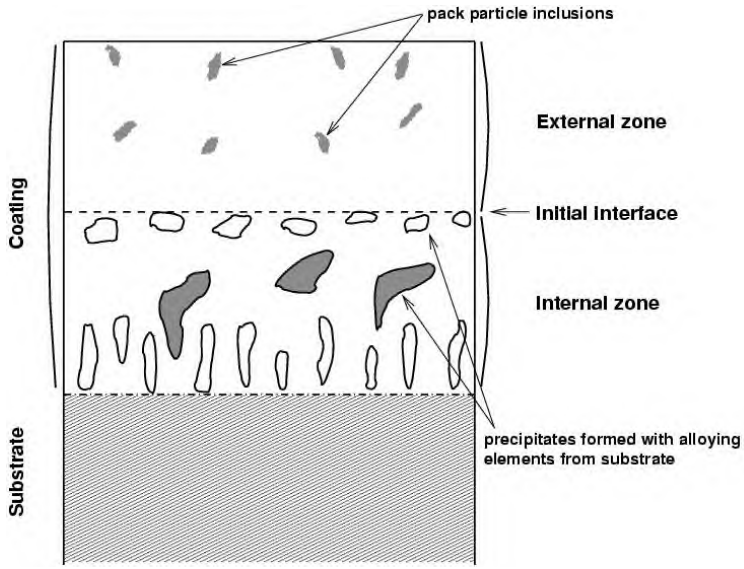

Figure 2.40: Schematic diagram of aluminide coating formed using low activity pack cementation [94]

2.5.10 High-activity aluminising

High-activity aluminides are usually characterized by the formation of δ- Ni_2Al_3 and the preferential diffusion of aluminium into the substrate, thus the initial surface is also the surface of the coated component. High activity aluminizing packs contain large quantities of aluminium as the source material. This increases the pack aluminium activity to unity.

In high activity/inward diffusion coatings, the alloying elements present in the substrate enter in the compound layer in solution, or as precipitates forming during the process. High activity aluminizing involves a lower temperature range (700^{o}C to 850^{o}C) to favour inward aluminium diffusion, whereas low activity aluminizing, at higher temperatures (up to 1150^{o}C) promotes outward nickel diffusion. The classification of aluminide coatings, proposed by Levine and Caves [93] is presented in Figure 2.41.

2.5.11 Vapour deposition using modifying elements

Mention has already been made that the performance of a standard aluminide may be improved by adding modifying elements such as a reactive elements; silicon, chromium or platinum. Silicon aluminising was chosen as the modifying element in the development of novel coatings and this with other modifying elements is described more fully in sections 8.3.4 and 8.3.5. Information is widely available in open literature on the CVD manufacturing methods of using modifying elements.

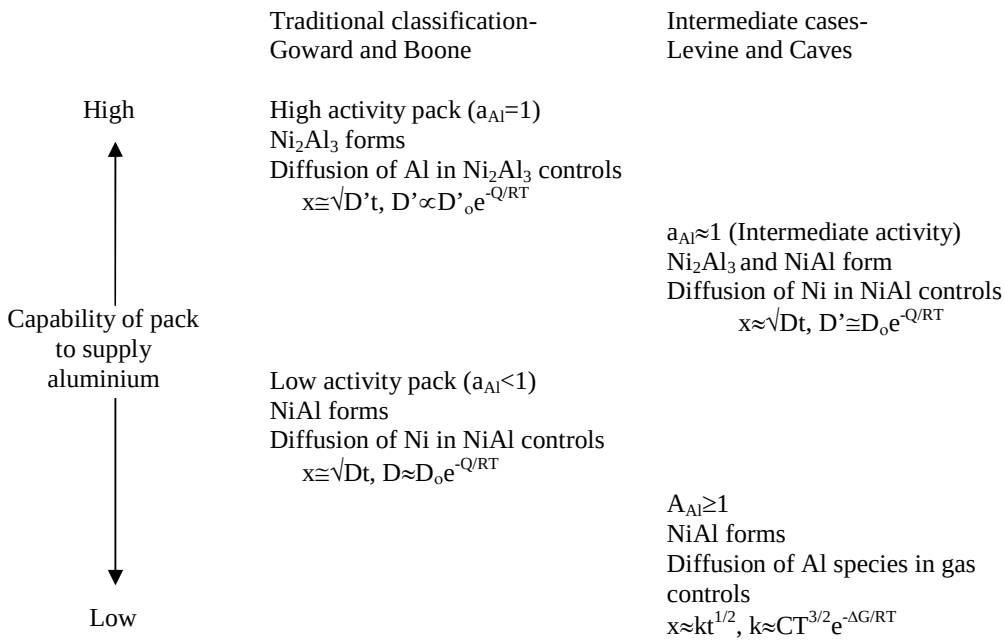

Figure 2.41: Classification of aluminide coatings proposed by Levine and Caves [93]

2.5.12 Reactive elements

Codeposition of aluminium by diffusion of yttrium, hafnium and zirconium [97] has been demonstrated. Multiple CVD co-deposition techniques have been demonstrated of forming enhanced platinum aluminide coatings with Al, Hf, Zr and Si [97]. Other workers have successfully codeposited reactive elements with chromium and aluminium using pack and slurry techniques and have also introduced reactive elements into the substrate as a superalloy addition and by using metallo-organics, evaporation and yttriumising [107].

2.5.13 Post pack-aluminising heat treatment

The chemical components at the surface of the alloy during pack aluminizing have been defined as [63,105,108]:

$$9AlX(g) + 4Ni(s) \longrightarrow 2Ni_2Al_3(s) + 3AlX_3(g) + Al \text{ in pack}$$

As δ- Ni_2Al_3 is brittle and has a low melting point it is not suitable as a high temperature protective coating. Post-aluminising heat treatment (1000°C to 1100°C) changes the coating phase to the more ductile β-NiAl, as the nickel diffuses out of the substrate.

The β-NiAl also has a higher melting point than δ- Ni_2Al_3. Micrographs of low-activity aluminide coatings before and after post-coating heat treatment are shown in Figure 2.42.

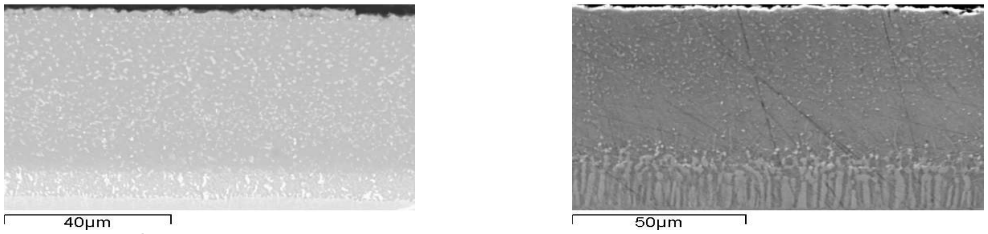

(a) before heat treatment (b) after heat treatment

Notes: different scales of images
: micrographs produced during aluminizing trials described in Chapter 8

Figure 2.42: Micrographs of a low-activity aluminide coating formed on IN738LC before and after post-aluminising coating heat treatment

After post-coating heat treatment the coatings transform into a pronounced three layer structure with:

1. An outer layer of aluminium-rich NiAl, which may contain substrate element precipitates;
2. Middle layer of NiAl with elements such as Cr, Co, Mo, etc in solution;
3. Diffusion layer that is nickel depleted containing secondary phases.

2.5.14 Diffusion-Barrier Concepts

Even with MCrAlX systems and with more advanced overlay coating concepts, element diffusion between the coating and substrate can affect coating performance. Outward diffusion of substrate alloying elements may adversely affect substrate integrity over time. Inward diffusion of coating elements may cause TCP phases to form at high temperatures, at the coating substrate interface, and thus degrade substrate strength. To provide long-term stability, it may be necessary to develop diffusion-barrier coatings that can minimize interdiffusion between coating and substrate [98].

As part of the novel coating development in this project, involving silicon-aluminide coatings, the high temperature oxidation and corrosion tests, particularly on the single crystal CMSX-4 coating, revealed extensive formation of potentially damaging TCP phases. For overlay coatings, precious metals, refractory elements, intermetallics and ceramics have been proposed as diffusion barriers [98]. This issue will be discussed further in Chapter 8.

3. Structure of thesis

The structure of the thesis reflects the series of activities which are involved in the development of novel coatings for gas turbines that burn biomass and waste-fuels. Common to all aspects of the project was the acquisition of knowledge and information, from published documentation and research material. These are set out in the literature review. Car was taken to avoid duplication of information provided in the literature review with that used to support test results, coating development and in discussions. The techniques and equipment, required in the project: to identify potential damaging trace species in fuel-gases, to test this potential on gas turbine substrates and commercial coatings, to develop and produce novel coatings, to test and evaluate their oxidation and hot corrosion performance, and to test their bonding capability for applying thermal barrier coatings, are described in the section on experimental methods and equipment.

The structure then reflects the main stages of original research, development and testing involved in developing and proving the performance of the novel coatings developed to protect gas turbines, burning biomass and waste-fuels, against hot corrosion.

The structure of this thesis is organised such that the results of the original work are presented and discussed within the respective sections. The conclusions contained in each section, in turn, provide the basis for proceeding with the next stage of work, contained in the following section. The structure of the thesis is shown below:

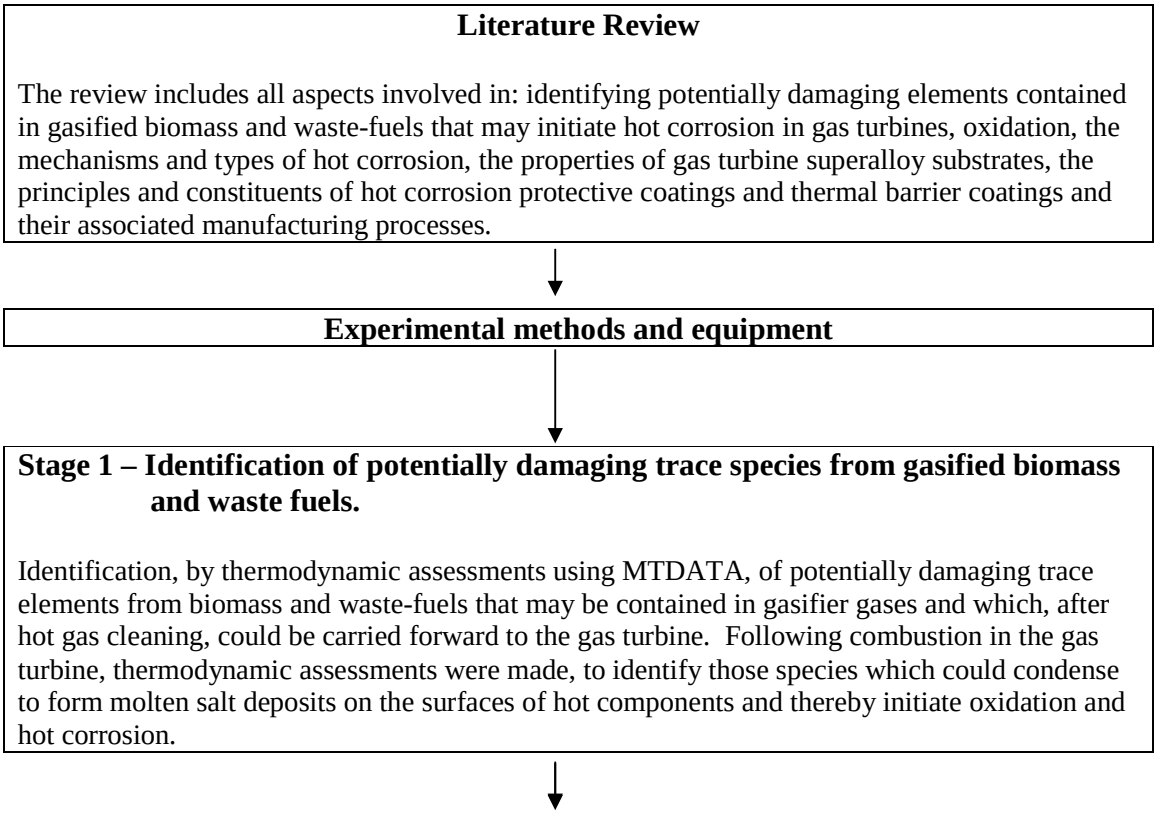

Stage 2 – Carry out two series of corrosion tests, on uncoated superalloys and on hot corrosion resistant commercial coatings.

The objectives of the corrosion tests were to confirm whether, and to what extent, the potentially damaging species, identified in Stage I, would initiate hot corrosion, on these substrates and coatings. Results of the tests were used to assist in the development of novel coatings and to provide comparisons of novel coating corrosion resistance.

↓

Stage 3 – Development of novel coatings.

Literature reviews and evaluation of the Stage 2 corrosion tests provided the bases for deciding on the materials, composition and manufacture of novel coatings, to provide enhanced hot corrosion resistance to the damaging species identified and proved in earlier stages.
Following a series of CVD aluminising and siliconising calibration trials, with post heat treatment, novel coatings were manufactured.

↓

Stage 4 – Performance testing of novel coatings.

Oxidation tests, at 950^{o}C and 1050^{o}C, were carried out to compare oxidation resistance of the novel silicon aluminide coatings and to select candidates for corrosion testing.
Corrosion test series, at 700^{o}C and 900^{o}C, were carried out on the selected novel silicon aluminide coatings, applied to superalloys IN738LC and CMSX-4, under similar conditions as those in the first two series of corrosion tests.

↓

Stage 5 –To test the bonding capability of the novel coating in EB-PVD deposition of TBC onto IN738LC turbine blades.

Produced the selected novel silicon aluminide coating on IN738LC turbine blades for quality evaluation and to determine its effectiveness for bonding a TBC coating to the turbine blades.
For these trials the TBC EB-PVD PYSZ ingots incorporated a thermoluminescent dopant.

↓

General Discussion

↓

Conclusions

↓

Future Work

↓

References

↓

Appendix

4. Experimental methods and equipment

4.1 Introduction

This chapter describes the equipment and methods used in this project to carry out the original research for:

- identifying potentially damaging trace species in gasifier gases which may form molten surface deposits and initiate hot corrosion on gas turbine hot components, and also used to produce binary and ternary phase diagrams for use in novel coating development;
- preparing samples for oxidation and corrosion testing, for weighing and, where applicable, for salt replenishment during testing;
- carrying out oxidation and corrosion tests, to confirm the extent of oxidation and, the initiation and extent of hot corrosion, in samples of superalloy substrates, commercial coatings and novel coatings;
- preparing samples, post testing, for evaluating their chemistry, microstructure and morphology;
- chemical vapour deposition (CVD) used in novel coating development;
- applying thermal barrier coatings (TBC) by electron beam-physical vapour deposition (EB-PVD) for trials on sample gas turbine blades and, post coating, for dividing samples and preparing sample surfaces to evaluate bonding effectiveness.

4.2 MTDATA software for thermodynamic and chemical assessments of contaminants in gases and for producing binary and ternary phase diagrams

MTDATA, the NPL databank for metallurgical thermochemistry, used as a tool in the analysis of problems in chemistry, metallurgy and materials science, was selected for the analyses/tests in this project. The basis for this choice was the applicability of MTDATA as a tool for problems associated with: hot and aqueous corrosion, coating, etching and crystal growth, molten salt chemistry and alloy development [109].

MTDATA comprises a suite of related modules which retrieve thermodynamic data from databases and carry out specified calculations on the data. MTDATA incorporates the following program modules:

- UTILITY ; database management and post processing,
- THERMOTAB ; thermodynamic functions and data management,
- ACCESS ; retrieval and selection of data for systems,
- MULTIPHASE ; flexible calculation of equalibria in multicomponent systems,
- UNARY ; data comparison and assessment,
- GPLOT ; thermodynamic functions of solution phases,
- BINARY ; calculation of binary phase diagrams,
- TERNARY ; calculation of ternary phase diagrams,
- APPLICATION ; determination of phase boundaries,
- COPLOT ; calculation of predominance area diagrams,
- FITANDPLOT ; checking, fitting and converting data.

The MTDATA internal databases used for in the thermodynamic assessments for identifying substances in gasifier gases were;
- SGTE Substance Database v.10.0 - 9 May, 2001,
- NPL Salts Database v. 2.0 – 28 November, 2001,
- SGTE Unary Database version v. 4.4 – 20 July, 2001.

Thermodynamic equilibrium composition in hot flue gas conditions was modelled using the MULTIPHASE module of MTDATA version 4.71. The gas phase was modelled as an ideal gas and the condensed phase as pure substances.

The MTDATA MULTIPHASE module used for the study [109] calculates multiphase, multicomponent equilibria. Phases may include alloys, molten salts, gases, aqueous solutions, slags and pure stoichiometric substances in combination. The equilibrium state for calculations is defined by specifying the temperature, pressure or volume, and quantity of substance. Data on elements, compounds, solutions and salts for use in the calculations are retrieved from the appropriate internal databases within MTDATA. Two types of calculations offered by MTDATA are; Stage 1, which uses true energy minimisation and gives very reliable results, and Stage 2, which achieves energy minimisation by equalising the chemical potentials of the components between the phases, which is used to calculate substances less than 10^{-6}. For the calculations used in this study, Stage 1 was used and proved to be effective in most cases. In all calculations in this study all species were included. Although MULTIPHASE is configured to deal with at least 200 substances, the actual limits depend on the type of computer being used, and in the few calculations that failed re-calculations were carried out over the narrower range of temperatures where the error occurred. Where further difficulty arose, the Robust Stage 2 option was used to confirm the result, as this option calculates equilibria in systems with large numbers of species. Robust Stage 2 is a combination of Stage 1 followed by Stage 2, which repeats Stage 1 only if equilibrium is not achieved after Stage 2, and if difficulties have arisen.

Prior to each simulation:
- the content of each element in the gases was keyed-into a standard screen format which converted ppm/mols automatically;
- selections were made of the species and phases to be used in each assessment calculation.

The MULTIPHASE module was also used for preparing ternary phase diagrams, to explore silicon content in CVD powder packs during the novel coating development stages described in Chapter 8.

4.3 Corrosion testing

The tests were executed in accordance with the Cranfield University Power Generation Technology Centre's Standard Operating Procedure for Sample Preparation and Spraying Salt Solutions on to Corrosion Specimens. These detailed the precautions to be taken and conditions for the tests with regard to the use of specified personal protective equipment, vented spray cabinet, methods of preventing contamination of surrounding areas, use of individual sprays and bottles for each salt, labelling of each item. Disposal of waste solution, gloves and other contaminated materials was carried out in accordance with Cranfield University regulations.

The series of laboratory tests used the well established deposit replenishment technique to investigate the effects of the compositions of the species selected on superalloys and coatings [19]. The test apparatus has evolved over a 20 year period and provides atmospheres in the furnace by closely controlling the inlet gases from pre-mixed gas bottles and the analysis of outlet gases. Sample preparation, the spraying of salt solutions and weighing activities pre- and post-tests were carried out strictly in accordance with the Power Generation Technology Centre (PGTC) standard operating procedure. The main procedures and equipment used in the tests are summarised below.

4.3.1 Sample preparation

Samples for corrosion test series 1 and 2 were provided in the form of bars of eleven chamfered cylinders, shown in Figure 4.1. For series 1 corrosion tests, samples of uncoated IN939, IN738LC and CMSX-4 were provided. Cylinders of IN738LC and CMSX-4, precoated with commercial coatings GT29+, Rt-22 or Sermaloy 1515 were used for corrosion test series 2. Samples used in novel coating development trials, for cyclic oxidation tests and corrosion test series 3 and 4, consistd of discs, approximately 4mm thick, cut from bars of IN738LC and CMSX-4.

For corrosion test series 1 and 2, deposits of the salts were sprayed on the outer body of each sample. Prior to exposure, the following preparatory operations on the cylindrical samples were carried out:

(a) Cutting; each sample was parted off in a precision cutting machine, using a cubic boron nitride wheel, at a distance of approximately 1.0-1.3mm from the end chamfer, so that a 2mm stub remained at the top. This stub enabled the sample to be manipulated during salt species spraying operations before and during the test programme.

(b) A grooved mark; 1mm deep, was cut in the top chamfer of each sample, for use as a reference point for; taking measurements, coating salts, mounting and post test analysis.

(c) Cleaning; each sample was cleaned by immersion in Volasil 344 in an ultrasonic bath for 15 minutes and then, using the same process, in isopropyl alcohol (IPA). After cleaning, samples were placed in individual, labelled plastic bags.

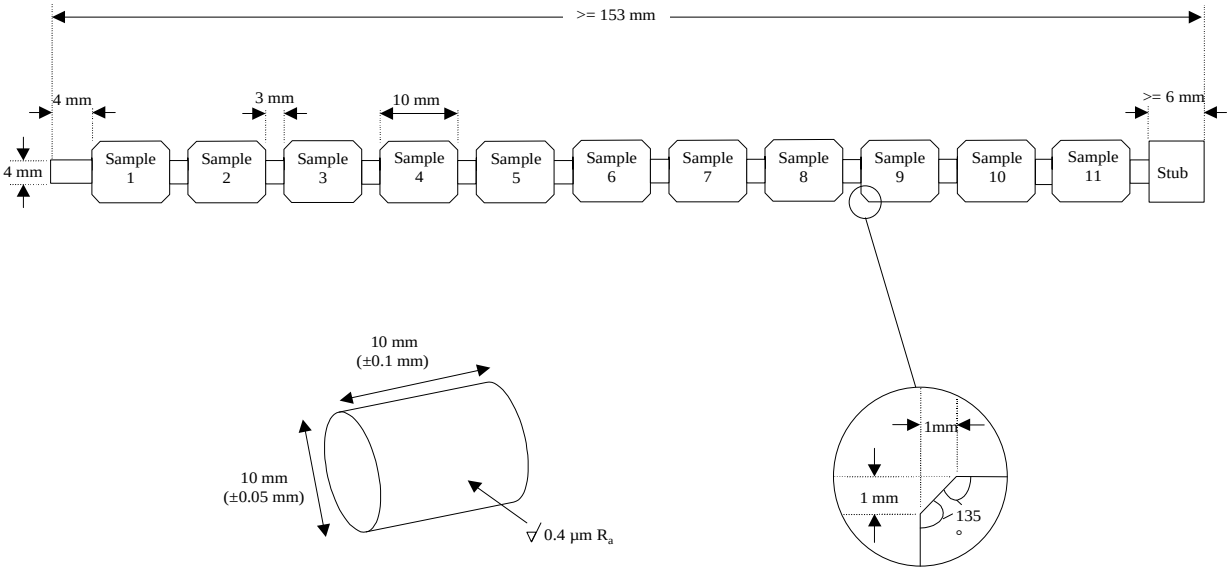

Figure 4.1: Illustration of samples as received, for series 1 and 2 corrosion tests [19]

(d) Cutting; each sample was parted off in a precision cutting machine, using a cubic boron nitride (CBN) wheel, at a distance of approximately 1.0-1.3mm from the end chamfer, so that a 2mm stub remained at the top. This stub enabled the sample to be manipulated during salt species spraying operations before and during the test programme.

(e) A grooved mark; 1mm deep, was cut in the top chamfer of each sample, for use as a reference point for taking measurements, for coating salts, mounting and post test analysis.

(f) Measurements; were made on each cylindrical sample diametrically, eight times, using a vernier micrometer having a resolution of ± 0.001mm. The first measurement on each sample was made at '9 o'clock', followed by clockwise rotation and measurement at every 45^{o}, as shown on Figure 4.2.

(g) Crucible cleaning; before placing samples into alumina crucibles, each crucible was cleaned in water and then IPA after which it was pre-heated at 1000^{o}C for 24 hours. Crucibles with samples were stored in a desiccator, containing regenerated desiccant, dedicated to this series of tests and labelled as such, prior to the test and then between each 100 hour exposure period.

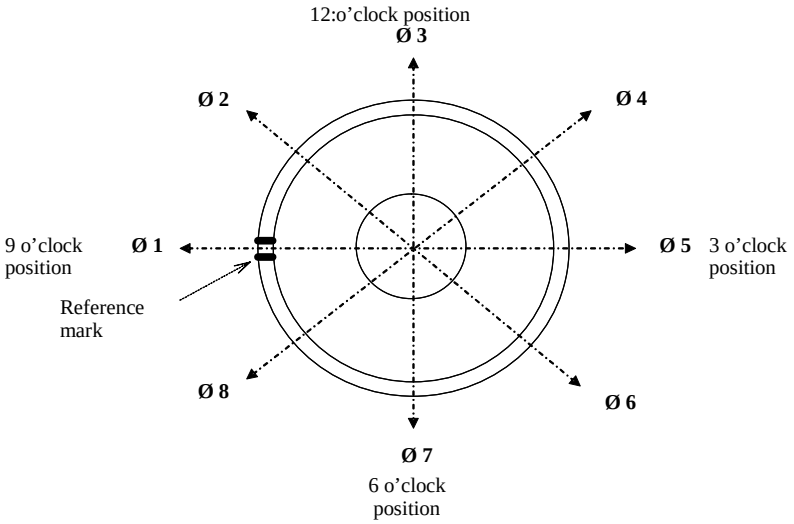

Figure 4.2: Cylindrical samples; micrometer diameter measuring procedure [19]

4.3.2 Furnace and equipment

A horizontal controlled atmosphere furnace was used for all four series of corrosion tests and a schematic diagram is shown in Figure 4.3. Prior to the corrosion tests, the furnace temperature was calibrated, to provide an average along the sample carrier of 700^{o}C. For example, for Type II corrosion tests the temperature controller was set at 725^{o}C to give an average temperature across the hot zone of 700^{o}C.

Two gases were used for all corrosion tests. In the proportion of 50:50 the gases were:

- 800ppm HCl, balance $N_{2;}$
- 500ppm SO_2, 41.9 %O_2, balance $N_{2,}$ for corrosion test series 1 and 2,
  500ppm SO_2, 39.0 %O_2, balance N_2, for corrosion test series 3 and 4.

Each gas bottle supplied its own mass controller, set at 25cc/min, to provide a total mass flow along the common main of 50cc/min.

Each sample was contained in its own alumina crucible for the duration of the tests. Throughout the test period when not in the furnace, samples and crucibles were stored on the labelled shelf of a dedicated dessicator.

4.3.3 Weighing and salt replenishment

4.3.3.1 Weighing

Weighing of samples and crucibles was carried out on a Sartorius microbalance, having a resolution of ± 0.01mg. Prior to the tests commencing each sample was weighed alone, then the crucible alone and then each crucible containing its sample.

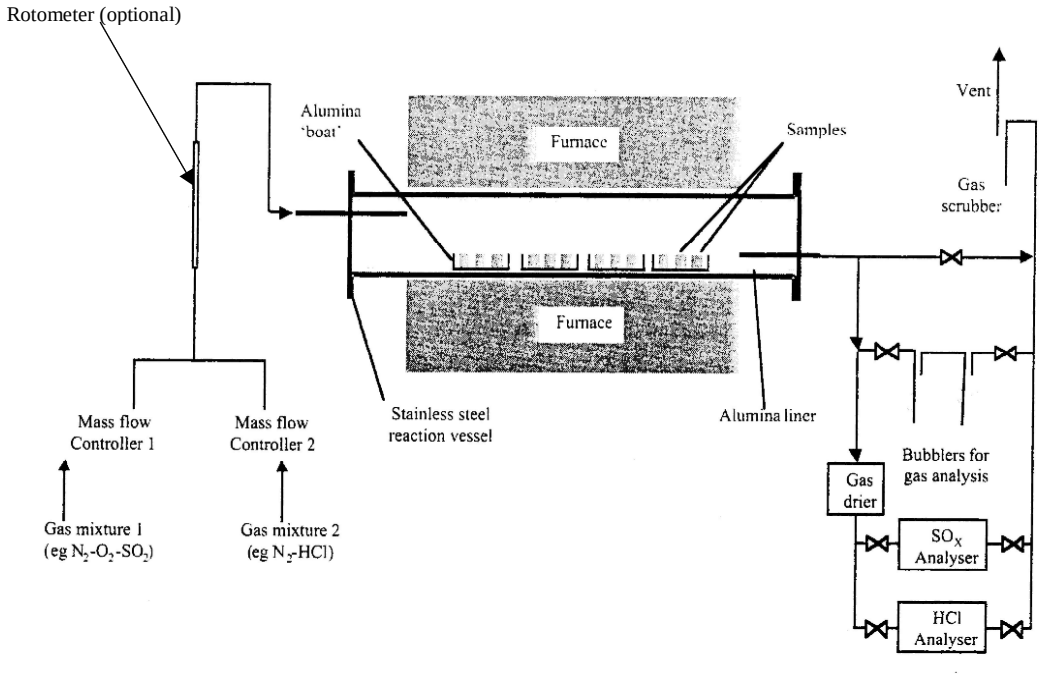

Figure 4.3: Schematic diagram of horizontal corrosion testing furnace [53]

During the salt spraying process, it was necessary to heat the samples on a hotplate to ensure that the water transporting the salt evaporated fully after each salt application. Finally, when the correct amount of salt(s) had been applied, the sample, crucible and crucible containing its sample, were weighed cold. The weighing and salt replenishment procedure, after each of the 100 hours test, consisted of:

(a) weigh crucible and sample together then weigh separately (cold)
(b) weigh sample (hot)
(c) spray salt
(d) weigh sample (hot) until correct amount of salt has been added
(e) weigh sample and crucible (cold)

4.3.3.2 Salt spraying process

Salt deposition was made by spraying a mist of the salt in water solution on to the pre-heated sample (100°C to 150°C), through an artist air brush. The water evaporates to leave an even layer of deposit uniformly around the sample surface. Figure 4.4, illustrates the spraying application technique, where variables such as distance of air brush from sample, air brush height and spray time, were calibrated and standardised. The spray controller setting was adjusted to provide an optimum spray rate, depending on the salt to be sprayed, after which each operation was repeatable. Any reduction in spray quantity during spray operations were caused by salt solidifying in the area of the nozzle, indicating it was necessary to clear the nozzle.

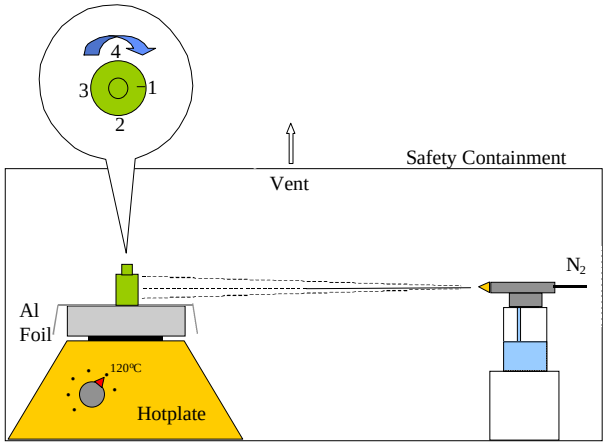

Figure 4.4: Illustration of salt spraying technique used in corrosion tests [69]

In accordance with the departmental COSSH procedure all salt spraying was carried out in the same dedicated, vented cabinet, with a separate spray container for each salt solution. Items of the equipment were uniquely identified and carried hazard notices.

4.3.4 Post corrosion test evaluation

4.3.4.1 Post corrosion test sample preparation

(a) Cylindrical samples

To prepare a section of each corroded sample to obtain data from microscopy image measurements, cylindrical samples were mounted vertically in a special jig. Shown in Figure 4.5, the mounting jig contains two locating pins and a knife edge which keeps the sample parallel against them. The sample is fixed in the jig by filling it with epoxy resin in combination with Potters ballotini (0.04 – 0.07 silica glass powder) and exposed to a vacuum to remove air bubbles. The knife edge touches the reference mark made before exposure (described in the pre-exposure sample preparation section), so that the knife edge will remain. This mark.will indicate the original positions of pre-exposure sample measurements and the right position for post-exposure image measurements.

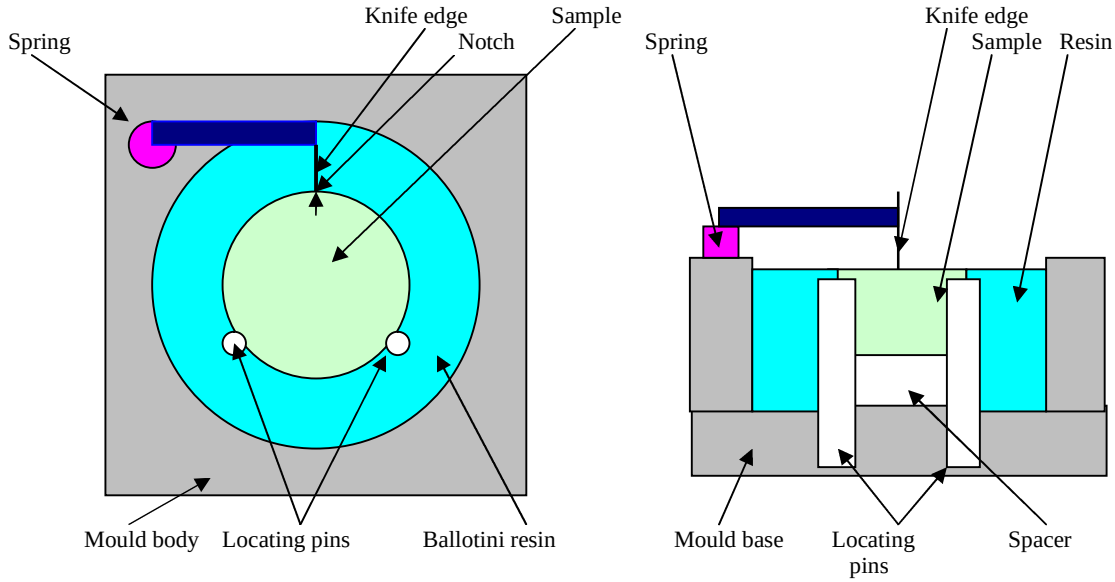

Figure 4.5: Diagram of mounting arrangement for cylindrical samples

When the epoxy resin has hardened, the samples are sectioned on their mid-point, using a Bueller Isomet 2000 precision saw with CBN cutter and then ground and polished, using mineral oil lubricants to ensure that water soluble species remained in the prepared sections, using semi-automated grinding and polishing machines.

(b) Sample discs

Post corrosion tested sample discs were sectioned using a Struers Isomet precision saw, with a 6" CBN wheel, cleaned in IPA, then mounted in conductive bakelite using the Bueller Simplimet 2000 auto-mounting press. After cleaning in IPA, the samples were ground and polished using mineral oil lubricants.

The typical grinding and polishing procedure for mounted cylindrical samples and discs, using a Bueller Metaserv Motopol 12 machine, consisted of:

Grinding

1st Grind: 120 grit grinding paper for 3.5 minutes at 170rpm, contra-rotation with a load of 50lbft, wash with IPA and blow dry;

2nd Grind: 240 grit grinding paper for 3.5 minutes at 170rpm, contra-rotation with a load of 50lbft, wash with IPA and blow dry;

3rd Grind: 240 grit grinding paper for 3.5 minutes at 170rpm, contra-rotation with a load of 50lbft, wash with IPA and blow-dry;

4th Grind: 1200 grit grinding paper for 3.5 minutes at 170rpm, same direction of rotation, with a load of 50lbft, wash with IPA and blow dry;

5th Grind: 1200 grit grinding paper for 3.5 minutes at 170 rpm, same direction of rotation, with a load of 50lbft, wash with IPA and blow dry;

Polishing

1st Polish: 6 micron hard grinding wheel, spray 3micron oil based liquid, for 2 minutes at <150rpm, same direction of rotation, with a load of 30lbft, wash with IPA and blow dry;

2nd Polish: 3 micron hard grinding wheel, spray 3micron oil based liquid, for 2 minutes at <150rpm, same direction of rotation, with a load of 30lbft, wash with IPA and dry;

Finally checks were made, by using optical microscope, that the sample was polished to an acceptable standard.

4.3.4.2 Post corrosion testing evaluation methods

Methods of evaluating results of corrosion tests were: mass change, and the use of metrology and scanning electron microscopy (SEM), to quantify the microstructural changes which occur by the end of each corrosion test series. Mass changes were derived from weighings of samples and crucibles, before and after each of the five 100 hours of exposure which comprised each corrosion test series. From these, the gross mass change, spall mass and net mass change were obtained for each test period.

The depths of degradation in coatings were measured, by metrology, as the change in sound metal. Microstructural changes which occur as high temperature corrosion of coated superalloys proceeds, which were characterised and measured by SEM, result from:

- outward growth of an oxide scale with partial or total detachment of this scale, particularly at the corners or edges;
- general internal penetration with a consequential loss in load-bearing cross-section;
- internal attack generally at grain or phase boundaries leading to an increase in stress concentration;
- depletion of the elements of the alloy matrix;
- precipitation of new phases now stable in the modified component of the alloy matrix.

(a) Metrology

By analysis of the pre-exposure and post-exposure dimensional measurements a set of data is produced that enables calculation of the material loss. This was achieved, for the cylindrical samples of corrosion test series 1 and 2, using a commercial Image Analysis System and reflected light microscope, with accurately calibrated x-y stages. This measures the position of the undamaged sample at a minimum of 24 locations round the circumference of the sample, and the depth of internal corrosion at each location.

The diagram in Figure 4.6 shows the principle by which the image analyser works. The procedure starts by selecting the position of the datum or origin, after which the microscope is moved by pre-selected stages round the sample and, at each stage, the analyser measures the angles and distance of the X and Y coordinates.

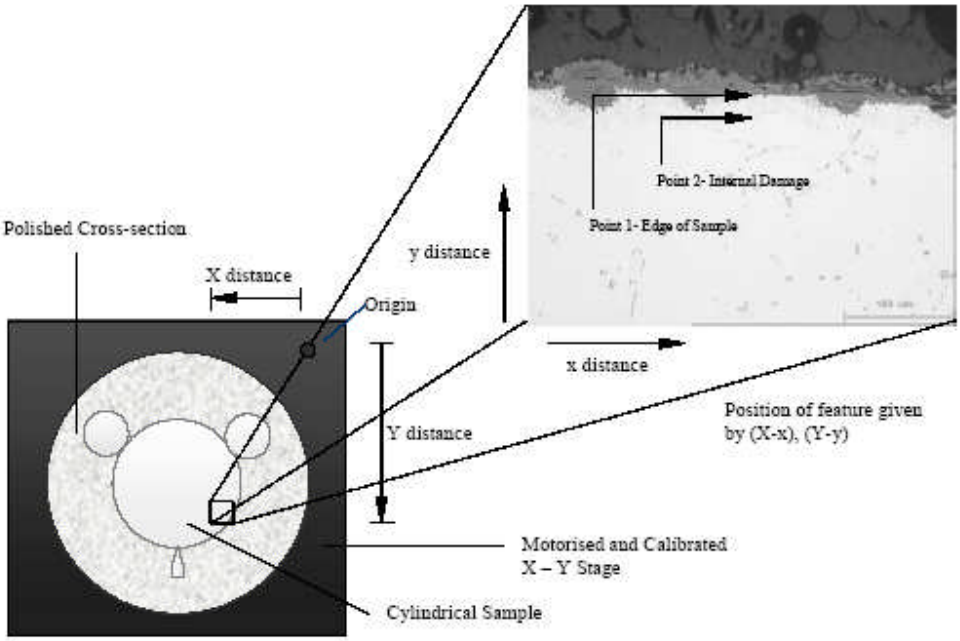

Figure 4.6: Post-exposure measurements process on image analyzer system [19]

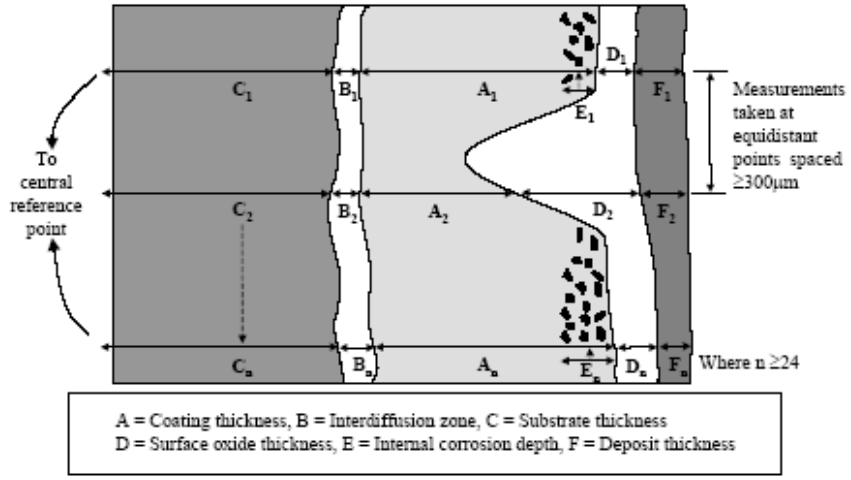

Figure 4.7: Diagram of post-exposure sample metrology procedure used to generate data for assessing coating corrosion performance [53]

The measurements and data provided by the image analyzer system for assessing coating performance are shown in Figure 4.7.

It was found when parting disc samples that, in some cases, the cutter veered during the operation, resulting in the two sides not being parallel. It was decided to measure the changes in sound metal for disc samples, after the cyclic oxidation tests and corrosion test series 3 and 4, by using the scanning electron microscope (SEM).

(b) Scanning electron microscope (SEM)

Scanning electron microscopes were used to optimise microstructure characterisation of, and make comparisons of, coated superalloy samples, for coating development and during odixation and corrosion testing.

The scanning electron microscope (SEM) used at Cranfield for the first two corrosion test series was the high resolution FEI XL30 SFEG analytical SEM. Evaluations of corrosion test series 3 and 4, cyclic oxidation tests and TBC bonding, were made using the FEI XL ESEM TMP SEM, in the high vacuum mode. In both cases the SEMs were equipped with Energy Dispersive X-ray (EDX) and back-scattering (BSE) imaging facilities. EDX calibration was carried out with a cobalt standard for the former SEM and with a nickel standard for the latter. The general approach was to produce BSE maps of the relevant elements, with an EDX line scan at locations through the coating, to provide the content (atomic%) of elements along the line.
Where relevant to provide more information on microstructures of degraded coatings, the approach was to repeat SEM analysis at higher magnification.

Thicknesses of scale and deposits and of degraded coatings in disc samples were determined by a series of measurements on the BSE images and then averaged. For the conductive bakelite mounted disc samples no additional conducting material was required when loading the sample into the SEM, whereas samples mounted in epoxy-ballotini, required bonding to the SEM carrier with conducting foil.

4.4 Novel coating production

4.4.1 Coating by chemical vapour deposition

The need to develop hot corrosion protective coatings for gas turbine blades, having internal cooling air passages, prevented the use of direct in-line transmitted methods of coating. Chemical vapour deposition (CVD) was the only feasible method to enable cooling-air passages within blades to be coated and the powder-pack CVD equipment was used for this purpose. The CVD chamber and its main components are shown diagrammatically in Figure 4.8.

Prior to loading the chamber, powder constituents of the appropriate purity and particle size had been mixed under controlled conditions. Trays to carry the powder and samples were grit blasted and cleaned in IPA, after which the powder and samples were loaded, ensuring that samples were separated from the top, bottom and sides by at least 10mm of powder.

Preparations for the deposition process aimed to avoid any impurities contaminating the powder pack, or the substrate, and the subsequent coating. The chamber base and tray support structure were cleaned, air-blown to remove dust and the sealing O-ring cleaned and smeared with silicon grease to ensure a seal when vacuum was raised.

After the chamber was boxed-up, purging and gas blanketing were carried out. On each occasion vacuum raising was achieved by a vacuum pumping set, consisting of a rotary pump and a Rootes blower, and ending when the target pressure of -0.95 Bar had been sustained for 15 minutes. The chamber was then backfilled with N4.8 argon on two occasions and on the third with N6.0 (99.99%) argon. After the third purging procedure argon was flowed through the chamber for 40 minutes at 10 – 15 lpm to remove any residual oxygen in the system. A water-based scrubbing system scrubbed the exhaust. Following completion of three purging and blanketing operations, the pre-heated furnace (to 1100^{o}C) was lowered over the chamber and switched on. Timing of the CVD soak period commenced when the internal chamber temperature reached 1050^{o}C, at which it was maintained for the required soak period. On completion of the soak period the furnace was switched off, lifted clear of the chamber and relocated on its trolley. When the chamber temperature had fallen to 900^{o}C, argon flow was resumed and controlled at between 2.0 lpm and 5.0 lpm to maintain a positive chamber pressure. Argon was shut off when the chamber temperature was below 300^{o}C.

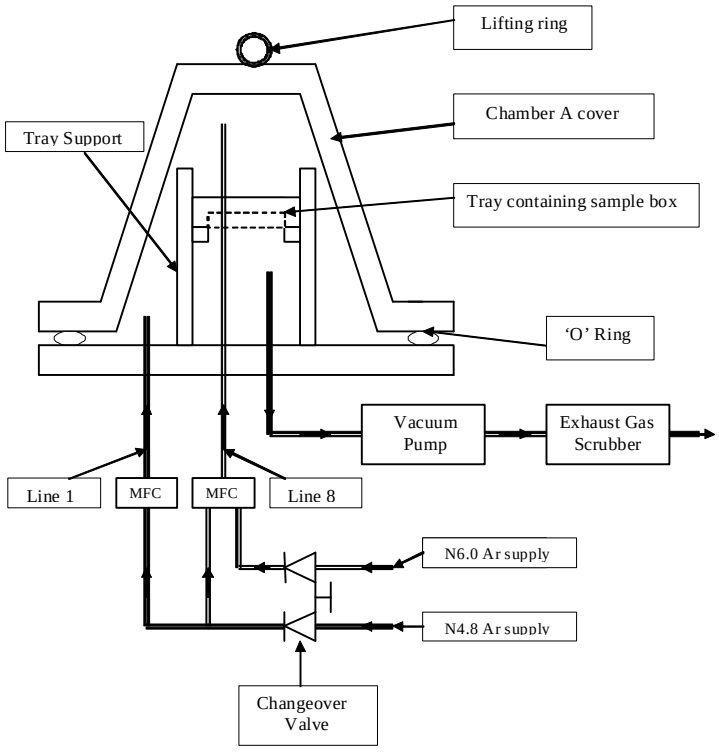

Figure 4.8: Schematic diagram of powder pack CVD equipment

The CVD equipment at Cranfield consisted of two chambers and all operations for this project were carried at in Chamber A, the left hand chamber seen in the photograph in Figure 4.9. When the chamber had stabilised at laboratory temperature, samples and trays were removed, residual powder packed, packaged and disposed of, in accordance with laboratory procedures.

The powder pack CVD process has two shortcomings, the main one being the variation in coating depths, between the bottom and top sides of sample discs. These adversely affect hot corrosion protection provided by novel coatings where the top side coating depth is significantly less than that of the bottom side. This phenomenon is described more fully in Chapters 9 and 10, dealing with oxidation and corrosion tests. The second shortcoming is the wastage of powder in the pack which is only used for one CVD operation before being disposed of. These shortcomings are overcome by true CVD whereby components(s) for coating are located inside, but not in contact with the CVD chemicals. The principle is shown in the schematic diagram of true CVD in Figure 2.39.

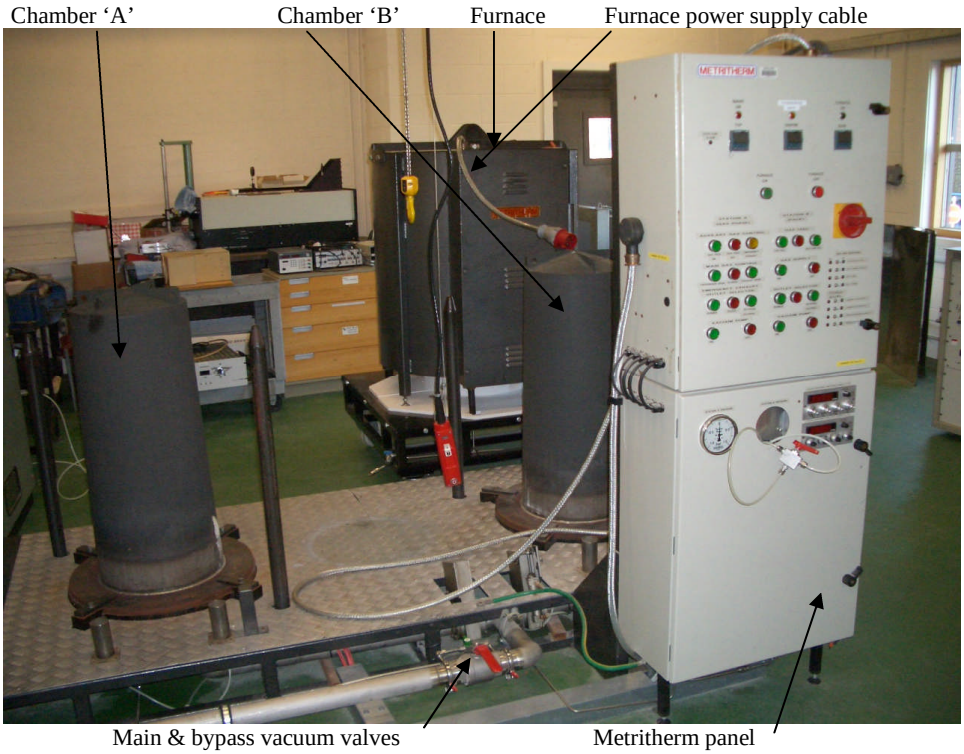

Figure 4.9: Photograph of the CVD equipment at Cranfield University

4.4.2 Post-CVD heat treatment

After chemical deposition, the diffusion coating process was completed by heat treatment in the Cranfield vacuum furnace, with the exception of twelve samples for the third and fourth series of corrosion tests, which were heat treated at TSTL. The vacuum furnace at Cranfield operated under high vacuum ($<10^{-4}$ mbar) which may have allowed evaporation of elements from samples at higher temperatures.

For description of the heat treatment/diffusion mechanism, reference should be made to section 2.5.13. The heat treatments used in coating production in this project were:

- IN738LC : 2 hours at 1120^{o}C and 24 hours at 843^{o}C;
- CMSX-4 : 2 hours at 1140^{o}C and 20 hours at 870^{o}C

4.5 Isothermal oxidation testing

The two isothermal oxidation test series were carried out using a horizontal, controlled atmosphere furnace. The dry combustion gas mixture, comprising nitrogen, oxygen, carbon dioxide and argon, was supplied to the furnace through a rotameter for flow measurement, bubbled through de-ionised water then supplied to the furnace through a heated tube. All sample preparations were the same as those used for the corrosion tests. Between each 100 hours test period samples and crucibles were weighed in a similar manner to those for the corrosion tests, as explained in section 4.2.3.1.

4.6 Thermal barrier coatings : electron beam-physical vapour deposition

The bonding trials of thermal barrier coatings (TBC) on IN738LC low pressure gas turbine blades are described in section 11. Several deposition methods for TBC systems are listed in section 2.5.5. This section describes the electron beam- physical vapour deposition (EB-PVD) equipment used in this project, shown in Figure 4.10.

The evaporation equipment used for the deposition of the TBC is a modified Electrotech 680 square chambered ion plater, consisting of an upper- and lower-chamber. Each chamber has its own pumping system of diffusion pump and vacuum pump. A separation plate between the two chambers allows different pressures to be maintained in the two chambers. The upper chamber operates at process pressure, the lower pressure in the lower chamber facilitates electron gun operation. The furnace and substrate manipulation system are located in the upper chamber, providing two rotating substrate positions above the source at a nominal distance of 15 cm and provide rotation speeds of between 0 and 60 rpm. The filament assembly and high voltage components of the electron beam gun, and the ingot rotation and elevation mechanisms, are located in the lower chamber.

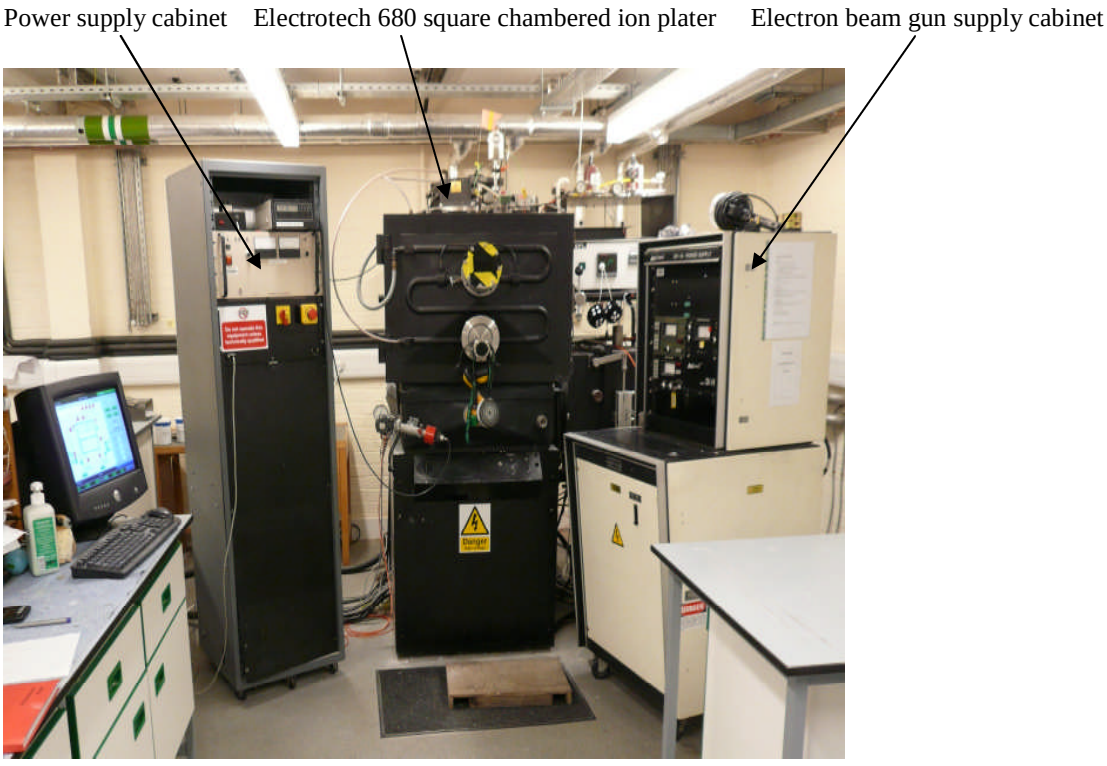

Figure 4.10: Electrotech 680 EB-PVD equipment for TBC deposition

A modified standard single hearth Temescal beam gun, driven by Temescal CV14 power supply, capable of operating the gun at a maximum power of 14 kW, was the evaporation source. A 33 mm hole drilled in the base of the crucible allows the ceramic ingots to rotate and rise within the hearth. Figure 4.11 shows the two blades, each welded to a Nimonic 75 plate carrier, mounted in the furnace, prior to EB-PVD and then after TBC deposition.

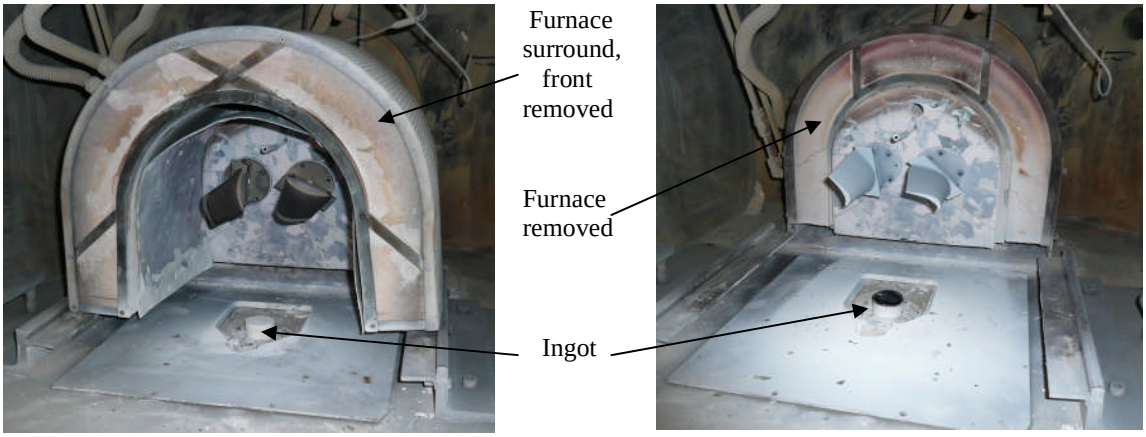

(a) Blades ready for EB-PVD & new ingot (b) Blades after EB-PVD & ingot residue

Figure 4.11: Photographs of blades mounted in the plater before and after EB-PVD

After the mounted blades were bolted to the rotating drives, the ingot was loaded into the gun hearth, the height of the ingot was adjusted to the operating position, and the furnace positioned around the substrates. Both chambers were then evacuated to a pressure below $5x10^{-5}$ mBar and the furnace switched on to heat up to at least 860°C. The process gas, comprising Ar(10 vol%)+O_2(90 vol%), was admitted to the upper chamber and the pressure maintained at $7x10^{-3}$ torr, the substrates rotated at a speed of 20 rpm and these conditions were maintained for one hour, to allow growth of the thermally grown oxide (TGO). After this period, the electron gun was switched on and the ingot adjusted in height for the beam to be directed to the surface of the ingot. The gun emission current was slowly increased until the top of the ingot was molten and optimum evaporation occurred, when the voltage was about 10 kV and emission current around 6 amp. The substrate temperatures were allowed to rise to 1000°C and upper chamber pressure to $1x10^{-2}$ torr. These conditions were maintained throughout the evaporation process for a period of 75 mins, when the required TBC thickness of 150 µm was achieved, the deposition rate being 2 µm/min.

4.7 Post EB-PVD sample preparation

Following TBC deposition, the blade surface was grit blasted at low pressure (1 Bar), using alumina brown grit, grade 220, and cleaned in acetone. Prior to cutting sections, in order to avoid cracking of the TBC, the blade was heated at 180°C for 30 minutes, brush coated with Araldite 8 resin, then heated to, and maintained at, 180°C for 15 minutes.

When cool, four sections, approximately 4 mm thick, were cut using the Struers Labotom-3 cut-off machine, with a Bueller 3H cutter disc.

Grinding and polishing of mounted samples was carried out using a Bueller Metaserv Motopol 12 machine, the first stage of which was to use 120 paper until all sections were totally level. The subsequent procedure consisted of: one contra-rotation run with 240 paper, then a series of same direction rotation runs; one run with 240 paper, two runs with 1200 paper, two runs with 2500 paper and one run with 4500 paper. In Figure 4.12(a), the four sections are coated with SiAl1 TBCs. The mounted sections in Figure 4.12(b) have been polished and are ready for SEM examination.

(a) Post EB-PVD Sections ready for mounting

(b) Mounted sections after surface preparation

Figure 4.12 : Sections of IN738LC turbine blade with SiAl1 coating after TBC deposition, and sections mounted in carrier after surface polishing

5. Identification of potentially damaging trace species in gases produced by gasification of biomass and waste-fuels

5.1 Introduction

In Chapter 2, it was explained how trace metallic elements, contained in biomass and waste-fuels, when deposited on high temperature gas turbine components, may initiate hot corrosion through basic and acidic fluxing mechanisms. This chapter is concerned with identifying metallic elements contained in biomass and waste-fuels which, following gasification, will be carried through in gasifier flue gases after gas cleaning to the gas turbine, and which, following combustion will form condensed trace metallic species on hot components of the gas turbine and thereby have the potential for initiating hot corrosion.

In this current study, the procedure for identifying potentially damaging trace species in gases produced by gasification of biomass and waste-fuels, involves five stages:

(i) Identify elements contained in typical biomass and waste-fuels using fuel analyses contained in the ECN PHYLLIS fuels database [115];

(ii) Using the MTDATA MULTIPHASE software module [109] carry out thermodynamic assessments, to identify trace species of the elements which will be contained in gases produced by gasification of these fuels;

(iii) Using the MTDATA MULTIPHASE software module, identify the trace species, in gaseous form, which will remain in the gases after flue gas cleaning, and be carried forward for combustion in the gas turbine;

(iv) Using the MTDATA MULTIPHASE software module, assess which trace species of these elements will be carried in the gas turbine gas path after combustion, and which will condense to form molten surface deposits, as they travel along the gas path to the exhaust;

(v) With the same software, determine the dew-point temperatures at which the trace species will condense, in order to identify the position in the gas path where molten surface deposits may form and have the potential to initiate hot corrosion.

In this chapter, each of the five stages is explained and the resulting trace species, which are forecast to form molten surface deposits on hot components in the gas turbine gas path are identified.

5.2 PHYLLIS database of biomass and waste-fuels

The PHYLLIS database is maintained by ECN Biomass (a knowledge centre in the Netherlands for technology development for energy and products). ECN Biomass focuses on the thermal conversion of biomass and waste, both theoretically and experimentally. Access and the use of PHYLLIS is free, so long as it is identified as the source of the data used. The database is very comprehensive and lists over 2000 biomass and waste-fuels. Each fuel data record has a unique ID-number and provides information on:

- Type of material (group);
- Subgroup;
- NTA classification code;
- Ultimate analysis: C, H, O, N, S, Cl, F and B;
- Proximate analysis: ash content, water content, volatile matter content and fixed C content;
- Biochemical composition;
- Calorific value;
- Alkali-metal content;
- Composition of the ash;
- Any specific information

Despite the comprehensive structure and content of PHYLLIS it was found that, of the over 2000 individual entries, most of the data on element content showed "nd" for "not determined". As the provision of data on trace elements contained in these fuels is vital for this project, the basis for selecting fuels was to select those which displayed data for each element or for most of the elements.

Samples of biomass fuels, including wheat-, barley- and rye-straw, treated and untreated waste wood, forest and park waste, sugar-cane bagasse and of waste fuels; municipal solid waste and sewage sludges (mechanically dried, granulates, aerodigested, thermally dried) were selected from the PHYLLIS database. Although there is limited elemental data displayed on this database, it was considered, at this stage, there were sufficient items of different biomass- and waste-fuels to support an investigation into those constituents which could cause hot corrosion damage to GT components.

The biomass- and waste-fuels selected from the PHYLLIS database were those for which data was provided on all or most constituents. The 23 fuels selected, their characteristics and elemental analyses are shown in Tables 5.1 and 5.2. As the basis for determining which trace metallic species could contaminate gasifier gases produced from these fuels, the typical value of each element was judged from the database entries, for example the lead content adopted was 400ppm.

Project - Stage 3: The Composition of Biomass and Waste Fuels

Sheet 1 - Data from ECN 'PHYLLIS' Database

	Biomass \ Waste Fuel			Proximate Analysis (wt.%)						Ultimate analysis (wt.%)														Calorific Value (kJ/kg)			
				Ash		Water		Volatiles		Carbon		Hydrogen		Oxygen		Nitrogen		Sulphur		Chlorine		Fluorene		Bromine		HHV		LHV	
Item	Group	Subgroup	ECN ID No	dry	ar	ar	dry	ar		dry	ar	dry	ar	dry	ar	dry	ar	dry	ar	dry	ar	dry	ar	dry	ar	dry	ar	dry	ar
1	straw	wheat	1129	4.7	4.2	10.3	77.7	69.7		47.3	42.5	5.87	5.30	41.3	37.1	0.58	0.52	0.07	0.06	0.17	0.15	nd	nd	nd	nd	18,940	16,999	17,659	15,599
2	straw	barley	432	4.9	nd	nd	nd	nd		46.8	49.2	5.53	5.8	41.9	44.1	0.41	0.43	0.06	0.06	0.41	0.43	nd	nd	nd	nd	18,780	19,739	17,563	18,460
3	straw	rye	547	4.6	nd	nd	nd	nd		47.5	nd	5.29	nd	41.7	nd	0.46	nd	0.06	nd	0.4	nd	nd	nd	nd	nd	18,792	nd	17,628	nd
4	trtd wood	compost'd	1089	42.8	37.3	12.8	43.0	37.5		29.0	25.3	3.26	2.80	23.8	20.8	0.89	0,78	0.15	0.13	0.04	0.03	0.01	0.01	nd	nd	11,120	9,697	10,409	8,764
5	untrt wood	pk waste	925	1.3	1.2	3.1	83.2	80.6		50.8	49.2	6.02	5.80	39.4	38.2	0.20	0.19	0.03	0.03	0.02	0.02	0.00	0.00	nd	nd	20,883	20,235	19,570	18,887
6	trtd wood	waste/dust	657	0.4	0.4	11.3	81.0	71.8		50.5	44.8	6.0	6.0	42.9	38.0	0.20	0.18	0.00	0.00	0.02	0.02	0.00	0.00	nd	nd	19,700	17,474	18,391	16,037
7	char	munwaste	1726	56.0	52.4	6.4	18.0	16.8		25.2	23.6	1.6	1.5	18.6	17.4	0.60	0.56	2.20	2.06	nd	nd	nd	nd	nd	nd	8,178*	7,655*	nd	nd
8	MSW	munwaste	1776	34.9	24.1	31.0	nd	nd		37.0	25.5	5.51	3.80	20.6	14.2	0.87	0.60	0.14	0.10	1.01	0.70	nd	nd	nd	nd	16,968*	11,708*	nd	nd
9	org/residu	orgdomws	1300	18.9	8.7	54.0	nd	nd		42.1	19.4	5.43	2.50	31.1	14.3	1.78	0.82	0.41	0.19	0.24	0.11	nd	nd	nd	nd	18,043	8,300	16,858	6,436
10	org/residu	mundom	393	4.5	nd	nd	nd	nd		48.1	nd	5.91	nd	40.7	nd	0.69	nd	0.04	nd	0.03	nd	nd	nd	nd	nd	17,300	nd	15,900	nd
11	others	biompellts	2238	38.1	34.3	10.0	nd	nd		28.0	25.2	3.56	3.2	28.9	26.0	0.91	0.82	0.45	0.40	0.16	0.14	0.01	0.01	nd	nd	11,604	10,443	10,827	9,500
12	org/residu	sugcnbag	894	2.4	2.2	10.4	85.6	76.7		48.6	43.6	5.87	5.3	42.8	38.4	0.16	0.14	0.04	0.04	0.03	0.027	nd	nd	nd	nd	18,994	17,021	17,713	15,619
13	org/residu	bagasse	1905	15.2	14.2	6.4	nd	nd		42.4	39.7	5.20	4.9	36.8	34.4	0.30	0.28	0.22	0.21	0.001	0.001	nd	nd	nd	nd	16,699*	15,630*	0.00	0.00
14	org/residu	sorgbagas	1401	8.1	7.2	10.7	73.4	65.6		39.5	35.2	7.51	6.7	43.0	38.4	1.10	0.98	0.22	0.20	0.604	0.540	nd	nd	nd	nd	17,894	15,987	16,255	14,262
15	char	sugcnbag	2344	5.5	0	0.0	15.4	0		81.5	0	3.1	0	9.1	0.0	0.80	0.00	0.00	0.00	0.00	0.00	nd	nd	nd	nd	30,622*	0.00	0.00	0.00
16	nonfossoil	sugcnbag	2343	0.1	0	13.8	0	0		54.6	47.1	6.45	5.6	38.1	32.8	0.73	0.63	0.10	0.09	-	-	nd	nd	nd	nd	25,986	22,400	24,579	20,850
17	sewsludge	granulates	941	36.0	32.2	10.6	52.6	47.0		33.4	29.9	4.65	4.20	19.6	17.6	4.52	4.04	1.67	1.49	0.096	0.086	0.028	0.025	nd	nd	14,800	13,231	13,785	12,065
18	sewsludge	sewsludge	658	35.0	31.5	9.9	53.5	48.2		34.0	30.6	4.90	4.4	20.0	18.0	4.70	4.23	1.30	1.17	0.080	0.072	0.013	0..012	nd	nd	15,100	13,605	14,031	12,400
19	sewsludge	mechdried	1777	39.1	11.7	70.1	-	-		30.7	9.2	5.01	1.5	21.7	6.5	3.34	1.00	0.13	0.04	0.033	0.010	nd	nd	nd	nd	13,736*	4,114*	0	0
20	sewsludge	aerodigest	2162	18.2	3.0	83.6	-	-		33.6	5.5	5.10	0.8	36.7	6.0	5.40	0.89	1.00	0.16	nd	nd	nd	nd	nd	nd	13,713	2,249	12,600	25
21	sewsludge	aerodigest	2160	26.4	7.2	72.8	-	-		29.2	7.9	4.70	1.3	35.8	9.7	2.90	0.79	1.00	0.27	nd	nd	nd	nd	nd	nd	12,496	3,399	11,470	1,342
22	sewsludge	driedthml	2191	44.0	39.6	10.0	-	-		27.8	25.0	5.00	4.5	15.1	13.6	5.00	4.50	1.56	1.40	1.556	1.400	0.020	0.018	nd	nd	13,585	12,226	12,494	11,000
23	sewsludge	driedthml	2188	35.3	30.8	12.8	-	-		34.1	29.7	5.73	5.0	18.3	15.9	4.47	3.90	1.95	1.70	0.183	0.160	0.011	0.010	nd	nd	15,371	13,404	14,120	12,000

Notes: Material Number* - the number allocated by ECN on Phyllis database.
Data obtained from; Phyllis, database for biomass and waste,
http://www.ecn.nl/phyllis
Energy Research Centre of the Netherlands

Table 5.1: Biomass and Waste Fuels selected from PHYLLIS Database – Proximate and Ultimate Analyses

Project - Stage 3: The Composition of Biomass and Waste Fuels

Sheet 2 - Elemental Analysis from ECN 'PHYLLIS' Database

	Biomass \ Waste Fuel			Elemental Analysis (mg/kg sample (dry)																											
Item	Group	Subgroup	ECN ID No	Al	As	B	Ba	Ca	Cd	Co	Cr	Cu	Fe	Hg	K	Mg	Mn	Mo	Na	Ni	P	Pb	Sb	Se	Si	Sn	Sr	Te	Ti	V	Zn
1	straw	wheat	1129	nd	nd	nd	nd	nd	nd	nd	nd	nd	nd	nd	5840	nd	nd	nd	140	nd	nd	nd	nd	nd	nd	nd	nd	nd	nd	nd	nd
2	straw	barley	432	nd	nd	nd	nd	nd	0.1	nd	nd	2.6	nd	0	nd	nd	nd	nd	nd	nd	nd	2.8	nd	nd	nd	nd	nd	nd	nd	nd	nd
3	straw	rye	547	nd	nd	nd	nd	nd	0	nd	nd	2.3	nd	0	nd	nd	nd	nd	nd	nd	nd	0.1	nd	nd	nd	nd	nd	nd	nd	nd	nd
4	trtd wood	compost'd	1089	8500	3.5	87	140	23000	0.6	10	320	29	5200	0.1	10200	2500	150	2.1	3900	1500	2200	210	1.6	0.7	35000	2	74	nd	200	13	180
5	untrt wood	pk waste	925	141	1.6	4.7	nd	1300	nd	0.6	14	160	200	nd	1500	260	16	nd	120	30	190	nd	nd	nd	380	nd	nd	nd	5.1	0.3	22
6	trtd wood	waste/dust	657	nd	nd	nd	nd	nd	nd	nd	nd	nd	nd	nd	nd	nd	nd	nd	nd	nd	nd	nd	nd	nd	nd	nd	nd	nd	nd	nd	nd
7	char	munwaste	1726	32000	nd	nd	61000	219000	nd	nd	nd	2000	53000	nd	14000	7000	nd	nd	6000	nd	nd	9000	nd	nd	73000	nd	nd	nd	10000	nd	13000
8	MSW	munwaste	1776	nd	nd	nd	nd	nd	nd	nd	nd	nd	nd	nd	nd	nd	nd	nd	nd	nd	nd	nd	nd	nd	nd	nd	nd	nd	nd	nd	nd
9	org/residu	orgdomws	1300	nd	nd	nd	nd	nd	nd	nd	nd	nd	nd	nd	nd	nd	nd	nd	nd	nd	nd	nd	nd	nd	nd	nd	nd	nd	nd	nd	nd
10	org/residu	mundom	393	nd	nd	nd	nd	nd	nd	nd	nd	nd	nd	nd	nd	nd	nd	nd	nd	nd	nd	nd	nd	nd	nd	nd	nd	nd	nd	nd	nd
11	others	biompellts	2238	43000	nd	nd	247	60900	4.1	0	74	253	13800	1.2	4200	5800	393	4.1	1400	30.9	9100	66	2.1	2.1	54900	nd	132	nd	2100	21	436
12	org/residu	sugcnbag	894	nd	nd	nd	nd	nd	nd	nd	nd	nd	nd	nd	nd	nd	nd	nd	nd	nd	nd	nd	nd	nd	nd	nd	nd	nd	nd	nd	nd
13	org/residu	bagasse	1905	nd	nd	nd	nd	nd	nd	nd	nd	nd	nd	nd	nd	nd	nd	nd	nd	nd	nd	nd	nd	nd	nd	nd	nd	nd	nd	nd	nd
14	org/residu	sorgbagas	1401	nd	nd	nd	nd	nd	nd	nd	nd	nd	nd	nd	nd	nd	nd	nd	nd	nd	nd	nd	nd	nd	nd	nd	nd	nd	nd	nd	nd
15	char	sugcnbag	2344	281.4	nd	nd	nd	5384.4	nd	1.5	2.4	15.3	950.1	nd	5536.7	2257.1	73.5	nd	448.8	2.6	1324.3	2.1	10.8	6.5	nd	nd	nd	nd	12.5	0.4	27.6
16	nonfossoil	sugcnbag	2343	10.1	nd	nd	nd	33.8	nd	0.1	0.6	2.3	105.8	nd	5.3	2.2	1.1	nd	21.5	1.1	3.3	4.9	7.7	0.2	nd	nd	nd	nd	0.2	0	43.7
17	sewsludge	granulates	941	20300	5.6	62	400	39000	1.4	6.6	64	450	50800	2.3	2250	3700	405	6.4	1600	170	21900	180	0.3	0.4	32600	24	350	nd	420	14	930
18	sewsludge	sewsludge	658	nd	nd	nd	nd	nd	nd	nd	nd	nd	nd	nd	nd	nd	nd	nd	nd	nnd	nd	nd	nd	nd	nd	nd	nd	nd	nd	nd	nd
19	sewsludge	mechdried	1777	nd	nd	nd	nd	nd	nd	nd	nd	nd	nd	nd	nd	nd	nd	nd	nd	nd	nd	nd	nd	nd	nd	nd	nbd	nd	nd	nd	nd
20	sewsludge	aerodigest	2162	15000	nd	100	400	58000	nd	nd	400	200	21000	nd	8000	8000	100	nd	1400	nd	nd	100	nd	nd	nd	nd	500	nd	nd	nd	12000
21	sewsludge	aerodigest	2160	34000	nd	nd	500	110000	nd	nd	4700	2200	7700	nd	1700	5800	100	nd	1200	1900	nd	100	nd	nd	nd	nd	900	nd	nd	nd	6800
22	sewsludge	driedthml	2191	nd	50	nd	1000	nd	20	50	150	600	nd	nd	20000	nd	1500	20	20000	200	50000	400	20	20	nd	50	nd	nd	nd	50	2500
23	sewsludge	driedthml	2188	nd	12	nd	650	nd	2.9	nd	70	660	nd	3	nd	nd	nd	nd	nd	40	nd	300	nd	nd	nd	nd	nd	nd	nd	nd	1500

Table 5.2: Biomass and Waste Fuels selected from PHYLLIS Database – Elemental Analysis

Identifying the trace metallic elements, from biomass and waste-fuels contained in gasifier gases, commenced with listing the trace metallic elements and their weights, in the 23 such fuels selected from the PHYLLIS database, as shown in Table 5.1.

Item	Group	Sub-group	ECN ID No.	Category
1	Organic residue	Municipal/Domestic	393	Waste
2	Straw	Barley	432	Biomass
3	Straw	Rye	547	Biomass
4	Treated wood	Waste/dust	657	Waste
5	Sewage sludge	Sewage sludge	658	Waste
6	Organic residue	Sugar bagasse	894	Biomass
7	Untreated wood	Park waste	925	Biomass
8	Sewage sludge	Granulates	941	Waste
9	Treated wood	Composted	1089	Waste
10	Straw	Wheat	1129	Biomass
11	Organic residue	Organ domesic waste	1300	Waste
12	Organic residue	Sorgam bagasse	1401	Biomass
13	Char	Municipal waste	1726	Waste
14	Municipal waste	Municipal waste	1776	Waste
15	Sewage sludge	Mechanically dried	1777	Waste
16	Organic residue	Bagasse	1905	Biomass
17	Sewage sludge	Aerobic digestion	2160	Waste
18	Sewage sludge	Aerobic digestion	2162	Waste
19	Sewage sludge	Thermally dried	2188	Waste
20	Sewage sludge	Thermally dried	2191	Waste
21	Others	Biomass pellets	2238	Biomass
22	Non fossil oil	Suger bagasse	2343	Biomass
23	Char	Sugar bagasse	2344	Biomass

Table 5.3: Selected fuels from the ECN PHYLLIS database, listed in order of their ECN identification numbers

Elements present in gas turbine superalloys, or are benign, were removed from the list namely; aluminium, cobalt, chromium, copper, iron, magnesium, nickel, silicon and titanium. Sodium and potassium were omitted as earlier studies which concentrated on alkali species [7], had already established that they would pass through to the gas turbine in vapour form and could then, after combustion, condense onto blades/vanes, as they passed along the gas turbine gas path.

The remaining elements were then divided into four groups, with each group containing elements near each other in the periodic table, and therefore likely to exhibit similar properties.

The content of each selected element was taken from the PHYLLIS database, as follows:

- Group A: As; 50ppm, Pb; 400ppm, Sb; 10ppm, Se; 5ppm, Sn; 50ppm, Te; 5ppm,
- Group B: Hg; 3ppm, Cd; 20ppm, Zn; 12000ppm,
- Group C: Ca; 200,000ppm, Sr; 900ppm, Ba; 62000ppm,
- Group D: Mo; 20ppm, Re; 5ppm, V; 50ppm.

Note : values of 5ppm were assumed for Te and Re as none were shown in the database.

The 23 biomass and waste-fuels selected from the PHYLLIS database contained sulphur, chlorine and fluorine, which have the potential to form sulphides, chlorides or fluorides. In the thermochemical calculations, to investigate the sensitivity of those species that would be formed, each metallic element in the four groups was tested in the presence of low, medium and high levels of sulphur, fluorine and chlorine. The low, medium and high values selected for these elements were taken from the 23 biomass and waste-fuels in the PHYLLIS database, as follows:

- Chlorine: 1000ppm, 7000ppm and 14000ppm;
- Fluorine: 100ppm, 200ppm, 300ppm;
- Sulphur : 1000ppm, 12000ppm, 20600ppm. .

5.3 Temperature range and common gasifier gas composition selected

The temperature range of 300^{o}C to 1200^{o}C was used, reflecting the typical air-blown gasifier operating temperatures. The calculations and plotting were generally based on 50^{o}C intervals. For each of the series of five tests, all the phases and the condensed and gaseous species were included, to ensure that no important species were omitted.

The common bulk gasifier gas composition, selected for the tests, was that identified by research into trace elements in gasification as proposed by Reed [116].

5.4 Minimum weights of trace contaminants in thermodynamic assessment

The cut-off point for the tests, below which any detected species would be judged to be insignificant, was set at 1ppb. As an example to illustrate where this content of species will occur, reference should be made to the MTDATA diagram in Figure 5.1, where the y-axis displays: *Log_{10} of the mass of the species per kg of the gases tested.*

Example: Assume the flow of gases to be 1 x 10^{6}g and the content of the trace metal to be 1ppm equivalent to say 1g; therefore the total weight of gases will be 1,000,001g. As the proportion of trace metal to total gases will be 1 x 10^{-6}, then 1ppb will equate to 1 x 10^{-9}g. The MTDATA Y-axis measures the mass in g/kg and therefore the ppb level in kg will be; 1 x 10^{-6}kg.

On Figure 5.1, the MTDATA graph the ppb level in this example will be $\log_{10}$ -6, therefore any species of the trace metal shown on the graph, above $\log_{10}$ -6, will be selected for further investigation.

5.5 Scope of group element assessments

Initially, a series of 27 assessments was carried out, to cover the full ranges of sulphur, chlorine and fluorine; high, medium and low, for several metals. This was done to determine whether the levels of these elements, individually, would have an identifiable effect on the species formed from the trace metals in the gasifier gas. The conclusion was that, although the test results showed an increase in the content of substances, from low levels of sulphur, chlorine and fluorine, through the medium levels to high levels, there was insufficient variation to justify carrying out all 27 tests for each metal.

5.6 First stage thermodynamic assessments

The MTDATA MULTIPHASE module used for the study [109] calculates multiphase, multicomponent equilibria. Phases may include alloys, molten salts, gases, aqueous solutions, slags and pure stoichiometric substances in combination. The equilibrium state for each calculation was defined by specifying the temperature, pressure or volume, and quantity of substance. Data on elements, compounds, solutions and salts for use in the calculations, were retrieved by the program, from the appropriate internal databases within MTDATA. Two types of calculations offered by MTDATA are; Stage 1, which uses true energy minimisation and gives very reliable results, and Stage 2 which achieves energy minimisation by equalising the chemical potentials of the components between the phases, which is used to calculate substances less than 10^{-6}. A more comprehensive description of MTDATA software is provided in section 4.1.

For all calculations, the MULTIPHASE Stage 1 proved to be effective in most cases. Although this stage is configured to deal with at least 200 substances, the actual limits depend on the type of computer being used, and in the few calculations that failed, re-calculations were carried out over the narrower range of temperatures where the error occurred. Where further difficulty arose, the Robust Stage 2 option was used to confirm the result (see Section 4.1 for explanations of these options).

For each thermodynamic assessment, all the species predicted to be present in the gasifier gases by the MULTIPHASE module were included, to ensure that none could be omitted due to misjudgement. Species included in the thermodynamic assessments, for each group, are shown in Tables 5.4, 5.5, 5.6 and 5.7.

As		Pb		Sb		Se		Sn		Te	
Cond	**Gas**	**Cond**	**Gas**	**Cond**	**Gas**	**Cond**	**Gas**	**Cond**	**Gas**	**Cond**	**Gas**
As	As	Pb	Pb	Sb	Sb	Se	Se	Sn	Sn	Te	Te
$AsCl_3$	As_2	$PbCl_2$	PbCl	$SbCl_3$	Sb_2	$SeCl_4$	Se_2	SnO	Sn_2	$TeCl_4$	Te_2
AsF_3	As_4	PbF_2	$PbCl_2$	SbF_3	Sb_3	Se_2Cl_2	Se_3	SnS	SnS	TeO_2	Te_3
As_2O_5	$AsCl_3$	PbS	$PbCl_3$	SbO_2	Sb_4	SeO_2	Se_4	Sn_2S_3	SnO		Te_4
As_4S_4	AsF	$Pb_3Cl_2O_3$	$PbCl_4$	SbClO	SbCl		Se_5	SnS_2	SnO_2		Te_5
As_2S_3	AsF_3	$PbCO_3$	PbF	Sb_2O_3	$SbCl_3$		Se_6	Sn_3S_4	SnF		Te_6
AsS	AsF_5	Pb_2CO_4	PbF_2	$Sb_2S_3O_{12}$	$SbCl_5$		Se_7	SnO_2	SnF_2		Te_7
	AsH	PbN_2O_6	PbF_3		SbF		Se_8	SnS_2O_8	SnF_3		$TeCl_2$
	AsH_2	PbO	PbF_4		SbF_3		SeC	SnF_2	SnF_4		$TeCl_2O$
	AsH_3	PbO_2	PbH		SbF_5		Se_2C	SnF_4	Sn_2F_4		$TeCl_4$
	AsN	Pb_2O_3	PbO		SbH		$SeCl_2$	$SnCl_2$	SnFO		TeF
	AsO	Pb_3O_4	PbO_2		SbH_3		Se_2Cl_2	$SnCl_4$	SnF_2O		TeF_2
	AsO_2	$PbSO_4$	PbS		SbN		SeF	$SnSO_4$	SnCl		TeF_4
	As_4O_6	Pb_2SO_5	PbS_2		SbO		SeF_2	SnN_2o_6	$SnCl_2$		TeF_5
	As_4O_7	Pb_2SO_7	Pb_2		SbO_2		SeF_4		$SnCl_3$		TeF_6
	As_4O_8	Pb_3SO_6			Sb_4O_6		SeF_5		$SnCl_4$		TeH
	As_4O_9	Pb_5SO			SbS		SeF_6		$SnCl_2O_2$		TeH_2
	As_4O_{10}						SeH		$SnCl_2O_4$		TeO
	AsS						SeH_2		SnH_4		TeO_2
	As_4S_4						SeN		SnS_2		Te_2O_2
							SeO		Sn_2S_2		TeS
							SeO_2				
							SeS				

Key: Cond ; condensed Gas ; gaseous

Table 5.4: Species of elements in Group A included in thermodynamic assessments

Hg		Cd		Zn	
Cond	**Gaseous**	**Cond**	**Gaseous**	**Cond**	**Gaseous**
Hg	Hg	Cd	Cd	Zn	Zn
HgCl	HgCl	$CdCO_3$	CdCl	$ZnCl_2$	ZnCl
$HgCl_2$	$HgCl_2$	$CdCl_2$	$CdCl_2$	$ZnCO_3$	$ZnCl_2$
Hg_2Cl_2	HgF	CdF_2	Cd_2Cl_4	ZnF_2	Zn_2Cl_4
HgF_2	HgF_2	CdH_2O_2	CdF	ZnH_2O_5S	ZnF
Hg_2F_2	HgH	CdN_2O_6	CdF_2	ZnH_4O_6S	ZnF_2
HgO	HgO	CdO	Cd_2F_4	$ZnH_{12}O_{10}S$	Zn_2F_4
$HgSO_4$	HgS	$CdSO_4$	CdH	$ZnH_{14}O_{11}S$	ZnOH
Hg_2SO_4		CdS	CdHO	ZnH_2O_2	ZnO_2H_2
HgS			CdH_2O_2	Zn_3N_2	ZnH
			CdO	$ZnSO_4$	ZnO
			CdCds	$Zn_3O_9S_2$	ZnS
				ZnO	
				ZnS	

Key: Cond ; condensed Gas ; gaseous

Table 5.5: Species of elements in Group B included in thermodynamic assessments

Ba		Ca			Sr	
Cond	**Gaseous**	**Cond**	**Cond**	**Gaseous**	**Cond**	**Gaseous**
Ba	Ba	Ca	$CaHO_{4.5}S$	Ca	Sr	Sr
BaC_2	Ba_2	CaC_2	CaH_4O_6S	Ca_2	$SrCO_3$	SrCl
$BaCO_3$	BaCl	$CaCN_2$	Ca_3N_2	CaCl	SrC_2	SrClHO
$BaCl_2$	$BaCl_2$	$CaCO_3$	CaN_2O_6	$CaCl_2$	$SrCl_2$	$SrCl_2$
BaF_2	BaClHO	$CaCl_2$	CaO	CaClOH	SrF_2	SrFHO
BaH_2	BaF	$CaCl_2O$	CaO_2	CaF	SrH_2O_2	SrF
BaH_2O_2	BaF_2	CaF_2	CaO_3S	CaF_2	SrH_2	SrF_2
Ba_3N_2	BaFHO	CaH_2	CaO_4S	CaFOH	Sr_3N_2	SrOH
BaN_2O_6	BaH	$CaH_4N_2O_8$	CaS	CaH	$SrSO_4$	SrH_2O_2
BaO	BaHO	$CaH_6N_2O_9$		CaHO	SrO	SrH
BaO_2	BaH_2O_2	$CaH_8N_2O_{10}$		CaH_2O_2	SrO_2	SrO
$BaSO_4$	BaO	CaH_2O_2		CaO	SrS	SrS
BaS	Ba_2O	$CaHO_{3.5}S$		CaS		Sr_2
	Ba_2O_2					
	BaS					

Key: Cond ; condensed Gas ; gaseous

Table 5.6: Species of elements in Group C included in thermodynamic assessments

Mo			Re		V	
Cond	**Gaseous**	**Gaseous**	**Cond**	**Gaseous**	**Cond**	**Gaseous**
Mo	Mo	$MoFO_2$	Re	Re	V	V
MoC	MoC_6O_6	MoF_2O	$ReCl_3$	ReF_6	V_2C	VCl_2
Mo_2C	MoCl	MoF_2O_2	ReO_2	ReO	VCl_3O	VCl_3O
Mo_3C_2	$MoCl_2$	MoF_3O	ReO_3	ReO_2	VCl_2	VCl_3
MoC_6O_6	$MoCl_3$	MoF_4O	Re_2O_7	ReO_3	VCl_3	VCl_4
$MoCl_2$	$MoCl_4$	MoOH	ReS_2	Re_2O_6	VCl_4	VF_2
$MoCl_3$	$MoCl_5$	MoO_2H	ReS_3	Re_2O_7	VF_2	VF_3
$MoCl_4$	$MoCl_6$	MoO_2H_2	Re_2S_7		VF_3	VF_4
$MoCl_5$	MoClO	MoO_3H_2	Re LIQ		VF_4	VF_5
$MoCl_6$	$MoClO_2$	MoO_4H_2	Re<HCP		VN	VN
$MoCl_2O$	$MoCl_2O$	Mo_2	-A3>		VO	VO
$MoCl_2O_2$	$MoCl_2O_2$	MoN			VO_2	VO_2
$MoCl_3O$	$MoCl_3O$	MoO			V_2O_3	V_4O_{10}
$MoCl_4O$	$MoCl_4O$	MoO_2			V_2O_4	
MoF_3	MoF	MoO_3			V_2O_5	
MoF_5	MoF_2	Mo_2O_6				
MoF_6	MoF_3	Mo_3O_9				
MoF_4O	MoF_4	Mo_4O_{12}				
Mo_2N	MoF_5	Mo_5O_{15}				
MoO_2	MoF_6	MoS				
MoO_3	Mo_2F_{10}	MoS_2				
MoS_2	Mo_3F_{15}					
Mo_2S_3	MoFO					

Key: Cond ; condensed Gas ; gaseous

Table 5.7: Species of elements in Group D included in thermodynamic assessments

5.7 Results of the first stage of thermodynamic assessments

Examples of MTDATA first stage thermodynamic assessments are shown in the graphs in Figure 5.1 for cadmium (20ppm) and Figure 5.2 for lead (400ppm).

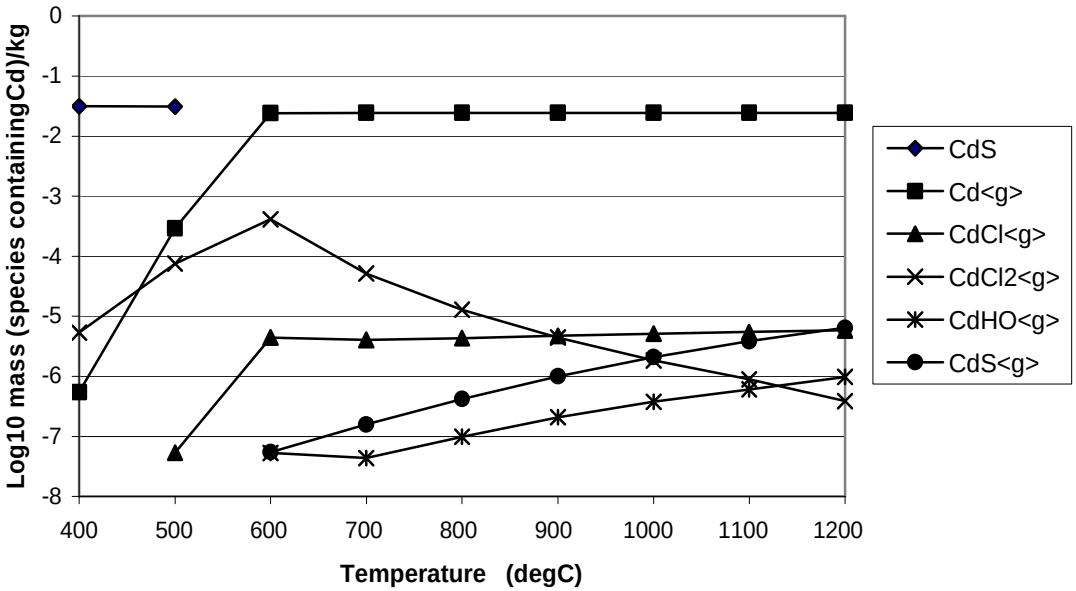

Key: species showing <g> are gaseous, otherwise the species are in condensed form

Figure 5.1: Graph of $\log_{10}$ mass (species containing 20ppm Cd)/kg in gasifier gases

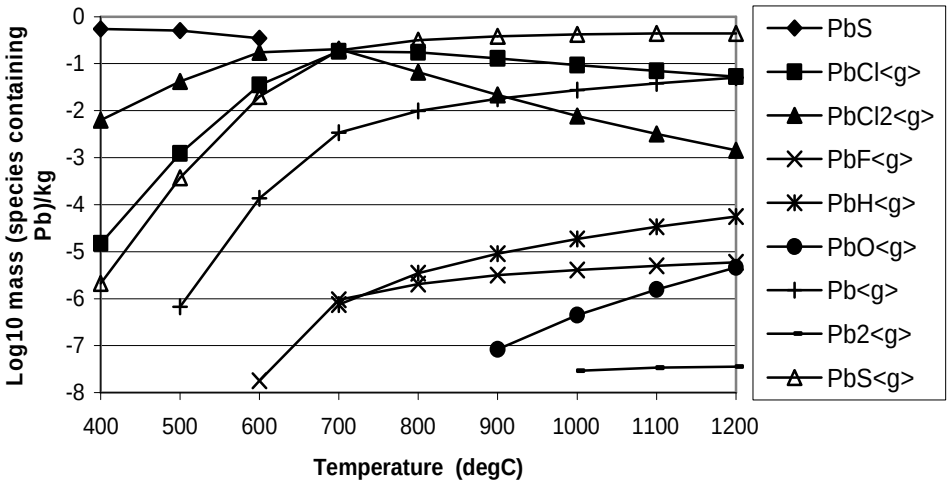

Key: species showing <g> are gaseous, otherwise the species are in condensed form

Figure 5.2: Graph of $\log_{10}$ mass (species containing 400ppm Pb)/kg in gasifier gases

Note that after the first series of tests involving the high, medium and low ranges of S, Cl and F, insufficient variation in the results occurred to justify carrying out all 27 tests for each metal. Therefore, only the high values of these elements were used in the assessments, namely; S = 20600ppm, Cl = 14000ppm and F = 300ppm.

The first round of MTDATA Multiphase calculations identified those trace species in biomass and waste-fuels which may be present in gasifier gases (above 1 ppb), prior to any gas cleaning or filtration stages. A summary of these species is shown in Table 5.8.

Element	Condensed Species	Gaseous Species
Group A As		As, As_2, As_4, AsH_2, AsH_3, AsO, AsN, AsS
Pb	PbS	Pb, PbS, PbCl, $PbCl_2$
Sb	Sb_2S_3	Sb, SbCl, $SbCl_3$, SbH, SbS
Se		Se, Se_2, SeH, SeH_2, SeS
Sn	SnS	Sn_2, SnCl, $SnCl_2$, SnO, SnS
Te	Te	Te, Te_2, Te_3, Te_5, $TeCl_2$, TeH, TeH_2, TeS
Group B Hg		Hg, HgS
Cd	CdS	Cd, $CdCl_2$,
Zn	ZnS, ZnS (wurzite)	Zn, ZnCl, $ZnCl_2$
Group C Ba	$BaCl_2$, BaF_2, BaS, $BaCO_3$	$BaCl_2$, BaClOH
Ca	$CaCl_2$, $CaCO_3$, CaF_2, CaO, CaS	$CaCl_2$
Sr	$SrCl_2$, SrS	$SrCl_2$, SrClOH
Group D Mo	MoS_2	$MoOCl_2$, $MoClO_2$, MoF_2O_2, $MoCl_2O_2$
Re	ReS_2, Re(HCP A3)	
V	VF_2, V_2O_3	VCl_2, VF_2

Table 5.8: Species in gasifier gases after first thermodynamic assessments

In Table 5.8 it will be noted that some species are shown to be present in both condensed and gaseous states, depending on the temperatures involved. Both states of such species have to be included for the calculations to work.

5.8 Identification of trace metallic elements in gasifier gases after gas cleaning

The objective of the next round of calculations, using the MULTIPHASE module, was to eliminate those trace species in gasifier gases which would be removed by gas cooling, filtration or hot gas cleaning. These treatments are necessary to meet the stringent quality requirements and environmental limits of high efficiency gas turbines. The fate of elements of an air-blown gasifier, used as the basis in this project, and described in the Literature Review (section 2.2), is illustrated diagrammatically in Figure 2.5.

Five types of gas phase contaminants were taken into account when determining what gas cleaning facilities should be provided; particulates, alkali compounds, tars, nitrogen-containing compounds and sulphur compounds [7]. These are explained more fully in section 2.2, as are the treatments for removing gas phase contaminants, albeit with attendant cost and efficiency penalties, and a schematic diagram of a gasifier with hot gas cleaning in an IGCC is shown in Figure 2.4.

5.8.1 Gas cleanup systems assumed for this project

A successful biomass gasification system requires that the gasifier, the accompanying gas conditioning technologies and the end-use application must be carefully designed as an integrated unit. Stevens [13] identifies four types of gas conditioning systems which can be adopted, based on the demands of the end-use of the gas and requiring different approaches to cleaning the product:

- Systems requiring minimal hot-gas conditioning that produce fuel gases for relatively undemanding end-use applications, examples would be where the fuel gas will be used in an existing coal-fired, steam-cycle power station;
- Systems requiring significant gas conditioning that produce cool (<100^{o}C) fuel gases for demanding applications, examples include gas engines or gas turbines for power generation;
- Systems requiring significant gas conditioning that produce warm or hot (>100^{o}C) fuel gases for demanding applications, for example high efficiency gas turbines;
- Systems requiring exceptional gas conditioning that produce synthesis gas for the manufacture of fuels and chemicals, or hydrogen for fuel cells.

For use with gas turbines systems requiring significant gas conditioning, cool or hot, are applicable. However, gas turbines achieve higher efficiencies by using hot fuel gases, as these gases retain part or most of the sensible heat from the gasification process, that heat then being available to generate additional electricity. Although the temperatures of cool systems are defined as <100^{o}C, most are nearer 35^{o}C, whereas the temperatures defined as warm or hot, range from 200-500^{o}C. As the optimization of gas turbine- and energy-efficiency are prime objectives, then the system requiring significant gas conditioning to produce warm or hot fuel gases will be adopted.

The equipment used in the ‘hot system’ will determine what temperatures will be applicable in the gas clean-up stages. Having taken into account the various temperatures required and use of appropriate catalysts for removing tars, alkali salts and ammonia, the gases in this project were assumed to be cooled to a temperature of 500^{o}C. This temperature was used in determining the fate of the species of metallic elements contained in the gasifier gases and was the major factor in determining whether they would be combusted in the gas turbine or filtered out before that stage.

5.8.2 Elimination of trace species by filtration and hot gas cleaning

The elimination of species after filtration and hot gas cleaning will be based on:

- all solids/condensate that will be removed by the filtration/hot gas cleaning or in the ash, during gasification, will be eliminated;
- those gaseous species that exceed the 1ppb value and which only exist below, but not above, the gasifier gas temperature of 500^{o}C, will have been removed by filtration/gas cleaning, hence they will be eliminated;
- those gaseous species that exist below and above 500^{o}C, will be carried through for combustion in the GT and therefore will be retained.

5.8.3 Fate of species after filtration and gas cleaning

The fates of species, identified to be in gasifier gases, which will be eliminated after filtration and gas cleaning, and proceed forward for combustion in the gas turbine, are summarised in table form.

Condensed Species	**Gaseous Species**	**Temp where species > 1ppb, degC**	**Elim'd**	**Go fwd (gaseous)**
	As	850 to 1200	✓	
	As_2	330 to 1200		✓
	As_4	300 to 1040		✓
	AsH_2	730 to 1200	✓	
	AsH_3	370 to 1200		✓
	AsN	910 to 1200	✓	
	AsO	920 to 1200	✓	
	AsS	490 to 1200		✓

Table 5.9: Fate of arsenic species after filtration and hot gas cleaning

Condensed Species	**Gaseous Species**	**Temp where species > 1ppb, degC**	**Elim'd**	**Go fwd (gaseous)**
	PbCl	440 to 1200		✓
	$PbCl_2$	300 to 1200		✓
	Pb	580 to 1200	✓	
	PbS	460 to 1200		✓
PbS		300 to 630	✓	

Table 5.10: Fate of lead species after filtration and hot gas cleaning

Condensed Species	Gaseous species	Temp where species > 1ppb, degC	Elim'd	Go fwd (gaseous)
	SbCl	300 to 1200		✓
	$SbCl_3$	300 to 440	✓	
	SbH	1120 to 1200	✓	
	SbS	920 to 1200	✓	
	Sb	1110 to 1200	✓	
Sb_2S_3		300 (spot reading)	✓	

Table 5.11: Fate of antimony species after filtration and hot gas cleaning

Condensed Species	Gaseous species	Temp where species > 1ppb, degC	Elim'd	Go fwd (gaseous)
	SeH	580 to 1200	✓	
	SeH_2	300 to 1200		✓
	SeS	550 to 1200	✓	
	Se	870 to 1200	✓	
	Se_2	830 to 1200	✓	

Table 5.12: Fate of selenium species after filtration and hot gas cleaning

Condensed species	Gaseous species	Temp where species > 1ppb, degC	Elim'd	Go fwd (gaseous)
	SnCl	470 to 1200		✓
	$SnCl_2$	300 to 1200		✓
	SnS	330 to 1200		✓
	Sn_2	390 to 620		✓
	SnO	1120 to 1200	✓	
SnS		300 to 340	✓	

Table 5.13: Fate of tin species after filtration and hot gas cleaning

Condensed species	Gaseous species	Temp where species > 1ppb, degC	Elim'd	Go fwd (gaseous)
	$TeCl_2$	300 to 930		✓
	TeH	340 to 1200		✓
	TeH_2	300 to 1200		✓
	TeS	300 to 1200		✓
	Te	430 to 1200		✓
	Te_2	300 to 1200		✓
	Te_3	300 to 670		✓
	Te_5	300 to 400	✓	
Te		300 to 310	✓	

Table 5.14: Fate of tellurium species after filtration and hot gas cleaning

Condensed species	Gaseous species	Temp where species > 1ppb, degC	Elim'd	Go fwd (gaseous)
	Hg	300 to 1200		✓
	HgS	At 1200	✓	

Table 5.15: Fate of mercury species after filtration and hot gas cleaning

Condensed species	Gaseous species	Temp where species > 1ppb, degC	Elim'd	Go fwd (gaseous)
	Cd	440 to 1200		✓
	$CdCl_2$	420 to 850		✓
CdS		300 to 540	✓	

Table 5.16: Fate of cadmium species after filtration and hot gas cleaning

Condensed species	Gaseous species	Temp where species > 1ppb, degC	Elim'd	Go fwd gaseous
	ZnCl	1080 to 1200	✓	
	$ZnCl_2$	560 to 1200	✓	
	Zn	780 to 1200	✓	
ZnS		300 to 1050	✓	
ZnS, wurzite		1100 (spot reading)	✓	

Table 5.17: Fate of zinc species after filtration and hot gas cleaning

Condensed species	Gaseous species	Temp where species > 1ppb, degC	Elim'd	Go fwd (gaseous)
	$CaCl_2$	990 to 1200	✓	
$CaCO_3$		300 to 680	✓	
$CaCl_2$		800 to 1200	✓	
CaF_2		300 to 1200	✓	
CaO		640 to 1200	✓	
CaS		300 to 1200	✓	
$CaCl_2$		300 to 730	✓	

Table 5.18: Fate of calcium species after filtration and hot gas cleaning

Condensed species	Gaseous species	Temp where species > 1ppb, degC	Elim'd	Go fwd (gaseous)
	SrClOH	1180 to 1200	✓	
	$SrCl_2$	860 to 1200	✓	
$SrCl_2$		300 to 1000	✓	
SrS		1000 to 1200	✓	

Table 5.19: Fate of strontium species after filtration and hot gas cleaning

Condensed species	Gaseous species	Temp where species > 1ppb, degC	Elim'd	Go fwd (gaseous)
	$BaCl_2$	910 to 1200	✓	
	BaClOH	1070 to 1200	✓	
$BaCl_2$		300 to 1200	✓	
BaF_2		300 to 700	✓	
BaS		300 to 1200	✓	
$BaCO_3$ BaS		300 to 530	✓	

Table 5.20: Fate of barium species after filtration and hot gas cleaning

Condensed Species	Gaseous species	Temp where species > 1ppb, degC	Elim'd	Go fwd (gaseous)
MoS_2		300 to 1200	✓	
	MoO_2F_2	800 to 1200	✓	
	$MoOCl_2$	1120 to 1200	✓	
	$MoClO_2$) $MoCl_2O_2$)	1100 to 1200	✓	

Table 5.21: Fate of molybdenum species after filtration and hot gas cleaning

Condensed species	Gaseous species	Temp where species > 1ppb, degC	Elim'd	Go fwd (gaseous)
ReS_2		300 to 600	✓	
Re (HCP A3)		650 to 1200	✓	

Table 5.22: Fate of rhenium species after filtration and hot gas cleaning

Condensed species	Gaseous species	Temp where species > 1ppb, degC	Elim'd	Go fwd (gaseous)
	VCl_2	820 to 1200	✓	
	VF_2	660 to 1200	✓	
VF_2		300 to 680	✓	
V_2O_3		720 to 1200	✓	

Table 5.23: Fate of vanadium species after filtration and hot gas cleaning

5.8.4 Species in gasifier gases that will go forward for combustion in the gas turbine

The species removed by cleaning or because their vapour phase contents were <1ppb were; zinc, calcium, molybdenum, rhenium, strontium and vanadium. The species in gasifier gases predicted by the MTDATA assessments to go forward for combustion in the gas turbine are listed in Table 5.24.

Element	Species in gases for combustion in GT
As	As_4, As_2, AsH_3, As
Pb	$PbCl_2$, PbCl, PbS
Sb	SbCl
Se	SeH_2
Sn	$SnCl_2$, SnS, SnS_2, SnCl
Te	Te_2, TeH_2, TeS, TeH, $TeCl_2$, Te_3, Te
Hg	Hg
Cd	Cd, $CdCl_2$

Table 5.24: Summary of species in gasifier gases to be combusted in gas turbine

5.9 Identification of condensed trace metallic elements in the gas turbine hot gas path after combustion

The next stage of MTDATA thermodynamic assessments was to eliminate those trace species, remaining after combustion in the gas turbine, whose dew-points would fall outside the range of 950^{o}C to 540^{o}C. This is the typical metal operating temperature range assumed in the gas turbine gas path, as can be seen in Figure 2.7.

5.9.1 Gas turbine combustion conditions

The air/fuel ratio for combustion in an industrial gas turbine was obtained from previous work carried out for a coal gasification/gas turbine cycle. In that case the mass flow at the filter exhaust was 27.8kg/s, the mass flow at the gas turbine exhaust was 144.6kg/s, thus the gas turbine air supply was 116.8kg/s.

Assuming that the low calorific value (CV) of coal derived fuel gas is equivalent to the CV of biomass fuel gas, then the air fuel ratio to be adopted was 116.8/27.8 or 4.20:1.

By using the MTDATA gas composition program, the constituents of the fuel gas going forward for combustion in the gas turbine, were keyed in for each species identified in Table 5.24. The next step was, for each of the species, to delete all the gas constituents but maintain the total mass flow and select the %vol(dry) compositions of 79.0% for nitrogen and 21.0% for oxygen.

Thus the mols at STP for each of these two gases, equivalent to full flow air was determined; for oxygen: 21600mols and nitrogen: 40600mols.

Using the air/fuel ratio above, the total air for inserting into the MULTIPHASE module for the combustion assessments consisted of:

For oxygen : (21600 x 4.2) + 17100 = 107820mols
For nitrogen: (40600 x 4.2) + 22600 = 193120mols

5.9.2 Inputs to MTDATA module for gas turbine combustion assessments

Having determined the air required for the combustion tests however, it was found that the ranges available in MTDATA MULTIPHASE for the thermodynamic assessments would be exceeded by these values of oxygen and nitrogen. Therefore, in order to remain within the MTDATA operating range, their values were halved. In order to maintain the correct proportions of the other constituents in the thermodynamic assessments, values were also halved for hydrogen, carbon, chlorine, fluorine, sulphur and the metallic element relevant to the particular test. The combustion pressure in the gas turbine was taken to be the mean pressure between the compressor outlet pressure of 203 psia or 1403 kPa, and the turbine inlet pressure of 195 psia or 1347 kPa (see Figure 2.7). The pressure adopted for the MULTIPHASE module assessments was set at 199 psia or 1375 kPa. Predictions at the lower pressures expected down the gas path are not included in this study, but are expected to be lower, therefore the conditions studied may be considered an upper case. It will be noted from Figure 2.7, that the temperature at the GT turbine exhaust is 546^{o}C. Therefore, for the purpose of this project, we are interested in those species that have a dew-point between 540^{o}C and 1200^{o}C.

5.9.3 Condensed species remaining after combustion in the gas turbine

In these assessments, the dew-points for the species; arsenic, cadmium, mercury, lead, antimony, selenium, tin and tellurium, were calculated using the MULTIPHASE module and the parameters from the previous series, but with the combustion air/fuel ratio 4.2 : 1. The assessments identified condensed species of cadmium, lead and antimony remaining after combustion of the gasifier derived gases produced from fuels having high levels of sulphur(20600ppm), chlorine(14000ppm) and fluorine(300ppm). The graphs of these MULTIPHASE assessment are shown in Figures 5.3, 5.4 and 5.5.

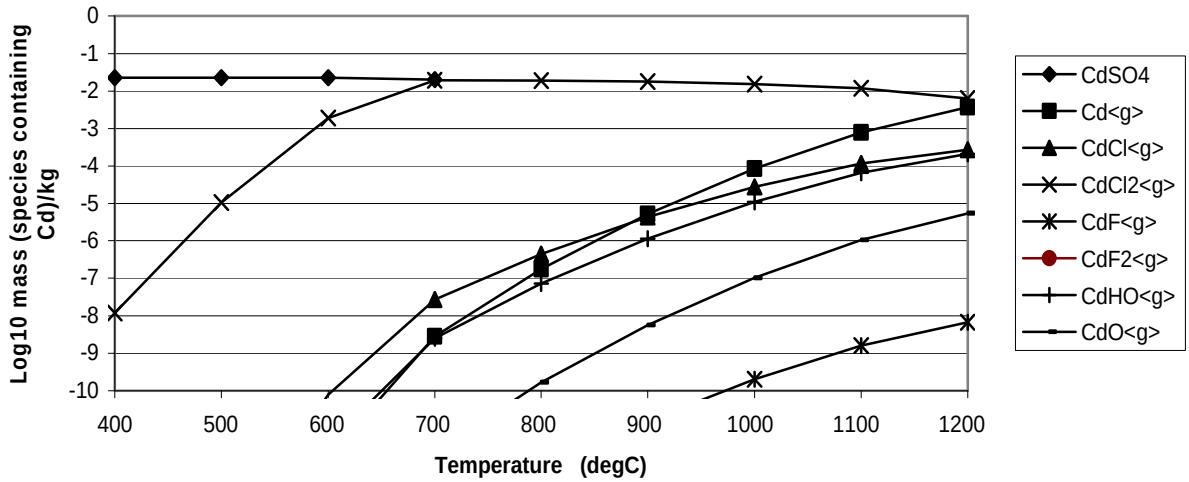

Key: species showing <g> are gaseous, otherwise the species are in condensed form
$CdSO_4$ is the only condensed species, having a dew-point of ~700^{o}C

Figure 5.3: Graph of mass of Cd species in the gas turbine gas path after combustion in gases from gasifier solid fuel composition containing S (20600ppm), Cl (14000ppm) and F (300ppm)

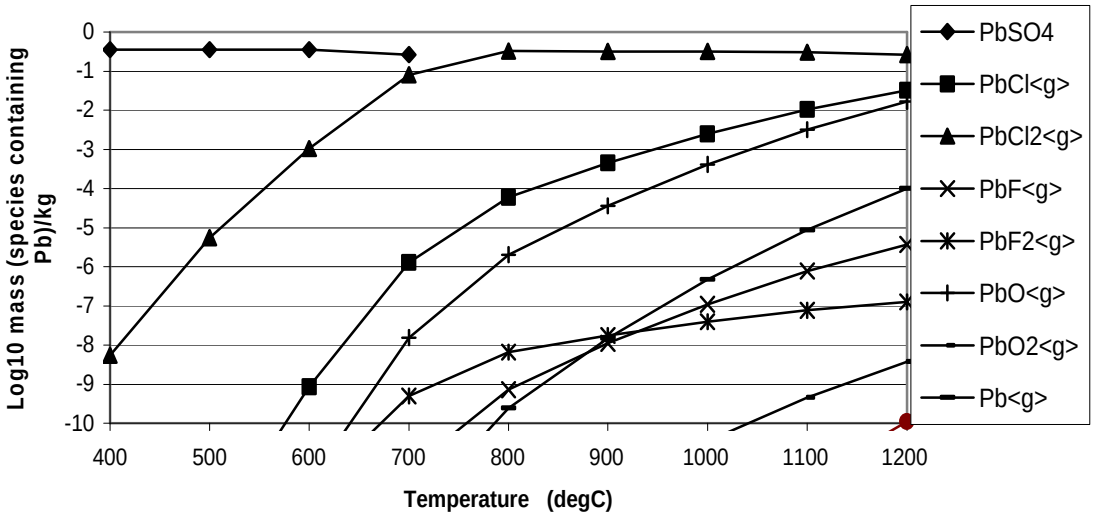

Key: species showing <g> are gaseous, otherwise the species are in condensed form

$PbSO_4$ is the only condensed species, having a dew-point of ~700°C

Figure 5.4: Graph of mass of Pb species in the gas turbine gas path after combustion in gases from gasifier solid fuel composition containing S (20600ppm), Cl (14000ppm) and F (300ppm)

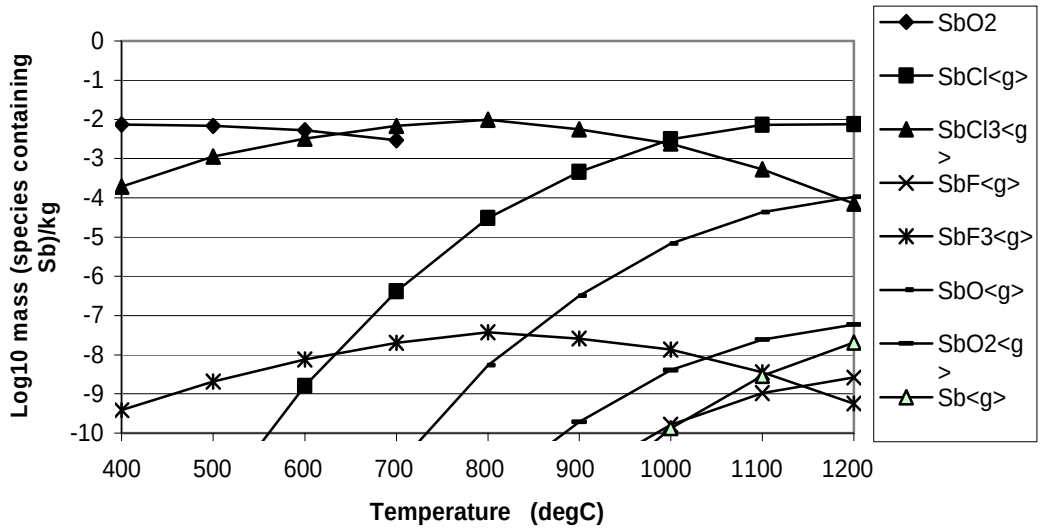

Key: species showing <g> are gaseous, otherwise the species are in condensed form

SbO_2 is the only condensed species, having a dew-point of ~700°C

Figure 5.5: Graph of mass of Sb species in the gas turbine gas path after combustion in gases from gasifier solid fuel composition containing S (20600ppm), Cl (14000ppm) and F (300ppm)

In order to determine the full range of dew-points for these condensed species, the tests were repeated for each high, medium and low level combination of S, Cl and F, 27 tests in all, with the resulting dew-points shown in Table 5.25. This shows that dew-points of $CdSO_4$ range from 640°C to 800°C, of $PbSO_4$ range from 730°C to 1020°C and of SbO_2 range from 700°C to 910°C, (dew-points rounded to the nearest 10°C in view of errors in calculations).

Test No.	Cl ppm	F ppm	S ppm	$CdSO_4$ Dew-pt °C	$PbSO_4$ Dew-pt °C	SbO_2 Dew-pt °C
1	1000	100	1000	730	900	910
2	1000	100	12000	790	1000	910
3	1000	100	20600	800	1020	910
4	1000	200	1000	730	900	910
5	1000	200	12000	790	1000	910
6	1000	200	20600	800	1020	910
7	1000	300	1000	730	900	910
8	1000	300	12000	790	1000	910
9	1000	300	20600	800	1020	910
10	7000	100	1000	670	770	900
11	7000	100	12000	740	840	900
12	7000	100	20600	750	860	900
13	7000	200	1000	670	770	900
14	7000	200	12000	740	840	900
15	7000	200	20600	750	860	900
16	7000	300	1000	670	770	900
17	7000	300	12000	740	840	900
18	7000	300	20600	750	860	900
19	14000	100	1000	640	730	700
20	14000	100	12000	700	800	700
21	14000	100	20600	720	820	700
22	14000	200	1000	640	730	700
23	14000	200	12000	700	800	700
24	14000	200	20600	720	820	700
25	14000	300	1000	640	730	700
26	14000	300	12000	700	800	700
27	14000	300	20600	720	820	700

Table 5.25 : Dew–points of $CdSO_4$, $PbSO_4$ and SbO_2 with high, medium and low levels of Cl, F and S, in gasified fuels (dew-points rounded to 10°C)

To assist interpretation of the data in Figure 5.25, graphs have been drawn, one for each of the three species, plotting dewpoint against chlorine content and sulphur content. It was considered that small values and ranges of fluorine content have little influence on the dewpoints of the three species and therefore no graphs of fluorine have been provided here. The three graphs are seen in Figures 5.6, 5.7 and 5.8.

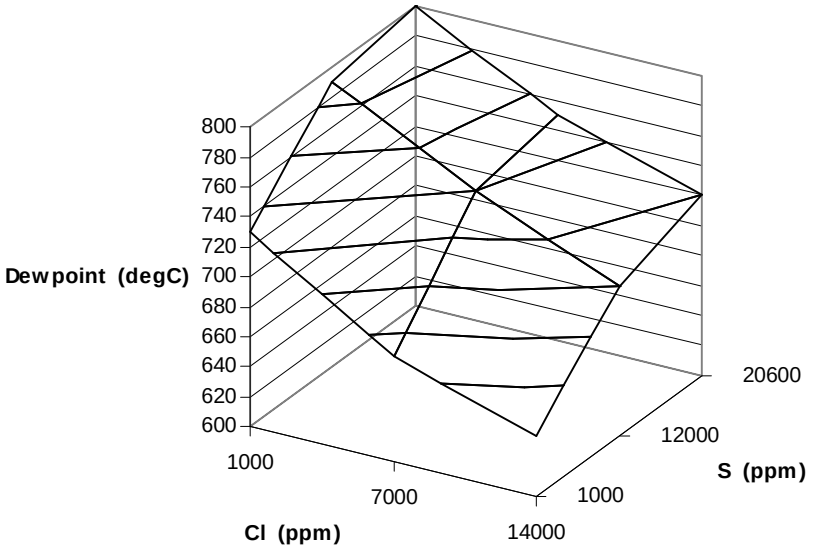

Figure 5.6: Fuel gases for combustion in gas turbines; plots of dewpoints of $CdSO_4$ with varying contents of sulphur and chlorine

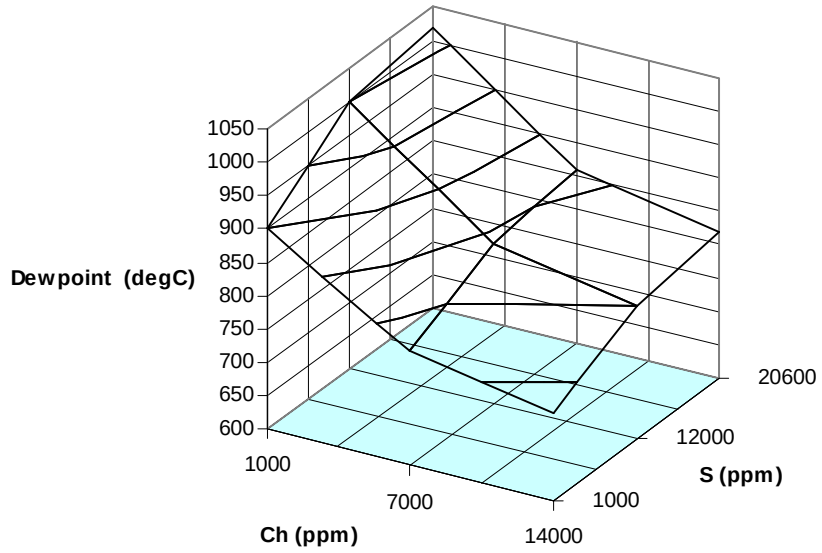

Figure 5.7: Fuel gases for combustion in gas turbines; plots of dewpoints of $PbSO_4$ with varying contents of sulphur and chlorine

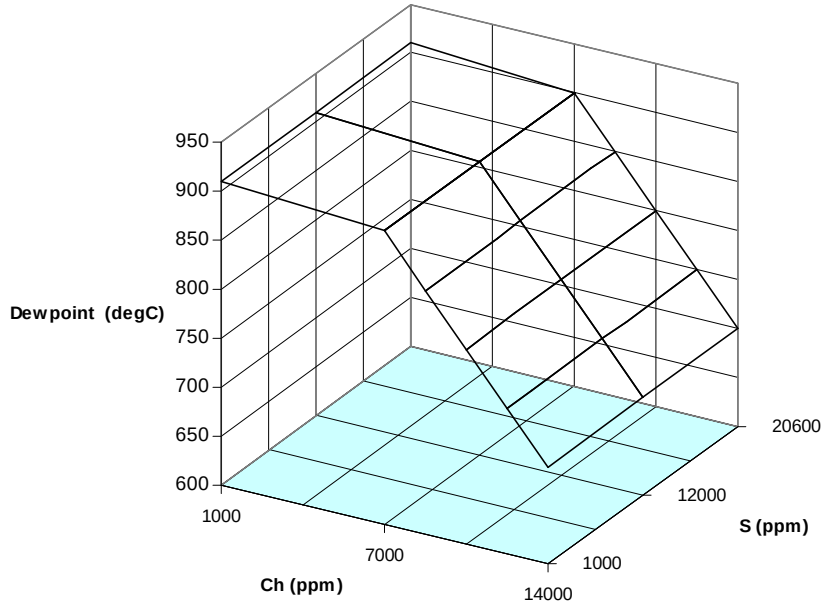

Figure 5.8: Fuel gases for combustion in gas turbines; plots of dewpoints of SbO_2 with varying contents of sulphur and chlorine

In all cases, the dew-point temperatures depend on the concentrations of S and Cl and, to a small extent, on F in the biomass and waste-fuels. With a dew-point temperature range of 160^{o}C, $CdSO_4$ is the least sensitive to variations in the content of these elements, whereas, with a dew-point temperature range of 290^{o}C, $PbSO_4$ is the most sensitive to their content.

The designs and operating pressures and temperatures of industrial gas turbines vary. However, if the surface of a hot component was at say 950^{o}C, the only one of these species which could condense and possibly initiate hot corrosion, would be $PbSO_4$, under specific combinations of S, Cl and F. If the surface temperature was 850^{o}C, $PbSO_4$ and SbO_2 could condense under certain combinations of S, Cl and F and possibly initiate hot corrosion. However, at a temperature of 750^{o}C, each of the Cd, Pb and Sb species could condense under certain combinations of S, Cl and F and possibly initiate hot corrosion. On components at temperatures below 640^{o}C, compounds of all three elements would condense. Components operating above 1050^{o}C would not be susceptible to deposition caused by Cd, Pb or Sb species. First stage turbine blades and vanes, which typically operate at temperatures of up to 950^{o}C, may have areas at much lower temperatures depending on the specific design and cooling methods. Film cooling holes and regions towards the base platforms may operate, in practice, at lower than optimum temperatures.

However, it should be borne in mind that condensation of these species would not occur in isolation. Earlier studies [53,79,80] have shown that alkali metals (Na and K) can also condense on turbine blades/vanes in this temperature range and most likely deposit in a mole ratio of 4:1, depending on the gas clean-up and S/Cl/F content of the fuels.

Therefore the composition of the deposits present on the surfaces of the blades/vanes will be a complex mix of salts. The stability of molten deposits needed for hot corrosion reactions will further depend on the partial pressures of gas phase species (eg. SO_3, HCl) and interactions of the salts with the underlying alloy/oxide layers (this is beyond the scope of study in this thesis).

5.10 Conclusions

The objective of this study was to identify whether trace elements contained in gases produced from the gasification of biomass and waste-fuels could form condensed surface deposits on the hot components of gas turbines, and thereby initiate hot corrosion.

In this study, elemental data on a number of biomass and waste-fuels contained in the PHYLLIS database, provided the inputs for thermodynamic assessments to be made, using the MTDATA MULTIPHASE thermodynamic software package. These assessments showed that, after hot gas cleaning at 500^{o}C, eight trace metals would remain in the fuel gas supplied to the gas turbine, namely mercury, cadmium, tellurium, antimony, selenium, tin, lead and arsenic, in addition to alkali metals.

Further calculations were then used to assess which trace species of these elements in the combusted gases, could condense on to critical components (ie blades and vanes) during their passage through the gas turbine hot gas path.

Overall, these thermodynamic assessments showed that, trace species of cadmium, lead and antimony could pass through the fuel gas path and form surface deposits on hot components, at different locations along the gas turbine gas path, depending on their dew-points.

The identified trace species, $CdSO_4$, $PbSO_4$ and SbO_2 would therefore have the potential to initiate hot corrosion at these locations, in addition to the alkali metal sulphates/chlorides that are normally considered in assessing gas turbine corrosion risks.

After having identified these trace species as having the potential to initiate hot corrosion, the next stage has been to carry out corrosion tests to determine whether, under similar combustion conditions as those in a gas turbine, they will initiate hot corrosion in typical substrate superalloys.

6. Series 1 corrosion tests – uncoated superalloys

6.1 Introduction

The objective of this project is to develop hot corrosion resistant coatings, for industrial gas turbines associated with integrated gasification combined cycle (IGCC) power generation units, fuelled by biomass and waste-fuels. However, these fuels are known to contain trace elements that could cause unacceptably high rates of hot corrosion in the hot components of gas turbines.

Developing novel coatings that will retard the rate of hot corrosion at optimum operating temperatures will provide the optimum conditions, when burning these fuels, of high efficiency and component life. The first stage of the study, reported in Chapter 5, involved thermodynamic assessments using the MTDATA MULTIPHASE software module. This enabled the identification of the trace species contained in gases produced by gasification of biomass and waste-fuels, and which would remain in the gases, following filtration and cleaning, to be carried through for combustion in the gas turbine. The second stage, reported in the same chapter, identified those trace species that, following combustion, would remain in the gas turbine gas path and could condense on gas turbine component surfaces and so have the potential to initiate hot corrosion.

Three species were identified as having the potential to form molten deposits on gas turbine hot components namely; cadmium sulphate ($CdSO_4$), lead sulphate ($PbSO_4$) and antimony dioxide (SbO_2) [117]. The aim of this first series of corrosion tests was to examine whether hot corrosion is initiated by two of these condensed species, $CdSO_4$ and $PbSO_4$, on three uncoated gas turbine substrate materials; polycrystalline IN738LC and IN939, and single crystal CMSX-4. These superalloys were selected as they are commonly used in gas turbine manufacture. Tests involving SbO_2 were postponed until a future date due to the risks of exposure to serious health hazards incurred when handling this species.

For the tests the same gasifier gas composition and similar gas turbine combustion conditions were used, to establish whether the thermodynamic assessment predictions would be realised in practice. A Type II hot corrosion temperature was used for five 100 hour exposure periods, with weighing and salt replenishment before and after each period. A high salt flux was adopted to accelerate the corrosion rate. The gas composition was that used in the thermodynamic assessments; however the tests were carried out at atmospheric pressure, and not the high pressures in normal practice.

This chapter describes the corrosion tests and gives the test results for $CdSO_4$ and $PbSO_4$ individually and in combination with Na_2SO_4 and K_2SO_4, on the three superalloys. The alkali sulphates are typically present in biomass and waste-fuels and their influence on corrosion rates had been assessed previously at Cranfield University [54].

6.2 Superalloys: IN738LC, IN939 and CMSX-4

Of the three superalloys to be used in this series of corrosion tests, IN738LC and IN939 are both polycrystalline and CMSX-4 is a commercial single-crystalline superalloy. They continue to be widely used by manufacturers of industrial gas turbines. The elemental analyses of these superalloys are shown in Table 6.1.

Mass%	Ni	Co	Cr	Al	Y	Si	Ta	Ti	Nb	Hf	Re	W	Mo
IN738LC	62.6	8	16	3.4	-	-	1.7	3.3	1	-	-	2.5	1.5
IN939	49.9	19	22	2	-	-	1.5	3.6	-	-	-	2	-
CMSX-4	60.4	10	6.6	5.5	-	-	6.5	1	-	0.1	3	6.4	0.6

Table 6.1: Elemental analyses of superalloys IN738LC, IN939 and CMSX-4

The major differences between IN738LC and IN939 are in the content of nickel, cobalt, chromium and aluminium, where the lower nickel content of IN939 results from its high levels of cobalt and chromium, the latter being at the highest level quoted for superalloys. The content of aluminium in IN939 is 37% less than in IN738LC, whereas it contains 27% more chromium. In the evaluation of the short- and long-term hot corrosion behaviour of some gas turbine superalloys, Desai [118] found that the superalloys IN738LC and IN939, with sufficient chromium content, showed excellent hot corrosion resistance due to the formation of a protective Cr_2O_3 scale, while superalloys with lower chromium content suffered hot corrosion attack. The catastrophic attacks to the latter alloys were caused by acidic fluxing due to the presence of high refractory elements of tungsten and/or molybdenum. Scale spalling occurred at test temperatures mainly due to the coalescence of pores and the formation of cracks underneath the oxide scale.

CMSX-4 contains significantly less chromium than the other two superalloys to be tested, but more aluminium, and their impact on oxidation and hot corrosion resistance, explained in Chapter 2, become apparent in this series of corrosion tests.

6.2.1. Superalloy IN738LC

IN738LC is a nickel-base superalloy which has been in widespread use for many years, for high stress GT components that operate at high temperatures and in aggressive environments, such as rotating blades. This results from its superior corrosion resistance, optimal thermal properties, strength (with ductility, creep, fatigue resistance) and weldability [118]. However, gas turbine manufacturers such as MHI [119] claim to have developed materials having the same creep strength but at 30^{o}C higher temperature than IN738LC and in another case, the same creep strength at 20^{o}C, while maintaining weldability.

The unique set of properties of IN738LC results from the 'fcc' nickel-base solid solution matrix which is hardened by solutes and precipitates. These are primarily the Ni_3(Al,Ti,Nb)-type intermetallic compounds and carbides, having structure, shape, size and distribution, that give the appropriate combination of properties and of resistance to microstructural changes, at high temperatures. However, the microstructural aspects that have a major influence on these high temperature properties result from morphology change and directional coalescence of γ' precipitates under static and cyclic creep conditions [118].

It was anticipated that this series of corrosion tests would show the extent of hot corrosion caused by acidic fluxing in IN738LC to be lower than for CMSX-4, due to the significant content (16%) of chromium. Examples of Type I and Type II Hot Corrosion of IN738LC are shown in Figure 6.1.

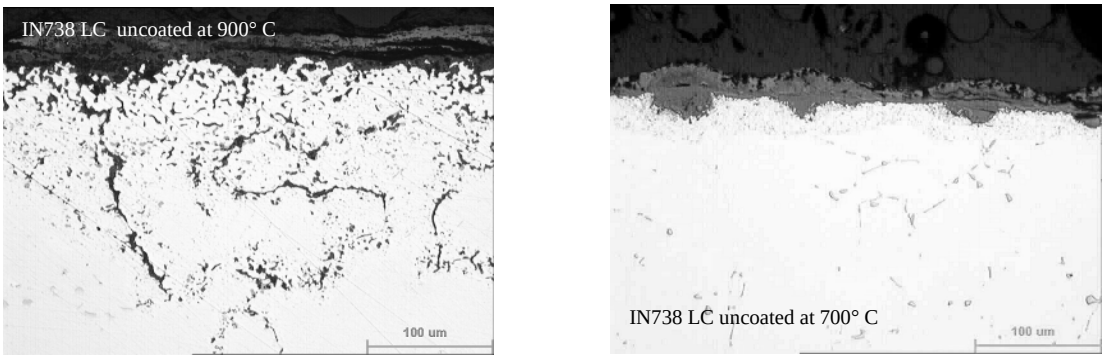

(a) (b)

Figure 6.1: Examples of Type I (a) and Type II (b) hot corrosion on IN738LC [19]

The Type I hot corrosion (above 800^{o}C), caused by either basic fluxing, alloy induced acidic fluxing or sulphidation, produces a corrosion morphology characterised by uniform broad front attack, with internal sulphidation and oxidation of the alloy ahead of the corrosion front.

The Type II hot corrosion (650^{o}C to 800^{o}C), caused by SO_3 present in the combustion gas inducing acidic fluxing or sulphidation, is characterised by a non-uniform distribution of pitting superimposed on the background broad front corrosion.

From her study of oxidation characteristics of IN738LC, Pampana [120] stated that the oxidation of IN738LC at temperatures of 1000^{o}C, 1090^{o}C, 1140^{o}C and 1190^{o}C follows the parabolic rate law, and that it loses weight at the two highest temperatures after certain intervals of time. The behavioural change is explained by the volatilisation of the oxides of chromium, tantallum and niobium at these higher temperatures. In particular, the Cr_2O_3 is converted to the volatile CrO_3.

6.2.2 Superalloy IN939

In the casting process, limitations of top filling aluminum alloys into casting moulds, due to oxide film formation, have been identified, and compared with the advantage of bottom filling to avoid the turbulence that leads to oxidation. In their tests to determine the effects on the Weibull modulus of tensile strength, using the top and bottom filling methods, Cox et al [121] carried out tests of tensile strengths on IN939 and IN738LC. The test results showed that reliability from bottom filling is advantageous for aluminium based investment castings. Comparing IN939 and IN738LC hipped specimens, the Weibull modulus from top filling was 14 and 35 respectively, whereas, for bottom filling through ceramic foam filters, the values were 22 and 41 respectively. Although IN939 is a lower tensile strength alloy than IN738LC, it is widely used in gas turbines which operate at high temperature due its resistance to oxidation at high temperatures. This protection against oxidation is achieved by the formation of an external layer of stable, slow growing oxide, such as Cr_2O_3, Al_2O_3 or SiO, from the selective oxidation of chromium, aluminium or silicon, respectively.

In this regard, although at 22wt%, the content of chromium in IN939 is at the highest end of the range for this element, tests by Lee et al [122] on IN939, without protective coatings, showed rapid weight loss at 3000 hours, due to scale spallation. At 2wt%, the aluminium content of IN939 is the lowest of the three project superalloys and the protection provided by aluminium will end once the selective oxidation reduces its content below the critical value. Enhanced efficiency and performance of gas turbines require hot section structural components with higher temperature capability and longer life. Therefore, in a typical alumina-forming high temperature superalloy, there is only a limited amount of excess aluminium above the critical value. Above this limit, the aluminium degrades the mechanical strength of the superalloy, so that under thermal cycling, protective scales crack and spall, due to the difference in thermal expansion between the alloy and the scale, thus accelerating aluminium loss, compared with that in isothermal expansion [122]. Tests of three NiAl-base coatings, a vapour phase aluminide (VPA), a pack aluminide (CODEP) and a slurry paint aluminide (Sermaloy J) on IN939 specimens showed excellent cyclic oxidation resistance to 10,000 hours [63].

IN939, unlike IN738LC, has low weldability, which limits the components for which it can be used. Weldability is defined as “the capacity of a material to be joined under imposed fabrication conditions into a suitable designed structure and to perform satisfactorily in the intended service” [123].

6.2.3. Superalloy CMSX-4

The increases in gas turbine operating temperatures means that the traditional corrosion resistant turbine blade alloys such as IN738LC and IN939 lack strength enough to offer the expected 25,000 – 30,000 hours minimum life, whereas the higher strength superalloys such as CMSX-4 do have the required creep strength [19,63,123].

CMSX-4 is a second generation, ultra high strength, nickel-base single crystal alloy containing 3wt% rhenium, whose application for GT turbine blades provides lives to overhaul of up to 30,000 hours. This performance results from the superalloy's combination of high creep rupture strength, mechanical and thermal fatigue, good phase stability after extensive high temperature stressed exposure, and oxidation, hot corrosion and coating performance [124]. These characteristics result from the single crystal casting, extensive vacuum and heat treatment and the use of hot-isostatic-pressing (HIP). The latter eliminates single crystal casting micropores which, together with the absence of the eutectic phase, carbides, stable oxide, nitride or sulphide inclusions, results in high mechanical fatigue properties. High temperature heat treatments are necessary to reduce the compositional gradients throughout the material and to disperse a second phase within it [124]. The additional treatments, although expensive, benefit creep and mechanical fatigue strength, with and without HIP, and coating performance.

However, the downside of CMSX-4 is its relatively poor hot corrosion resistance and hence the need for coatings to prevent severe and life limiting damage [123]. Based on this statement, the results of the corrosion tests that follow should show marked differences in the corrosion resistances of IN738LC and IN939 and that of CMSX-4.

6.3 Description of the series 1 corrosion tests

6.3.1 General conditions

The corrosion tests used the combusted fuel gas composition selected for the second stage thermodynamic assessments, at atmospheric pressure. The tests were carried out at 700^{o}C, within the total exposure period of 500 hours per test series. The salt species were replenished at 100 hour intervals to maintain a flux of approximately 15 mg/cm^{2}/hr and samples were weighed at the same intervals.

This flux rate was chosen to reflect the content of the species in the gas flows produced by the gasifier selected for this project. The same ratings for gasifier gas production and flows and of combustion conditions in the gas turbine were assumed, with the exception that the tests were at atmospheric pressure. This contrasts with the GT combustion pressure of approximately 13 bar and reducing pressure gradient to the turbine exhaust. The schedule of superalloys and salt species applied is shown in Table 6.1.

For more information on the equipment and methods used in corrosion testing, reference should be made to Chapter 4.

6.3.2 Gas composition

Two gases were used for the corrosion tests, each providing 50% of the total flow::

- 800ppm HCl, balance N_2;
- 500ppm SO_2, 41.9% O_2, balance N_2.

Each gas bottle supplied a mass controller, set at 25cc/min to provide a total mass flow along the common main of 50cc/min.

Sample No.	Superalloy	Salt/species
1.01	IN738LC	$CdSO_4$
1.02	CMSX-4	$CdSO_4$
1.03	IN939	$CdSO_4$
1.04	IN738LC	$CdSO_4 + (Na_2SO_4(80) + K_2SO_4(20))$
1.05	CMSX-4	$CdSO_4 + (Na_2SO_4(80) + K_2SO_4(20))$
1.06	IN939	$CdSO_4 + (Na_2SO_4(80) + K_2SO_4(20))$
1.07	IN738LC	$(Na_2SO_4(80) + K_2SO_4(20))$
1.08	CMSX-4	$(Na_2SO_4(80) + K_2SO_4(20))$
1.09	IN939	$(Na_2SO_4(80) + K_2SO_4(20))$
1.10	IN738LC	$PbSO_4$
1.11	CMSX-4	$PbSO_4$
1.12	IN939	$PbSO_4$
1.13	IN738LC	$PbSO_4 + (Na_2SO_4(80) + K_2SO_4(20))$
1.14	CMSX-4	$PbSO_4 + (Na_2SO_4(80) + K_2SO_4(20))$
1.15	IN939	$PbSO_4 + ((Na_2SO_4(80) + K_2SO_4(20))$

Table 6.2: Schedule of superalloys and salt species in series 1 corrosion tests

6.3.3 Salt solutions applied in the corrosion tests

The salt solutions were a mixture of the salt and water, in a proportion balanced between not being so concentrated that the salt would not remain in solution at room temperature, but sufficiently concentrated that the water evaporated quickly in order to leave an evenly deposited layer of salt on the surface of the sample. The selected salts required a water solubility that is high enough to spray well. Where mixed salts were to be sprayed, care was taken to avoid precipitation by using three separate sprays and bottles, one for each solution; $CdSO_4$, $PbSO_4$ and $(Na_2SO_4 + K_2SO_4)$.

Lead sulphate causes difficulties in a water solution as the salt will precipitate from the mixed solution. Therefore, for these tests, lead nitrate $Pb(NO_3)_2$ was used in sufficient quantities that the lead reacted with SO_2 and HCl in the gases to produce $PbSO_4$, PbCl, PbO and NOx. As $Pb(NO_3)_2$ was being used in place of $PbSO_4$, an allowance had to be made for the difference in weight of these salts.

Therefore, where 5 mg of $PbSO_4$ was to be added at the start of the tests and at each of the 100 hour intervals, the value 5.6 mg $Pb(NO_3)_2$ was applied. Trial and error were used to determine the maximum amount of salt that should be added to the water without precipitation, to prevent the spray solution being allowed to crystallise, thus altering the ratio of salts being applied.

6.3.4 Safety precautions, procedures and equipment

The salt species being used in the corrosion tests are hazardous to varying degrees, as shown in the individual Control of Substances Hazardous to Health (COSHH) Assessments. The tests were executed strictly in accordance with the Cranfield University Power Generation Technology Centre's Standard Operating Procedure for Sample Preparation and Spraying Salt Solutions on to Corrosion Specimens, and the individual COSHH assessment sheets. These detailed the precautions to be taken and conditions for the tests with regard to the use of specified personal protective equipment, vented spray cabinet, methods of preventing contamination of surrounding areas, use of sprays and bottles dedicated to each salt and labelling of each item. Disposal of waste solution, gloves and other contaminated materials were also carried out in accordance with these regulations.

6.3.5 Methodology

The series of laboratory tests used the well established deposit replenishment technique [19,63] to investigate the effects of the compositions of the three species selected on each of the three substrate superalloys. The test apparatus has evolved over a 15 year period and provides atmospheres in the furnace by closely controlling the inlet gases from pre-mixed gas bottles and the analysis of outlet gases.

Reference should be made to Chapter 4 for information on sample preparation, the spraying of salt solutions and weighing activities pre- and post-corrosion tests.

6.4 Series 1 corrosion tests – results and evaluation

On completion of the corrosion tests, samples were mounted and cross-section surfaces prepared in accordance with the procedures described in Chapter 4. Photographs of the tested and untested samples, prior to being mounted are shown in Figure 6.2.

Evaluations of the samples were carried out by assessing mass change, metrology to determine accurately the extent and character of corrosion damage, by optical microscopy to identify the extent of corrosion and scale formation, and by scanning electron microscope (SEM) to identify the dispersion of main elements in the corrosion damage.

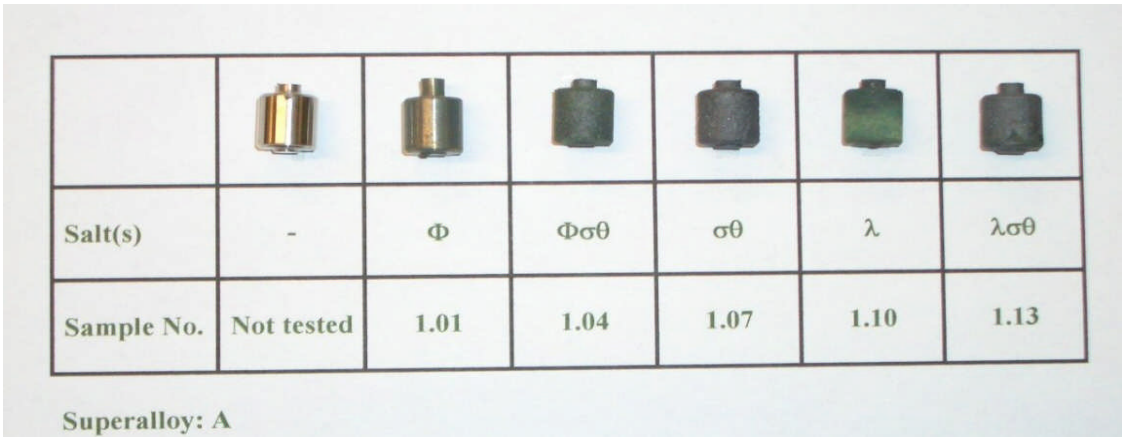

Salt(s)	-	Φ	Φσθ	σθ	λ	λσθ
Sample No.	Not tested	1.01	1.04	1.07	1.10	1.13

Superalloy: A

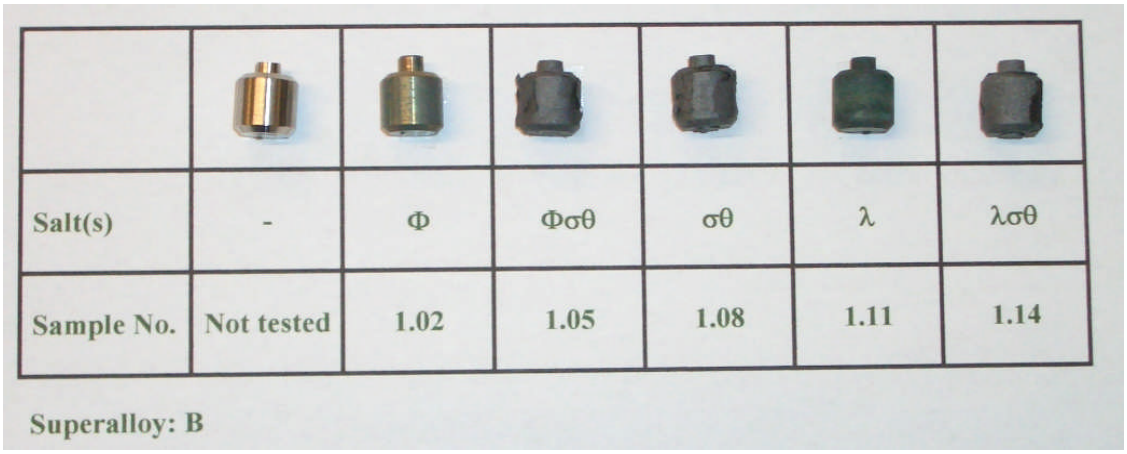

Salt(s)	-	Φ	Φσθ	σθ	λ	λσθ
Sample No.	Not tested	1.02	1.05	1.08	1.11	1.14

Superalloy: B

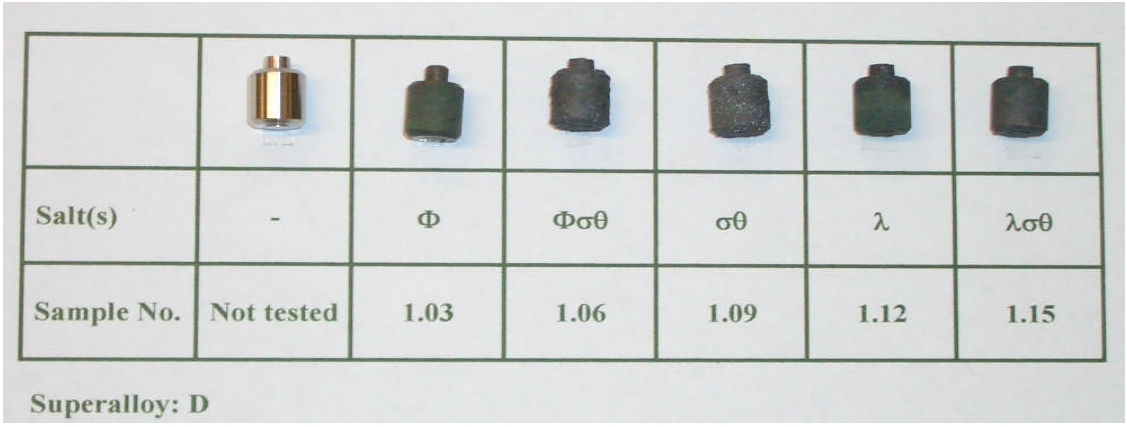

Salt(s)	-	Φ	Φσθ	σθ	λ	λσθ
Sample No.	Not tested	1.03	1.06	1.09	1.12	1.15

Superalloy: D

Codes: Superalloy; A, IN738LC, B, CMSX-4, D, IN939
Salts; $\Phi = CdSO_4$, $\sigma = Na_2SO_4$, $\theta = K_2SO_4$, $\lambda = PbSO_4$

Figure 6.2: Photographs of samples on completion of the series 1 corrosion tests

6.4.1 Results for IN738LC

6.4.1.1 IN738LC – Mass change

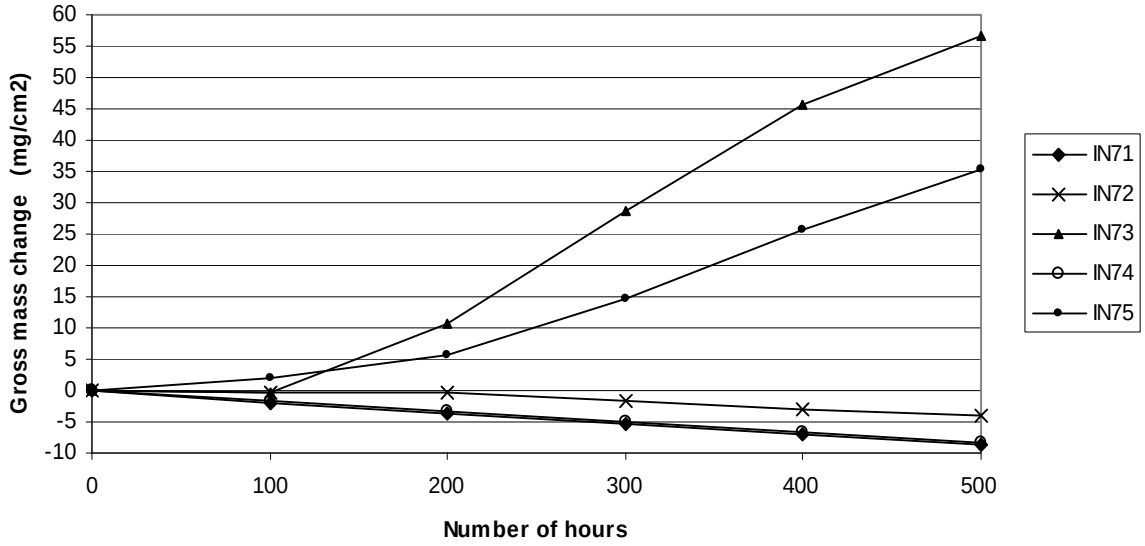

Key: IN71; $CdSO_4$ IN72; $CdSO_4$+(Na_2SO_4(80)+K_2SO_4(20)) IN73; (Na_2SO_4(80)+K_2SO_4(20))
IN74; $PbSO_4$ IN75; $PbSO_4$+(Na_2SO_4(80)+K_2SO_4(20))

Figure 6.3: IN738LC; comparison of gross mass changes from different salt species after 500 hours corrosion testing at 700°C

The gross mass change graphs for IN738LC are shown in Figure 6.3. The samples solely carrying sulphates of cadmium and lead and, the sample carrying $CdSO_4$+(Na_2SO_4(80)+K_2SO_4(20)), indicate that very little Type II hot corrosion is being initiated. The inference is that most of these species are evaporating, without condensing on the surfaces of samples, then being exhausted from the furnace. This is particularly the case for cadmium, even when in combination with sodium and potassium salts. The (Na_2SO_4(80)+K_2SO_4(20)) species initiates hot corrosion in IN738LC more aggressively than when in combination with lead, but still remaining in the incubation stage.

Reference to the net mass change graphs, shown in Figure 6.4, reflect these phenomena but some hot corrosion may be initiated by the $CdSO_4$+(Na_2SO_4(80)+K_2SO_4(20)) combination (IN72) after 300 hours of testing. Comparison of the two sets of graphs indicate that no scale spallation occurs when these salt species are corrosion tested on IN738LC at 700°C.

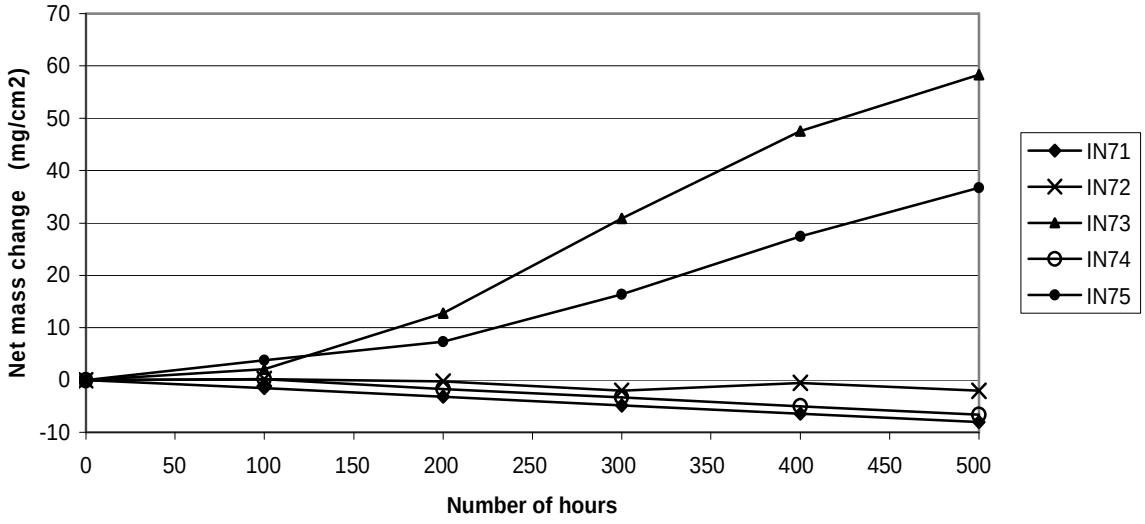

Key: IN71; $CdSO_4$ IN72; $CdSO_4$+(Na_2SO_4(80)+K_2SO_4(20)) IN73; (Na_2SO_4(80)+K_2SO_4(20))
IN74; $PbSO_4$ IN75; $PbSO_4$+(Na_2SO_4(80)+K_2SO_4(20))

Figure 6.4: IN738LC; comparison of net mass changes from different salt species after 500 hours corrosion testing at 700°C

6.4.1.2 IN738LC – Metrology

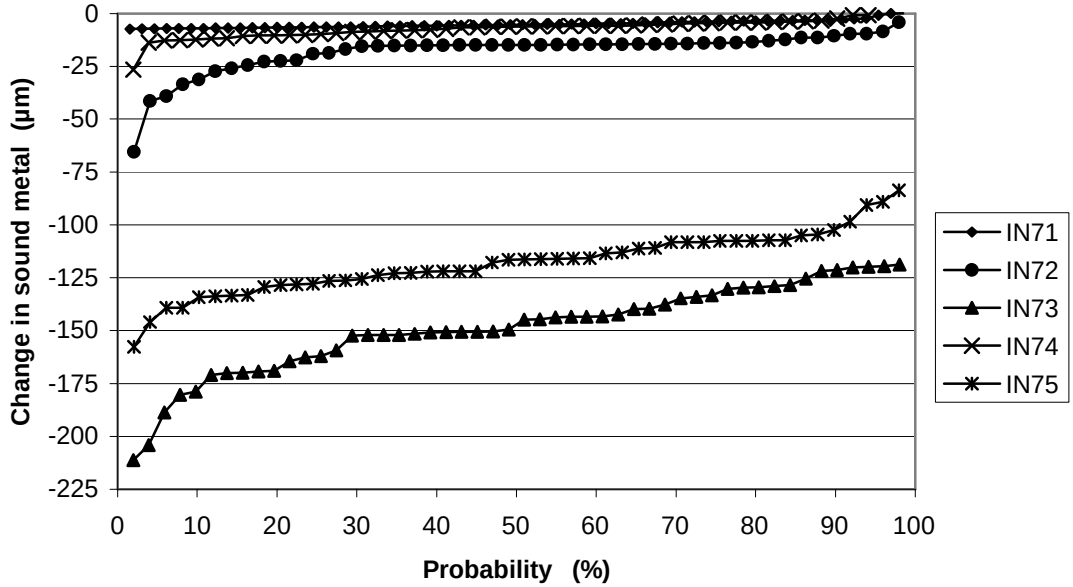

Key: IN71; $CdSO_4$ IN72; $CdSO_4$+(Na_2SO_4(80)+K_2SO_4(20)) IN73; (Na_2SO_4(80)+K_2SO_4(20))
IN74; $PbSO_4$ IN75; $PbSO_4$+(Na_2SO_4+K_2SO_4)

Figure 6.5: IN738LC; comparisons of change in sound metal after 500 hours corrosion testing at 700°C

The graphs in Figure 6.5, showing changes in sound metal following 500 hours corrosion tests at 700°C, confirm the degree of hot corrosion initiated by these species, shown in the mass change graphs above. The graphs indicate considerable pitting in IN73 and IN75. The summary of the ranges of changes in sound metal in IN738LC, resulting from the corrosion tests, are presented in Table 6.3.

Sample code	Φ wt%/ mol%	σ wt%/ mol%	θ wt%/ mol%	λ wt%/ mol%	Change in sound metal µm
1.01	83.8/100				0 to -7.5
1.04	41.9/50	38.3/40	11.7/10		-4 to -40
1.07		76.5/80	23.5/20		-120 to -200
1.10				154.8/100	-1 to -13
1.13		76.5/40	23.5/10	77.4/50	-80 to -160

Key : Φ - cadmium, σ - sodium, θ - potassium, λ - lead

Table 6.3 : Summary of change in sound metal for IN738LC after 500 hours corrosion tests at 700°C

6.4.1.3 IN738LC – Optical microscopy

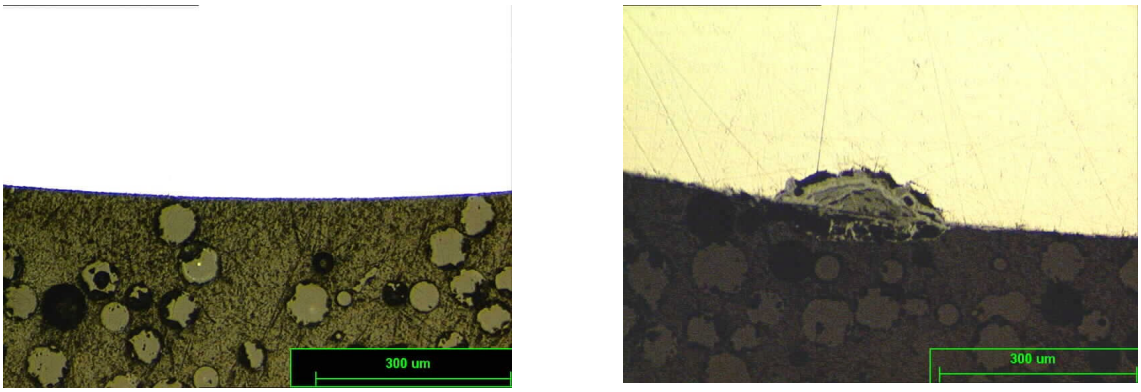

(a) IN738LC - $CdSO_4$ (b) IN738LC - $CdSO_4$+(Na_2SO_4+K_2SO_4)

Figure 6.6: IN738LC samples after 500 hours corrosion testing at 700°C, (a) with $CdSO_4$ and (b) with $CdSO_4$+(Na_2SO_4(80)+K_2SO_4(20))

Figure 6.6 shows optical micrographs of IN738LC samples, one carrying $CdSO_4$ and the other carrying the $CdSO_4$+(Na_2SO_4(80)+K_2SO_4(20)) combination. As shown by graphs of mass change and change in sound metal, for these combinations, no hot corrosion has been initiated on the sample carrying cadmium sulphate. Image (b) on Figure 6.6 shows a localised growth of scale and pitting formed by Type II hot corrosion, accompanied by a very fine general layer of scale deposits, again bearing out graphs in Figures 6.3 and 6.5.

The micrograph of the sample carrying (Na_2SO_4+K_2SO_4), in Figure 6.7, shows the significant Type II hot corrosion pitting and scale formation following 500 hours corrosion testing at 700°C. The pits are approximately 70µm in depth. This combination of salts initiates the most severe hot corrosion damage of all the combinations in these tests, on IN738LC, as shown in Table 6.3.

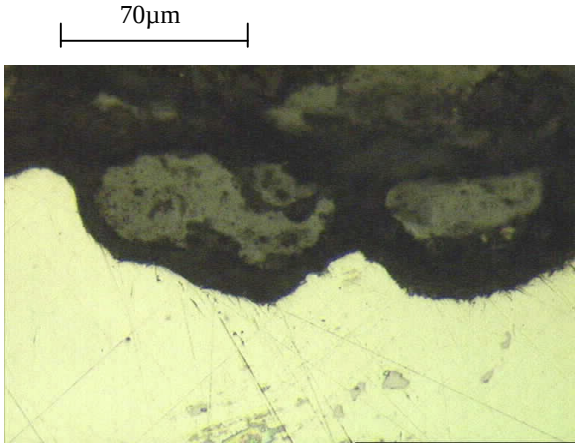

Figure 6.7: IN738LC with (Na_2SO_4(80)+K_2SO_4(20)) after 500 hours corrosion testing at 700°C

The micrographs of $PbSO_4$ and combined $PbSO_4$+(Na_2SO_4(80)+K_2SO_4(20)) samples, Figure 6.8 shows no hot corrosion has been initiated by lead sulphate alone. The scale formation and pitting resulting from Type II hot corrosion are to be seen in the sample tested with the $PbSO_4$+(Na_2SO_4+K_2SO_4) combination, shown in Figure 6.8(b). These results are consistent with the mass changes and changes in sound metal for these salts, seen in Figures 6.3 and 6.5.

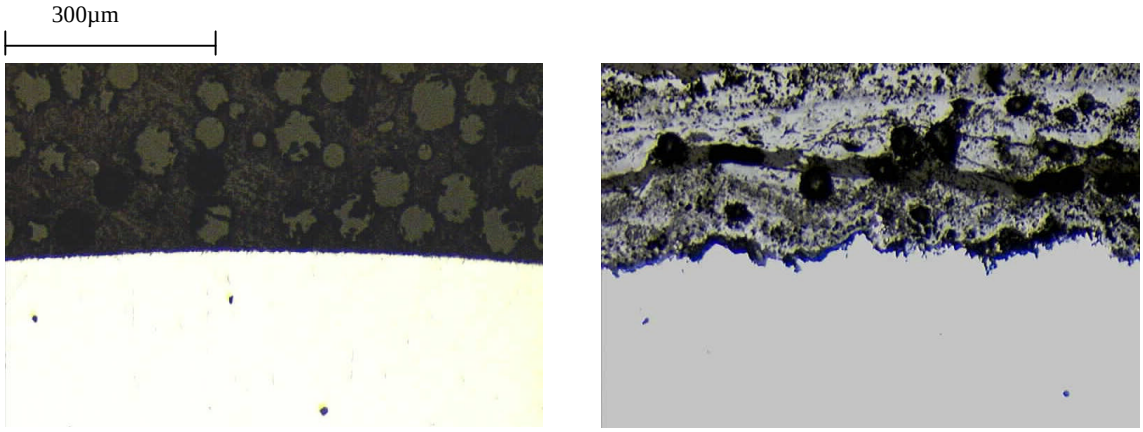

(a) IN738LC - $PbSO_4$

(b) IN738LC-$PbSO_4$+(Na_2SO_4(80)+K_2SO_4(20))

Figure 6.8: IN738LC samples after 500 hours corrosion testing at 700°C, (a) with $PbSO_4$ and (b) with $PbSO_4$+(Na_2SO_4(80)+K_2SO_4(20))

6.4.1.4 IN738LC – Micrograph and element analyses by scanning electron microscope

The objective of the first series of corrosion tests, at 700°C, was to investigate whether the trace salt species, cadmium sulphate and lead sulphate, would initiate hot corrosion in gas turbine superalloys, as predicted by the thermodynamic assessments reported in Chapter 5.

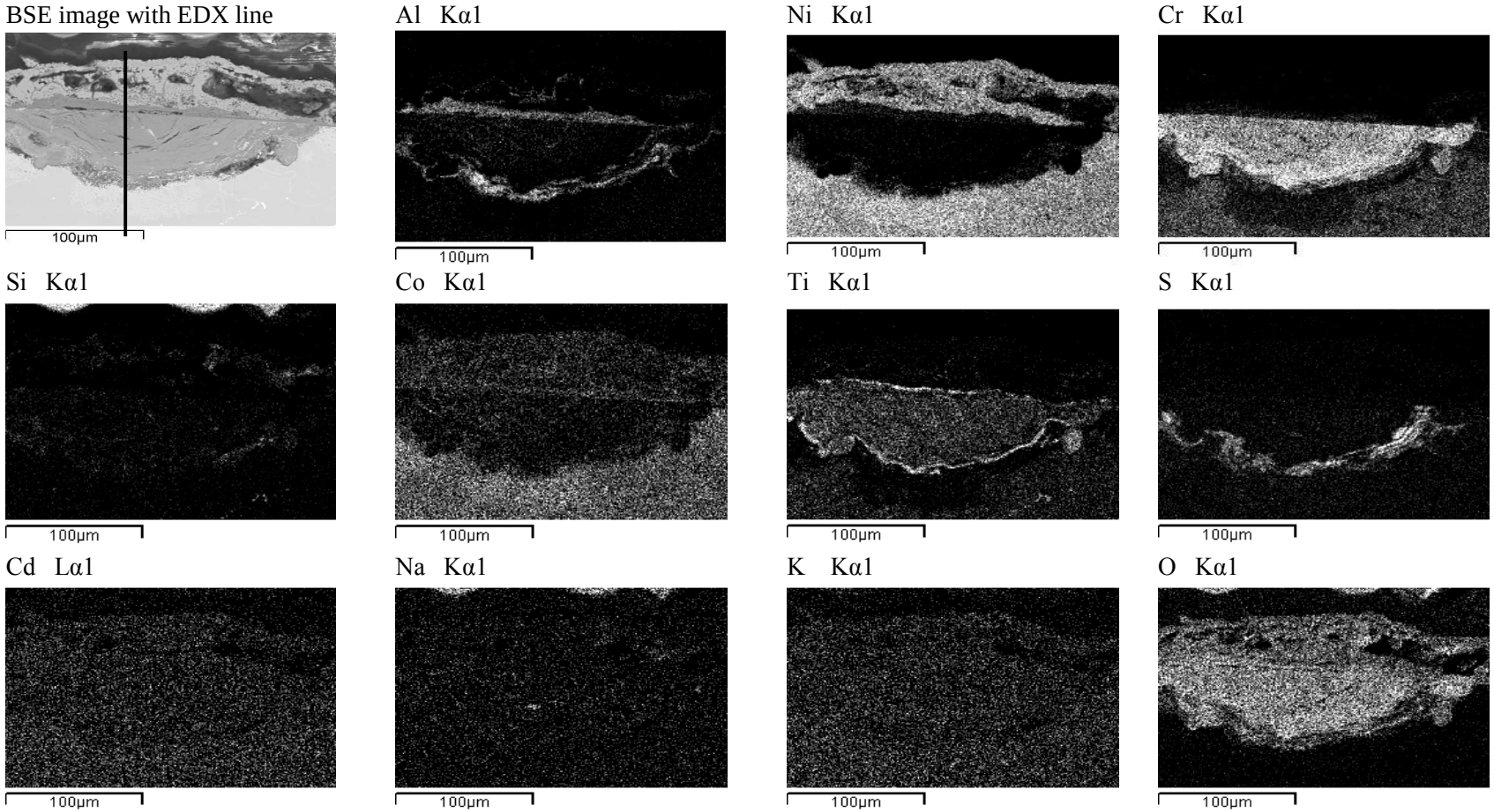

Figure 6.9: IN738LC after corrosion testing for 500 hours at 700^{o}C with $CdSO_4$+(Na_2SO_4(80)+K_2SO_4(20)) – element maps

Of the IN738LC samples tested, little significant hot corrosion had been initiated in those carrying either $CdSO_4$ or $PbSO_4$ alone. In samples tested with (Na_2SO_4(80)+K_2SO_4(20)), or in combination with either cadmium sulphate or lead sulphate, significant Type II hot corrosion had been initiated, as shown by the mass changes, changes in sound metal and optical microscopy. It was decided that, analysis by scanning electron microscope (SEM) would not proceed for the samples carrying cadmium sulphate or lead sulphate.

(a) IN738LC corrosion tested with $CdSO_4$+(Na_2SO_4(80)+K_2SO_4(20)) salt combination

The element maps for the corrosion tests on this salt combination are shown in Figure 6.9. The element analysis along the EDX line shown in the BSE image in Figure 6.9 is shown in Figure 6.10. From the maps, the scale is seen to consist predominantly of oxides of nitrogen, cobalt, silicon, cadmium, sodium, potassium, and aluminium. Lesser oxides of titanium and sulphur are present in the scale. The chromium present in the scale is mainly located, as a thin layer, at the interface between the scale and the surface of the corrosion pit. The scale aluminium is present along the scale surface and at the pit surface, the latter area in combination with the chromium. Taking into account the reduced nickel in the same area, they are having a retarding effect on the corrosion rate.

The corrosion pit consists of oxides of chromium, titanium, cadmium, potassium , and to lesser extents, aluminium, silicon, sodium, cobalt and sulphur. At the inner face of the substrate, there are concentrated layers of aluminium, chromium, titanium and sulphur. Sulphidation and oxidation are the corrosion mechanisms, being retarded by aluminium and chromium, with the substrate levels of nickel, cobalt, cadmium, sodium, potassium, remaining uniform. The corrosion pit base and outer oxidation zones contain aluminium and added protection is provided by chromium in the pit, particularly along the chromium rich bottom region.

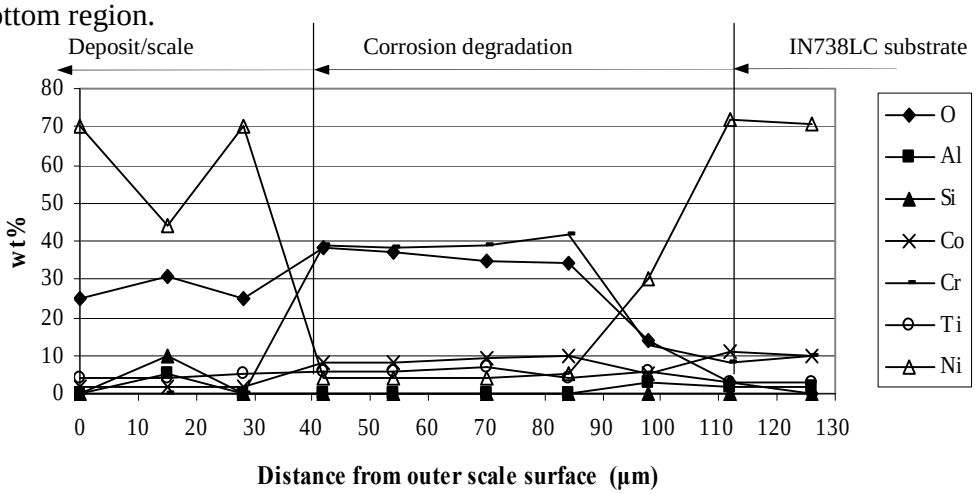

Salt combination : $CdSO_4$ + (Na_2SO_4(80) + K_2SO_4(20)) Salt flux : 15.0µg/cm^2/hr
Test conditions: 500 hours at 700^{o}C

Figure 6.10: IN738LC; main elements along EDX line shown in Figure 6.9

(b) IN738LC corrosion tested with the (Na_2SO_4(80)+K_2SO_4(20)) salt combination

Figure 6.11 shows the main elements along the EDX line indicated in the BSE image map of Figure 6.12. The depth of degradation in the sample shown in Figure 6.11 and the element maps in Figure 6.12, approximately 100µm, consists of oxides of nickel, cobalt and, to a much lesser extent, aluminium, titanium, sulphur, molybdenum, sodium, potassium and a trace level of chromium. Oxide layer cracking can be seen in the BSE image, but this is not apparent in the element maps.

The lower corrosion layer below the scale, with a depth of approximately 300µm, consists of oxides of chromium, titanium, aluminium and molybdenum, with uniformly distributed sodium and potassium. Chromium appears to retard sulphidation at the corrosion zone interface with the substrate. Sulphur and molybdenum peaks, seen in the element maps ar in the same region indicated by the EDX results.

Oxidation and sulphidation are involved in the pitting developing at the substrate/ corrosion zone interface.

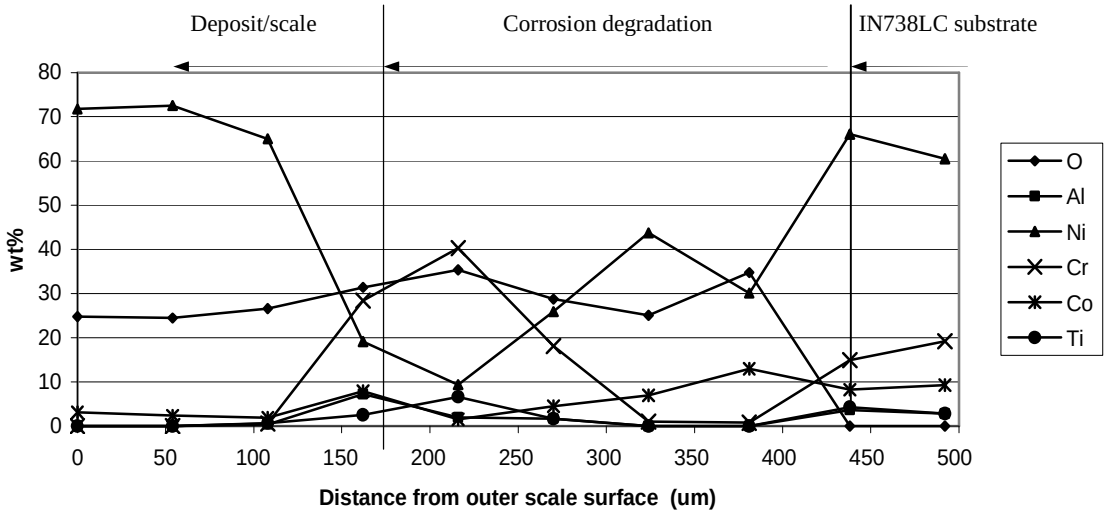

Figure 6.11: IN738LC; main elements along EDX line shown in Figure 6.12

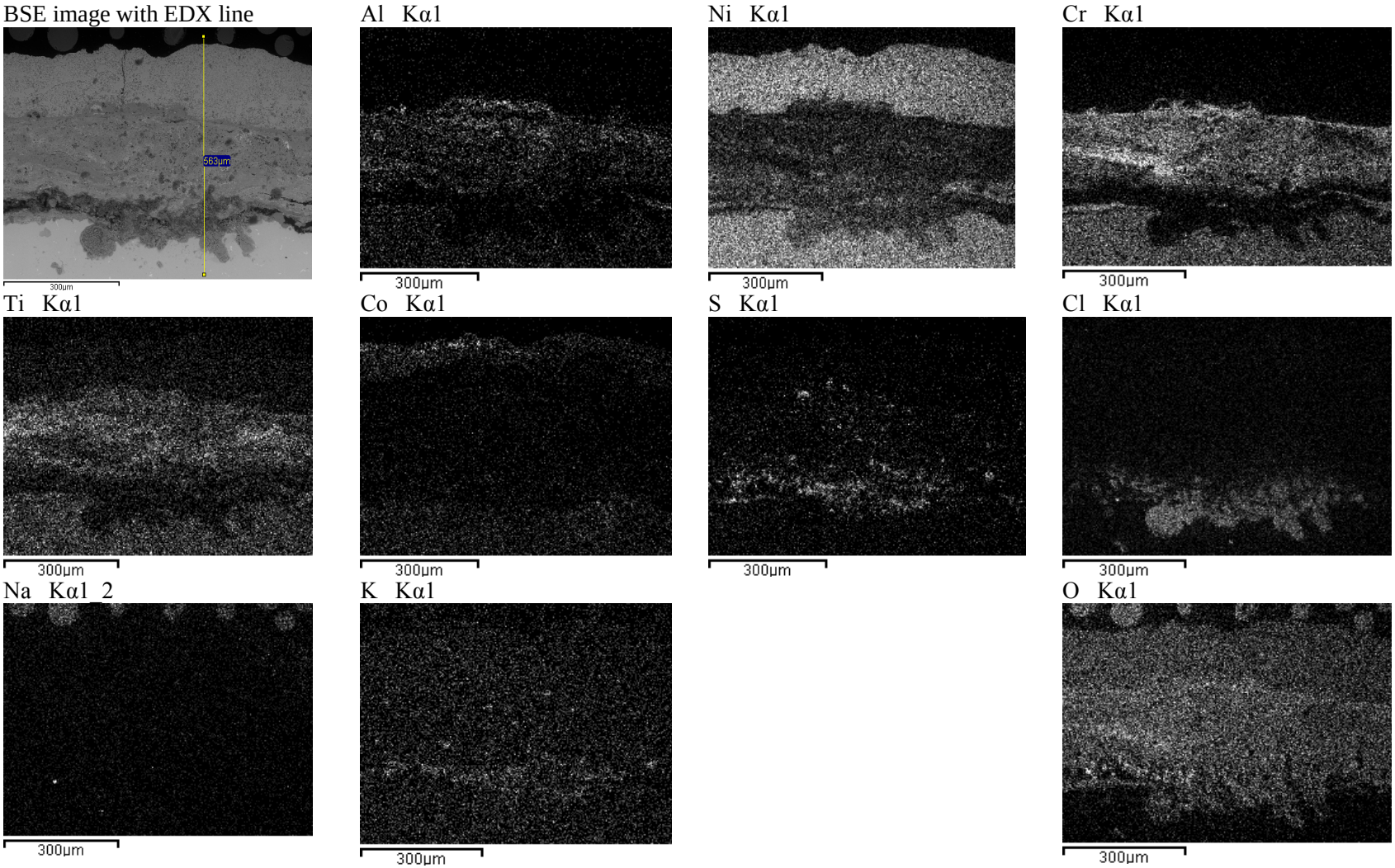

Figure 6.12: IN738LC after 500 hours corrosion tests at 700°C with (Na_2SO_4(80) + K_2SO_4(20)) – element maps

(c) IN738LC corrosion tested with $PbSO_4$+(Na_2SO_4(80)+K_2SO_4(20) salt combination

Element analyses in Figure 6.13 and the element maps presented in Figure 6.14 show the individual 100 hour test periods. The scale from the first two test periods is dominated by nickel and cobalt oxides, with much lower content oxides of aluminium, chromium, titanium, sulphur, sodium and potassium. The element map shows a uniform light distribution of lead oxide throughout the scale, with the EDX results showing this to be <1 at%Pb. Oxidation precedes sulphidation in development of the corrosion mechanism.

Corrosion retarding concentrations of aluminium and chromium occur where both the oxidation and sulphidation mechanisms have been occurring, with aluminium at the leading edge of the corrosion.

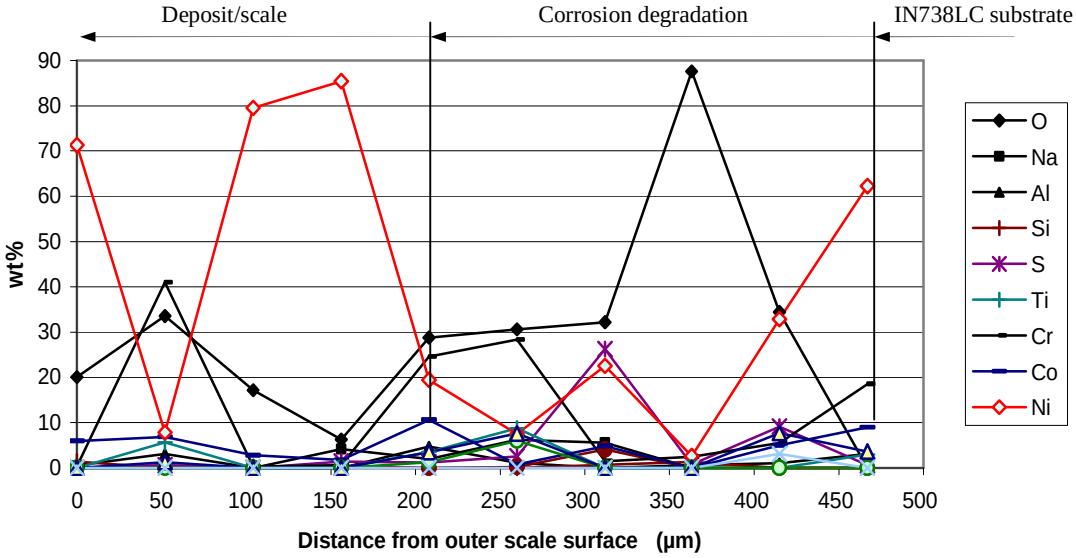

Figure 6.13: IN738LC; main elements along EDX line shown in Figure 6.14

Comparisons of the corrosion morphology produced by the three salt combinations on IN738LC, shown in Figures 6.9, 6.12 and 6.14, show that cadmium, in combination with sodium and potassium, is the least corroding. Under the conditions of this corrosion test series, which has the comparatively high salt flux of 15 µg/cm^2/h, the corrosion rates of the lead/sodium/potassium combination and that of sodium/potassium alone are similar.

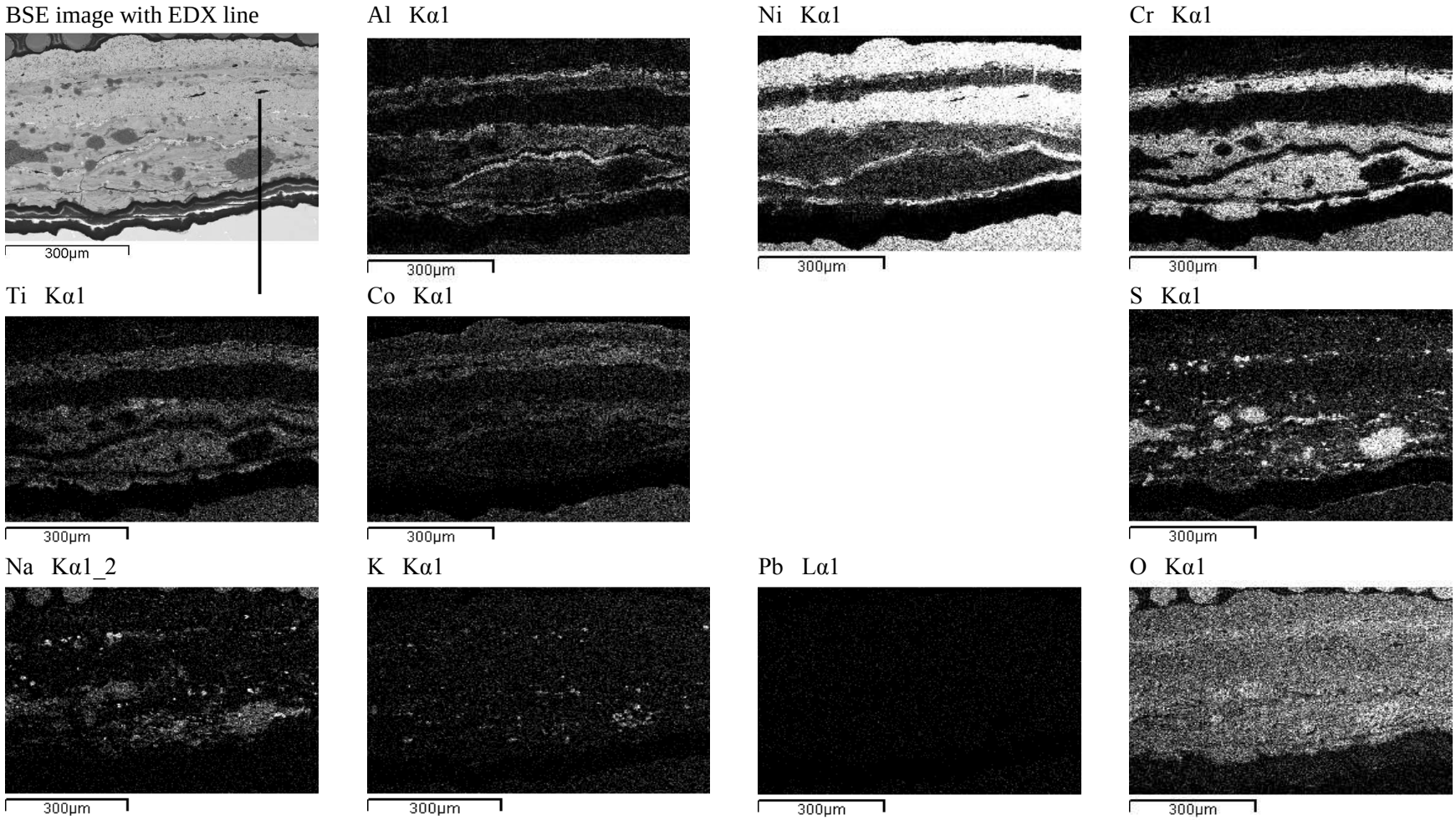

Figure 6.14: IN738LC after 500 hours corrosion tests at 700°C with $PbSO_4$ + (Na_2SO_4(80) + K_2SO_4(20)) – element maps

6.4.2 Results for CMSX-4

6.4.2.1 CMSX-4 – Mass change

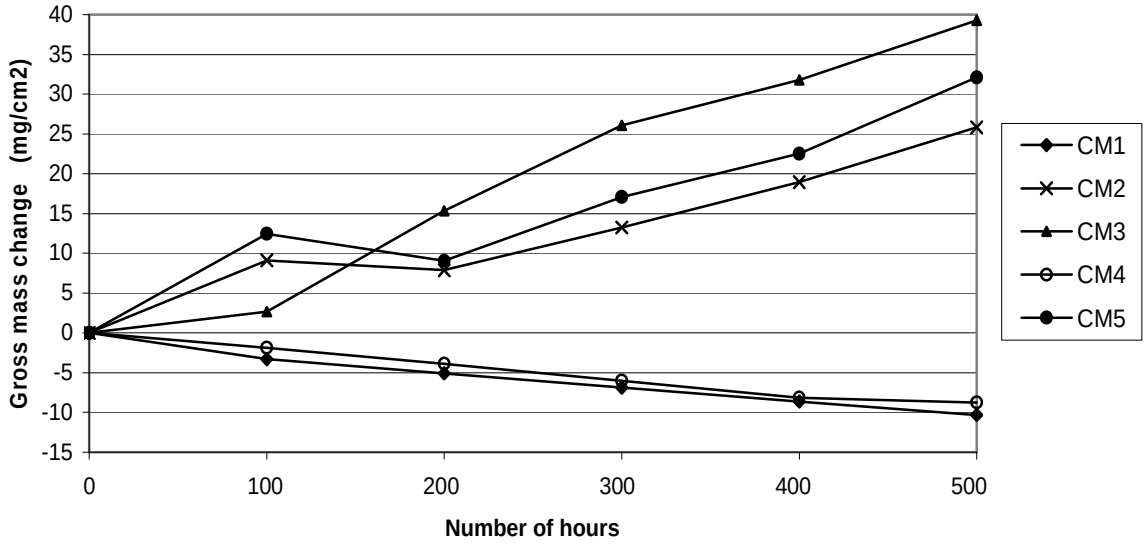

Key: CM1; $CdSO_4$ CM2; $CdSO_4$+(Na_2SO_4(80)+K_2SO_4(20)) CM3; (Na_2SO_4(80)+K_2SO_4(20))
CM4; $PbSO_4$ CM5; $PbSO_4$+(Na_2SO_4(80)+K_2SO_4(20))

Figure 6.15: CMSX-4; comparison of gross mass changes from different salt species after 500 hours corrosion testing at 700^{o}C

The gross mass change graphs for CMSX-4 are shown in Figure 6.15. The samples solely carrying sulphates of cadmium and lead indicate that very little corrosion is being initiated. The inference is that evaporation of these species is occurring the products being exhausted from the furnace, corrosion is still in incubation. However, for CMSX-4, cadmium in combination with sodium and potassium salts initiates hot corrosion at a similar rate to the lead/sodium/ potassium combination. The (Na_2SO_4(80)+K_2SO_4(20)) species initiates hot corrosion in CMSX-4 less aggressively than when they are in combination with cadmium or lead.

Reference to the net mass change graphs, shown in Figure 6.16, reflect these phenomena but more hot corrosion is initiated by both the $CdSO_4$+(Na_2SO_4(80)+K_2SO_4(20)) combination (CM2) and the $PbSO_4$+(Na_2SO_4(80)+K_2SO_4(20)) combination (CM4), than (Na_2SO_4(80)+K_2SO_4(20)) alone (CM3), after 300 hours of testing. Comparison of the two sets of graphs indicate that no scale spallation occurs when these salt species are corrosion tested on CMSX-4 at 700^{o}C.

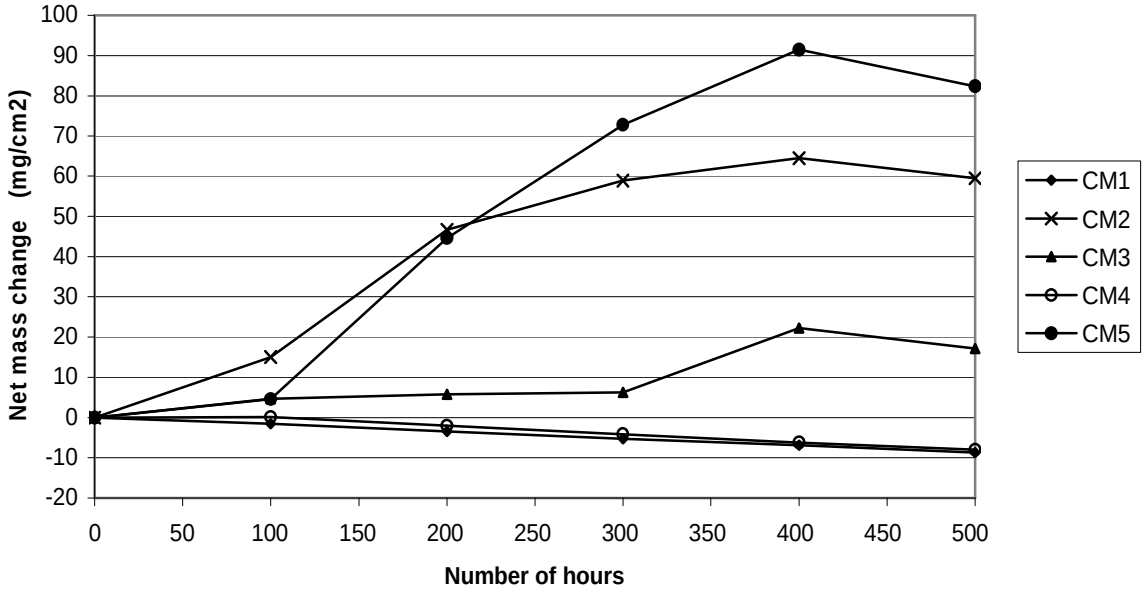

Key: CM1; $CdSO_4$ CM2; $CdSO_4(Na_2SO_4(80)+K_2SO_4(20))$ CM3; $(Na_2SO_4(80)+K_2SO_4(20))$
CM4; $PbSO_4$ CM5; $PbSO_4+(Na_2SO_4(80)+K_2SO_4(20))$

Figure 6.16: CMSX-4; comparison of net mass changes from different salt species after 500 hours corrosion testing at 700°C

6.4.2.2 CMSX-4 – Metrology

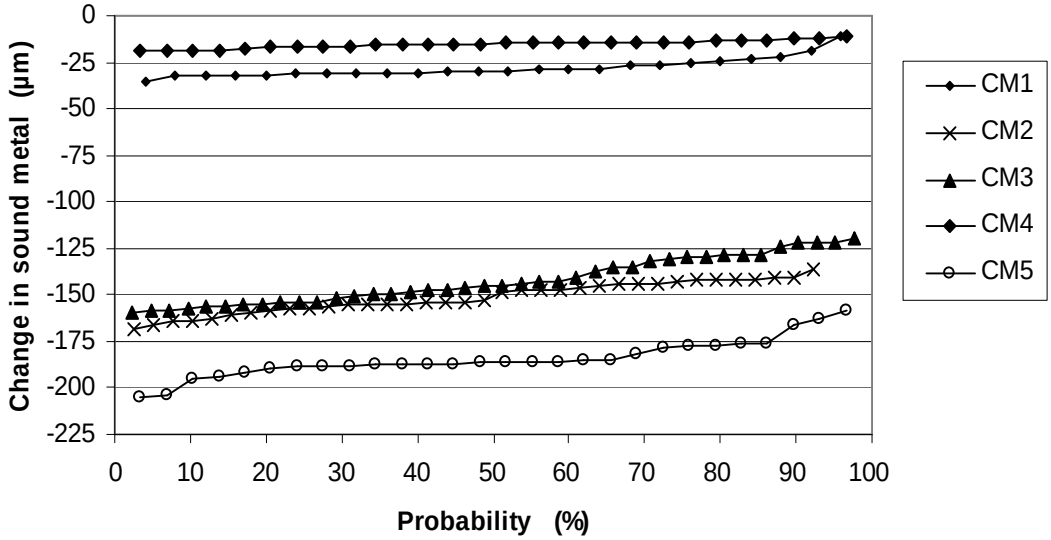

Key: CM1; $CdSO_4$ CM2; $CdSO_4+(Na_2SO_4(80)+K_2SO_4(20))$ CM3; $(Na_2SO_4(80)+K_2SO_4(20))$
CM4; $PbSO_4$ CM5; $PbSO_4+(Na_2SO_4(80)+K_2SO_4(20))$

Figure 6.17: CMSX-4; comparisons of change in sound metal after 500 hours corrosion testing at 700°C

The graphs in Figure 6.17, showing changes in sound metal following 500 hours corrosion tests at 700°C, confirm the degree of hot corrosion initiated by these species shown in the mass change graphs above. The graphs alos indicate uniform degradation round the samples, with little pitting. The summary of the ranges of changes in sound metal in CMSX-4, resulting from the corrosion tests are presented in Table 6.4.

Sample code	Φ wt%/ mol%	σ wt%/ mol%	θ wt%/ mol%	λ wt%/ mol%	Change in sound metal µm
1.02	83.8/100				0 to -25
1.05	41.9/50	38.3/40	11.7/10		-135 to -170
1.08		76.5/80	23.5/20		-120 to -155
1.11				154.8/100	0
1.14		76.5/40	23.5/10	77.4/50	-155 to -205

Key : Φ - cadmium, σ - sodium, θ - potassium, λ - lead

Table 6.4: Summary of change in sound metal in CMSX-4 samples after series 1 corrosion tests

6.4.2.3 CMSX-4 – optical microscopy

Figure 6.16 shows optical micrographs of CMSX-4 samples, one carrying $CdSO_4$ and the other carrying the $CdSO_4$+(Na_2SO_4+K_2SO_4) combination. As shown by graphs of mass change and change in sound metal, for these combinations, significantly less hot corrosion has been initiated on the sample carrying cadmium sulphate, where only light pitting has occurred.

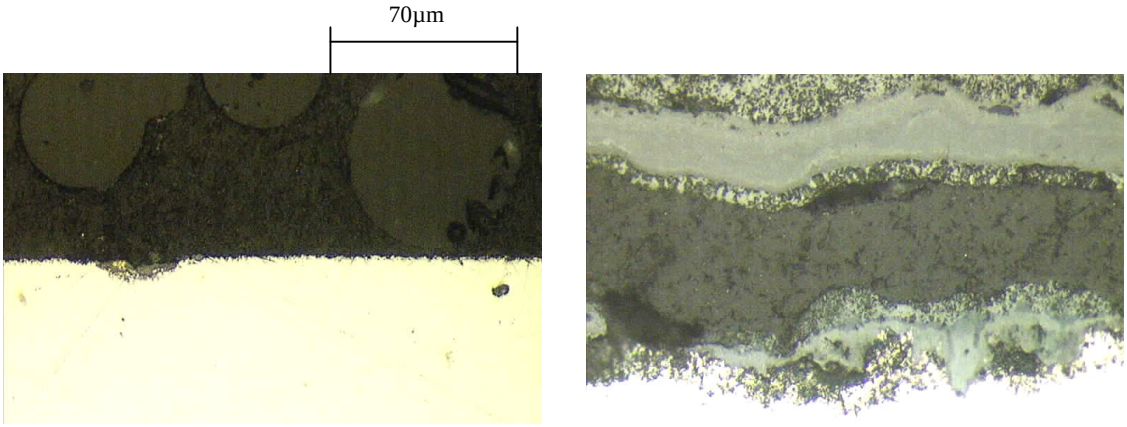

(a) $CdSO_4$ (b) $CdSO_4$ +(Na_2SO_4(80)+K_2SO_4(20))

Figure 6.18: CMSX-4 samples after 500 hours corrosion testing at 700°C, (a) with $CdSO_4$ and (b) with $CdSO_4$+(Na_2SO_4(80)+K_2SO_4(20))

Figure 6.18(b) shows the heavy Type II hot corrosion initiated in CMSX-4 by the salt species $CdSO_4$+(Na_2SO_4(80)+K_2SO_4(20)), again bearing out the mass changes shown earlier in this section.

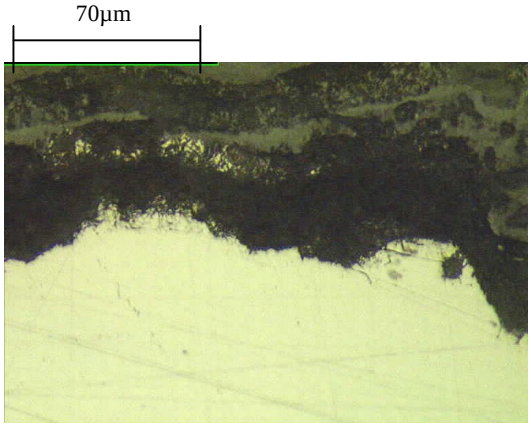

Figure 6.19: CMSX-4 after testing with (Na_2SO_4(80)+K_2SO_4(20))

Significant Type II hot corrosion occurs in CMSX-4 after 500 hours testing at 700°C by Na_2SO_4(80)+K_2SO_4(20), as shown in Figure 6.19. However, this combination of salt species causes less change in sound metal, in CMSX-4, than the cadmium and lead combinations with sodium and potassium.

Micrographs of $PbSO_4$ alone and the species (Na_2SO_4(80)+K_2SO_4(20)), seen in Figure 6.20, show the very light surface pitting initiated by the former and heavier Type II hot corrosion pits initiated by the latter. These results are consistent with the mass changes and changes in sound metal, for these species, shown in Figures 6.15, 6.16 and 6.17.

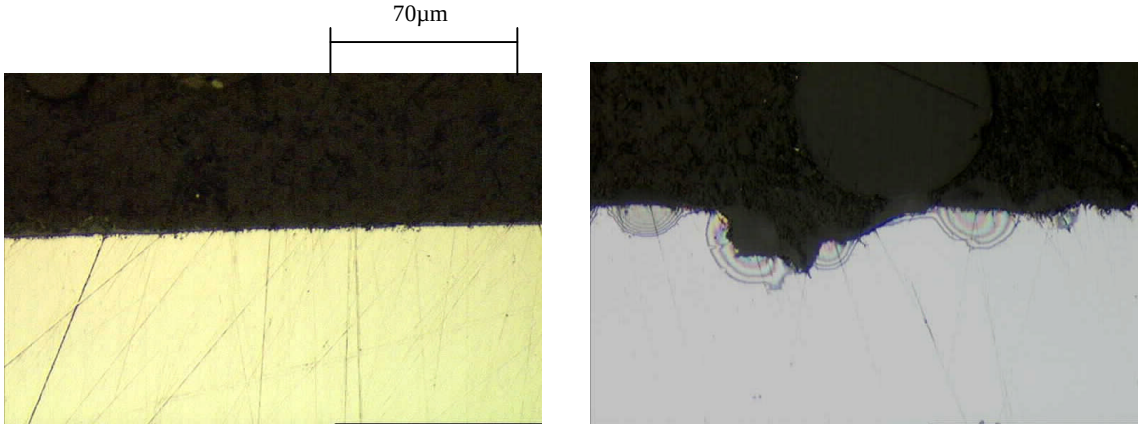

(a) $PbSO_4$ (b) $PbSO_4$+(Na_2SO_4+K_2SO_4)

Figure 6.20: CMSX-4 samples after 500 hours corrosion testing at 700°C, (a) with $PbSO_4$ and (b) with $PbSO_4$+(Na_2SO_4(80)+K_2SO_4(20))

6.4.2.4 CMSX-4 – Micrograph and element analyses by scanning electron microscope

(a) CMSX-4 tested with $CdSO_4$+(Na_2SO_4(80)+K_2SO_4(20))

The SEM BSE element maps for this salt combination, after corrosion testing for 500 hours at 700°C, are shown in Figure 6.21.

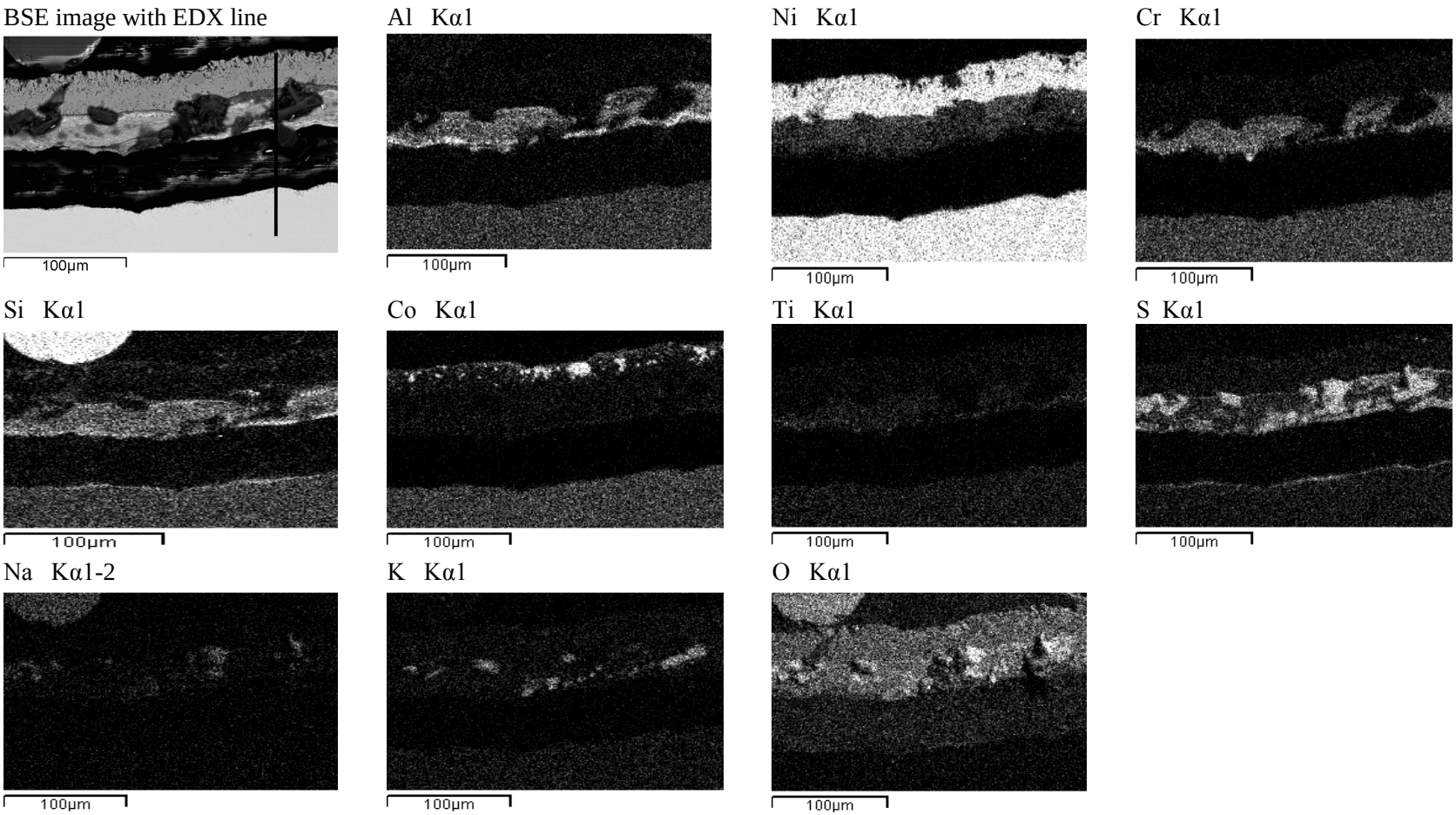

Figure 6.21: CMSX-4 corrosion tests with $CdSO_4$+(Na_2SO_4(80)+K_2SO_4(20)) for 500 hours at 700^{o}C - element maps

The element maps in Figure 6.21 show the scale, having an outer layer consisting of oxides of aluminium, nickel and cobalt, and an inner layer caused by sulphidation of chromium and silicon, has spalled from the substrate. This is confirmed by the EDX analyses shown in Figure 6.23, from which the gap between the spalled scale and substrate is shown to occur from approximately 60µm to 100µm from the scale surface. The main layers are illustrated in Figure 6.22.

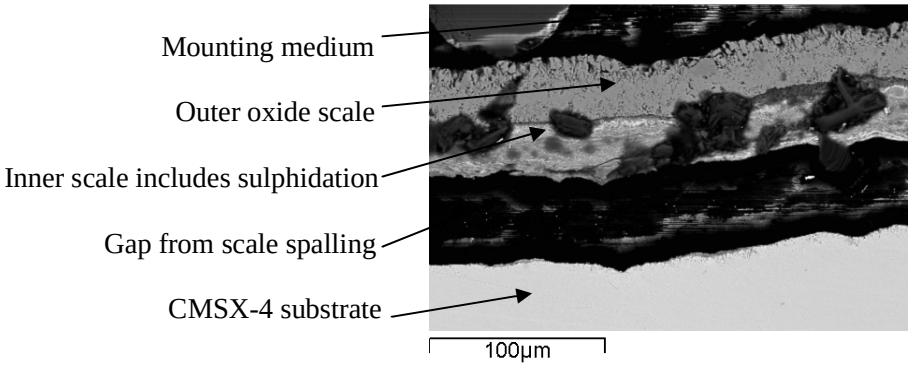

Figure 6.22: CMSX-4 with $CdSO_4$+(Na_2SO_4(80)+K_2SO_4(20)) after 500 hours corrosion testing at 700°C – BSE image showing spalling

The maps show that, following the scale spalling, broad front pitting is occurring at the substrate surface, resulting from oxidation and sulphidation. There is an aluminium concentration along the inner edge of the spalled scale which is leaving the substrate surface without a protective aluminium rich layer. This may be due to scale spallation having taken the aluminium rich layer from the surface.

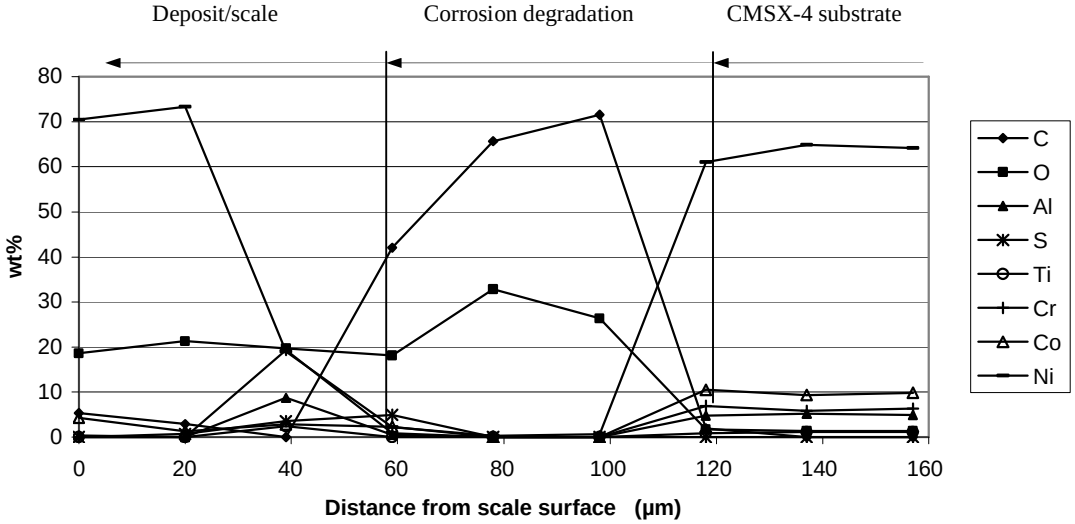

Figure 6.23: CMSX-4; main elements along EDX line shown in Figure 6.21

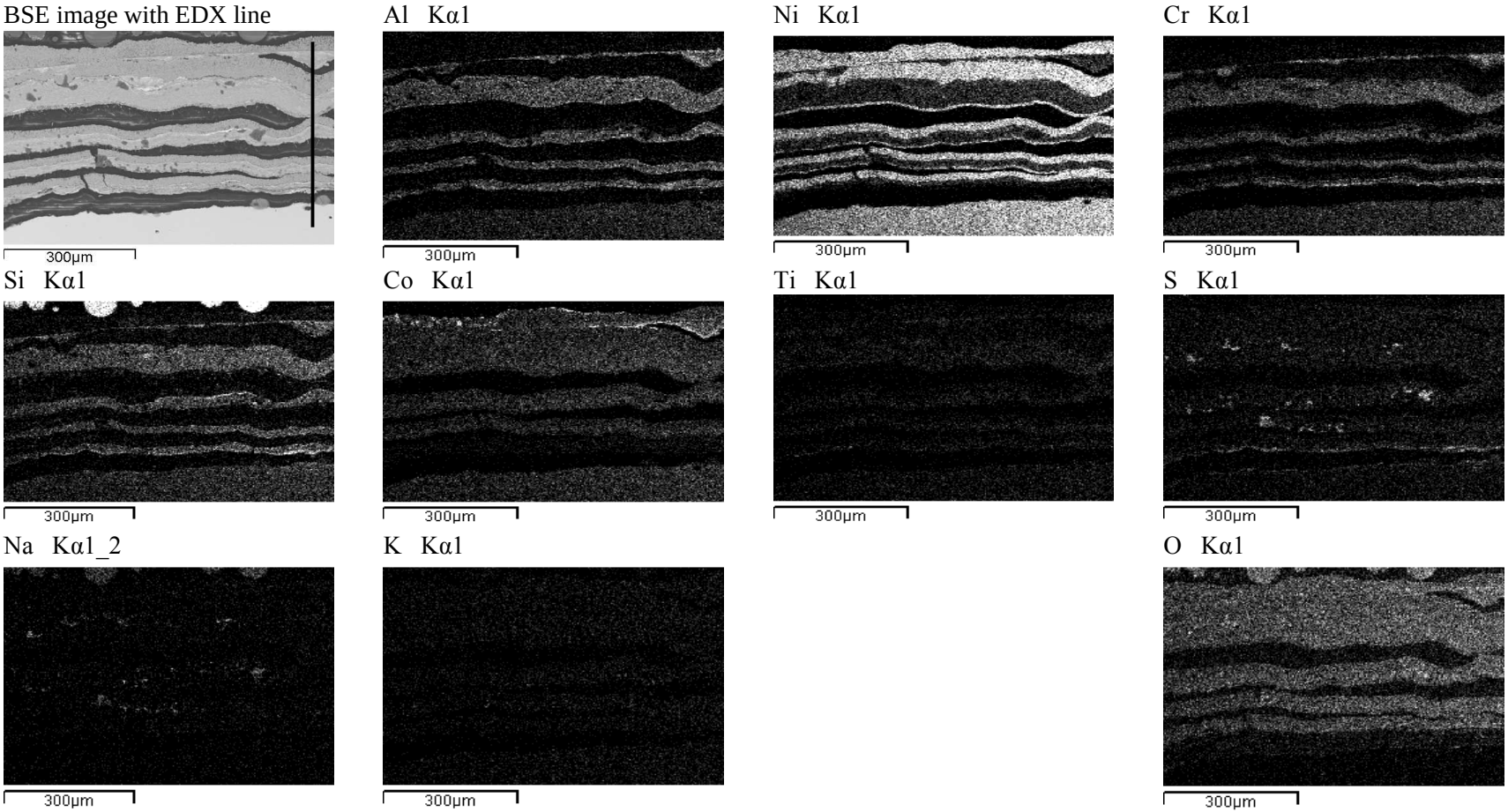

Figure 6.24: CMSX-4 corrosion tests with (Na_2SO_4(80)+K_2SO_4(20)) for 500 hours at 700^{o}C - element maps

(b) CMSX-4 tested with ($Na_2SO_4(80)+K_2SO_4(20)$)

Scale formation for each of the five test periods can be seen on the element maps shown in Figure 6.24. Oxidation and sulphidation mechanisms are involved in each test period. The propensity for spalling, shown in the cadmium/sodium/potassium test maps, in Figure 6.21, is more pronounced in these sodium/potassium salt combination corrosion tests.

The main elements along the EDX line shown in Figure 6.24, plotted in Figure 6.25 confirm the microstructure in the BSE maps. When compared with the changes in sound metal for CMSX-4, for the same salt combination, which range from -120µm to -155µm, (see Table 6.4).

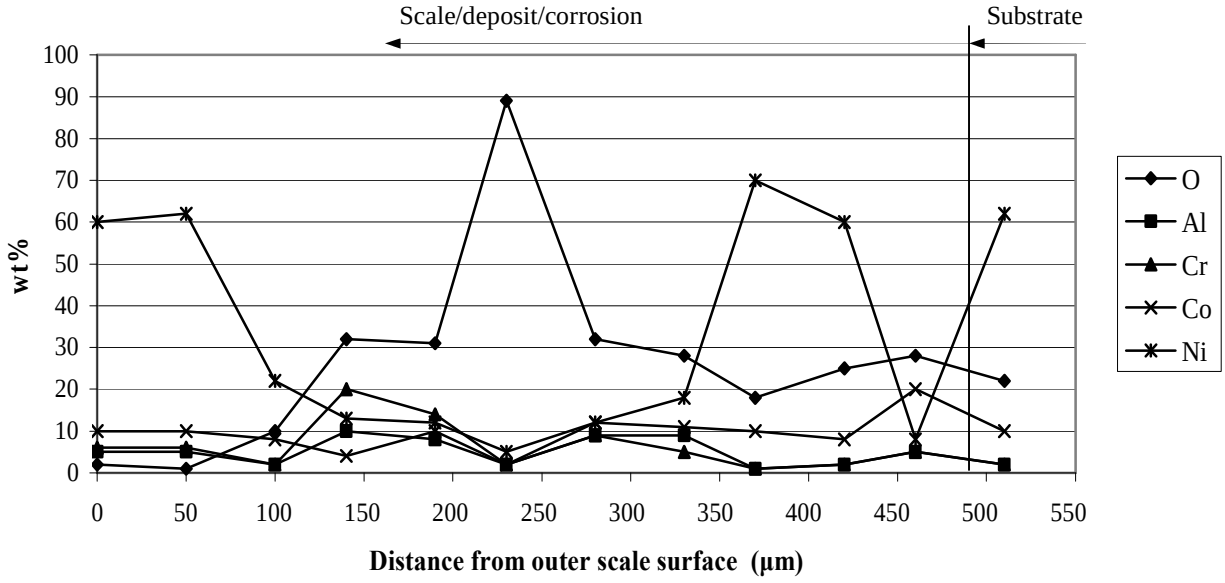

Figure 6.25: CMSX-4; main elements along EDX line shown in Figure 6.24

(c) CMSX-4 tested with $PbSO_4$+($Na_2SO_4(80)+K_2SO_4(20)$)

Element maps for this salt combination when tested on CMSX-4 are shown in Figure 6.26, with the element analysis along the EDX line, shown in Figure 6.27. The scale mainly comprises oxides of nickel, tantalum, cobalt, titanium, potassium, sodium and lead. At the base of the scale are concentrations of aluminium and chromium.

Within the scales, oxides and sulphides of aluminium, tantalum occur, with needles of sodium sulphide also present. Aluminium provides protection in the base of the pit, with chromium retarding corrosion on the outward area of the pit, under the base of the scale. Depletion of titanium and tantalum occurs within the pit. The figures illustrate Type II hot corrosion.

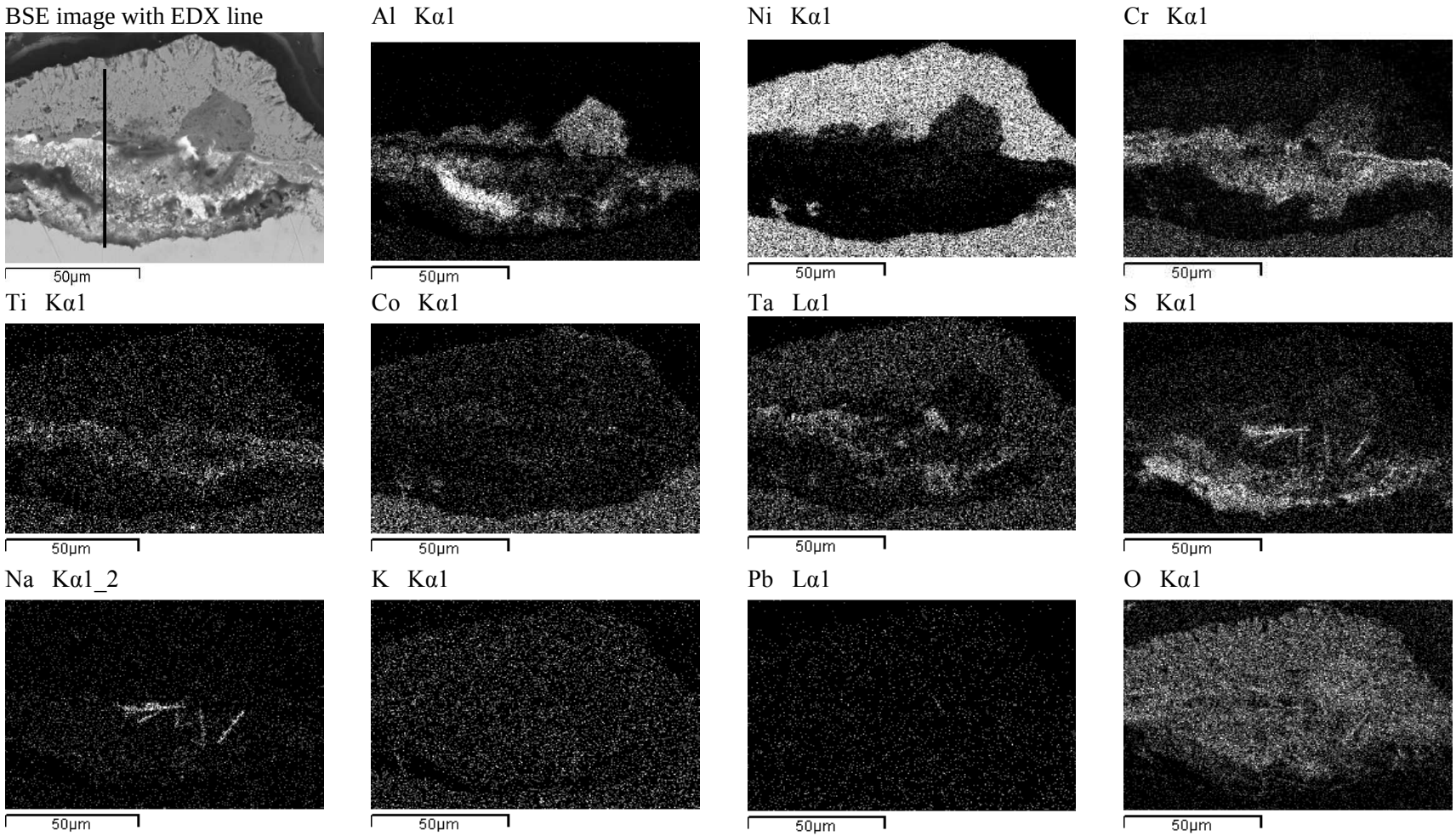

Figure 6.26: CMSX-4 corrosion tests with $PbSO_4$ + (Na_2SO_4(80)+K_2SO_4(20)) for 500 hours at 700^{o}C - element maps

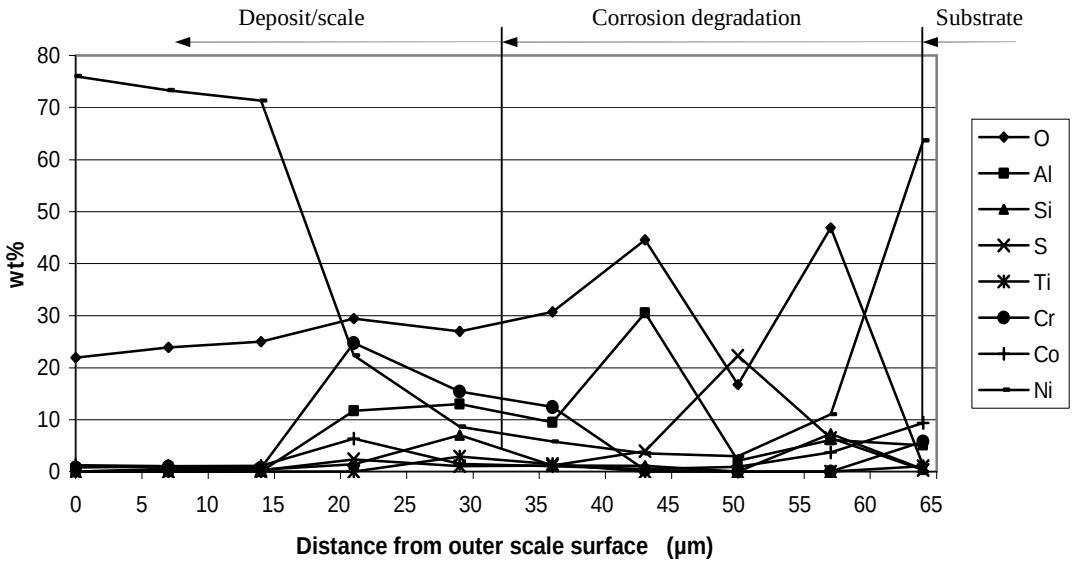

Figure 6.27: CMSX-4; main elements along EDX line shown in Figure 6.26

6.4.3 Results for IN939

6.4.3.1 IN939 – Mass change

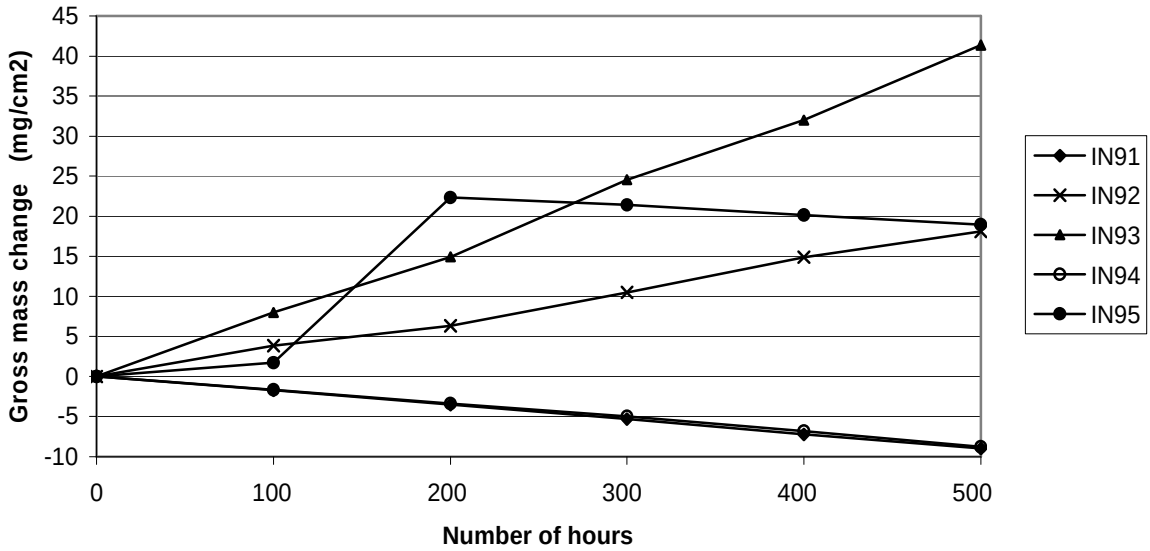

Key: IN91; $CdSO_4$ IN92; $CdSO_4$+(Na_2SO_4(80)+K_2SO_4(20)) IN93; (Na_2SO_4(80)+K_2SO_4(20))
IN94; $PbSO_4$ IN95; $PbSO_4$+(Na_2SO_4(80)+K_2SO_4(20))

Figure 6.28: IN939; comparison of gross mass changes from different salt species after 500 hours corrosion testing at 700^{o}C

The gross mass change graphs for IN939 are shown in Figure 6.28. The samples solely carrying sulphates of cadmium and lead indicate that very little corrosion is being initiated. As with both IN738LC and CMSX-4 samples, the inference is that cadmium and lead sulphates, when applied individually, evaporate and are carried through to the exhaust. However, for IN939, the Cd+alkali combination initiates hot corrosion at a similar rate to that initiated by the Pb+alkali combination. The (Na_2SO_4(80)+K_2SO_4(20)) species initiate hot corrosion in IN939 more aggressively than when they are in combination with cadmium or lead.

Reference to the net mass change graphs, shown in Figure 6.29, reflect these phenomena but hot corrosion is initiated by both $CdSO_4$+(Na_2SO_4(80)+K_2SO_4(20)) and the $PbSO_4$+(Na_2SO_4(80)+K_2SO_4(20)) combinations after 300 hours of testing. However, after this period, (Na_2SO_4(80)+K_2SO_4(20)) alone initiate the most hot corrosion. Comparison of the two sets of graphs indicate that no scale spallation occurs when these salt species are corrosion tested on IN939 at 700^{o}C.

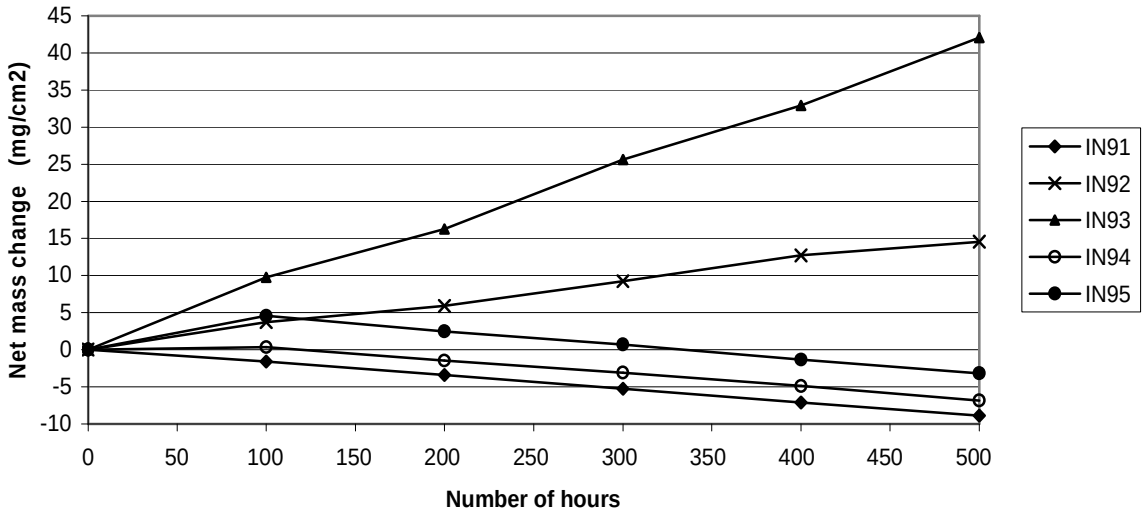

Key: IN91; $CdSO_4$ IN92; $CdSO_4$+(Na_2SO_4(80)+K_2SO_4(20)) IN93; (Na_2SO_4(80)+K_2SO_4(20))
IN94; $PbSO_4$ IN95; $PbSO_4$+(Na_2SO_4(80)+K_2SO_4(20))

Figure 6.29: IN939; comparison of net mass changes from different salt species after 500 hours corrosion testing at 700^{o}C

6.4.3.2 IN939 – metrology

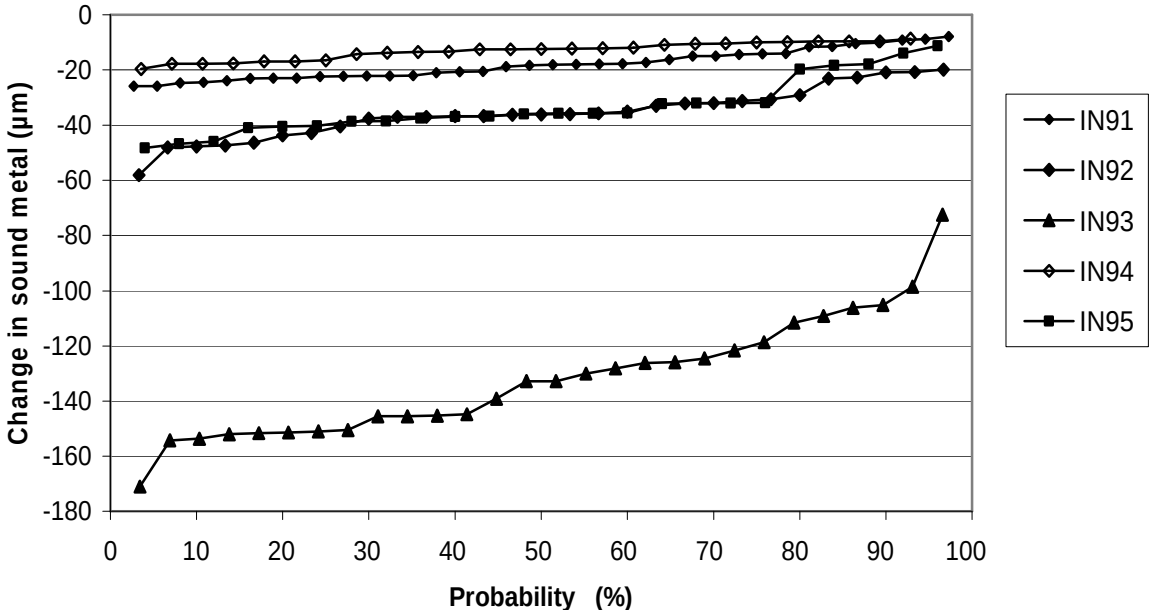

Key: IN91; $CdSO_4$ IN92; $CdSO_4$+(Na_2SO_4(80)+K_2SO_4(20)) IN93; (Na_2SO_4(80)+K_2SO_4(20))
IN94; $PbSO_4$ IN95; $PbSO_4$+(Na_2SO_4(80)+K_2SO_4(20))

Figure 6.30: IN939; comparisons of change in sound metal after 500 hours corrosion testing at 700°C

The graphs in Figure 6.30, showing changes in sound metal following 500 hours corrosion tests at 700°C, confirm the degree of hot corrosion initiated by these species shown in the mass change graphs above. The summary of the ranges of changes in sound metal in IN939, resulting from the corrosion tests, are presented in Table 6.5.

Sample code	Φ wt%/ mol%	σ wt%/ mol%	θ wt%/ mol%	λ wt%/ mol%	Change in sound metal µm
1.03	83.8/100				-10 to -25
1.06	41.9/50	38.3/40	11.7/10		-20 to -55
1.09		76.5/80	23.5/20		-70 to -170
1.12				154.8\100	-10 to -50
1.15		76.5/40	23.5/10	77.4/50	-10 to -50

Key : Φ - cadmium, σ - sodium, θ - potassium, λ - lead

Table 6.5 : Summary of loss of sound metal in IN939 samples after corrosion testing for 500 hours at 700°C

6.4.3.3 IN939 – optical microscopy

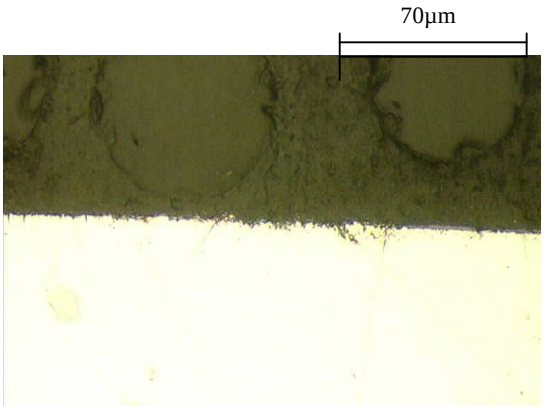

(a) $CdSO_4$

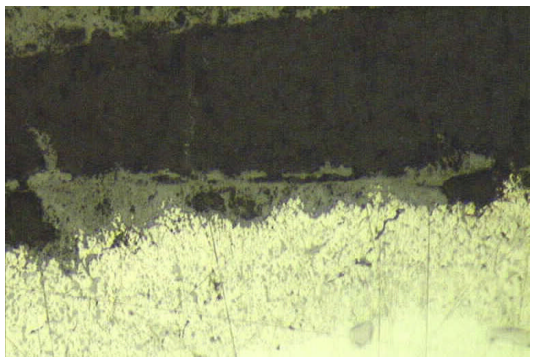

(b) $CdSO_4$+(Na_2SO_4(80)+K_2SO_4(20))

Figure 6.31: IN939 samples after 500 hours corrosion testing at 700°C, (a) with $CdSO_4$ and (b) with $CdSO_4$+(Na_2SO_4(80)+K_2SO_4(20))

Figure 6.31 shows optical micrographs of IN939 samples, one carrying $CdSO_4$ and the other the $CdSO_4$ + (Na_2SO_4(80)+K_2SO_4(20)) combination. The graphs of mass change and change in sound metal, for the cadmium containing tests, show that only very minor surface pitting has occurred in the cadmium sulphate sample, compared with the heavy Type II hot corrosion pitting initiated by the cadmium/sodium/potassium salt combination, shown in Figure 6.31(b). The incipient Type II pitting in the cadmium sulphate sample contrasts with the absence of any pitting in the IN738LC sample carrying the same salt, seen in Figure 6.6a. This is unexpected, because of the greater chromium content of IN939 compared with that of IN738LC.

Significant Type II hot corrosion occurs in IN939 after 500 hours testing at 700°C, when tested with (Na_2SO_4(80)+K_2SO_4(20)), confirming the mass change and change in sound metal results in Figures 6.28 and 6.30.

Micrographs of $PbSO_4$ alone and with the species $PbSO_4$+(Na_2SO_4(80)+K_2SO_4(20)), seen in Figure 6.33, show similar patterns of Type II hot corrosion to those for CMSX-4 and IN939.

The results are consistent with the mass changes and changes in sound metal, for these species, in Figures 6.28 and 6.30.

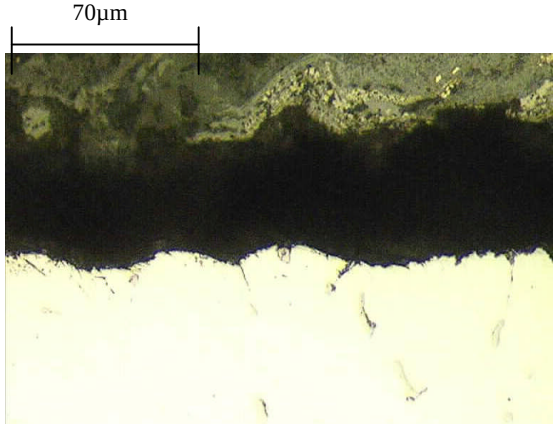

Figure 6.32: IN939 after testing with (Na_2SO_4(80)+K_2SO_4(20))

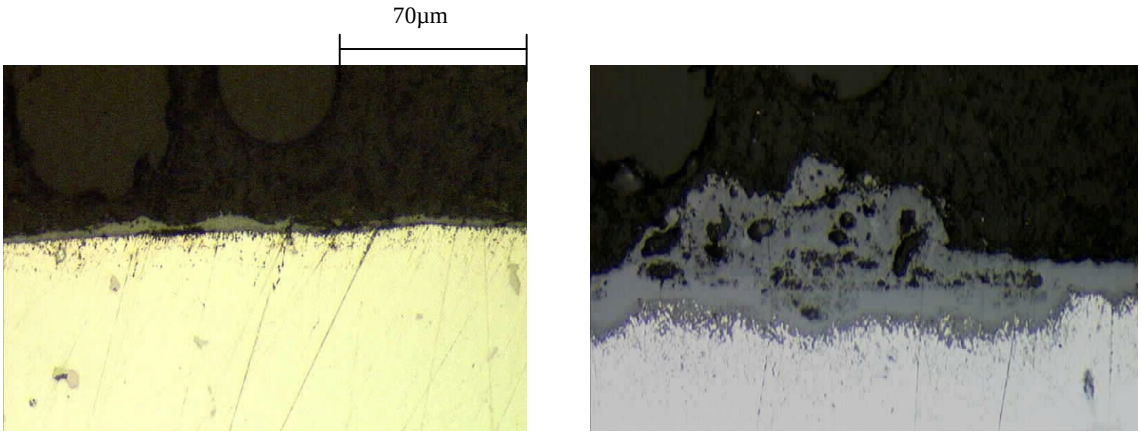

(a) $PbSO_4$ (b) $PbSO_4$+(Na_2SO_4(80)+K_2SO_4(20))

Figure 6.33: IN939 samples after 500 hours corrosion testing at 700°C, (a) with $PbSO_4$ and (b) with $PbSO_4$+(Na_2SO_4(80)+K_2SO_4(20))

6.4.3.4 IN939 – Micrograph and element analyses by scanning electron microscope

(a) IN939 tested with $CdSO_4$+(Na_2SO_4(80)+K_2SO_4(20))

The element maps in Figure 6.35 show Type II hot corrosion pitting and scale growth from the internal face of the pit, to a stage where spalling is commencing in the outer scale. The outer scale surface is nickel rich. The scale is composed of oxides of aluminium, cobalt, chromium, titanium and sulphur, and to a lesser extent of sodium and potassium. Sulphides of these elements occur strongly in the pit. The high content of chromium in the scale is consistent with its high content in IN939.

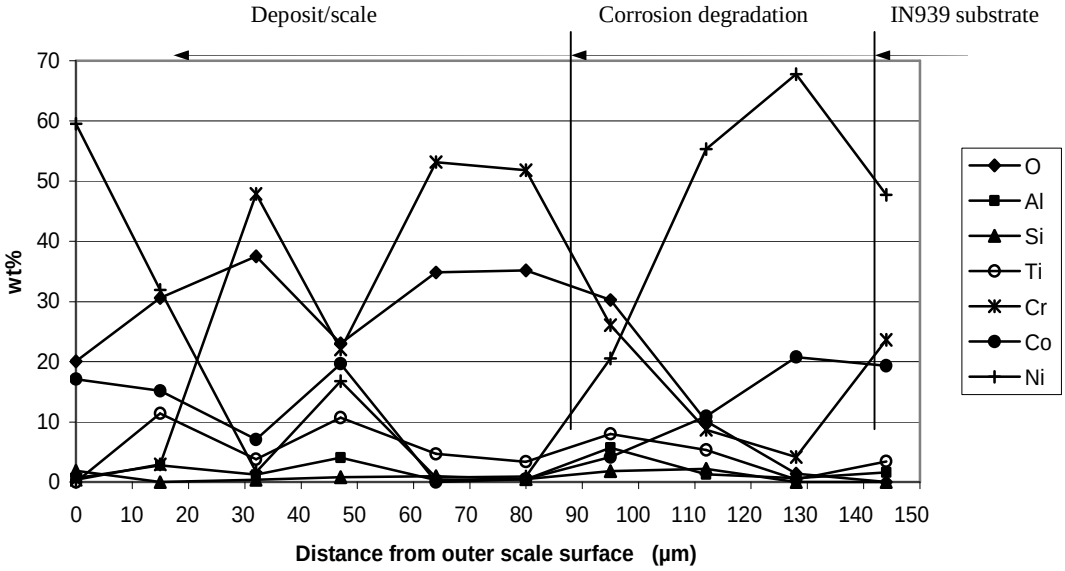

Figure 6.34: IN939; main elements along EDX line shown in Figure 6.35

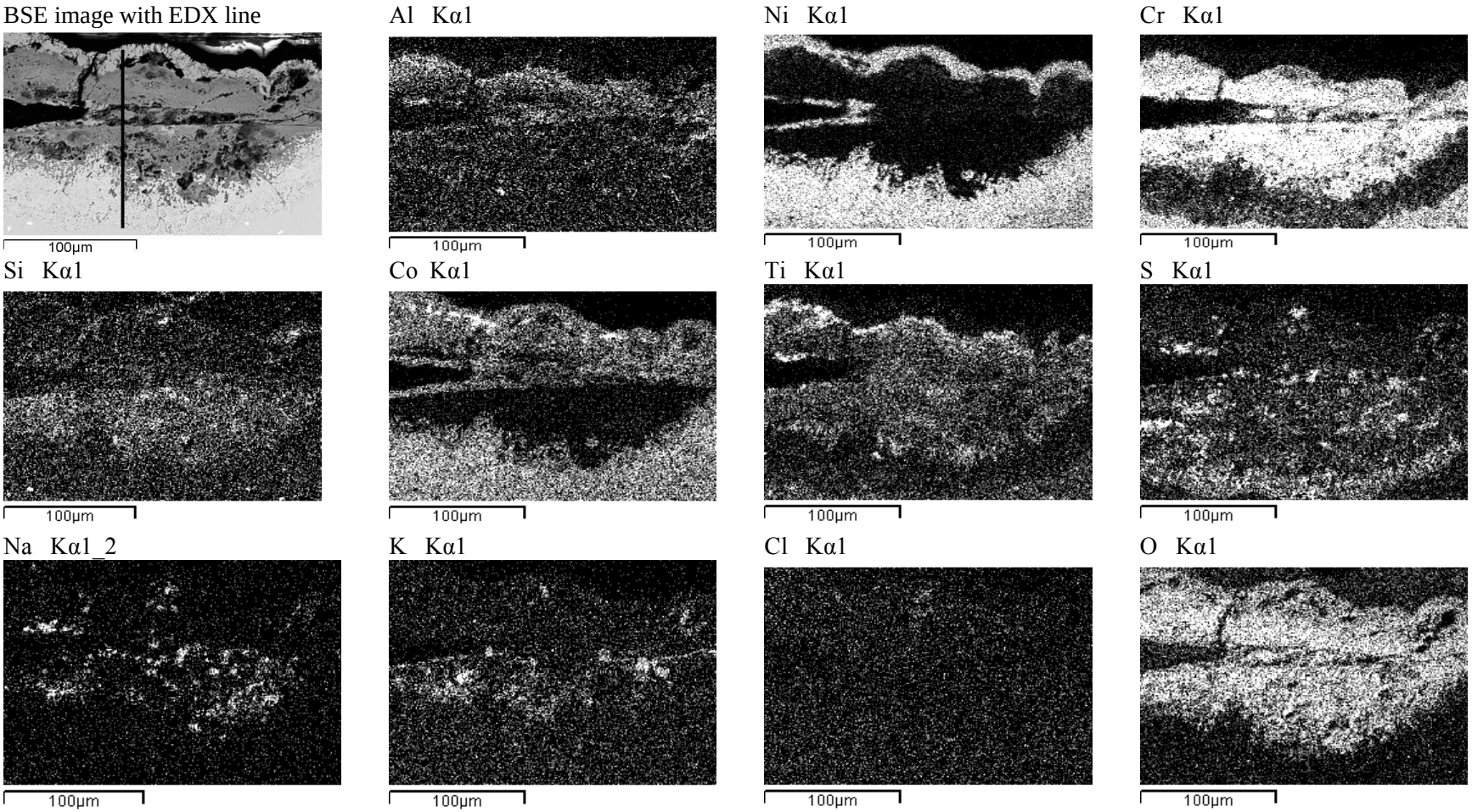

Figure 6.35: IN939; after corrosion testing for 500 hours at 700°C with $CdSO_4$+(Na_2SO_4(80) + K_2SO_4(20)) – element maps

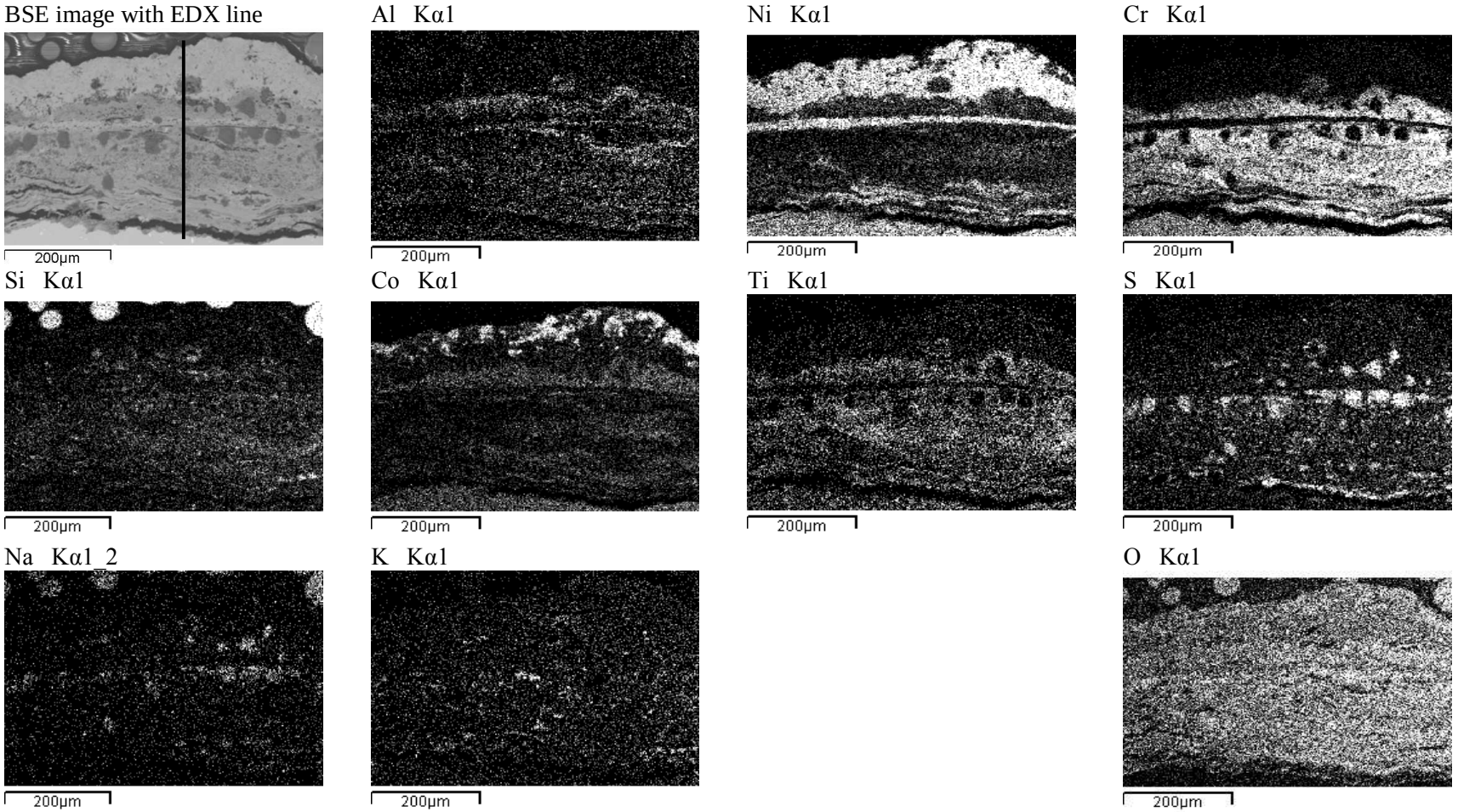

Figure 6.36: IN939; after corrosion testing for 500 hours at 700°C with (Na_2SO_4(80) + K_2SO_4(20)) – element maps

(b) IN939 tested with (Na_2SO_4(80)+K_2SO_4(20))

The element maps in Figure 6.36 show the broad front Type II hot corrosion and scale formation. In this case the outer scale is seen to be rich in oxides of nickel and cobalt, with the inner scale layer rich in oxides of chromium and aluminium. The inner scale contains sulphates of sodium and to a lesser extent, of potassium. This microstructure is reflected in the EDX element analysis shown in Figure 6.37.

Aluminium is uniformly distributed in the inner scale and pitting down to the substrate interface. Oxidation is seen to be uniform whereas two intermediate 'layers' of sulphur have been formed, the lower layer along the superalloy interface. Of the substrate alloying elements, oxides of titanium are contained in the inner scale.

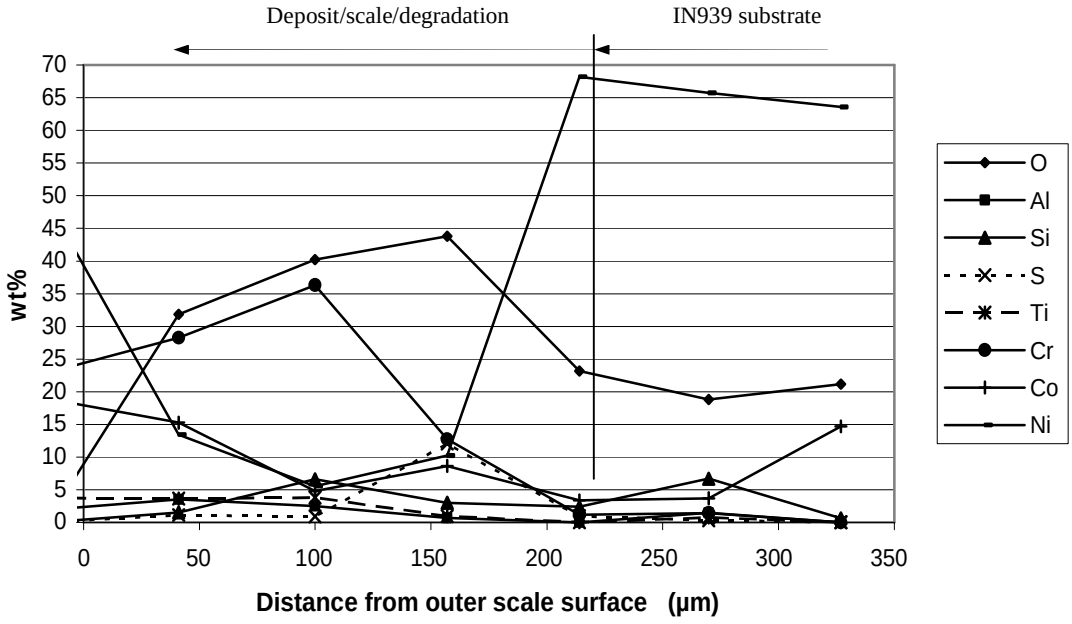

Figure 6.37: IN939; main elements along EDX line shown in Figure 6.36

(c) IN939 tested with $PbSO_4$+(Na_2SO_4(80)+K_2SO_4(20))

The element maps in Figure 6.39 illustrate the typical Type II hot corrosion. The scale consists of two basic layers, one rich in oxides of nickel, chromium, cobalt and titanium, to a lesser extent, silicon and sulphur. The second layer is rich in oxides of chromium and titanium, with sulphur in the lower region.

The maps in Figure 6.39 show aluminium sulphides at scale/metal interface, with nickel sulphide as internal precipitates in a cobalt depleted zone below the metal surface. Precipitates of titanium silicide are locally present further into the substrate. Oxides of titanium are contained in the scale outside the sulphur rich layer. The EDX element analyses seen in Figure 6.38 confirm the compositions shown by the element maps.

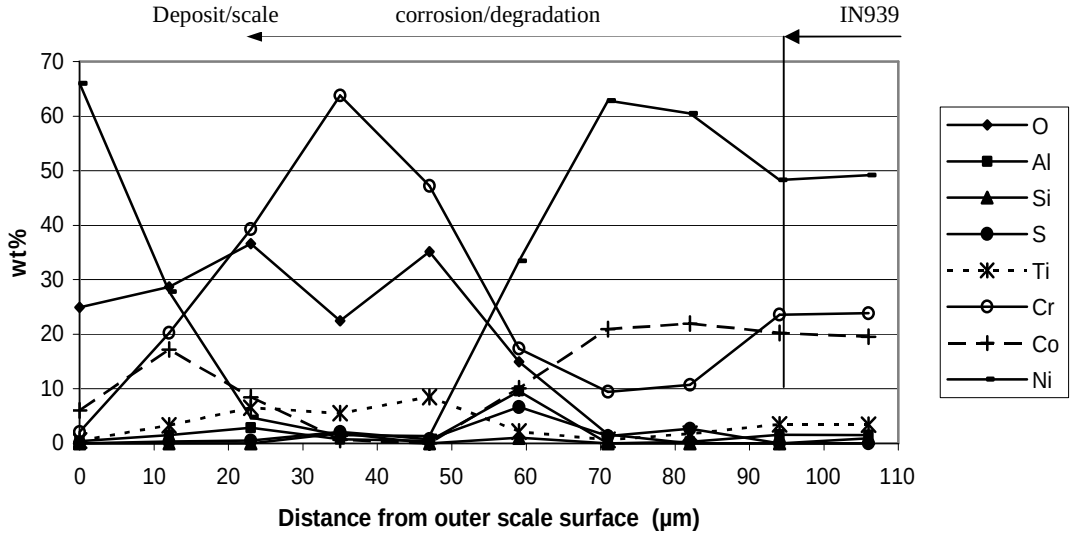

Figure 6.38: IN939; main elements along EDX line shown in Figure 6.39

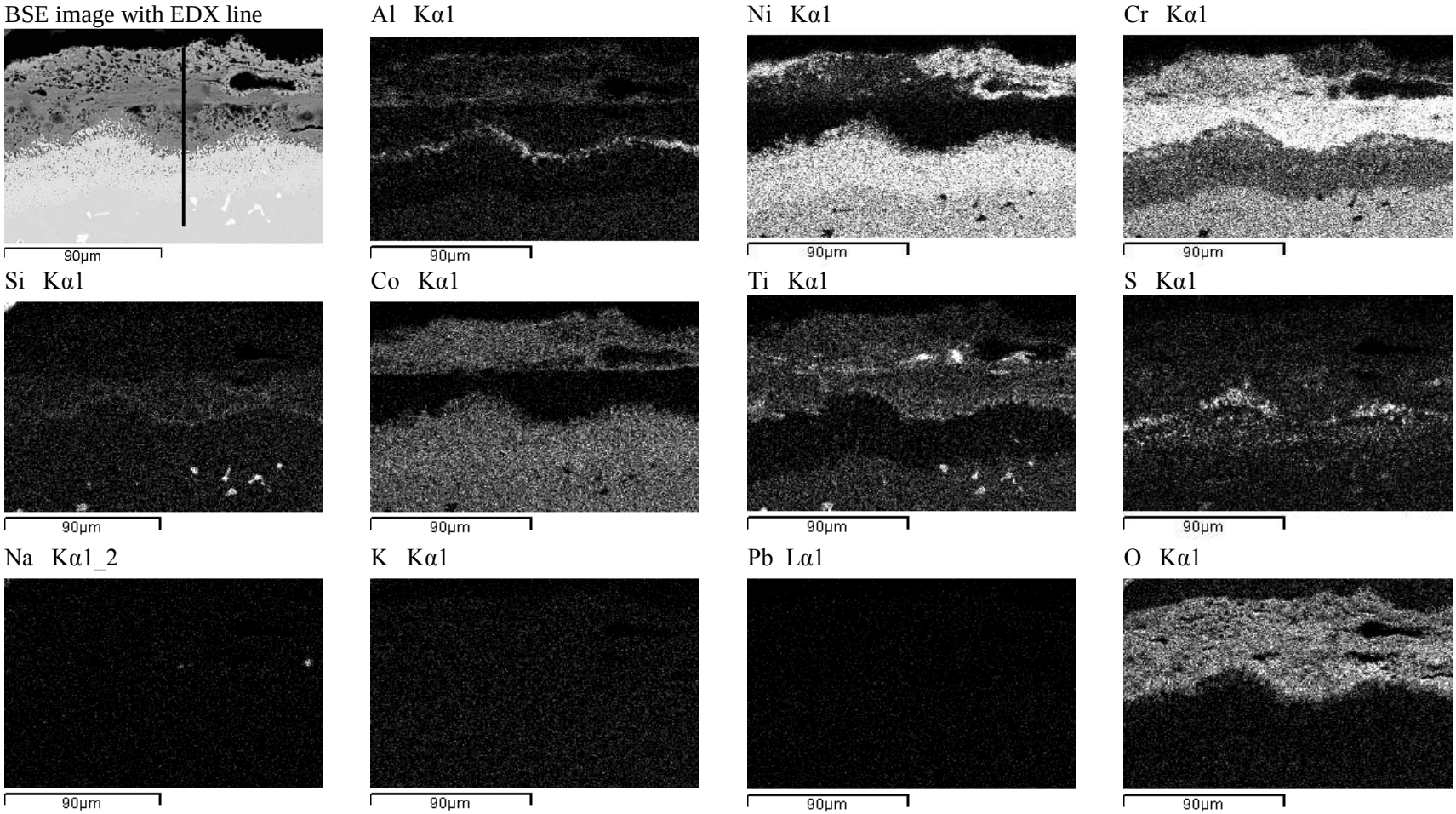

Figure 6.39: IN939; after corrosion testing for 500 hours at 700°C with $PbSO_4$ + (Na_2SO_4(80) + K_2SO_4(20)) – element maps

6.5 Series 1 corrosion tests - conclusions

In the thermodynamic assessments, in Chapter 5, it was predicted that the species $CdSO_4$ and $PbSO_4$, when contained in gases produced from the gasification of biomass and waste-fuels, would condense on the surfaces of hot components in gas turbines. It was concluded that these species, when combusted in the presence of sulphur, chlorine and fluorine, from these fuels, had the potential to initiate hot corrosion in gas turbine gas path components such as turbine blades and vanes. The purpose of this first series of corrosion tests was to confirm whether, and to what extent, cadmium sulphate and lead sulphate would initiate hot corrosion in the superalloys: IN738LC, CMSX-4 and IN939.

The corrosion tests consisted of 500 hours testing at 700°C, with sample and crucible weighing and salt replenishment, to maintain the salt flux of 15µg/cm^2/h, before and after each 100 hours period. Tests were carried out at atmospheric pressure with a 50:50 mix of two gases. One gas contained 800ppm HCl with the balance N_2 and 500ppm SO_2, 40 wt%O_2 and balance of N_2, to simulate gases combusted in the gas turbine. A comparatively high salt flux, of 15 µm/cm^2/h, was used as a means of accelerating the tests, for each of the five salt species on each superalloy:

- $CdSO_4$
- $CdSO_4$+(Na_2SO_4(80) + K_2SO_4(20))
- (Na_2SO_4(80)+K_2SO_4(20))
- $PbSO_4$
- $PbSO_4$ + (Na_2SO_4(80) + K_2SO_4(20))

As shown by the graphs of mass change and metrology and optical microscopy, the two single species, $CdSO_4$ and $PbSO_4$, initiated very little oxidation or Type II hot corrosion in any of the superalloys. In the case of $CdSO_4$, no oxidation or corrosion was initiated in IN738LC, with only very minor pitting and scale formation on CMSX-4 and IN939. Mass change graphs show that insufficient $CdSO_4$ deposits start on the sample surface – they may evaporate or may not melt (or form low melting point eutectics). The results for $PbSO_4$ alone, showed similar limited pitting, mass changes, and changes in sound metal to those for $CdSO_4$, although their values are marginally higher. These results also indicate that, for $PbSO_4$ at 700°C, even if there is no evaporation, surface deposits may not melt but remain solid. As shown in Table 5.25, the dew points of these two species varied, depending on the individual contents, and their combinations, of sulphur, chlorine and fluorine contained in the gases, albeit at high pressure. The range of dew point temperatures were: from 640°C to 800°C for $CdSO_4$ and, from 730°C to 1020°C for $PbSO_4$. It could be assumed that, if these corrosion tests had been carried out at 650°C, the lowest value in the Type II hot corrosion temperature range, then even at atmospheric pressure, if no evaporation occurs, they may not melt. In practice, biomass and waste-fuels contain a variety of elements, not cadmium or lead individually, which may interact with them to affect dew points and the rates of oxidation and hot corrosion. No further attention will be given here to the results for $CdSO_4$ and $PbSO_4$ individually.

As a result of previous research into the gasification of biomass and waste fuels at Cranfield University [53], the salt combination of (Na_2SO_4(80)+K_2SO_4(20)) was included in this series of corrosion tests, both alone and when combined 50:50 with $CdSO_4$ and $PbSO_4$. All these combinations of species initiated significant Type II hot corrosion in IN738LC, CMSX-4 and IN939. The effect on melting point temperatures of sulphates of sodium and potassium with cadmium sulphate are shown in the ternary diagram in Figure 6.40.

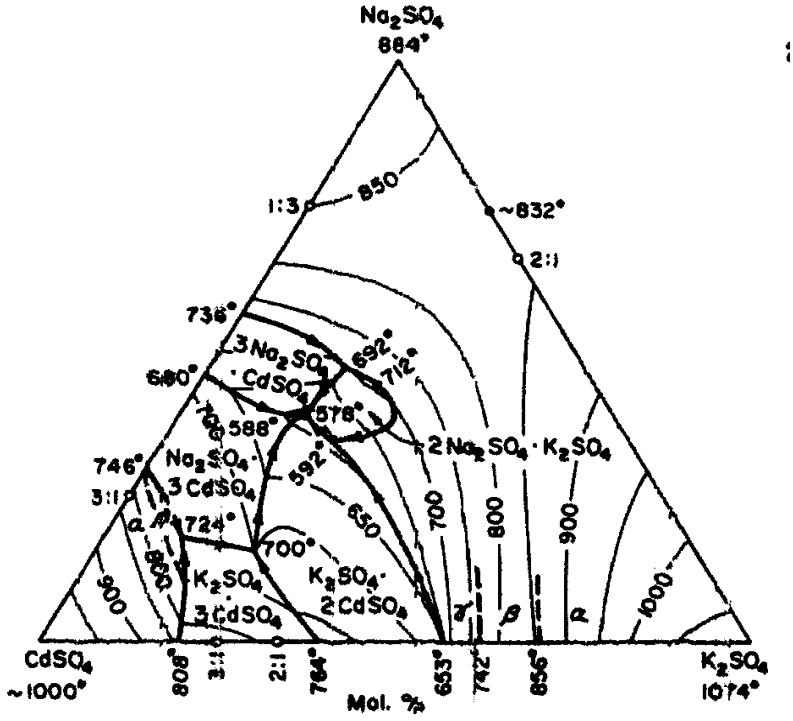

Figure 6.40 : Ternary phase diagram of the K_2SO_4 - Na_2SO_4 - Cd_2SO_4 system [130]

From this diagram it can be seen that the lowest melting point temperature of this combination of species, of 578^{o}C, occurs when their proportions are approximately 80 mol% Na_2SO_4, 20 mol% K_2SO_4 and 50 mol% $CdSO_4$.

In this series of corrosion tests, Type II hot corrosion was initiated by the three salt combinations. A summary of changes in sound metal for each salt combination on each superalloy is shown in Table 6.6. In the IN939 samples less hot corrosion has been initiated by all the species tested, due to this superalloy containing the largest chromium content. CMSX-4, having the lowest chromium content, is heavily corroded in comparison with the other two for species 1 and 2. Species 2 initiates the heaviest hot corrosion in the superalloys with the exception of CMSX-4, where the change in sound metal is the lowest of the three superalloys, possibly due to the high aluminium content of this superalloy. The initiation of hot corrosion by the cadmium containing combination is less than that of the lead containing combination.

In all cases titanium is contained within the pitting and scale, with lower levels of molybdenum, tungsten and tantalum also present.

	Species 1	Species 2	Species 3
IN738LC	-4 to -40	-120 to -200	-80 to -160
CMSX-4	-135 to -170	-120 to -155	-155 to -205
IN939	-20 to -55	-70 to -170	-10 to -50

Key: Species 1; $CdSO_4$+(Na_2SO_4(80) + K_2SO_4(20))
Species 2; (Na_2SO_4(80)+K_2SO_4(20))
Species 3; $PbSO_4$ + (Na_2SO_4(80) + K_2SO_4(20))

Table 6.6: Summary of changes in sound metal for superalloy samples after 500 hours corrosion tests at 700^{o}C (µm)

It is concluded that these corrosion tests have confirmed that, at atmospheric pressure, $CdSO_4$ and $PbSO_4$, when combined separately with Na_2SO_4(80)+K_2SO_4(20)), will initiate Type II hot corrosion in the superalloys IN738LC, CMSX-4 and IN939. These results bear out the predictions produced by the thermodynamic assessments set out in Chapter 5.

7 Series 2 corrosion tests - commercial coatings

7.1. Introduction

The first series of corrosion tests confirmed that the trace species $CdSO_4$ and $PbSO_4$ would initiate hot corrosion in hot components of gas turbines burning biomass and waste-fuels, as forecast by thermodynamic assessments and reported in section 5. The corrosion tests showed that these two species, when deposited in the proportion 50:50 with (Na_2SO_4(80) + K_2SO_4(20)), with a comparatively high salt flux of 15 µg/cm^2/h, will initiate hot corrosion in the commonly used superalloys IN738LC, IN939 and CMSX-4.

The next stage in the project was to determine to what extent these trace species, in the same proportions, would initiate hot corrosion in commercially available coatings.
Evaluation of the nature and extent of hot corrosion initiation identified by these corrosion tests would then provide the basis for developing novel coatings having enhanced resistance to hot corrosion initiation in gas turbines burning biomass and waste-fuels. The commercial coatings selected were GT29+, RT-22, and Sermaloy1515, applied to the superalloys IN738LC and CMSX-4.

7.2. Corrosion test series 2 ; superalloys and coatings selected

7.2.1. Superalloys IN738LC and CMSX-4

The second series of corrosion tests were divided between the widely used general purpose IN738LC and the commercial single-crystalline CMSX-4. Their elemental analyses are shown in Table 6.1. The superalloy IN939 was omitted from the second corrosion test series due to its lower aluminium content (2 wt%) providing less mechanical strength under thermal cycling due to cracking and spalling of the protective scale. This results from the difference in thermal expansion between alloy and scale. IN939 is also lower in weldability than IN738LC and in general terms is considered to be less attractive as a general purpose superalloy for developing new coatings in this project. More detailed descriptions of the superalloys used in the first series of corrosion tests are provided in section 6.2.

7.2.2. Selected commercial coatings

The three commercial coatings selected for the second series of corrosion tests were; GT29+, RT-22 and Sermaloy1515

7.2.2.1 Commercial coating GT29+

GT29+ is a CoCrAlY overlay coating with aluminium diffused into the outer part of the coating. As seen in the BSE maps in Figure 7.1, chromium and cobalt dominate the elemental content, with limited intrdiffusion at the coating/substrate interface.

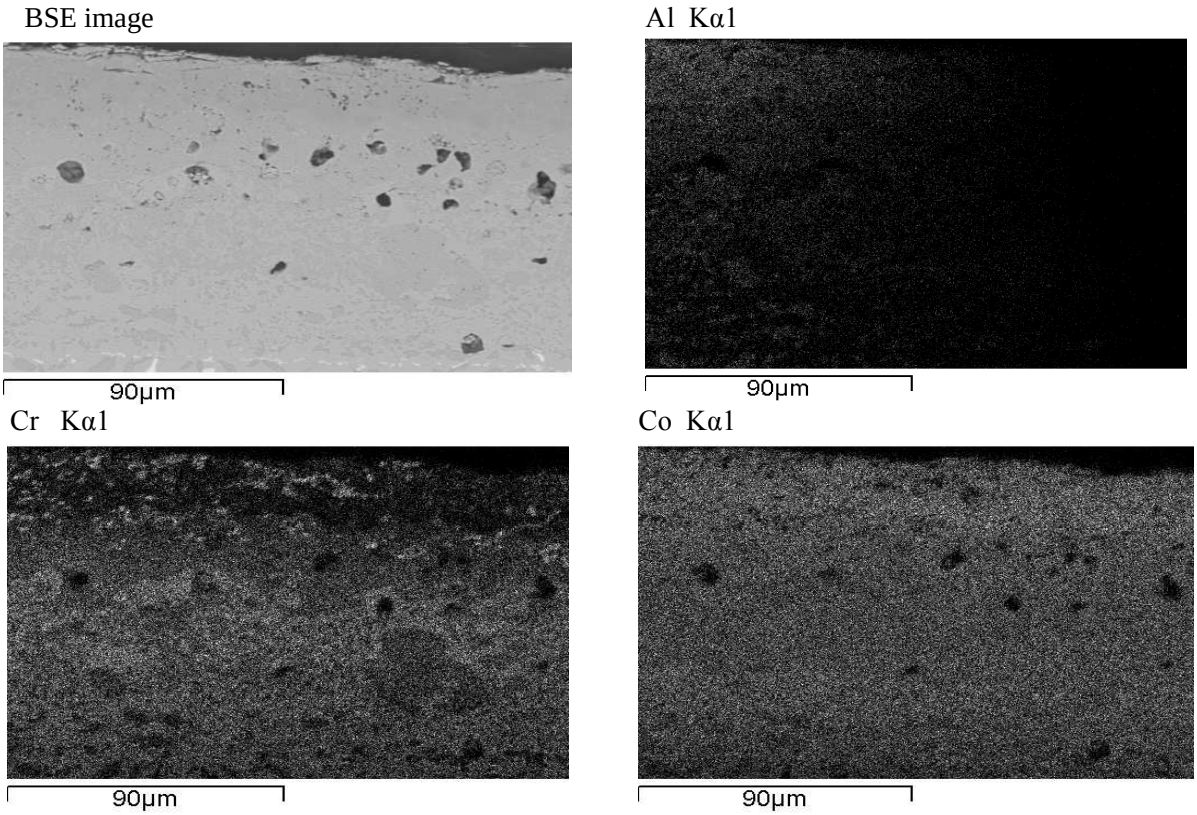

Figure 7.1: IN738LC coated with GT29+ - element maps

7.2.2.2 Commercial coating RT-22

RT-22 is an aluminide diffusion coating with an outer platinum rich layer, having an overall depth of approximately 110µm. Maps of the main elements in RT-22, in Figure 7.2 show the clearly defined platinum-rich outer layer, with a typical depth of 30µm. The element analyses in Figure 7.18 show the outer platinum-rich layer, whose content falls from 43 at%Pt at the surface to 8 at%Pt at the interface between the platinum-rich layer and the aluminide coating, to zero content at the substrate surface . Within the platinum-rich layer, aluminum (20 at%Al) and nickel (18 at%Ni) are the other main elements, with chromium (6 at%Cr) and traces of titanium also being present. The layers within the coating are mainly composed of nickel (50 at%Ni to 62 at%Ni), aluminum (26 at%Al falling away to 5 at%Al), cobalt (consistently at 6 at%Co) and titanium (4 at%Ti).

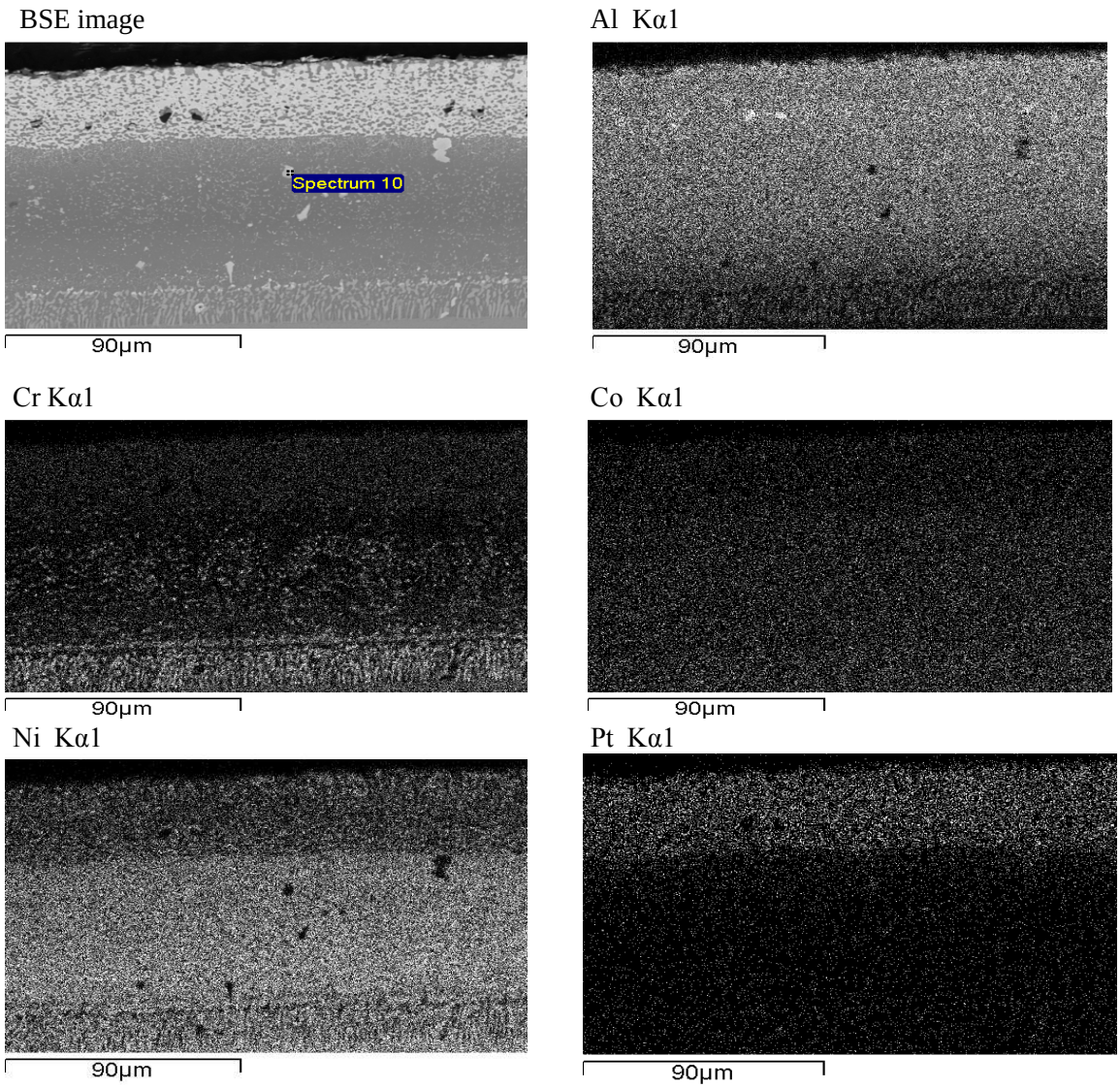

Figure 7.2: IN738LC coated with RT-22 - element maps

7.2.2.3 Commercial coating Sermaloy1515

Sermaloy 1515 is a triple layered silicon aluminide coating. Each of the three layers consists of one sub-layer rich in chromium, silicon and titanium, the second sub-layer being rich in aluminum, nickel and molybdenum, as can be seen in Figure 7.3. The overall depth of the coating is approximately 40µm, with variations in the depths of each of the triple layers. Table 7.2 shows typical depths of the layers.

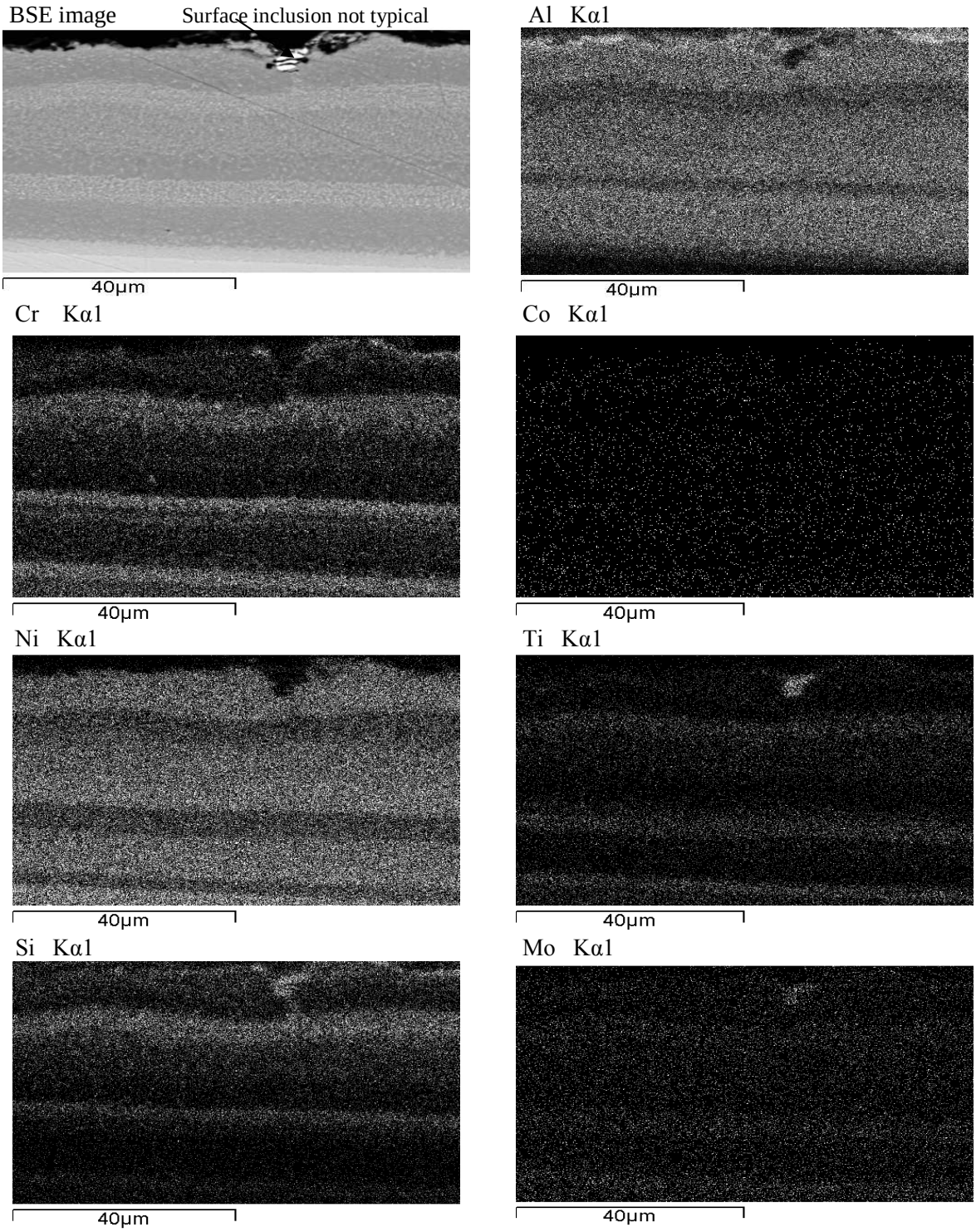

Figure 7.3: IN738LC coated with Sermaloy1515 – element maps

Layer	Cr/Ti/Si rich sub-layer	Al/Ni rich sub-layer
Inner	3	8
Centre	5	14
Outer	4	7

Note: 'inner' is at the substrate interface

Table 7.1: Depths of individual layers of Sermaloy1515 coating – (μm)

7.3 Description of series 2 corrosion tests

7.3.1 General conditions

The same test conditions were used as those for series one, with five 100 hour exposure periods at 700^{o}C, with weighing and salt replenishment before and after each 100 hours test period. Their descriptions are contained in sections 2 and 6. The schedule of superalloys, coatings and salt fluxes are shown in Table 7.3. There was no reference sample for CMSX-4 coated with Sermaloy 1515. Where any need arose to compare a sample with untested Sermaloy 1515, the sample of IN738LC coated with Sermaloy 1515 was referred to.

7.3.2 Gas compositions

As for series 1 corrosion tests, the total volume gas flow was 50cc/min and the gases used for series 2 tests were [800ppm HCl, balance N_2(50) + 500ppm SO_2, 41.9% O_2, balance N_2(50)]. This gives; 400ppm HCl, 250ppm SO_2, 20.9 % O_2 – bal. N_2 entering the furnace.

7.3.3 Salt compositions and salt fluxes

In the second test series, lower salt fluxes of 1.5 mg/cm^2/hr and 5 mg/cm^2/hr were used, compared with the high flux of 15 μg/cm^2/h in the first test series. These were selected to reflect the low levels of trace species that could be anticipated, in practice, when burning gases from biomass and waste-fuels. It was also desirable that some coating would be left at the end of the testing to analyse.

7.3.4 Safety precautions, procedures and equipment

Series two corrosion tests used the same furnace, weighing and salt spraying equipment, methods, evaluation techniques and safety procedures as those used in the first series.

Sample No.	Salt species	Salt Flux ($\mu g/cm^2/h$)	Coating	Superalloy
2.01	$CdSO_4$+(Na_2SO_4(80)+ K_2SO_4(20))	1.5	GT29+	IN738LC
2.02	$CdSO_4$+(Na_2SO_4(80)+ K_2SO_4(20))	5.0	GT29+	IN738LC
2.03	$CdSO_4$+(Na_2SO_4(80)+ K_2SO_4(20))	1.5	RT-22	IN738LC
2.04	$CdSO_4$+(Na_2SO_4(80)+ K_2SO_4(20))	5.0	RT-22	IN738LC
2.05	$CdSO_4$+(Na_2SO_4(80)+ K_2SO_4(20))	5.0	Sermaloy1515	IN738LC
2.06	$CdSO_4$+(Na_2SO_4(80)+ K_2SO_4(20))	1.5	Sermaloy1515	CMSX-4
2.07	$CdSO_4$+(Na_2SO_4(80)+ K_2SO_4(20))	5.0	Sermaloy1515	CMSX-4
2.08	$PbSO_4$+(Na_2SO_4(80)+ K_2SO_4(20))	1.5	GT29+	IN738LC
2.09	$PbSO_4$+(Na_2SO_4(80)+ K_2SO_4(20))	5.0	GT29+	IN738LC
2.10	$PbSO_4$+(Na_2SO_4(80)+ K_2SO_4(20))	1.5	RT-22	IN738LC
2.11	$PbSO_4$+(Na_2SO_4(80)+ K_2SO_4(20))	5.0	RT-22	IN738LC
2.12	$PbSO_4$+(Na_2SO_4(80)+ K_2SO_4(20))	5.0	Sermaloy1515	IN738LC
2.13	$PbSO_4$+(Na_2SO_4(80)+ K_2SO_4(20))	1.5	Sermaloy1515	CMSX-4
2.14	$PbSO_4$+(Na_2SO_4(80)+ K_2SO_4(20))	5.0	Sermaloy1515	CMSX-4
2.15	*Untested, reference sample*	*0*	*GT29+*	*IN738LC*
2.16	*Untested, reference sample*	*0*	*RT-22*	*IN738LC*
2.17	*Untested, reference sample*	*0*	*Sermaloy1515*	*IN738LC*

Table 7.2: Corrosion tests series 2 – schedule of superalloys, coatings and salt fluxes tested

7.3.5 Methodology

The series of laboratory tests used the well established deposit replenishment technique [ ] to investigate the effects of the compositions of the species selected on each of the combinations of superalloy and commercial coating. The tests, at atmospheric pressure, were carried out in the furnace by closely controlling the inlet gas flows from pre-mixed gas bottles by mass controllers. Information on sample preparation, spraying of salt solutions and weighing activities during pre- and post-test periods is provided in Chapter 4.

7.4 Series 2 corrosion tests – results and evaluation

Mass change assessments were used to evaluate corrosion test results. Then, after mounting and surface preparation, described in section 4, evaluation of the samples was carried out by metrology to determine accurately the extent and character of corrosion damage, by optical microscopy and by SEM to identify the dispersion of main elements in the corrosion damage. Photographs of the samples, post testing and before mounting are shown in Figure 7.3.

The order of presenting results and evaluation commences with SEM backscatter (BSE) microstructures of the IN738LC and GT29+ combination, then of IN738LC and RT-22, of IN738LC and Sermaloy1515, and lastly CMSX-4 and Sermaloy1515.

(a) Salts : $CdSO_4$+(Na_2SO_4(80)+K_2SO_4(20))

2.01	**2.02**	**2.03**	**2.04**	**2.05**	**2.06**	**2.07**
IN738LC	IN738LC	IN738LC	IN738LC	IN738LC	CMSX-4	CMSX-4
GT29	GT29	RT-22	RT-22	Serm1515	Serm1515	Serm1515
1.5 µg/cm^2/hr	5.0 µg/cm^2/hr	1.5 µg/cm^2/hr	5.0 µg/cm^2/hr	5.0 µg/cm^2/hr	1.5 µg/cm^2/hr	5.0 µg/cm^2/hr

(b) Salts : $PbSO_4$+(Na_2SO_4(80)+K_2SO_4(20))

2.08	**2.09**	**2.10**	**2.11**	**2.12**	**2.13**	**2.14**
IN738LC	IN738LC	IN738LC	IN738LC	IN738lC	CMSX-4	CMSX-4
GT29	GT29	RT-22	RT-22	Serm1515	Serm1515	Serm1515
1.5 µg/cm^2/hr	5.0 µg/cm^2/hr	1.5 µg/cm^2/hr	5.0 µg/cm^2/hr	5.0 µg/cm^2/hr	1.5 µg/cm^2/hr	5.0 µg/cm^2/hr

(c) Untested reference samples:

2.15	**2.16**	**2.17**
IN738LC	IN738LC	IN738LC
GT29	RT-22	Serm1515

Figure 7.4: Photographs of samples after series 2 corrosion tests, prior to mounting

7.4.1 Microstructures of IN738LC samples coated with GT29+

7.4.1.1 $CdSO_4$+(Na_2SO_4(80)+ K_2SO_4(20)) with salt flux of 1.5 µg/cm^2/h

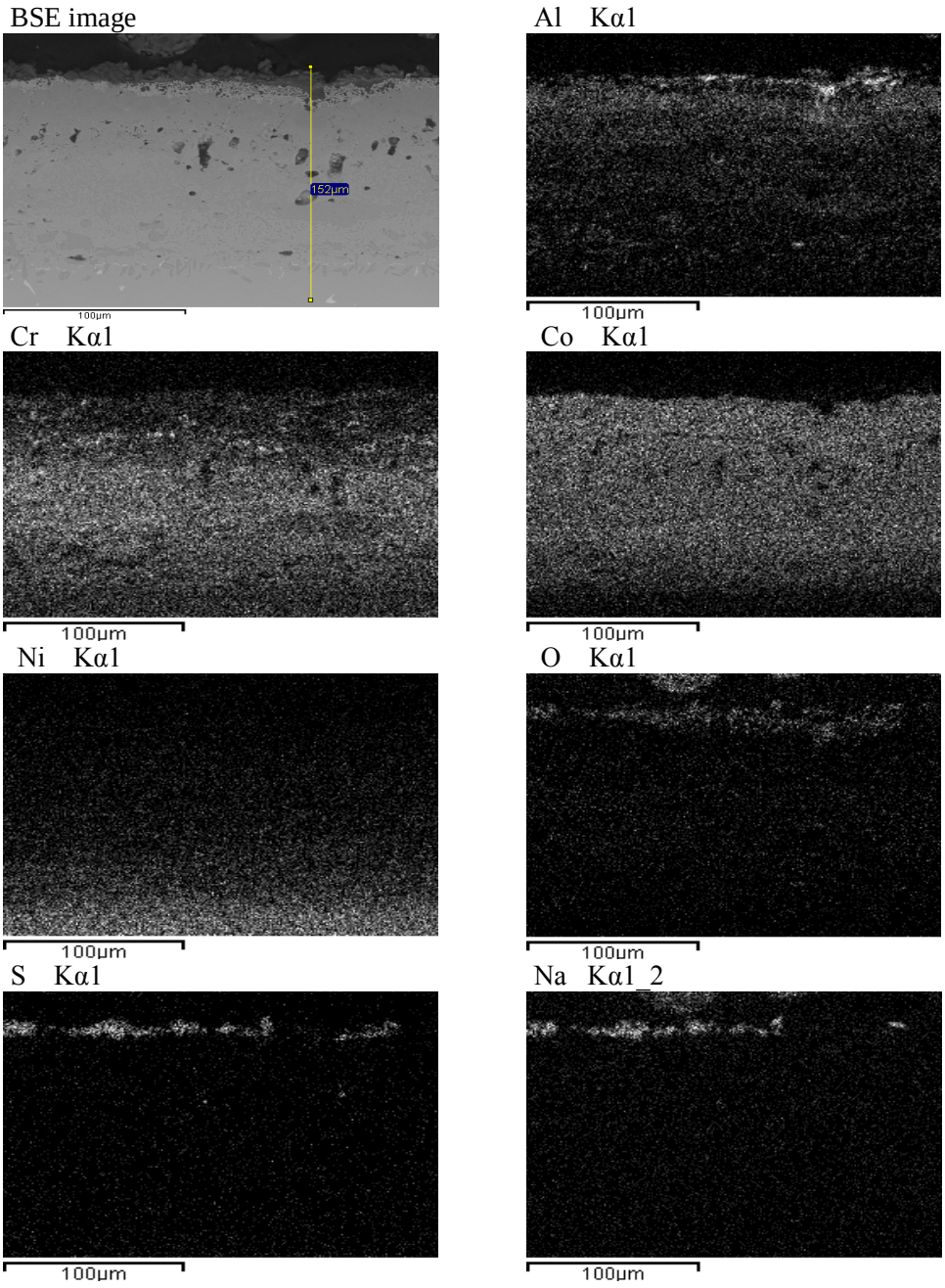

Figure 7.5: IN738LC and GT29+; with $CdSO_4$+(Na_2SO_4(80)+ K_2SO_4(20)) salt flux 1.5 µg/cm^2/h, after corrosion testing for 500 hours at 700^{o}C – element maps

Oxidation and the light pitting and scale formation caused by Type II hot corrosion can be seen in the BSE maps shown in Figure 7.5. The scale/deposit consists of oxides of chromium and aluminium and also contains cobalt, sulphur and sodium.

7.4.1.2 $CdSO_4$+(Na_2SO_4(80)+ K_2SO_4(20)) with salt flux of 5.0 µg/cm^2/h

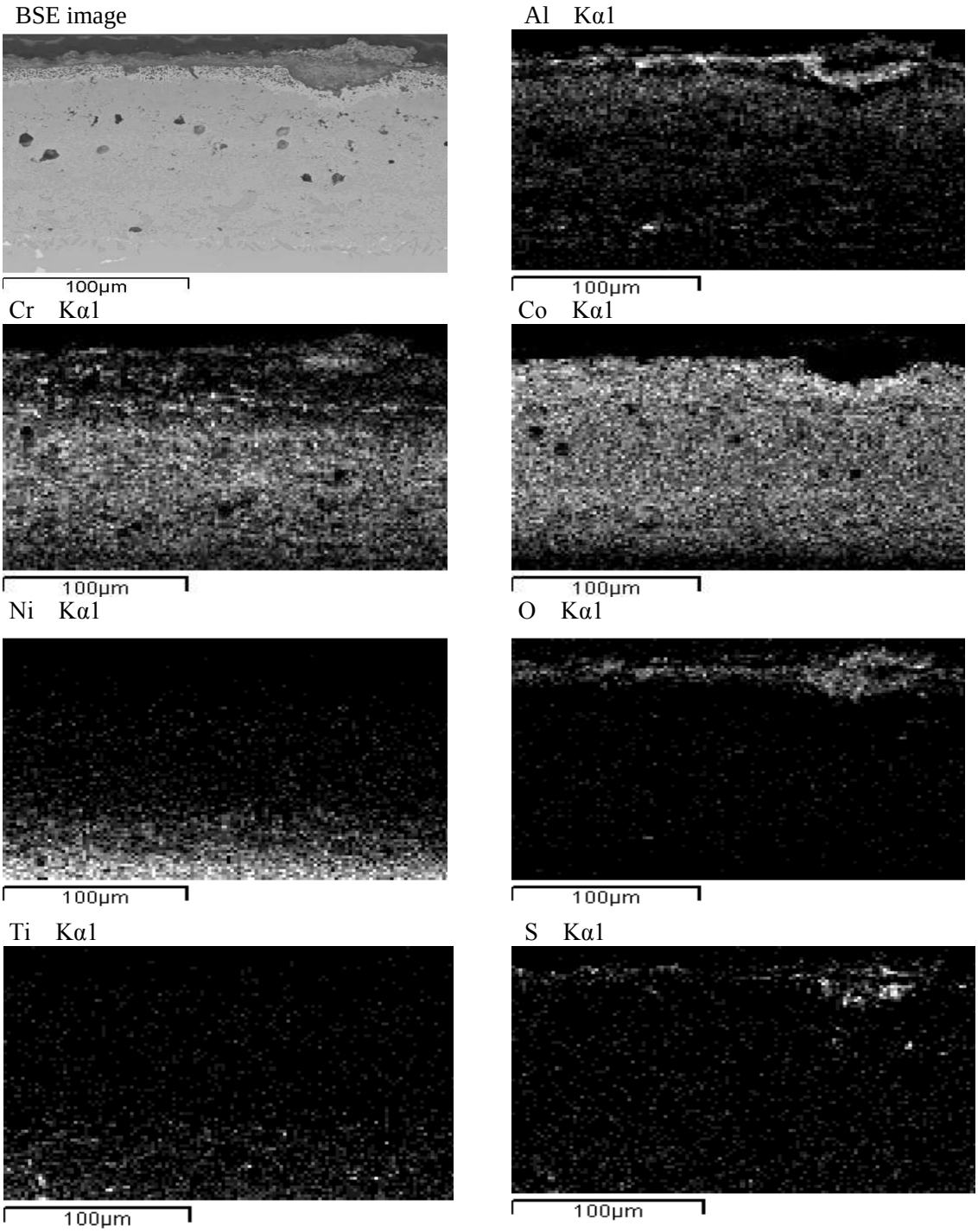

Figure 7.6: IN738LC and GT29+; with $CdSO_4$+(Na_2SO_4(80)+ K_2SO_4(20)), salt flux 5.0 µg/cm^2/h, after corrosion testing for 500 hours at 700^{o}C – element maps

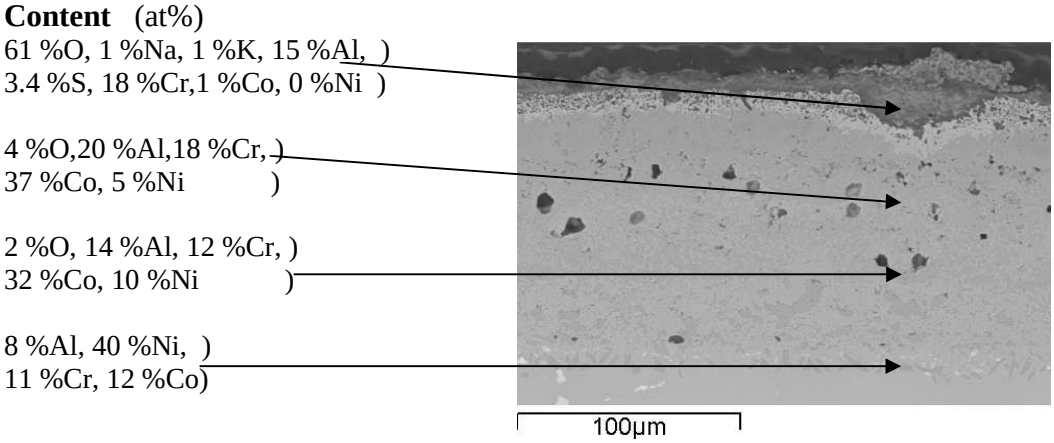

Figure 7.7: IN738LC and GT29+; with $CdSO_4$+(Na_2SO_4(80)+ K_2SO_4(20)), salt flux 5.0 µg/cm^2/h, after corrosion testing for 500 hours at 700^{o}C – main elements at selected layers

The heavier oxidation, Type II hot corrosion and scale formation in this sample, resulting from the higher salt flux of 5.0 µg/cm^2/h, seen in the element maps in Figure 7.6, can be compared with those from the low salt flux sample, seen in Figure 7.5. The higher salt flux in this test sample has caused significantly deeper pitting as a result of oxidation and sulphidation, as sown in th sulphur map in Figure 7.6. The heavy aluminium oxide layer along the bottom of the pitting and the coating surface, seen in Figure 7.6, has provided hot corrosion protection.

The outer layer of the uniformly distributed cobalt, seen in Figure 7.7, shows incipient oxidation and sulphidation but is more protective than chromium in the same region. The EDX results in Figure 7.7 show little outward diffusion of titanium has occurred, to impair its role as a alloying component of the substrate.

Despite the local heavy pitting resulting from Type II hot corrosion, from the higher level of salt flux in this sample, the figures show that the aluminium, chromium and cobalt in GT29+ continue to provide hot corrosion protection for IN738LC. Although the outer aluminium rich coating layer has been degraded, there remains approximately 30µm of sound coating remaining at the deepest point of the pit to continue to provide hot corrosion protection for the substrate.

7.4.1.3 $PbSO_4$+(Na_2SO_4(80)+ K_2SO_4(20)) with salt flux of 1.5 µg/cm^2/h

BSE image

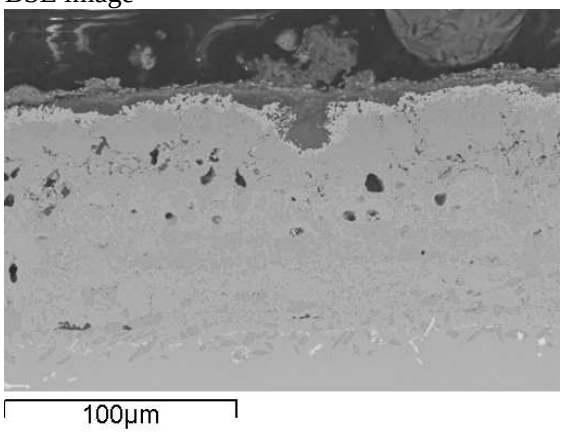

Figure 7.8: IN738LC and GT29+; with $PbSO_4$+(Na_2SO_4(80)+ K_2SO_4(20)), salt flux 1.5 µg/cm^2/h, after corrosion testing for 500 hours at 700^{o}C – BSE image

It is apparent that the sample with the lead/sodium/potassium combination, with the low salt flux, seen in Figure 7.8, is more heavily degraded than the low salt flux cadmium/ sodium/potassium sample seen in Figure 7.5. This is evidenced by the deeper pitting and increased scale formation of the sample having the lead combination.

.

7.4.1.3 $PbSO_4$+(Na_2SO_4(80)+ K_2SO_4(20)) with salt flux of 5.0 µg/cm^2/h

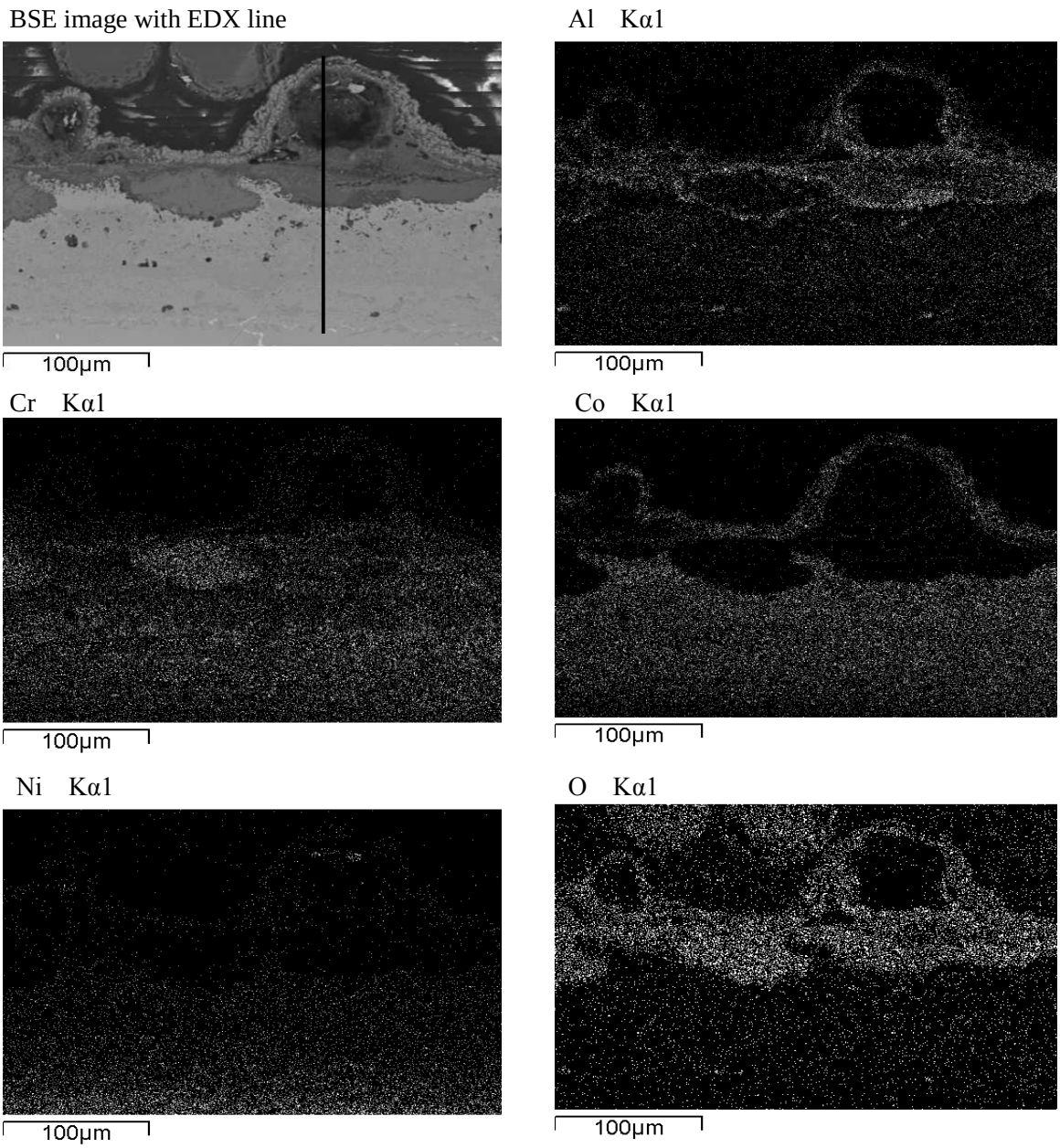

Figure 7.9: IN738LC and GT29+; with $PbSO_4$+(Na_2SO_4(80)+ K_2SO_4(20)), salt flux 5.0 µg/cm^2/h, after corrosion testing for 500 hours at 700^{o}C – element maps

The high salt flux lead/sodium/potassium combination has caused the heaviest degradation of the four combinations tested on IN738LC coated with GT29+. In Figure 7.9, the BSE image shows that the initial morphology of Type II pitting, seen in previous samples, in this case has developed on a broader front. The scale is rich in oxides of aluminium and cobalt, whereas the corrosion product in the pitting is chromium-rich.

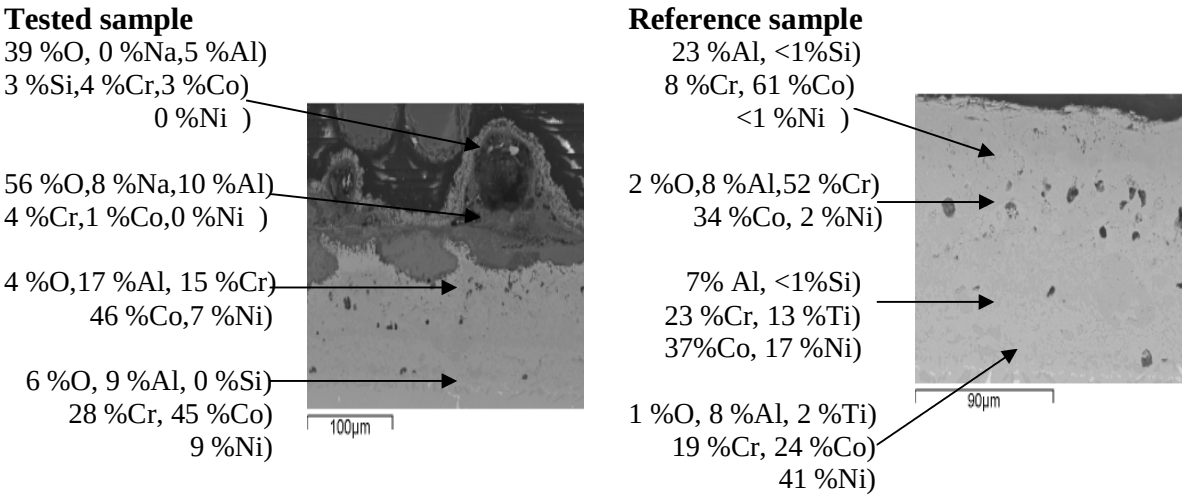

Figure 7.10: IN738LC and GT29+; with $PbSO_4$+(Na_2SO_4(80)+ K_2SO_4(20)), salt flux 5.0 µg/cm^2/h, after corrosion testing for 500 hours at 700^{o}C – comparison of tested and reference samples (at%)

Quantitative analysis, along the EDX line (in Figure 7.9), displayed in Figure 7.11, confirms Type II hot corrosion with 7 at%S, 51 at%O, and oxides formed from 2 at%Na and 2 at%K in the outer layer. The inner layer of the pitting consists of 18 at%O, 9 at%Al, 17 at%Cr, 33 at%Co and 6 at%Ni.

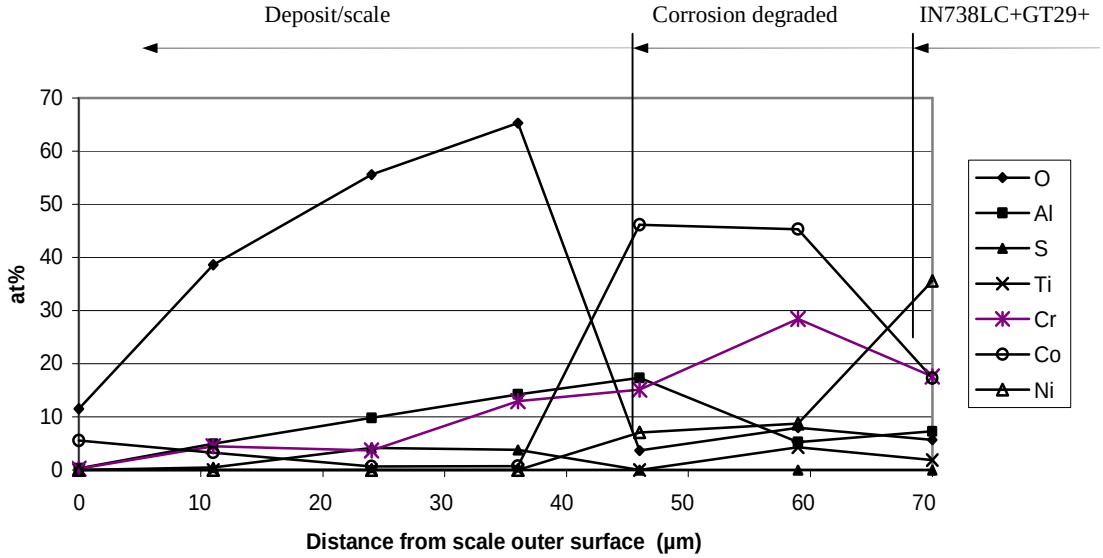

$PbSO_4$ + (Na_2SO4(80)+K_2SO_4(20)) Salt flux 5.0 µg/cm^2/hr

Figure 7.11 IN738LC and GT29+; with $PbSO_4$+(Na_2SO_4(80)+ K_2SO_4(20)), salt flux 5.0 µg/cm^2/h, after corrosion testing for 500 hours at 700^{o}C – main elements on EDX line in Figure 7.9.

7.4.1.5 IN738LC coated with GT29+ - discussion

GT29+ is a CoCrAlY overlay coating with an outer, aluminium-rich diffusion layer, to provide enhanced corrosion protection. Of the samples of IN738LC/GT29+ tested, only in the high salt flux Pb+alkali sample has corrosion progressed through the outer aluminium-rich layer. In the high salt flux Cd+alkali sample, pitting has progressed through half of this outer layer, a similar depth to that in the low salt flux Pb+alkali sample. Only minor pitting has occurred in the low salt flux Cd+alkali sample. The microstructures show that GT29+ is more protective of cadmium containing salt species, than it is of species containing lead.

Oxide scale growth is proportional to pitting depths in the samples, but only in the high salt flux Pb+alkali sample is the scale seen to be on the point of spalling. The outer layer of scale is rich in aluminium oxide, whereas scale growth within the pitting is chromium-rich and also contains sulphur. The latter indicates that sulphidation occurs in the propagation stages of Type II hot corrosion.

In summary, the microstructures indicate that the GT29+ coating provides protection to IN738LC, against oxidation and Type II hot corrosion, to a higher degree for cadmium + alkali sulphates containing species than for lead + alkali sulphate species.

7.4.2 Microstructures of IN738LC samples coated with RT-22

7.4.2.1 $CdSO_4$+(Na_2SO_4(80)+ K_2SO_4(20)) with salt flux of 1.5 µg/cm^2/h

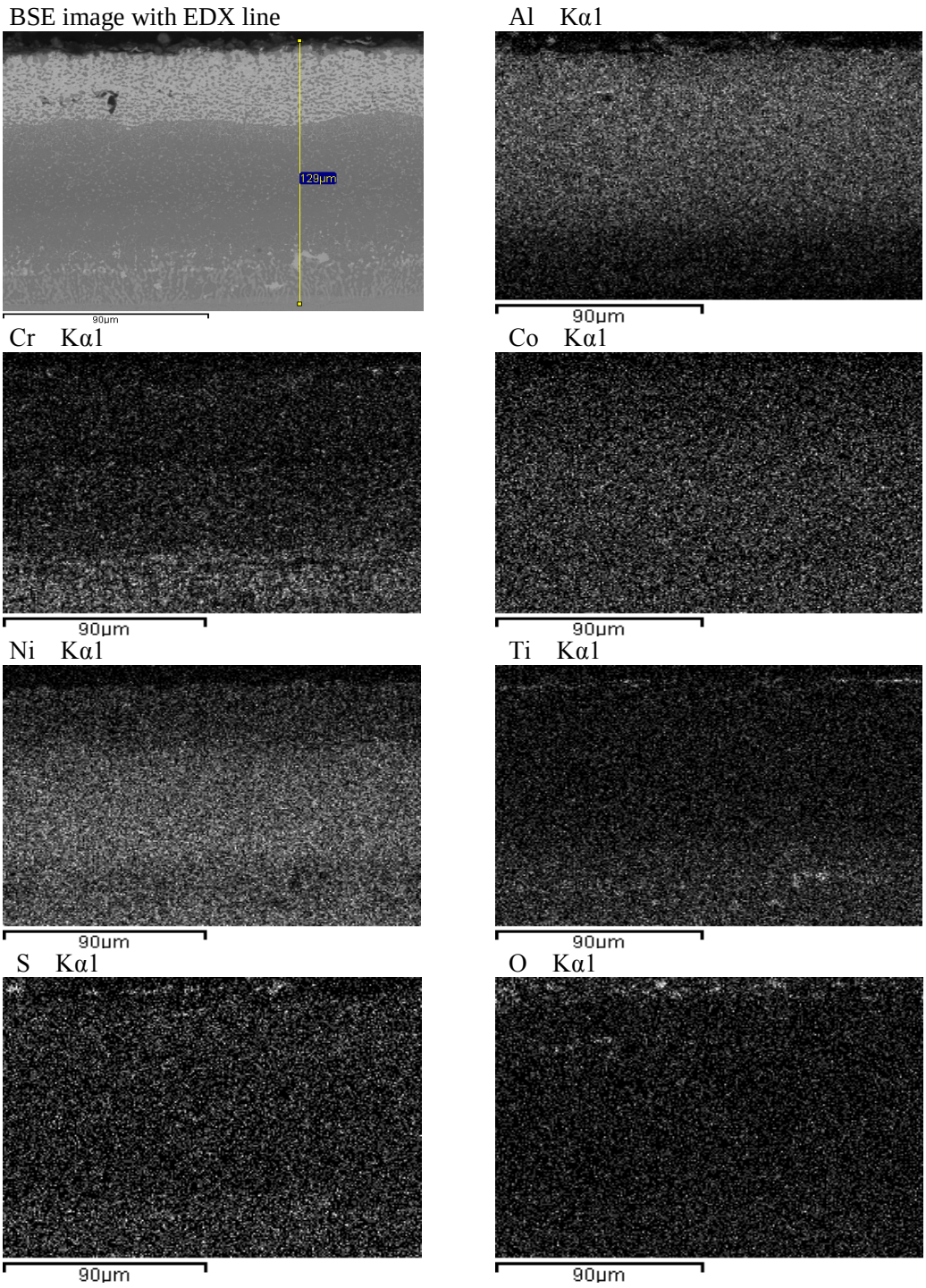

Figure 7.12: IN738LC and RT-22 with $CdSO_4$ + ($NaSO_4$(80)+K_2SO_4(20)); salt flux 1.5 µg/cm^2/h, after corrosion testing for 500 hours at 700^{o}C – element maps

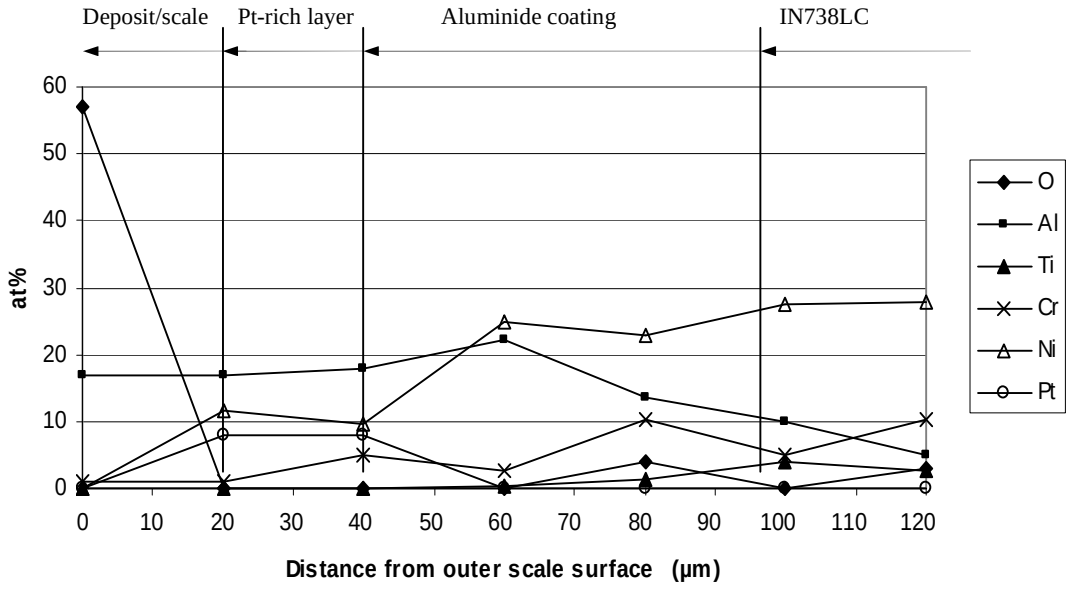

Figure 7.13: IN738LC and RT-22; with $CdSO_4$+(Na_2SO_4(80)+ K_2SO_4(20)), salt flux 1.5 µg/cm^2/h, after corrosion testing for 500 hours at 700^{o}C – main elements on EDX line in Figure 7.12

The microstructure of the low salt flux Cd+alkali sample map, seen in Figure 7.12, shows very shallow pitting and oxide scale groth along the platinum-rich outer layer of the coating. Quantitative analysis of the scale shows it to be rich in oxides of aluminium and also sodium, sulphur, potassium, with a trace of cadmium; 57 at%O, 17 at%Al, 4 at%S, 3 at%Na, <1 at%K and <0.1 at%Cd.

The EDX line analysis in Figure 7.13 shows that from the 20µm distance between analysis points, oxygen content falls to zero, whereas platinum content rises from zero at the scale surface, to 8 at%Pt at the base of the scale, approximately 40µm from the scale surface. Chromium content, averages 7 at%Cr through the coating to the base of the platinum-rich layer, from where it falls to 2 at%Cr through to the scale surface.

These results show that RT-22 provides a high level of corrosion protection to IN738LC when the cadmium+alkali sulphate species, of a low salt flux, are deposited in an industrial gas turbine.

7.4.2.2 $CdSO_4$+(Na_2SO_4(80)+ K_2SO_4(20)) with salt flux of 5.0 µg/cm^2/h

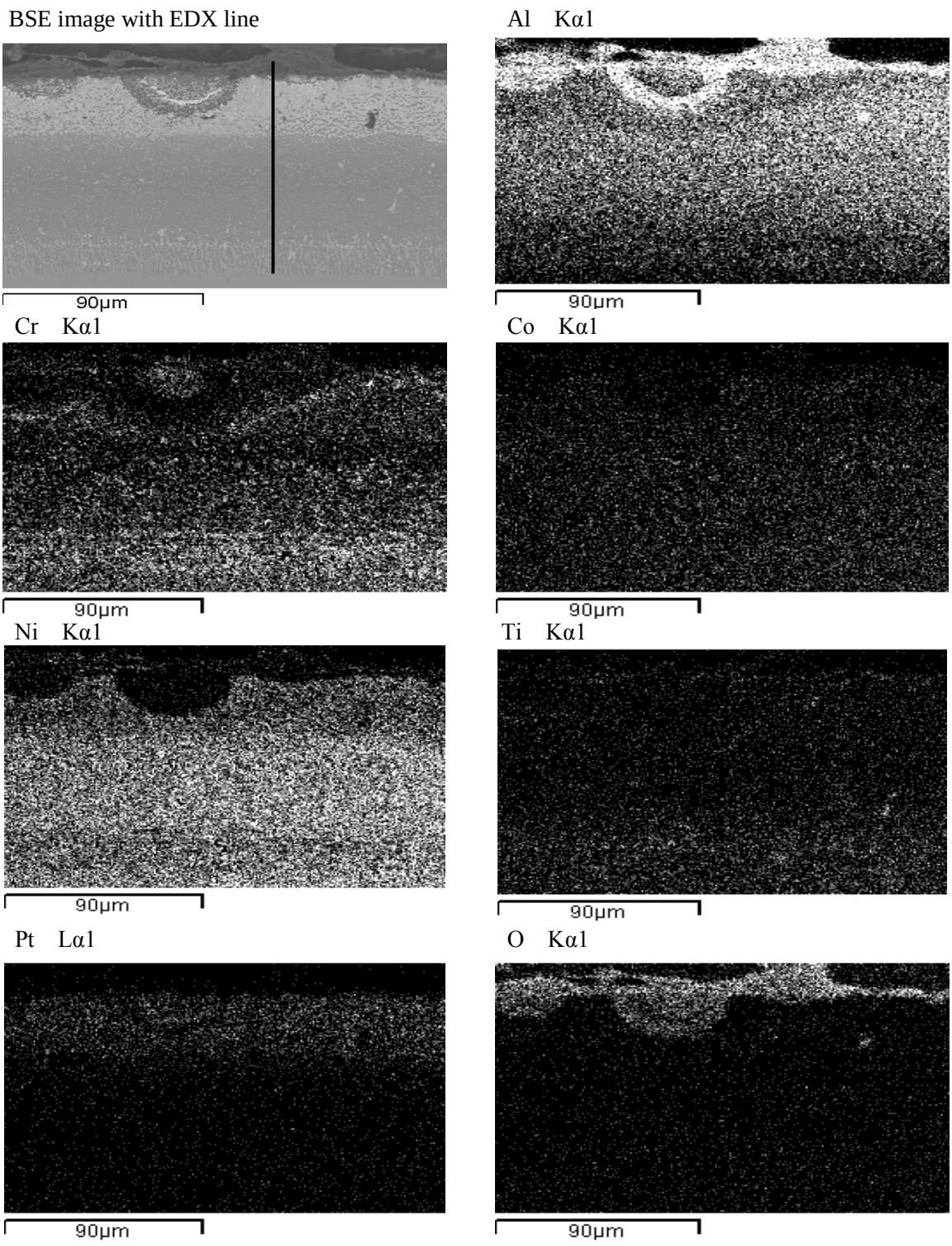

Figure 7.14: IN738LC and RT-22 with $CdSO_4$ + ($NaSO_4$(80)+K_2SO_4(20)); salt flux 5.0 µg/cm^2/h, after corrosion testing for 500 hours at 700°C – element maps

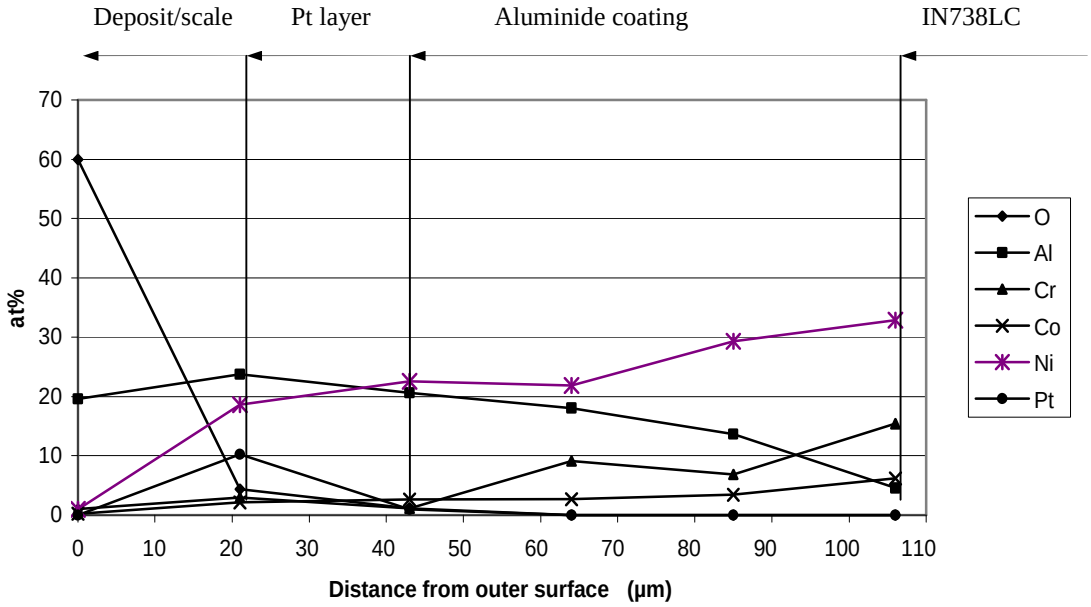

Figure 7.15 : IN738LC and RT-22; with $CdSO_4$+(Na_2SO_4(80)+ K_2SO_4(20)), salt flux 5.0 µg/cm^2/h, after corrosion testing for 500 hours at 700^{o}C – main elements on EDX line in Figure 7.14

The BSE image in Figure 7.14 shows that, compared with the low salt flux Cd+alkali sample (in Figure 7.12) significant Type II hot corrosion pitting has been caused by the high salt flux of the same species. The base of the major site of degradation remains in the platinum-rich layer but oxidation is approaching the platinum-rich layer interface with the remaining coating. The platinum map in Figure 7.14 shows some reduction in its content in the less oxidised centre of the pit.

The scale and inner ring and outer layer of the coating are rich in aluminium oxide. However, the coating adjacent to the oxidation is aluminium depleted before its content increases again in the remaining coating. In the depleted aluminium, a chromium-rich layer runs along the base of the platinum layer and the protection provided by aluminium and chromium appears to combine in a complex manner.

Quantitative analysis confirms that the scale and outer, degraded layer is mainly aluminium oxide (60 at%O, 20 at%Al) with lesser oxides of chromium, sodium, sulphur, potassium and nickel being present (>1 at%Na, 1 at%S, <1 %K, 1 at%Cr, 1 at%Ni).

As a contribution to understanding the changes in outer coating microstructure, in the vicinity of the heavily degraded site, elements in this area and in the reference sample are compared in Figure 7.16. It can be seen that, oxidation has penetrated deep into the platinum layer in the tested sample, that the aluminium content remains similar in both samples, whereas chromium in the tested sample is present as an oxide, in contrast to that in the reference sample.

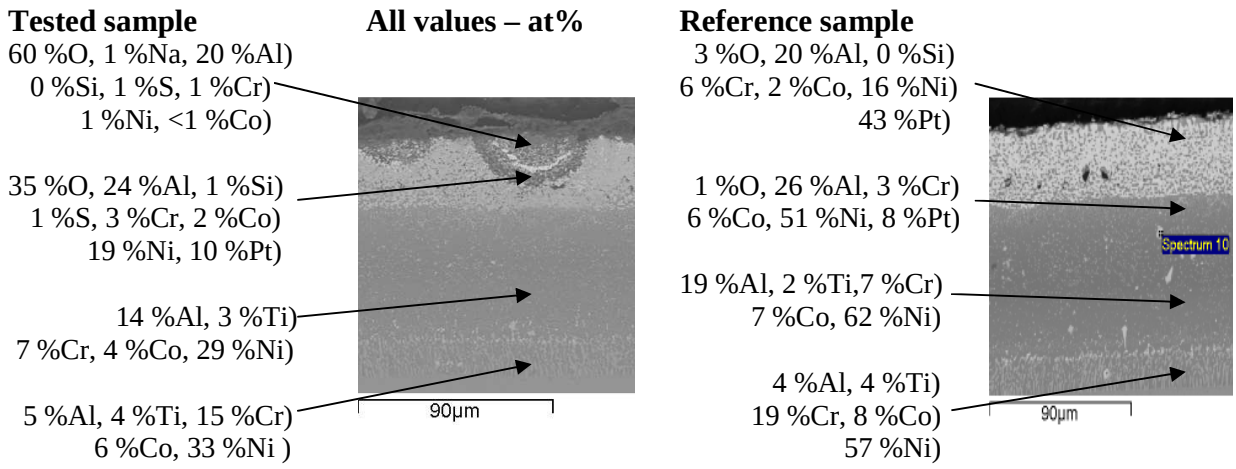

Figure 7.16: IN738LC and RT-22 with $CdSO_4$ + ($NaSO_4$(80)+K_2SO_4(20)); salt flux 5.0 µg/cm^2/h, after corrosion testing for 500 hours at 700^{o}C – elements in tested and reference samples

Analysis of this sample so far has provided a more general overview of the coating, and as such omits detailed examination of the heavily degraded sites. The second stage of the analysis concentrates on the major degraded area, the element maps for which are shown in Figure 7.17.

The whole degraded area comprises oxides of aluminium and platinum, with the central degraded area also containing chromium and platinum oxides. The advance of degradation at this site is led by oxidation and oxidation is already to be seen in the coating under the lower edge of the ‘ring’.

The scale mainly contains oxides of nickel and, to a lesser extent, aluminium, chromium and platinum. Titanium has diffused outwards through the coating to the surface with only a small proportion being contained in the scale. The maps indicate that scale spallation has commenced but are inadequate to provide information on its extent.

Quantitative analyses of elements contained in the heavily degraded area of the tested sample are compared with the reference sample in Figure 7.18.

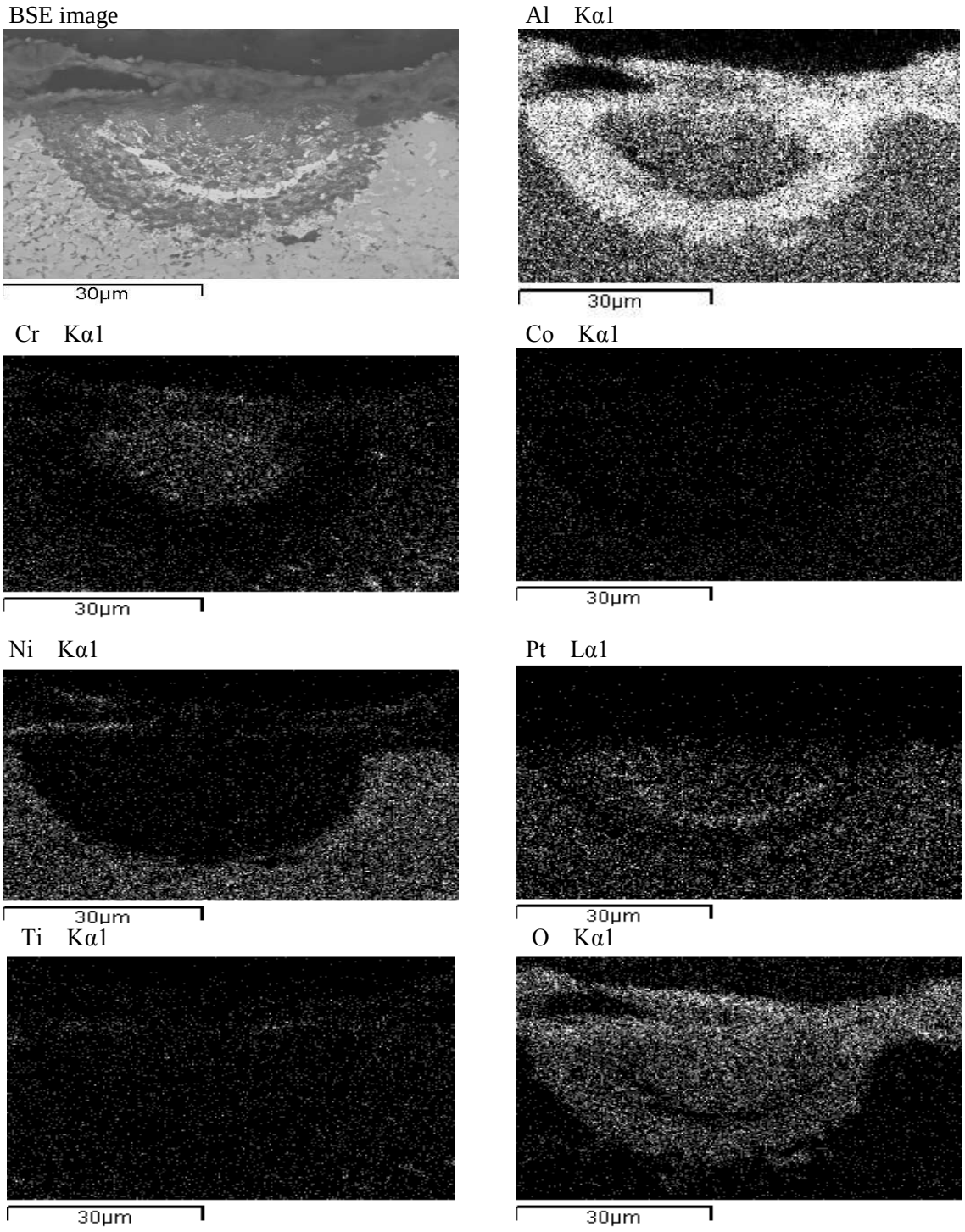

Figure 7.17: IN738LC and RT-22 with $CdSO_4$ + ($NaSO_4$(80)+K_2SO_4(20)); salt flux 5.0 µg/cm^2/h, after corrosion testing for 500 hours at 700^{o}C – element maps of oxidation and corrosion site shown in Figure 7.14

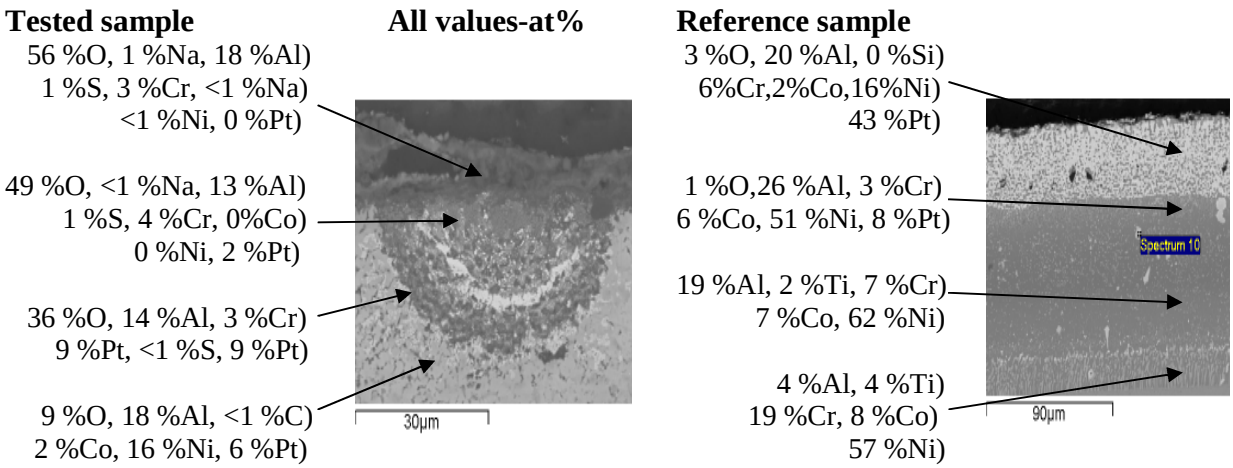

Figure 7.18: IN738LC and RT-22 with $CdSO_4$ + ($NaSO_4$(80)+K_2SO_4(20)); salt flux 5.0 µg/cm^2/h, after corrosion testing for 500 hours at 700^{o}C – elements in the tested sample

Figure 7.18 shows details of the main elements contained in the tested sample and compares values in the reference sample. The figure is for illustrative purposes and should not be used for measuring depths.

In addition to the elements quantified in Figure 7.18, traces of potassium and titanium are contained in the two outer sites. There are no traces of cadmium in any of the sites, however, the presence of sodium, potassium and sulphur indicates Type II hot corrosion has been initiated. The oxidation under the base of the degraded area shows that the platinum-rich layer has been degraded to a depth of approximately 22µm, compared with a total depth of this layer, of 30µm. The platinum-rich 'beads' have provided corrosion protection and, as seen in the platinum map in Figure 7.17, appear to retard oxidation locally.

7.4.2.3 $PbSO_4$+(Na_2SO_4(80)+ K_2SO_4(20)) with salt flux of 1.5 µg/cm^2/h

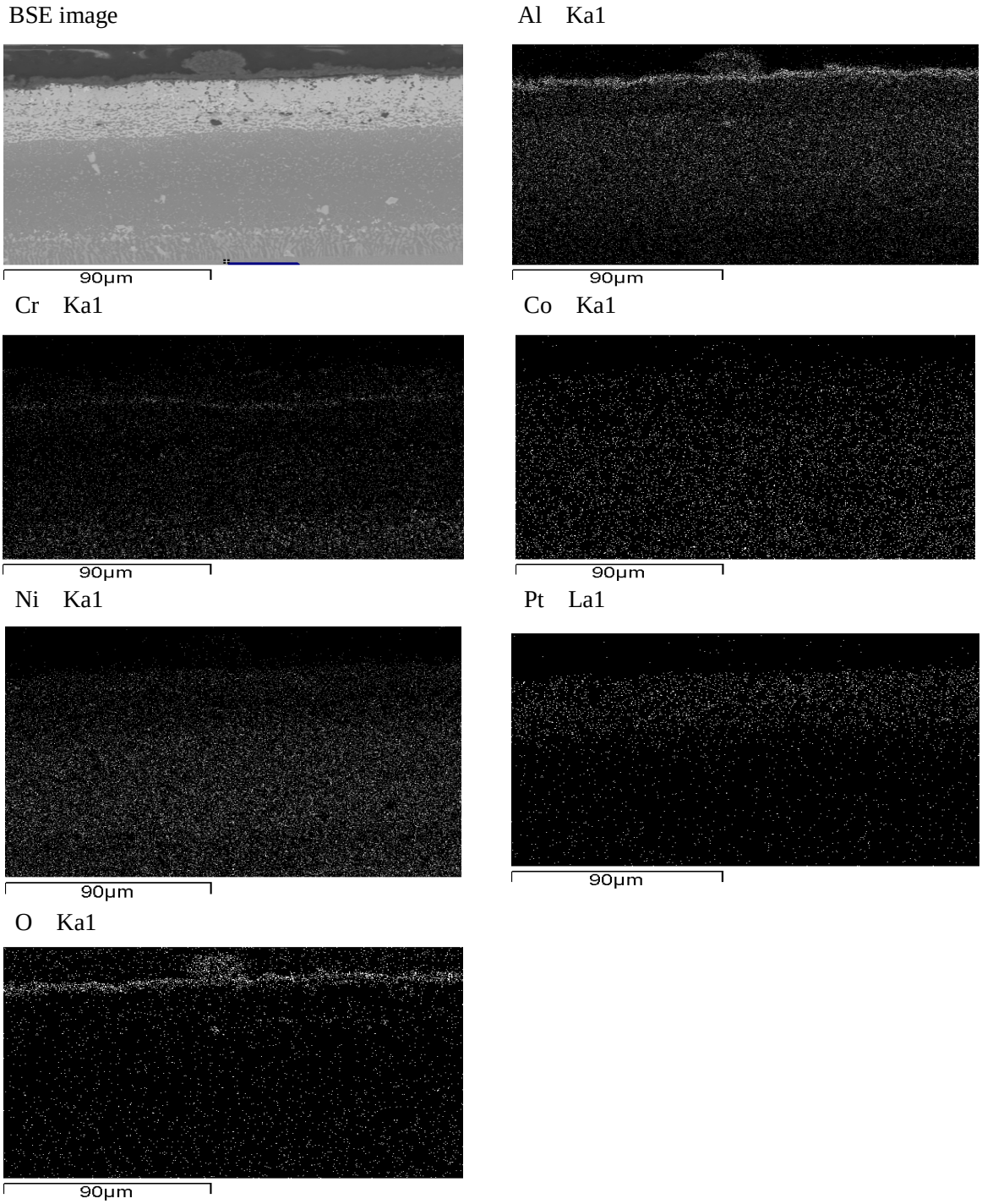

Figure 7.19: IN738LC and RT-22 with $PbSO_4$ + ($NaSO_4$(80)+K_2SO_4(20)); salt flux 1.5 µg/cm^2/h, after corrosion testing for 500 hours at 700^{o}C – element maps

7.4.2.4 $PbSO_4$+(Na_2SO_4(80)+ K_2SO_4(20)) with salt flux of 5.0 µg/cm^2/h

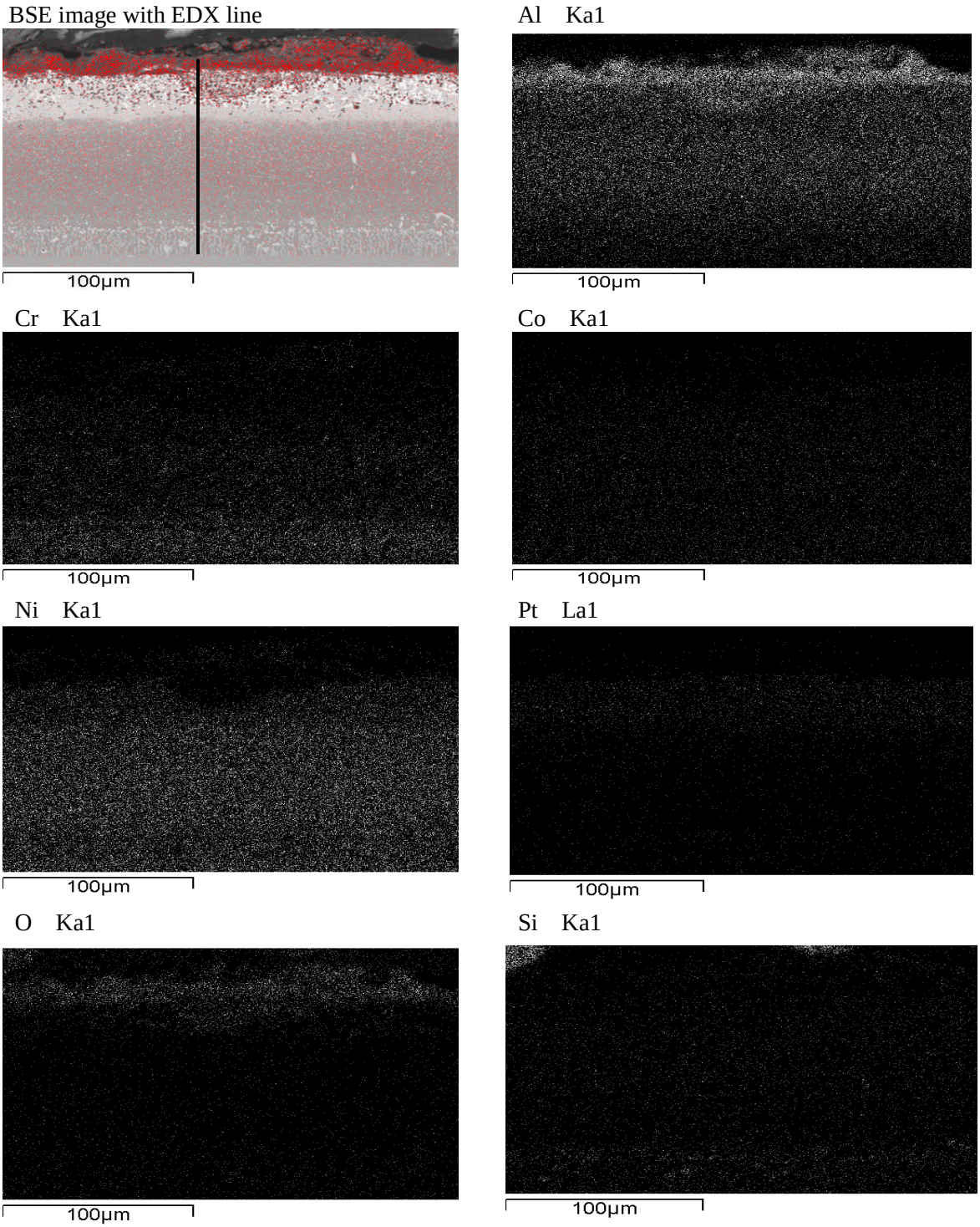

Figure 7.20: IN738LC and RT-22 with $PbSO_4$ + ($NaSO_4$(80)+K_2SO_4(20)); salt flux 5.0 µg/cm^2/h, after corrosion testing for 500 hours at 700°C – element maps

The element maps of the low salt flux Pb+alkali sample, seen in Figure 7.19, show that little oxidation or corrosion has been initiated in the RT-22 coating. The generally thin scale contains oxides of aluminium, whereas lower in the platinum-rich layer of the coating, there is a thin chromium-rich oxide layer.

Quantitative analysis of the elements in the scale shows the composition to be 39 at%O, 17 at%Al, 6 at%Ni, 4 at%Cr, 2 at%Co, 1 at%Pt, 1 at%Ti and traces of sulphur.

In contrast to the minimal degradation caused to RT-22 by the low salt flux Pb+alkali combination, the high salt flux combination has initiated significant Type II hot corrosion in RT-22. This is shown in the element maps for this sample shown in Figure 7.20. The scale and area of major degradation are rich in oxides of aluminium and nickel.

The elemental analysis along the EDX line seen in Figure 7.20, set out graphically in Figure 7.21, shows the aluminium oxide rich scale, in which the platinum content of 10 at%Pt falls to zero at the outer surface of the scale. The corrosion product within the degraded area contains traces of sulphur on the outer layer, which become richer in the base of the same area. Oxidation is seen to be progressing into the platinum-rich layer below the main degraded area, which is approaching the base of the layer.

Quantitative analysis of the outer degraded area shows the composition to be 17 at%O, 17 at%Al, 16 at%Ni, 4 at%Cr, 2 at%Co, 1 at%Ti, 1 at%Pt and <1 at%S. The composition changes within the area, as oxidation reduces and sulphidation increases towards the lower edge. The content of elements at the base confirm this, as follows; 0 at%O, 8 at%Al, 44 at%Ni, 21 at%Cr, 8 at%Co, 4 at%Ti, 0 at%Pt and 1 at%S.

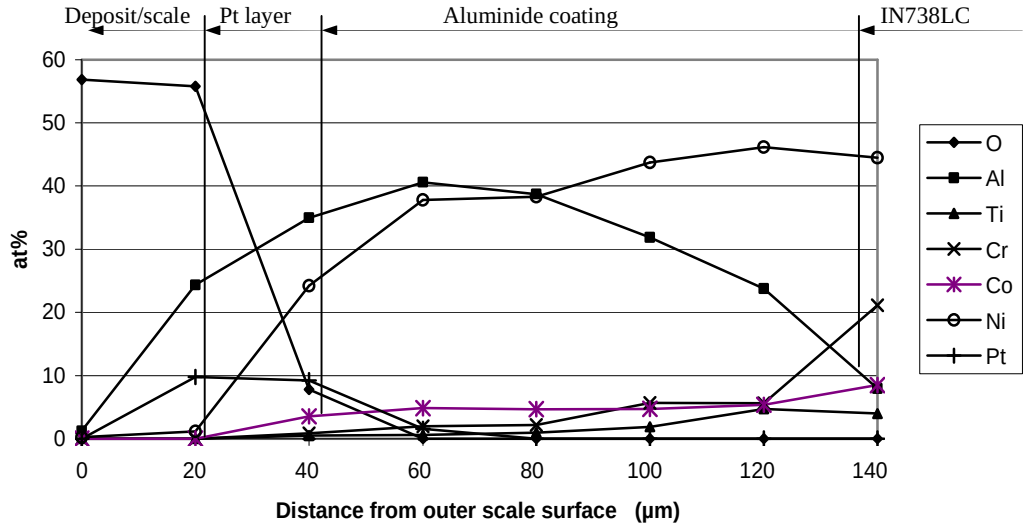

Figure 7.21: IN738LC and RT-22; with $PbSO_4$+(Na_2SO_4(80)+ K_2SO_4(20)), salt flux 5.0 µg/cm^2/h, after corrosion testing for 500 hours at 700^{o}C – main elements on EDX line in Figure 7.20

7.4.2.5 IN738LC coated with RT-22 – discussion

The outer platinum-rich layer of the aluminide diffusion coating RT-22 is effective in retarding the initiation of hot corrosion, and these tests show that in low salt flux samples of the Cd+alkali and Pb+alkali combinations, minimal degradation of this layer has occurred. In each case, only a thin uniform layer of scale been formed along the surface. With such minimal degradation and thin scale formation, it can be concluded that RT-22 will be highly protective against the initiation of Type II hot corrosion.

Both high salt flux samples exhibit heavy degradation of the platinum-rich layer of the coating resulting from oxidation and Type II hot corrosion. In each case degradation has penetrated more than half way through the platinum-rich layer, with oxidation already approaching its interface with the aluminium-rich layer of the coating. There is little difference between the depths of degradation exhibited by the high salt flux samples. However, in the Cd+alkali species sample, the heavily degraded area is more closely defined, with less incipient oxidation outside the area. In the Pb+alkali sample, oxidation is apparent on a broader front, along the layer, outside the heavily degraded area. Compared with the platinum-rich layer, it can be expected that there will be an acceleration in the initiation of hot corrosion once degradation of the aluminium-rich layer commences.

7.4.3 Microstructures of IN738LC samples coated with Sermaloy 1515

Only high salt flux samples of the IN738LC/Sermaloy 1515 combination were tested in this series of corrosion tests. Figure 7.22 shows main elements in the Cd+alkali species sample along the EDX line shown in Figure 7.23.

7.4.3.1 $CdSO_4$+(Na_2SO_4(80)+ K_2SO_4(20)) with salt flux of 5.0 µg/cm^2/h

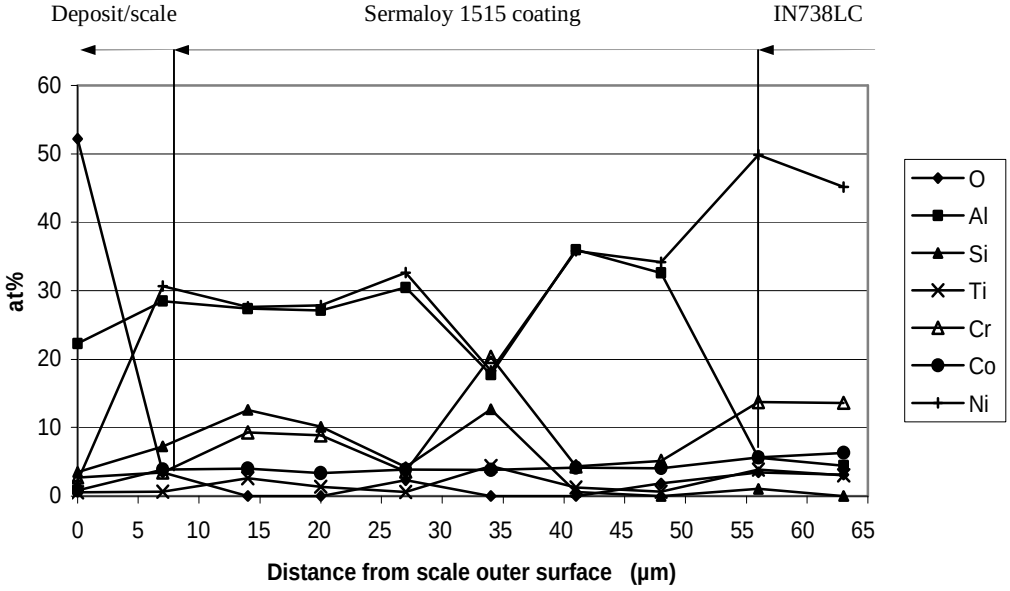

Figure 7.22: IN738LC & Serm1515; with $CdSO_4$+(Na_2SO_4(80)+ K_2SO_4(20)), salt flux 5.0 µg/cm^2/h – main elements on EDX line in Figure 7.23

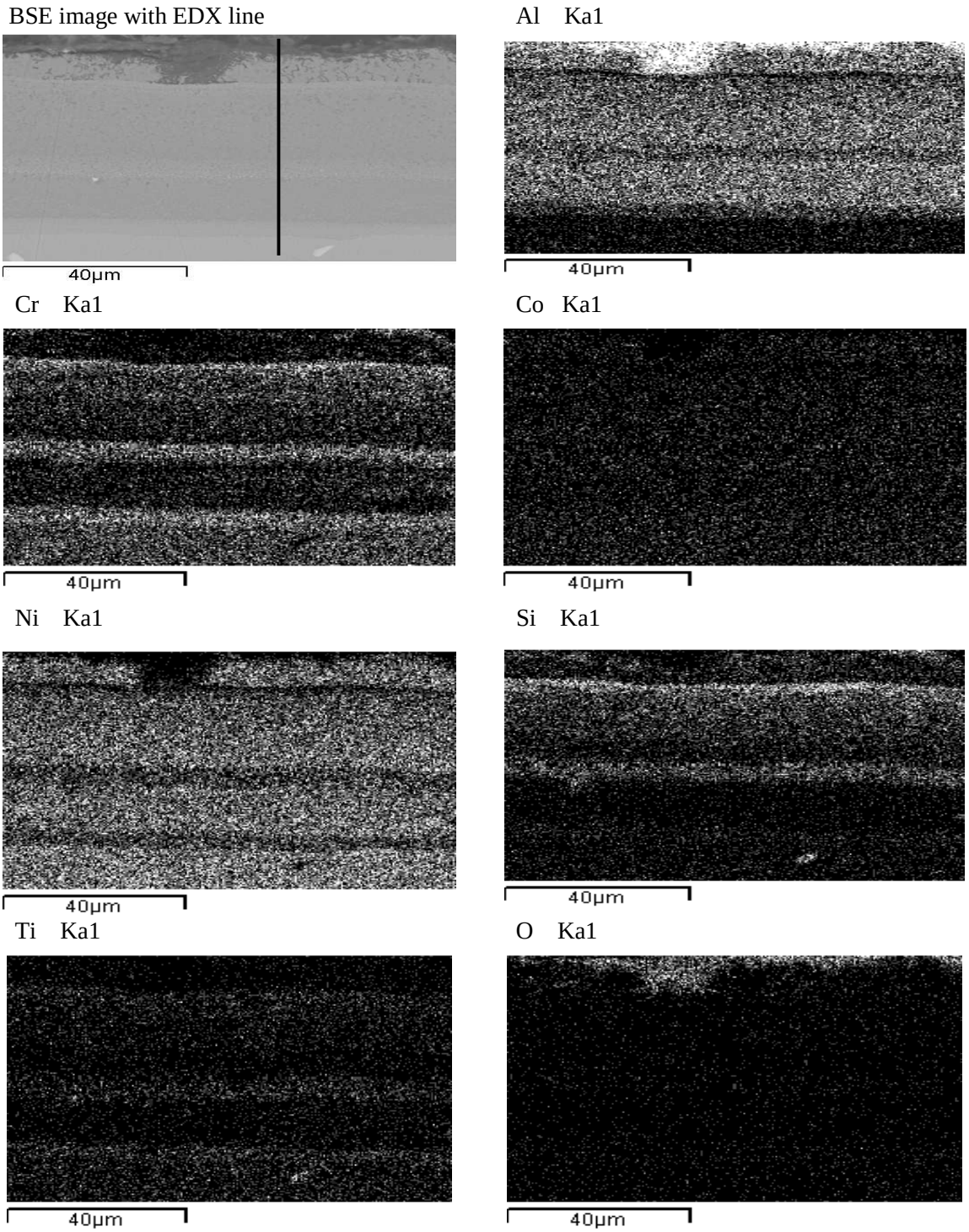

Figure 7.23: IN738LC & Sermaloy 1515 with $CdSO_4$ + ($NaSO_4$(80)+K_2SO_4(20)); salt flux 5.0 µg/cm^2/h, after corrosion testing for 500 hours at 700^{o}C – element maps

Quantitative analysis shows the scale and pitting to contain oxides of aluminium and silicon with lesser content in the scale of chromium and titanium.

7.4.3.2 $PbSO_4$+(Na_2SO_4(80)+ K_2SO_4(20)) with salt flux of 5.0 µg/cm^2/h

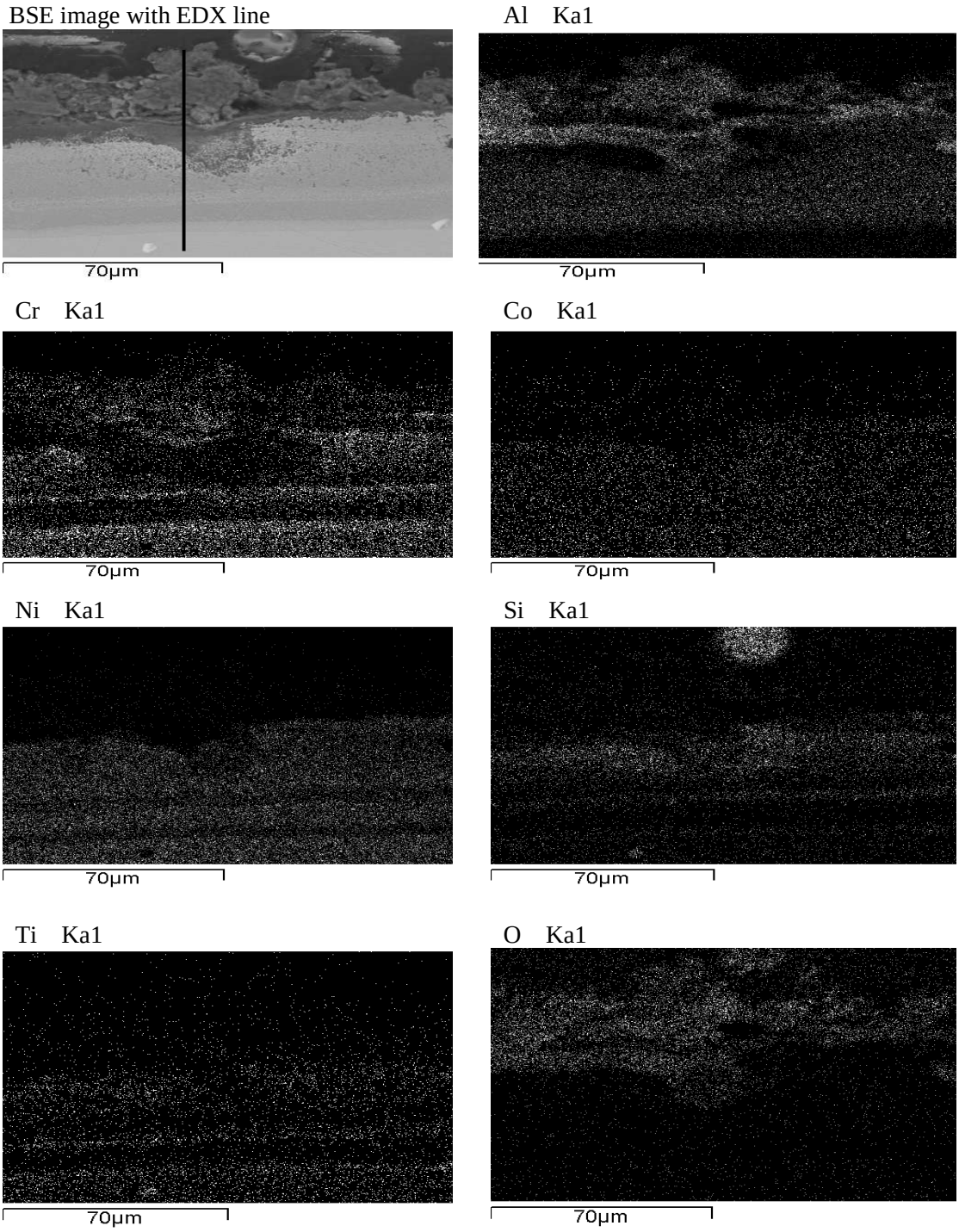

Figure 7.24: IN738LC and Sermaloy 1515 with $PbSO_4$ + ($NaSO_4$(80)+K_2SO_4(20)); salt flux 5.0 µg/cm^2/h, after corrosion testing for 500 hours at 700^{o}C – element maps

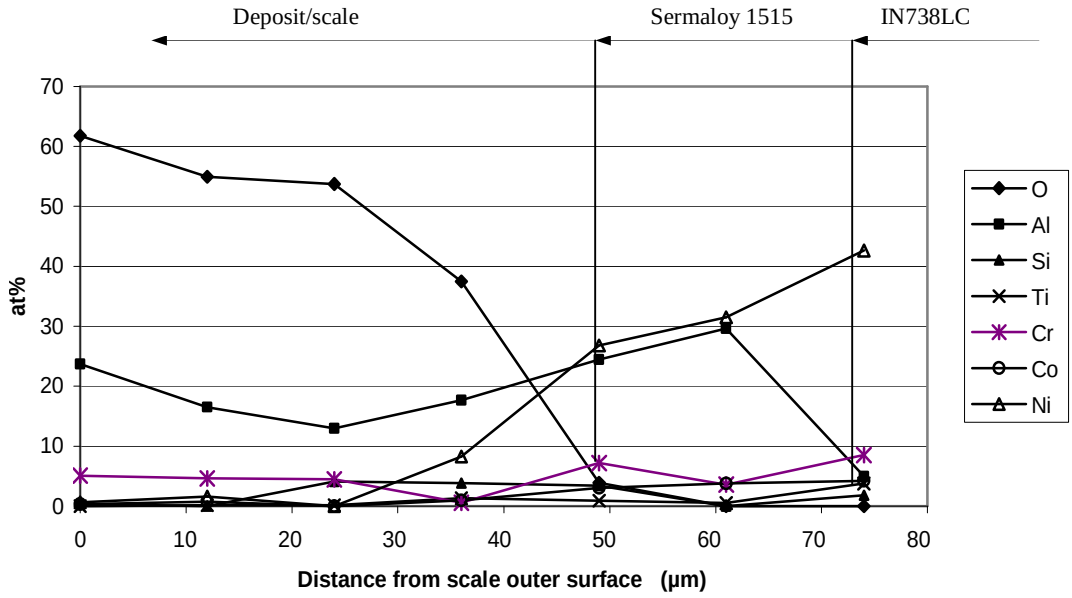

Figure 7.25: IN738LC & Serm1515; with $PbSO_4$+(Na_2SO_4(80)+ K_2SO_4(20)), salt flux 5.0 µg/cm^2/h, after corrosion testing for 500 hours at 700^{o}C – main elements on EDX line in Figure 7.24

The element maps in Figure 7.24 show that the high salt flux of the Pb+alkali species has caused heavy degradation of the IN738LC/Sermaloy 1515. The degraded area and scale contain oxides of aluminium, chromium, and to a lesser extent, of titanium from the coating. The quantitative analyses of samples for both species, show the sulphur-rich scale and pitting of Type II hot corrosion, degradation of each being of a similar extent .

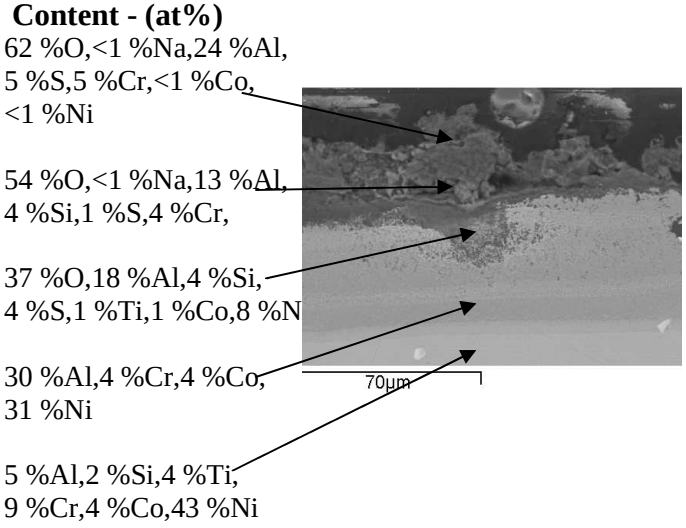

Figure 7.26: IN738LC & Serm1515; with $PbSO_4$+(Na_2SO_4(80)+ K_2SO_4(20)), salt flux 5.0 µg/cm^2/h, after corrosion testing for 500 hours at 700^{o}C – elements at selected layers

7.4.4 Micrographs of CMSX-4 samples coated with Sermaloy 1515

7.4.4.1 $CdSO_4$+(Na_2SO_4(80)+ K_2SO_4(20)) with salt flux of 1.5 µg/cm^2/h

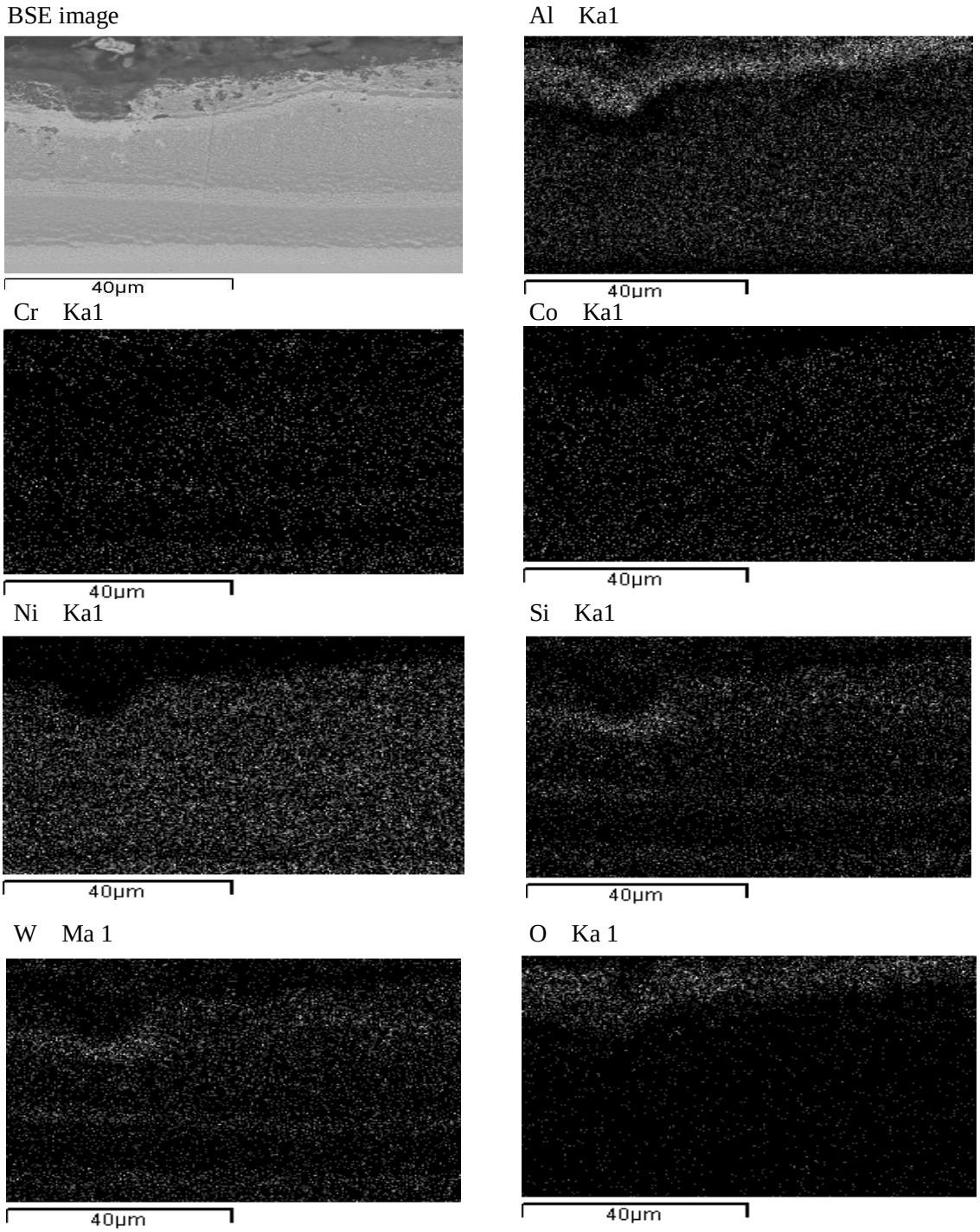

Figure 7.27: CMSX-4 and Sermaloy 1515 with $CdSO_4$ + ($NaSO_4$(80)+K_2SO_4(20)); salt flux 1.5 µg/cm^2/h, after corrosion testing for 500 hours at 700^{o}C – element maps

The maps in Figure 7.27 show the significant degradation of Sermaloy 1515 caused by Type II hot corrosion, after testing with the low salt flux, Cd/Na/K species.

7.4.4.2 $CdSO_4$+(Na_2SO_4(80)+ K_2SO_4(20)) with salt flux of 5.0 µg/cm^2/h

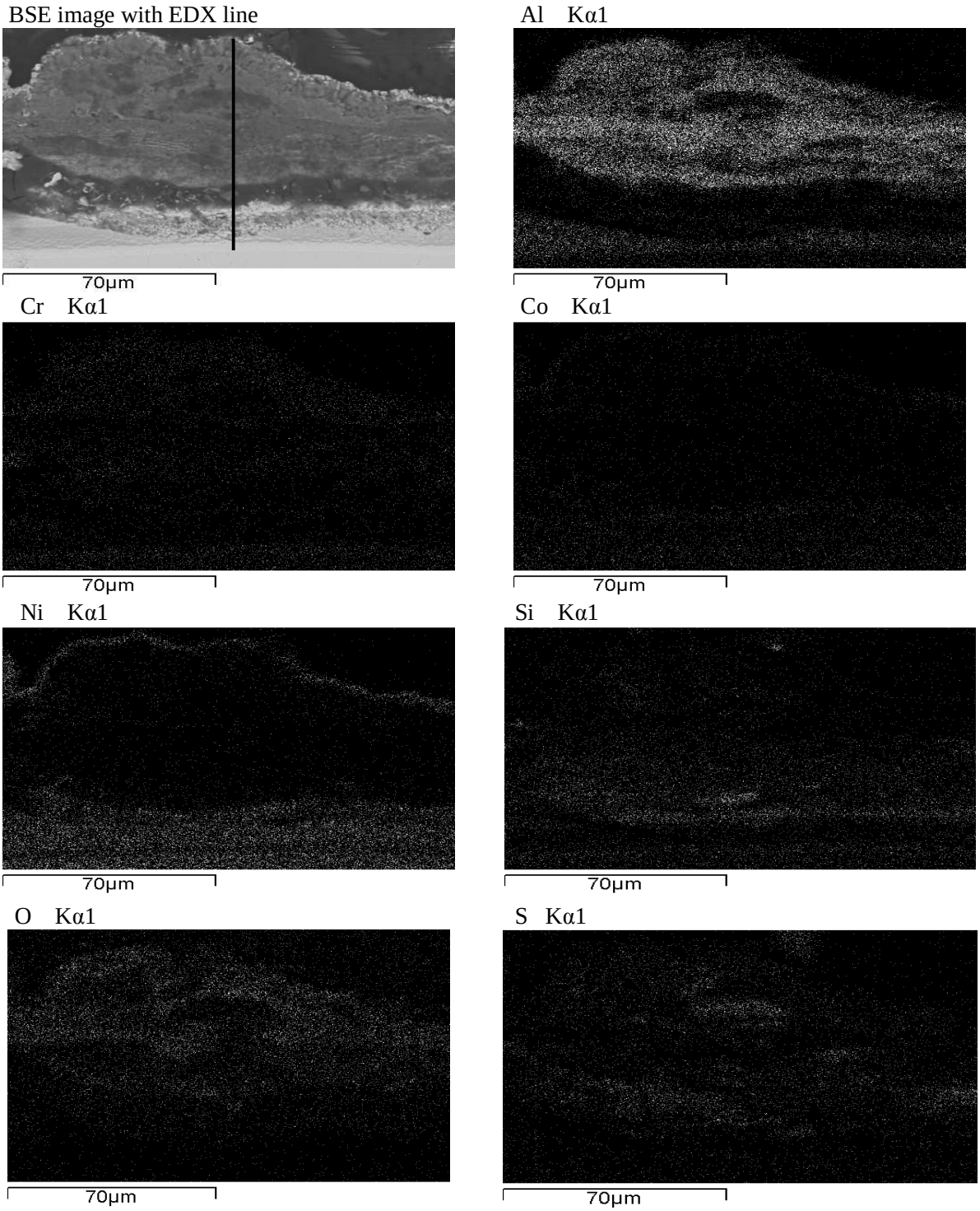

Figure 7.28: CMSX-4 and Sermaloy 1515 with $CdSO_4$ + ($NaSO_4$(80)+K_2SO_4(20)); salt flux 5.0 µg/cm^2/h, after 500 hours corrosion testing at 700^{o}C–element maps

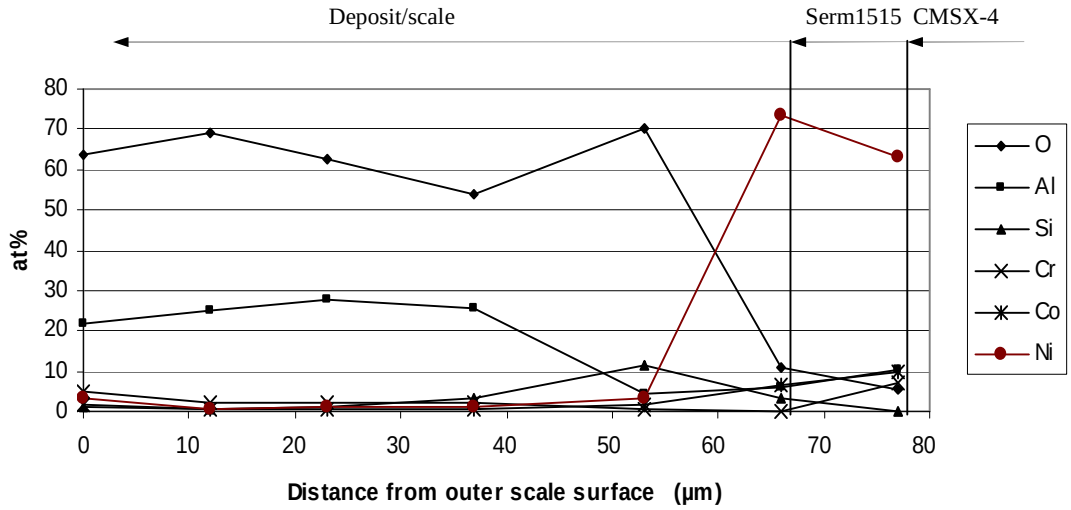

Figure 7.29: CMSX-4 & Serm1515; with $CdSO_4$+(Na_2SO_4(80)+ K_2SO_4(20)), salt flux 5.0 µg/cm^2/h, after 500 h corrosion testing at 700^{o}C – elements with high content on EDX line in Figure 7.28

The maps in Figure 7.28 show the very heavy degradation caused by Type II hot corrosion from the high salt flux Cd+alkali species to the Sermaloy 1515 coating on CMSX-4. The outer scale contains oxides of aluminium, chromium, silicon and sulphur. However, there are sulphides also contained in small areas of the scale. Graphs of the main elements along the EDX line in Figure 7.28, presented in Figure 7.29, show oxidation has degraded the coating down to the inner aluminium- and nickel-rich layer. Graphs of the low content elements along the same EDX line, in Figure 7.30, illustrate that sulphidation of sodium and potassium, the acid-fluxing of Type II hot corrosion, commences at a similar coating depth to that of oxidation. However, the corrosion develops at a slower rate than that of oxidation. The differences in rate of corrosion, of the low salt flux sample, compared with that of the high salt flux sample, are clear from Figures 7.27 and 7.28.

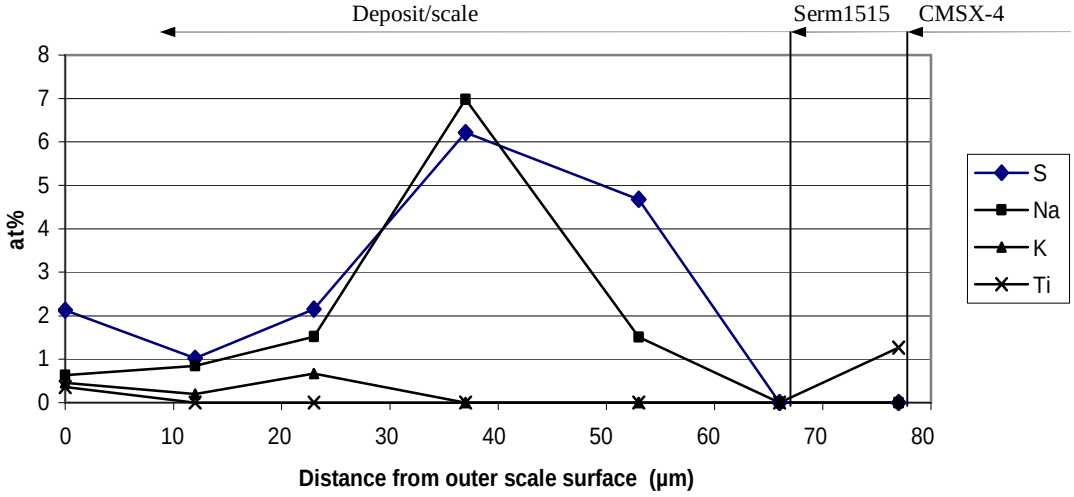

Figure 7.30: CMSX-4 & Serm1515; with $CdSO_4$+(Na_2SO_4(80)+ K_2SO_4(20)), salt flux 5.0 µg/cm^2/h, after 500h corrosion testing at 700^{o}C – elements with low content on EDX line in Figure 7.28

7.4.4.3 $PbSO_4$+(Na_2SO_4(80)+ K_2SO_4(20)) with salt flux of 1.5 µg/cm^2/h

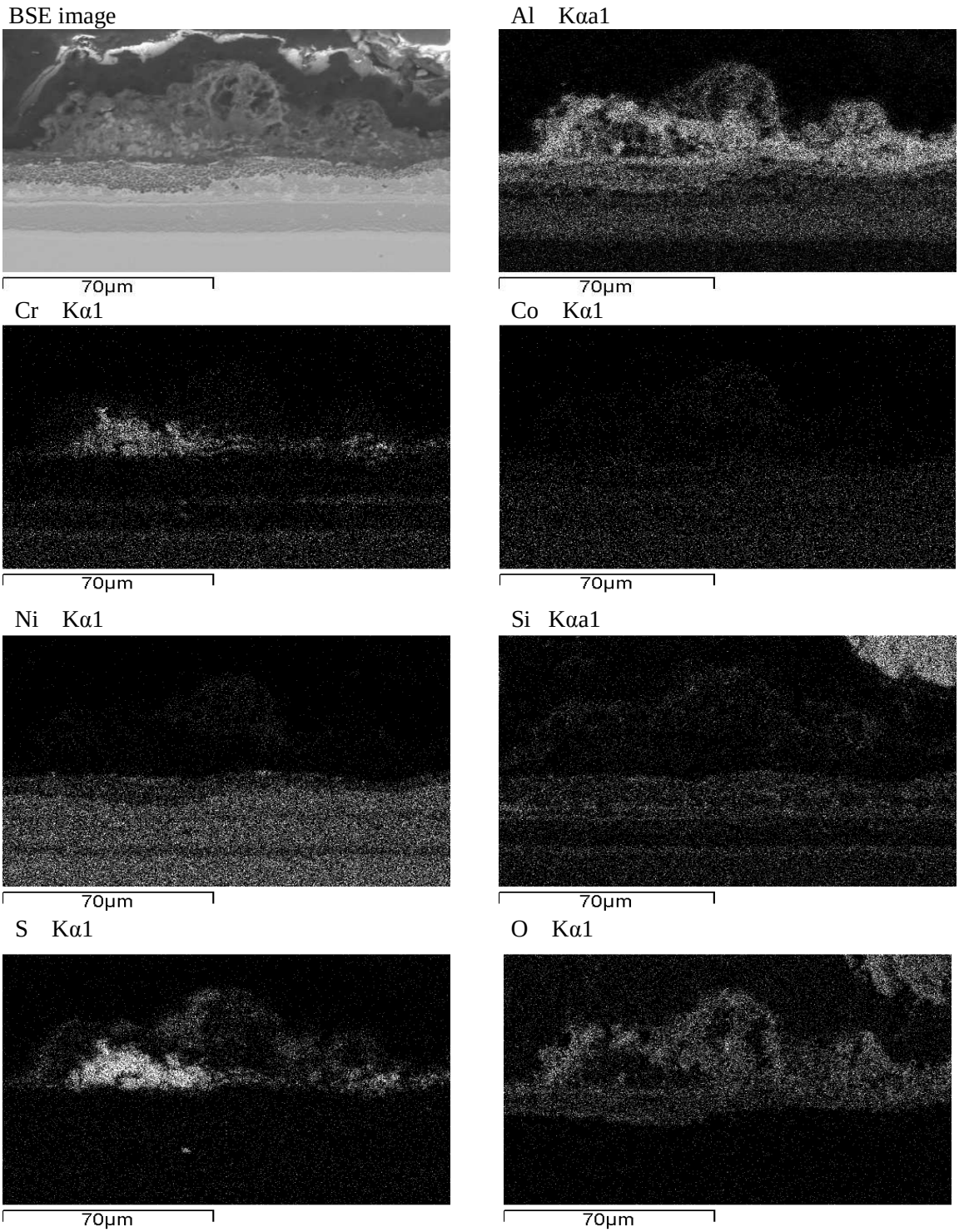

Figure 7.31: CMSX-4 and Sermaloy 1515 with $PbSO_4$ + ($NaSO_4$(80)+K_2SO_4(20)); salt flux 1.5 µg/cm^2/h, after 500h corrosion testing at 700^{o}C – element maps

The element maps in Figure 7.31 show the corrosion in this sample consists of oxides of aluminium, silicon, cobalt, and sulphur, with heavy sulphidation of chromium.

The corrosion from the low salt flux species has penetrated through approximately half the depth of the Sermaloy 1515 coating. In the high salt flux sample, as seen by the maps in Figure 7.32, corrosion degradation has penetrated through the full depth of the coating.

7.4.4.4 $PbSO_4$+(Na_2SO_4(80)+ K_2SO_4(20)) with salt flux of 5.0 µg/cm^2/h

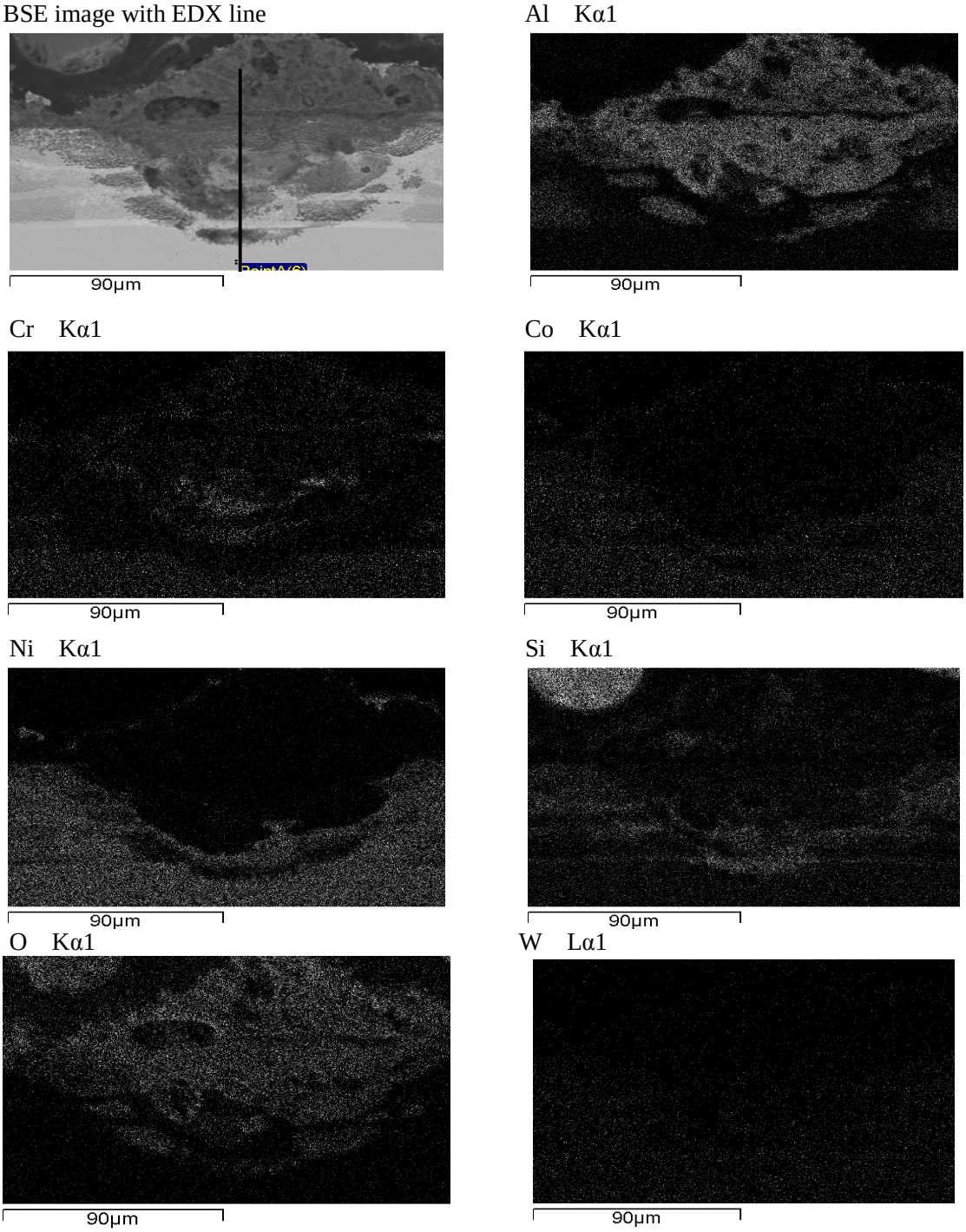

Figure 7.32: CMSX-4/Sermaloy 1515 with $PbSO_4$ + ($NaSO_4$(80)+K_2SO_4(20)); salt flux 5.0 µg/cm^2/h, after corrosion testing for 500h at 700^{o}C – element maps

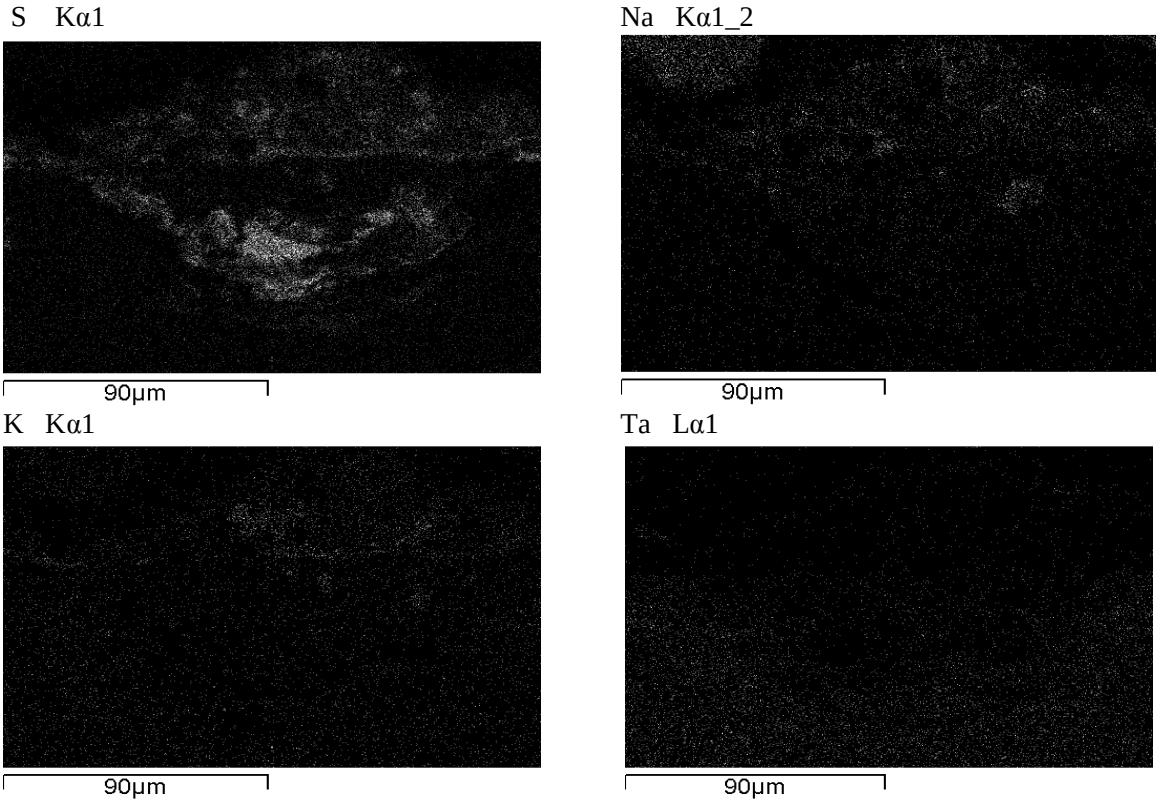

Figure 7.33: CMSX-4 & Serm1515; with $PbSO_4$+(Na_2SO_4(80)+ K_2SO_4(20)), salt flux 5.0 µg/cm^2/h, after corrosion testing for 500 hours at 700^{o}C – maps of elements of lesser content in the sample

Element maps for this sample, seen in Figures 7.32 and 7.33, show the outer regions of scale and degradation consist of oxides of aluminium, silicon, sodium, potassium and sulphur. Areas of the inner layers are deficient of oxidation but rich in sulphides of chromium and silicon. Although the maps of the high salt flux sample show that Sermaloy 1515 has been fully degraded, the Cr/Ti/Si rich layers have been more corrosion resistive than the Al/Ni-rich layers.

Graphs in Figure 7.34, show the content of elements along the EDX line in Figure 7.32, and particularly, the 'sulphur-rich' depth of the Type II hot corrosion produced by the high salt flux species of this sample. These factors lead to the conclusion that the corrosion resistance of Sermaloy 1515 to the species tested, could be significantly improved by adopting deeper Cr/Ti/Si-rich and AL/Ni-rich layers.

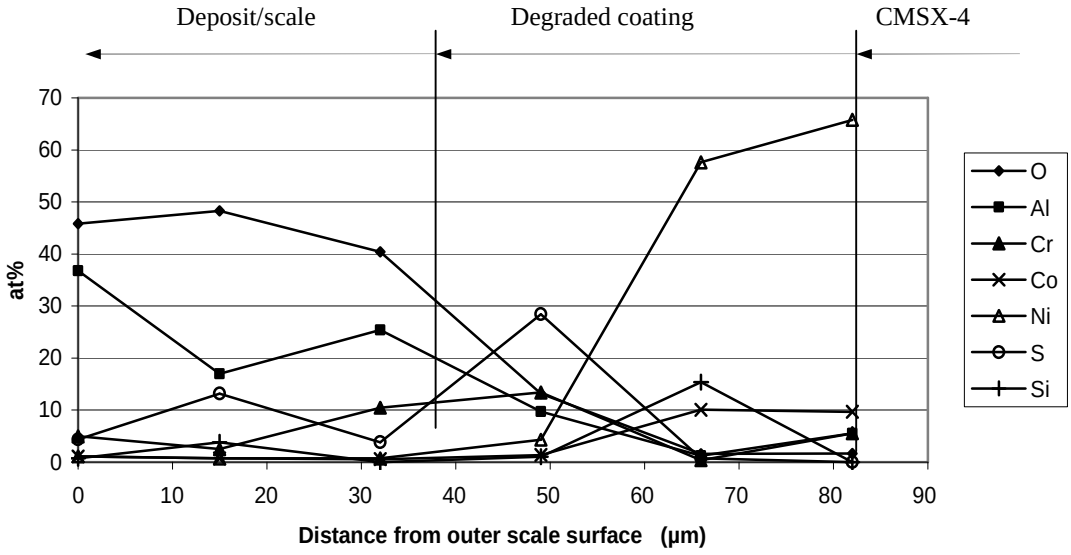

Figure 7.34: CMSX-4 & Serm1515; with $PbSO_4$+(Na_2SO_4(80)+ K_2SO_4(20)), salt flux 5.0 µg/cm^2/h, after corrosion testing for 500 hours at 700^{o}C – elements on EDX line in Figure 7.32

7.4.4.5 Microstructures of CMSX-4 coated with Sermaloy 1515 – conclusions

Both the low salt flux species and high flux species cause significantly deeper oxidation and Type II hot corrosion in CMSX-4 coated with Sermaloy 1515, than they do in IN738LC coated with Sermaloy 1515. This is attributable to the low chromium content of the single crystal CMSX-4 (6 at%C) compared with the polycrystalline IN738LC (16 at%Cr).

The Sermaloy 1515 coated CMSX-4 provides more hot corrosion protection for the Cd+alkali species tested than it does for the Pb+alkali species, in both the low salt flux and high salt flux samples. In the case of the high flux Cd+alkali species, the Sermaloy 1515 coating is degraded down to the inner of the six layers, whereas the degradation has penetrated the whole coating into the CMSX-4 substrate in the case of the high salt flux Pb+alkali species.

7.5 Conclusions from series 2 corrosion tests

7.5.1 Mass change

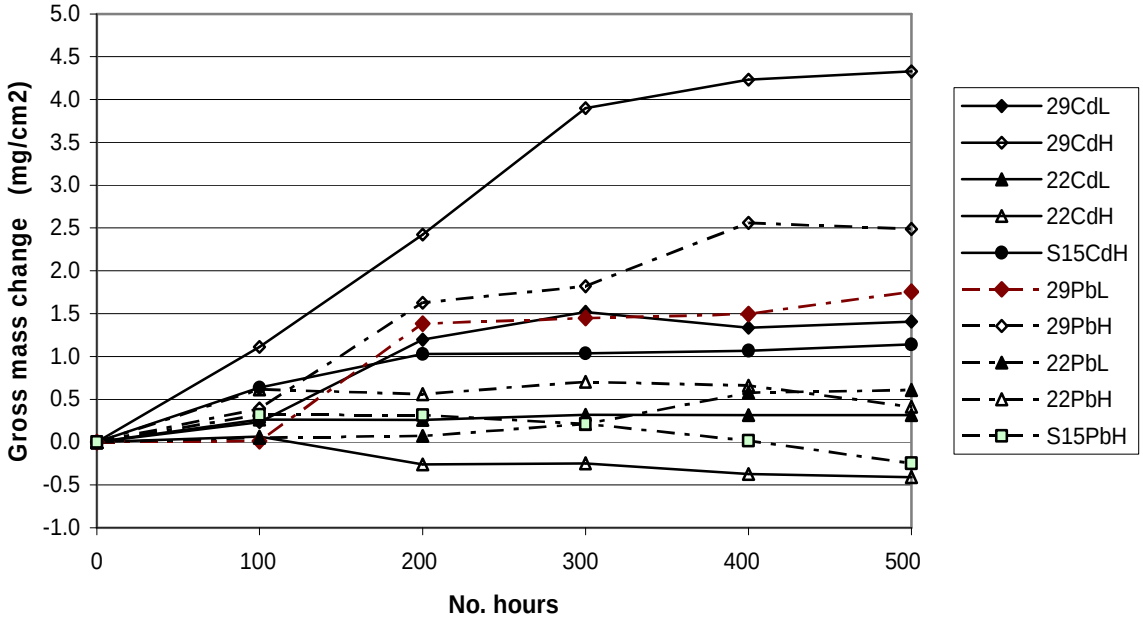

Key: 29CdL; GT29+, $CdSO_4$ + (Na_2SO_4(80)+K_2SO_4(20)); salt flux 1.5 µg/cm^2/h
29CdH; GT29+, $CdSO_4$ + (Na_2SO_4(80)+K_2SO_4(20)); salt flux 5.0 µg/cm^2/h
22CdL; RT-22, $CdSO_4$ + (Na_2SO_4(80)+K_2SO_4(20)); salt flux 1.5 µg/cm^2/h
22CdL; RT-22, $CdSO_4$ + (Na_2SO_4(80)+K_2SO_4(20)); salt flux 5.0 µg/cm^2/h
S15CdH; Sermaloy 1515, $CdSO_4$ + (Na_2SO_4(80)+K_2SO_4(20)); salt flux 5.0 µg/cm^2/h
29PbL; GT29+, $PbSO_4$ + (Na_2SO_4(80)+K_2SO_4(20)); salt flux 1.5 µg/cm^2/h
29PbH; GT29+, $PbSO_4$ + (Na_2SO_4(80)+K_2SO_4(20)); salt flux 5.0 µg/cm^2/h
22PbL; RT-22, $PbSO_4$ + (Na_2SO_4(80)+K_2SO_4(20)); salt flux 1.5 µg/cm^2/h
22PbH; RT-22, $PbSO_4$ + (Na_2SO_4(80)+K_2SO_4(20)); salt flux 5.0 µg/cm^2/h
S15PbH; Sermaloy 1515, $PbSO_4$ + (Na_2SO_4(80)+K_2SO_4(20)); salt flux 5.0 µg/cm^2/h

Figure 7.35: IN738LC; 500 hours corrosion tests at 700^{o}C - gross mass change

The gross mass changes for IN738LC samples, with all three coatings, and for each low and high salt flux are displayed in Figure 7.35. The key identifies the combinations of coating, species composition and salt flux, for each caption in the legend.

The gross mass changes for the Cd+alkali species, for both low and high salt fluxes, for GT29+ show consistent mass gain in proportion to the salt flux. Thus the peak gross mass change for the high salt flux Cd+alkali species of 4.3 mg/cm^2, compared with 1.9 mg/cm^2 for the low salt flux sample. For RT-22 the peak mass change for the low flux Cd+alkali species is 0.6 mg/cm^2 against that of the high salt flux sample, which crosses the zero point on the X-axis after 100 hours, and reduces to a minimum of -0.6 mg/cm^2 after 500 hours testing.

The only samples where their mass change crosses the zero-line are the high flux Cd+alkali species on RT-22 and the high salt flux sample of Pb+alkali species on Sermaloy 1515. This result appears inconsistent with the degradation and scale formation shown by microstructures shown in Figures 7.14 and 7.24 respectively.

The net mass change results for IN738LC, seen in Figure 7.36, reflect similar slopes, sample for sample as those for gross mass change. The values in the net mass change curves are close to those for gross mass, for example the gross and net mass change values, after 500 hours, for the high salt flux Cd+alkali species on GT29+ are 4.3 mg/cm^2 and 4.2 mg/cm^2 respectively. For the high salt flux Pb+alkali species on GT29+, these values are 2.5 mg/cm^2 and 2.0 mg/cm^2. These results generally indicate minor spalling in the IN738LC samples. Of the net mass change IN738LC samples, three cross the X-axis; the high salt flux Cd+alkali on RT-22 crosses after 100 hours, the high salt flux Pb+alkali on Sermaloy 1515 crosses after 330 hours and the low salt flux sample on RT-22 crosses after 400 hours.

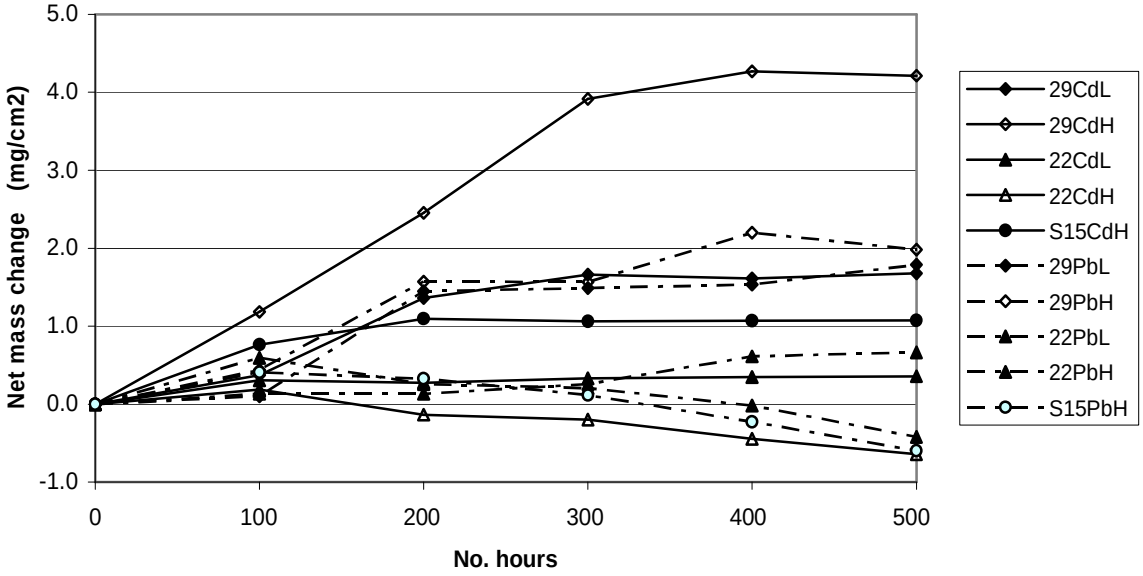

Key: 29CdL; GT29+, $CdSO_4$ + (Na_2SO_4(80)+K_2SO_4(20)); salt flux 1.5 µg/cm^2/h
29CdH; GT29+, $CdSO_4$ + (Na_2SO_4(80)+K_2SO_4(20)); salt flux 5.0 µg/cm^2/h
22CdL; RT-22, $CdSO_4$ + (Na_2SO_4(80)+K_2SO_4(20)); salt flux 1.5 µg/cm^2/h
22CdL; RT-22, $CdSO_4$ + (Na_2SO_4(80)+K_2SO_4(20)); salt flux 5.0 µg/cm^2/h
S15CdH; Sermaloy 1515, $CdSO_4$ + (Na_2SO_4(80)+K_2SO_4(20)); salt flux 5.0 µg/cm^2/h
29PbL; GT29+, $PbSO_4$ + (Na_2SO_4(80)+K_2SO_4(20)); salt flux 1.5 µg/cm^2/h
29PbH; GT29+, $PbSO_4$ + (Na_2SO_4(80)+K_2SO_4(20)); salt flux 5.0 µg/cm^2/h
22PbL; RT-22, $PbSO_4$ + (Na_2SO_4(80)+K_2SO_4(20)); salt flux 1.5 µg/cm^2/h
22PbH; RT-22, $PbSO_4$ + (Na_2SO_4(80)+K_2SO_4(20)); salt flux 5.0 µg/cm^2/h
S15PbH; Sermaloy 1515, $PbSO_4$ + (Na_2SO_4(80)+K_2SO_4(20)); salt flux 5.0 µg/cm^2/h

Figure 7.36: IN738LC; 500 hours corrosion tests at 700^{o}C - net mass change

The gross mass change curves for CMSX-4 coated with Sermaloy 1515, seen in Figure 7.37 show similar rates of mass change for both low salt flux samples and similar rates for both high salt flux samples. As with IN738LC, the rates of net mass change in Figure 7.38, for CMSX-4 coated with Sermaloy 1515, are similar to those of gross mass change.

As with IN738LC samples, the differences between gross and net mass changes in CMSX-4 samples are minor and indicate little spalling associated with this coating.

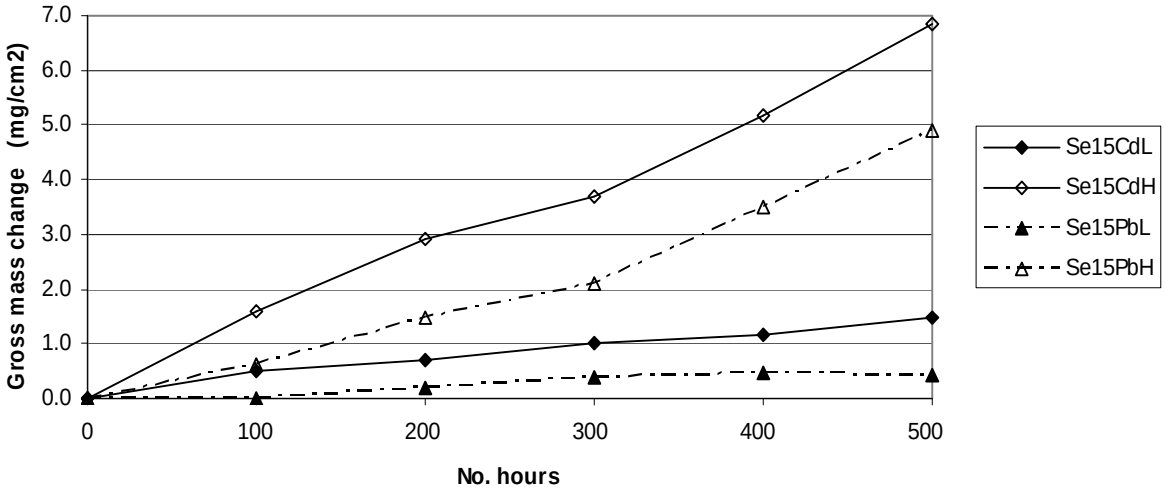

Key: Se15CdL; Sermaloy 1515, $CdSO_4$ + (Na_2SO_4(80)+K_2SO_4(20)); salt flux 1.5 µg/cm^2/h
Se15CdH; Sermaloy 1515, $CdSO_4$ + (Na_2SO_4(80)+K_2SO_4(20)); salt flux 5.0 µg/cm^2/h
Se15PbL; Sermaloy 1515, $PbSO_4$ + (Na_2SO_4(80)+K_2SO_4(20)); salt flux 1.5 µg/cm^2/h
Se15PbH; Sermaloy 1515, $PbSO_4$ + (Na_2SO_4(80)+K_2SO_4(20)); salt flux 5.0 µg/cm^2/h

Figure 7.37: CMSX-4; 500 hours corrosion tests at 700°C - gross mass change

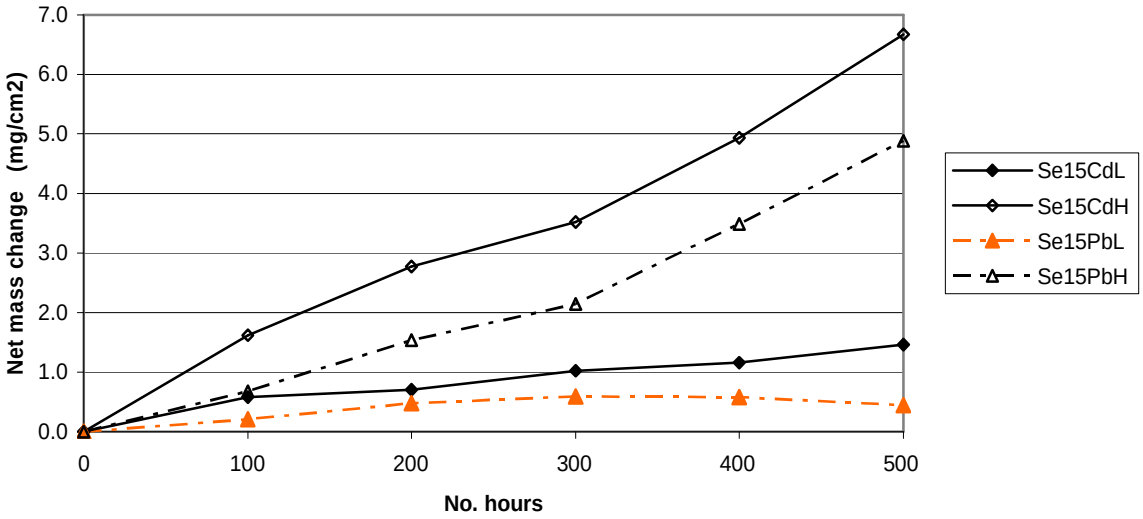

Key: Se15CdL; Sermaloy 1515, $CdSO_4$ + (Na_2SO_4(80)+K_2SO_4(20)); salt flux 1.5 µg/cm^2/h
Se15CdH; Sermaloy 1515, $CdSO_4$ + (Na_2SO_4(80)+K_2SO_4(20)); salt flux 5.0 µg/cm^2/h
Se15PbL; Sermaloy 1515, $PbSO_4$ + (Na_2SO_4(80)+K_2SO_4(20)); salt flux 1.5 µg/cm^2/h
Se15PbH; Sermaloy 1515, $PbSO_4$ + (Na_2SO_4(80)+K_2SO_4(20)); salt flux 5.0 µg/cm^2/h

Figure 7.38: CMSX-4; 500 hours corrosion tests at 700°C - net mass change

7.5.2 Metrology

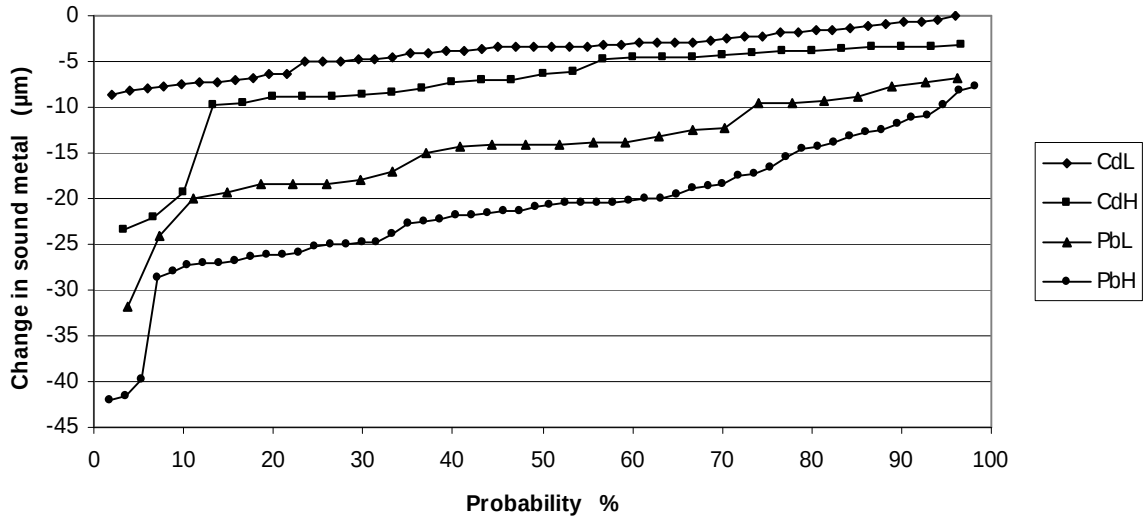

Key: CdL; $CdSO_4$ + (Na_2SO_4(80)+K_2SO_4(20)); salt flux 1.5 µg/cm^2/h
CdH; $CdSO_4$ + (Na_2SO_4(80)+K_2SO_4(20)); salt flux 5.0 µg/cm^2/h
PbL; $PbSO_4$ + (Na_2SO_4(80)+K_2SO_4(20)); salt flux 1.5 µg/cm^2/h
PbH; $PbSO_4$ + (Na_2SO_4(80)+K_2SO_4(20)); salt flux 5.0 µg/cm^2/h

Figure 7.39: IN738LC with coating GT29+ after 500 hours corrosion testing at 700^{o}C – change in sound metal

The changes in sound metal shown for IN738LC samples coated with GT29+, shown in Figure 7.39, indicate that GT29+ provides more hot corrosion protection for cadmium containing species than for those containing lead. There is less degradation of both the high- and low salt flux cadmium species than the low salt flux lead species. The three samples, other than the low salt flux cadmium species, having heavy degradation in the early stages, indicate Type II hot corrosion pitting.

The change in sound metal graphs for IN738LC with RT-22, seen in Figure 7.40, are presented separately for the cadmium and lead species, to assist in separating the individual curves. In Figure 7.40(a), the heavy degradation in the high salt flux cadmium species reflects the mass change curves, in Figures 7.35 and 7.36, which show the mass changes crossing the X-axis after 100 hours. Similarly, for the Pb+alkali species the mass change curves indicated similar rates of corrosion for the low and high salt flux samples.

The coating RT-22 provides similar levels of hot corrosion protection to the low salt flux samples of both species but is significantly less protective against hot corrosion in high salt flux cadmium species. This contrasts with GT29+ which provides higher corrosion protection for cadmium species than those of lead.

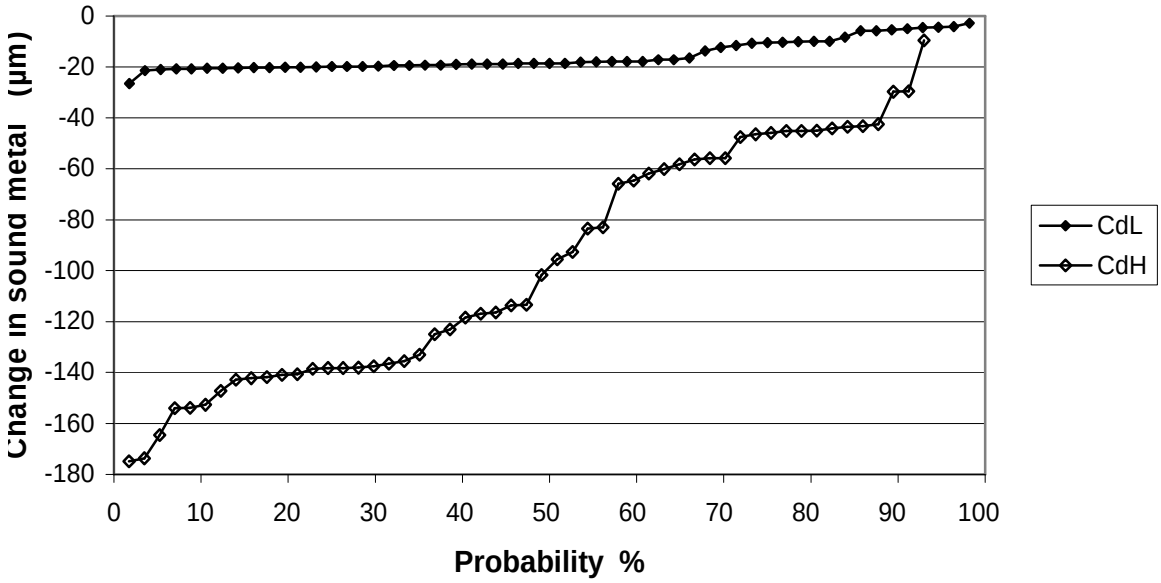

Key: CdL; $CdSO_4$ + (Na_2SO_4(80)+K_2SO_4(20)); salt flux 1.5 µg/cm^2/h
CdH; $CdSO_4$ + (Na_2SO_4(80)+K_2SO_4(20)); salt flux 5.0 µg/cm^2/h

Figure 7.40(a): IN738LC with coating RT-22 after 500 hours corrosion testing at 700°C – change in sound metal from Cd/Na/K species

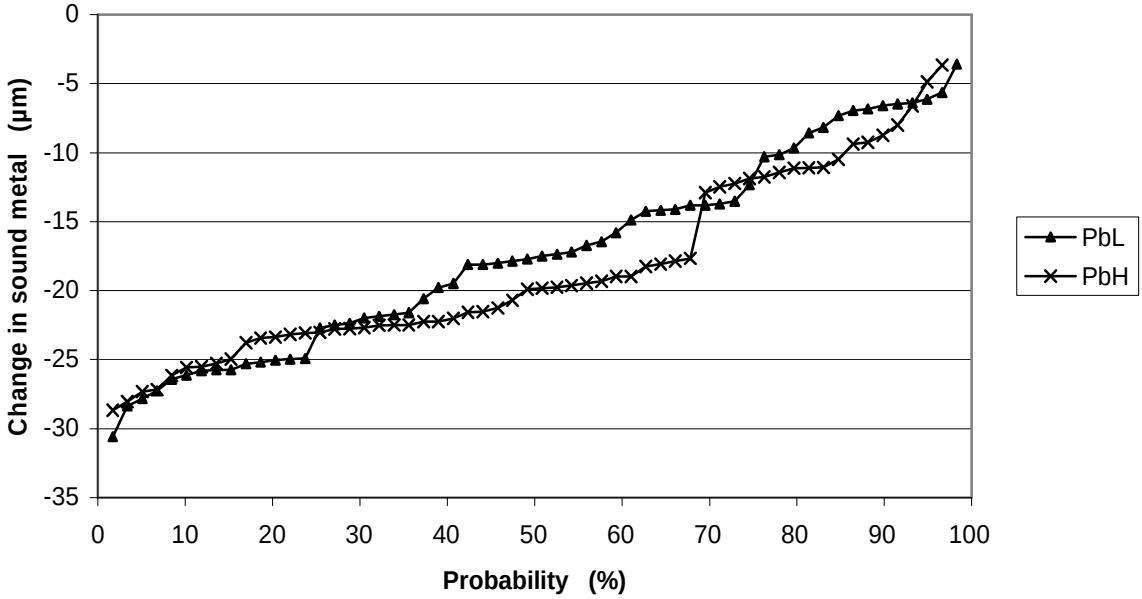

Key: PbL; $PbSO_4$ + (Na_2SO_4(80)+K_2SO_4(20)); salt flux 1.5 µg/cm^2/h
PbH; $PbSO_4$ + (Na_2SO_4(80)+K_2SO_4(20)); salt flux 5.0 µg/cm^2/h

Figure 7.40(b): IN738LC with coating RT-22 after 500 hours corrosion testing at 700°C – change in sound metal from Pb/Na/K species

IN738LC coated with Sermaloy 1515 was tested with the high salt fluxes of both species. In Figure 7.41 it can be seen that this substrate/ coating combination provides higher corrosion protection for the cadmium species than that of lead. Heavy Type II pitting is occurring from the lead species, whereas the incipient pitting from the cadmium species is significantly lighter.

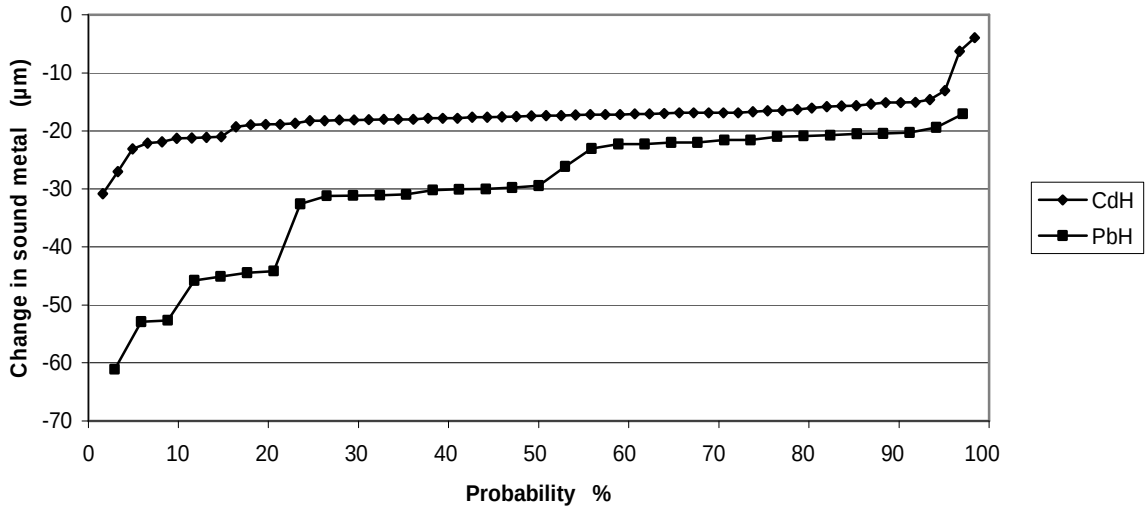

Key: CdH; $CdSO_4$ + (Na_2SO_4(80)+K_2SO_4(20)); salt flux 5.0 µg/cm^2/h
PbH; $PbSO_4$ + (Na_2SO_4(80)+K_2SO_4(20)); salt flux 5.0 µg/cm^2/h

Figure 7.41: IN738LC with coating Sermaloy 1515 after 500 hours corrosion testing at 700^{o}C – change in sound metal

As seen in Figure 7.42, CMSX-4 coated with Sermaloy 1515 provides hot corrosion protection for the low salt flux samples of both species and for the high salt flux lead species. However, Sermaloy 1515 is a comparatively low depth coating and small loss of sound metal can diminish protection over a short time period.

In the same substrate/coating combination, incipient Type II hot corrosion pitting in the low salt flux cadmium sample has penetrated deep into the coating, and comparatively deep pitting, along a broader front, is caused by the high salt flux lead species. In the high salt flux cadmium sample, the Sermaloy 1515 has totally failed to protect the substrate. In this case, Type II hot corrosion has penetrated through the coating to deep into the substrate.

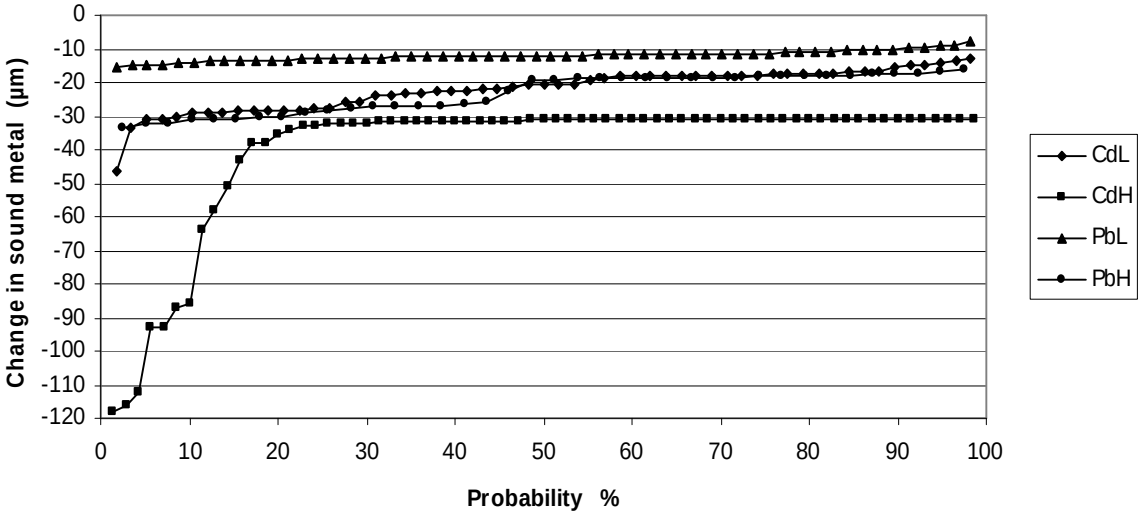

Key: CdL; $CdSO_4$ + (Na_2SO_4(80)+K_2SO_4(20)); salt flux 1.5 µg/cm^2/h
CdH; $CdSO_4$ + (Na_2SO_4(80)+K_2SO_4(20)); salt flux 5.0 µg/cm^2/h
PbL; $PbSO_4$ + (Na_2SO_4(80)+K_2SO_4(20)); salt flux 1.5 µg/cm^2/h
PbH; $PbSO_4$ + (Na_2SO_4(80)+K_2SO_4(20)); salt flux 5.0 µg/cm^2/h

Figure 7.42: CMSX-4 with coating Sermaloy 1515 after 500 hours corrosion testing at 700^{o}C – change in sound metal

7.5.3 Comparisons of commercial coatings after corrosion testing for 500 hours at 700^{o}C

There were four combinations of substrate and commercial coatings tested. The commercial coatings varied in depth and composition, which may influence rates of degradation. As an example, the platinum-rich outer layer of RT-22 may have been deeply but not completely degraded. However, after penetration of hot corrosion into the inner layer, degradation may accelerate. The result, when compared with the deeper diffusion coating GT29+, the substrate may be degraded earlier in the RT-22 coated IN738LC combination. Of the combinations of IN738LC tested, the RT-22 coating was least degraded for all low and high salt flux salt species, with the 60% and 70% of the outer platinum-rich layer remaining un-degraded for the low salt flux cadmium and lead species, respectively. The outer layer was approximately 75% degraded by both the high salt flux species. The IN738LC/GT29+ combination proved to be hot corrosion protective for all species. The outer aluminide layer was only fully degraded by the high salt flux species. The outer aluminium-rich layer provides significant hot corrosion protection compared with the inner, deeper CoCrAlY coating. The Sermaloy 1515 coated IN738LC combination was least Type II hot corrosion protective, whereby in both the high salt flux cadmium and lead species tested approximately 50% of the coating was degraded.

Each of the four CMSX-4/Sermaloy 1515 combinations was not as corrosion protective as the other combinations. In both of the low salt flux species, 50% of the coating was degraded.

Over 80% of the coating was degraded by the high salt flux cadmium species. In the case of the high salt flux lead species, the coating was fully degraded and degradation penetrated approximately 10μm into the CMSX-4. The low chromium content of CMSX-4 (6%) compared with IN738LC (16%) was a major factor in the reduced corrosion protection provided by CMSX-4.

7.6 Conclusions from corrosion tests on commercial coatings

The prime purpose of this series of corrosion tests was to determine whether, and to what extent, cadmium and lead containing species, when combusted under gas turbine operating conditions, would initiate hot corrosion in commercial, corrosion protecting coatings. The secondary purpose of the tests was to provide data on commercial coating corrosion protection, for comparison with novel coatings to be developed in this project.

This series of tests followed the first series which confirmed that the cadmium and lead species, when combusted under gas turbine operating conditions, initiated Type II hot corrosion, to differing degrees, on the uncoated superalloys IN738LC, IN939 and CMSX-4. The first corrosion test series were reported in section 5 of this thesis. The second series of corrosion tests involved the commercial coatings GT29+, RT-22 and Sermaloy 1515, when applied to superalloys IN738LC and CMSX-4. The testing methods, equipment and conditions were the same as for the first series of tests.

The results of these corrosion tests, consisting of 500 hours at 700^{o}C, confirmed that Type II hot corrosion was initiated in all four coatings, to varying degrees. Three of the tests involved GT29+, RT-22 and Sermaloy 1515, on IN738LC. Of these coatings, RT-22 proved to be the most protective, with all degradation being contained within the platinum-rich outer layer, although being significantly degraded by the high salt flux species. The coating GT29+ also protected the substrate against Type II hot corrosion degradation, although, in the case of the high salt flux lead species, degradation had penetrated into the lesser corrosion resistant overlay layer. The Sermaloy 1515 coating proved to be the least corrosion protective of the three coatings applied to IN738LC, being deeply degraded, although it maintained its protection of the substrate.

The corrosion tests on CMSX-4 coated with Sermaloy 1515 showed this combination to be the least protective than any of those involving IN738LC. In this combination, 50% of the coating was degraded by both low salt flux salt species, 80% was degraded by the high salt flux Cd+alkali species, and the coating was totally degraded in the high salt flux lead species.

This series of corrosion tests has confirmed that Type II hot corrosion was initiated in typical commercial coatings by cadmium and lead containing species, after 500 hours testing at 700^{o}C. Evaluation of the coatings has provided data on the hot corrosion protection provided by a range of commercial coatings. These will enable comparisons to be made with the protection provided by novel coatings to be developed in this project.

8. Development of novel coatings

8.1 Introduction

The main objective of this project was to develop novel coatings to protect superalloys in hot components of gas turbines fuelled by biomass and waste-fuels, from degradation mechanisms caused by oxidation and hot corrosion. However, in developing coatings for this purpose, other constraints were taken into account; that substrate properties are maintained, that economic lives of coating and substrate are achieved and that coating costs are commercially competitive. In earlier stages of the project, potentially damaging trace species contained in biomass and waste-fuels were identified by thermodynamic assessments. Two series of corrosion tests were then carried out to confirm the results of these assessments. These tests confirmed that the identified species, when exposed in combustion gases, at 700^{o}C, would initiate Type II hot corrosion on the uncoated superalloys IN738LC, IN939 and CMSX-4, and in the commercial coatings GE29^{+}, RT-22 and Sermaloy1515 (when applied to IN738LC and CMSX-4). Evaluation of the corrosion test results, showed the nature and extent of oxidation and hot corrosion on the commercial coatings. Also shown, were the extent of diffusion of substrate elements into the coatings, which could degrade the substrate structure and thus reduce its mechanical integrity.

In this chapter, evidence from literature reviews and comparisons with the performances of commercial coatings found in the corrosion tests are used to decide on the composition of basic coatings and suitable manufacturing methods. The approach adopted, was to minimise the material costs and production processes used in developing novel coatings, which would then be technically and commercially competitive.

8.2 Rationale for type of coating to be developed

The novel coatings to be developed for protecting hot components of gas turbines, fired by biomass and waste-fuels, from high temperature oxidation and hot corrosion, should have the following properties:

- ability to form a stable, slow-growing, surface oxide to provide a barrier between the coating/alloy and the environment, and thus to provide oxidation and hot corrosion resistance;
- thermodynamic stability to maintain their protective properties over the optimum service life despite being subject to high temperatures, with near stoichiometric compositions, low defect concentrations and low diffusion rates;
- the coating should be resistant to cracking; to maintain its integrity when subject to thermally induced and mechanical stresses.

As explained more fully in Chapter 2, hot-corrosion is caused by salt contaminants (eg Na_2SO_4, NaCl) which combine, with oxidation products/gases, to produce low-melting-point deposits that dissolve protective oxide scales on the coatings.

The general classification of hot corrosion, is based on varying fluxing mechanisms causing different corrosion morphologies; high- temperature hot corrosion (Type I, 800-950^{o}C), low-temperature hot corrosion (Type II, 600-800^{o}C), and vanadic corrosion (535-950^{o}C).

The novel coating protective mechanism should provide an oxide film that repairs the protective surface-oxide scales, to maintain the initiation stage, before the surface oxide film breaks down, ideally for the life of the component. Otherwise, after surface oxide film breakdown, the propagation phase will cause rapid consumption of the alloy. Commonly, the oxide film providing this protection mechanism for nickel based substrates is alumina (Al_2O_3), whereas chromia (Cr_2O_3) and/or silica (SiO_2) provides protection for cobalt based substrates and chromia, or chromia plus silica, protects ferrous based substrates [63]. Alumina will be the basis for protecting substrates in this project.
To provide hot corrosion protection, the novel coating will involve a complex interplay of surface-, coating-, and substrate-related properties. Additionally, these need to provide interface stability, good adhesion between coating and substrate and sufficient mechanical strength.

8.2.1 Oxidation /corrosion resistance

The degradation processes of oxidation and hot corrosion, acting on gas turbine components, set out by Simms et al [53] are:

- elevated temperature gas phase induced corrosion: including oxidation and sulphidation;
- corrosion induced by surface deposits: either particles derived from the gasifier, species condensed onto these particles or species condensed onto component surfaces;
- interaction of any of the above degradation modes with mechanical factors, e.g. creep or fatigue, to produce synergistic degradation, e.g. creep-corrosion or corrosion fatigue; and
- spallation of corrosion products: spalled scale may cause erosion damage in components along the gas path, and may be initiated by erosion, caused by particles from components earlier in the gas path.

In practice, several material degradation modes may occur on gas turbine components in the hot gas path and different combinations of degradation modes may be found in the hot gas path components. However, in this project, samples will only be subjected to oxidation and corrosion tests, to identify their resistance to these mechanisms. No testing of mechanical factors, such as fatigue or erosion, were undertaken.

The microstructural changes which occur as high temperature corrosion of gas turbine alloys proceeds can be summarised as:

- Outward growth of an oxide scale with partial or total detachment of this scale, particularly at the corners or edges;
- General internal penetration of oxidation/corrosion products, with a consequential loss in load-bearing cross-section;
- Internal attack generally at grain or phase boundaries leading to an increase in stress concentration;

- Depletion of some elements of the alloy matrix;
- Precipitation of new phases in the modified component system, consisting of the alloy matrix/coating.

To sustain formation of the oxide scale the novel coating requires a sufficient reservoir of aluminium that forms the scale, and chromium, to maintain the initiation phase of hot corrosion for as long as the scale forming component lasts.

8.2.2 Interface stability

To provide stability at the novel coating/substrate interface, requires a low rate of interdiffusion at operating temperatures, limited compositional changes across the interface and the absence of embrittling phase formation. In aluminide coatings, by these provisions, degradation of the outer β-NiAl phase, caused by the formation of a γ'-Ni_3Al network, will be prevented. Otherwise, in time, the β-phase would be penetrated and with the γ' leaders acting as short-circuit paths, cause rapid failure of the coating.

The diffusion of elements between the substrate and coating can be a major factor for coating performance and, to provide long-term stability at higher temperatures, the development of diffusion-barrier coatings to minimise the interdiffusion between the coating and the substrate to limit movement of problematic elements, may be necessary. However, some interdiffusion is required to provide good adhesion and to provide protective elements for the coating, such as chromium. If the concept of a diffusion barrier is proven to be effective for giving good interface stability, then substrate compatibility is no longer needed for specifying the overlay coating composition and the overlay coating can be designed for optimised oxidation or corrosion resistance. Different base-alloy compositions can provide optimum performance, depending on temperature and environment, and in this context, with particular Cr and Al levels, a Ni-Cr-Al-Y system provides the optimum hot-corrosion-resistant composition for coatings [36,63].

8.2.3 Thermal stability of coatings

To maintain thermal stability, the novel coatings must prevent degradation by providing scale-forming elements to the surface, and also by interdiffusion from the substrate [36]. These will assist structural stability and protective properties over extended periods of operation at high temperatures. Studies into the thermal stability of a number of diffusion coatings, including pack-aluminide, chromium-aluminide and platinum-aluminide variants, showed that the thermal stability of β-NiAl can be improved by the addition of platinum and that the two-layered $PtAl_2$-β structure degrades to single-phased β with no γ' leaders, even after long periods of time [36,110,111]. This contributes to the improved corrosion resistance of platinum-aluminide coatings, compared with conventional aluminides.

8.2.4 Mechanical properties of coatings

Resistance of coatings at high temperature, to cracking by thermally induced stresses and the effects of the transition from ductile to brittle condition, are critical. Of coating material bases, the ductile-to-brittle transition temperature (DBTT) of aluminides is higher than that of many of the overlay coatings. Since peak tensile surface strains on turbine blades occur at relatively low temperatures, diffusion coatings may have inadequate ductility for relatively high strain applications in turbine blades. Transition from ductile to brittle behaviour, as the temperature reduces, is significant during gas turbine thermo-mechanical cycling over its service lifetime and may cause cracking of the coating, crack propagation into the substrate or separation at the coating/substrate interface, reducing component life.

Development of novel diffusion coatings therefore needs to take account of the interdiffusion between the coating and the substrate. However, some interdiffusion is required to provide good adhesion, but this must limit the movement of particularly problematic elements while permitting transport of protective elements which are not contained in the original coating, such as chromium. Thus the coating must be an element selective diffusion barrier. Also, the mechanical behaviour of coated components will be an important factor in the development of novel coatings.

8.2.5 Types of hot corrosion resistant coatings

Two generic types of coatings provide hot corrosion resistance; diffusion and overlay. Combinations of these coatings to form Smartcoat systems can be used, which are ‘custom made’ to retard hot corrosion in the most durable and economical manner. Explanations of these coatings are provided more fully in Chapter 2. Further, thermal barrier coatings may also be added to reduce metal surface temperatures, whilst limiting salt deposition through condensation reactions.

8.3 Selection of the type of novel coating

8.3.1 Diffusion or overlay coatings

The first consideration was whether to use the diffusion or overlay types of coating as the basis for developing the novel coating for use in gas turbines fired by gasified biomass and waste-fuels. Both aluminide diffusion and MCrAlY overlay coatings can provide high corrosion protection for gas turbine superalloys, as has been explained in Chapter 2. Aluminising is the most common coating used by gas turbine manufacturers to enhance resistance to oxidation and corrosion of hot components [36,63], as it forms a slow growing, stable thermally grown oxide (TGO) as a surface scale, which acts to prevent oxygen penetrating into the component, thus retarding the oxidation process. Although aluminium may form part of an overlay MCrAlY coating, the deciding factor for rejecting overlay coatings is that they cannot be used to coat internal cooling air passages, to resist Type II hot corrosion caused by contaminants in the air drawn from the local atmosphere [23]. A diffusion coating formed by vapour deposition has the potential to coat all the component, including internal passages.

8.3.2 Diffusion aluminide coatings

Diffusion aluminide coatings are based on the intermetallic compound β-NiAl, which provides stability through the temperature range of the gas turbine gas path, from combustion to the exhaust. This is shown in the phase diagram in Figure 8.1. Chemical vapour deposition (CVD), is the most widely used process to form aluminide coatings, being inexpensive, well adapted to coating small components, and not limited to straight line application. In CVD for this project, components were immersed in a powder pack containing alumina, particles of aluminum and ammonium halide activators. After being heated to, and maintained at, 800°C-1050°C, in argon or hydrogen atmospheres, aluminium halides form and diffuse through the pack, to react with the substrate to form an aluminium-rich intermetallic. Thermodynamics and kinetics of the CVD process are set out in Chapter 2, with the Cranfield CVD equipment being described in Chapter 4.

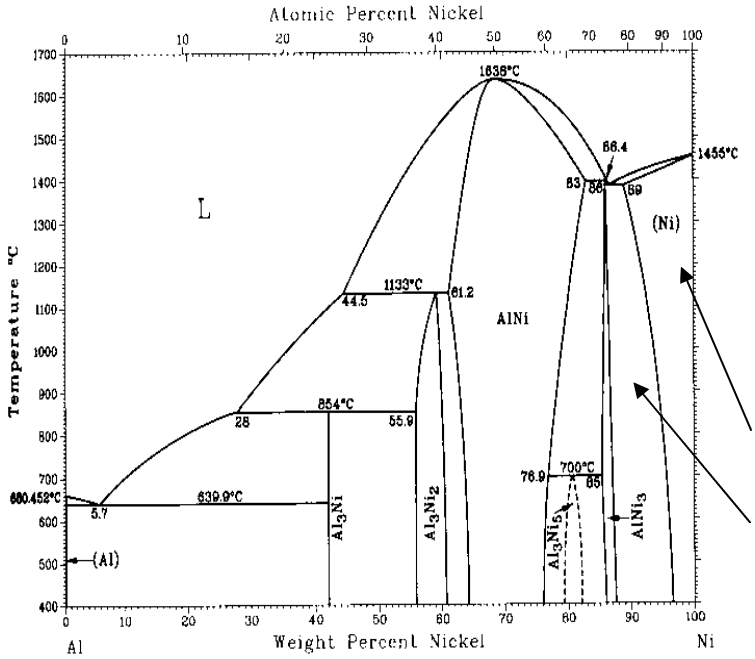

Phase (1050°C)	Composition (wt%Ni)	(at%Ni)
Al_3Ni_2	55.9 to 60.7	39 to 42
AlNi	61 to 83	44 to 76
$AlNi_3$	85 to 87	76 to 77
(Ni)	88 to 100	85 to 100

γ

γ+γ'

Figure 8.1: Al-Ni phase diagram and phase composition [112]

8.3.3 Coating thermodynamics and kinetics

Solid-state diffusion and gas-phase diffusion have been identified as the limiting factors in aluminizing by several authors [36,91,93,105] and Knudsen diffusion is important when aluminizing narrow cooling passages [93]. The coating profile on a complex substrate will be irregular and irreproducible if the process is limited by gas-phase diffusion. Solid-state diffusion has the advantages of providing an excess of aluminum at the substrate surface and of limiting diffusion into the surface, thus providing a more uniform coating profile. Diffusion controlled coating growth rate is defined by the Arrhenius equation [93]:

$$(Thickness)^2 \alpha\, e^{-Q/RT}$$

For diffusion process within the solid state the thickness of the coating is also proportional to the square root of the coating time:

$$(Thickness)^2 \alpha k_o(Time)$$

These equations imply that only limited thicknesses can be achieved in practice. The diffusion rate can be increased by higher temperatures, but if they are too high a liquid phase may be formed on the substrate surface, the pack powder can be depleted locally and the process becomes gas-diffusion limited [105].

8.3.4 Modified aluminide diffusion coatings

The next stage of novel coating development, is to consider whether aluminium diffusion coatings can be modified to improve protection against hot corrosion. Widely reported routes to performance improvement in aluminide coatings include; platinum-modified aluminide coatings, silicon-containing aluminide diffusion coatings and chromised and chrome-aluminised diffusion coatings. Nicholls [36] has reviewed a range of diffusion coatings with regard to their hot-corrosion protection, with the following results:

- Platinum-modified aluminide diffusion coatings; perform exceptionally well under high-temperature oxidation conditions and Type I hot-corrosion environments, less well under Type II hot corrosion conditions, but outperform conventional aluminides;
- Silicon-containing aluminide diffusion coatings; perform well under Type II hot-corrosion conditions;
- Chromised and chrome-aluminised diffusion coatings; have been observed to provide protection under Type II hot corrosion conditions in industrial turbine environments, but were no better than conventional aluminides in laboratory and burner tests.

These levels of performance were also reflected in the second series of corrosion tests reported in Chapter 7. These Type II hot corrosion tests, for a duration of 500 hours at 700^{o}C, showed that trace levels of cadmium sulphate and lead sulphate, in the presence of sodium sulphate and potassium sulphate, when exposed in typical combustion conditions, caused less severe Type II hot corrosion on CMSX-4 and IN738LC, when coated with the platinum aluminide commercial coating RT-22, than the aluminised overlay coating GT29+ and multilayered silicon aluminide Sermaloy 1515. Long [63], in his report on investigations into potential enhanced performance offered by platinum-, chromium- and silicon-aluminides, over standard vapour aluminides, considered that, as platinum could not be deposited in internal cooling passages without using a metal-organic species, and on the basis of unit cost and coating quality, the process could not be justified. The report also concluded, from assessment of the level of chromium that could be held in solid-solution in the beta phase, it was not high enough to offer any benefit to the aluminide diffusion coating. The solid solution limit in the beta phase was found to be only 6 wt% chromium. It also reported that the cyclic oxidation performance of the two-phase chromium aluminides, at 1100^{o}C, was worse than a standard aluminide.

Therefore, for developing novel coatings in this project, it was concluded that platinum- and chromium-modification were not suitable for improving the performance of aluminide vapour diffusion coatings, given the need to coat internal passages as well as the external blade surfaces.

Aluminide diffusion coatings containing silicon were reported [63] to have demonstrated good oxidation and hot corrosion resistance, attributed to the formation of glassy silica sub-scales having low oxygen diffusion coefficients. Silica formed on a silicon-aluminide coating also has minimal solubility in highly acidic melts, providing significant resistance to acidic deposits typical of Type II hot corrosion. It was concluded that development of novel coatings based on silicon modified aluminide diffusion should be explored further.

8.3.5 Silicon-aluminide diffusion coatings

Commercial silicon containing coatings which offer effective hot corrosion resistance are readily available, Sermaloy J being a prime example. This is a slurry coating, applied manually before heat treatment to diffuse the coating into the substrate. This coating can perform as well as platinum aluminide coatings in resisting Type I and Type II hot corrosion. However, there is concern that brittleness may result from the relatively high silicon content of the coating (18 wt%Si). An engine test by Rolls-Royce of Sermaloy 1515, reported by Long [63], a multi-layer version of Sermaloy J, did not exhibit any cracking or substrate corrosion, indicating that the silicon content can be reduced below those in Sermaloy J, without reducing coating performance and without any coating cracking being exhibited.

In research reported by Swadzbe [106], on silicon-aluminide coatings produced by a pack cementation process, using soak temperatures between 600^{o}C and 950^{o}C, results showed increased silicon content in the aluminide coating, without reducing the aluminum content. This research concluded that silicon-aluminides with <6 wt%Si performed better in Type I hot corrosion than slurry aluminides containing 19 wt%Si to 22 wt%Si, and thermo-mechanical testing had found that pack cementation silicon-aluminide coatings had better mechanical properties, compared with aluminised, chromium-aluminised, chrome silicon-aluminised and chrome silicon diffusion coatings.

From this evidence, coupled with the potential ability of silicon-aluminide diffusion coatings to coat blade and vane air internal cooling passages, it was concluded that these coatings would be the basis for developing the novel coatings in this project.

8.3.6 Manufacture of novel silicon aluminide diffusion coatings

There are two basic routes for manufacturing silicon-aluminide diffusion coatings; a two-step process of siliconising followed by aluminising, or a single-step silicon-aluminising process. Both routes involve chemical vapour deposition (CVD), followed by heat treatment to complete diffusion of the coating into the substrate. Research at Cranfield University [63], had previously identified that the two-step process has the advantage of better control of the quantities of aluminium and silicon deposited in the coating. However, its disadvantages include the formation of brittle and poorly adhered outer coating layer, and poor coating quality.

This research has also indicated that the simpler, and lower cost, single stage process produced a coating providing good hot corrosion protection. As the single step silicon-aluminising process also has the inherent advantage of avoiding another process and its associated risks, it was decided that the single stage silicon-aluminising CVD process would be adopted for developing the novel hot corrosion resistant coatings.

8.3.7 Low and high activity powder packs

Low activity aluminide coatings are so called because the aluminium activity in the pack is low, $a_{Al}<1$ [93], the coating phase formed is β-NiAl, from the preferential outward diffusion of nickel from the substrate into the coating, and an interdiffusion region rich in precipitates is formed between the substrate and coating. These precipitates may be enriched by refractory elements; chromium, tungsten, tantalum, rhenium, cobalt and molybdenum, and will contain secondary phases such as Laves, Sigma and Mu. In low activity/outward diffusion coatings, the alloying elements present in the substrate tend to diffuse into the coating to a depth depending on their solubility (see Chapter 2).

High-activity aluminides are usually characterized by the formation of δ-Ni_2Al_3 and the preferential diffusion of aluminum into the substrate, thus the initial surface is also the surface of the coated component. High activity aluminizing packs contain large quantities of aluminum as the source material, which increases the aluminum activity in the pack to unity. In high activity/inward diffusion coatings, the alloying elements present in the substrate enter in the compound layer in solution, or as precipitates formed during the process. High activity aluminizing involves a lower temperature range (700^{o}C to 850^{o}C) to favour inward aluminum diffusion, whereas low activity aluminizing, at higher temperatures (up to 1150^{o}C) promotes outward nickel diffusion.

The basis for developing the novel coatings in this project is to produce a coating with an aluminide rich intermetallic compound in the coating which, during scale growth under oxidation and hot corrosion conditions, will be supported by outward diffusion of aluminium from the coating/substrate system. This requirement may be satisfied by the use of a low activity powder pack.

8.4 Novel coating development – aluminising and silicon-aluminising trials

The approach to novel coating manufacture, by powder pack chemical vapour deposition (CVD), followed by post heat treatment, was carried out in two stages. The first stage was to carry out four aluminising CVD calibration trials, all having the same soak temperature of 1050^{o}C, but for varying soak periods. These trials provided the depths of coatings, which increased with longer soak period durations, and details of their microstructures. The second stage was to carry out silicon modified aluminising CVD trials, in which both the soak periods and soak temperatures were varied. In this chapter, the two stages of trials are described and analysed, followed by more detailed evaluation of the silicon modified aluminising CVD trial results, from which the preferred novel coatings were selected for oxidation and hot corrosion testing.

8.4.1 Aluminising trials

8.4.1.1 Introduction and process

The Cranfield University CVD equipment used for the trials, shown diagrammatically in Figure 8.2, is described more fully in Chapter 4. Each CVD operation required the furnace, after reaching, and soaking at, a temperature of 1100^{o}C, to be switched off and positioned over the CVD chamber. The furnace was then switched on again and the chamber temperature was raised to 1050^{o}C, where it was maintained for the required period. At the end of the soak period, the furnace was switched off and moved clear of the chamber.

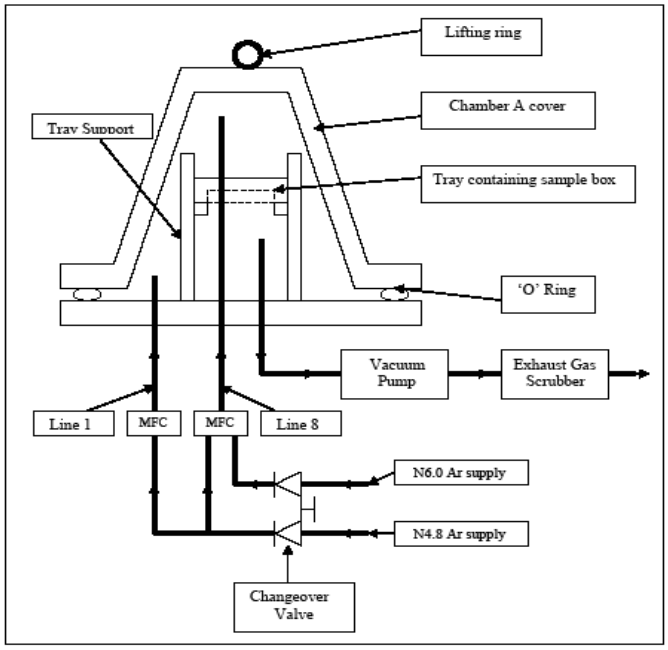

Key: *MFC – mass flow controller, for controlling argon supply to the chamber*

Figure 8.2: Diagram of CVD chamber and associated systems [63]

Furnace positioning operations and furnace and chamber temperature raising profiles are unique to the particular CVD equipment being used. It can be seen from Figure 8.3 that the chamber temperature gradients for the Cranfield equipment, after the furnace had been positioned over the chamber and switched on, from the 800^{o}C level at which vapourising commences, varied slightly for each of the four runs. These variations, when considered over the durations of the soak periods were not considered to have caused inconsistencies in coating microstructure or compositions.

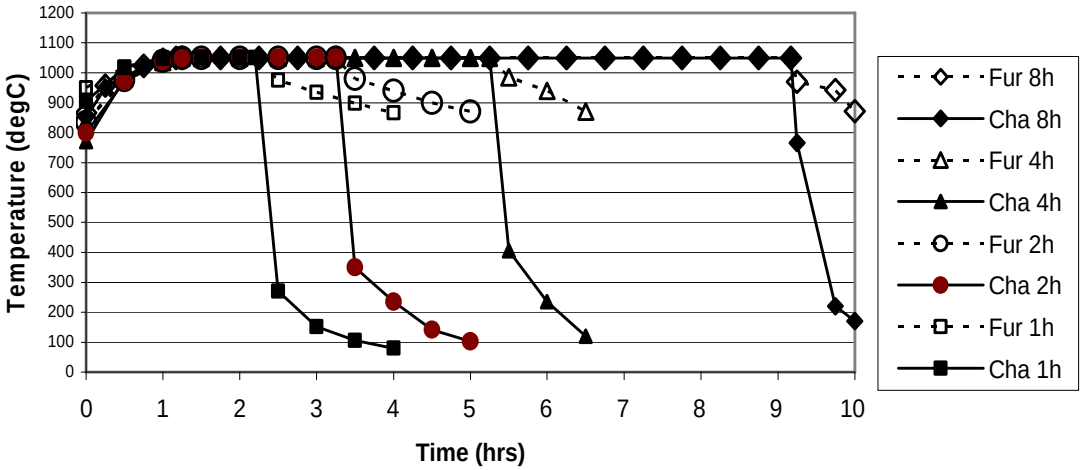

Key: Fur; furnace, Cha; chamber

Figure 8.3: Aluminising trial runs; furnace and CVD chamber temperature profiles

One sample disc each of IN738LC and CMSX-4, was coated in each run, after surface preparation using 120, 240 and 1200 grade silicon carbide papers, and followed by ultrasonic cleaning in isopropyl alcohol (IPA). Sample discs were located horizontally in the powder pack, in the tray, and located so that the depths of powder, above, below and at the sides of the samples, were at least 10mm.

A low-activity powder pack, developed after MTDATA assessments [63] was used for the aluminising trials, containing fluoride activators NaF and KFHF to generate a stable vapour pressure. The powder pack was composed of:

Al; 1.39%-17%, NaF; 0.88%, KFHF; 0.07%, NH_4Cl; 0.17%, H_2O; 0.1%, balance Al_2O_3

8.4.1.2 Aluminising trials – results and discussion

Figure 8.4 shows photographs of the samples taken after the trial aluminising runs. The coatings are seen to become progressively deeper in colour as the soak periods increase.

After CVD, each sample was cut diametrically, with only one half of each sample being heat treated in the vacuum furnace, to complete diffusion, the other half was not heat treated, and remained in the as-deposited state. Heat treatment programmes consisted of:

IN738LC - 2 hours at 1120^{o}C and 24 hours at 843^{o}C
CMSX-4 - 2 hours at 1140^{o}C and 20 hours at 870^{o}C

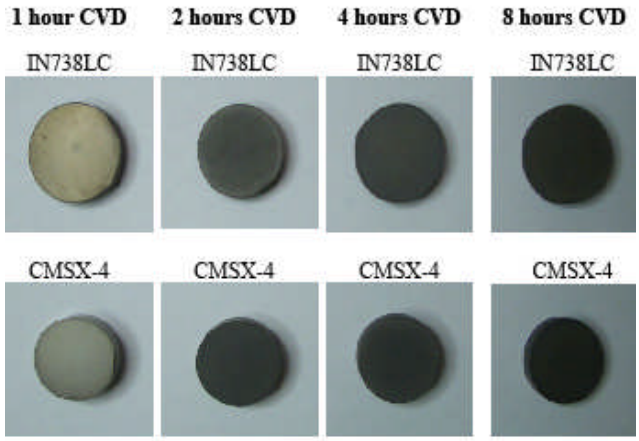

Figure 8.4: Photographs of samples after aluminizing CVD trials at 1050^{o}C

(a) Coating depths

The SEM backscatter (BSE) images, shown in Figure 8.5, illustrate the different microstructures of the interdiffusion zone that occurred during the deposition processes compared to the diffusion zone of a heat treated sample. These images illustrate the results of post heat treatment in providing interdiffusion paths and hence the development of the microstructure of the coating to the substrate.

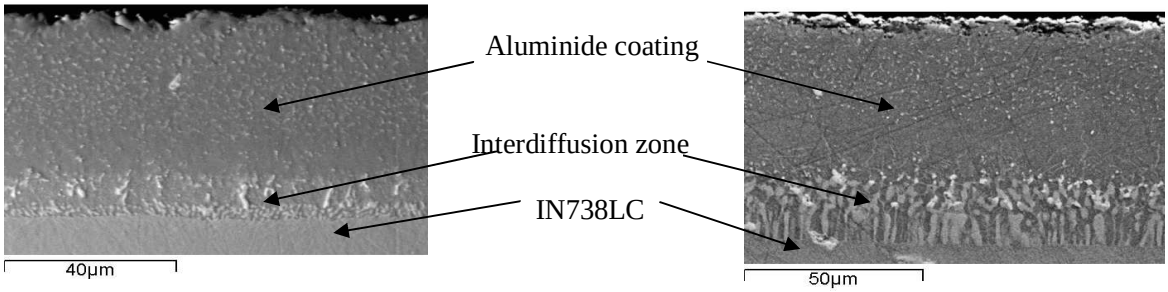

Not heat treated after 1h CVD *Heat treated after 1h CVD*

Figure 8.5: BSE images of IN738LC samples, heat treated and not heat treated, after aluminising CVD for 1h at 1050^{o}C

The limited diffusion zone formed as a result of the CVD process can be seen to be increased in size and transformed by post heat treatment. This heat treatment changes the coating phase to β-NiAl, by interdiffusion of nickel from the substrate. The interdiffusion zone (IZ) is nickel depleted and contains other secondary phases, rich in chromium and refractory metals. Coating depths of samples, after CVD but prior to post heat treatment, will be used in determining activation energies in section 8.4.2.3. As the calibration trials are concerned with fully processed aluminide diffusion coatings, no further consideration will be given to non-heat treated samples. Heat treatment is discussed in Chapter 2.

Coating depths were measured, by optical microscope, on both sides of each sample disc. Where there is a variation in the depths of coatings on the sides of a sample, this is attributed to the top side being open to gas and vacuum pump suction, thus depleting pack composition. The tray bottom prevents depletion of pack composition on the lower side.

Table 8.1 lists the depths of aluminising chemical vapour deposition (CVD) of IN738LC and CMSX-4, for trial CVD soak periods of one, two, four and eight hours, at 1050^{o}C, one half of each sample being heat treated, the other half not heat treated.

IN738LC	**Ht trt'd**	**Side**	**Depth** (μm)	**1h soak**	**2h soak**	**4h soak**	**8h soak**
	x	1	Al coating	36	45	51	54
	x	2	Al coating	35	44	50	53
	✓	1	Al coating	43	50	56	62
	✓		IZ	21	22	22	21
	✓	2	Al coating	32	40	57	61
	✓		IZ	20	20	20	20
CMSX-4	x	1	Al coating	54	67	85	98
	x	2	Al coating	52	65	85	98
	✓	1	Al coating	53	60	75	86
	✓		IZ	27	27	27	29
	✓	2	Al coating	53	63	71	94
	✓		IZ	27	27	27	29

Key: IZ – interdiffusion zone

Table 8.1: Depths of coatings after aluminising CVD trials of IN738LC and CMSX-4, for 1h, 2h, 4h and 8h soak periods, at 1050^{o}C

(b) Aluminising trials – resulting microstructures

Microstructures of the mounted and surface-prepared aluminised and heat treated samples of IN738LC and CMSX-4 were inspected using the ESEM backscatter (BSE) facility. Maps of main elements, for visual presentation of the microstructures, and EDX line scans for elemental analyses, were produced for each trial coating.

In this section, for each trial soak period, the BSE element maps, EDX line scan and brief discussion, are presented for the respective sample of IN738LC and CMSX-4.

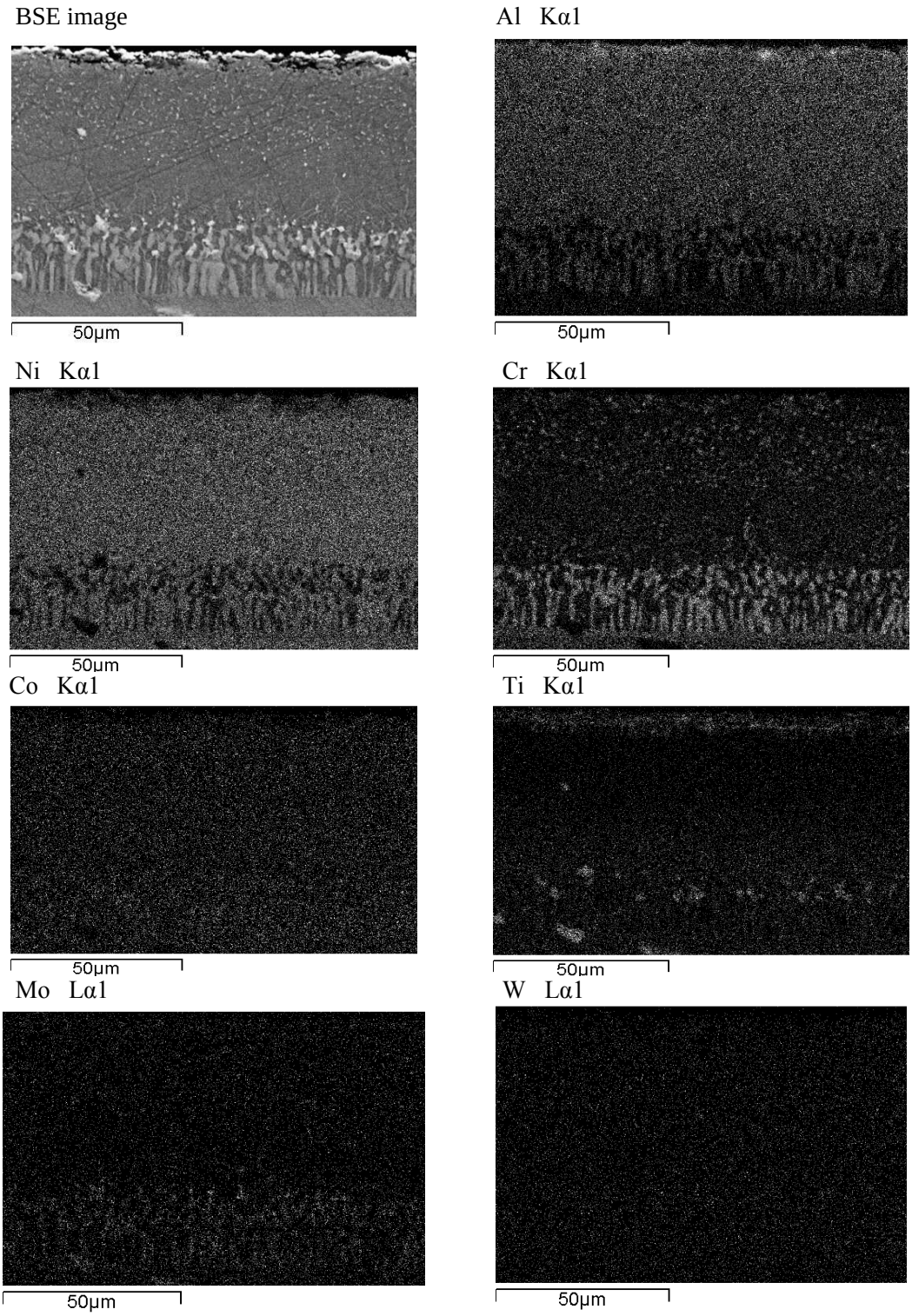

Figure 8.6: Aluminising trials; IN738LC one hour aluminising CVD at 1050^{o}C, element maps

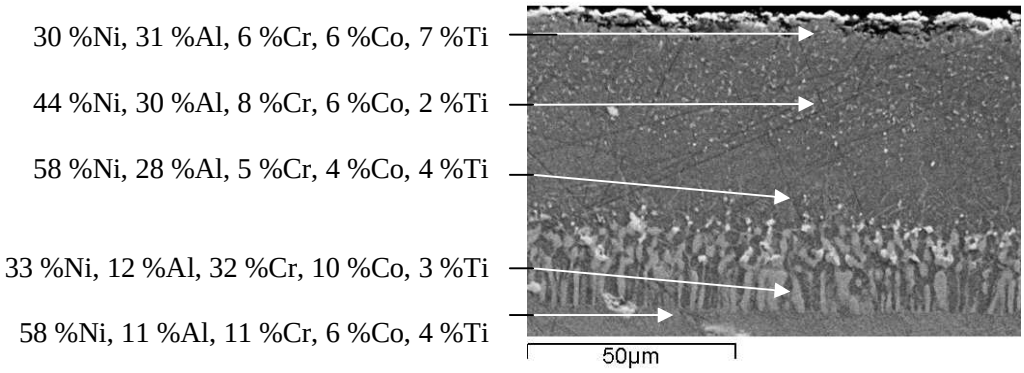

Figure 8.7: IN738LC; one hour aluminising CVD at 1050^{o}C, main elements

The first sample assessed was aluminised IN738LC in-pack at 1050^{o}C for one hour. The microstructure is shown by the BSE image in Figure 8.6. The maps in Figure 8.6 clearly show the aluminium uniformly distributed through the coating to become aluminium rich at the coating surface. In Figure 8.7, the EDX results of the main elements show the nickel content of 58 at% Ni in the substrate, to 33 at% Ni midway through the diffusion zone, then increasing to 58 at% Ni in the coating, 38µm from the outer coating surface, then reducing at a constant gradient to 30 at%Ni, at the coating surface. The EDX results do not include the coating surface. The β-NiAl phase continues through the coating to the Al-rich edge of this phase field at the surface.

Chromium generally occurs in the coating with an average content of 6 at% Cr and chromium rich precipitates can be seen in the outer part of this coating. Cobalt is also present at a uniform level of 6 at% Co. Titanium rich particles occur at the interdiffusion zone/coating interface and as a layer at the coating surface of 6 at% Ti. Lower levels of molybdenum and tungsten diffuse outward into the coating also.

Although the NiAl phases are satisfactory, the depth of aluminised coating, averaging 43µm, could limit the duration of hot corrosion protection this combination offers.

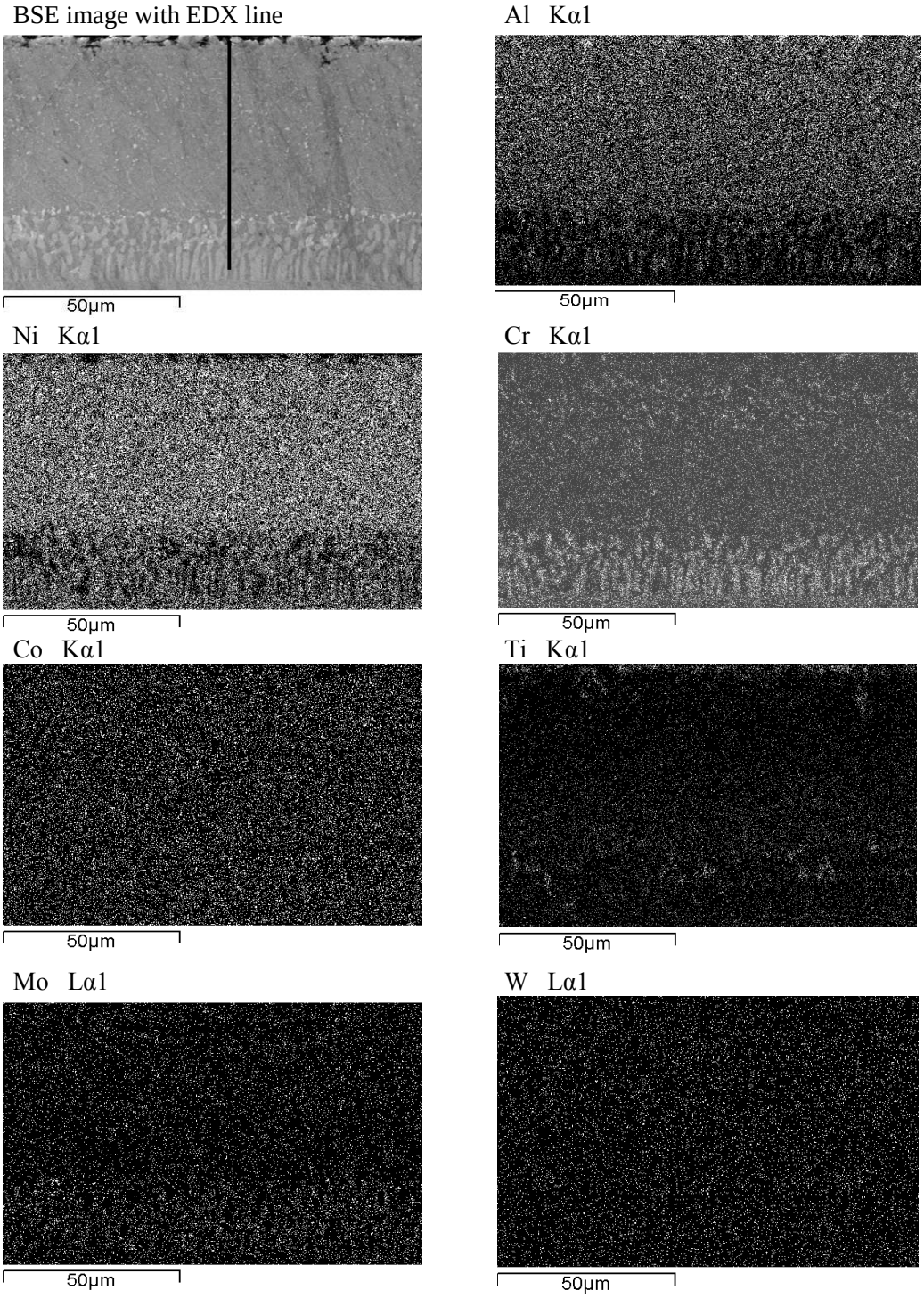

Figure 8.8: Aluminising trials; IN738LC two hours aluminising CVD at 1050^{o}C, element maps

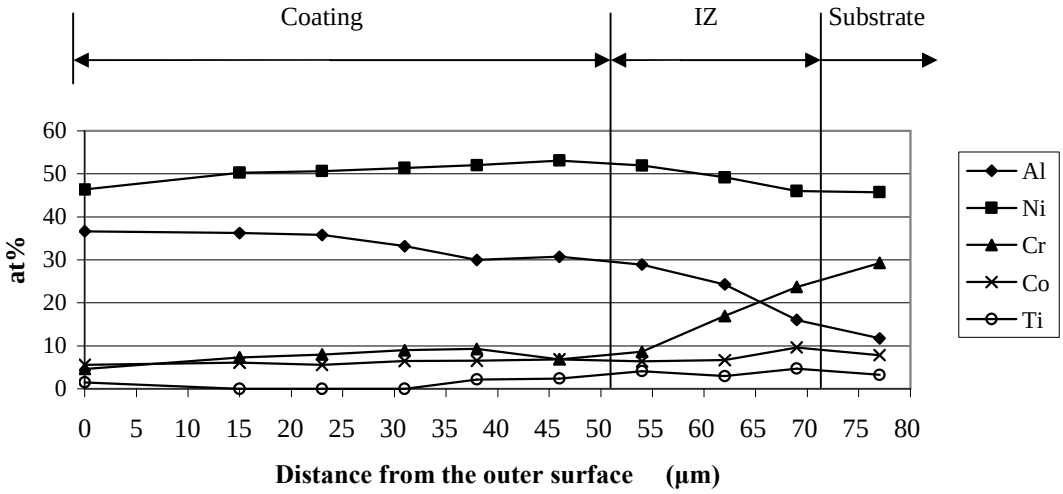

Figure 8.9: IN738LC; two hours aluminising CVD at 1050°C, main elements on EDX line shown in Figure 8.8

The sample assessed was IN738LC after aluminising CVD at 1050°C for two hours. The microstructure is shown by the BSE image in Figure 8.8, which also presents the EDX line scan position. In Figure 8.8, the Al map indicates a uniform distribution across the coating to the surface where it is aluminum rich. In Figure 8.9, the spacing of EDX points has resulted in the content of elements being distorted. As a result, the graph cannot show all peaks which causes inaccuracies, particularly through and in the vicinity of the interdiffusion zone. The main advantage of the EDX scan is to show phase stability and phase trends through the coating, and it is also necessary to refer to the element maps, when analysing the results. To assist in understanding EDX line scan results, in Figure 8.9, the approximate positions of the interfaces of the coating/ interdiffusion zone (IZ) and IZ/substrate are marked. These interfaces will be identified on similar graphs in this report. The figure shows that interdiffusion of nickel occurs from the substrate, where the content is 58 at% Ni, to 51 at%Ni at the IZ/coating interface, then continuing in the βNiAl phase to 47 at% Ni at the coating surface

Interdiffusion of Cr into the coating matrix proceeds at a similar gradient, from 10 at%Cr at the substrate/coating interface, to 5 at%Cr at the coating surface. Again chromium rich precipitates are observed in the outer part of the coating. The content of cobalt in the coating, resulting from interdiffusion from the substrate, remains constant at 5 at%Co, through the coating to the surface. Of the substrate alloying elements, interdiffusion of titanium within the matrix at 2 at%Ti occurs and also forms an intermetallic layer at the outer surface and precipitates at the coating/diffusion zone interface. Maps in Figure 8.8 show uniform but lesser content of molybdenum and tungsten. The CVD soak period in this case produced an aluminide diffusion coating having a average depth of 50µm.

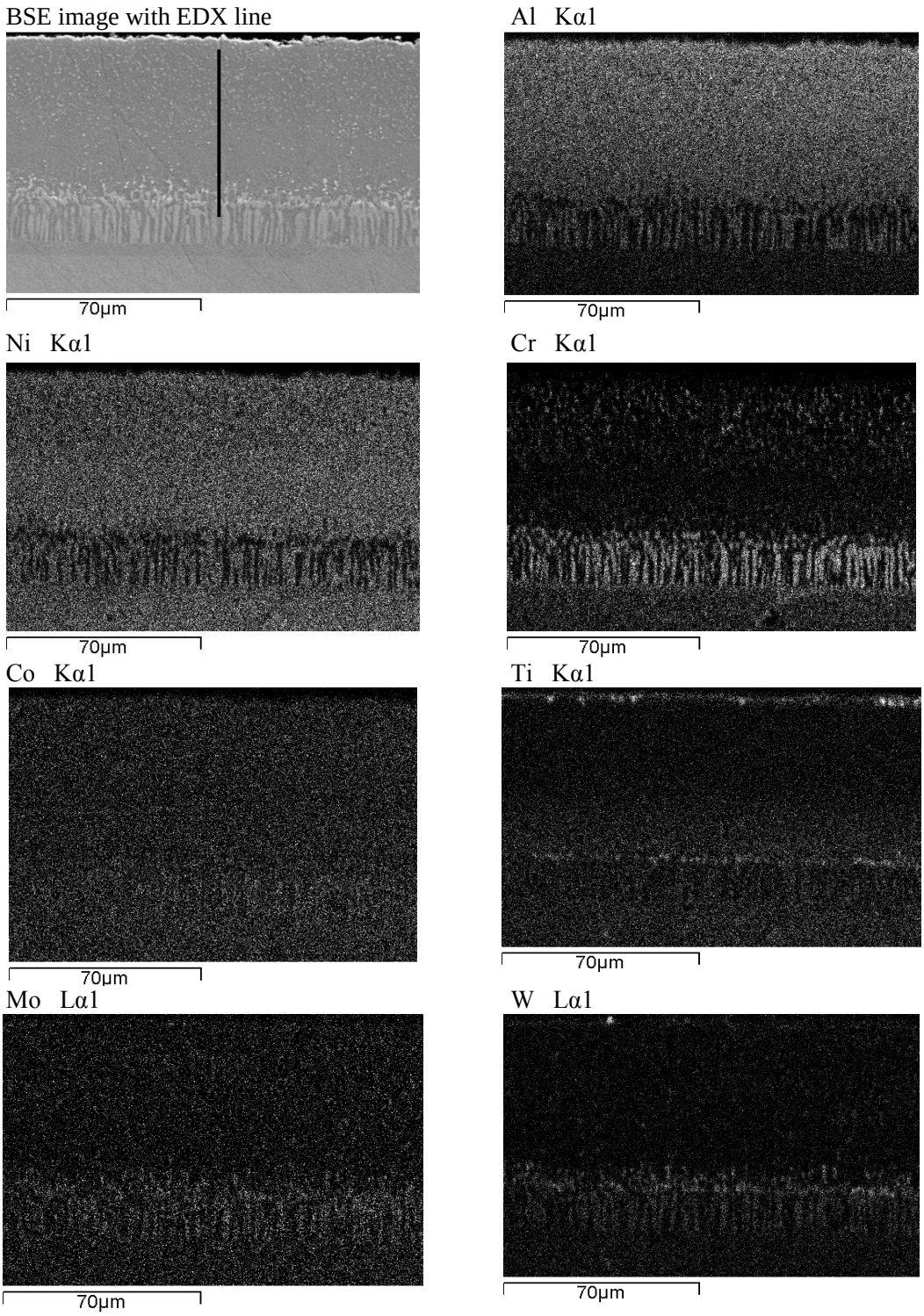

Figure 8.10: Aluminising trials; IN738LC four hours aluminising CVD at 1050^{o}C, element maps

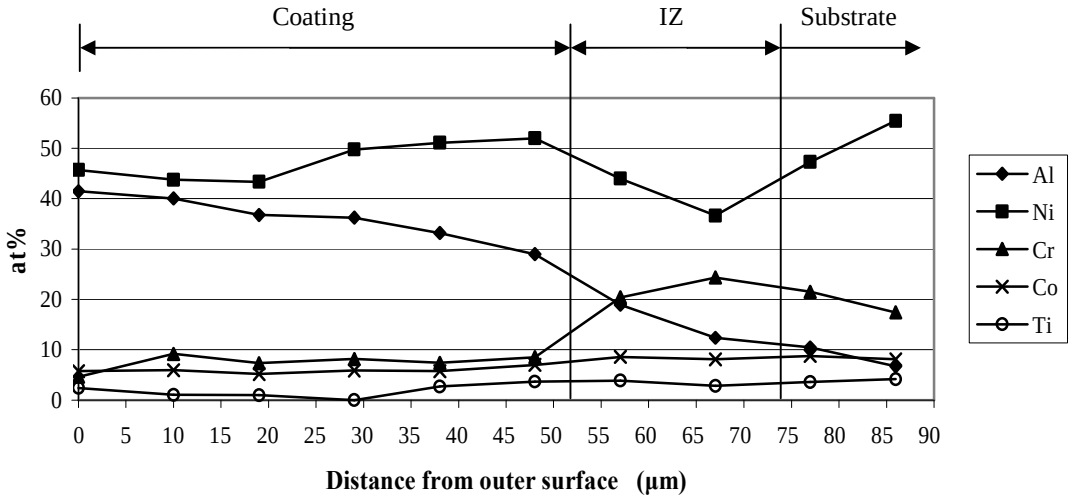

Figure 8.11: IN738LC; four hours aluminising CVD at 1050°C, main elements on EDX line shown in Figure 8.10

The sample assessed was aluminised IN738LC in-pack at 1050°C for four hours. The microstructure is shown by the BSE image in Figure 8.10, which also presents the EDX line scan position. The Al map in Figure 8.10 indicates a uniform distribution through the coating. The element map shows outward diffusion of chromium, which is of a lower order through the first half of the coating above the coating/IZ interface, then becoming chromium rich in the outer half of the coating. The microstructure of cobalt is uniform, with its content falling from 7 at%Co at the coating/IZ interface to 4 at%Co at the coating surface.

In Figure 8.11, the approximate positions of the coating/IZ, and IZ/substrate interfaces are shown. The figure shows the β-NiAl phase at the coating/ diffusion zone interface, remaining stable but increasingly Al-rich as the matrix proceeds to the coating surface where it lies at the Al-rich edge of the NiAl field.

The maps in Figure 8.10 shows the coating to contain substrate strengthening elements, titanium, molybdenum and tungsten. Titanium forms intermetallic layers at the coating/IZ interface and outer coating surface. In the matrix, titanium content remains generally constant at ~3 at%Ti. Molybdenum and tungsten occur in the coating, at <0.65 at%Mo and <1 at%W respectively, although the maps suggest that that these values are low.

The four hours soak period in this trial provides an aluminide coating having an average depth of 56µm.

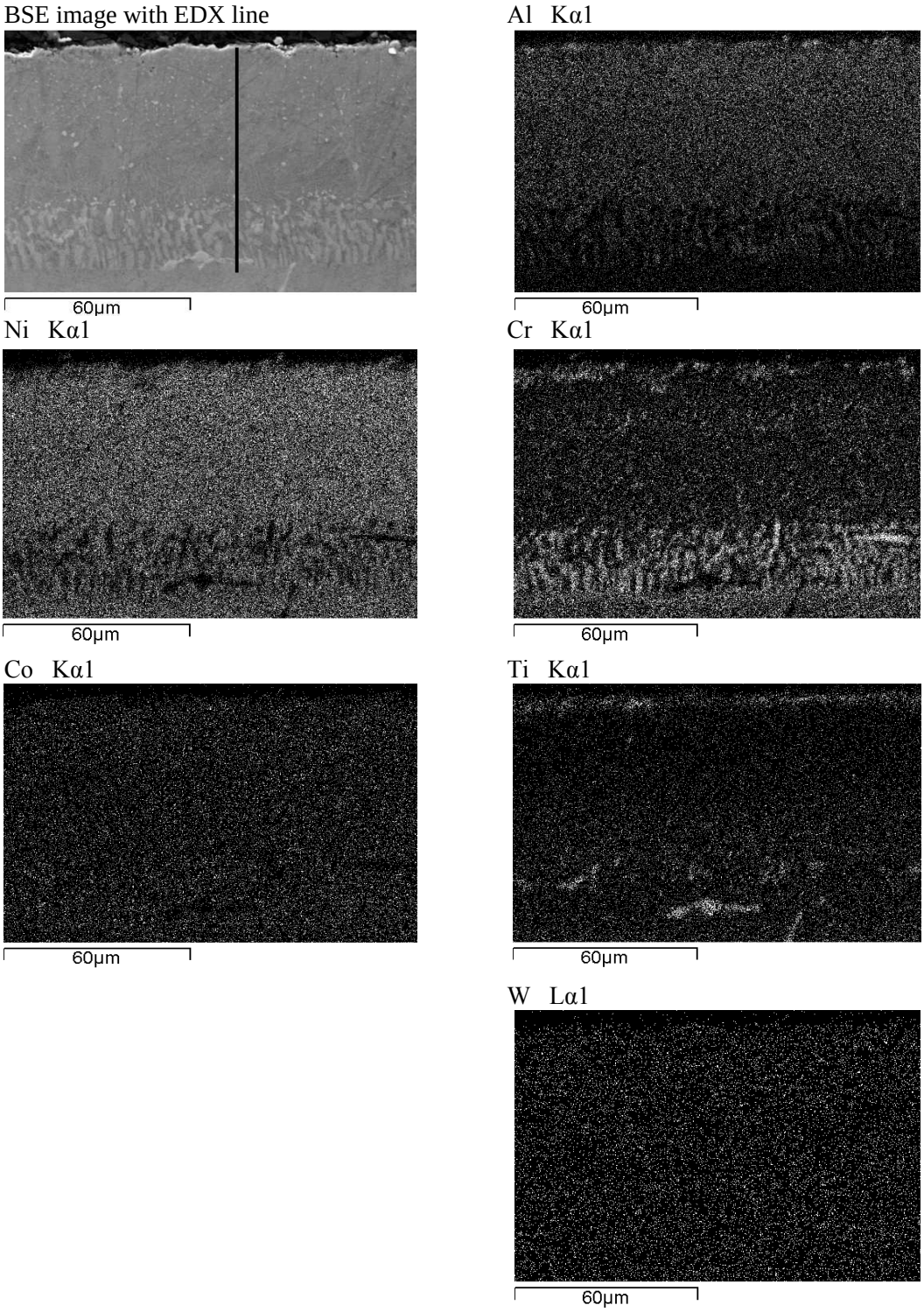

Figure 8.12: Aluminising trials; IN738LC eight hours aluminising CVD at 1050^{o}C, element maps

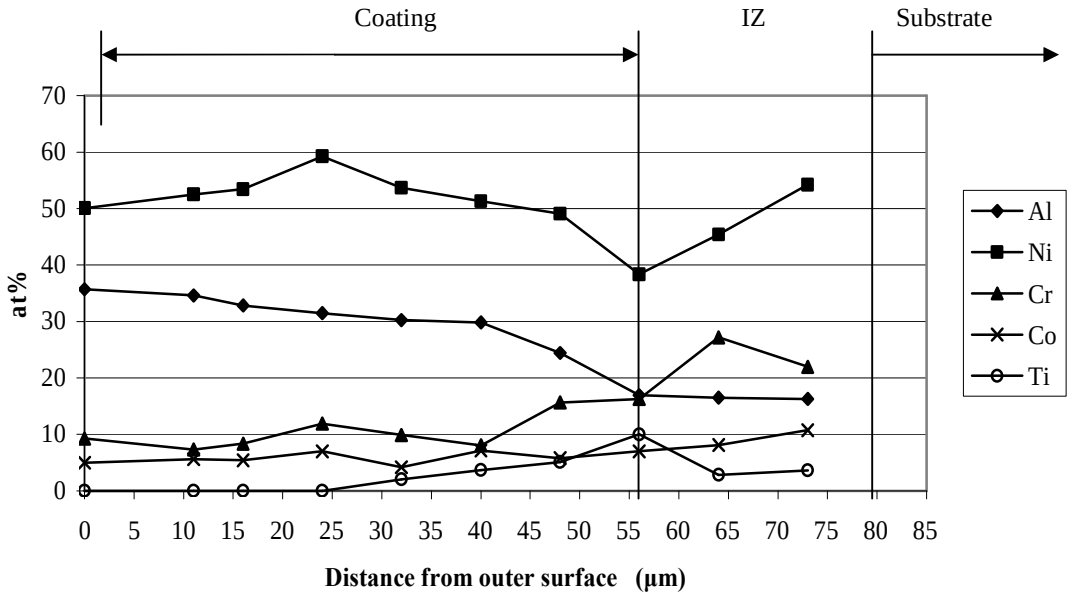

Figure 8.13: IN738LC; eight hours aluminising CVD at 1050^{o}C, main elements on EDX line shown in Figure 8.12

The sample assessed was aluminised IN738LC in-pack at 1050^{o}C for eight hours. The microstructure is shown by the BSE image in Figure 8.12, which also shows the position of the EDX line scan.

Figure 8.13 shows the stable coating commencing at the IZ/coating interface, as nickel rich β-phase with a high chromium content, with the composition changing towards the centre of β-NiAl phase at the coating surface.

In Figure 8.12 the map shows uniform distribution of chromium in the coating through to the chromium rich surface. It can be seen, from the EDX line scan shown in Figure 8.12, that, through the IZ, the substrate content of ~16 at%Cr rises to ~28 at%Cr in the IZ, then reduces, at a constant gradient to ~9 at%Cr, at the coating surface. Interdiffusion of cobalt proceeds from a level of 8 at%Co, at the IZ/coating interface, with an average content through the coating of 6 at%Co, to 5 at%Co at the surface. With the ~60µm deep stable NiAl matrix and high content of chromium and cobalt, the coating should provide good protection against hot corrosion.

As with the three previous aluminising trials, titanium is the main substrate alloying element which outwardly diffuses from the IN738LC into the coating. In this trial, as seen in the map in Figure 8.12, titanium proceeds uniformly with a content averaging 2 at%Ti after the IZ, to form a titanium rich layer at the coating surface. Tungsten in the substrate interdiffuses into the coating but at levels below 1 at%W.

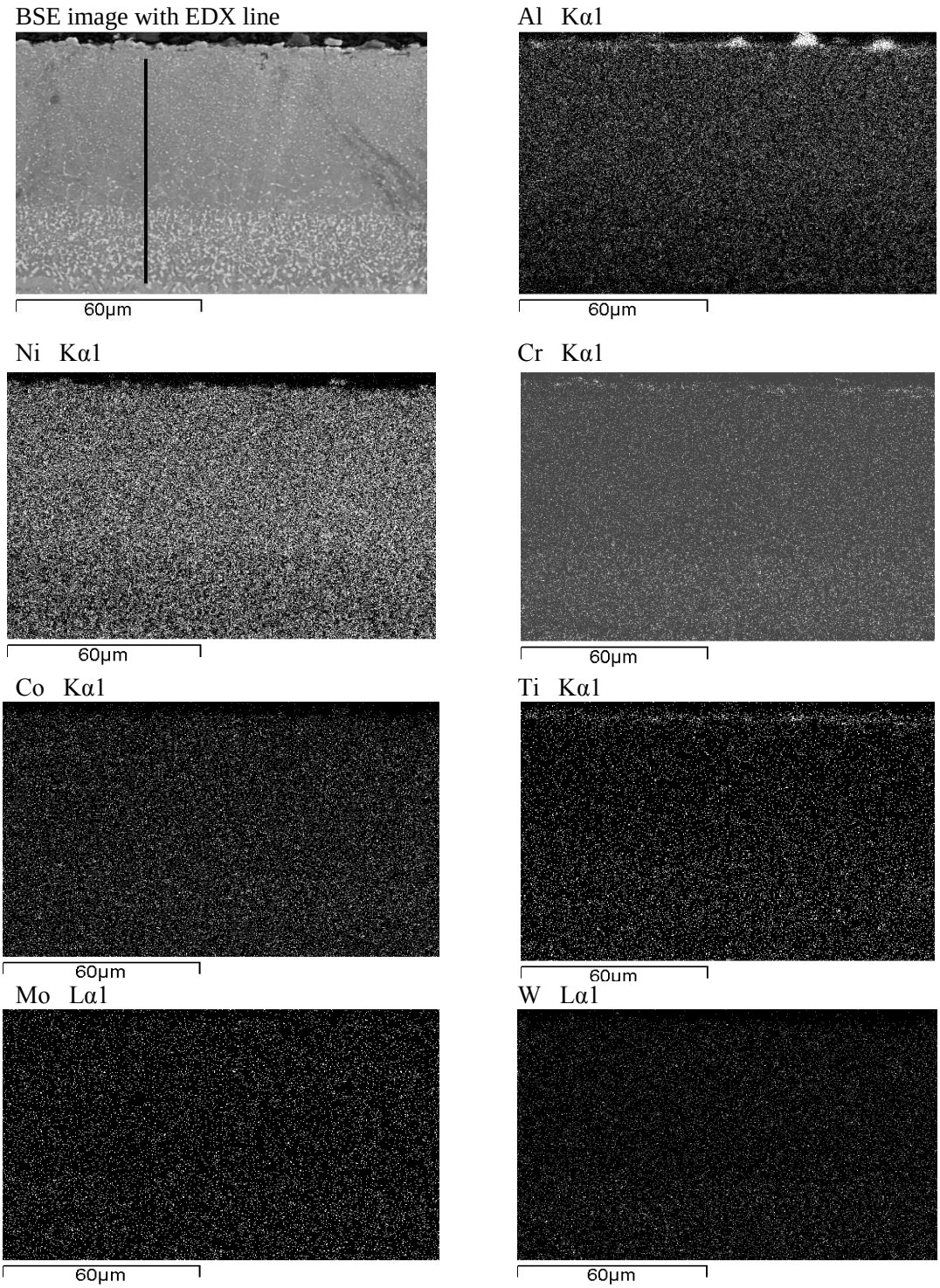

Figure 8.14: Aluminising trials; CMSX-4, one hour aluminising CVD at 1050^{o}C, element maps

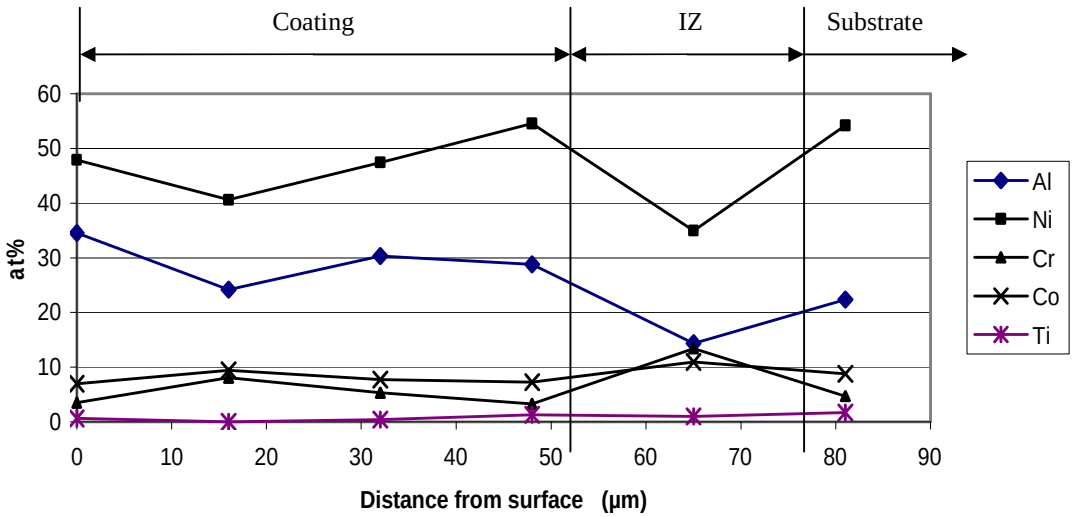

Figure 8.15: CMSX-4; one hour aluminising CVD at 1050°C, main elements on EDX line shown in Figure 8.14

The sample assessed was aluminised CMSX-4 in-pack at 1050°C for one hour. The microstructure is shown by the BSE image in Figure 8.14, which also shows the position of the EDX line scan.

The stable β-NiAl phase coating proceeds from the interdiffusion zone to the coating surface. The graphs in Figure 8.15 show the microstructures of outward diffusing elements are uniform reflecting the absence of grain boundaries in CMSX-4. The lower content of chromium contained in CMSX-4, compared with IN738LC, averages 5 at%Cr in the coating, to 4 at%Cr at the surface. Cobalt content in CMSX-4 (9 at%Co) continues at similar levels through to 8 at%Co at the coating surface.

Titanium, molybdenum and tungsten occur uniformly, but titanium, with a content averaging 1.3 at%Ti through the coating, is the only element >1 at%.

The one hour aluminising CVD soak period in this trial produced a coating depth averaging 53µm.

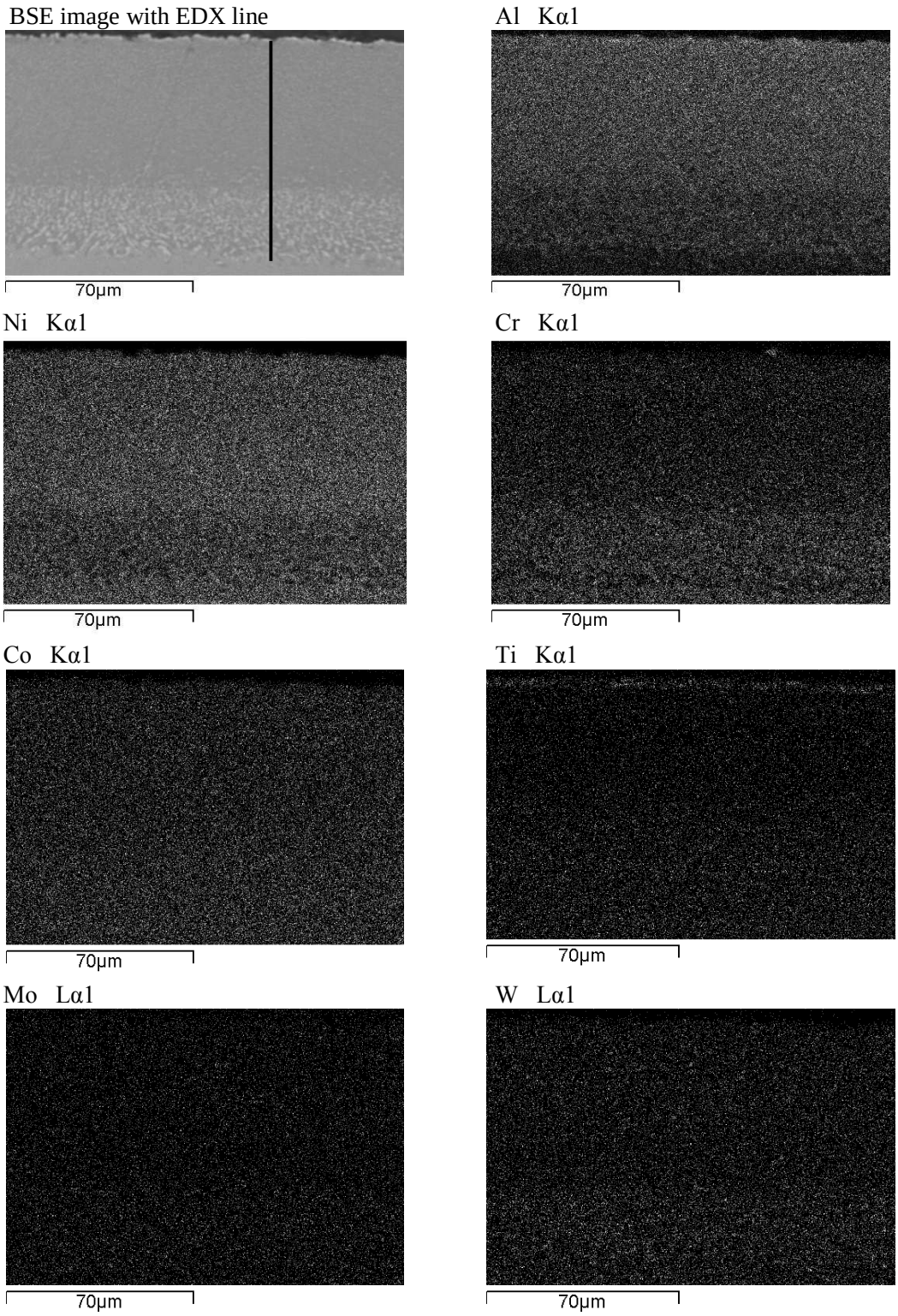

Figure 8.16: Aluminising trials; CMSX-4, two hours aluminising CVD at 1050^{o}C, element maps

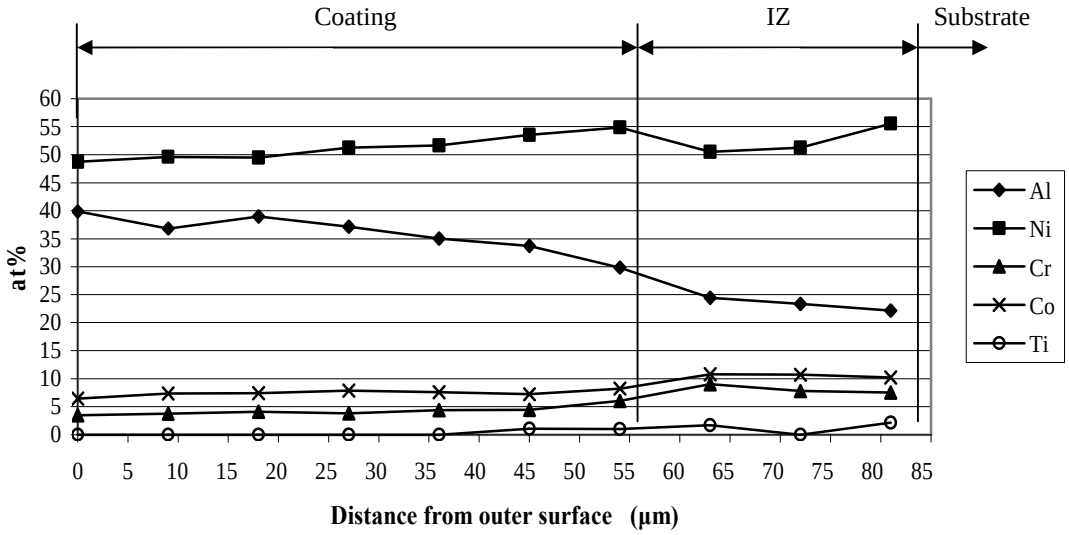

Figure 8.17: CMSX-4; two hours aluminising CVD at 1050°C, main elements on EDX line shown in Figure 8.16

The sample assessed was aluminised CMSX-4 in-pack at 1050°C for two hours. The BSE secondary image, with the EDX line scan indicated, and element maps, for this trial, are shown in Figure 8.16. From the maps in this figure, it is seen that element microstructures are very similar to those for the aluminising CVD one hour trial, shown in Figure 8.14.

The element analyses in Figure 8.17 show the β-NiAl phase at the IZ/ substrate interface is stable as it proceeds through the coating, becoming more Al-rich, to the surface, where its position is central in the β-NiAl field.

Substrate elements occur at near constant rates from the IZ, with the chromium content averaging 5 at%Cr through the coating to the surface. Cobalt content reduces at a constant gradient from 8 at%Co to 6 at%Co at the surface. Molybdenum and tungsten are distributed uniformly through the coating, generally <1 at%. Titanium forms part of the intermetallic at the coating surface, as it did in the one hour aluminising trial.

The two hours aluminising CVD soak period in this trial produced a coating depth averaging 60µm.

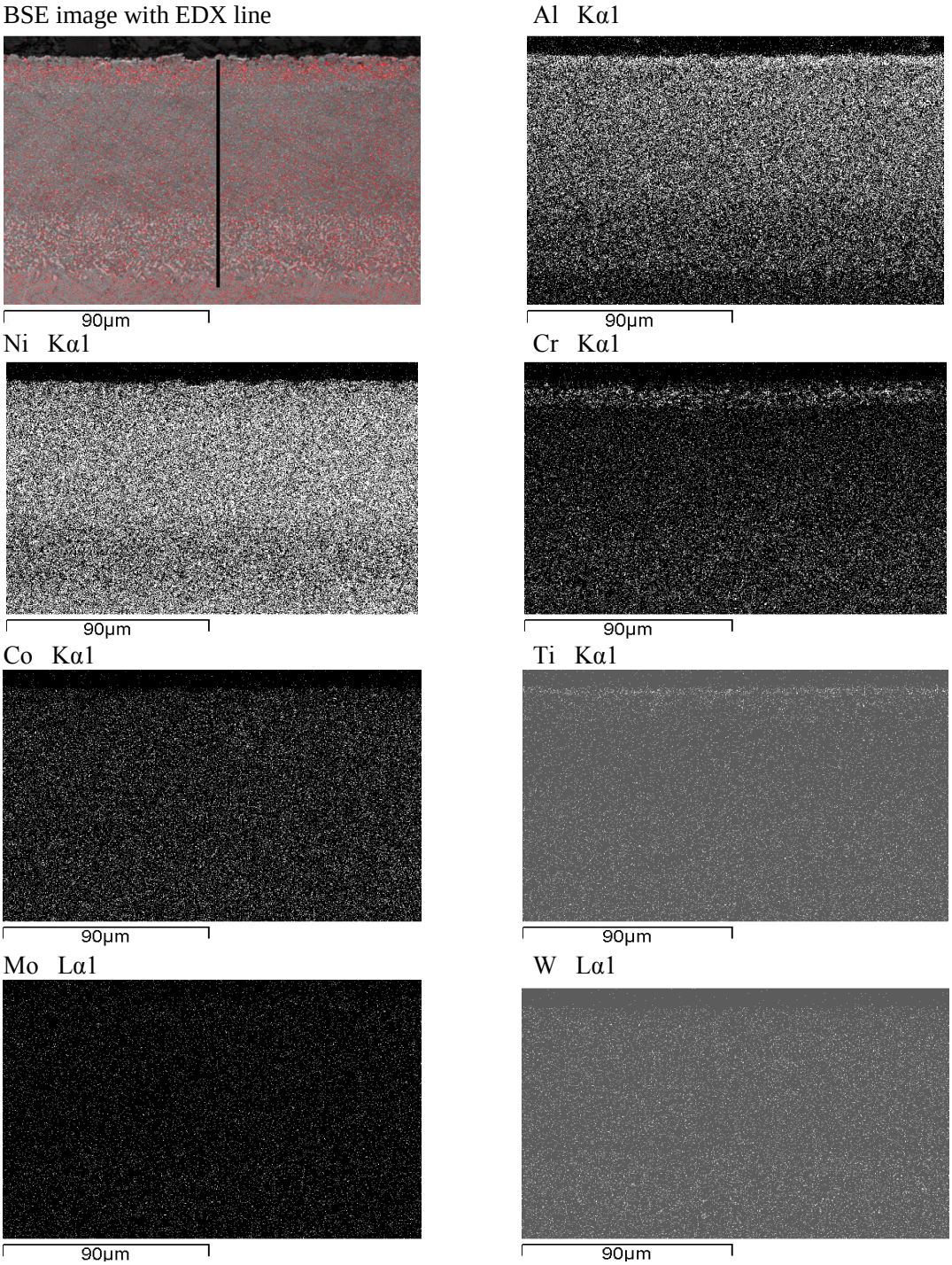

Figure 8.18: Aluminising trials; CMSX-4, four hours aluminising CVD at 1050°C, element maps

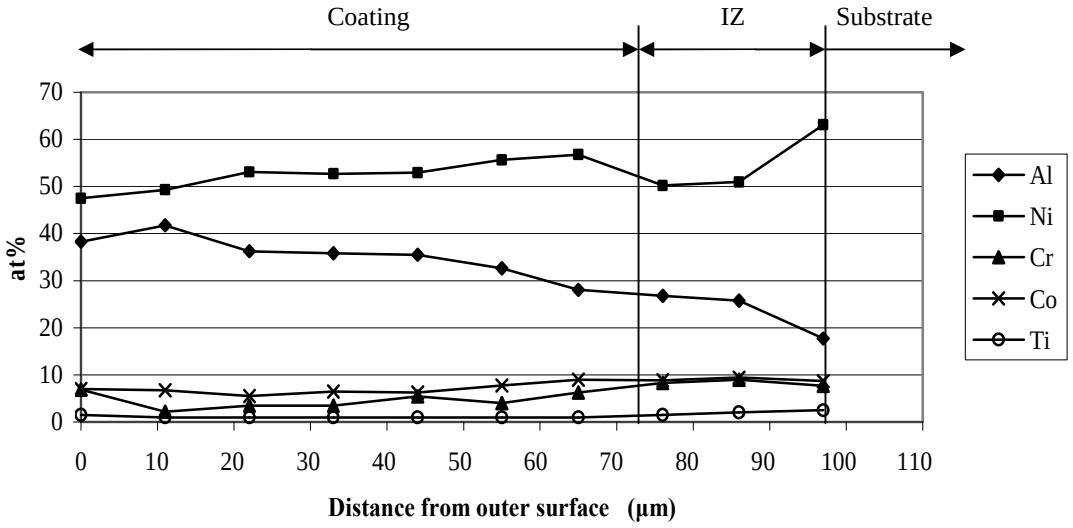

Figure 8.19: CMSX-4; four hours aluminising CVD at 1050°C, main elements on EDX line shown in Figure 8.18

The sample assessed was aluminised CMSX-4 in-pack at 1050°C for four hours. The BSE image with EDX line scan and element maps are shown in Figure 8.18, the EDX results being shown in Figure 8.19.

The EDX scan graphs in Figure 8.19 show that, from the Ni-rich edge of the β-NiAl phase field at the IZ/coating interface, to the coating surface, the matrix remains stable. Aluminium content increases through the coating and, from a position ~10µm from the surface, aluminium and nickel contents decrease, possibly picking up some oxidation. However, at the surface, the phase is central in the β-NiAl phase field.

EDX graphs show contents of elements are generally very similar in composition to those of the two previous aluminising trials on CMSX-4 at this soak temperature, the main differences being in the coating depths which reflect the different soak periods..

In contrast to the two earlier CMSX-4 aluminising trials, the BSE maps of aluminium and chromium, seen in Figure 8.18 both show intermetallic layers containing these two elements enriched at the coating surface. The EDX line scan graphs do not reflect the increasing content of these elements at the surface, being very similar to those in the earlier CMSX-4 aluminising trials. Throughout the coating the cobalt content averages 8 at%Co. Titanium, molybdenum and tungsten occur, uniformly distributed, generally with contents <1 at%.

The four hours aluminising CVD soak period in this trial produced a coating depth on the substrate of 75µm.

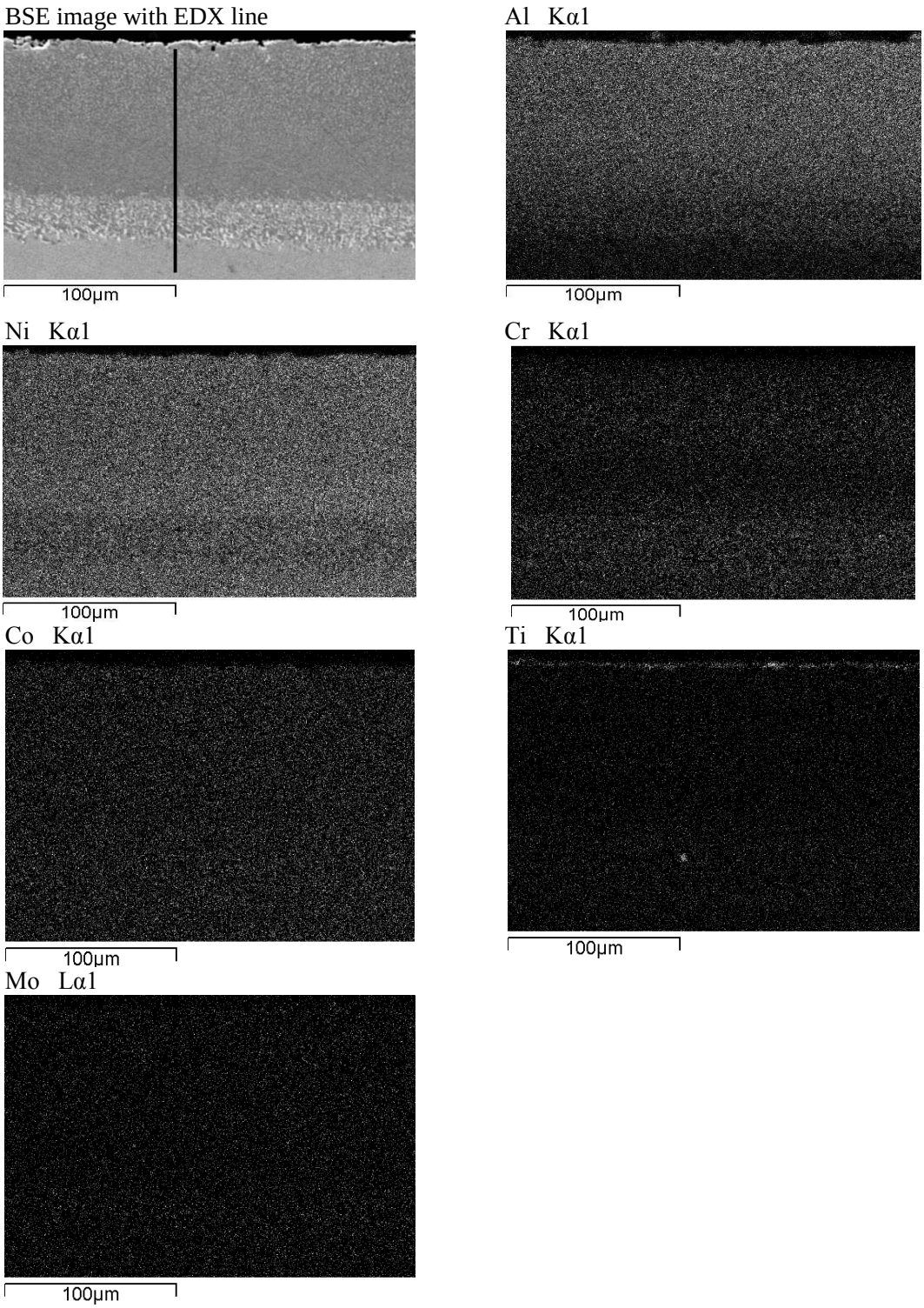

Figure 8.20: Aluminising trials; CMSX-4, eight hours aluminising CVD at 1050^{o}C, element maps

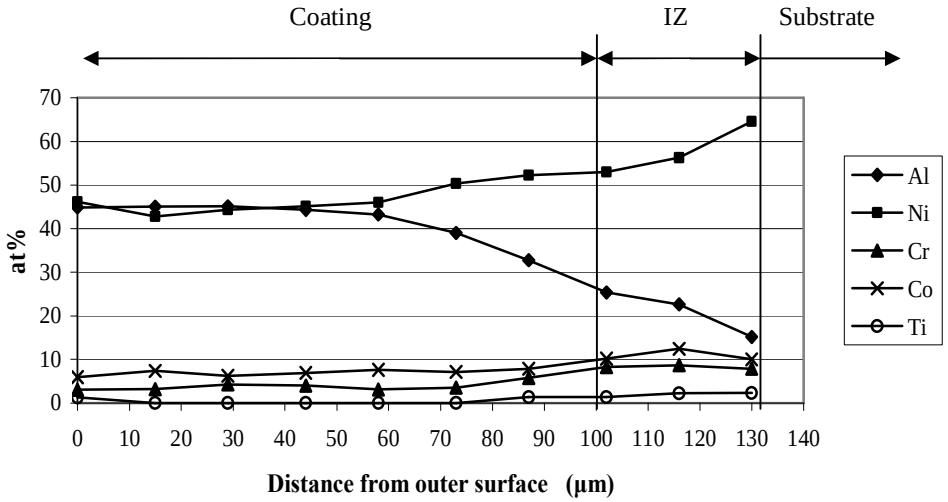

Figure 8.21: CMSX-4; eight hours aluminising CVD at 1050^{o}C, main elements on the EDX line shown in Figure 8.20

The sample assessed was aluminised CMSX-4 in-pack at 1050^{o}C for eight hours. In common with the previous three aluminising runs, the NiAl phases developed through the coating, from β-NiAl at the diffusion zone, to the Al-rich edge of the β-NiAl field, at the coating surface.

The microstructures are generally very similar in composition to those of the previous three aluminising trials on CMSX-4 at this soak temperature.

The eight hours aluminising CVD soak period of eight hours produced an average coating depth of 86µm.

8.4.1.3 Aluminising trials – general discussion and conclusions

Aluminising trials are the first step in the development of novel silicon modified diffusion coatings for protecting hot components of gas turbines fired by biomass and waste-fuels. The main features required of such coatings and the features to be assessed in the aluminised coatings produced in these trials are:

- sufficient depth of coating to maintain the incubation stage of hot corrosion throughout the component's service life;
- stable β-phase NiAl matrix should be sustained through the coating;
- interdiffusion of superalloy strengthening elements into the coating should not jeopardise its mechanical integrity.

In the four aluminising runs for each substrate, at a CVD soak temperature of 1050^{o}C, carried out to calibrate coating depth against time, the difference in diffusion coefficients between IN738LC and CMSX-4 resulted in the average depths shown in Table 8.2. Although the nominal CVD soak times were 60 -, 120-, 240- and 480-minutes, CVD chamber temperature ramp-up times significantly extended the CVD heating time. In Figure 8.3, it is seen that all ramping times from 750^{o}C, when it was assumed that pack vapourising commenced, to 1050^{o}C, were in excess of 60 minutes. Figure 8.22 illustrates the significant differences in coating rates on IN738LC, between nominal CVD soak times and then with the addition of 75 minutes ramping times. When assessing the aluminising trial results, a ramping time of 75 minutes was added to the CVD soak times, to provide the CVD heating times adopted. Table 8.2 shows the CVD heating times and average aluminide coating thicknesses used in assessing aluminising trial results.

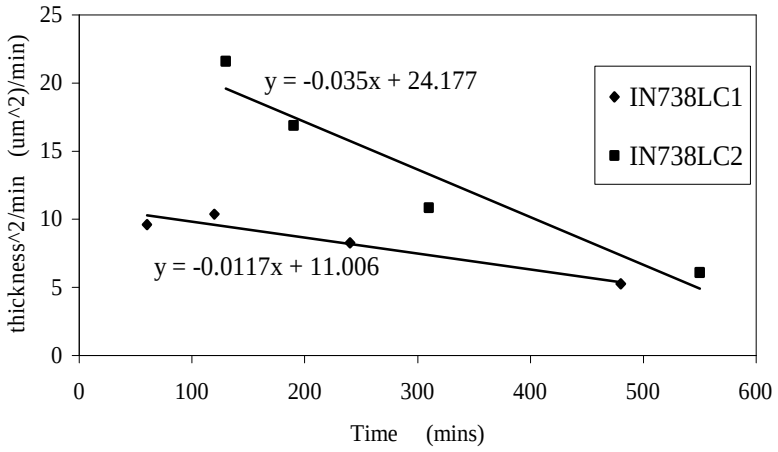

Key: IN738LC1; nominal CVD soak times IN738LC2;CVD soak times + 75 mins ramp times

Figure 8.22: Aluminising trials on IN738LC samples; effect of ramping time on aluminide coating thickness

CVD heating time (mins)		135	195	315	555
IN738LC	(μm)	36	45	51	54
CMSX-4	(μm)	53	66	85	98

Table 8.2: Aluminising CVD trials of IN738LC and CMSX-4 at 1050°C; average coating thickness and CVD heating times

Average values of the top and bottom side depths of samples were used in the assessments, recognising that the thickness of the top side coating is less, as a result of the top surface of the powder being exposed to the chamber and tending to leak vapour. In contrast, the underside of the pack is constrained by the tray bottom allowing no leakage to the chamber, thus producing a thicker coating. The Arrhenius plots in Figure 8.23 consist of the heating time against (coating thickness)^2 for IN738LC and CMSX-4, showing coating thickness grew parabolically with respect to time ((*thickness*)^2 α *time),* the coating rate slowing with time. The linearity of the plots indicate that coatings grew by a diffusion controlled processes [114]. In general, the rate of aluminium diffusion increases with CVD heating time in both substrates, with that in CMSX-4 higher than in IN738LC. However, the aluminium diffusion rates in both substrates are very similar, as shown by the gradients in Figure 8.23.

All coatings exhibited consistent microstructures due to diffusion kinetics remaining the same through the coatings. In the trials of both superalloys, the β-phase formed at the coating/interdiffusion zone interface, continued to the Al-rich edge of the β-NiAl field at the surface, providing stability through the coatings. The only exception to this pattern was in the eight hours aluminising CVD trial on IN738LC. In this case, as shown in Figure 8.13, γ+γ' phase appears approximately mid-way through the coating, which rapidly recovers to β-NiAl phase through to the coating surface. The coatings on both substrates contain alloying elements, In IN738LC coatings these form small particles. In CMSX-4 there are no particles, probably due to the absence of grain boundaries in the single crystal substrate. It is concluded that the aluminide coatings on both substrates are formed by outward diffusion.

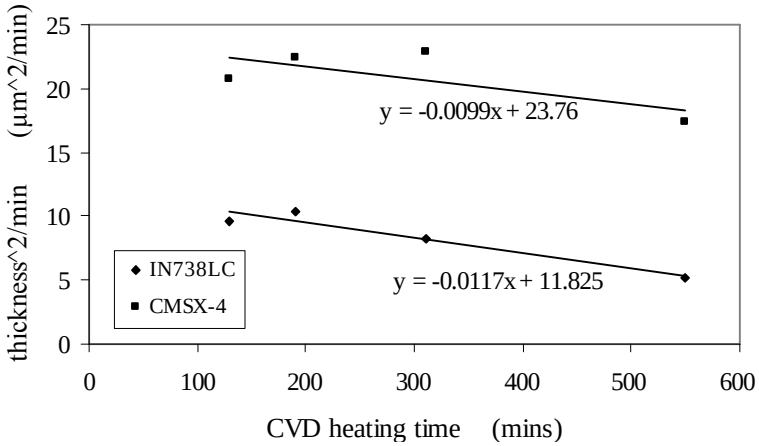

Figure 8.23: Aluminising CVD trials at 1050°C; Arrhenius plots of aluminide coating thickness against CVD heating time for IN738LC and CMSX-4

For IN738LC, the chromium content increased with heating times: content ranged from; 4 at%Cr to 8 at%Cr in the one hour trial, 5 at% to 9 at%Cr in the two hours trial, with 13 at%Cr average and 6 at%Cr at the coating surface, after the four hours trial and from 3 at% to 15 at%Cr in the eight hours trial. Chromium content in the coated CMSX-4 ranged from 5 at%Cr through the coating to 4 at%Cr at the surface, in all the trials. Cobalt interdiffused uniformly throughout the coatings, the content in each IN738LC sample being in the range 4 at%Co to 6 at%Co, but higher in CMSX-4 where the range averaged 7 at%Co.

Titanium was the alloying element with the highest content in the coatings, the content in IN738LC ranged from 2 at%Ti to 3 at%Ti, but averaged 1 at%Ti in samples of CMSX-4. The contents of molybdenum and tungsten in the coatings were at levels generally <1 at%. Depths of coatings ranged from; 41µm for the one hour CVD process to 62µm for the eight hours run, for IN738LC and, 53µm for the one hour CVD run to 88µm for the eight hours run, for CMSX-4

The next stage of novel coating development was to commence the silicon-aluminising trials.

8.4.2 Silicon-aluminising trials

8.4.2.1 Introduction and process

The objective of the silicon-aluminising trials was to determine the CVD soak temperature and soak period required to produce a novel coating having the following features:

- a stable silicon modified aluminide diffusion coating having the depth required to provide optimimum hot corrosion protection over a viable operational life;
- by interdiffusion into the coating of the hot corrosion protective elements chromium and cobalt, enhance its hot corrosion protection properties;
- avoid the formation of brittle silicide phases;
- avoid the interdiffusion of substrate strengthening elements into the coating, sufficient to jeopardise the mechanical strength of the substrate or to reduce hot corrosion protection provided by the coating.

For silicon-aluminising trials a low activity powder pack was used consisting of alumina, aluminum, silicon (content less than 10 wt%) and the activator aluminium fluoride, the proportions of which had been determined from MTDATA assessments. The five silicon-aluminising trials, carried out on sample discs of IN738LC and CMSX-4, used the same Cranfield University CVD equipment and methods as those for the aluminising trials. The CVD parameters of the first silicon-aluminising trial run, of a one hour soak period at a soak temperature of 1050^{o}C, followed on directly from the aluminising trials. The second and third silicon-aluminising trials, had soak periods of one hour, but were carried out at lower temperatures, to explore whether coating quality could be maintained, despite reducing process costs. Following the second and third silicon-aluminising CVD runs, it was concluded that the lower temperatures were inadequate to produce coatings of sufficient depth and stability. The decision was made to adopt a soak temperature of 1050^{o}C, but for the next silicon-aluminising trials to adopt shorter CVD soak periods, again with a view to reducing process costs. The fourth and fifth trials at this temperature, were carried out for CVD soak periods of 15 minutes and 30 minutes respectively. In summary, the following programme of siliconising trials, on IN738LC and CMSX-4, was carried out, the results being reported in this order, in this chapter:

(i) One hour CVD soak period at a temperature of 1050^{o}C,
(ii) One hour CVD soak period at a temperature of 800^{o}C,
(iii) One hour CVD soak period at a temperature of 850^{o}C,
(iv) Fifteen minutes CVD soak period at a temperature of 1050^{o}C,
(v) Thirty minutes CVD soak period at a temperature of 1050^{o}C.

8.4.2.2 Silicon-aluminising trials – results and discussion

Photographs of samples, taken after CVD at 800^{o}C for one hour, and before being divided, are shown in Figure 8.24, as typical examples. After cutting in half, one half sample was heat treated. All samples were then cleaned and mounted in conductive bakelite, then surface prepared and ultrasonically cleaned in IPA.

Figure 8.24: IN738LC and CMSX-4 samples after silicon-aluminising CVD for 1h at 800^{o}C

The heat treatment programme for IN738LC was: 2 hours at 1120^{o}C and then 24 hours at 843^{o}C and for CMSX-4, 2 hours at 1140^{o}C followed by 20 hours at 870^{o}C. The transformation to silicon containing diffusion coating by heat treatment is shown in Figure 8.25, which shows the changes in coating and interdiffusion zone microstructures.

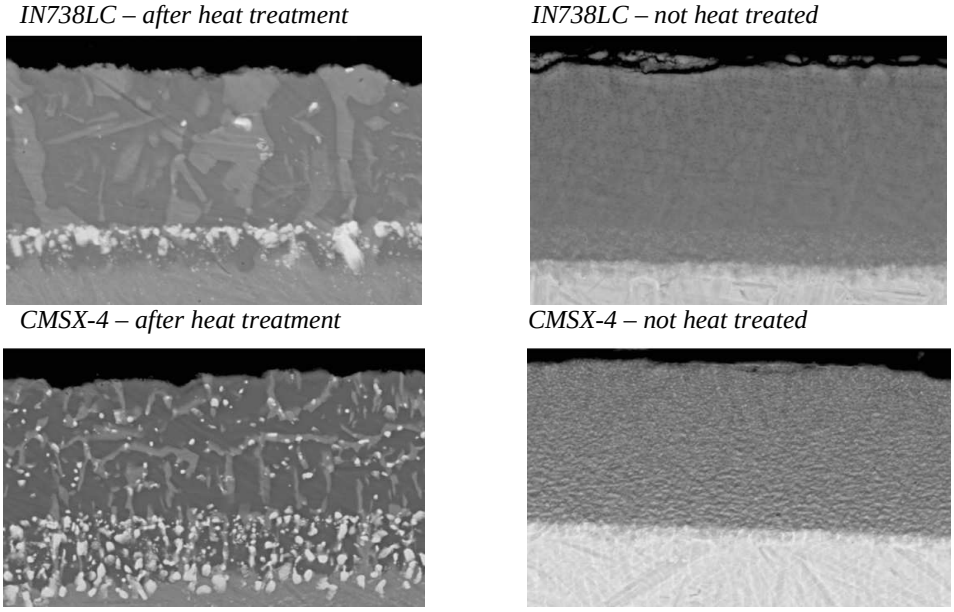

Figure 8.25: Silicon-aluminising CVD of one hour at 800^{o}C, BSE images of heat treated and not heat treated samples of IN738LC and CMSX-4

Coating depths in the non-post heat treatment state will be used in calculating activation energies, as for the aluminising trials, otherwise results will be considered only for post-CVD heat treated samples.

8.4.2.2 Silicon-aluminising trials; one hour silicon-aluminising CVD at 1050°C

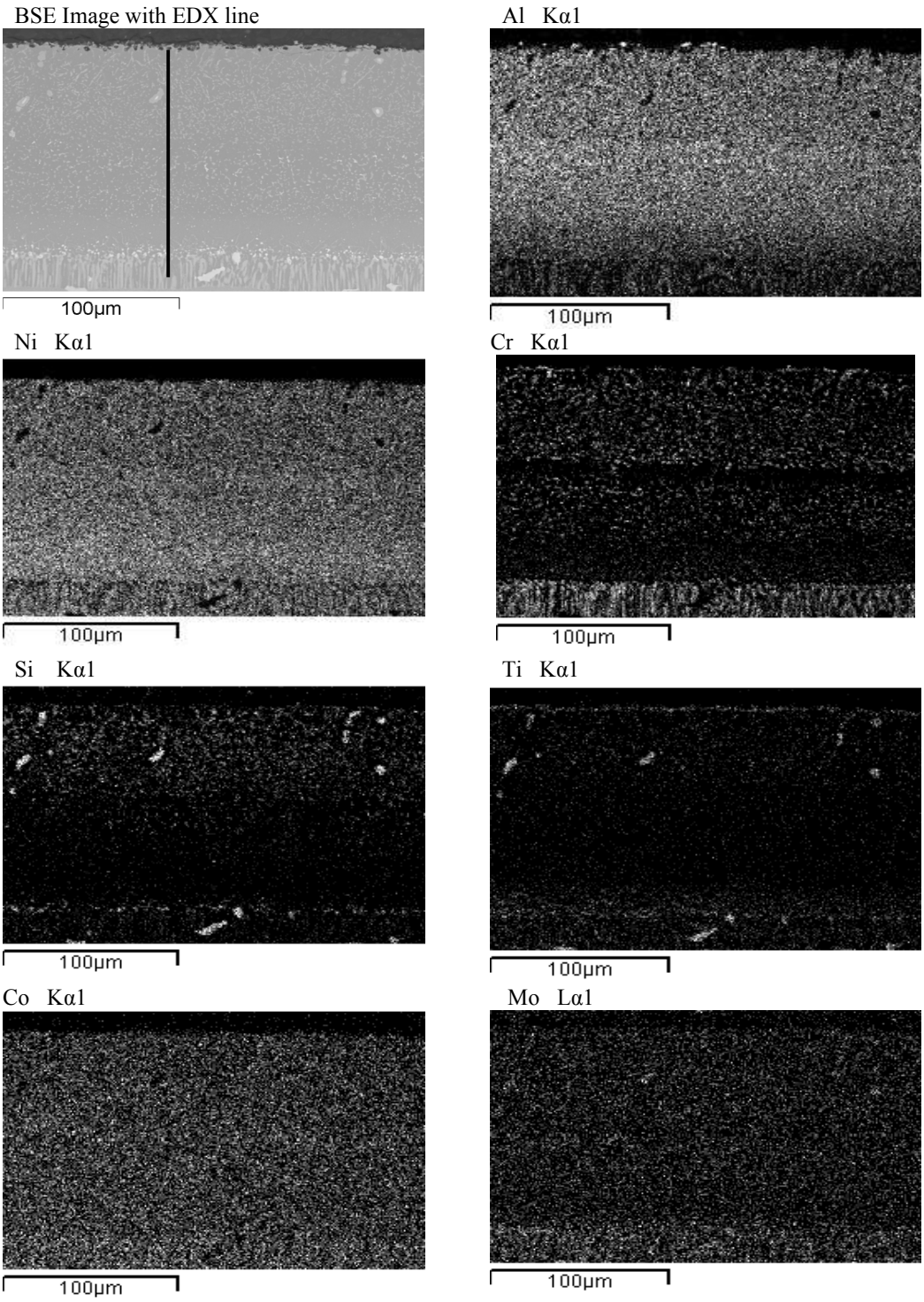

Figure 8.26: Silicon-aluminising trials; IN738LC, one hour silicon-aluminising CVD at 1050°C, element maps

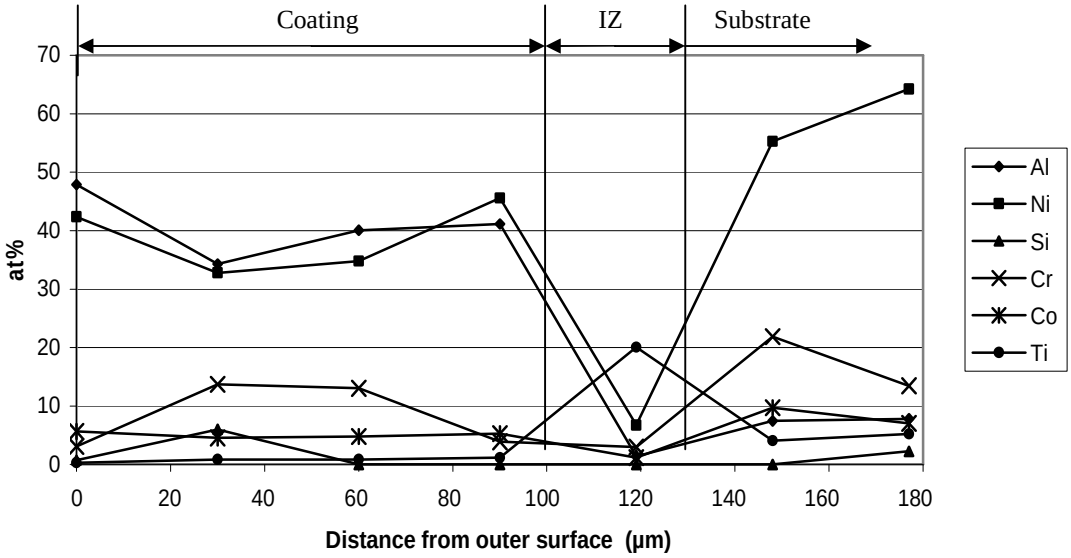

Figure 8.27: IN738LC; one hour silicon-aluminising CVD at 1050°C, main elements on EDX line scan shown in Figure 8.25

The BSE image map in Figure 8.26 shows the β-NiAl phase at the diffusion zone/ coating interface being stable as it proceeds through to the coating surface. The EDX line scan in Figure 8.27 indicates that this development commences approximately 100µm from the coating surface, and continues to the surface on the Al-rich edge of β-NiAl phase field. The stable, aluminium rich coating is enhanced by chromium interdiffusing from the substrate to a level of 14 at%Cr which falls away from a position 25µm from the surface, to 3 at%Cr at the surface. Cobalt interdiffuses to form a near constant 4 at%Co through to the coating surface.

Silicon is concentrated over the outer 60µm of the coating, the content averaging 3 at%Si. The average content of titanium which interdiffuses into the coating from the substrate is approximately 1 at%Ti. Silicon and titanium maps show local particles of titanium silicide or chromium silicide with titanium dissolved in it, from titanium precipitating from the substrate. Figure 8.28 shows one particle in the β-NiAl matrix as an example. The particle is also rich in outwardly diffused Cr, Co, and precipitates of Ta and W. Nucleation of these elements may have caused the particle to form.

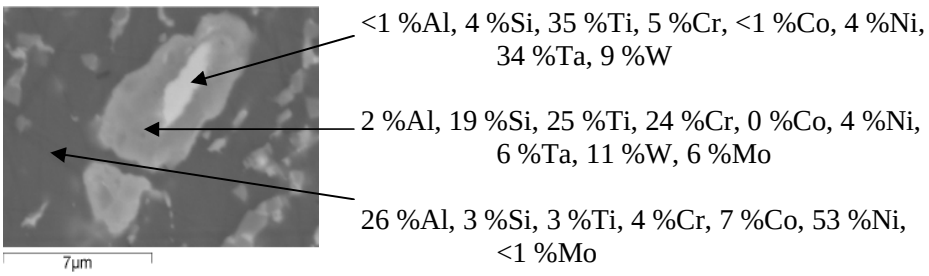

Figure 8.28: IN738LC; 1h silicon-aluminising CVD at 1050°C; elements in coating particle (at%)

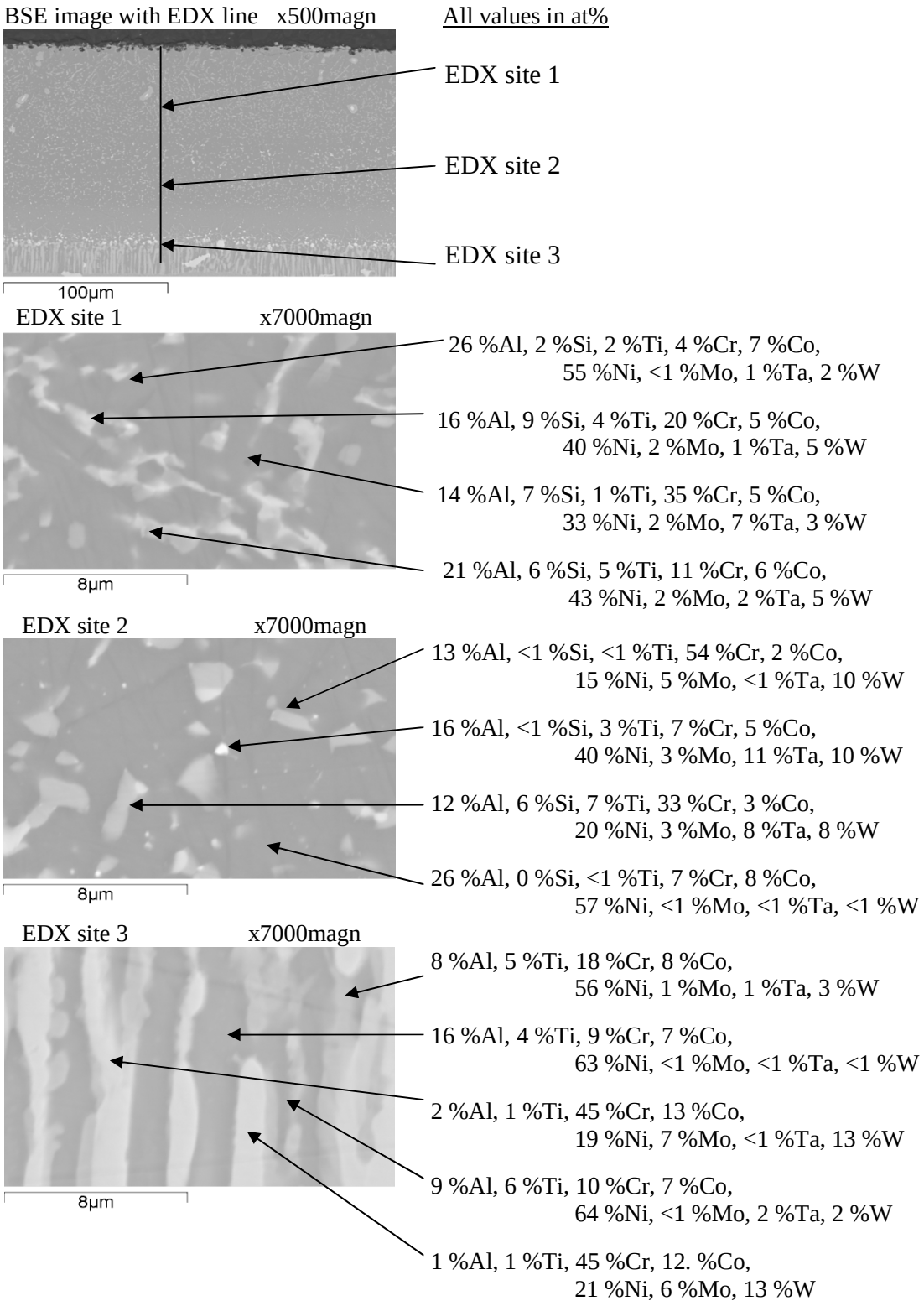

Figure 8.29: IN738LC, one hour silicon-aluminising CVD at 1050^{o}C, high magnification EDX element analyses of selected locations in coating

Figure 8.29 shows the transformation of the β-NiAl phase matrix through the diffusion zone to the Al rich edge of the β-NiAl phase field in the coating. The two phased microstructure interdiffusion zone with Ti, Cr, Co, Mo, Ta and W is seen in EDX site 3.

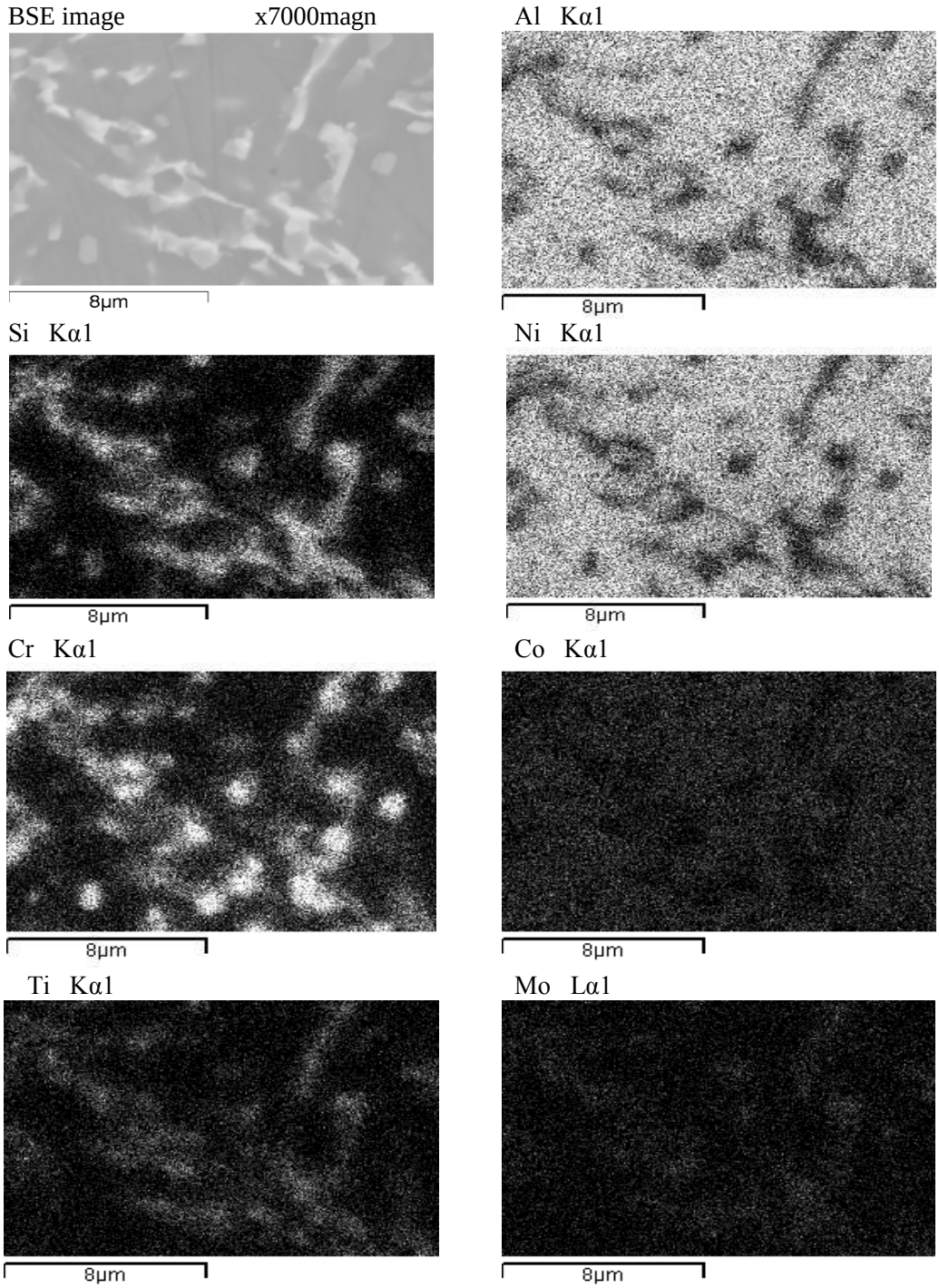

Figure 8.30: IN738LC; one hour silicon-aluminising CVD at 1050^{o}C, element maps of EDX site 1 in Figure 8.29

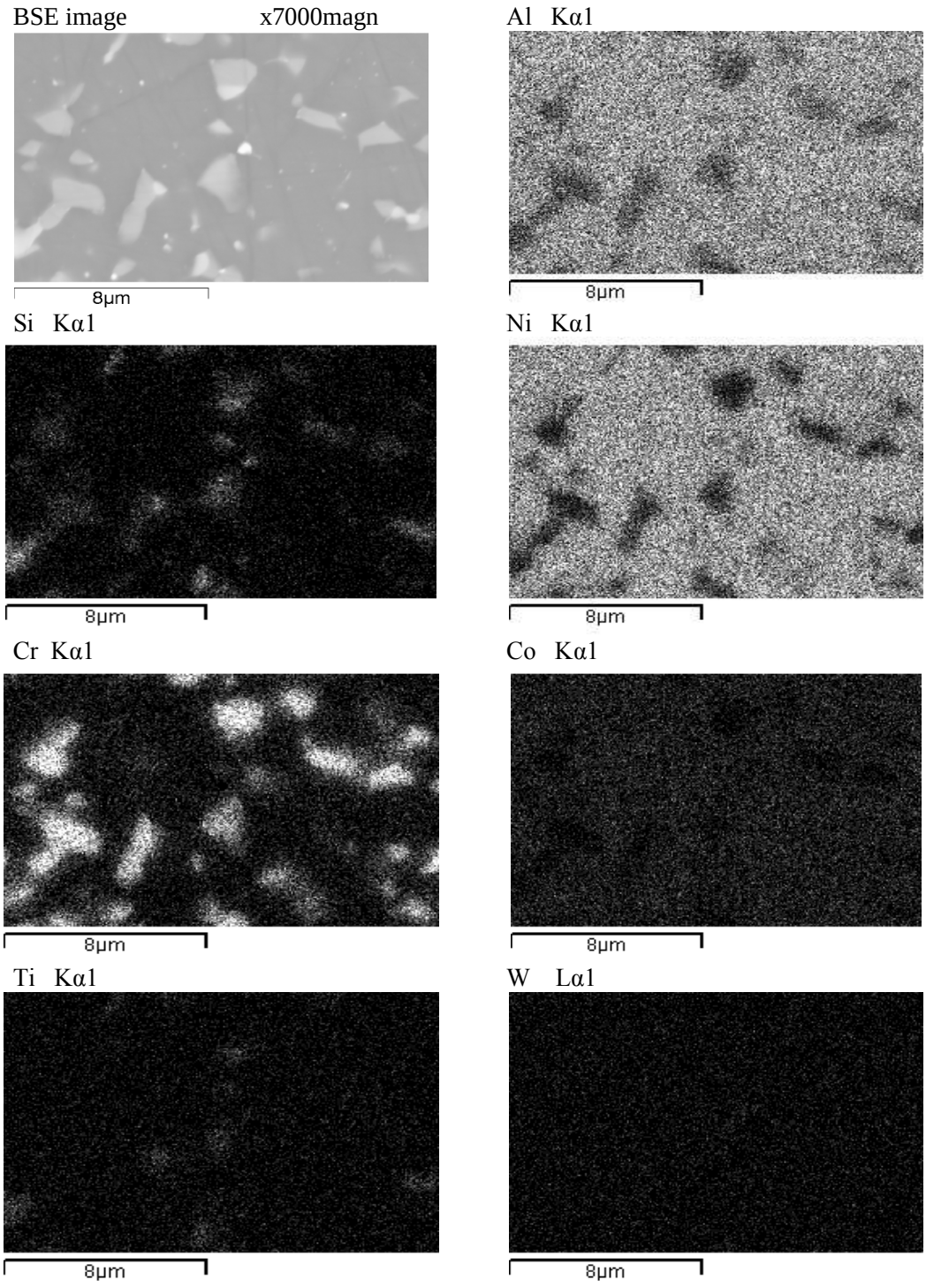

Figure 8.31: IN738LC; one hour silicon-aluminising CVD at 1050^{o}C, element maps of EDX site 2 in Figure 8.29

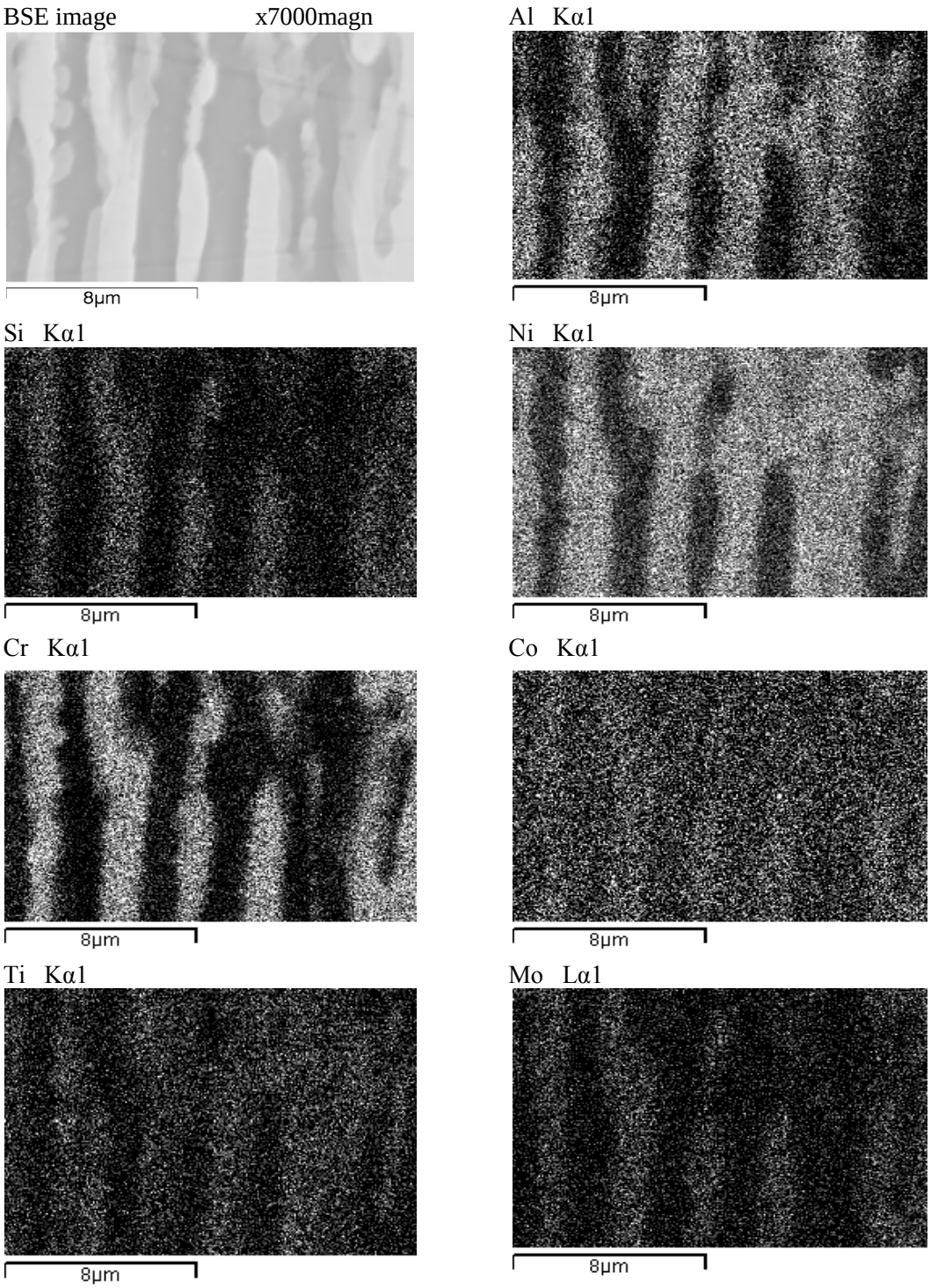

Figure 8.32: IN738LC; one hour silicon-aluminising CVD at 1050^{o}C, element maps of EDX site 3, the interdiffusion zone, in Figure 8.29

Maps in Figures 8.30 and 8.31 show that, following the silicon-aluminising CVD of IN738LC, for a soak period of one hour at 1050^{o}C, the stable β-phase NiAl matrix proceeds through the coating. Chromium silicides with lesser content of titanium and molybdenum continue in the matrix. At the surface the content of elements is typically in the region of 5 at%Cr, 6 at%Co, 1 at%Si, 1 at%Ti, 2 at%Mo, 2 at%Ta, 1 at%W. Titanium silicides, with compositions in the ranges 2-9 at%Si/2-5 at%Ti are present as pack particle inclusions in the outer region of the coating.. At the coating surface titanium forms a shallow titanium enriched intermetallic layer.

The maps in Figure 8.32 and element compositions set out in EDX site 3 on Figure 8.29 shows the interdiffusion zone and presence of substrate elements. From the interdiffusion zone, β-NiAl matrix forms as a result of the deposition of aluminium from the CVD pack. The coating proceeds to the surface which has a composition close to the Al-rich edge of the beta phase field. Diffusion of titanium and cobalt occurs through the coating, as shown in the higher magnification BSE in Figures 8.30 and 8.31. Chromium and molybdenum occur through the interdiffusion zone leading to precipitates of these elements in the coating. Precipitation requires supersaturation, this implies entrapment of Cr and Mo particles or solubility at temperature and precipitation on cooling.

The silicon and titanium BSE maps in Figure 8.32 show the intermetallic titanium silicide layer at the diffusion zone/ coating interface. From the silicon map in Figure 8.32 interdiffusion of silicon into the diffusion coating can be seen, but the EDX results show the silicon content to be too low to register. Titanium and chromium silicides, with compositions in the ranges 2-9 at%Si/1.5-5 at%Ti/4-35 at%Cr occur as pack particle inclusions towards the surface.

Silicon modification of the aluminide diffusion coating for IN738LC, has resulted in an average coating depth of 104μm, compared with 46μm for the aluminide coating, for the same CVD soak temperature and similar CVD heating time.

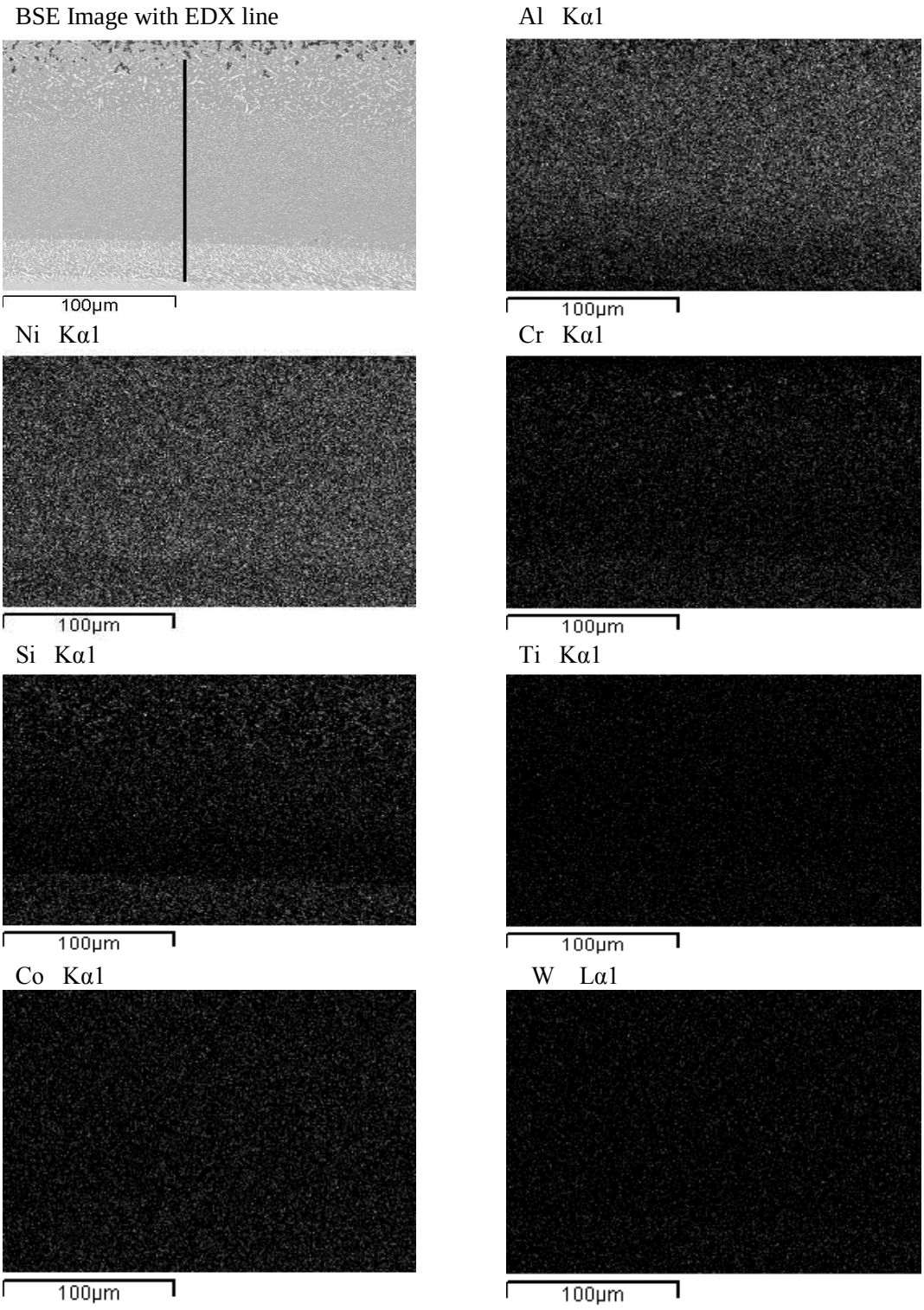

Figure 8.33: Silicon-aluminising trials; CMSX-4 one hour silicon-aluminising CVD at 1050^{o}C, element maps

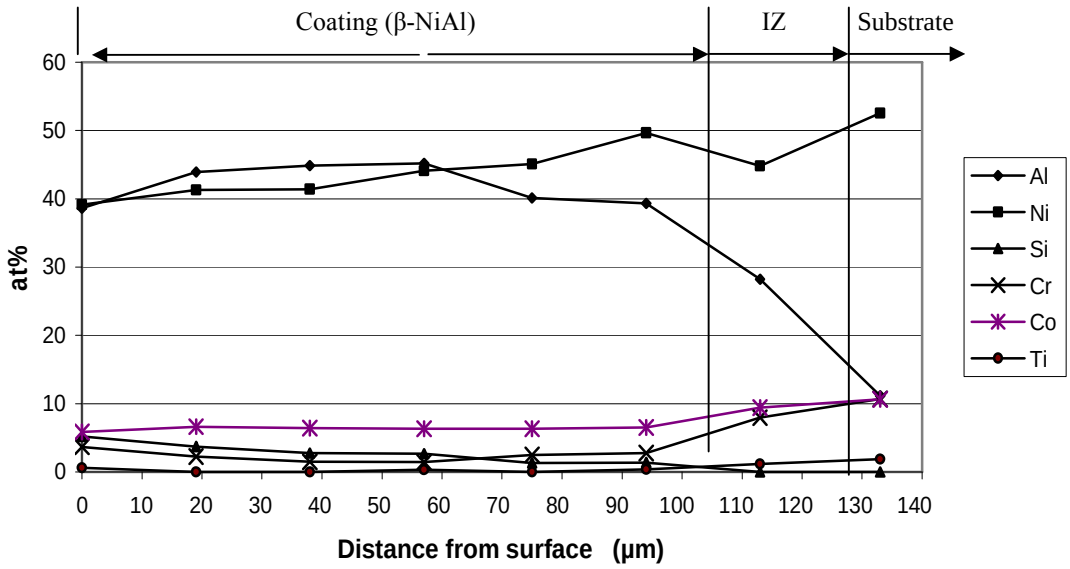

Figure 8.34: CMSX-4; one hour silicon-aluminising CVD at 1050°C, main elements on EDX line scan shown in Figure 8.33

Reference should be made to Figures 8.33 and 8.34 to obtain the overall results of the siliconising of CMSX-4, for one hour CVD soak period at 1050°C. Figure 8.35 provides the EDX elemental analyses, at higher magnification, at three sites in the coating. These results are supported by BSE maps of main elements at these sites, contained in Figures 8.36, 8.37 and 8.38. It is contended that a general description of the elemental analysis and microstructure will provide the reader with sufficient understanding of the results of this siliconising run. No individual, detailed analysis of each site will be provided here but reference to the high magnification figures will be made where additional clarification is required to explain a point, either here or in the discussion at the end of this chapter.

For this silicon-aluminising run, Figure 8.34 shows the consistent and stable β-NiAl phase matrix being maintained throughout the coating. Cobalt interdiffuses in the matrix at constant levels typically of 7 at%Co, to the coating surface. The coating contains concentrations of titanium, tantalum and tungsten silicides, formed from precipitates of these elements. Chromium rich silicides also containing some molybdenum and tungsten in solution (not shown in the figure to aid clarity) are uniformly distributed in the coating. The coating in general has a uniform microstructure, having no pronounced layers of the intermetallic compounds. Typical content of elements in the vicinity of the surface is; 0.54 at%Ti, 1.7 at%Cr, 8.8 at%Co, 0.64 at%Mo, 3.2 at%Ta and 3.9 at%W. Reference to Figure 8.36 shows there is little silicon and chromium contained in the matrix. Mid-coat, as seen in Figure 8.35, the particles are much smaller mid way through the coating, becoming larger in the outer one-third of the coating. In contrast, the interdiffusion zone, shown in Figure 8.38, has a well defined two phase structure where chromium, silicon, tantalum and tungsten, are partitioned to one phase with nickel, cobalt, aluminium to the second.

The average coating depth of 141μm of silicon modified aluminide coating of CMSX-4, after one hour silicon-aluminising CVD at 1050°C, can be compared with the average depth of 53μm after aluminising under the same CVD conditions.

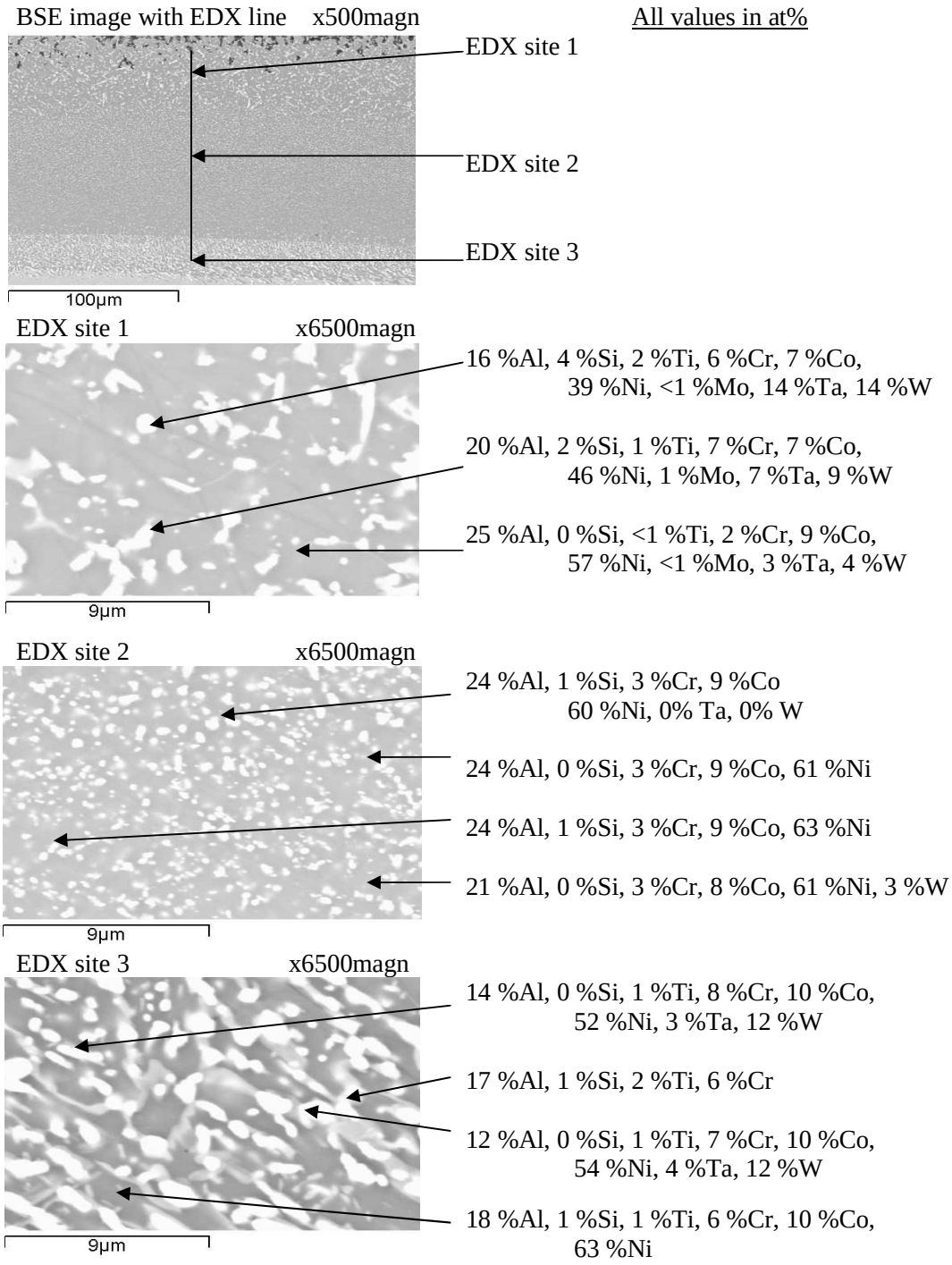

Figure 8.35 : CMSX-4; one hour silicon-aluminising CVD at 1050^{o}C, EDX element analyses of selected locations in coating

BSE element maps of the three EDX sites shown in Figure 8.35 are contained in Figures 8.36 (site 1), 8.37 (site 2) and 8.38 (site 3).

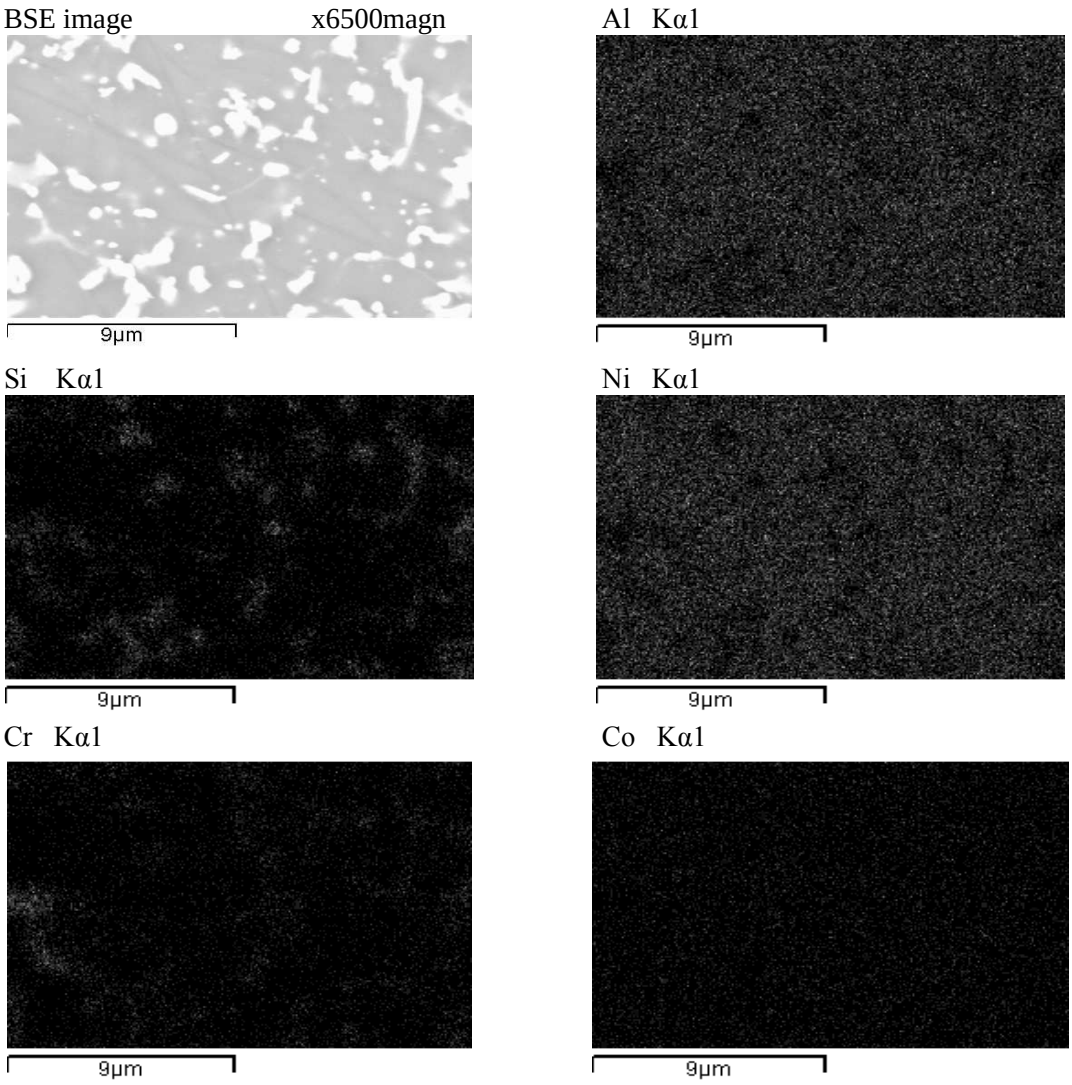

Figure 8.36 : CMSX-4; one hour silicon-aluminising CVD at 1050^{o}C, element maps of EDX site 1 in Figure 8.35

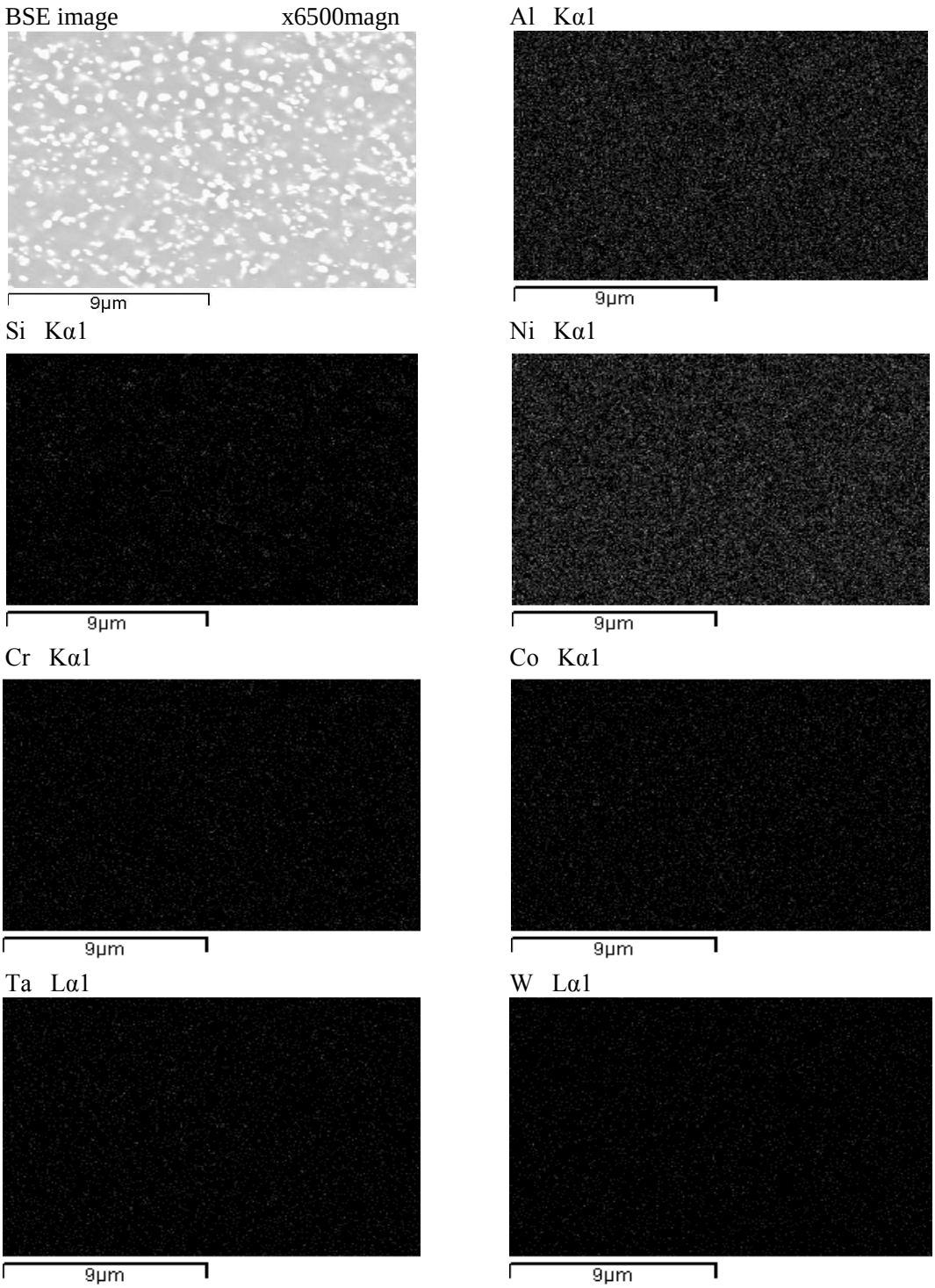

Figure 8.37 : CMSX-4; one hour silicon-aluminising CVD at 1050^{o}C, element maps of EDX site 2 in Figure 8.35

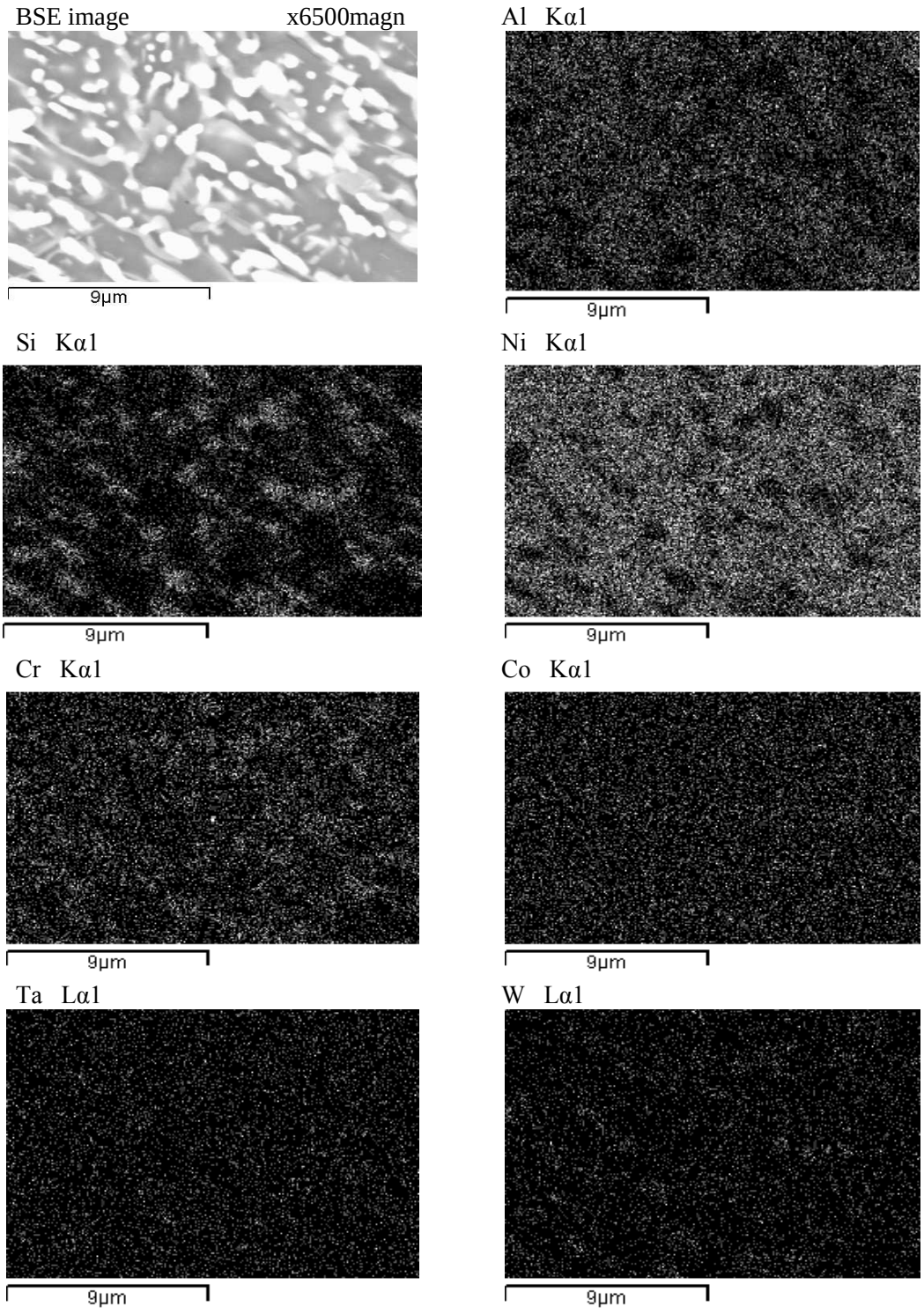

Figure 8.38 : CMSX-4; one hour silicon-aluminising CVD at 1050^{o}C, element maps of EDX site 3 in Figure 8.35

8.4.2.2 Silicon-aluminising trials: one hour silicon-aluminising CVD at 800°C

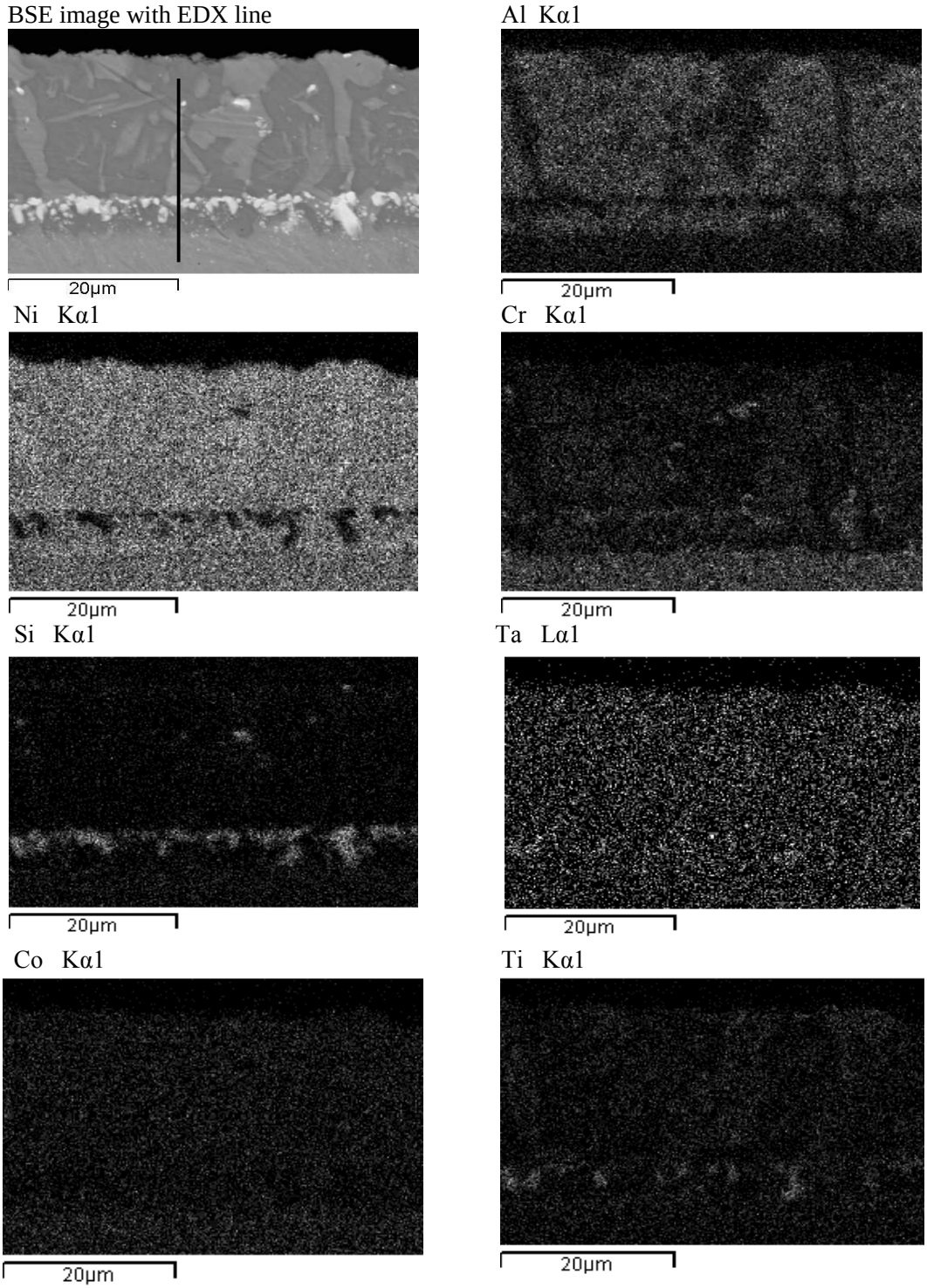

Figure 8.39: Silicon-aluminising trials; IN738LC, one hour silicon-aluminising CVD at 800°C, element maps

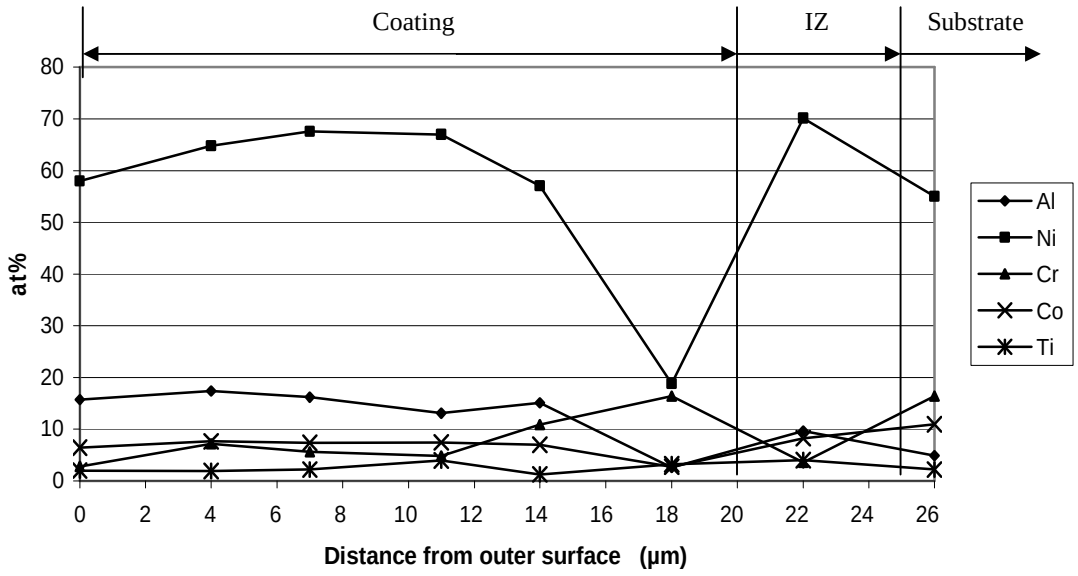

Figure 8.40: IN738LC; one hour silicon-aluminising CVD at 800°C, main elements on EDX line scan shown in Figure 8.39

The maps in Figure 8.39 clearly show that the lower soak temperature of 800°C results in a low aluminium containing coating, probably γ' Ni_3(Al, Ti) some 16 - 20 µm thick. Thus this diffusion treatment does not provide sufficient energy for the vapour deposition process to form a β-NiAl coating having the required content of aluminium, to provide hot corrosion protection. This lack of corrosion protection is compounded by the observed chromium which has been displaced by the aluminising front towards the IZ and matrix. Thus, the chromium content is low in the same areas of the coating where the aluminium content is also low. Areas deficient in both elements are clearly to be seen in the maps, and are expected to provide little hot corrosion protection, through the coating to the substrate.

From the map it can be seen that silicon is mainly concentrated at the IZ/ coating interface and there is insufficient process energy to enable it to modify the composition of the coating. The only silicon content identified in the EDX results was <1 at%Si at the coating surface.

The EDX results in Figure 8.40 confirm that, where aluminium is present the content is low, typically at 16 at%Al, through to the coating surface. The coating depth, averaging 19µm, is also inadequate to provide hot protection for a sufficient component life, even if the coating composition had been hot corrosion protective.

In summary, this coating is not expected to provide satisfactory hot corrosion protection and will not be adopted as a novel coating in this project.

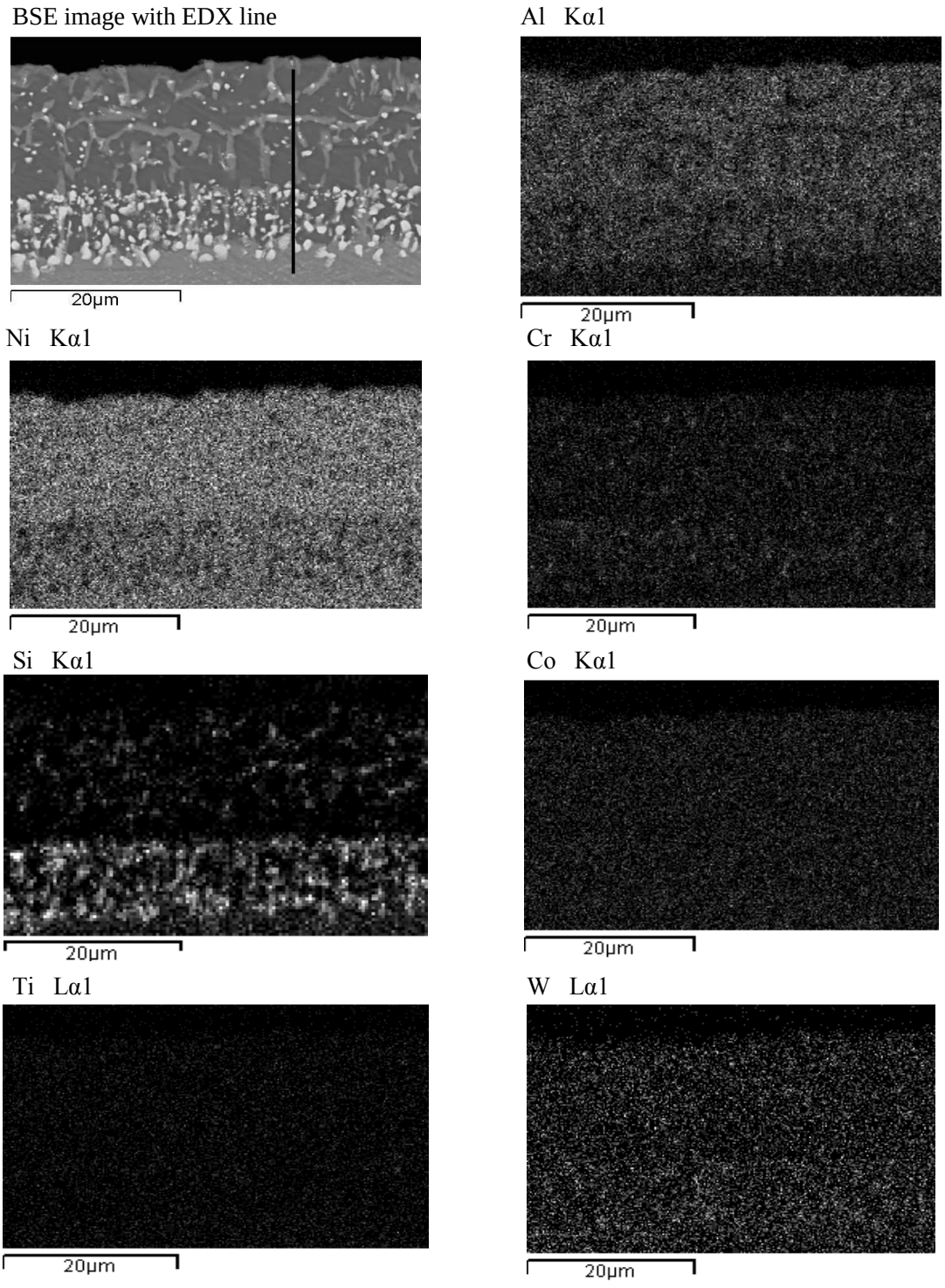

Figure 8.41: Silicon-aluminising trials; CMSX-4 one hour silicon-aluminising CVD at 800^{o}C, element maps

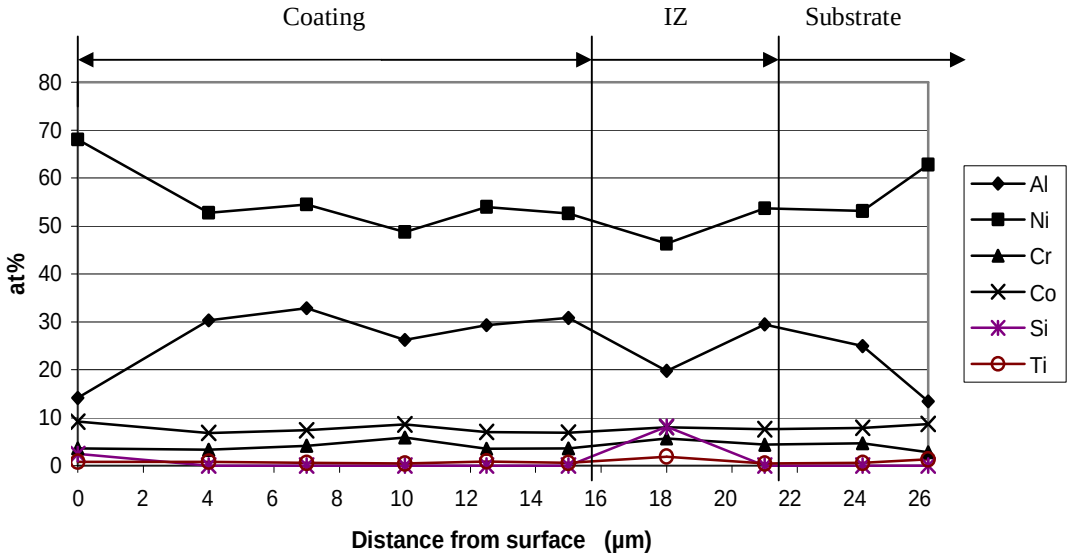

Figure 8.42: CMSX-4; one hour silicon-aluminising CVD at 800°C, main elements on EDX line scan shown in Figure 8.41

Figure 8.42 shows the β-NiAl phase from the IZ to the surface of the coating where it becomes Ni_3Al. This phase change results in an expected reduction of hot corrosion protection at the coating surface. Hot corrosion protection provided by chromium is also jeopardised by its formation due to outward nickel diffusion from the matrix, causing chromium deficiency which coincide with areas of lower aluminium content. These deficiencies are thought to be due to the formations of regions of γ', which can only contain up to 8 at%Cr in solution. Silicon remains concentrated at the coating/substrate interface with the diffusion zone.

Further, the average depth of coating produced by these CVD soak conditions was 15µm, which is inadequate for the proposed hot corrosion service.

In summary, the silicon modified aluminised coating produced by a one hour CVD soak period at a temperature of 800°C is not considered suitable for providing hot corrosion protection coatings for CMSX-4 and in this thesis no further consideration will be given to its adoption as a novel coating.

8.4.2.3 Silicon-aluminising trials: one hour silicon-aluminising CVD at 850°C

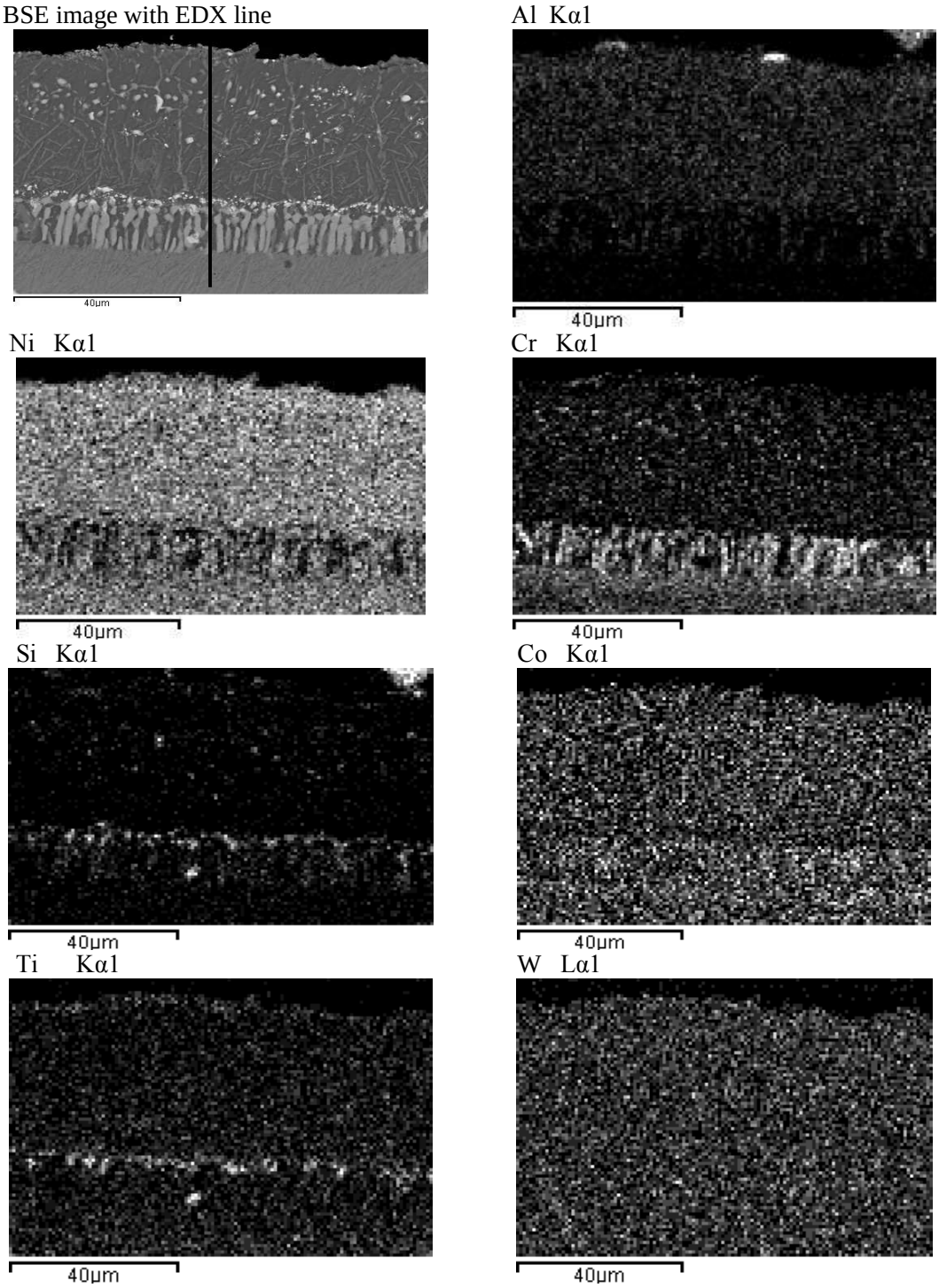

Figure 8.43: Silicon-aluminising trials; IN738LC one hour silicon-aluminising CVD at 850°C, element maps

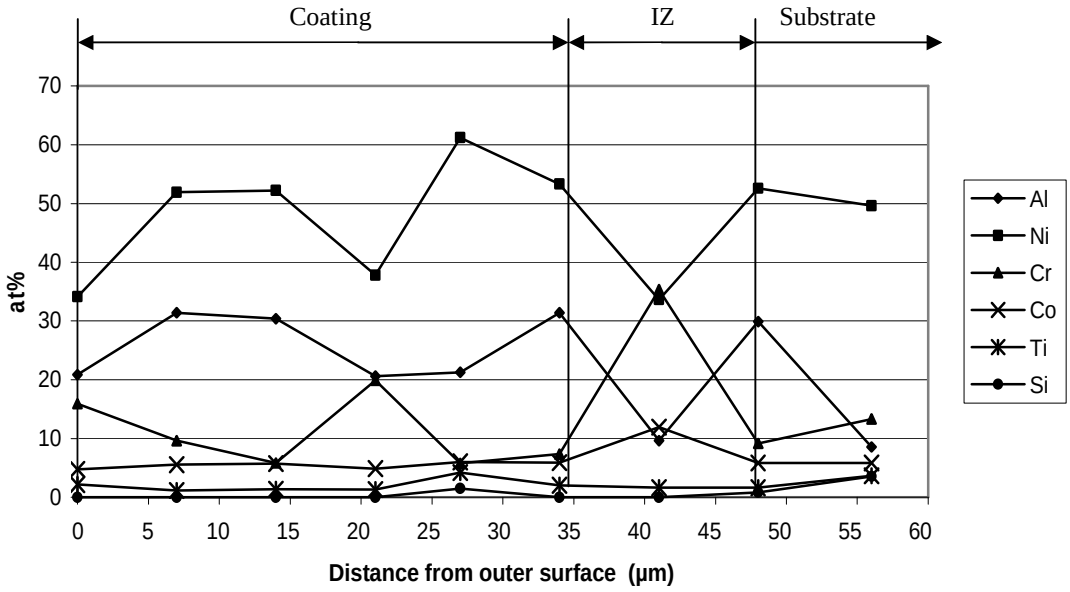

Figure 8.44: IN738LC; one hour silicon-aluminising CVD at 850°C, main elements on EDX line scan shown in Figure 8.43

The maps seen in Figure 8.43, show that the β-NiAl coating at the IZ/ coating interface progresses through a γ' phase approximately 27µm from the coating surface, then remains stable β-phase to the surface. At the coating surface the reducing content of nickel and aluminium may be due to partially analysing a surface oxide.

This coating should provide satisfactory hot corrosion protection, possibly enhanced by the chromium content, although some of this, as shown in the chromium map, could be in the form of chromium intermetallics in the chromium rich precipitates.

The higher CVD soak temperature of this trial provides a deeper coating, having an average depth of 35µm, than that from the silicon-aluminising trial at 800°C. However, the coating from the CVD soak conditions in this trial is not expected to provide hot corrosion protection for sufficient duration and it will not be considered further in this coating development programme.

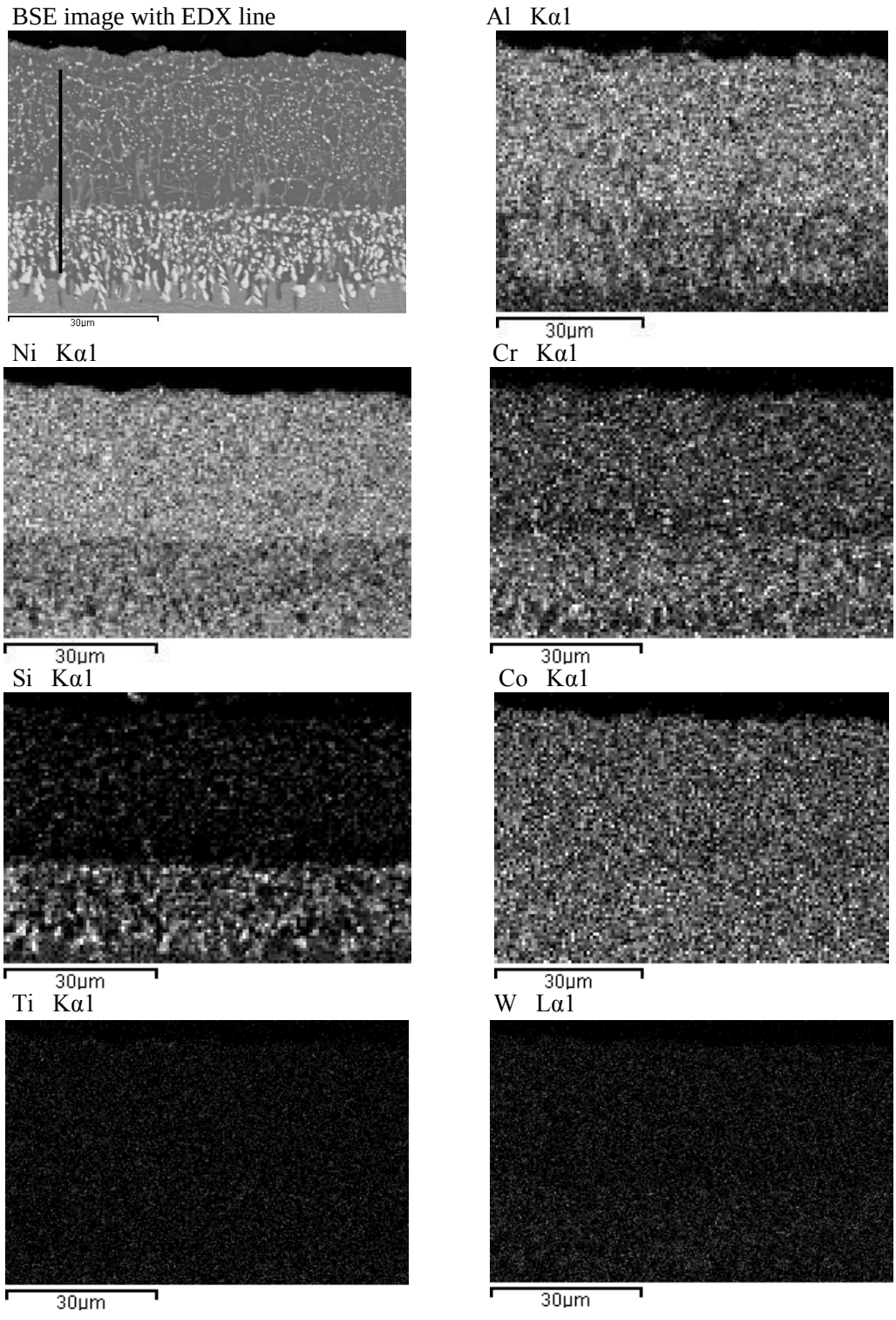

Figure 8.45: Silicon-aluminising trials; CMSX-4 one hour silicon-aluminising CVD at 850^{o}C, element maps

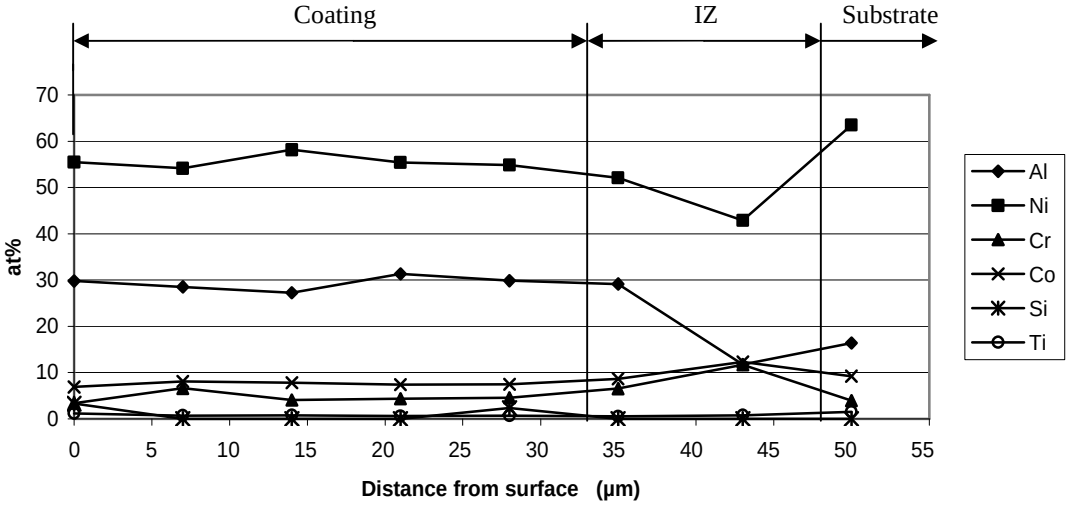

Figure 8.46: CMSX-4; one hour silicon-aluminising CVD at 850^{o}C, main elements on EDX line in Figure 8.45

The EDX results in Figure 8.46 show the β-phase remaining generally stable throughout the coating. The figure also shows the content of aluminium remains at around 30 at%Al in the coating.

The microstructures of alloying elements in the coating are similar to those seen in previous trials. Chromium and cobalt are uniformly distributed in the coating and also in the IZ. In this sample silicon is uniform in the coating but provides a silicon rich IZ, this is typical for CMSX-4 samples, whereas in IN738LC samples, it is mainly the IZ/coating region which is rich in silicon.

It is considered that the energy created from the CVD soak temperature of 850^{o}C, for a soak period of one hour, provides an adequate aluminium rich coating through to the surface. However, the average coating depth of 33µm is considered to be inadequate for industrial service in aggressive environments and, leads to the conclusion that the coating will not be sufficiently hot corrosion protective to justify consideration in this study. Thus, the CVD conditions used in this trial will not be considered further for developing novel coatings in this project.

8.4.2.4 Silicon-aluminising trials: fifteen minutes silicon-aluminising CVD at 1050^{o}C

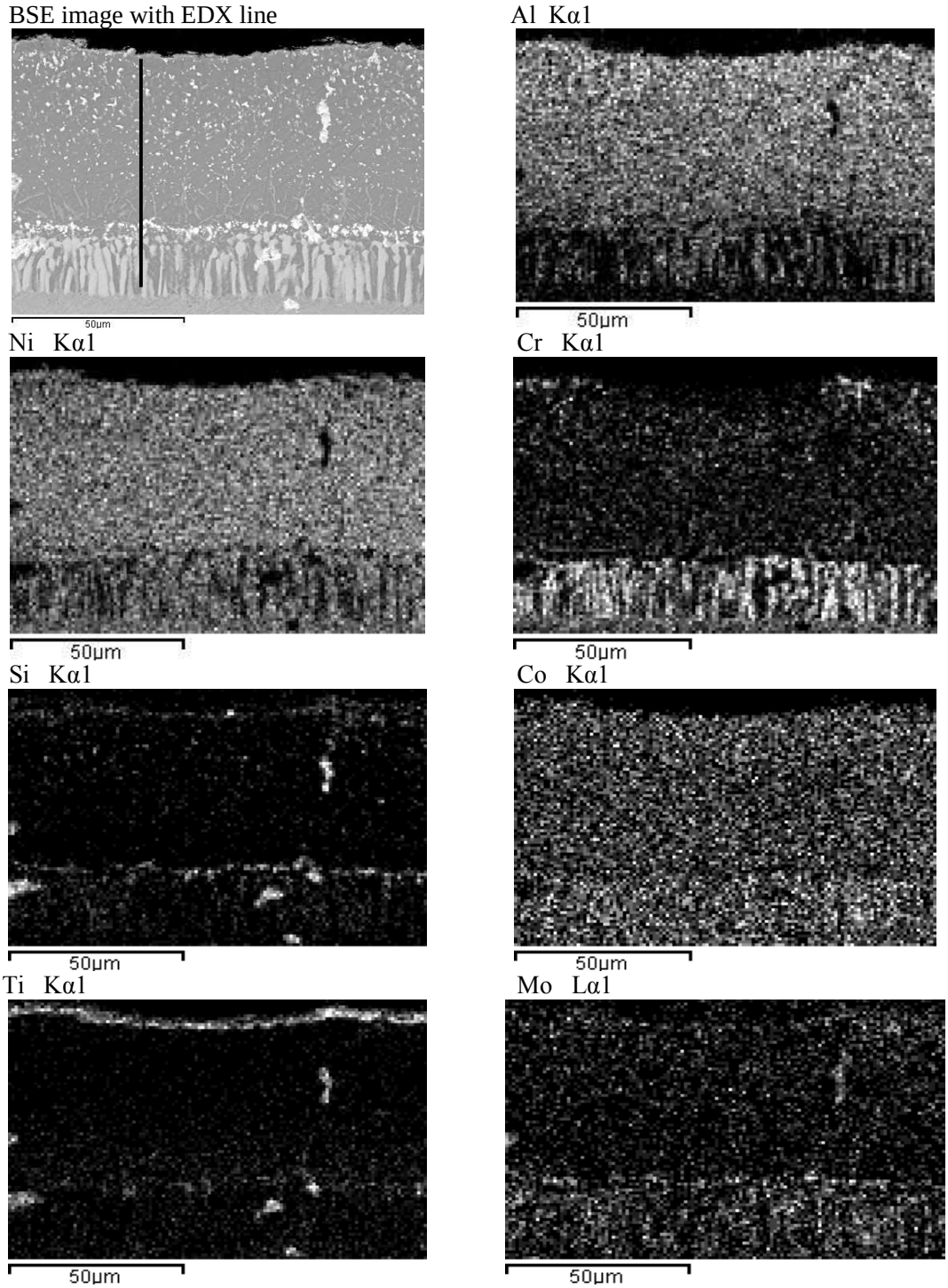

Figure 8.47: Silicon-aluminising trials; IN738LC, 15 minutes silicon-aluminising CVD at 1050^{o}C - element maps

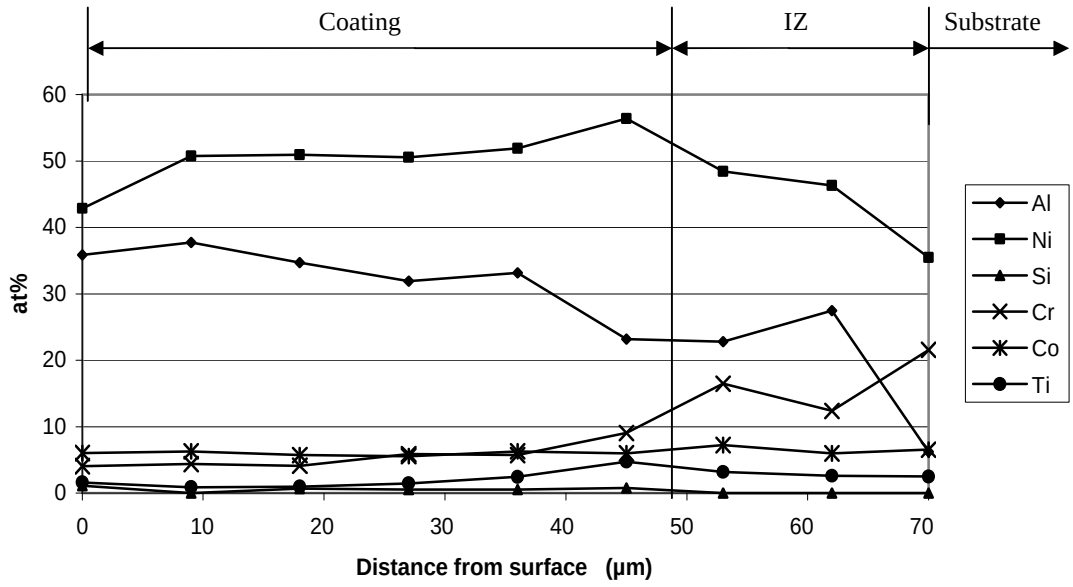

Figure 8.48: IN738LC; 15 minutes silicon-aluminising CVD at 1050^{o}C, main elements on EDX line in Figure 8.47

The maps in Figure 8.47 illustrate how the increased thermal energy provided by the higher CVD soak temperature, compared with the previous lower temperature trial runs, has produced a uniform, aluminium rich coating. The EDX results in Figure 8.48 show the stable β-phase proceeding through the coating, becoming increasingly aluminium rich to the surface, where the content is 36 at%Al. Hot corrosion protection will be enhanced by the outward diffusion of chromium and cobalt, averaging 5 at%Cr and 7 at%Co respectively, from the substrate into the coating matrix. Thus this coating has acceptable thickness and composition to be considered for service under hot corrosion conditions.

Silicon and titanium are generally distributed in the coating with contents of around <1 at%Si and 2 at%Ti, and form thin intermetallic layers at the IZ/coating interface and coating surface. Particles rich in silicon, titanium and, to a lesser extent molybdenum, randomly occur in the coating.

The average coating depth of 49µm, resulting from 15 minutes CVD soak time at 1050^{o}C, may be sufficient to provide hot corrosion protection for viable operational service.

In summary, it is considered that the coating produced in this trial run has the potential to provide hot corrosion protection for IN738LC, for a limited service life. Low levels of outward diffusion of titanium and molybdenum may reduce mechanical integrity of the substrate. However, this coating offers sufficient hot corrosion protection to consider it as a novel coating in this project.

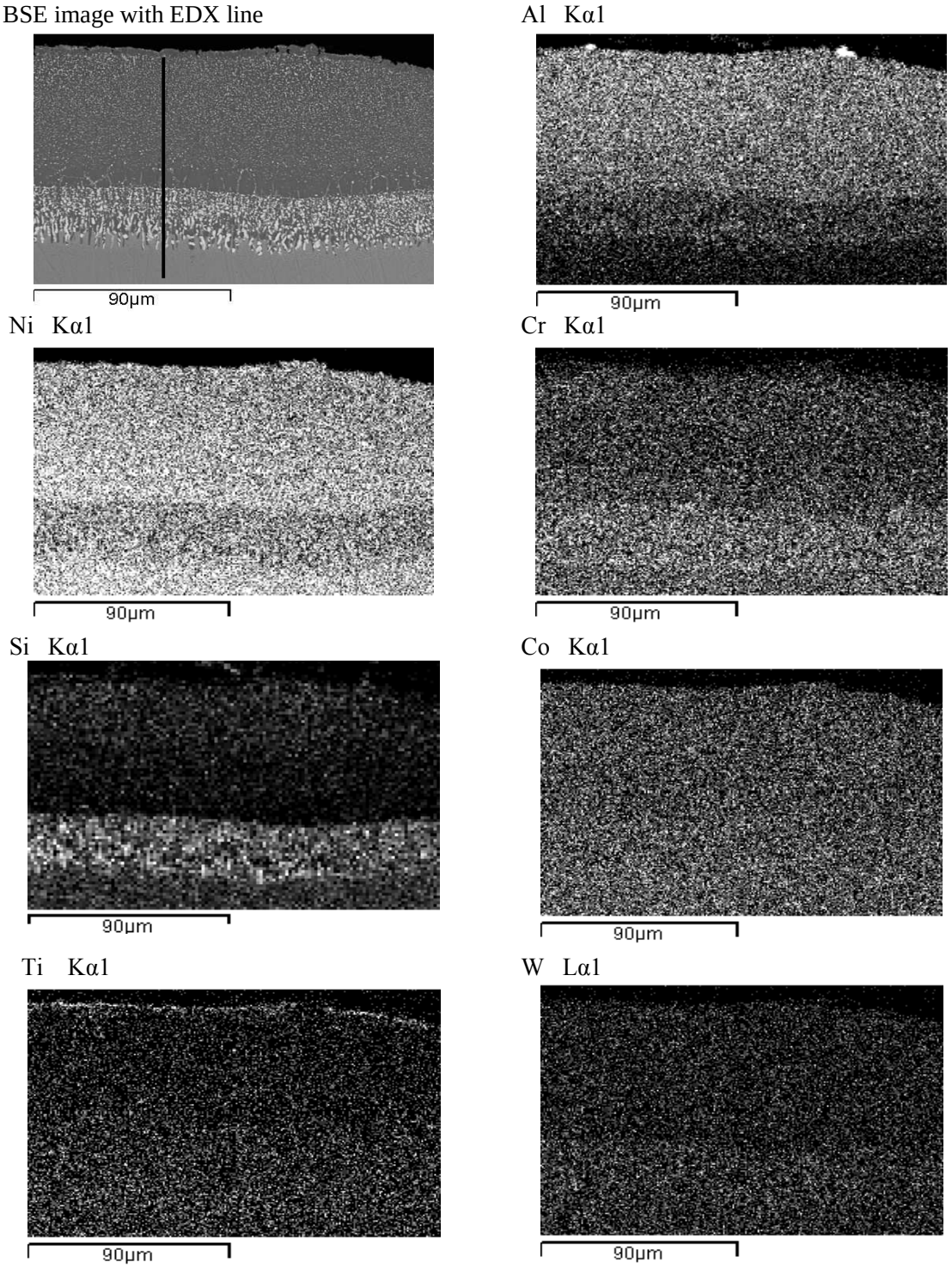

Figure 8.49: Silicon-aluminising trials; CMSX-4, 15 minutes silicon-aluminising CVD at 1050^{o}C - element maps

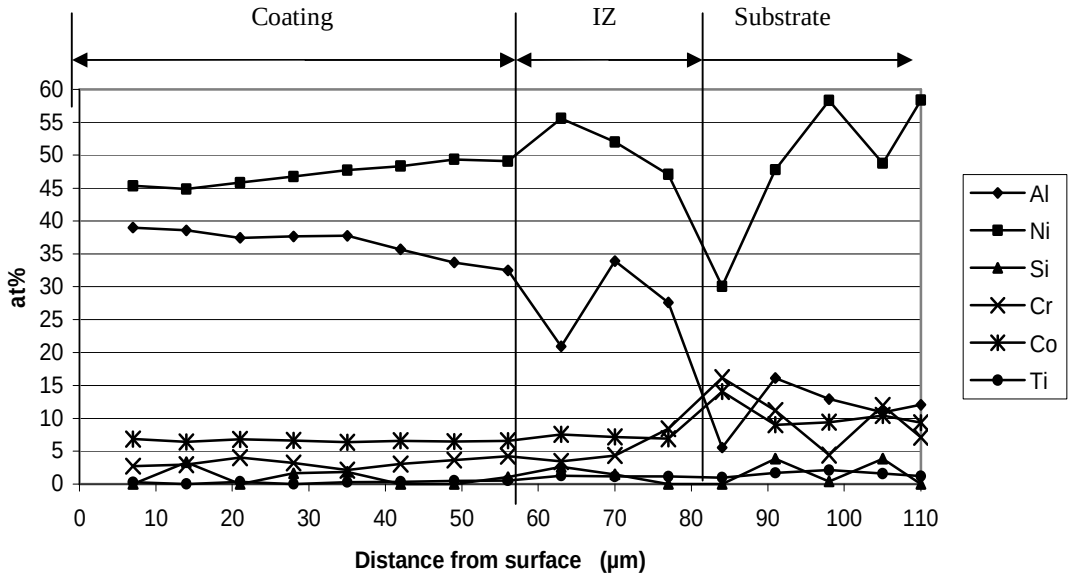

Figure 8.50: CMSX-4; 15 minutes silicon-aluminising CVD at 1050°C, main elements on EDX line scan shown in Figure 8.49

The maps in Figure 8.49 show the uniform microstructures of nickel and aluminium in the coating. From the EDX data in Figure 8.50, it is seen that the β-NiAl phase coating remains stable through the coating, the increasing aluminium content being countered by the reducing nickel content. There may be some γ'-phase (Ni_2Al) formed at grain boundaries, towards the outer region of the IZ, in Figure 8.49 the γ'-phase occurs around 63µm from the coating surface. From this region, β-NiAl phase continues with increasing aluminium content to the surface. At the coating surface, the 38 at%Al has the potential, to sustain scale growth and hence maintain the initiation stage of hot corrosion.

It is doubtful whether the low chromium content through the coating, averaging 3 at%Cr, could enhance hot corrosion protection of this coating. Cobalt, which averages 7 at%Co, in the coating matrix, may contribute to hot corrosion protection provided by the coating .

Outward diffusion of titanium forms a titanium enriched intermetallic at the coating surface, where the content is 2 at%Ti. Particles rich in molybdenum and tungsten are uniformly distributed in the coating.

This coating has the potential to protect CMSX-4 against hot corrosion, and having an average depth of 56µm, it will be considered further as a novel coating in this project.

8.4.2.5 Silicon-aluminising trials: thirty minutes silicon-aluminising CVD at 1050°C

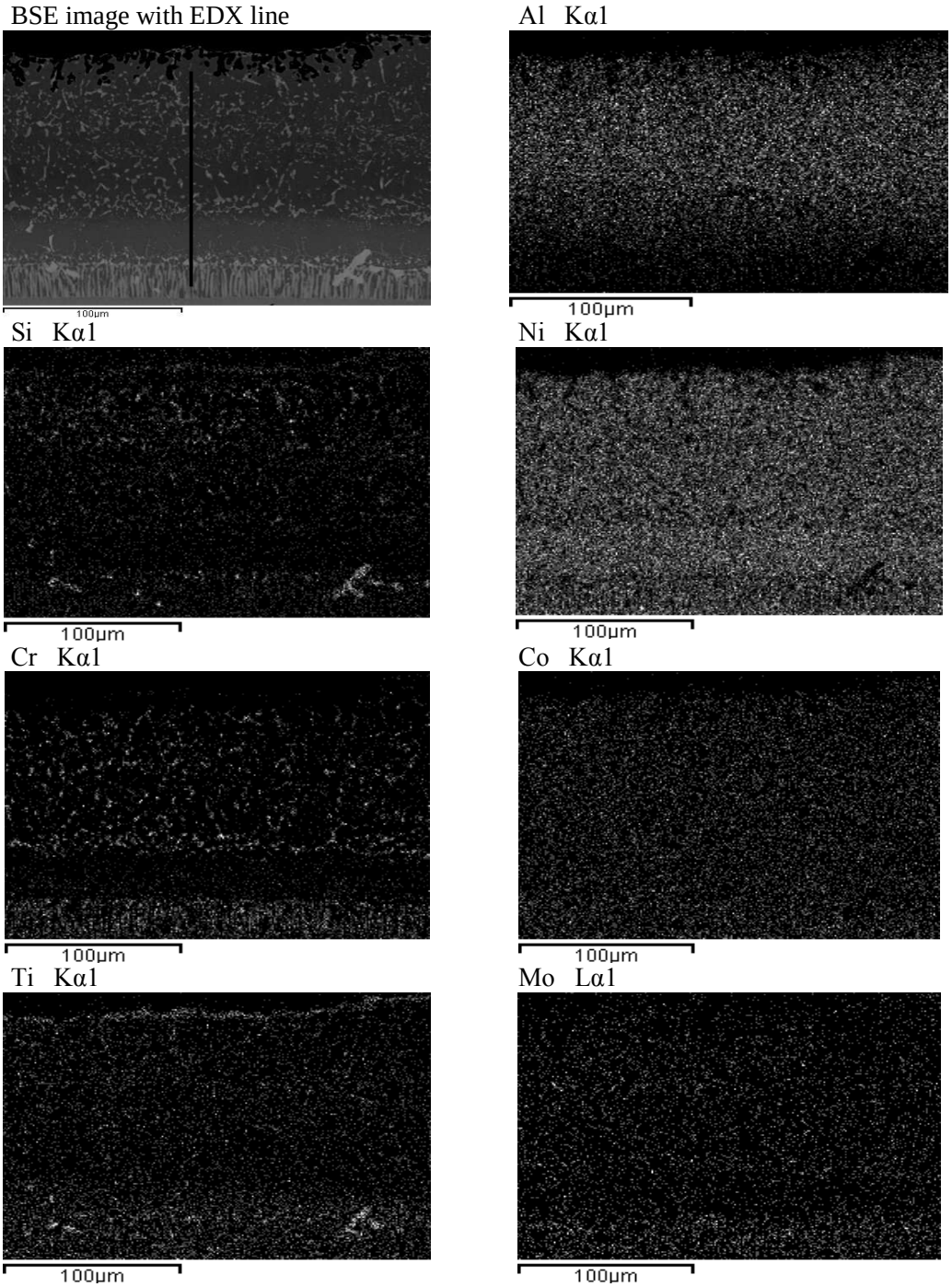

Figure 8.51: Silicon-aluminising trials; IN738LC, 30 minutes silicon-aluminising CVD at 1050°C - element maps

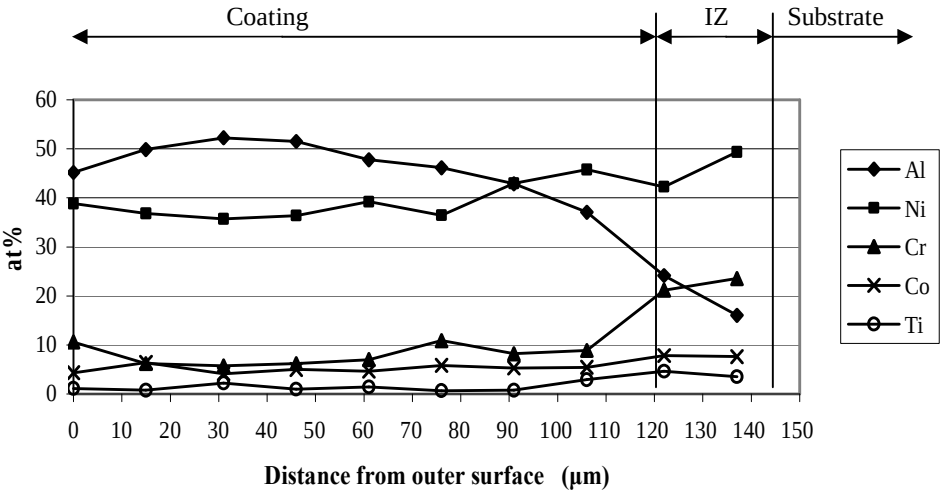

Figure 8.52: IN738LC; 30 minutes silicon-aluminising CVD at 1050°C, main elements on EDX line scan shown in Figure 8.51

The maps in Figure 8.51 show a generally stable and uniform β-NiAl phase through the coating. In Figure 8.52 the coating matrix is seen to progress at the Al-rich edge of the β-phase field. Through the uniform coating the aluminium content averages 50 at%Al, thus providing feedstock for scale growth to maintain the initiation stage in a hot corrosion initiating environment. The outer 5µm of the coating is very coarse and shows some internal oxidation and is expected to be less protective in such an environment.

Chromium interdiffuses from the substrate into the coating and, as seen in Figure 8.53, the matrix in EDX site 1 contains 8 at%Cr and 5 at%Co, enhancing hot corrosion protection provided by the coating. Also randomly distributed in the matrix, in EDX site 1, are particles which consist of 46 at%-57 at%Cr, 16 at%-20 at%Si, 3 at%-4 at%Ti, <1 at%-3 at%Ta and 3 at%-5 at%W. The layer of coating seen in EDX site 2 also contains 7 at%Cr in the matrix and particles containing 7 at%Mo, <1 at%-3 at%Ta and <1 at%-14 at%W.

In both EDX sites 1 and 2, shown in Figure 8.53, titanium outwardly diffuses into the coating in the range <1 at%-2 at%Ti and in randomly distributed particles, with content in the range <1 at%-5 at%Ti. These particles also contain traces of Mo, Ta and W.

It is concluded that the coating produced from 30 minutes silicon-aluminising CVD, at a soak temperature of 1050°C, should provide significant hot corrosion protection for IN738LC, mainly resulting from the Al-rich matrix and its average depth of 96µm. This coating is considered to be suitable for testing as a novel coating in this project.

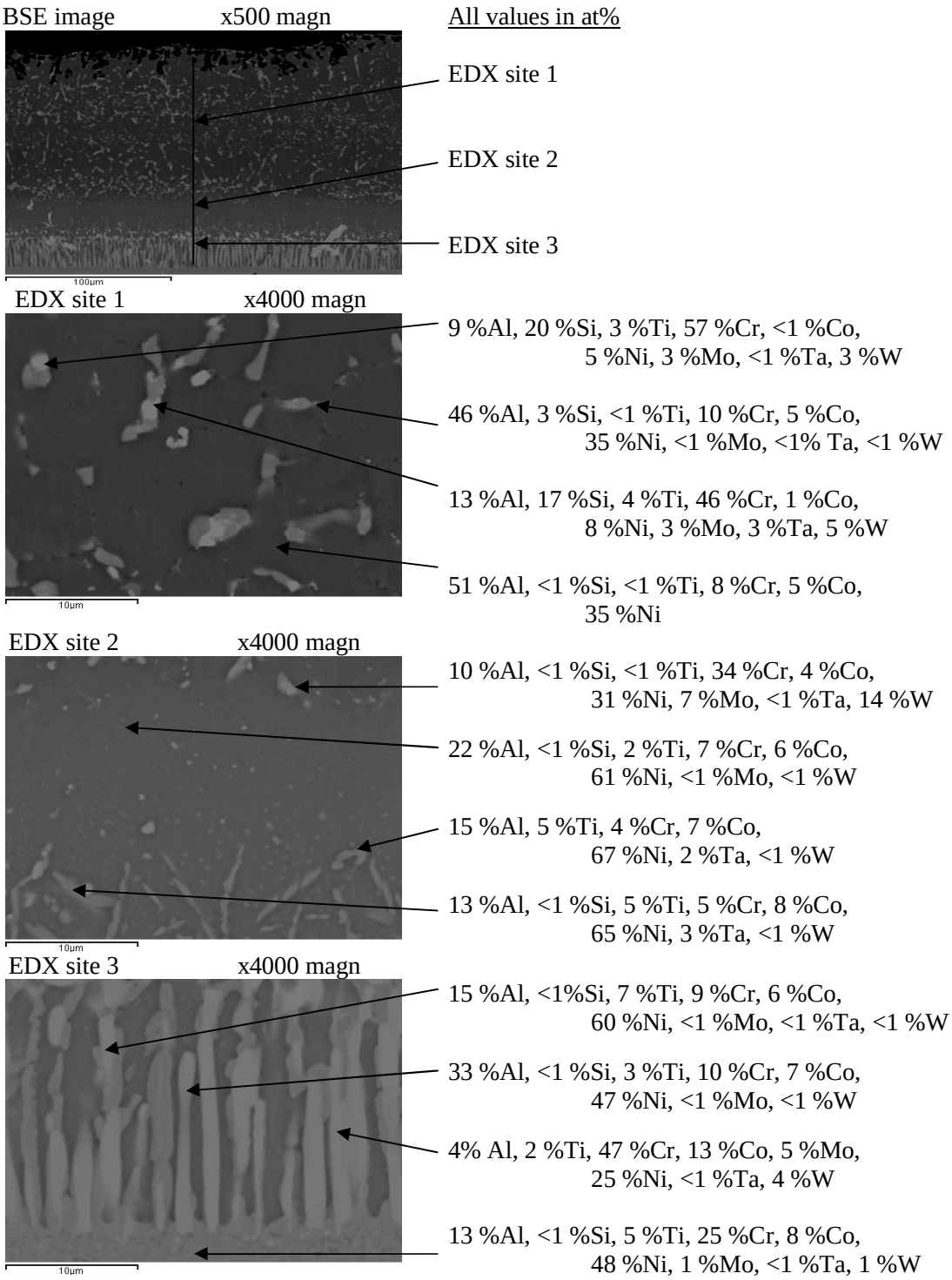

Figure 8.53: IN738LC; 30 minutes silicon-aluminising CVD at 1050^{o}C, high magnification EDX element analyses of selected sites in the coating

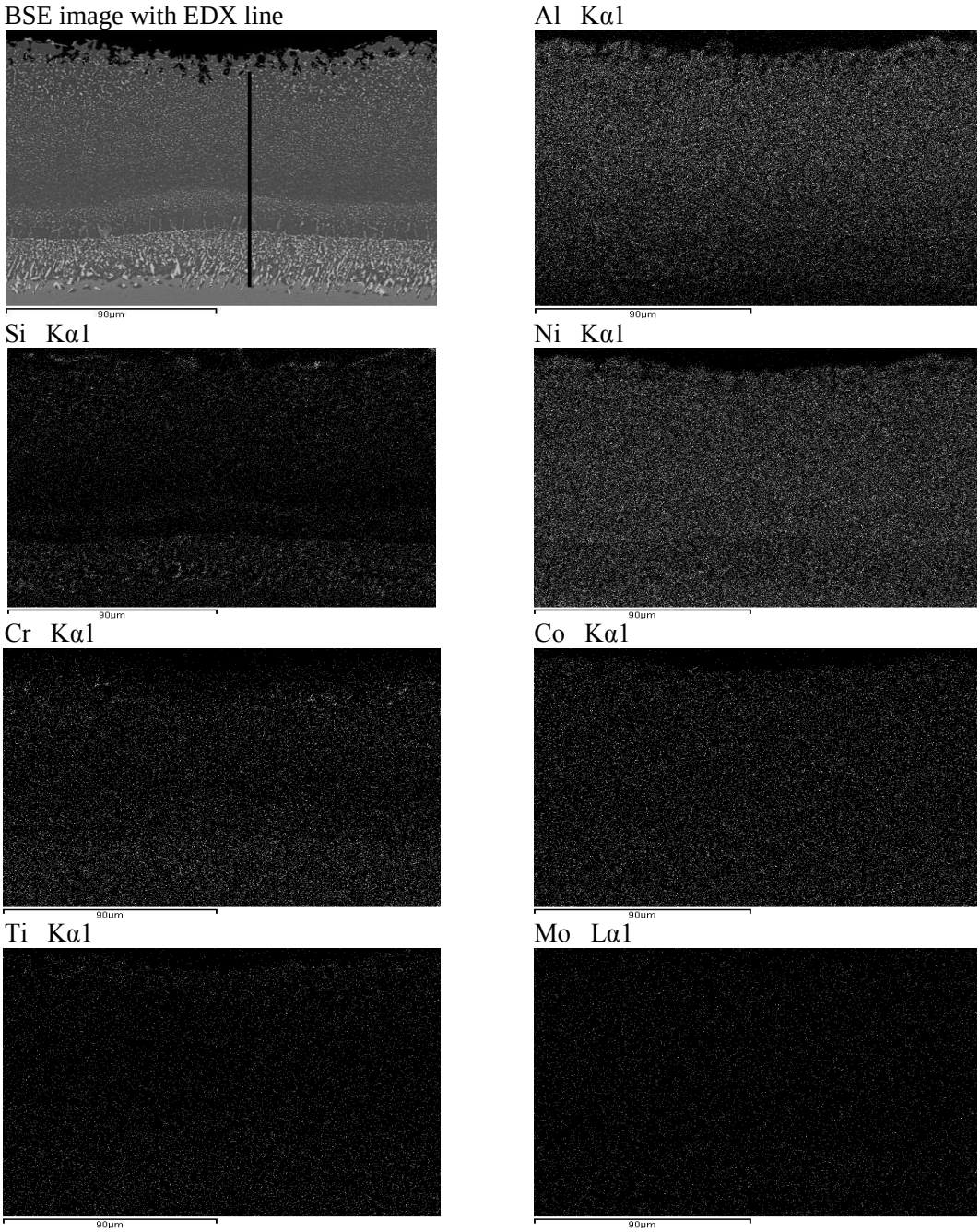

Figure 8.54: Silicon-aluminising trials; CMSX-4, 30 minutes silicon-aluminising CVD at 1050^{o}C - element maps

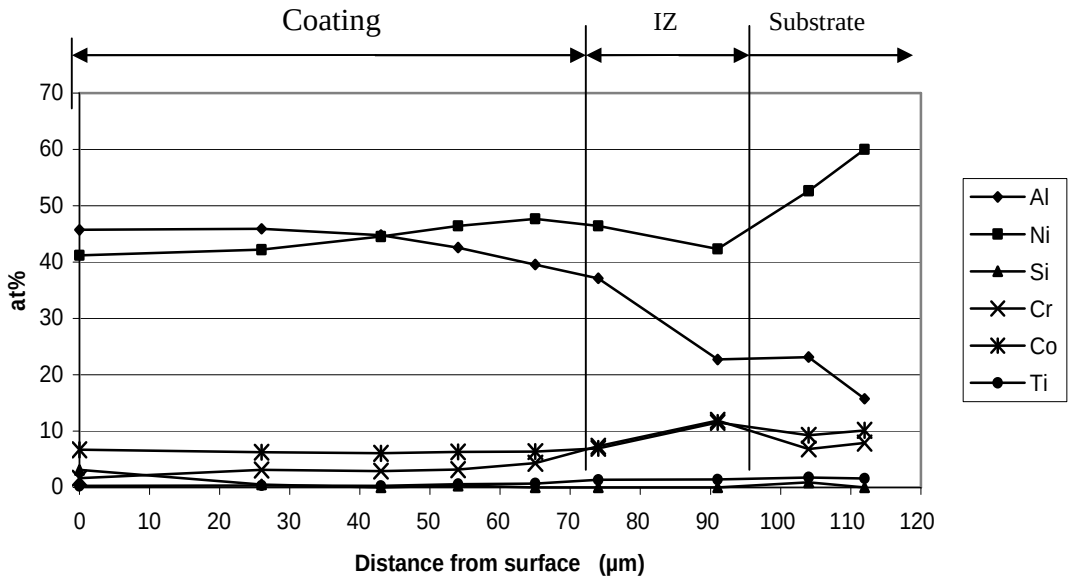

Figure 8.55: CMSX-4; 30 minutes silicon-aluminising CVD at 1050^{o}C, main elements on EDX line shown in Figure 8.54

The uniform microstructure of the coating and main elements which result from silicon-aluminising CVD on CMSX-4, at a soak temperature of 1050^{o}C for 30 minutes, are clearly seen in Figure 8.54. As there are no grain boundaries in CMSX-4, particles are smaller and more closely located to each other, when compared with those seen for IN738LC, in Figure 8.53. The β-phase NiAl is stable throughout the coating, with progression to the Al-rich edge of the β-phase field at the surface.

It is anticipated that 46 at%Al content through the coating, shown in Figure 8.55, will provide satisfactory hot corrosion protection which will be enhanced by outward diffusion of chromium, averaging 4 at%Cr, and cobalt, averaging 6 at%Co.

Titanium outwardly diffuses into the matrix and also forms particles rich in Ta, Mo and W. Chromium silicides with precipitates of Ta, Ti, Mo and W also occur. However, as seen in Figure 8.56, particles in the coating are too closely spaced to differentiate elements and to measure them accurately.

In summary, this β-NiAl phase coating, containing significant levels of Cr and Co, and having an average depth of 108µm, should provide good hot corrosion protection for CMSX-4, for a viable service life. This coating will be included as a novel coating for use with CMSX-4 in this project.

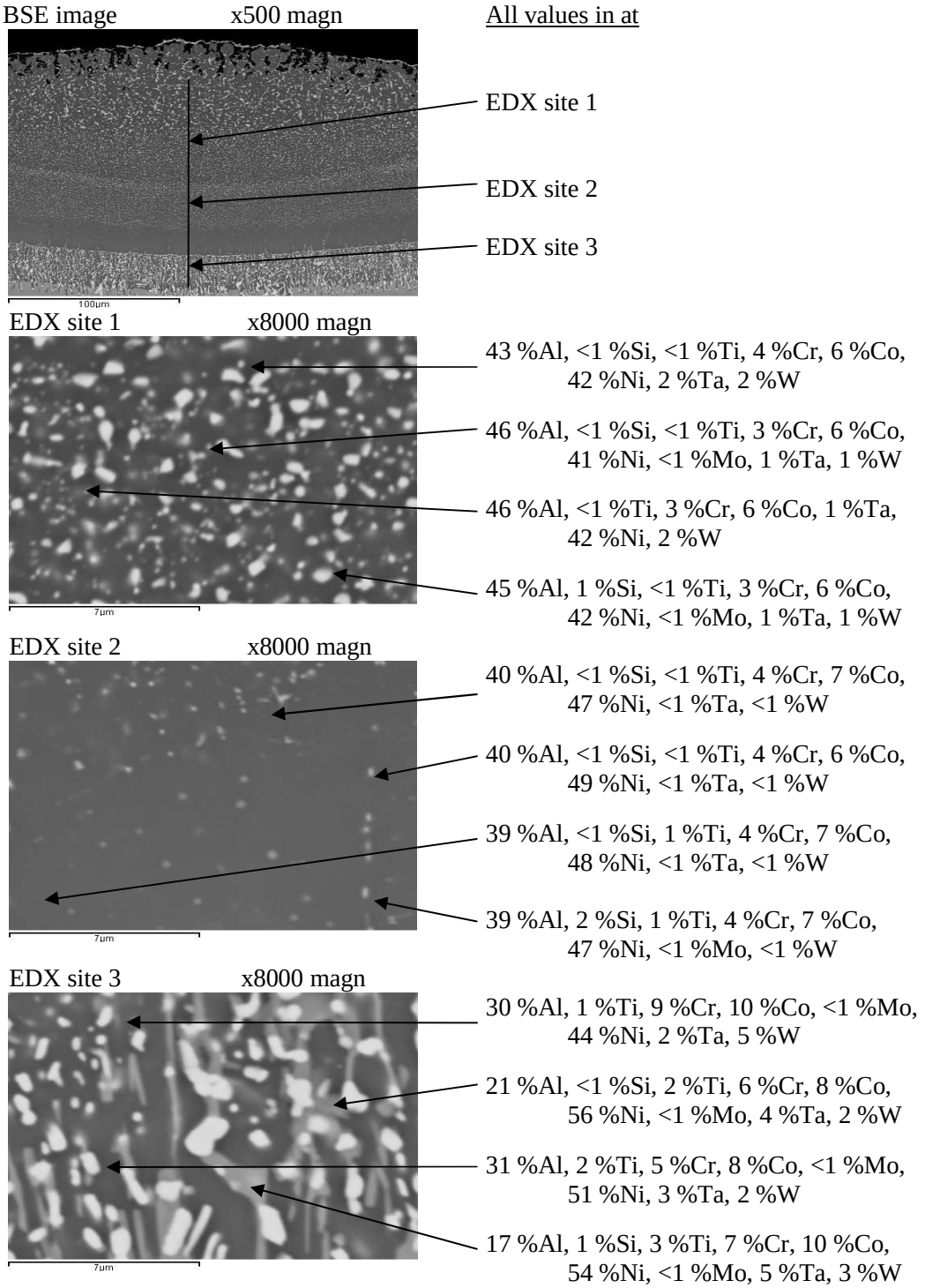

Figure 8.56: CMSX-4; 30 minutes silicon-aluminising CVD at 1050^{o}C, high magnification EDX element analyses of selected locations in coating

8.5 Silicon-aluminising trials – general discussion and conclusions

The CVD soak conditions for the first silicon-aluminising trial were 1050^{o}C for a period of one hour. This trial produced a coating which had the potential to provide good hot corrosion protection for IN738LC and CMSX-4. For both superalloys, the coating contained chromium interdiffused from the substrate, the higher chromium content in IN738LC being reflected in the coating on IN738LC, compared with CMSX-4. However, the lower hot corrosion protection expected for the coating on CMSX-4, may be possibly compensated by its average depth of 108µm offering a larger aluminium reservoir to maintain the initiation stage, compared with that of 96µm on IN738LC. Outward diffusion rates of titanium appeared low, and molybdenum precipitates were significant in the IN738LC trial but minimal in CMSX-4. The incidence of particles rich in tantallum and tungsten were comparable in both substrates. It was concluded that the one hour CVD soak period at 1050^{o}C potentially offered acceptable levels of hot corrosion protection for IN738LC and CMSX-4.

Continuing the low cost approach to novel coating development, it was decided to explore whether silicon-aluminised coatings produced by the same CVD soak period, but at the lower operating cost soak temperature of 800^{o}C, could offer viable levels of hot corrosion protection. The trials produced average depths of coatings on both substrates that were not adequate and would not be expected to provide sufficient hot corrosion protection. The conditions chosen for the third trial were to retain the one hour CVD soak period, with the higher temperature 850^{o}C, to explore whether the higher thermal energy in this process would produce coating microstructures capable of protecting against hot corrosion, at the more economic temperature than 1050^{o}C. This third trial produced deeper coatings with higher aluminium contents then those in the second trial, at 800^{o}C, but these were still considered inadequate to provide viable hot corrosion protection for both of the substrates.

The next stage in coating development was to retain the CVD soak temperature of 1050^{o}C, which produced potentially viable hot corrosion protective coatings, but for shorter CVD soak periods. The fourth trial was carried out at 1050^{o}C for a CVD soak period of 15 minutes.

During the fourth trial, while the chamber temperature was being raised to 1050^{o}C, the electricity supply to the furnace tripped and was off for a period of 4 minutes until restored, and the temperature increase resumed. During the 4 minutes period, the chamber temperature was above 900^{o}C and pack vapourisation and deposition would have continued. This would have extended the soak period for four minutes, significant in the context of a target CVD soak time of 15 minutes, shown in Figure 8.57. This was the only occasion, on either the aluminising or silicon-aluminising trials, when the CVD temperature heating profile was not consistent with that proposed, as shown in Figure 8.3. The net effect would have been to add depth to the coatings in this trial compared with the other trials. The fourth trial produced uniform and stable coatings which were considered to be suitable for testing as novel coatings.

To gain more understanding of the depths of coatings produced at 1050^{o}C, for shorter soak times then one hour, a soak time of 30 minutes was selected for the fifth siliconising trials. It should be noted that, immediately before the fifth silicon-aluminising trials, the furnace was overhauled and a broken element replaced. The replaced furnace element was the central one of three, which was at the same level as the sample tray containing the powder pack. As a result of the furnace overhaul there was a 15 minutes reduction in the time for the chamber to reach the target soak temperature of 1050^{o}C after the furnace was placed in position over the chamber. Figure 8.57 shows the temperature increase graphs for silicon-aluminising trials at 1050^{o}C, to illustrate the effects of the furnace electricity supply trip in trial 4 (15 minutes) and the ramp rate increase after the furnace was overhauled, prior to trial 5 (30 minutes).

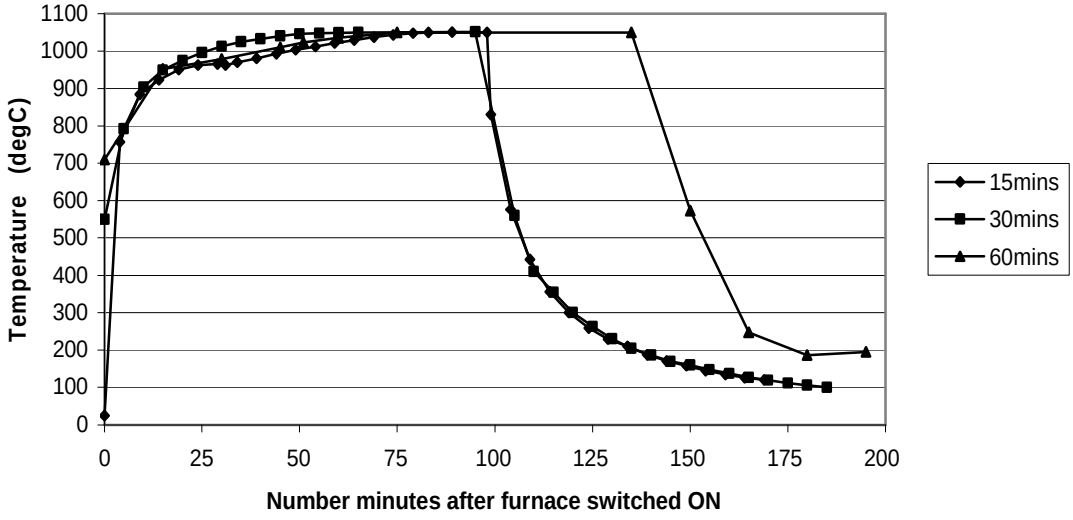

Figure 8.57: Silicon-aluminising CVD trials at 1050^{o}C; graphs of chamber temperatures after furnace placed in position and switched on

The effects, of the delayed temperature rise in trial 4 after the furnace trip, and the improved ramp rate following furnace overhaul before trial 5, caused the times during which the chamber temperatures were in excess of 900^{o}C, to the ends of the soak periods of the two trials, to be nearly the same. This should have resulted in similar coating depths however, due to the improved ramp rate, the coating depths differed significantly between trials 4 and 5, even though the total process time was similar. The average coating depths for the silicon-aluminising trials are presented in Table 8.3.

CVD soak temperature CVD soak period	800°C 60mins	850°C 60mins	1050°C 60mins	1050°C* 30mins	1050°C** 15mins
IN738LC					
Coating depth (µm)	19	35	121	126	46
Interdiff'n zone depth (µm)	4	14	24	20	22
CMSX-4					
Coating depth (µm)	17	29	141	108	69
Interdiff'n zone depth (µm)	10	18	28	23	28

*Note: *- CVD run after furnace overhaul **- Furnace electricity supply tripped, off for 4 mins*

Table 8.3: Summary of average coating depths from silicon-aluminising CVD trials – following post-CVD heat treatment

For determining the coating growth rate, the CVD heating times were assessed iin the same way as for aluminising. In this case, the assumption was made that vapourising commenced at 750°C, recognising that vapourising had commenced before 800°C, in the silicon-aluminising trial at this temperature. Sensitivity tests showed the ramping period differences between 800°C and 750°C were not significant in the total heating time. Thus the total heating times used in coating rates, diffusion assessments and Arrhenius plots, consisted of the ramping time from 750°C to the CVD soak temperature, plus the period at the CVD soak temperature. The heating times and thicknesses of coatings used in these assessments are summarised in Table 8.4.

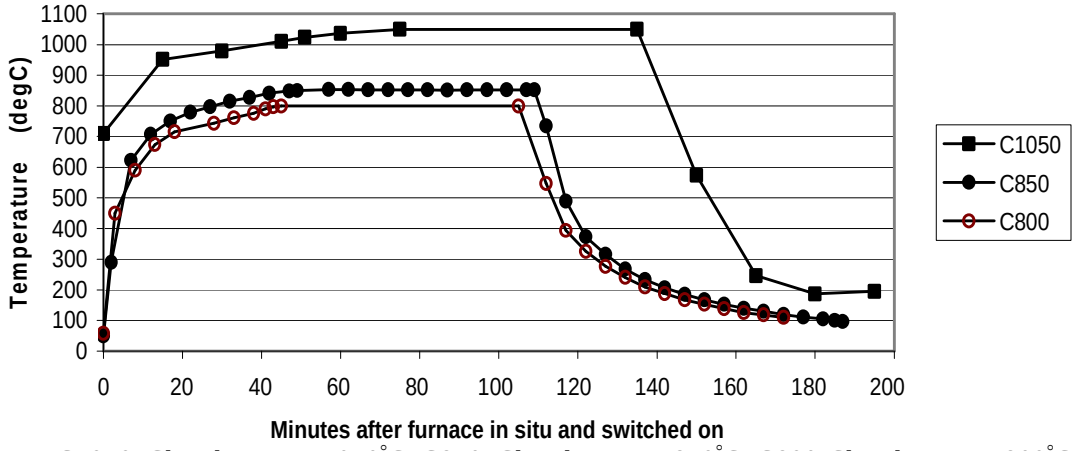

Key: C1050–Chamber temp 1050°C, C850–Chamber temp 850°C, C800-Chamber temp 800°C

Figure 8.58: Silicon-aluminising one hour trials; CVD chamber temperatures after furnace in situ and switched on

The results of the one hour silicon-aluminising CVD trials, at 800°C, 850°C and 1050°C, were used in preparing the Arrhenius plots for IN738LC and CMSX-4 seen in Figure 8.59. Both plots show the coatings to be diffusion controlled, with the R^2 values, 1 for the IN738LC plot and 0.999 for the CMSX-4 plot, confirming linear correlation in both cases.

Substrate	CVD temperature	Time at temperature mins	Avge coating depth (μm)
IN738LC	800°C	73	18
	850°C	87	33
	1050°C	132	118
CMSX-4	800°C	73	15
	850°C	87	27
	1050°C	132	133

Table 8.4: Silicon-aluminising one hour CVD trials; times at temperature and average depths of coatings – without post-CVD heat treatment

The Arrhenius plots indicate that the IN738LC substrate promoted a thicker coating compared with the CMSX-4 substrate, due to the lower activation energy for IN738LC (145kJ/mole), than that for CMSX-4 (176kJ/mole). Janssen and Rieck [113] found that the activation energy for diffusion of nickel in the beta phase was 172kJ/mol. However, as shown by the crossover point, where the coatings on IN738LC in the first two trials, were thicker than those on CMSX-4, the CMSX-4 coating was thicker after the third trial. Taking into account the errors in measuring coating thickness and the assumptions made about CVD heating times, there appears to be little difference in coating rates produced by single-step silicon-aluminising for IN738LC and CMSX-4 samples.

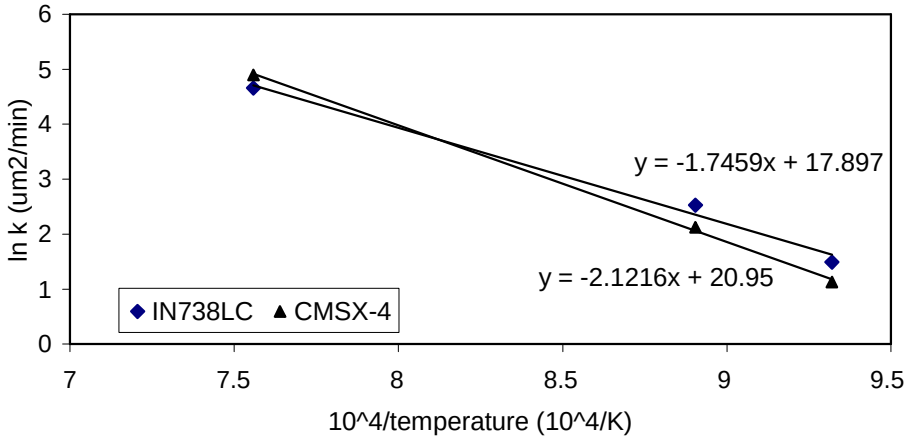

Figure 8.59: Silicon-aluminising one hour CVD trials; Arrhenius plots of silicon-aluminide coating thickness against CVD heating time for IN738LC and CMSX-4

The various BSE maps show that coatings of both substrates contain alloying elements, in particulate form in CMSX-4 samples as well as in IN738LC samples. Thus, the single-step silicon-aluminide coatings produced in these coating development trials are outward diffusion coatings.

The single-step silicon-aluminising trials showed that the coatings expected to offer the best hot corrosion protection, for both IN738LC and CMSX-4, were those produced at a CVD soak temperature of 1050^{o}C. Each of the three trials coatings had stable aluminium-rich β-phase NiAl and were of sufficient thickness to maintain protection and retard the initiation stage of hot corrosion.

Of these, the 15 minutes CVD trial produced coatings of comparatively low thickness. However, from the temperature profile of the overhauled furnace which showed, an increased depth of coating produced by a soak period of 30 minutes, one may expect that the 15 minutes process should produce a deeper coating than was produced in the trial.

Hot corrosion resistance can be expected to be further enhanced by the outward diffusion of chromium and cobalt into the coatings. Another contribution to protecting substrates against hot corrosion, provided by the single-step CVD process is the absence of grit lines, caused by contamination introduced between steps in two- or more-steps of coating production. A BSE image of the microstructure of a silicon multilayer and aluminised coating, which contains grit lines, is shown in Figure 8.60. Similarly, the single-step silicon-aluminides do not exhibit Kirkendall voids, which may also be introduced by multi-step coating processes [63].

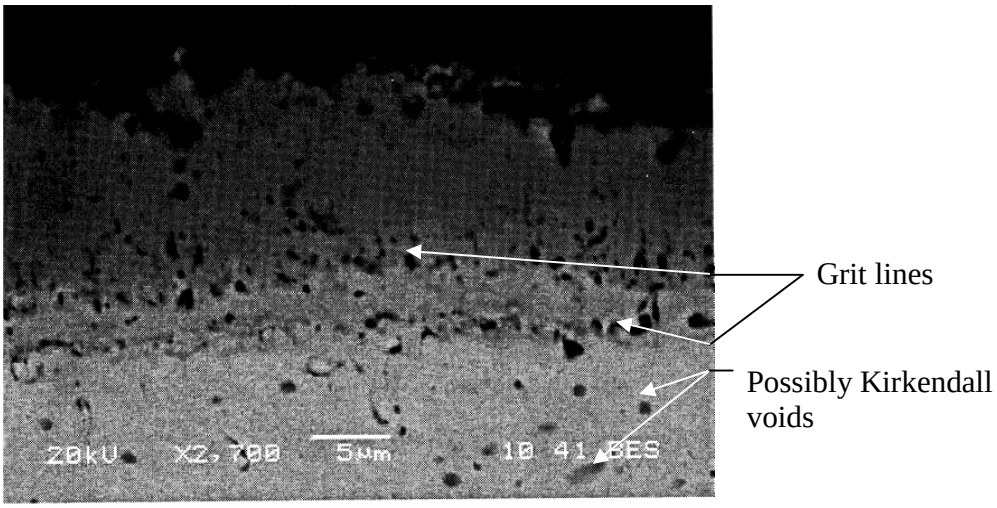

Figure 8.60: BSE image of the microstructure of a Ni-Cr substrate, Si multilayer, heat treated and aluminised trial sample [63]

Titanium outwardly diffused into the coating in each trial, with higher content in IN738LC than in CMSX-4. In the IN738LC trial, it also forms randomly distributed particles rich in molybdenum, tantallum and tungsten precipitates. Smaller particles, rich in these elements are more uniformly distributed through the coatings on CMSX-4, their content being lower, at <1 at%Ti, than those on IN738LC (2 at%Ti).

These particles may reduce hot corrosion protection and, additionally impair mechanical integrity. However, the main objective here is to select novel coatings on the basis of the expected hot corrosion protection they offer, any adverse behaviour due to minor elemental additions they may contain will be considered in a later chapter in this thesis.

Following assessment of the single-step silicon-aluminising trials the decision was made to select each of the three trial coatings produced by silicon-aluminising CVD at 1050^{o}C, for oxidation and corrosion tests, to evaluate the protection they may provide.

9. Novel coatings – cyclic oxidation tests

As reported in Section 8, three silicon modified aluminide coatings were considered to have the potential to protect hot components of gas turbines, fuelled by gasified biomass and waste-fuels, from hot corrosion. The next stage of coating development, was to establish whether the three novel coatings would provide cyclic oxidation protection.

Two series of cyclic oxidation tests were undertaken, the first series at 950^{o}C for 1000 hours, the second series was carried out at 1050^{o}C for 3000 hours.

9.1 Description of cyclic oxidation tests

9.1.1 Procedures and equipment

The horizontal, cylindrical furnace used, sat continuously at 950^{o}C or 1050^{o}C, with the samples fed in and out of the furnace manually. After each test period samples were cooled on the bench in laboratory air prior to being weighed. Between test periods, samples were stored in a dedicated desiccator containing regenerated silica-gel desiccant. Furnace calibration followed the same procedure as that for corrosion tests described in Section 4.2.

Both test series consisted of strictly adhered to 100 hour periods, samples being weighed when at laboratory temperature, before and after each test period. Samples were each contained in an alumina crucible to contain scale spall. Weighing was conducted on a Sartorius 5 decimal point balance. At each weighing, the crucible plus sample it contained were weighed first, then the sample and crucible were weighed separately. This procedure provided the gross mass change, spall mass and net mass change for each test period.

Of the two duplicate samples for oxidation testing, one was omitted from the first oxidation cycle but included in the second and subsequent cycles, to check consistency and provide back-up in the event of malfunction. All samples were tested over ten 100 hour periods. After completion of the ten test periods at 1050^{o}C, one of the two duplicate samples was selected for continued testing to failure, the second was cut, mounted, ground and polished, for evaluation. Each second sample was oxidation tested for 3000 hours.

9.1.2 Novel coatings tested

All substrate samples of IN738LC and CMSX-4 for oxidation testing were coated by CVD at 1050^{o}C. Five samples of each superalloy were coated using a CVD soak period of 15 minutes, five samples using a soak period of 30 minutes and five using a soak period of 60 minutes. A reference sample from each CVD period and substrate remained untested. For CVD operations, the samples were randomly placed, horizontally, in the powder pack. Each sample was separated by 10mm from its neighbour and the depths of powder, above and below each sample, were 10mm. The schedule of samples and their positions in the test programme are shown in Table 9.1.

Sample number	**Superalloy**	**CVD Period** (mins)	**Role in test programme**
IN151	IN738LC	15	Oxidn tst1 950^{o}C
IN152	IN738LC	15	Oxidn tst1 950^{o}C
IN153	IN738LC	15	Oxidn tst2 1050^{o}C
IN154	IN738LC	15	Oxidn tst2 1050^{o}C
IN155	*IN738LC*	*15*	*Reference sample*
CM151	CMSX-4	15	Oxidn tst1 950^{o}C
CM152	CMSX-4	15	Oxidn tst1 950^{o}C
CM153	CMSX-4	15	Oxidn tst2 1050^{o}C
CM154	CMSX-4	15	Oxidn tst2 1050^{o}C
CM155	*CMSX-4*	*15*	*Reference sample*
IN301	IN738LC	30	Oxidn tst1 950^{o}C
IN302	IN738LC	30	Oxidn tst1 950^{o}C
IN303	IN738LC	30	Oxidn tst2 1050^{o}C
IN304	IN738LC	30	Oxidn tst2 1050^{o}C
IN305	*IN738LC*	*30*	*Reference sample*
CM301	CMSX-4	30	Oxidn tst1 950^{o}C
CM302	CMSX-4	30	Oxidn tst1 950^{o}C
CM303	CMSX-4	30	Oxidn tst2 1050^{o}C
CM304	CMSX-4	30	Oxidn tst2 1050^{o}C
CM305	*CMSX-4*	*30*	*Reference sample*
IN601	IN738LC	60	Oxidn tst1 950^{o}C
IN602	IN738LC	60	Oxidn tst1 950^{o}C
IN603	IN738LC	60	Oxidn tst2 1050^{o}C
IN604	IN738LC	60	Oxidn tst2 1050^{o}C
IN605	*IN738LC*	*60*	*Reference sample*
CM601	CMSX-4	60	Oxidn tst1 950^{o}C
CM602	CMSX-4	60	Oxidn tst1 950^{o}C
CM603	CMSX-4	60	Oxidn tst2 1050^{o}C
CM604	CMSX-4	60	Oxidn tst2 1050^{o}C
CM605	*CMSX-4*	*60*	*Reference sample*

Table 9.1: Schedule of samples used in the oxidation test series

Photographs of the samples prepared for oxidation testing (Figure 9.1) show that coatings on bottom faces are less uniform than those on the top faces. The differences in deposition and oxidation protection provided by the top and bottom faces, will form part of the post oxidation test evaluations.

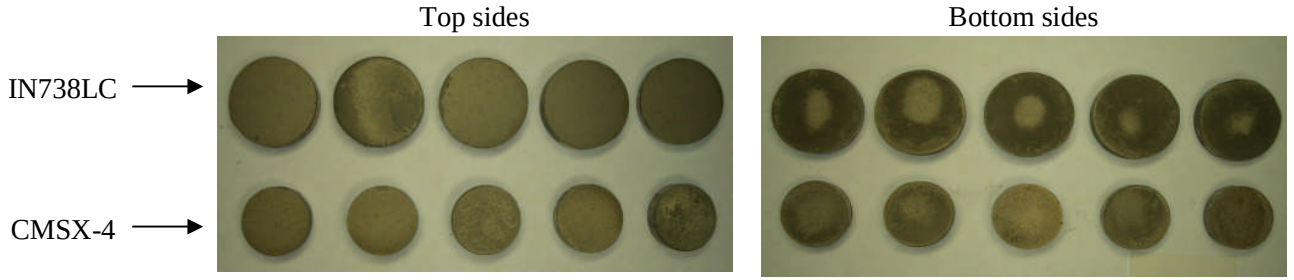

(a) : Siliconising : 15mins CVD at 1050^{o}C

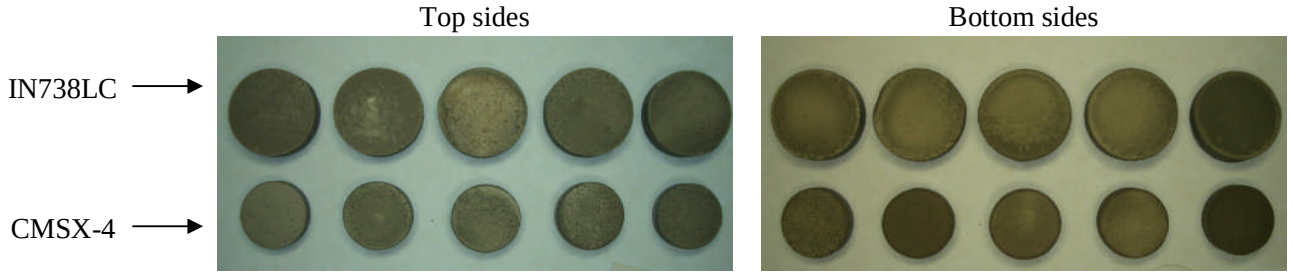

(b) : Siliconising : 30mins CVD at 1050^{o}C

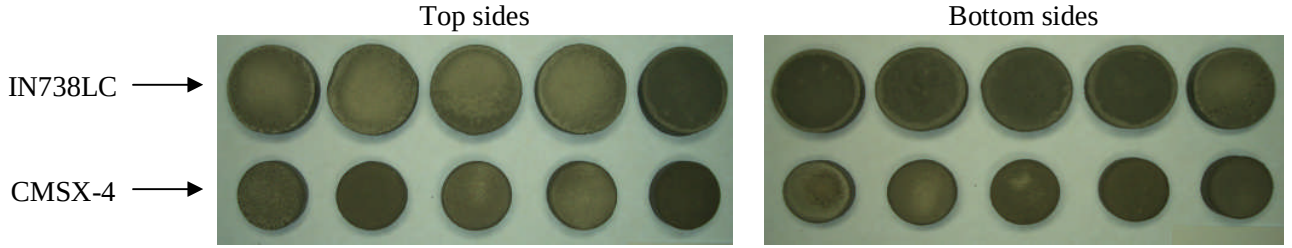

(c) : Siliconising : 60mins CVD at 1050^{o}C

Figure 9.1: Oxidation test preparations; IN738LC and CMSX-4 superalloys coated by CVD, after heat treatment

9.2 Oxidation Test Results

Two series of oxidation tests were planned, the first series of oxidation tests, at 950^{o}C, to serve as a screening test. If samples exhibit poor performance under this less onerous oxidation test, then there would be nothing to be gained in proceeding to the much more onerous second series of oxidation tests. The performance of coatings in the first series was considered to be satisfactory and so the second series, at 1050^{o}C, was completed. The results of the two series of oxidation tests are presented below.

9.2.1 Oxidation test series 1; 1000 hours at 950^{o}C – results

Photographs of the post series one samples are exhibited in Figure 9.2. Photographs are provided of both sides of each sample, but they do not identify whether the top or bottom side is shown, as in Figure 9.1.

The purpose of the first series of oxidation tests was to assess whether the novel coatings provided sufficient oxidation protection to justify commencing the more onerous, higher temperature, second series of tests. Mass change was used to evaluate the first series of tests.

9.2.2 Mass change

In the oxidation tests, as oxidation proceeds the oxide scale will grow and mass will increase. When the oxide scale reaches a certain thickness, often quoted to be 5µm-7µm, the scale may spall. Spalling continues for the duration of the remainder of the test or, until the coating loses it's protective capacity, through loss of aluminium or chromium, and is the point where the net mass change falls to zero [63]. Figure 9.3 shows the gross mass changes, in all samples, during the 1000 hours of testing at 950^{o}C.

In Figure 9.3 it can be seen that there is no direct correlation between the number of hours at CVD soak temperature and the gross mass observed. For example, the mass change of the 30 minutes CVD sample 2 (IN302) is greater than that of both the 15 minutes CVD sample 2 and 60 minutes CVD sample 2, and all three are significantly higher than sample 1 of all the soak periods. Similarly, for number one IN738LC samples, the 30 minutes CVD sample has the lowest mass change of the three, in contrast to the number two samples, where the 30 minutes CVD sample has the highest gross mass change of the three.

The lowest mass gains were observed for samples IN151, IN301 and IN601, with mass gains of 0.3-0.4 mg/cm^{2} after 1000 hours.

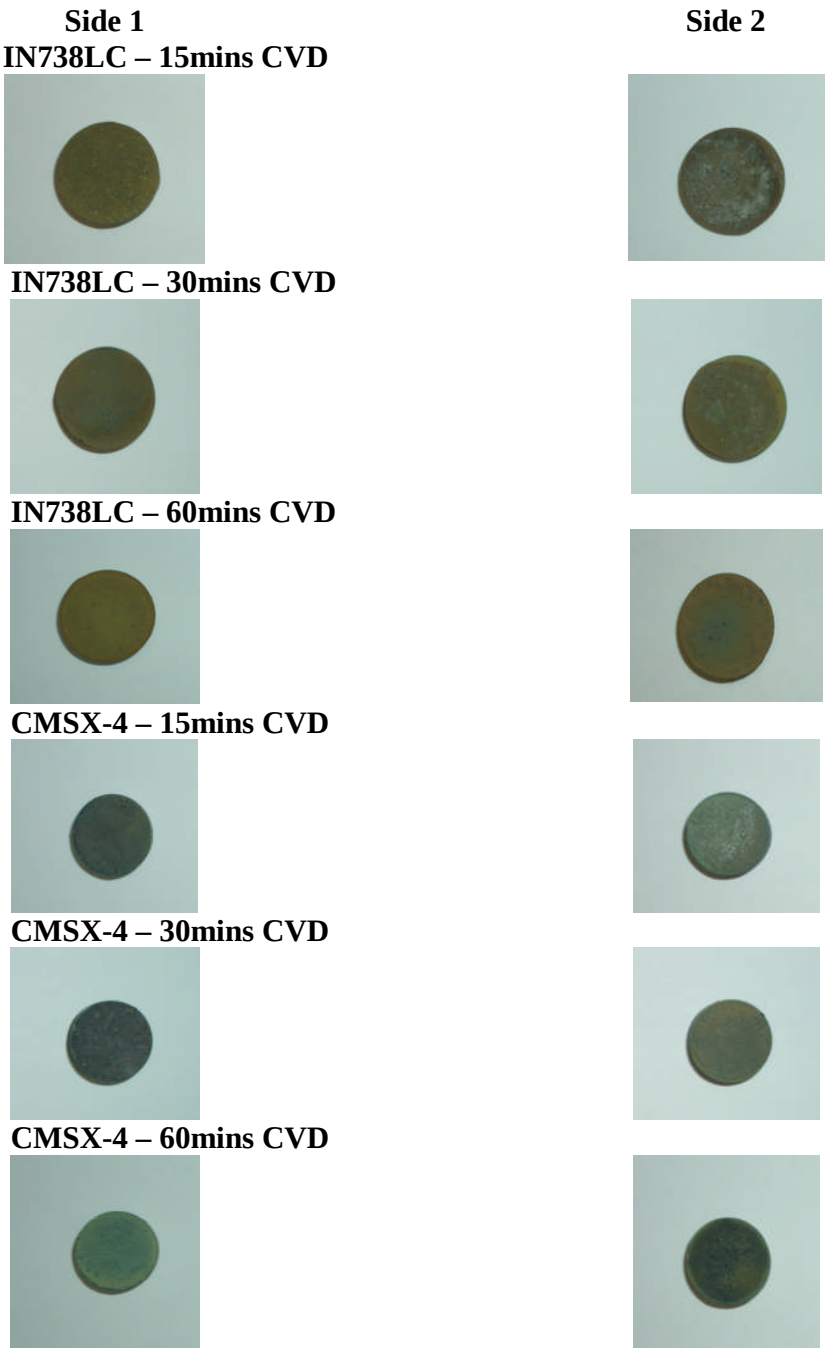

Figure 9.2: Photographs of samples after 1000 hours oxidation testing at 950^{o}C

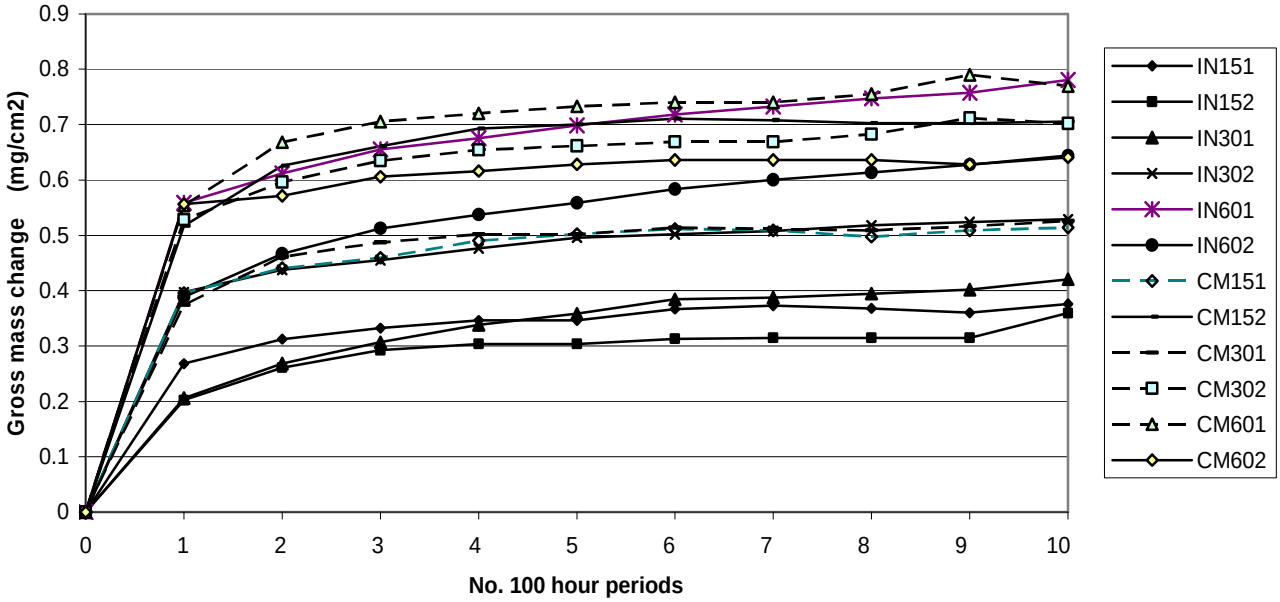

Key to codes: IN = IN738LC and CM = CMSX-4, the next two digits denote the no. of minutes CVD, the final digit denotes the number of the sample.
Example; IN151 = IN738LC, 15 minutes CVD, sample number 1

Figure 9.3: Oxidation test series; 1000 hours at 950^{o}C, gross mass change

In Figure 9.4, showing the gross mass changes for IN738LC samples, it is seen that, during the first 100 hours period, the mass of all samples rise from zero to a range of 0.2mg/cm^2 to 0.56mg/cm^2 after which the gradient levels off to a follow a consistent slope for the remaining periods. The differences in initial mass gain, during the first 100 hours of oxidation testing are caused by a combination of minor variations in coating depths and minor variations in CVD temperature, which depend on the position of the sample on the furnace carrier. The latter could occur because the temperatures along the furnace hot zone vary slightly, being lower at the ends than in the centre, the loaded length of the furnace carrier being 200mm. The effect will be cumulative, because for every 100 hours test period, each sample occupied the same position on the carrier.

After 300 hours of testing, mass changes generally maintain similar gradients. There is a marked increase in gradient after 900 hours testing for IN151, IN301 and IN601. The graphs of spall mass changes for silicon-aluminide IN738LC are to be seen in Figure 9.5. These show that, for these three samples, spalling occurs earlier than in the remainder. For IN151, heavy spalling occurs between 100 and 200 hours, and for both IN301 and IN601, high spalling occurs between 500 hours and 600 hours. Then, after 900 hours heavy spalling occurs in all samples except IN602.

The general pattern of spalling for IN738LC, shown in Figure 9.5, is for scale to grow over several 100 hour periods before reaching the critical thickness, presumed to be between 5µm and 7µm [63] caused by thermal expansion mismatch or, an excessively thick oxide scale where the oxide scale breaks away.

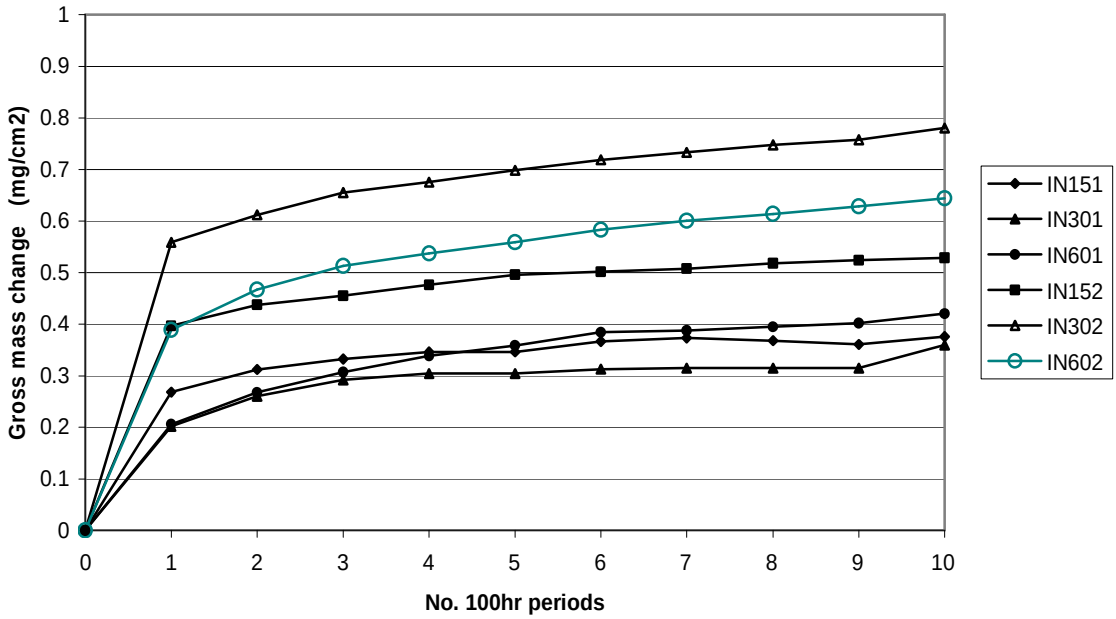

Figure 9.4: IN738LC; after 1000 hours oxidation testing at 950°C – gross mass change

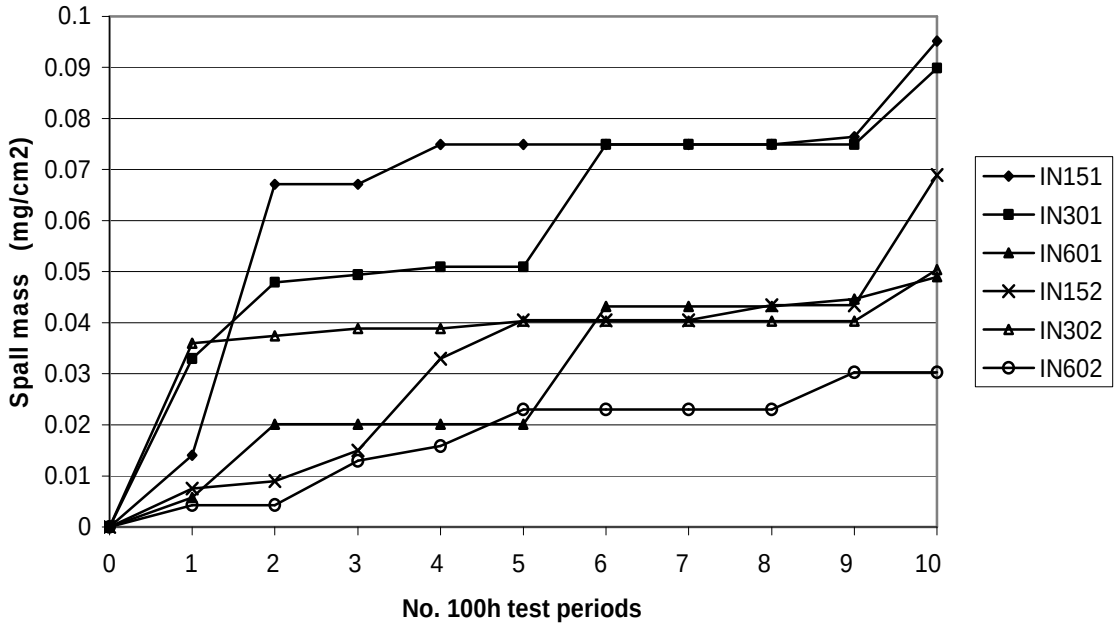

Figure 9.5: IN738LC; after 1000 hours oxidation testing at 950°C – spall mass

The mass changes, after the first 100 hours for silicon-aluminised CMSX-4, as shown in Figure 9.6, rise at similar gradients from the range 0.38 mg/ cm^2 - 0.57 mg/ cm^2 to the range 0.50 mg/ cm^2 - 0.76 mg/cm^2, for the remaining 900 hours. These are similar ranges to those coatings on IN738LC. As with the IN738LC based samples, there is no clear distinction between samples of one CVD soak period and those of other soak periods.

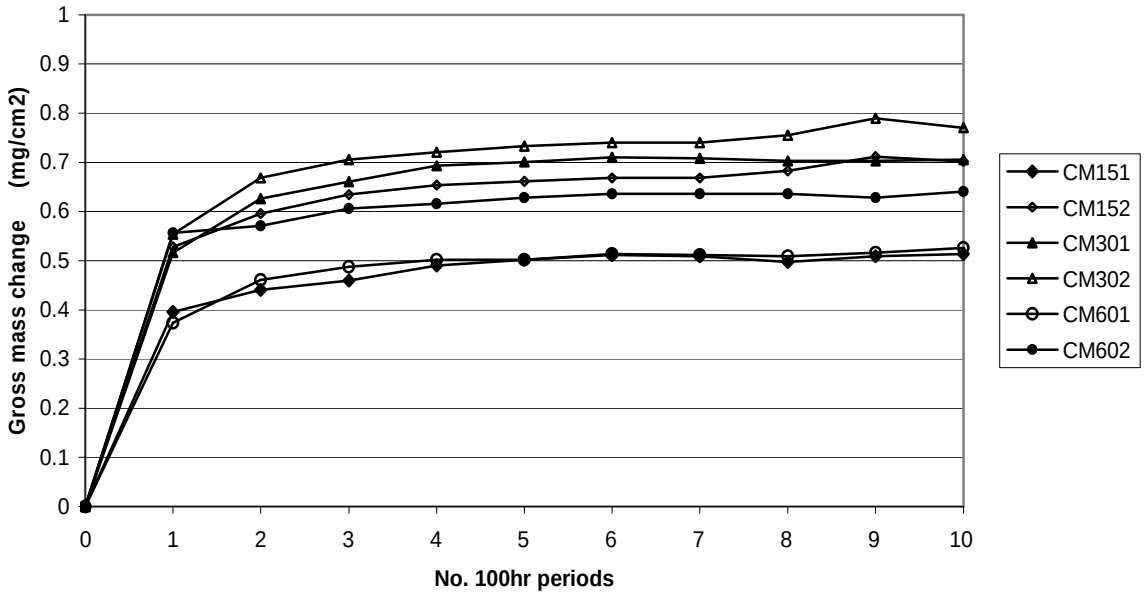

Figure 9.6: CMSX-4; after 1000 hours oxidation testing at 950°C – gross mass change

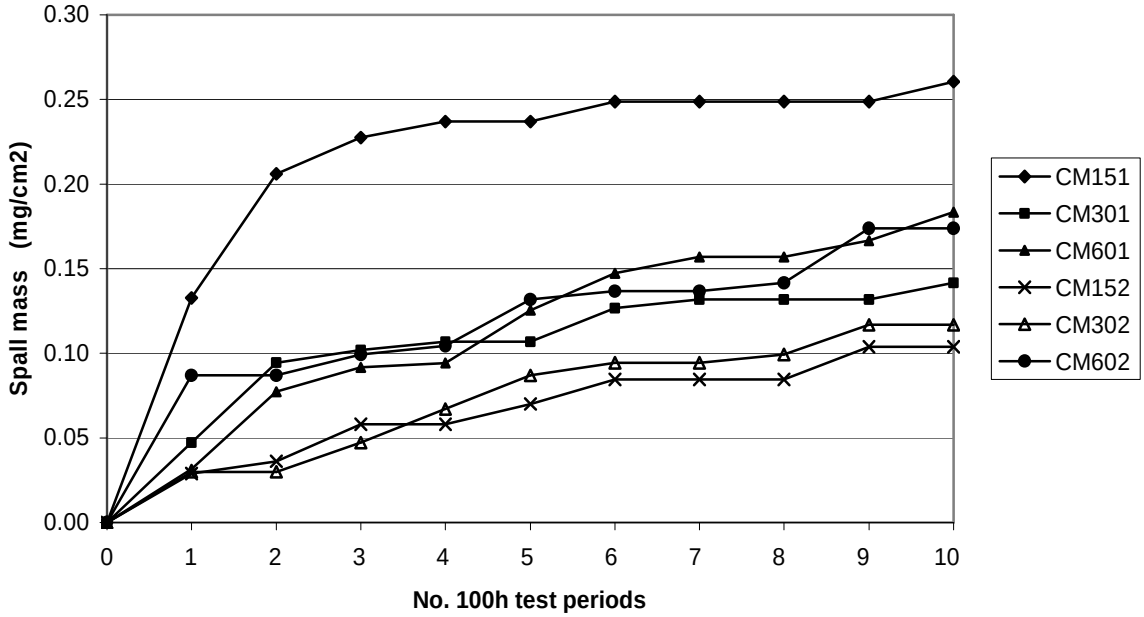

Figure 9.7: CMSX-4; after 1000 hours oxidation testing at 950°C – spall mass

Scale spalling of the silicon-aluminised coatings on CMSX-4, seen in Figure 9.7, is again not proportional to CVD soak periods, this being particularly applicable to sample CM151, with spall rates of between 0.2 mg/cm^2 and 0.26 mg/cm^2 for the last 800 hours of oxidation testing. The other five samples have much closer spall rates, within the range of 0.025 mg/cm^2 to 0.08 mg/cm^{2}after 200 hours, rising to a range of 0.10 mg/cm^2 to 0.18 mg/cm^{2}after 1000 hours. There is a trend for spalling to increase over about 200 hours, then to level off for about 200 hours. The figures for spall mass show there is more spall from coated CMSX-4 samples than for coated IN738LC samples.

9.2.3 Oxidation test series 1 - Conclusion

From the various mass change results it was concluded that the silicon-aluminide coatings had provided sufficient protection after a period of 1000 hours cyclic oxidation at 950°C, to justify ceasing further oxidation tests at this temperature. The decision was made to proceed with the second series of cyclic oxidation tests, at the more onerous temperature of 1050°C.

9.3 Oxidation test series 2; at 1050°C - results

The methods of evaluating oxidation test results are: mass change and examination by scanning electron microscope (SEM). Comparisons will be made of the coating depths and elemental analyses after this series of oxidation testing, with those of the reference samples.

9.3.1 Mass change

The gross mass changes of IN738LC based and CMSX-4 based novel coatings, after 1000 hours oxidation tests at 1050°C, are shown in Figures 9.8 and 9.9 respectively. These provide direct comparisons with gross mass changes of similar samples after 1000 hours at 950°C, shown in Figures 9.4 and 9.6. In Figure 9.8 it is seen that the gross mass changes of the coated IN738LC samples, after 100 hours at 1050°C, range from 0.42 mg/cm^2 to 1.22 mg/cm^2, compared with a range of 0.2 mg/cm^2 to 0.56 mg/cm^2 for the same period, at 950°C. The ranges for the higher temperature tests are approximately double those of the first series. After 100 hours testing the gradients of gross mass change graphs are similar for both series of tests.

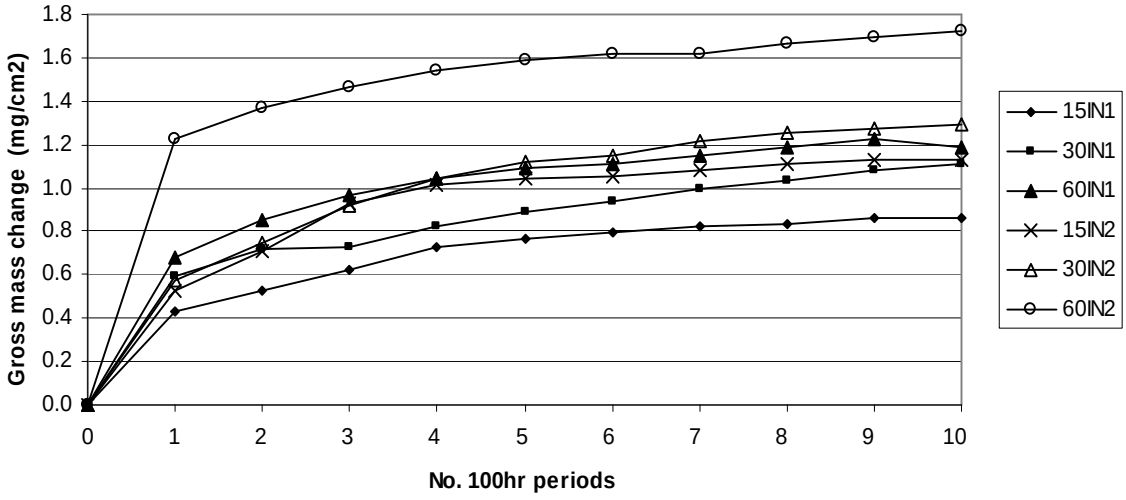

Figure 9.8: IN738LC; after 1000 hours oxidation testing at 1050°C – gross mass change

The gross mass changes for CMSX-4 based novel coatings, seen in Figure 9.9, show a wider range of mass gains, after 100 hours testing at 1050°C, than those for IN738LC based coatings. After 100 hours, for CMSX-4 based coatings, the gross mass changes range from 0.47mg/cm^2 to 1.6 mg/cm^2, compared with 0.38mg/cm^2 to 0.57 mg/cm^2 in the first test series.

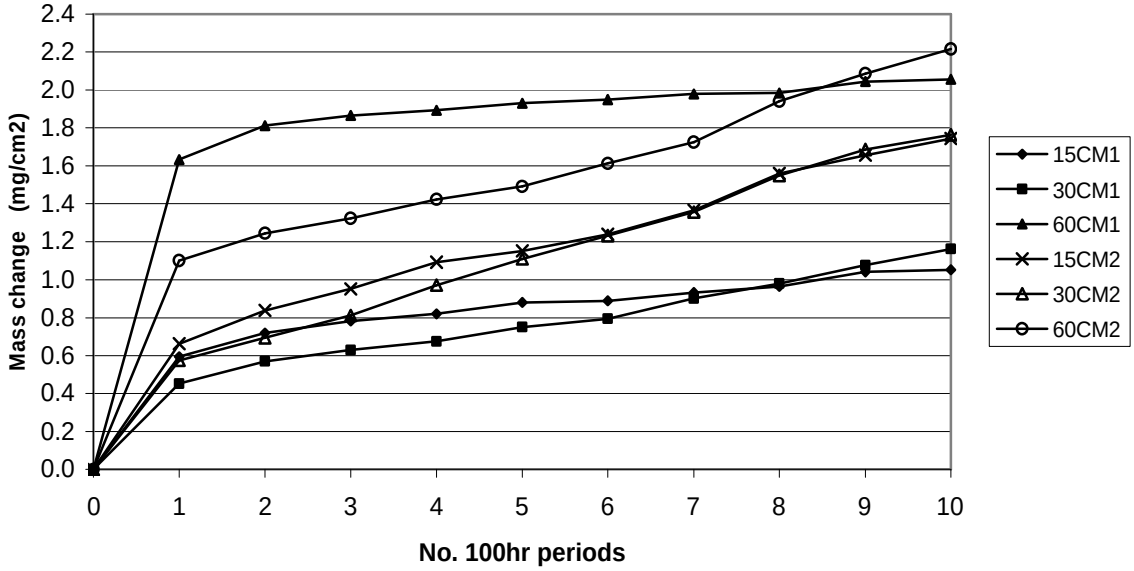

Figure 9.9: CMSX-4; after 1000 hours oxidation testing at 1050^{o}C – gross mass change

There are marked differences in gradients of gross mass changes from 100 hours to 1000 hours, seen in Figure 9.9, when compared with those in Figure 9.6. Although of differing values, the gradients for all samples except that of 60CM1 are similar, with higher oxidation rates occurring after 600-700 hours.

On completion of the first 1000 hours of oxidation testing at 1050^{o}C, the decision was made to continue the test, to failure, of the worst performing sample of each duration of CVD coating for IN738LC and CMSX-4 samples. However, as no mass change graphs had turned down positively after 1000 hours, the selection was made on a random basis. The samples selected for testing to failure were: the IN738LC-based IN151, IN302 and IN602, and the CMSX-4-based CM152, CM301 and CM601.

The mass change graphs for these samples, for the full 3000 hours of oxidation testing, are shown in; Figure 9.10 for gross mass change, Figure 9.11 for spall mass and Figure 9.12 for net mass change. In Figure 9.12, it can be seen that, of the six samples tested, five of the IN738LC samples had crossed the zero mass line, and only IN602 had not crossed the zero mass line, after 3000 hours testing. In Figure 9.10, the gross mass change curves show that, after around 600 hours of testing, the mass change rates of the CMSX-4 coated samples CM152 and CM301 increase significantly. The curves converge with that of CM601 and, after 1900 hours testing, the gradients and gross mass change values of the three CMSX-4 samples are very similar. The gross mass changes for the 60 minutes CVD CMSX-4 sample (CM601) show the highest value, whereas those for the other two CMSX-4 samples are very similar.

The gross mass change curves for coated IN738LC samples are more consistent than for coated CMSX-4 samples and the gradients remain similar for all three samples. The curves for different CVD durations are consistent for IN738LC samples, the lowest being the 15 minutes CVD sample, and the highest being the 60 minutes CVD sample. The spall mass curves in Figure 9.11 show consistency with the gross mass changes for coated IN738LC and coated CMSX-4, seen in Figure 9.10.

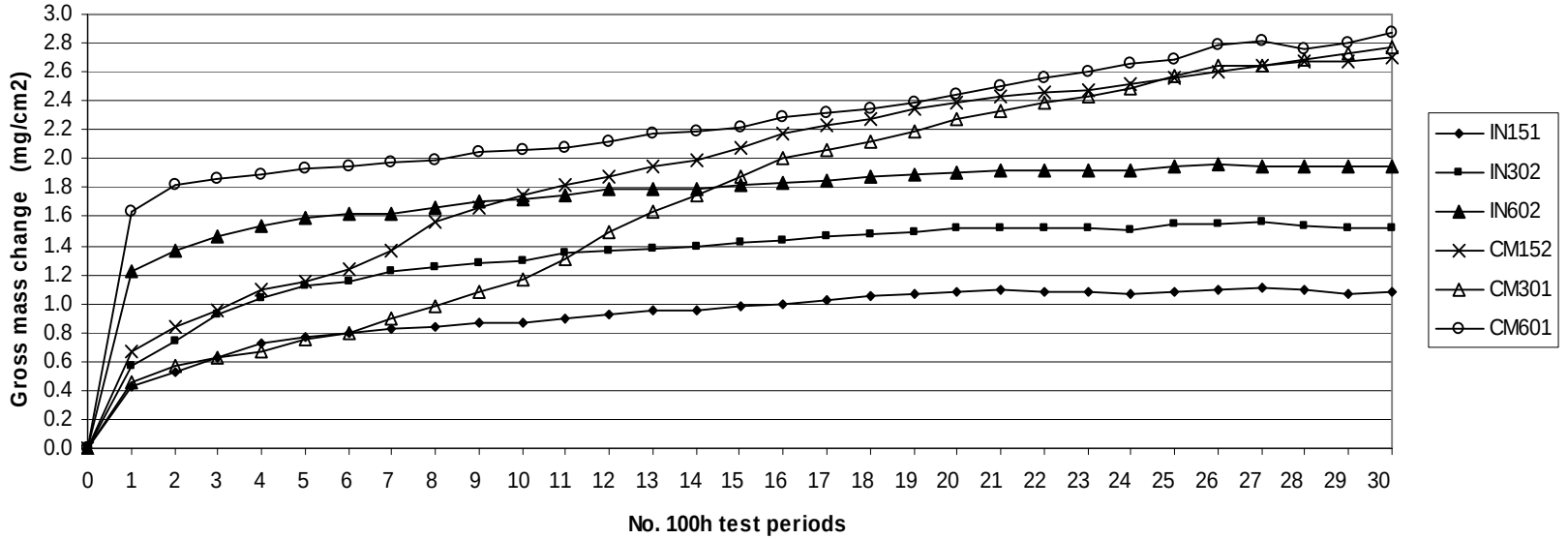

Figure 9.10: Oxidation test series 2; 3000 hours at 1050^{o}C – gross mass change

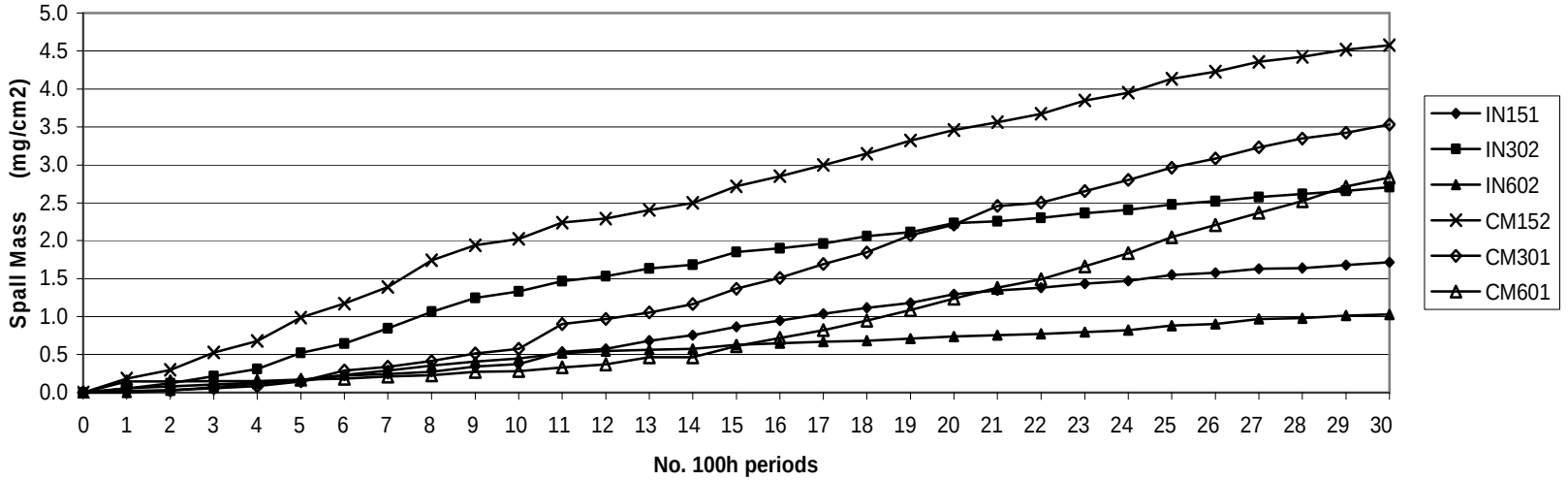

Figure 9.11: Oxidation test series 2; 3000 hours at 1050^{o}C – spall mass

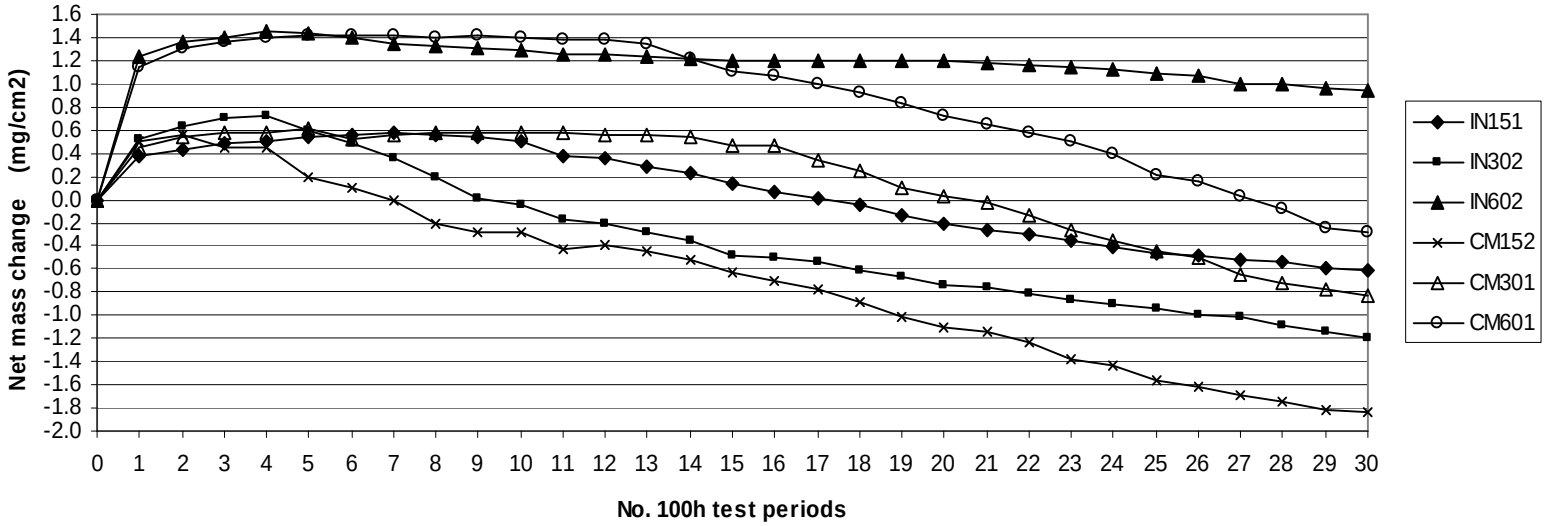

Figure 9.12: Oxidation test series 2; 3000 hours at 1050^{o}C – net mass change

Spall rates of CMSX-4 samples are higher than those for IN738LC, particularly after 700 hours, when values for each substrate diverge. The spall mass curves for IN738LC are not consistent with the coating depths expected from the CVD soak durations. For example, the spall mass produced by the 30 minutes CVD sample is higher than the 60 minutes CVD sample, for this substrate. In the CMSX-4 based samples, the spall mass values for the 15 minutes CVD sample are the highest of the three samples, with those for the 60 minutes CVD being the lowest of the three. These results are indicative of the variations in coating depths on the performance of individual samples.

The net mass change graphs, in Figure 9.12, reflect the differences in expected performance of the coatings, shown by the spall mass graphs, particularly for the 15 minutes CVD and 30 minutes CVD samples. However, the 15 minutes CVD sample should cross the zero line after the lowest testing period, as shown by CM152 crossing zero after 700 hours, whereas IN151 crosses zero after 2000 hours. Mass growths of 15 and 30 minutes CVD samples, in the first 100 hours, range from 0.4 to 0.55mg/cm^2. Those for the 60 minutes CVD samples range from 1.18 to 1.23 mg/cm^2 over 100 hours. However, the 15 minutes and 30 minutes CVD samples cross zero significantly sooner than those from 60 minutes CVD. Sample IN602 had not crossed the zero line after 3000 hours testing and CM601 crossed the zero line after 2850 hours. The conclusion is that, based on mass changes, only the 60 minutes CVD, IN738LC- and CMSX-4-based samples, with novel silicon aluminide coatings, provide viable protection against cyclic oxidation at 1050^{o}C.

9.3.2 Microstructures of samples after 1000 hours cyclic oxidation testing at 1050°C

9.3.2.1 IN738LC with a silicon-aluminide coating produced using 15 minutes CVD at 1050°C

After 1000 hours oxidation the sample discs were parted, cleaned, and mounted in conducting bakelite for examination in optical and scanning electron microscopes. On examination it was observed that there were variations in depths of the coatings on the top and bottom sides of the sample discs. This is illustrated as an example in Figure 9.13, where low magnification BSE images show the differences in depths and morphology, between the top and bottom surfaces of a sample of IN738LC, with a novel coating produced using 15 minutes CVD at 1050°C.

Variations in depths occur in most samples and are the result of the gap between the surface of the powder on top of the samples, and the tray lid and the position of samples in relation to the gap. This gap allowed some of the vapourised AlF_3 activator to rise above the main powder pack and thereby reduce the activity around the top face of the sample. Under the bottom face of the sample, the pack, including AlF_3, could not escape, thus retaining full activity.

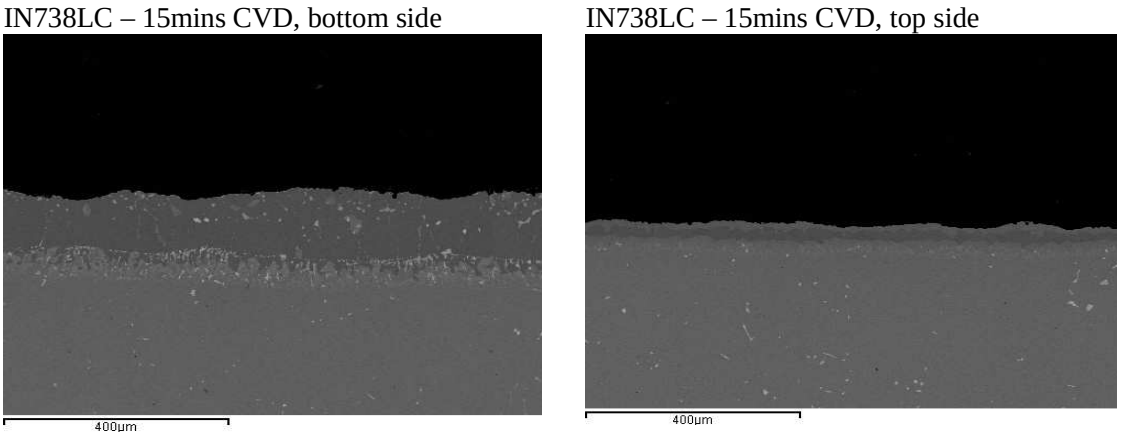

Figure 9.13: BSE images of IN738LC sample with novel coating, produced by 15mins CVD, after 1000 hours oxidation testing at 1050°C

BSE element maps of the IN738LC sample with novel coating produced following 15 minutes CVD at 1050°C, after 1000 hours oxidation testing at 1050°C, and comparisons with the appropriate untested reference samples, are shown in Figure 9.14. The maps show that, on both faces, the aluminium has been depleted other than for the outer surface. Chromium, is rich in the diffusion zone in both sides, but particles have also become distributed in the coating, mainly towards the surface. Chromium protection is still being provided by the bottom side, but not by the top side and, it can be concluded that, due to the inadequacy of the top side, the coating has failed.

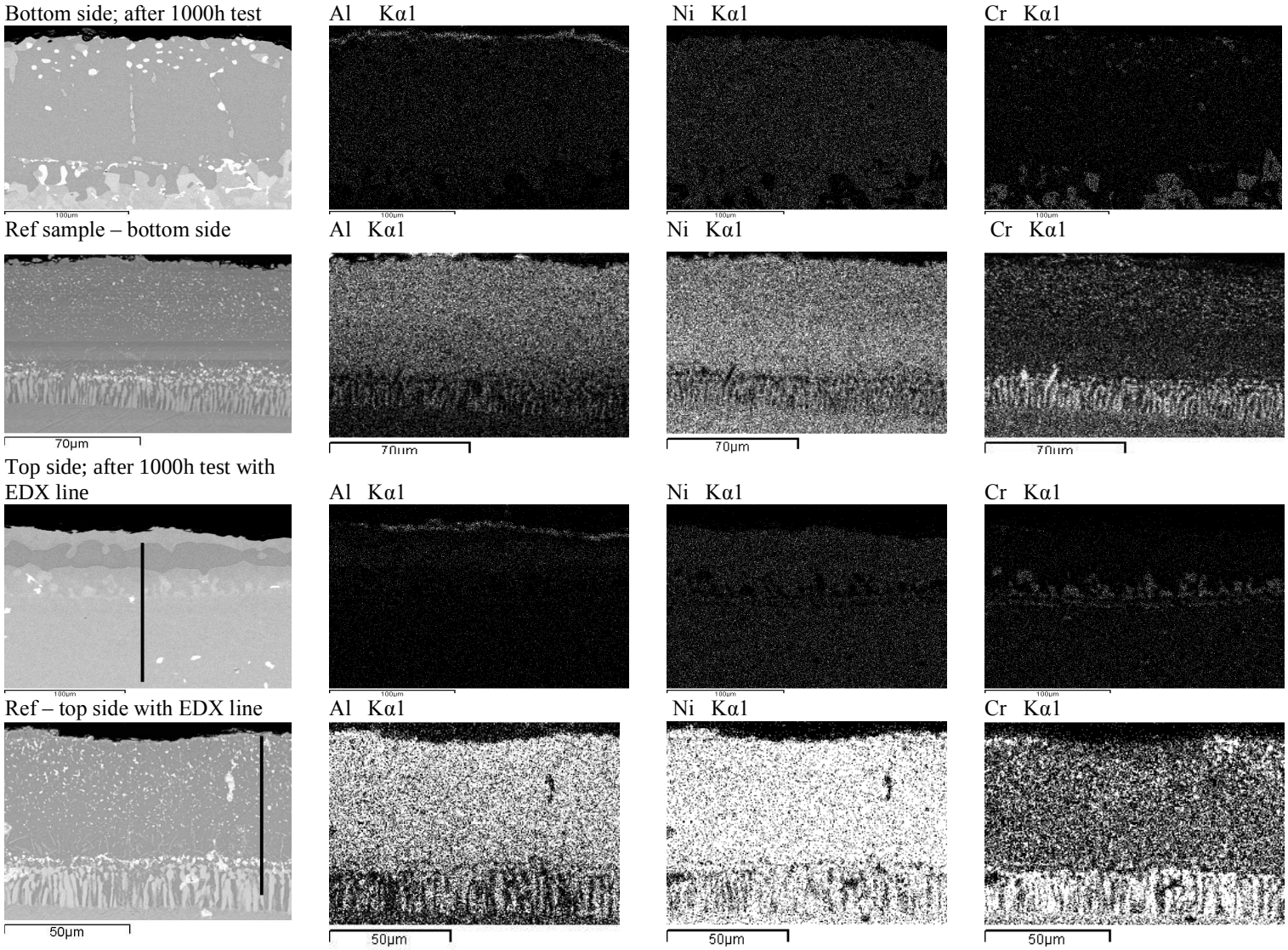

Figure 9.14: Oxidation Test; 1000 hours at 1050^{o}C, IN738LC with 15mins CVD novel coating, element maps of tested and reference samples (note different magnifications)

Microstructures in Figure 9.14 show the alumina scale formed from oxidation at the coating surface of the tested sample, compared with the uniform aluminium morphology of the reference sample. The diffusion zone morphology has become less uniform due to interdiffusion, without having any extreme effect on nickel content. After 1000 hours cyclic oxidation, chromium within the diffusion zone outwardly diffuses less uniformly into the coating and then tends to form precipitates towards the outer coating surface. The elemental compositions of the tested and reference samples are shown in Figures 9.15 and 9.16, with points analysed every 20-30µm. Aluminium has depleted to 25 at%Al in the surface region of the coating after oxidation, from 52 at% in the reference coating. At this stage in the oxidation testing there remains sufficient aluminium at the coating surface to feed scale growth. The thickness of the coating after oxidation testing has increased due to interdiffusion.

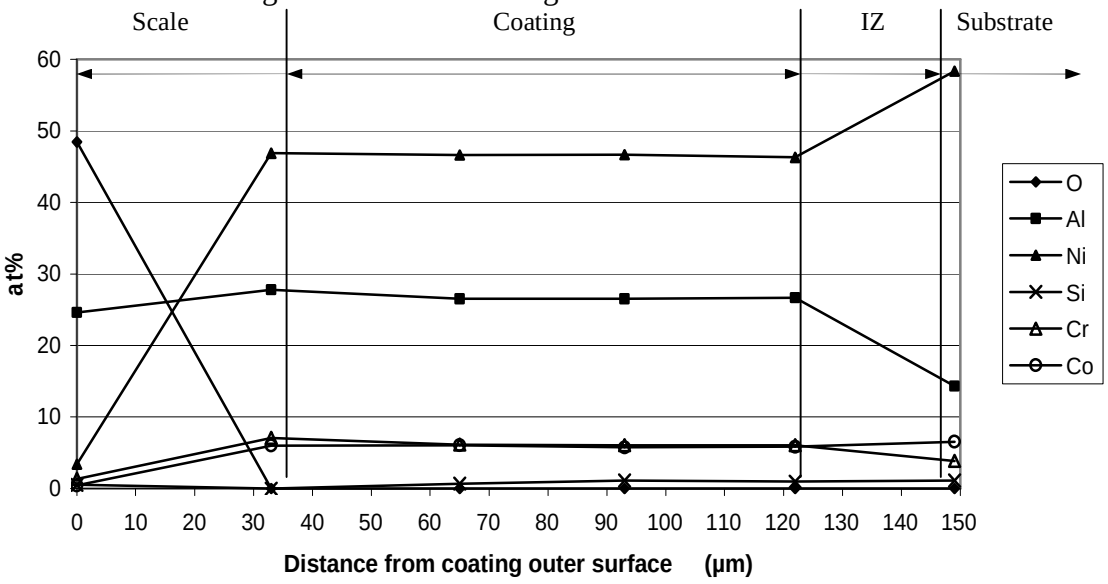

Figure 9.15: IN738LC with 15mins CVD novel coating, after 1000 hours oxidation tests at 1050°C – elements along EDX line in Figure 9.14

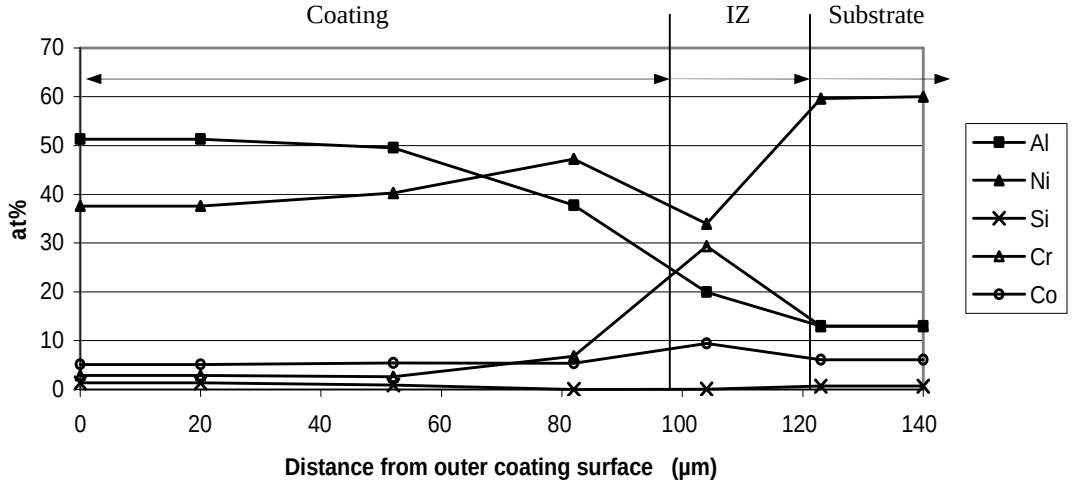

Figure 9.16: IN738LC with 15mins CVD novel coating, untested reference sample – elements along EDX line in Figure 9.14

9.3.2.2 IN738LC with silicon-aluminide coating produced following 30 minutes CVD at 1050^{o}C

The BSE maps of the main elements in the top side of the post oxidation test sample are shown in Figure 9.17. Microstructures of elements show similar morphology to those in IN738LC samples with the 15mins CVD coating.

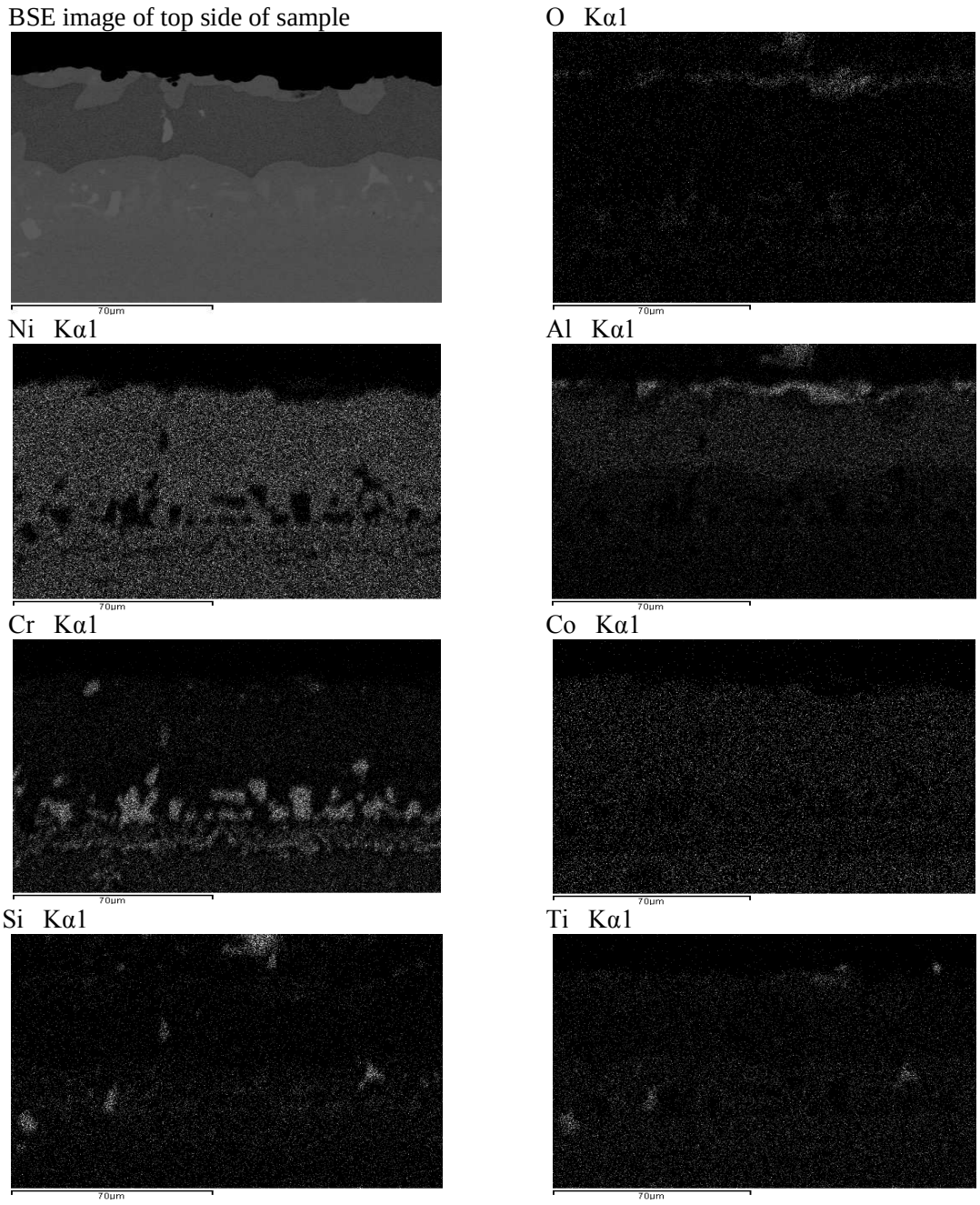

Figure 9.17: Oxidation test; 1000 hours at 1050^{o}C, top side of IN738LC sample with 30mins CVD silicon aluminide coating - element maps

As seen in Figure 9.12, the second sample of IN738LC with the 30mins CVD silicon aluminide coating (IN302), which was selected as the poorer performer of the two, crossed the zero-line after 1000 hours. The net mass change, of the sample being evaluated here (sample no. IN301), had not crossed the zero-line at the 1000 hours testing stage. Maps in Figure 9.17 and EDX results in Figure 9.18 show 28 at% Al is contained in the outer part of the coating and at the diffusion zone /coating interface, to retard oxidation. Chromium rich particles are present at the outer edge of the coating, in addition to outwardly diffused chromium, to enhance oxidation resistance and it is concluded that the coating still has sufficient aluminium to maintain an alumina scale. This consistent with the fact that the cyclic oxidation had not crossed the zero-line. Figure 9.18 shows that some internal oxidation has occurred.

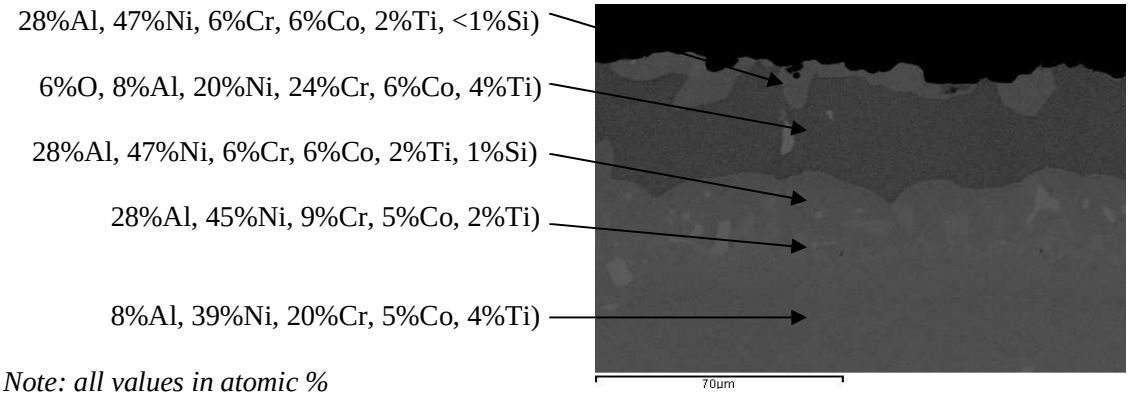

Note: all values in atomic %

Figure 9.18: Oxidation test; 1000 hours at 1050^{o}C, top side of an IN738LC sample with a 30mins CVD silicon-aluminide coating – EDX element analysis

Maps and EDX results quoted here are for the top side of the sample, which is expected to provide less oxidation protection than the bottom, because it has been found to be thinner.

9.3.2.3 IN738LC with silicon aluminide coating produced following 60 minutes CVD at 1050°C

The BSE images of the IN738LC sample with 60mins CVD silicon aluminide coating, after 1000 hours oxidation testing at 1050°C, and of the untested reference sample are shown in Figure 9.19. Coatings on both sides of the tested sample have grown by a ratio of 1.7:1 compared with the untested reference sample, due to interdiffusion between the coating and substrate.

Bottom side of oxidation tested sample
Average depth of coating: 154µm

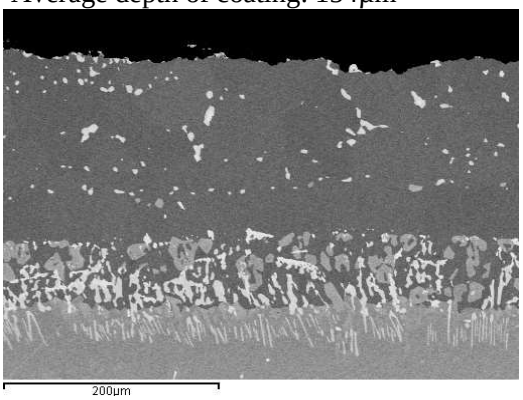

Reference sample – bottom side
Average depth of coating: 93µm

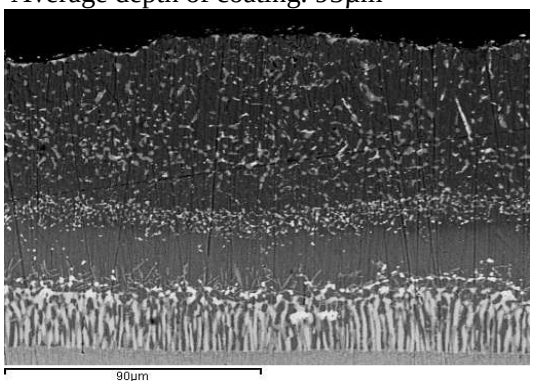

Top side of oxidation tested sample
Average depth of coating: 128µm

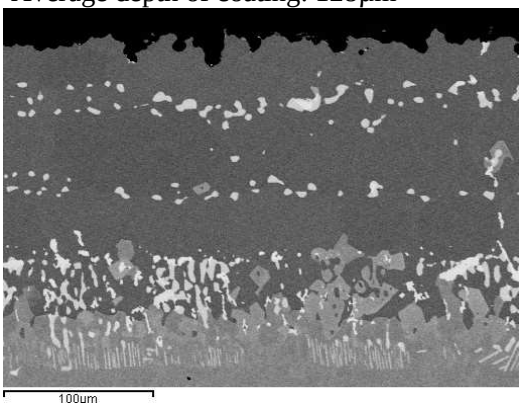

Reference sample – top side
Average depth of coating: 74µm

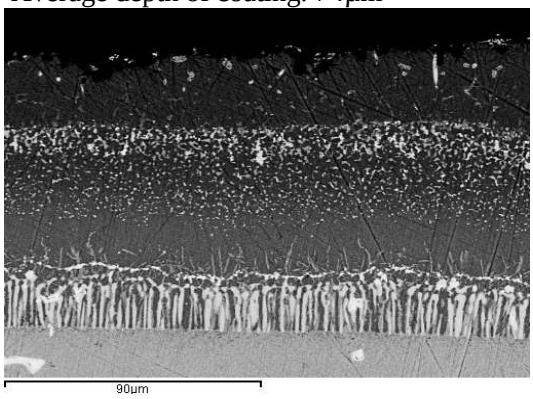

Figure 9.19: Oxidation test; 1000 hours at 1050°C, BSE images of IN738LC sample with 60mins CVD silicon aluminide coating compared to the reference sample (note the different magnifications)

The morphologies of both sides of the tested sample are similar, although there are some phase differences between the sides of the reference sample. Despite these apparent phase differences, they have not been reflected in the performance of the tested sample. The element maps of the top side of the tested sample, seen in Figure 9.20, suggest there is sufficient aluminium in the coating to continue feeding scale growth for a significant period. This is borne out by the performance of its partner sample (IN602), the net mass change of which had not crossed the zero-line after 3000 hours, as can be seen in Figure 9.12.

The maps in Figure 9.20 show that the oxide scale developed at the outer coating surface, most probably alumina but containing some titanium oxides, indicates that protective oxides continue to be formed. Precipitates rich in chromium, silicon and titanium, some of which are oxides of these elements, are concentrated along the interdiffusion zone, with particles comprising these elements distributed in the coating scale.

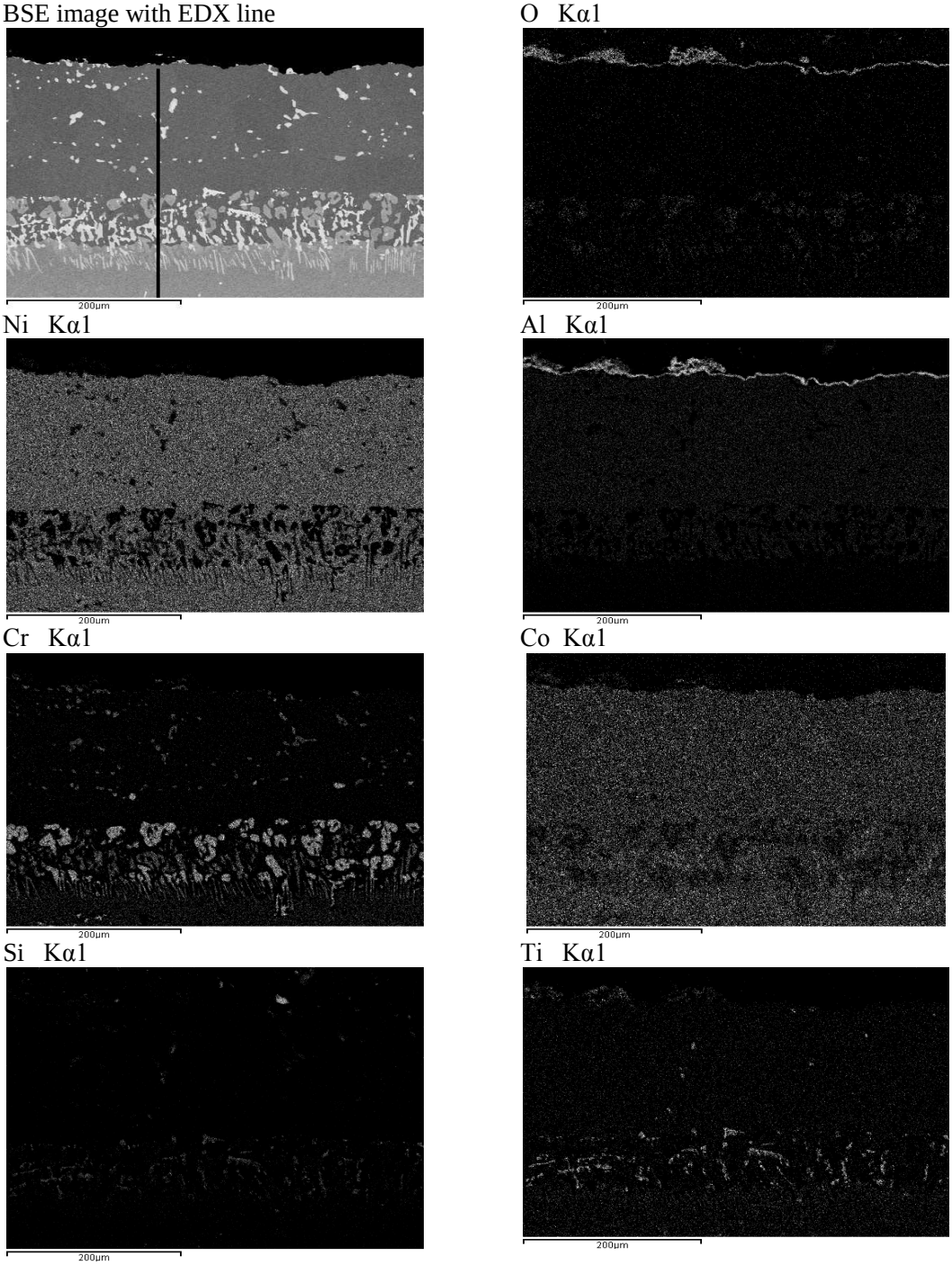

Figure 9.20: Oxidation test; 1000 hours at 1050^{o}C, bottom side of IN738LC sample with 60mins CVD silicon-aluminide coating - element maps

The EDX results in Figure 9.21 indicate that a region of second phase particles occurs 50µm from the surface and coincides with the peaking of titanium, tantalum and refractory metals precipitates mentioned above. These results are reflected in those for the reference sample seen in Figure 9.22. The coating was 93µm thick before the test, with 50 at% aluminium and an average of 2 at% silicon, as seen in the reference sample in Figure 9.22(a). After the test the coating was over 160µm thick and had an aluminium content of 27 at% in areas where the coating was β-NiAl.

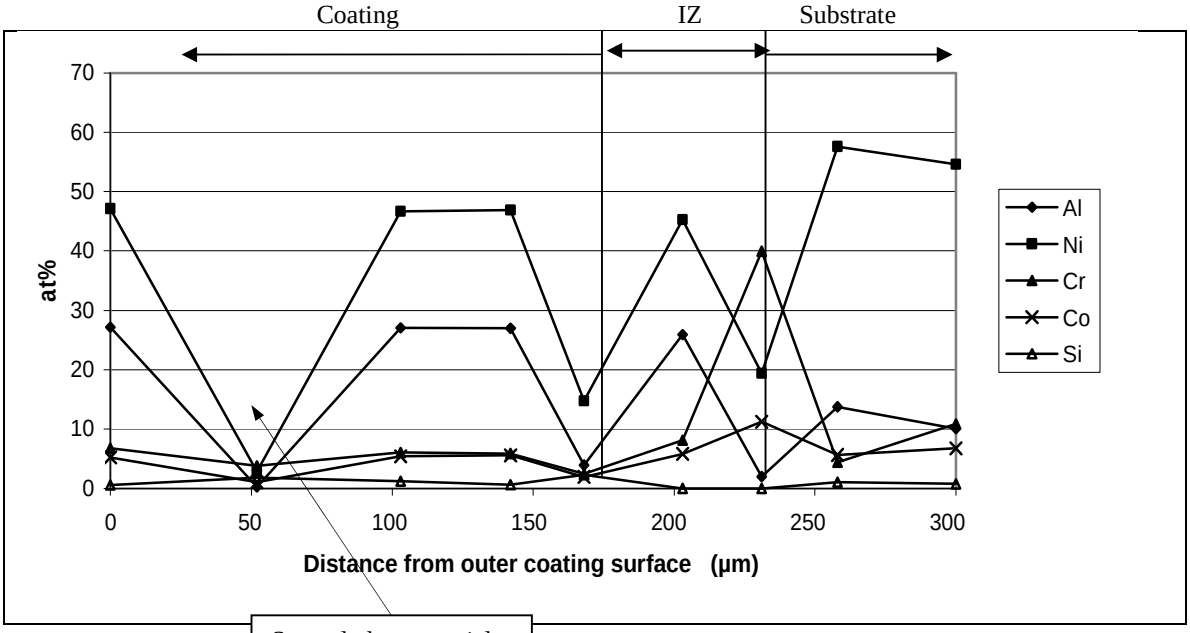

(a) : Main elements

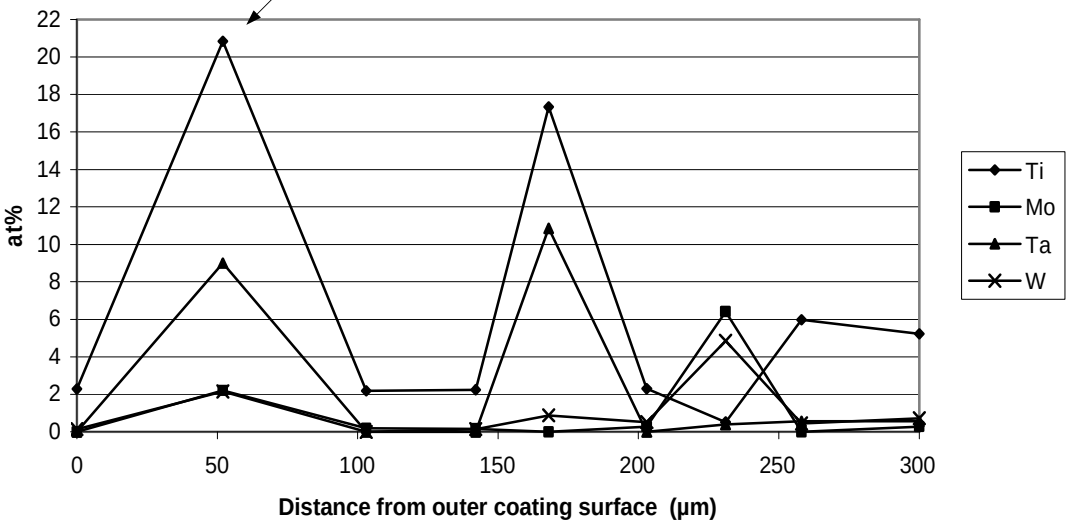

(b) : Alloying elements

Figure 9.21: Oxidation test; 1000 hours at 1050^{o}C, bottom side of IN738LC sample with 60mins CVD silicon-aluminide coating - EDX line elements in Figure 9.20

Comparison of the EDX results of tested and reference samples show the depletion of aluminium to give the γ'-Ni_3Al phase, in the former. After 1000 hours testing at 1050°C, outward diffusion of titanium, molybdenum, tantalum and tungsten has occurred, peaking in the region 50μm from the outer scale surface, due to the formation of second phase particles here. More generally, these metals, in the tested sample, have double the content in the coating and scale, of those in the reference sample.

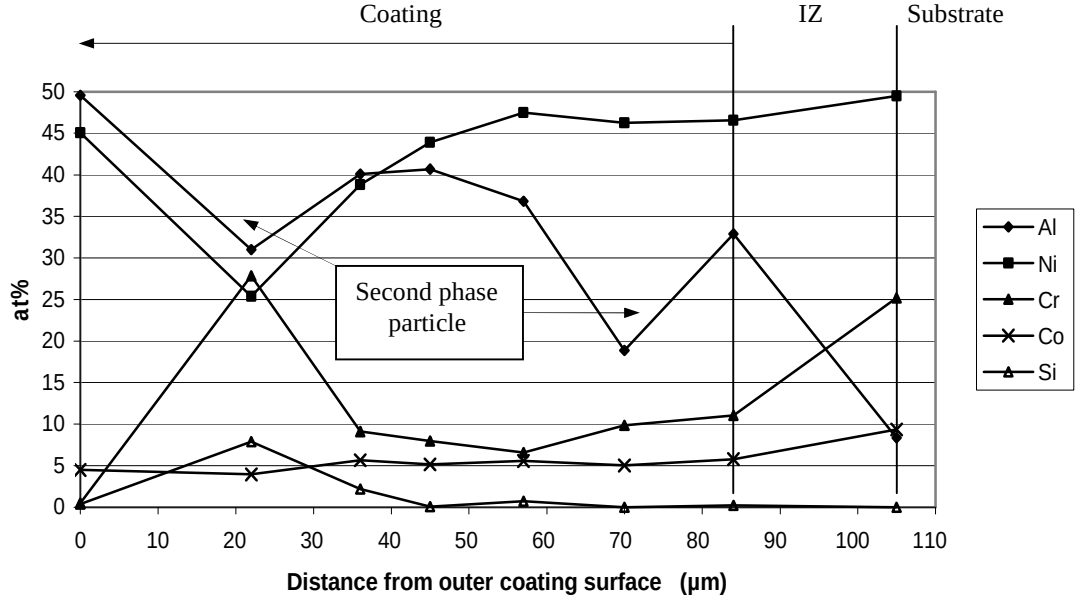

(a) : Main elements

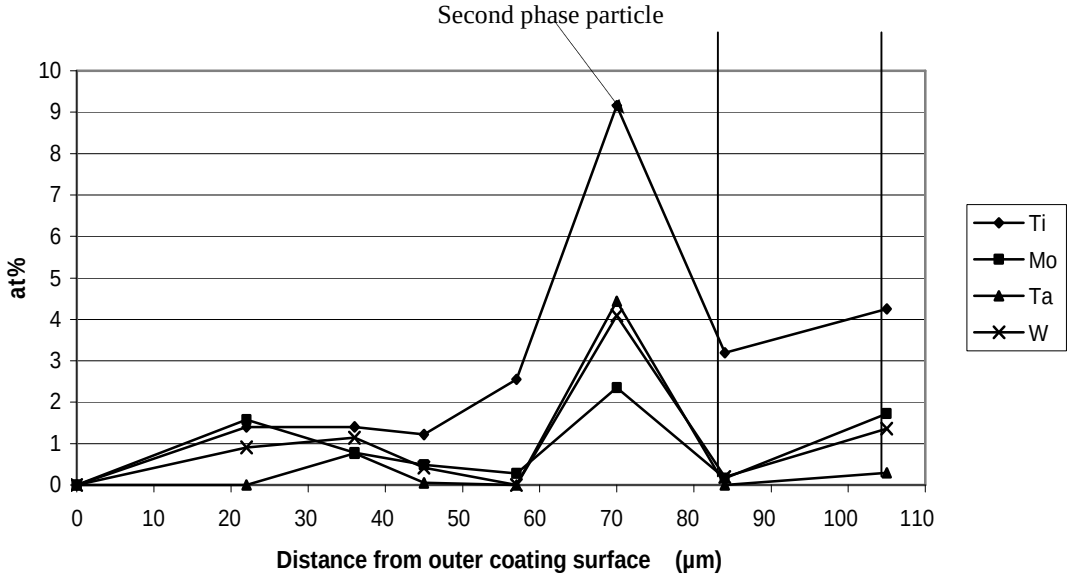

(b) : Alloying elements

Figure 9.22: Reference sample of IN738LC with 60mins CVD silicon-aluminide coating, bottom side – elements

9.3.2.4 CMSX-4 with silicon aluminide coating produced following 15 minutes CVD at 1050^{o}C

The BSE images of the CMSX-4 sample with 15mins CVD silicon aluminide coating, after 1000 hours oxidation testing at 1050^{o}C, and of the untested reference sample are shown in Figure 9.23. It is apparent that oxide scale has continually spalled and, that interdiffusion has occurred with the substrate. In this sample there is less difference between the depths of coatings on the top sides of the tested and reference samples, compared with those on the bottom sides.

Tested sample – bottom side
Average depth of coating: 72µm

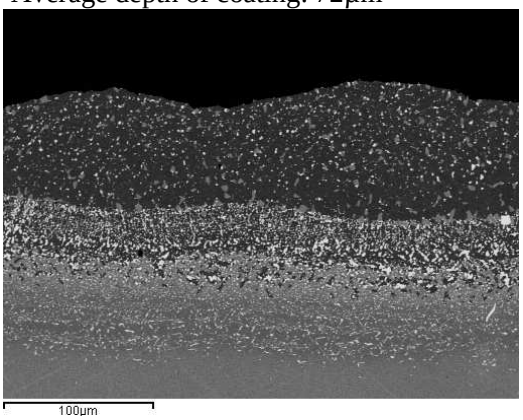

Reference sample – bottom side
Average depth of coating: 50µm

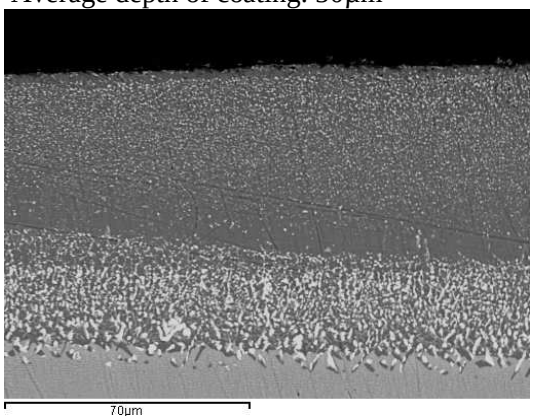

Tested sample – top side
Average depth of coating: 46µm

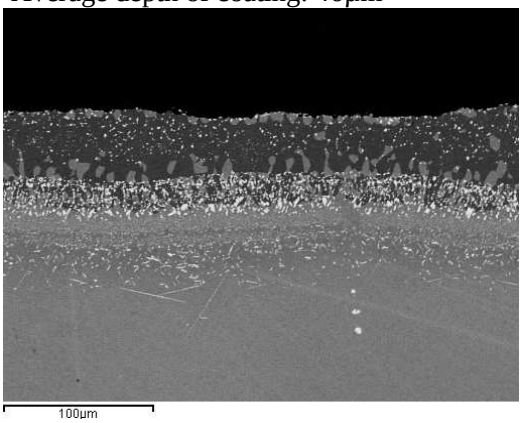

Reference sample – top side
Average depth of coating: 43µm

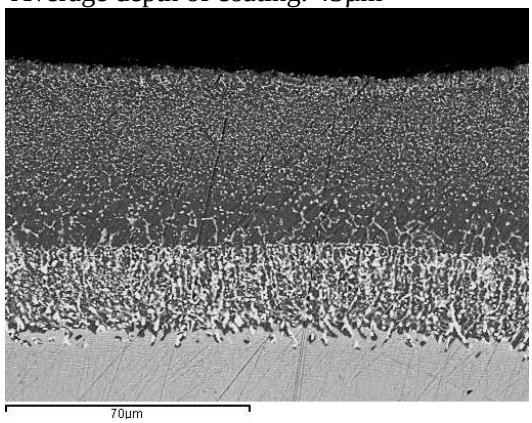

Figure 9.23: BSE images of CMSX-4 sample with 15mins CVD silicon-aluminide coating after 1000 hours oxidation testing at 1050^{o}C, and reference sample (Note different magnifications)

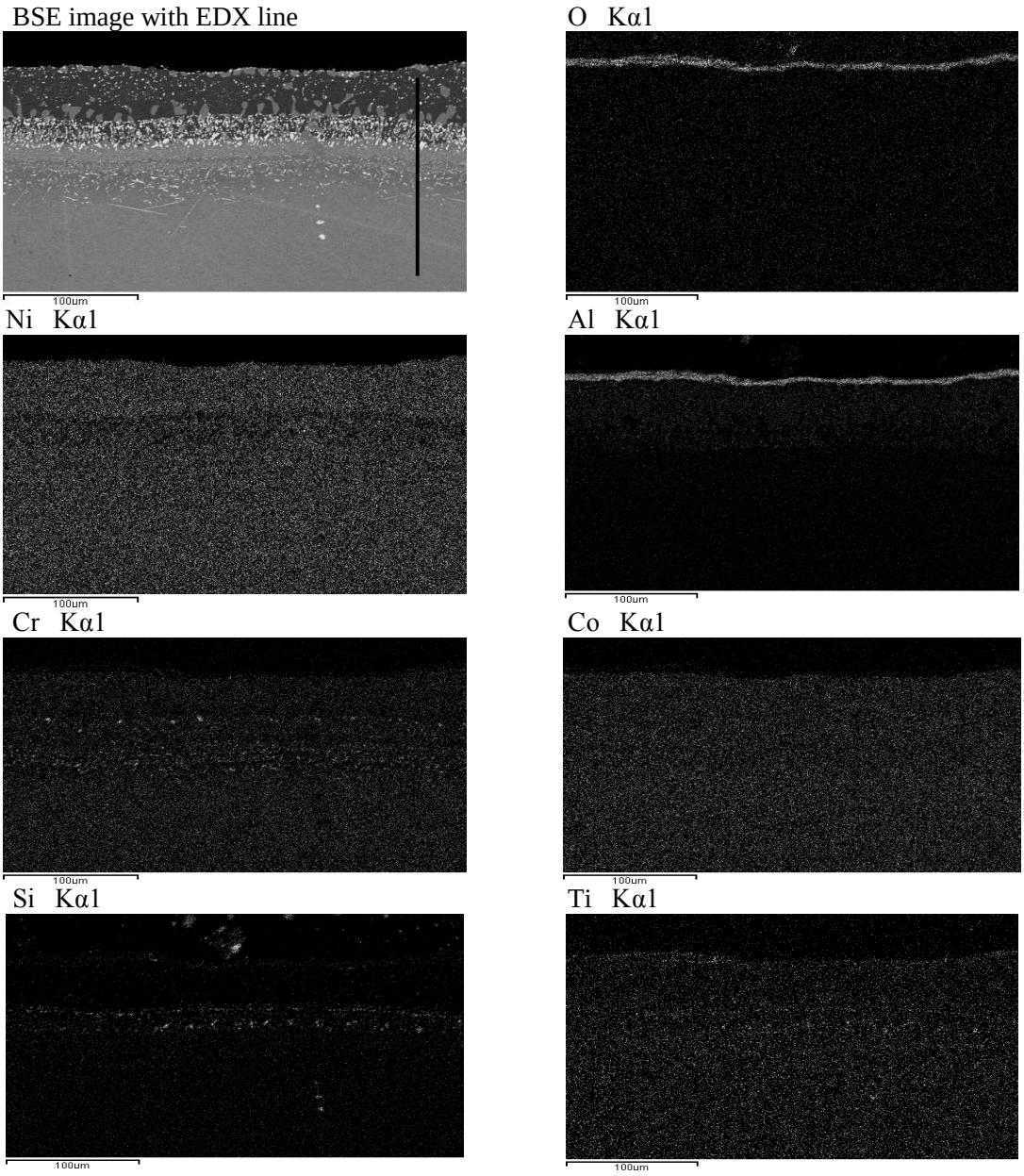

Figure 9.24: Oxidation test; 1000 hours at 1050^{o}C, top side of CMSX-4 sample with 15mins CVD silicon-aluminide coating - element maps

The maps in Figure 9.24 show that the oxide scale, developed at the outer coating surface, most probably alumina, will continue to form protective scale. The EDX results, shown in Figure 9.25, confirms there is an average aluminium content of 30 at% along 40µm of the β-NiAl phase nearest to the surface, remaining in the coating after 1000 hours of oxidation testing at 1050^{o}C. This compares with 32 at% aluminium through the coating, in the reference sample: the reference coating being 50 µm thick. Towards the surface, the aluminium has depleted, resulting in γ'-Ni_3Al phase in this region.

Chromium and cobalt diffuse outward during cyclic oxidation testing , having average contents of 4 at% Cr and 7 at% Co, compared with 2 at% Cr and 5 at% Co in the reference coating. During oxidation testing, the silicon content of 1 at% Si uniformly distributed in the reference coating, seen in Figure 9.25(a), becomes dislocated and only emerges in the oxidation region, where it continues to maintain alumina, or in the interdiffusion zone as a secondary phase.

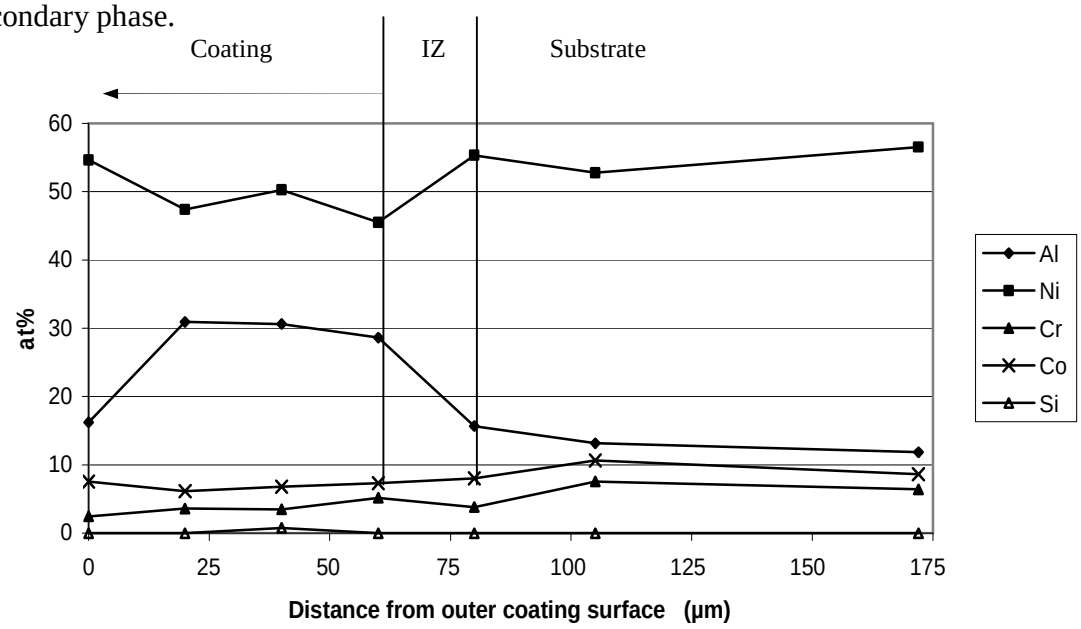

(a): Main elements

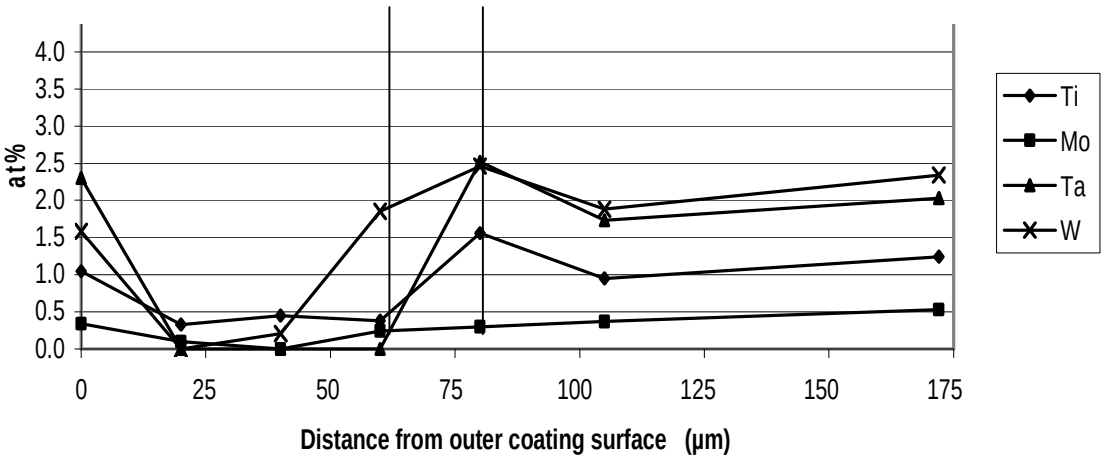

(b) : Alloying elements

Figure 9.25: Oxidation test; 1000 hours at 1050^{o}C, top side of CMSX-4 sample with 15mins CVD silicon-aluminide coating – EDX line elements in Figure 9.24

In the oxidation sample, EDX results in Figure 9.25(b) show higher levels of outward diffusion of titanium, molybdenum, tantalum and tungsten have occurred, rising to 1 at% Ti, 0.25 at% Mo, 2.3 at% Ta and 1.6 at% W at the coating surface. Contents of these elements in the untested coating, as shown in Figure 9.26, generally follow a downward outward trend through the coating, to levels of <1 at% of titanium, tungsten, molybdenum and tantalum, at the coating surface.

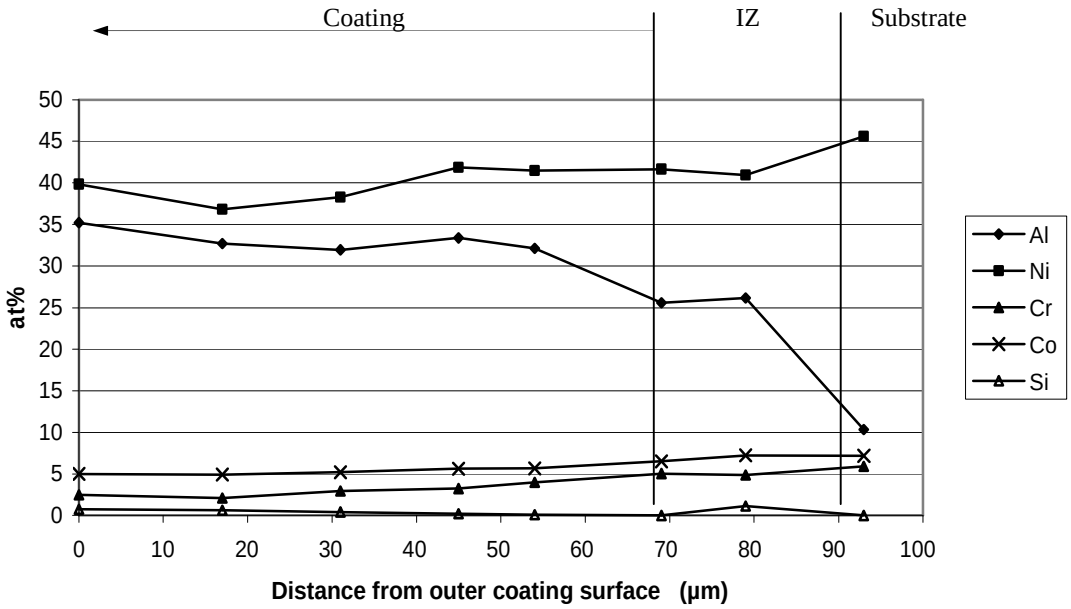

(a) : Main elements

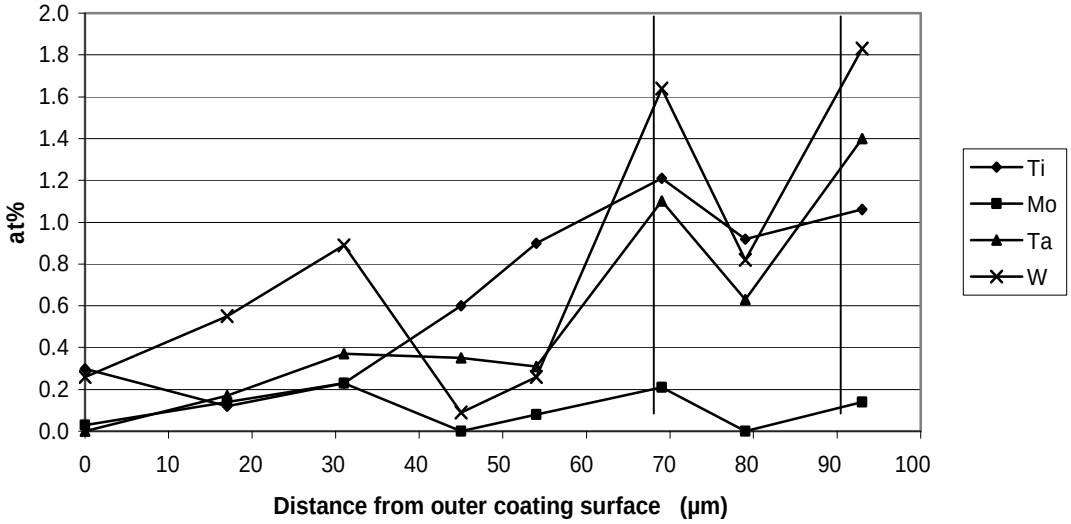

(b) : Alloying elements

Figure 9.26: Reference sample of CMSX-4 with 15mins CVD silicon-aluminide coating, (top side) – elements

9.3.2.5 CMSX-4 with silicon-aluminide coating produced from 30 minutes CVD at 1050°C

The BSE images of both sides of the tested and reference samples, seen in Figure 9.31, show similar morphologies in the respective samples. In the tested sample, there is evidence of inward diffusion, in a similar manner to that seen in the CMSX-4 sample with the 15 minutes CVD silicon-aluminide coating. The differences in depths of coatings, between those of the tested and reference samples, are consistent.

Bottom side of oxidation tested sample
Average depth of coating: 74µm

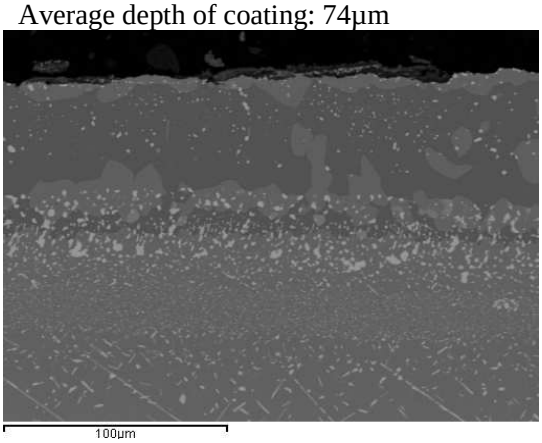

Reference sample – bottom side
Average depth of coating: 70µm

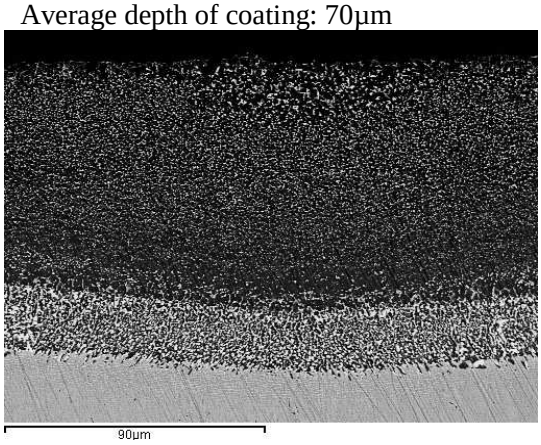

Top side of oxidation tested sample
Average depth of coating: 58µm

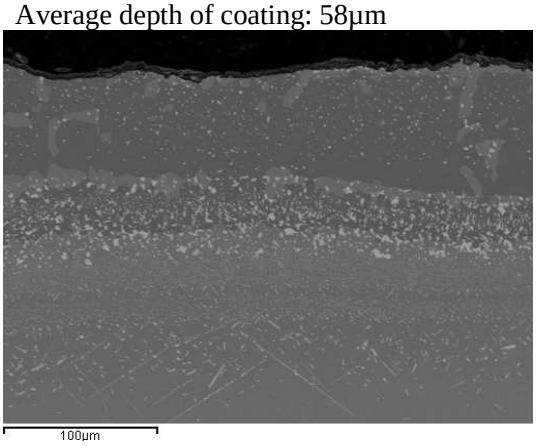

Reference sample – top side
Average depth of coating: 56µm

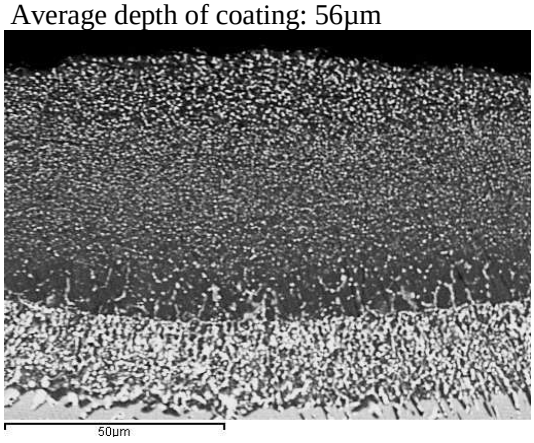

Figure 9.27: BSE images of CMSX-4 sample with 30mins CVD silicon-aluminide coating after 1000 hours oxidation testing at 1050°C, and the untested reference sample (Note different magnifications)

The element maps in Figure 9.28 show there is reducing aluminium content in the coating to feed the growth of the oxide scale. There is little chromium outwardly diffusing from the substrate to enhance corrosion protection. Inward diffusion of silicon has occurred and the diffusion zone/substrate initerface is silicon rich.

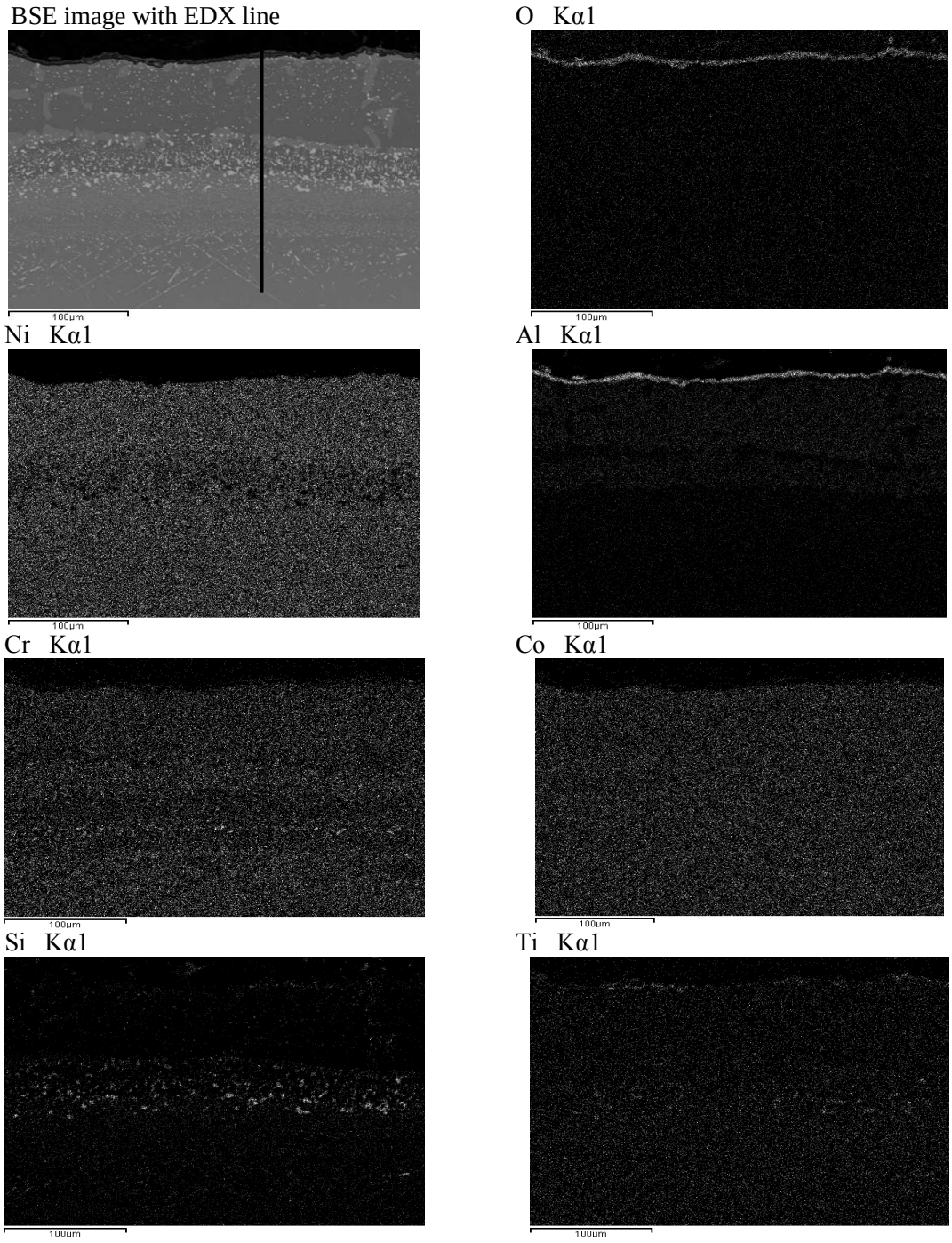

Figure 9.28: Oxidation test; 1000 hours at 1050^{o}C, top side of CMSX-4 sample with 30mins CVD silicon-aluminide coating - element maps

Comparison of the EDX results for the tested sample in Figure 9.29(a), with those of the reference sample seen in Figure 9.30(a), shows that after 1000 hours at 1050^{o}C, the aluminium content is significantly depleted. However, it is seen from Figures 9.28 and 9.29(a) that a depth of aluminium of ~50µm remains in the coating to provide oxidation protection.

This depth compares with the average depth of the remaining top side coating of the 15 minutes CVD sample, of ~45µm, showing that the latter coating will fail before that produced following 30 minutes CVD.

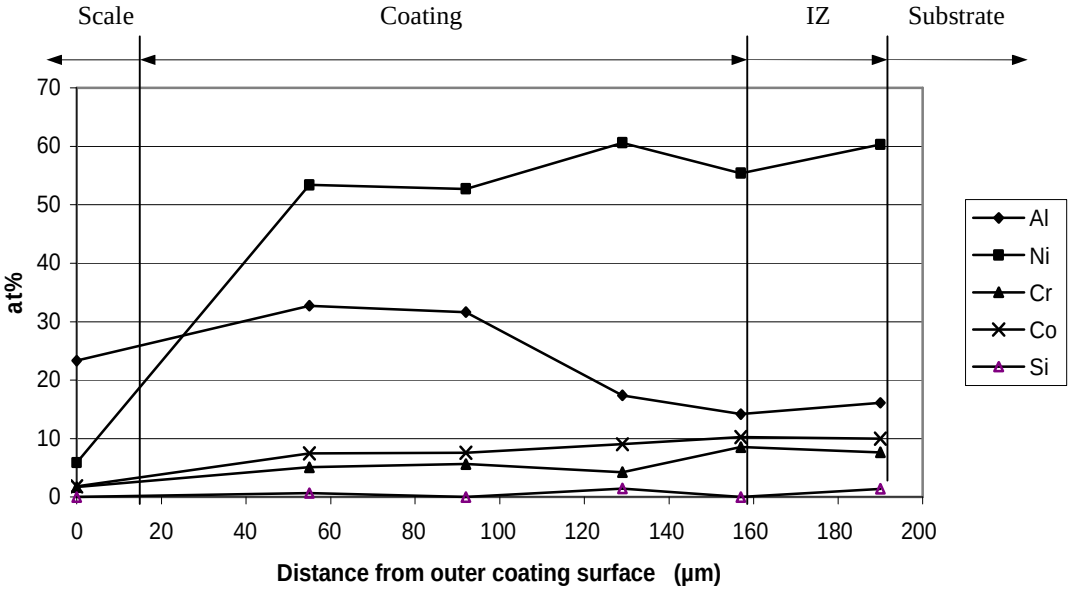

(a) : Main elements

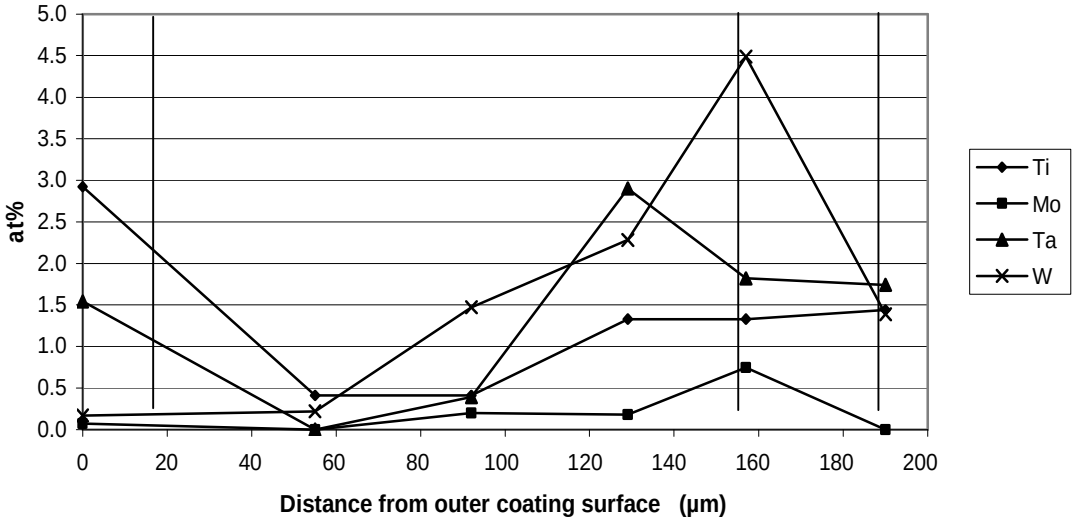

(b) : Alloying elements

Figure 9.29: Oxidation test; 1000 hours at 1050°C, top side of CMSX-4 sample with 30mins CVD silicon-aluminide coating – EDX line elements in Figure 9.28

The EDX results for titanium, molybdenum, tungsten and tantalum, in the tested sample, seen in Figure 9.29(b), show the high level of outward diffusion of these metals, compared with their content in the reference sample, displayed in Figure 9.30(b), where they are concentrated in the interdiffusion zone.

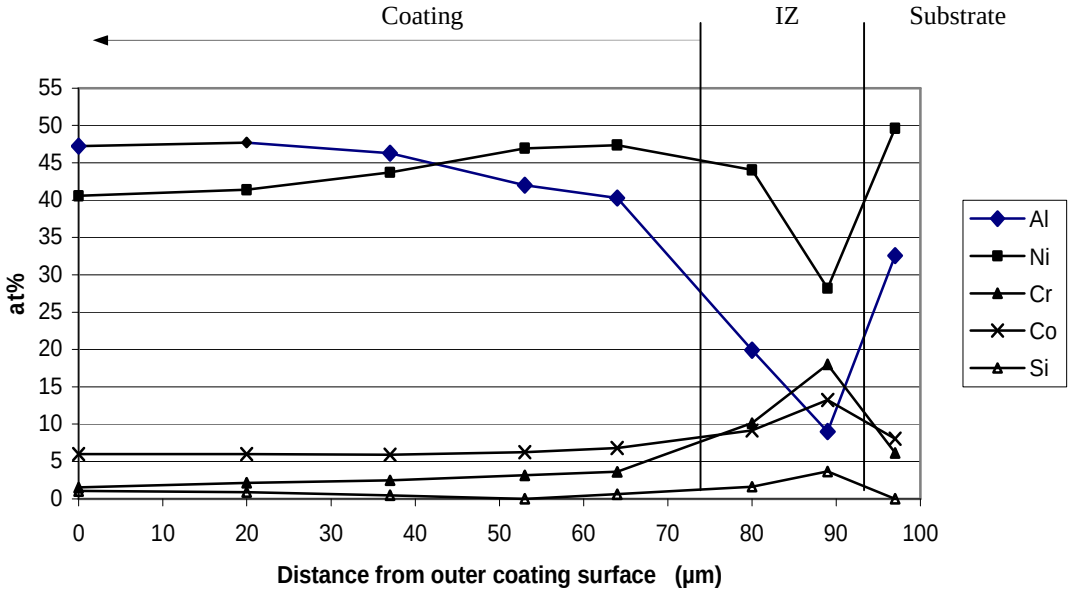

(a) : Main elements

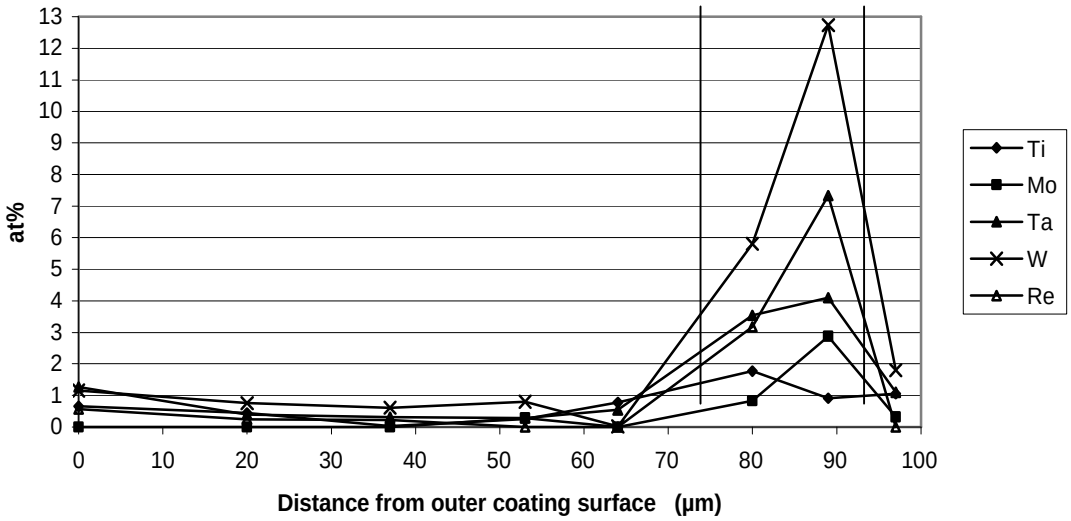

(b) : Alloying elements

Figure 9.30: Reference sample of CMSX-4 with 30mins CVD silicon-aluminide coating, (top side) – elements

9.3.2.6 CMSX-4 with silicon-aluminide coating produced from 60 minutes CVD at 1050°C

Figure 9.31 shows that, in contrast to coatings produced by 15 minutes CVD and 30 minutes CVD, there is no significant difference between the average depths of the two sides of the reference sample, produced by 60 minutes CVD. There is a significant difference in coating depths of the two sides, after oxidation, of 114µm and 75µm, which will result in earlier failure of the latter side coating. Heavy spalling has occurred during 1000 hours oxidation testing at 1050°C. The differences in the microstructures of the two sides of the reference sample will be considered later in this section.

Bottom side of oxidation tested sample
Average depth of coating: 114µm

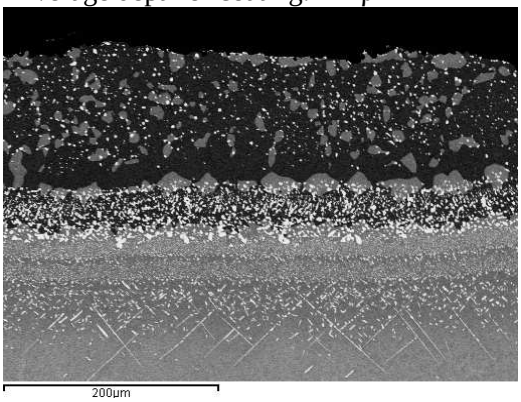

Reference sample – bottom side
Average depth of coating: 127µm

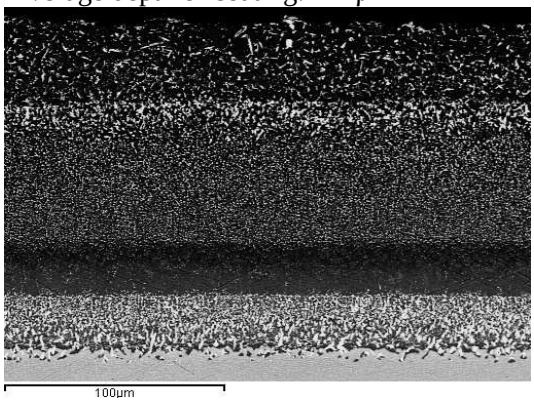

Top side of oxidation tested sample
Average depth of coating: 75µm

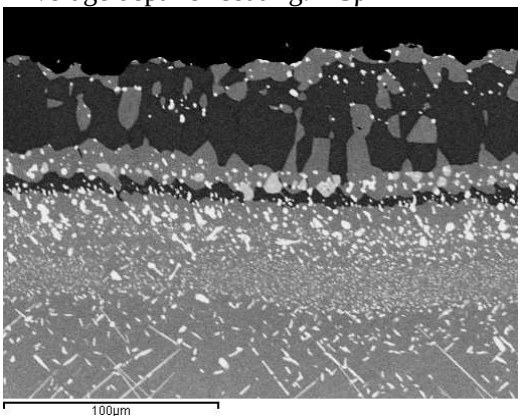

Reference sample – top side
Average depth of coating: 124µm

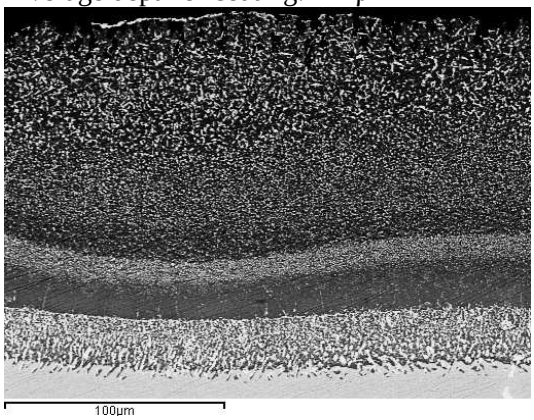

Figure 9.31: BSE images of CMSX-4 sample with 60mins CVD silicon-aluminide coating after 1000 hours oxidation testing at 1050°C, and the untested reference sample (note different magnifications)

Element maps in Figure 9.32 show typical microstructures of CMSX-4 having substantial depths of silicon aluminide coating remaining. The mapped elements fail to show any differences in the region of the substrate underneath the diffusion zone. These may be identified in the EDX scans. Degradation of the substrate is apparent, due to the TCP phases enriched in chromium, molybdenum and silicon, which have penetrated 150µm into the substrate.

The diffusion zone is rich in silicon, chromium and titanium, with little of these metals having outwardly diffused into the coating. Some silicon is found in the outer part of the coating. The aluminium and oxygen maps show the alumina rich oxide surface and uniform aluminium in the coating matrix that remains, with the darker phase in the BSE more aluminium rich.

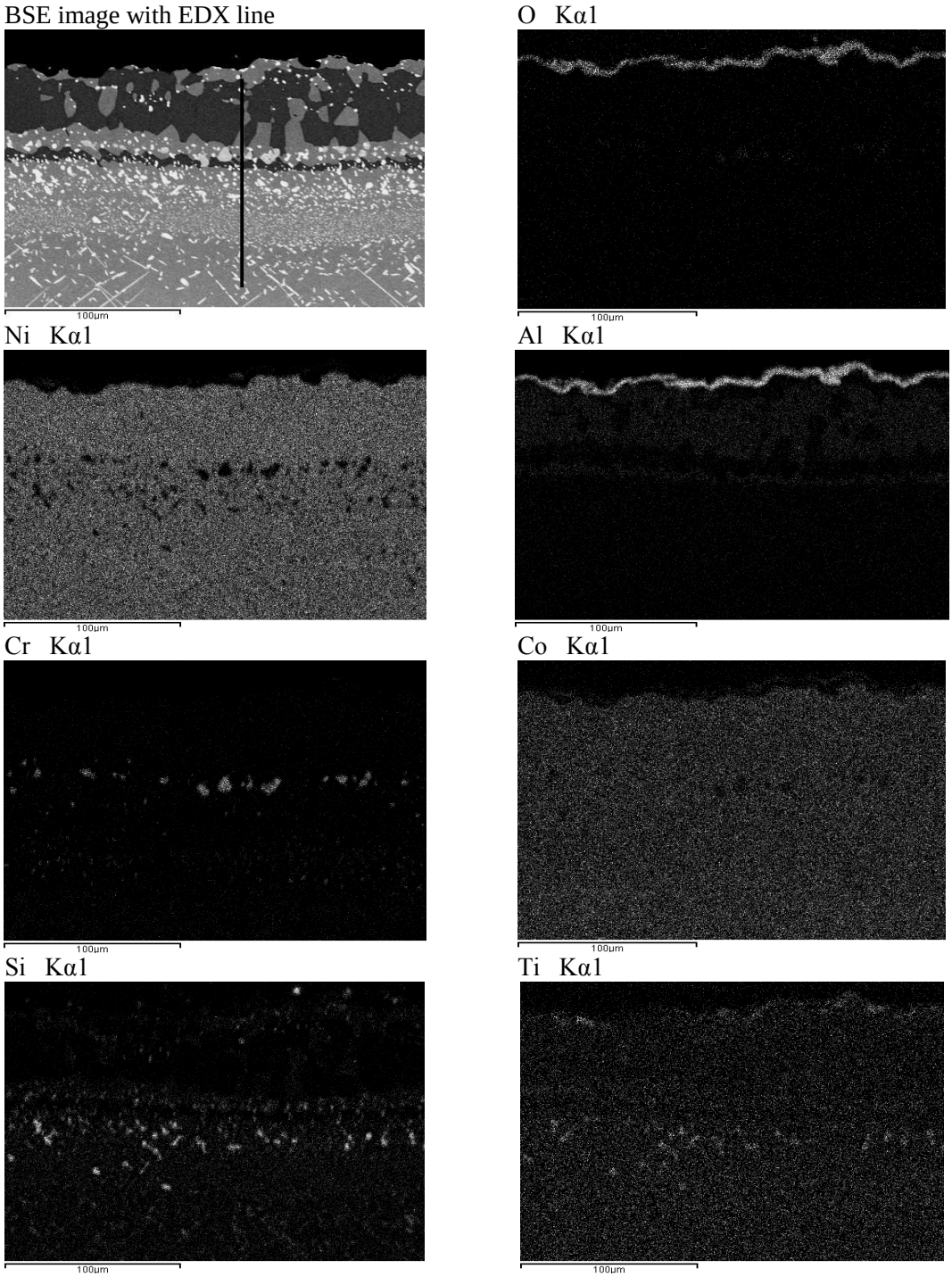

Figure 9.32: Oxidation test; 1000 hours at 1050^{o}C, top side of CMSX-4 sample with 60mins CVD silicon-aluminide coating - element maps

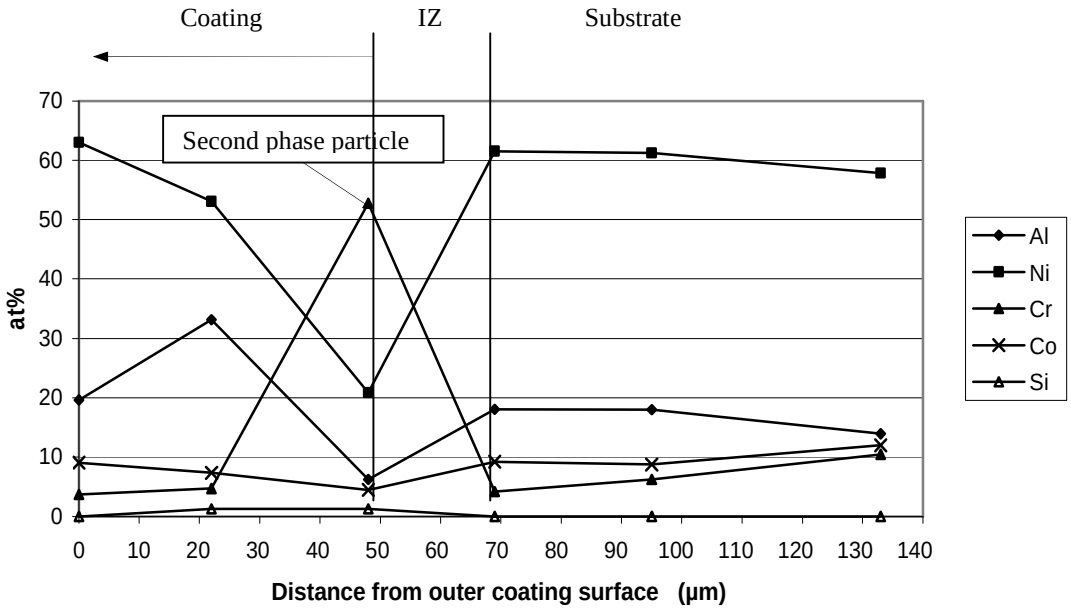

(a) : Main elements

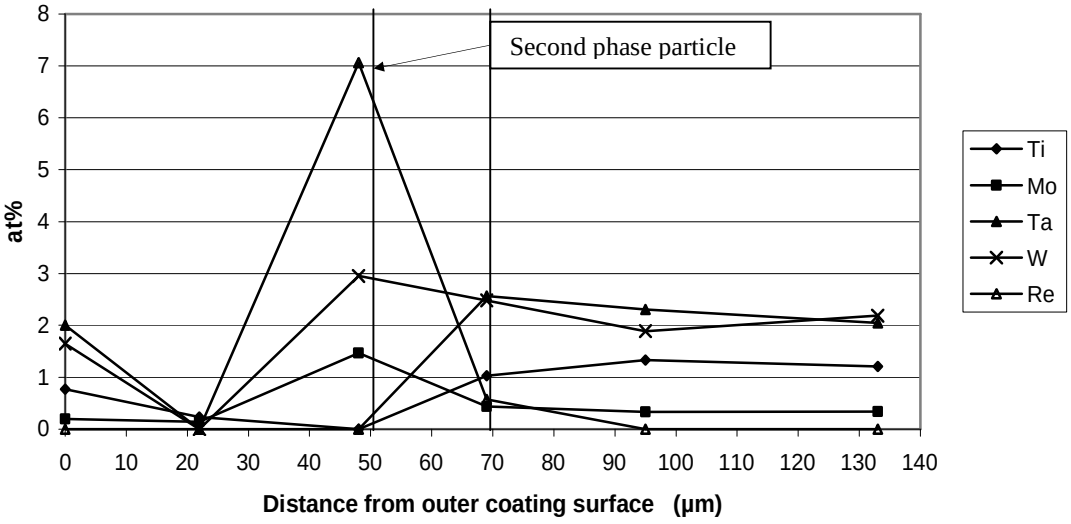

(b) : Alloying elements

Figure 9.33: Oxidation test; 1000 hours at 1050^{o}C, top side of CMSX-4 sample with 60mins CVD silicon-aluminide coating – EDX line elements in Figure 9.32

The EDX results in Figure 9.33 and the BSE image in Figure 9.32 show that around 30-40µm depth of silicon-aluminide coating remains in the top side of the tested sample. The diffusion zone is rich in chromium and tantalum, which peak at 53 at% Cr and 7 at% Ta, then reduce to 4 at% Cr and <1 at% Ta at the coating surface. These values compare with 2 at% Cr and 1.5 at% Ta in the interdiffusion zone and 2 at% Cr and <1 at% Ta in the coating, of the reference sample. Oxidation testing for 1000 hours at 1050^{o}C has transformed the more aluminium rich β-NiAl phase of the reference sample to γ'NiAl phase at the coating surface.

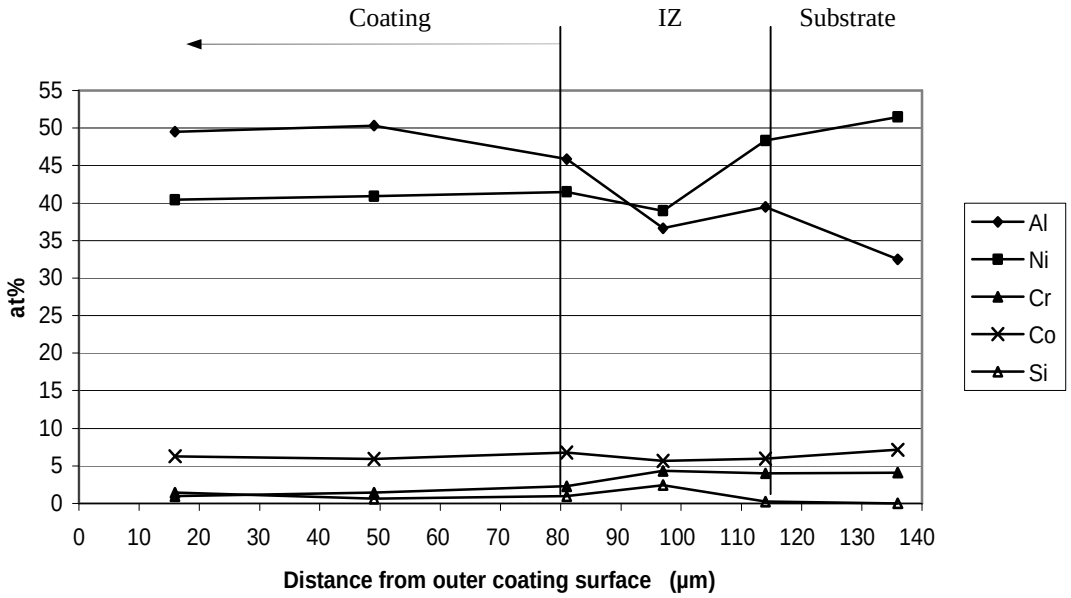

(a) : Main elements

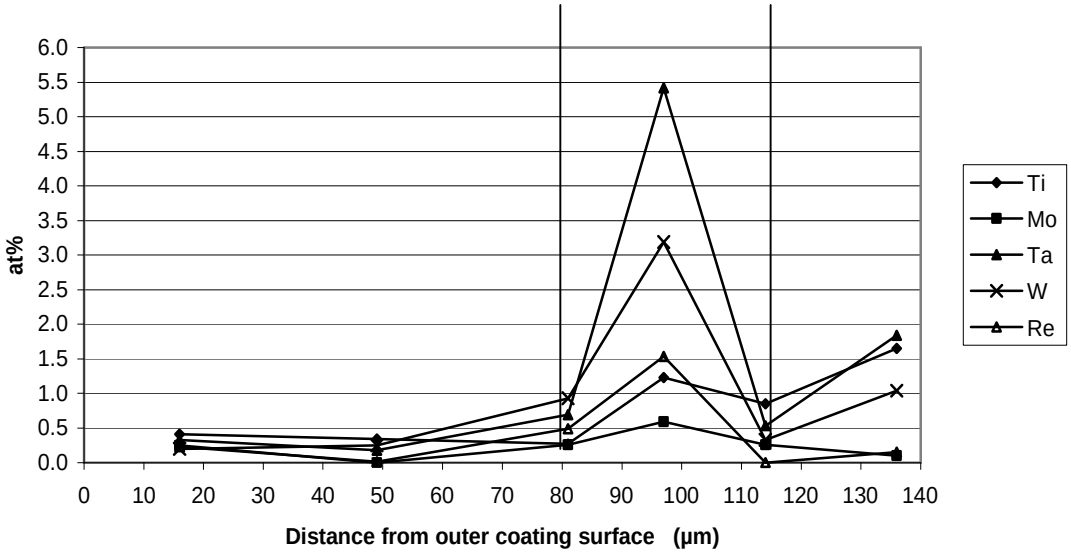

(b) : Alloying elements

Figure 9.34: Reference sample of CMSX-4 with 60mins CVD silicon-aluminide coating, (top side) – elements

9.3.2.7 Microstructures after 1000 hours oxidation testing at 1050^{o}C – summary

Depths of remaining coatings after oxidation testing, for the various CVD soak periods, for IN738LC samples were higher than in the respective CMSX-4 samples. For both substrates, the coatings produced following 60 minutes CVD proved more oxidation resistant then those for the shorter soak periods. There were larger differences in depths of coatings, on each side of samples, produced from the 15 and 30 minutes CVD soak periods, than those from samples produced following 60 minutes CVD soak periods.

9.3.3 Microstructures of samples after 3000 hours cyclic oxidation testing at 1050°C

It was concluded in section 9.3.2.1 that, after 3000 hours oxidation testing at 1050°C, only the IN738LC and CMSX-4 samples with the 60 minutes CVD novel coatings, could still provide acceptable oxidation protection. As seen in Figure 9.12, the IN738LC sample (IN602) with this novel coating had not crossed the zero line after 3000 hours, whereas the CMSX-4 sample (CM601) crossed the zero line after 2850 hours. The four samples with novel coatings, produced following 15 minutes CVD or 30 minutes CVD, failed after significantly fewer hours of oxidation testing at 1050°C, and were not considered to be viable for long term service in an industrial gas turbine burning biomass derived fuels. Their microstructures are not evaluated in this section. The following evaluations of samples IN602 and CM601 include microstructures of each side (top and bottom).

9.3.3.1 IN738LC with silicon-aluminide coating produced by 60 minutes CVD at 1050°C

Bottom side of oxidation tested sample
Average depth of coating: 135µm

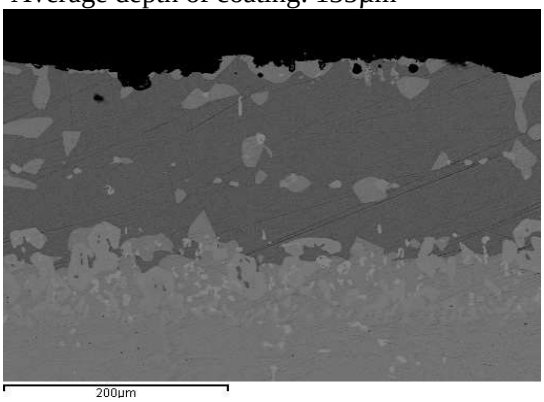

Reference sample – bottom side
Average depth of coating: 93µm

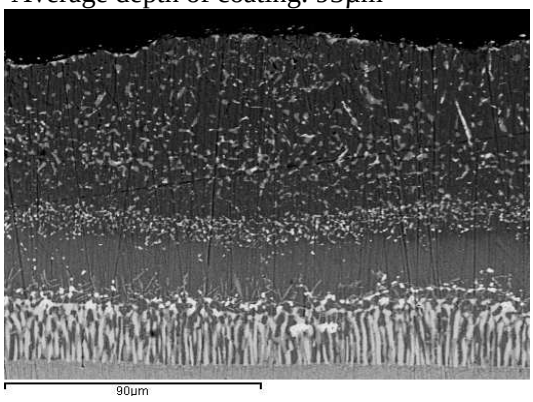

Top side of oxidation tested sample
Average depth of coating: 93µm

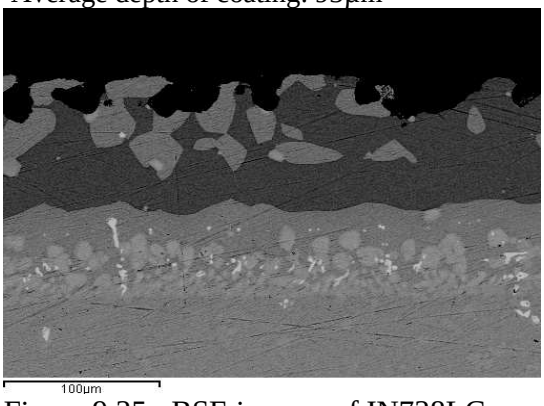

Reference sample – top side
Average depth of coating: 74µm

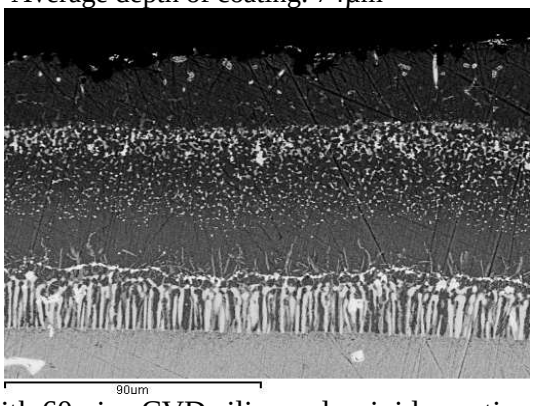

Figure 9.35: BSE images of IN738LC sample with 60mins CVD silicon-aluminide coating after 3000 hours oxidation testing at 1050°C, and reference sample (note different magnifications)

The BSE images of tested and untested samples, seen in Figure 9.35, show the extensive coating degradation after 3000 hours oxidation testing. However, it should be noted that the net mass change of this sample did not cross the zero-line during the test period.

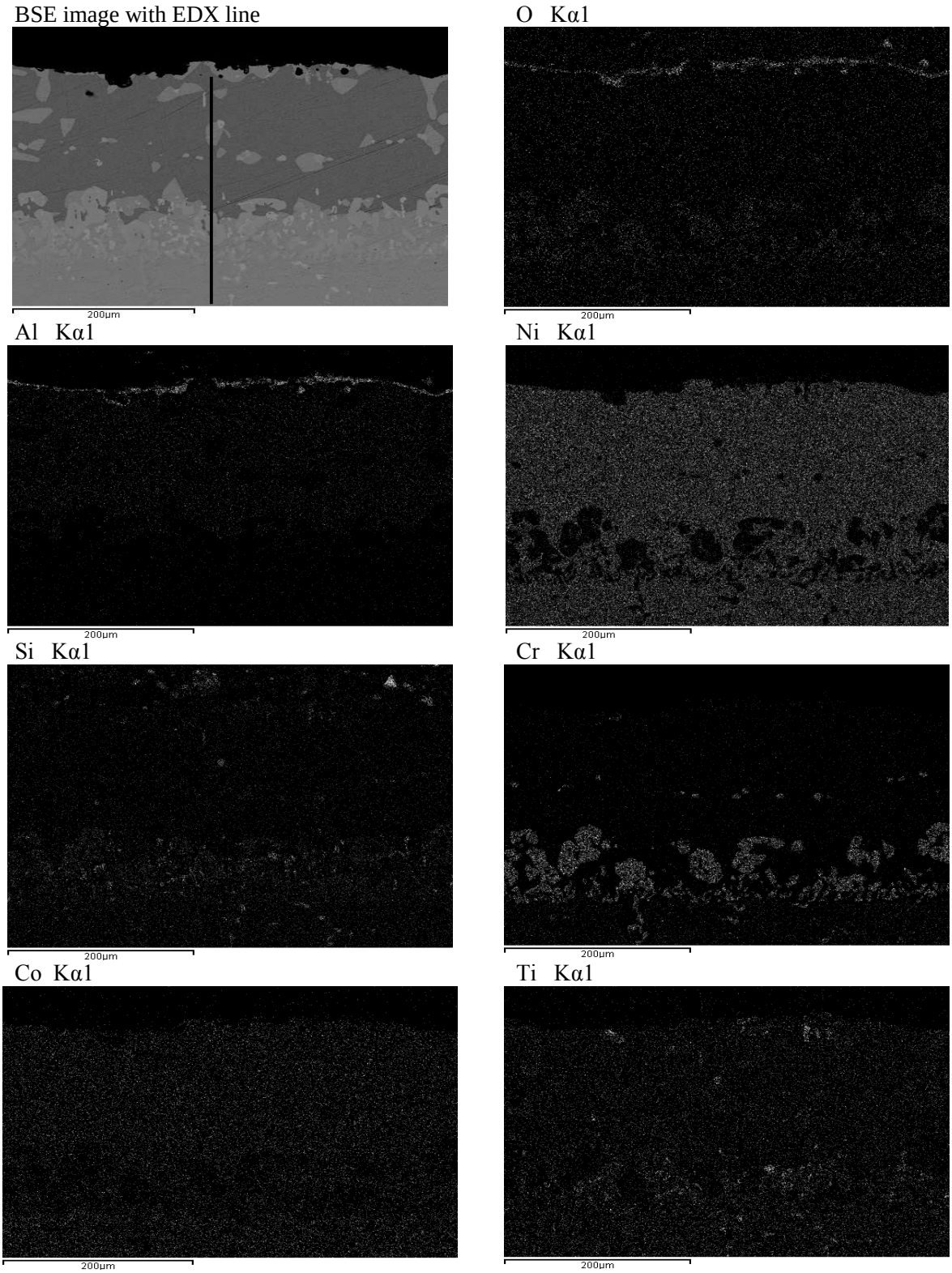

Figure 9.36: Oxidation test: 3000 hours at 1050^{o}C, bottom side of IN738LC sample with 60mins CVD silicon-aluminide coating – element maps

Element maps in Figure 9.36 show the relatively uniform matrix. This is confirmed by EDX results in Figure 9.37, where the nickel content averages about 50 at% Ni through the coating, whereas aluminium commences an increasing trend from the interdiffusion zone, rising to 27 at% at the coating surface. The matrix consists of γ'-NiAl phase, throughout the coating, with a surface α-Al_2O_3 scale. Outward diffusion of chromium proceeds fom the interdiffusion zone through the scale, with a line of chromium rich particles half way through the coating. Levels of chromium, cobalt and silicon are steady through the coating (4 at% Cr, 6 at% Co, 1 at% Si).

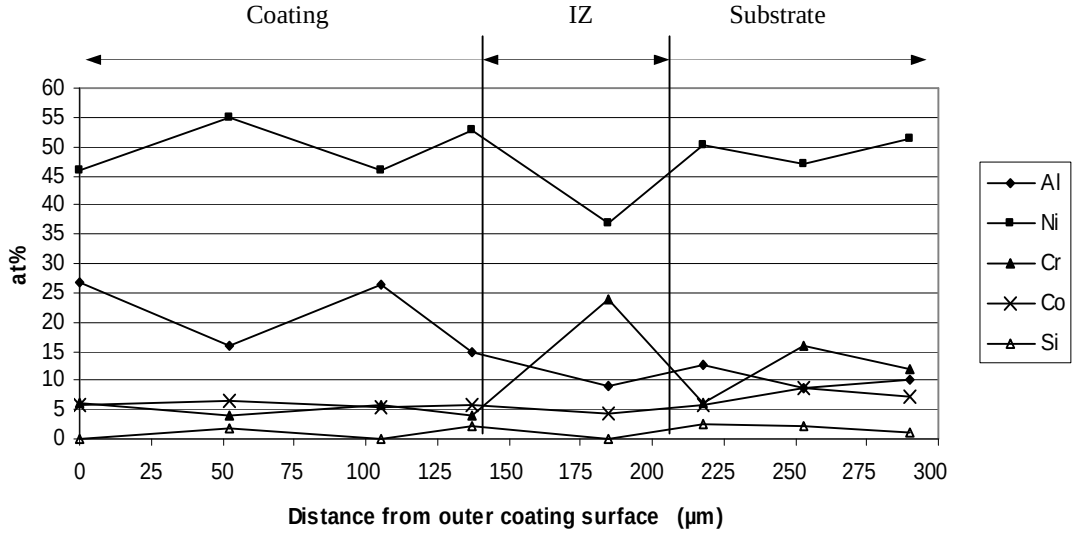

(a) : Main elements

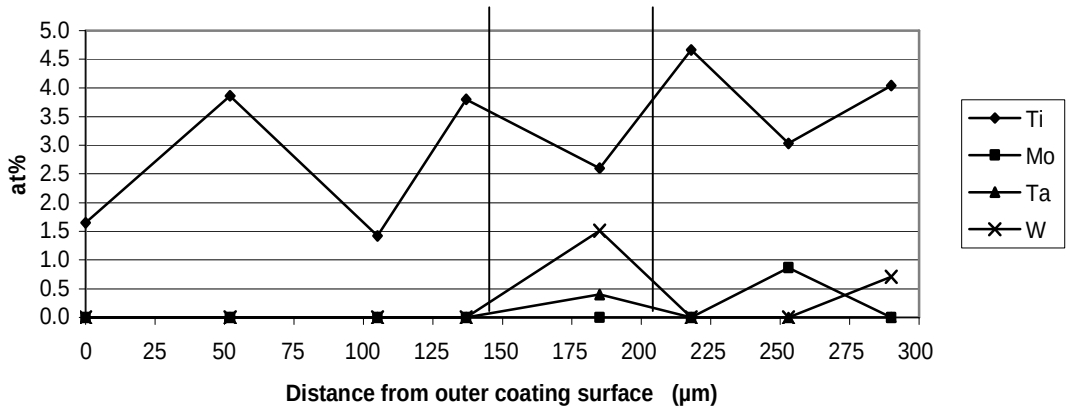

(b) : Alloying elements

Figure 9.37: Oxidation test; 3000 hours at 1050°C, bottom side of IN738LC sample with 60 mins CVD silicon-aluminide coating - EDX line elements in Figure 9.36

As seen in Figure 9.37, of the four metals seen to outwardly diffuse into the coating during oxidation testing, only titanium continues its outward diffusion through the coating with a fluctuating content of between 1.4 at% Ti and 3.8 at% Ti. Molybdenum, tantalum and tungsten remain at the coating/interdiffusion zone interface.

The element maps of the top side of the same sample are shown in Figure 9.38. These show similar morphologies to those of the bottom side elements.

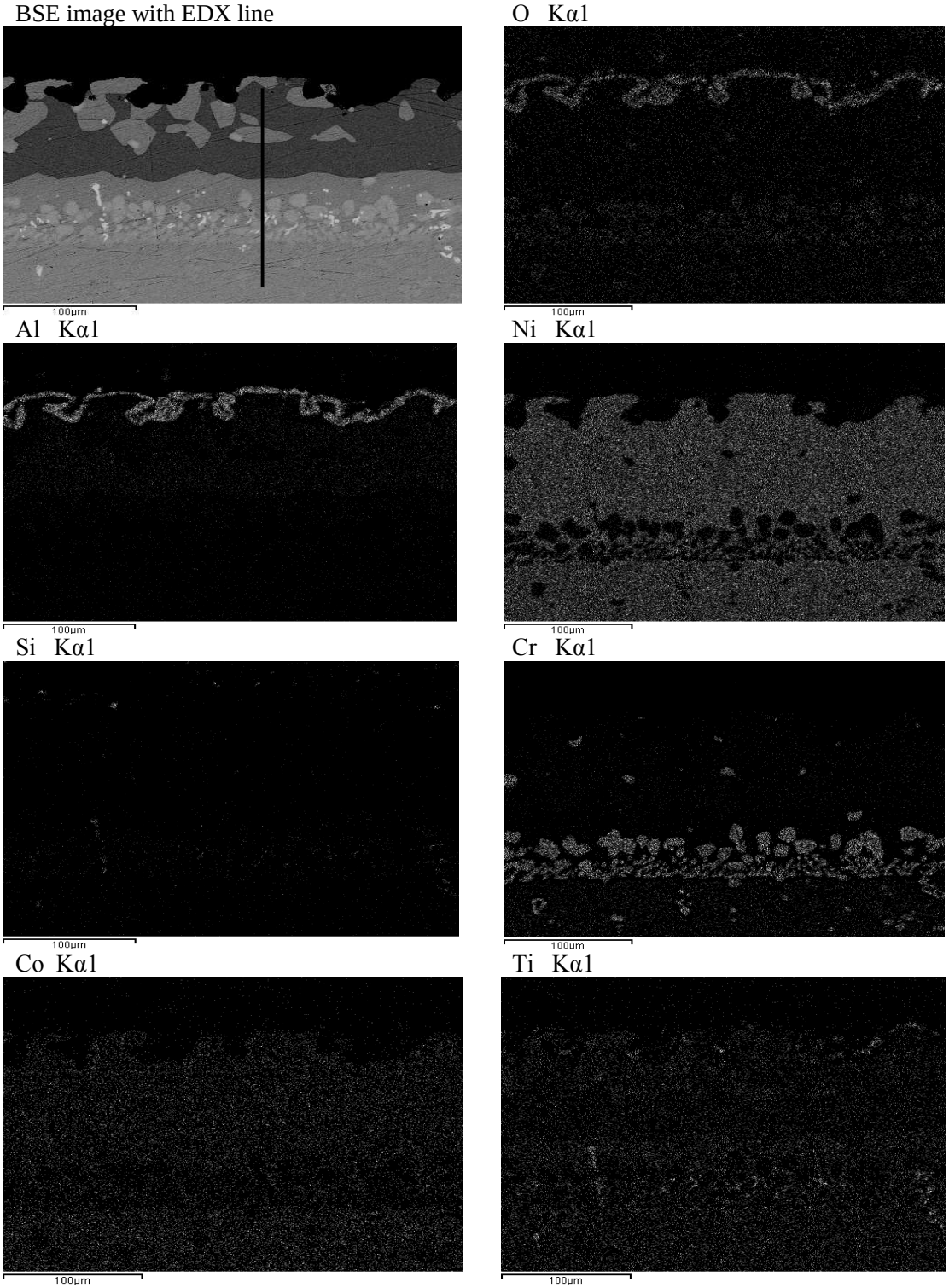

Figure 9.38: Oxidation test: 3000 hours at 1050^{o}C, top side of IN738LC sample with 60mins CVD silicon-aluminide coating – element maps

Element maps in Figure 9.38 show two main phases in the degraded NiAl coating after 3000h oxidation at 1050°C. The results in Figure 9.39(a), taken along the EDX line in Figure 9.37, confirm these are γ'-NiAl phase and γ-Ni, containing up to 15 at%Al, similar to those in the bottom side of the sample. However, in the top side the phases are irregularly distributed in patches, where as, in the bottom side they progress uniformly from diffusion zone to surface. The levels of aluminium content through the coating/scale in the top side are very similar to those in the bottom side of the sample. Nickel content at the surface of the top side, of 36 at% Ni, is significantly less than that in the bottom side, 46 at% Ni.

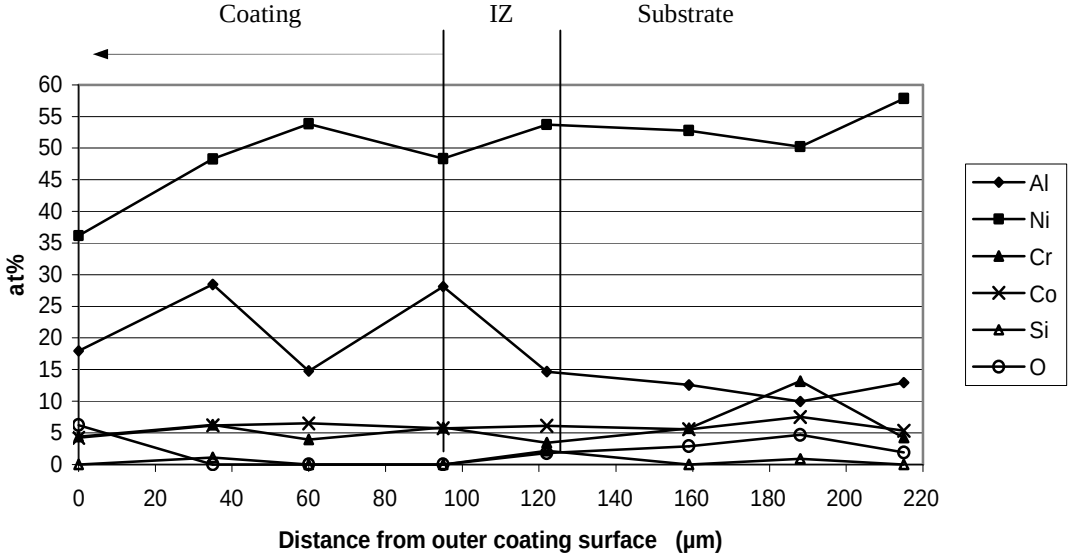

(a) : Main elements

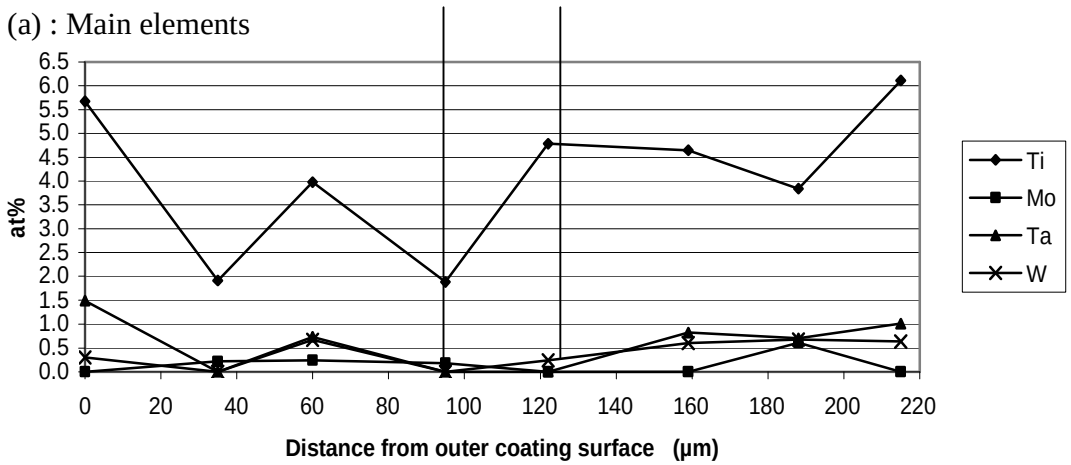

(b): Alloying elements

Figure 9.39: Oxidation test; 3000 hours at 1050°C, top side of IN738LC sample with 60mins CVD silicon-aluminide coating - EDX line elements in Figure 9.38

Outward diffusion of titanium in the top side, seen in Figure 9.39, is at similar levels to those in the bottom side, seen in Figure 9.37. The content of outward diffusion of molybdenum, tantalum and tungsten in the top side appears higher than in the bottom side of the sample. However, it is considered that the differences in their content, between the two sides of the sample, are small.

9.3.3.2 CMSX-4 with silicon-aluminide coating produced from 60 minutes CVD at 1050°C

The net mass change for this sample (CM601) had crossed the zero-line after 2750 hours of cyclic oxidation testing at 1050°C (Figure 9.12). As seen in Figure 9.40, the depths of coating on this sample are the same on the bottom and top sides. This is also the case for the reference sample. In the tested sample, Figure 9.40 shows that, on both sides, the coating is degraded due to diffusion, with a thin oxide scale remaining.

Bottom side of oxidation tested sample
Average depth of coating: 143µm

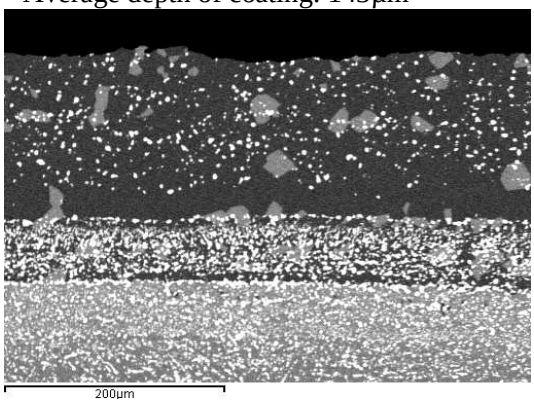

Reference sample – bottom side
Average depth of coating: 120µm

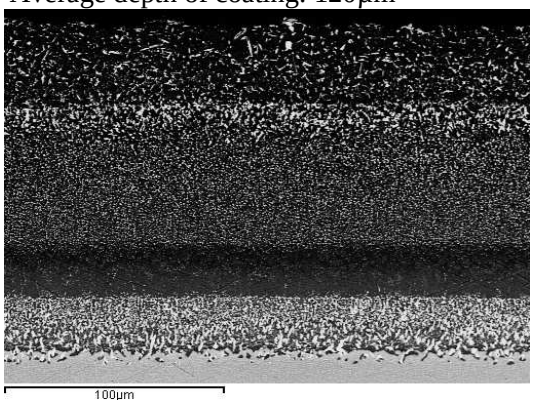

Top side of oxidation tested sample
Average depth of coating: 143µm

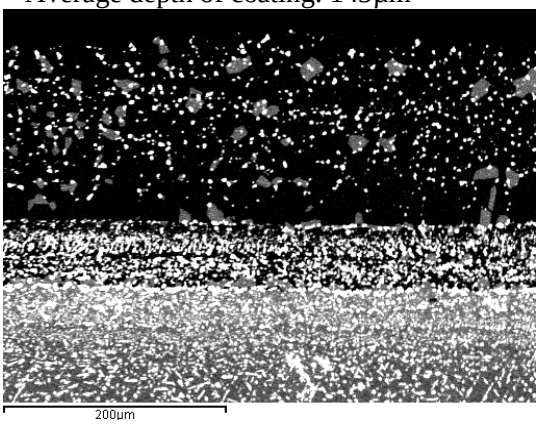

Reference sample – top side
Average depth of coating: 120µm

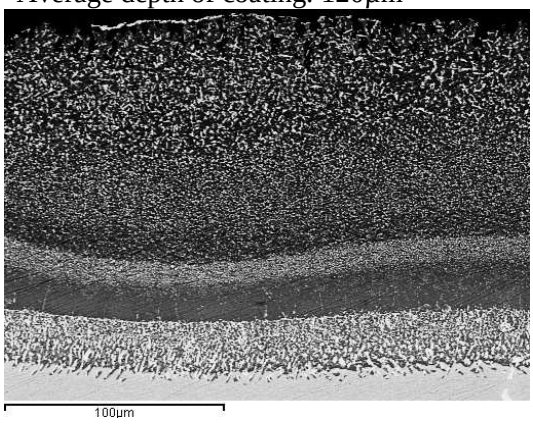

Figure 9.40: BSE images of CMSX-4 sample with 60mins CVD silicon-aluminide coating after 3000 hours oxidation testing at 1050°C, and the reference sample (note different magnifications)

The element maps in Figure 9.41 illustrate the coating failure due to interdiffusion with the substrate, showing near complete uniformity of oxygen, aluminium, nickel, chromium, cobalt and titanium, as they progress from within the substrate through to the coating surface. Silicon is distributed within the coating/scale, and has inwardly diffused through the interdiffusion zone into the substrate.

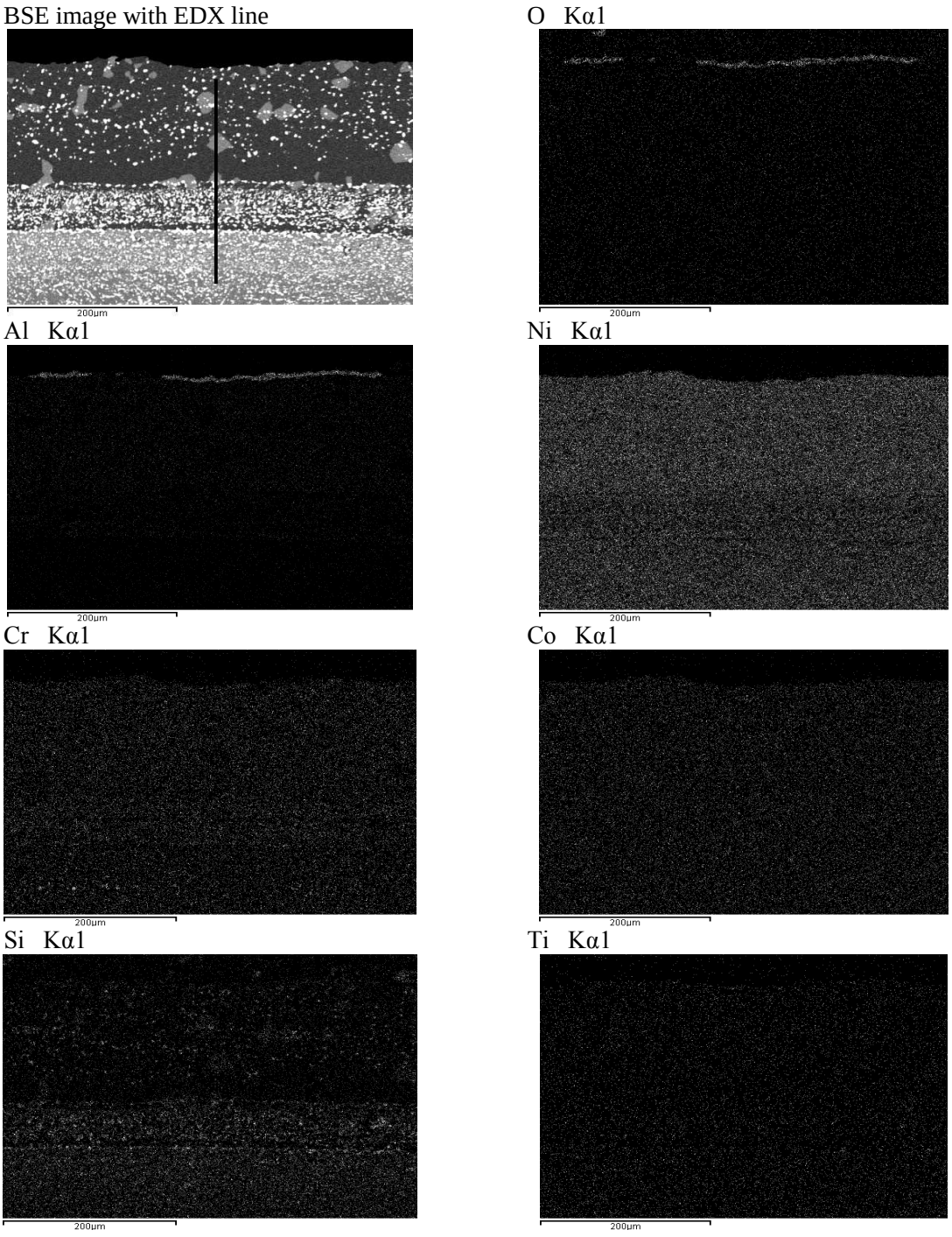

Figure 9.41: Oxidation test: 3000 hours at 1050^{o}C, bottom side of CMSX-4 sample with 60mins CVD silicon-aluminide coating – element maps

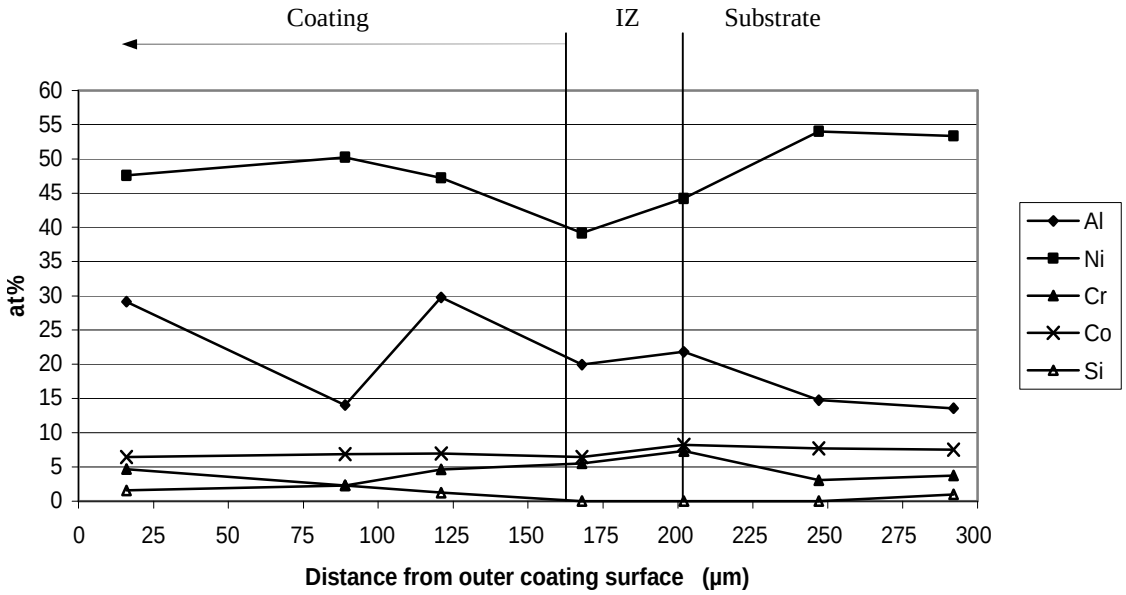

(a) : Main elements

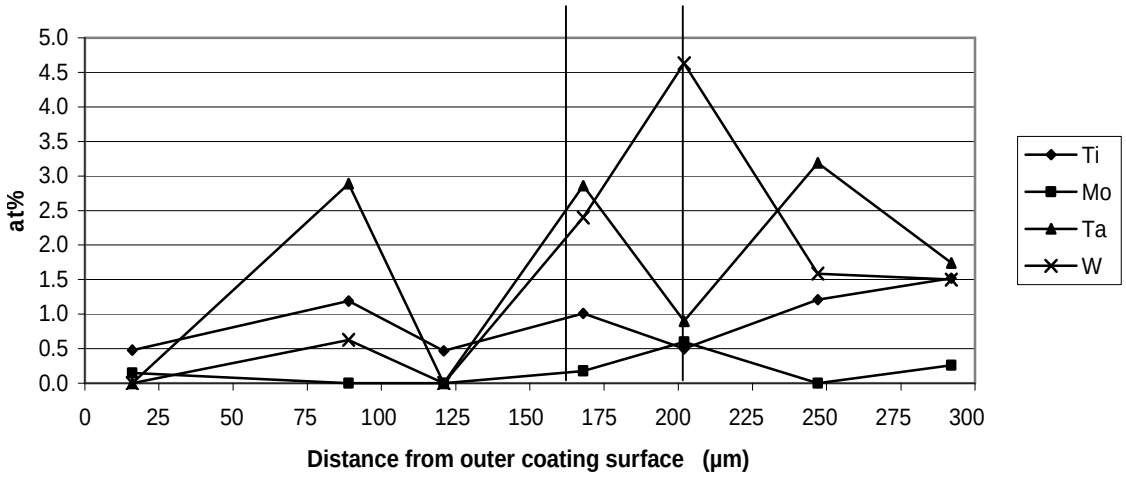

(b) : Alloying elements

Figure 9.42: Oxidation test; 3000 hours at 1050°C, bottom side of CMSX-4 sample with 60mins CVD silicon-aluminide coating - EDX line elements in Figure 9.41

Figure 9.42(a) shows progress of the degraded β-NiAl phase matrix through the coating to the interdiffusion zone/coating interface, 240µm from the scale/coating surface. From this position, there is a rapid transition to γ'-NiAl phase then, with increasing aluminium content from silicon modification, there is movement to α-Ni, with aluminium in solution. Within the substrate there is increasing inward diffusion of silicon, also borne out by the silicon map in Figure 9.51. Outward diffusion of titanium, molybdenum, tantalum and tungsten occurs in the bottom side of the tested sample, as seen in Figure 9.42(b).

The similarities, in depths of coatings and extent of substrate deterioration, in the tested sample, are shown in Figure 9.43. These differences are investigated further in comparisons of EDX results in each side. The BSE image of the top side and the EDX line is shown in Figure 9.44.

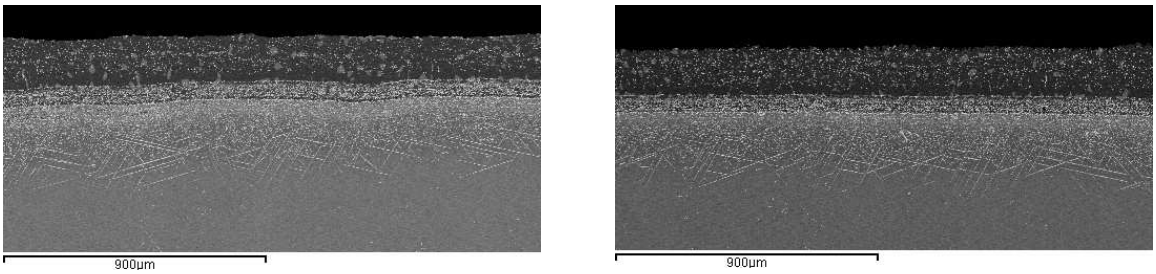

Bottom side Top side

Figure 9.43: Oxidation test, 3000 hours at 1050^{o}C, BSE images of bottom and top sides of CMSX-4 sample with 60mins CVD silicon-aluminide coating

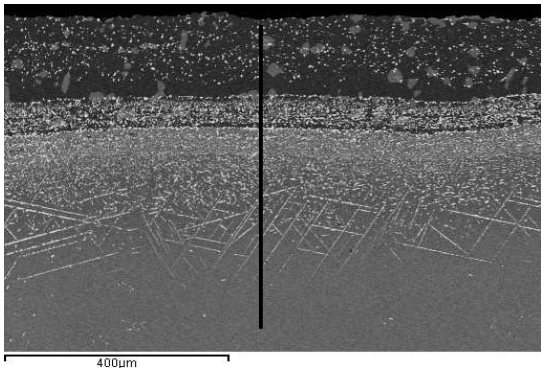

Figure 9.44: BSE image of the top side of tested CMSX-4 sample with 60mins CVD silicon-aluminide coating, with EDX line

The EDX results in Figures 9.42 and 9.45 indicate that the coating degradation, due to interdiffusion of aluminium into the substrate, in the top side preceded that of the bottom side. In the top side , aluminium content at a position 35µm from the scale/coating surface had reduced to 15 at% Al. This content will be insufficient to feed protective oxide scale growth. In the bottom side, the aluminium content at a distance from the surface of approximately 18µm, was 29 at% Al, sufficient to support scale growth for a longer period than that in the top side. It can be assumed that, if the phase change in the top side had been similar to that in the bottom side, coating failure would have occurred some time after the 2850 hours achieved by the tested sample.

In Figure 9.45(b), TCP phases depending on tungsten, molybdenum, chromium and cobalt are seen to have degraded the substrate to a depth in excess of 300 µm.

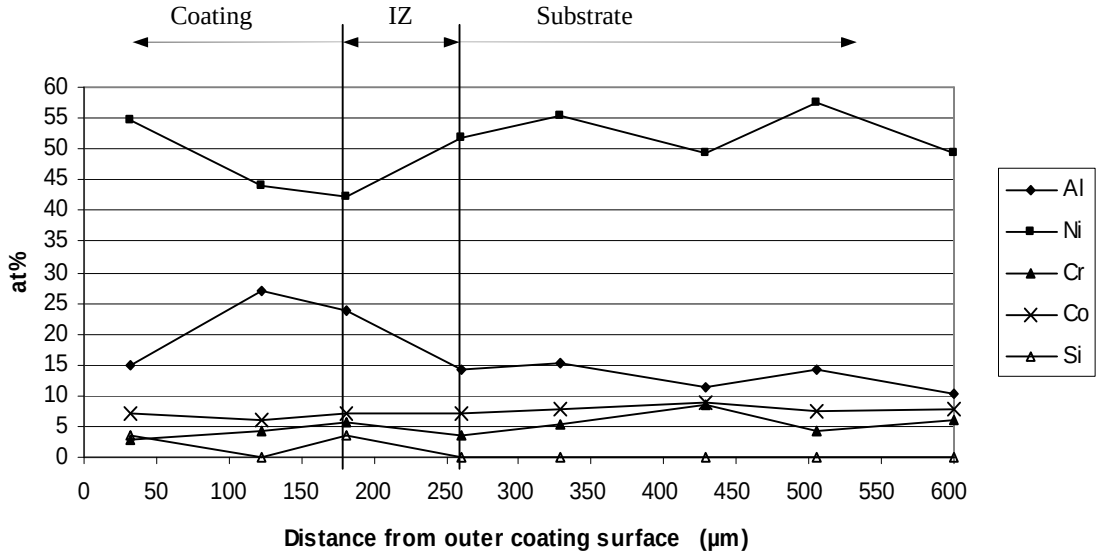

(a) : Main elements

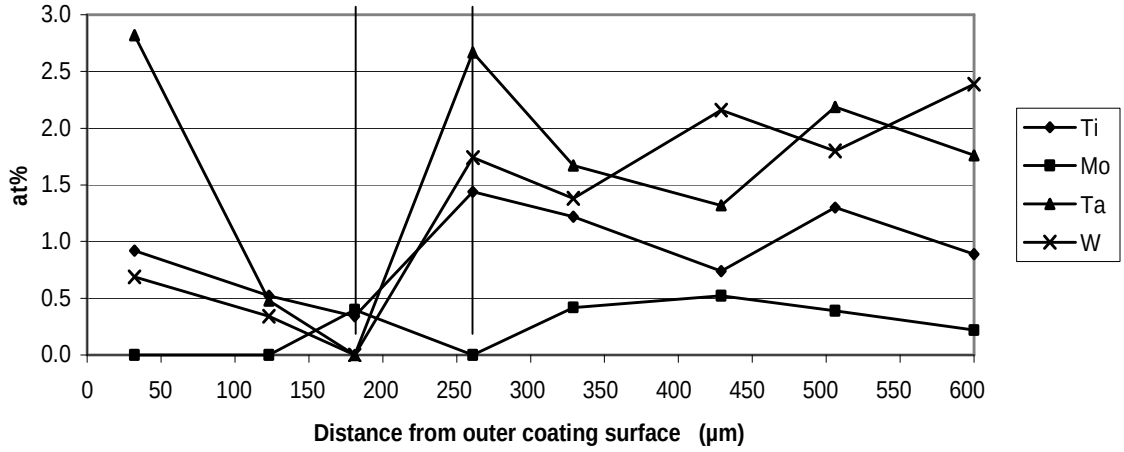

(b) : Alloying elements

Figure 9.45: Oxidation test; 3000 hours at 1050°C, top side of CMSX-4 sample with 60mins CVD silicon-aluminide coating - EDX line elements in Figure 9.44

EDX results of titanium, molybdenum, tantalum and tungsten content in the top side of the tested sample, shown in Figure 9.45(b), indicate their outward diffusion progresses to the surface, which is then comparatively rich in these metals. In contrast, Figure 9.42 shows the outward diffusion of these metals in the bottom side, to peak at a distance from the surface of 88µm, after which they reduce to trace levels at the surface. The γ-Ni phase is now present through the coating. Refractory metal additions are more soluble in γ-Ni.

9.4 Cyclic oxidation tests, evaluation of oxidation protection provided by novel coatings

9.4.1 Cyclic oxidation tests of novel coatings for 1000 hours at 950^{o}C

The first series of cyclic oxidation tests, of 10 x 100 hours testing periods at 950^{o}C, was used as a filtration process, to eliminate any silicon aluminide novel coatings, produced from different CVD soak periods, which may have failed in less than 1000 hours. The tests revealed inconsistencies in the mass changes of some coatings when compared with their duplicates. In some cases, involving both IN738LC and CMSX-4 samples, the mass changes in one coating, produced by 30 minutes CVD, would be significantly different to the mass changes produced by its duplicate sample (produced for the same CVD soak period). The mass changes from the coating produced for the same CVD soak period, in some cases were higher or, in other cases, lower than samples coated using 15 minutes or 30 minutes CVD soak periods. Variations such as these are considered in more detail in evaluation of the oxidation tests at 1050^{o}C.

It was concluded that all coatings performed sufficiently well at 950^{o}C for them to be subject to cyclic oxidation testing at 1050^{o}C. No further evaluation of the oxidation tests at 950^{o}C was undertaken as it was deemed that the coatings would last well over 3000 hours, beyond the remaining time for this thesis. Instead the cyclic oxidation studies focussed on 1050^{o}C.

9.4.2 Cyclic oxidation tests of novel coatings for 3000 hours at 1050^{o}C

In this series of cyclic oxidation tests, two samples of each substrate with silicon aluminide coatings produced by CVD at 1050^{o}C, with soak periods of 15 minutes, 30 minutes and 60 minutes, a total of twelve samples, were tested. After 1000 hours testing, the worst performing sample of each combination was removed from the test programme, for evaluation. Oxidation testing of the best performer of each combination was then resumed, for an extended period. After 3000 hours, the net mass change of the IN738LC sample with a silicon-aluminide coating produced from 60 minutes CVD soak period, was the only sample not to have crossed the zero-line for net mass gain as a result of scale spallation. The decision was made to stop oxidation testing at this point.

9.4.2.1 Influence of CVD soak periods on oxidation performance

Evaluation of samples, post 1000 hours and post 3000 hours oxidation testing, showed that coating depths varied between the top and bottom sides of samples and varied, to some extent, between samples formed by the same CVD soak period. These variations were caused by the surface of the powder pack on the top side of the sample being exposed to gas during CVD, whereas the bottom side, sitting directly on the base of the tray was completely separated from the gas. The position of the sample in the CVD tray could also influence the depth of coating, particularly for the samples produced by shorter CVD soak periods. Samples farthest from the gas entry aperture could be less exposed to allow leakage than those close to the gas entry point. These factors are explained in detail in Section 4.3. The net effect on oxidation protection of the coatings is that those on the top side of samples would fail before the deeper, bottom coatings, these generally had a thicker silicon-aluminide coating.

A major activity in further coating development of silicon aluminide coatings, produced by CVD, will be to rectify this difference in coating depths.

The cyclic oxidation tests at 1050^{o}C showed that samples of IN738LC and CMSX-4, with the silicon aluminide coatings produced by CVD soak periods of 15 minutes and 30 minutes, all failed early, between 700 hours and 2100 hours of testing.

The samples of IN738LC and CMSX-4 with silicon aluminide coatings produced by CVD soak periods of 60 minutes provided the best cyclic oxidation protection. Net mass change of the CMSX-4 sample crossed the zero-line after 2850 hours of testing, signifying the mass of oxygen lost by scale spallation equalled the mass of oxygen gained by the sample in the oxidation process. The net mass change of the IN738LC sample, with the silicon-aluminide coating produced by a soak period of 60 minutes, had not crossed this zero-line after 3000 hours of testing. At this stage in the testing, the net mass change of 0.95 mg/cm^2 was reducing at a rate of 0.0025 mg/cm^2 per hour. For the same sample, the gross mass change of 1.95 mg/cm^2 had been unchanged for 400 hours, during which time the spall mass of 1 mg/cm^2 was rising at a rate of 0.0005 mg/cm^2. Crossing of the zero-line could be expected after a further 1400 hours of oxidation testing.

9.4.2.2 Oxidation resistance of IN738LC and CMSX-4 with silicon-aluminide coatings

IN738LC and CMSX-4 substrates with similar silicon aluminide coatings exhibit differing mass change and spall rates when cyclic oxidation tested at 1050^{o}C.. In general terms, all IN738LC samples, irrespective of the CVD soak periods, had similar mass change and spall mass gradients. This was also the case for CMSX-4 samples, with all gradients being steeper than those for IN738LC samples. The initial gross mass changes, over the first 100 hours, were of a similar order for the 15 minutes CVD and 30 minutes CVD soak period samples, whereas rates were much higher for the 60 minutes CVD soak period samples; 1.2mg/cm^2 for the IN738LC sample and 1.6mg/cm^2 for the CMSX-4 sample.

For the next 1000 hours of testing, the rates of gross mass change followed a similar gradient then diverged with an increasing rate for the CMSX-4 sample. Over the first 1000 hours the spall mass gradients were similar for the two substrates, after which that of the CMSX-4 sample followed an increasing trend. Of significance was the oxidation rate in the first 100 hours, for the two samples with 60 minutes CVD soak periods. Despites the net mass changes, in this period, of approximately 1.2mg/cm^2 for both IN738LC and CMSX-4 samples, subsequent gradients were similar until after approximately 1300 hours of testing, when the gradient for the CMSX-4 sample changed negatively, resulting in the earlier failure of this sample, compared with the IN738LC sample mentioned above.

In summary, the oxidation protection provided by the coating formed on samples of IN738LC and CMSX-4, with silicon aluminide coatings formed from 60 minutes CVD soak periods, was significantly higher that that provided by these substrates having coatings formed from the shorter CVD soak periods. These shorter CVD period samples provided non-viable oxidation protection, for industrial gas turbines expected to burn biomass derived fuels.

Substrate degradation, due to interdiffusion and the formation of topologically close packed (TCP) phases, such as σ, μ and laves occurs in all the CMSX-4 samples, but is very high in the sample with the silicon-aluminide coating produced by 60 minutes CVD. In this sample, the substrate degradation caused by TPC depletes the matrix of the alloying elements; cobalt, molybdenum, tungsten, rhenium and chromium. This degradation may diminish the rupture strength and ductility of the CMSX-4 substrate.

9.4.2.3 Assessment of residual post-oxidation test silicon-aluminide coatings

The BSE images and attendant EDX results for the oxidation tested IN738LC and CMSX-4 samples coated with novel silicon-aluminide coatings provided oxidation resistance to varying degrees depending on depths of coatings applied. These results also showed there were residual coatings, although as shown earlier, in some cases they were heavily degraded. In order to determine whether, and to what extent, residual coatings would provide further oxidation resistance, a series of X-ray defraction (XRD) assessments were carried out on selected samples. These would show the depths of residual coatings, what compounds remained in them, originating from those in the reference samples, and the presence of oxidised metals from the substrate which would demonstrate the extent of degradation. XRD plots would also show differences in thickness of the sides of reference and residual coatings.

In EDX, an electron beam vertically hits the surface and scattered electrons are collected to provide an elemental composition. XRD provides crystallographic information on the compounds present in the sample. In XRD an X-ray beam with wavelength λ is incident on lattice planes in a crystal at angle θ. The crystal lattice is a regular 3-dimensional distribution of atoms in space, arranged so that they form a series of parallel planes separated from each other by a distance d, which varies according to the nature of the material. For any crustal, planes exist in a number of different orientations, each with its own specific d. Diffraction occurs when the distance travelled by the rays reflected from successive planes differs by a complete number n of wavelengths. Diffraction is governed by Braggs Law: $n\lambda = 2d\sin\theta$

By varying the angle θ, the Braggs Law conditions are satisfied by different spacings in polycrystalline materials. Plotting the angular positions and intensities of the resultant diffraction peaks produces a pattern which is characteristic of the sample. The result of an XRD measurement is a diffractogram which shows the phases present (peak positions), phase concentrations (peak heights), amorphous content (background bump) and crystallite size/strain (peak widths). The interplanar spacing between crystal planes is very precise and subjective, matching database patterns to sample patterns. Full descriptions of XRD are readily available [125,126]. The XRD machine used at Cranfield for measurements of post oxidation test samples was a Siemens X-Ray Diffractometer D5005, which uses radioactive copper for X-ray diffraction measurements. Figure 9.46 shows the resulting diffractogram.

The samples selected for XRD examination were IN738LC and CMSX-4 with silicon-aluminide coatings produced from 30 minutes CVD and 60 minutes CVD. The coatings produced from 15 minutes CVD were not considered to be viable for service in industrial gas turbines burning biomass and waste-fuels.

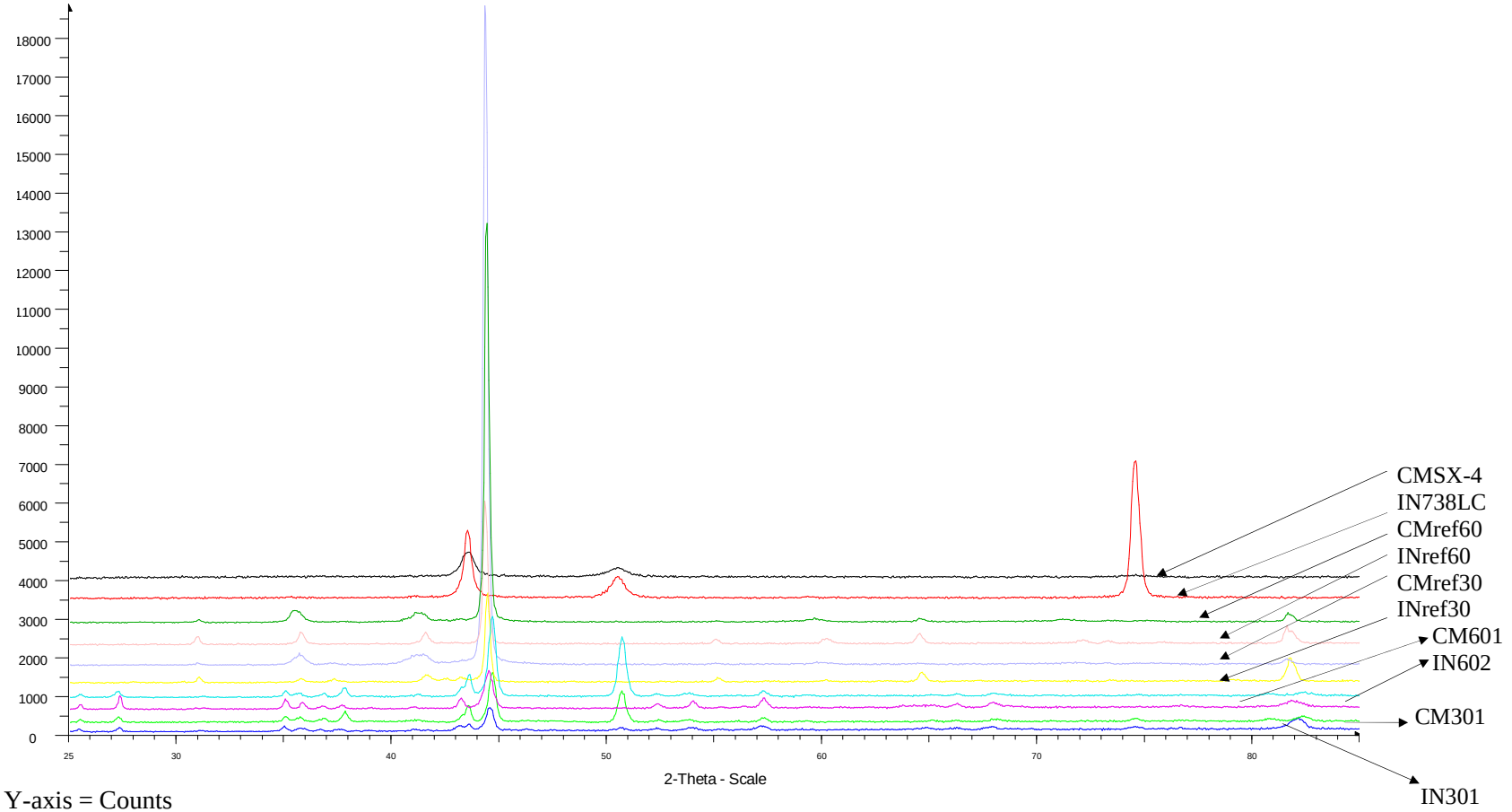

Y-axis = Counts

Figure 9.46: Oxidation Test Series 2; 3000 hours exposure at 1050^{o}C, XRD results of selected samples

In Figure 9.46, for each exposed, reference and substrate sample, additional counts (Y-axis) have been added to separate them, in a 'stepped' presentation, for ease of identification. The samples measured were:

- IN301 ; exposed sample of IN738LC with SiAl coating produced from 30 minutes CVD,
- IN602 ; exposed sample of IN738LC with SiAl coating produced from 60 minutes CVD,
- CM301 ; exposed sample of CMSX-4 with SiAl coating produced from
- 30 minutes CVD,
- CM601 ; exposed sample of CMSX-4 with SiAl coating produced from
- 60 minutes CVD,
- INref30 ; unexposed reference sample of IN738LC with SiAl coating produced from 30 minutes CVD,
- INref60 ; unexposed reference sample of IN738LC with SiAl coating produced from 60 minutes CVD,
- CMref30 ; unexposed reference sample of CMSX-4 with SiAl coating produced from 30 minutes CVD,
- CMref60 ; unexposed reference sample of CMSX-4 with SiAl coating produced from 60 minutes CVD,
- IN738LC; unexposed, uncoated IN738LC substrate,
- CMSX-4 ; unexposed, uncoated CMSX-4 substrate.

The peaks in Figure 9.46 and the compounds they contain are listed in Table 9.2. It should be noted that, as this XRD process cannot see small fractions of <5%, any silicon containing compounds will not show up. The peaks at 43.7 identify the uncoated substrates. The peaks at 44.4 are associated with all reference and exposed SiAl coated samples and appear to be degraded β-NiAl from the loss of Al. The peaks at 50.7 are associated with the two substrates and exposed CM301 and CM 601.

Peak 2-Theta-Scale	**Compound**
25.5	Al_2O_3
27.5	TiO_2
35.0	Al_2O_3
41.5	Al_2O_3, TiO_2
43.7	Ni_3Al, Al_2O_3
44.4	NiAl, TiO_2, CrO_3
50.7	Ni_3Al, CrO_3, Co_3O_4
54.0	CoO, TiO_2
57.7	Al_2O_3, CoO
74.5	NiO, Co_3O_4
82.0	TiO_2, CrO_3

Table 9.2 : Oxidation tests; XRD analyses, compounds associated with peaks shown in XRD plots in Figure 9.46

To identify remnant coatings and differences in coating differences on each side of each sample, a series of four XRD plots are presented, one for each of the four exposed samples.

The scale of the X-axis on each graph is 42.75 to 45.25, and include peaks for the substrate, and all exposed and reference samples. On each graph, the plots for the respective reference coating and for the uncoated substrate are included for comparison purposes. Note that the four graphs are to be used for illustrative purposes, their scale and depths having been adjusted to differentiate individual lines better.

In Figure 9.47, the results are associated with IN738LC with the SiAl coating produced from 60 minutes CVD. It can be seen that coatings remain after exposure but of lesser thickness. In both reference and exposed samples there are differences in the depths of coatings on the sides of the samples. These XRD results confirm respective EDX results explained earlier in this chapter.

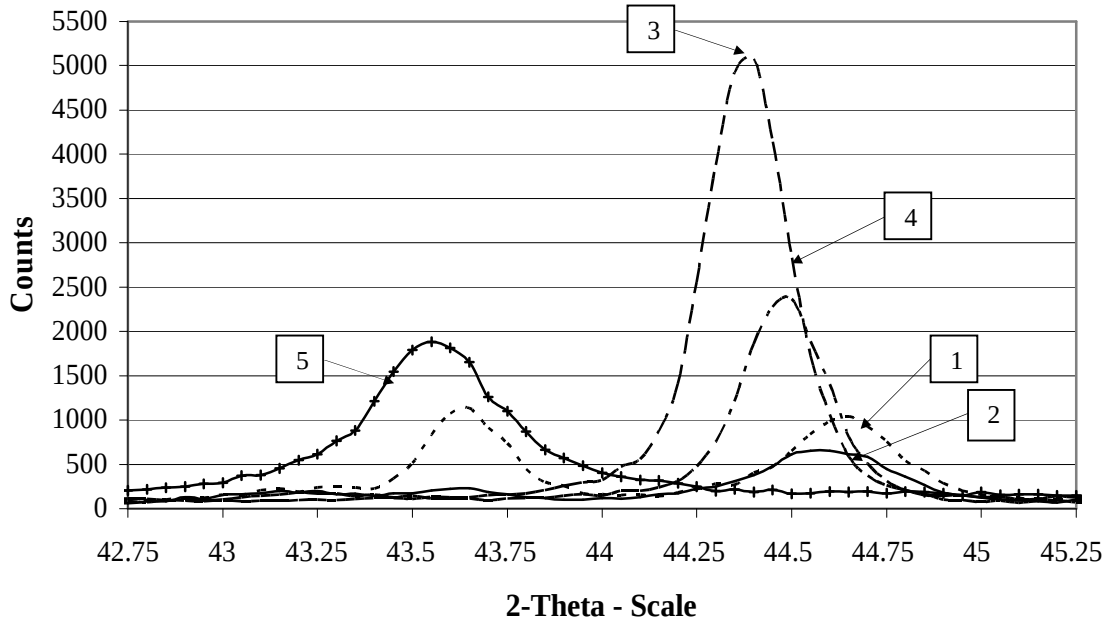

Peaks: 1; Exposed IN738LC with SiAl coating, sample IN601 (side 1)
2; Exposed IN738LC with SiAl coating, sample IN602 (side 2)
3; Unexposed SiAl reference coating (side 1) :
4; Unexposed SiAl reference coating (side 2) :
5; Uncoated IN738LC substrate : Ni_3Al

Figure 9.47 : Oxidation tests; 3000 hours at 1050°C, XRD plots of IN738LC with SiAl1 coating formed from 60 minutes CVD, exposed and reference samples

The XRD plots in Figure 9.48 are for the IN738LC sample with SiAl coating produced from 30 minutes CVD. Peaks are similar to those for the IN738LC sample produced from 60 minutes CVD but with a reduced depth of coating. There are also similar variations in depths of remanent coatings as for those produced from the longer CVD period.

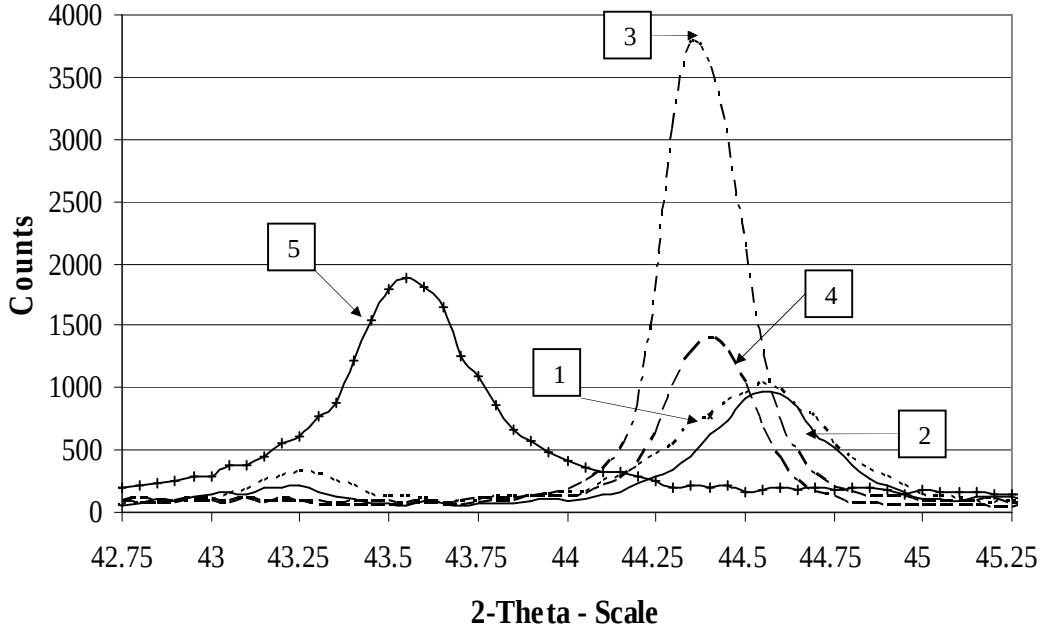

Peaks: 1; Exposed IN738LC with SiAl coating, sample IN301 (side 1)
2; Exposed IN738LC with SiAl coating, sample IN301 (side 2)
3; Unexposed SiAl reference coating (side 1) :
4; Unexposed SiAl reference coating (side 2) :
5; Uncoated IN738LC substrate : Ni_3Al

Figure 9.48 : Oxidation tests: 3000 hours at 1050°C; XRD plots of IN738LC with SiAl1 coating formed from 30 minutes CVD, exposed and reference samples

Figures 9.49 and 9.50 show the XRD results for CMSX-4 samples with SiAl coatings produced from 60 minutes and 30 minutes CVD respectively. In both cases, post-oxidation coatings having similar depths remained. The coatings on both sides of the 60 minutes CVD sample were nearly the same, whereas, in the case of the 30 minutes CVD sample there was a greater difference between the depths of the coating on each side. The coating depths on the 30 minutes CVD sample were closer than those on the 60 minutes CVD sample. These differences and those on the IN738LC samples, mentioned previously, confirm differences in coating depths between sides of the same sample, which were identified in the microstructures obtained from BSE images earlier.

The reference coatings on CMSX-4 were consistently of a much greater depth than those on the IN738LC reference coatings. These findings are also consistent with depths seen on BSE images of the respective coatings. The CMSX-4 substrate has a much 'flatter' peak than that of IN738LC, reflecting the former substrate being a single crystal whereas IN738LC is a polycrystalline superalloy.

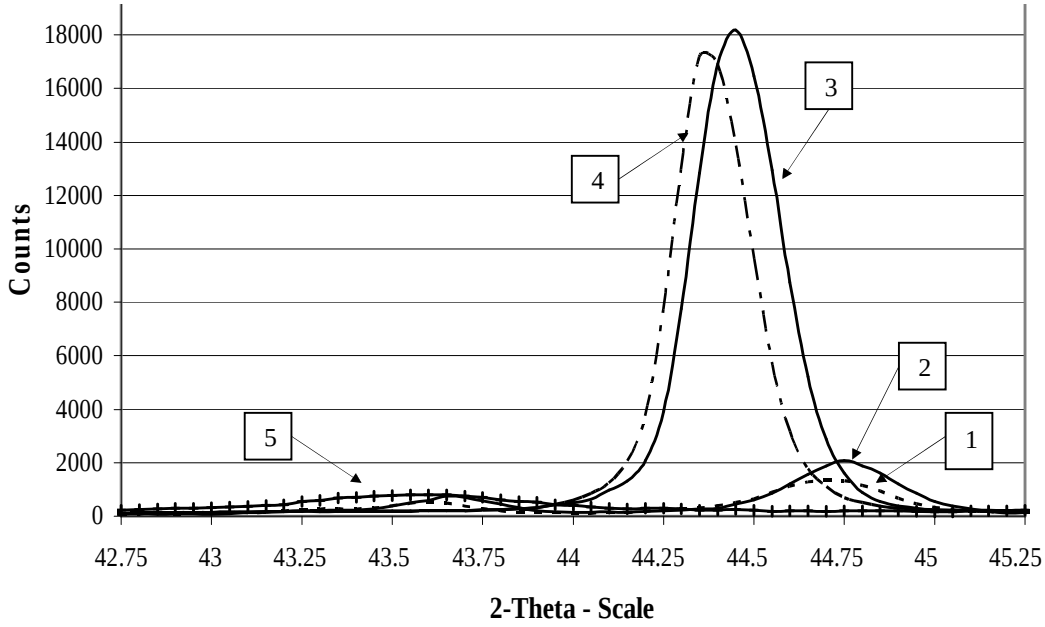

Peaks : 1 ; Exposed CMSX-4 with SiAl coating, sample CM601 (side 1)
2 ; Exposed CMSX-4 with SiAl coating, sample CM601 (side 2)
3 ; Unexposed reference coating (side 1)
4 ; Unexposed reference coating (side 2)
5 ; Uncoated CMSX-4 substrate: Ni_3Al

Figure 9.49 : Oxidation tests; 3000 hours at 1050°C, XRD plots of CMSX-4 with SiAl coating formed from 60 mins CVD, exposed- and reference samples

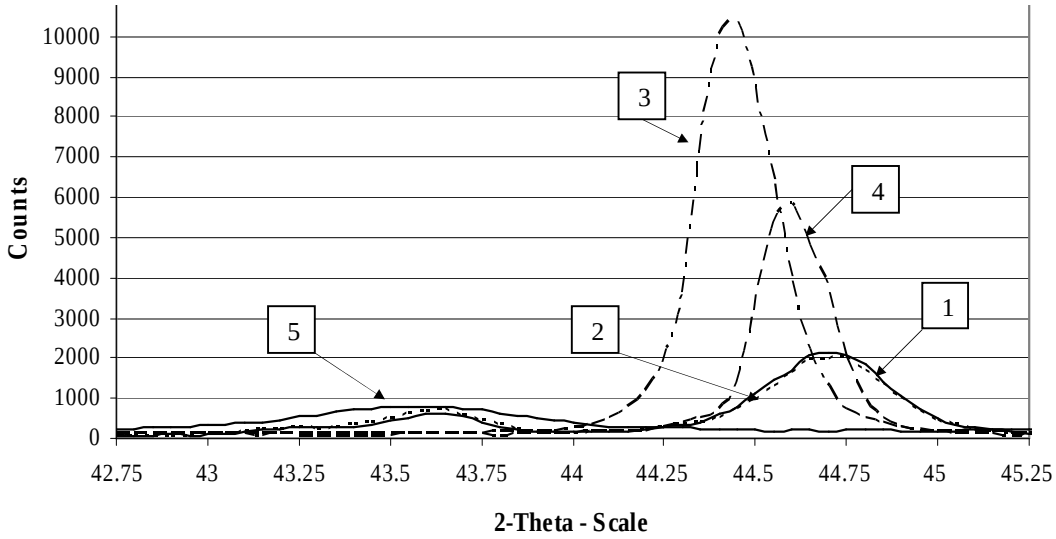

Peaks: 1; Exposed CMSX-4 with SiAl coating, sample CM301 (side 1)
2; Exposed CMSX-4 with SiAl coating, sample CM301 (side 2) – (dotted line)
3; Unexposed SiAl1 reference coating (side 1) :
4: Unexposed SiAl1 reference coating (side 2) :
5: Uncoated CMSX-4 substrate : Ni_3Al

Figure 9.50 : Oxidation tests: 3000 hours at 1050°C; XRD plots of CMSX-4 with SiAl coating formed from 30 minutes CVD, exposed and reference samples

9.4.2.4 Comparisons of oxidation protection for CMSX-4 provided by novel silicon aluminide coatings and commercial coatings

Previous oxidation tests on CMSX-4, carried out at Cranfield University, allow some comparison with the oxidation protection provided by the novel silicon aluminide coating developed in this project. The previous oxidation tests were not carried out under identical conditions to those described in this section but will serve as some measure of the coating's performance. In the first comparison of oxidation test results, the net mass changes of CMSX-4 samples coated with RT-22 [19] and with the silicon aluminide coating, were tested at 950°C and 1050°C. For the cyclic oxidation testing of the silicon aluminide coatings, weighings were carried out at 100 hours intervals. The isothermal oxidation tests on CMSX-4 samples coated with RT-22 were weighed at 1000 hours intervals. Comparisons are presented in Table 9.3.

No. hours tested	**SiAl* 950°C** mg/cm^2	**RT-22 950°C** mg/cm^2	**SiAl 1050°C** mg/cm^2	**RT-22 1050°C** mg/cm^2
1000	0.36 to 0.48	0.40 to 0.45	1.4	0.55 to 0.64
2000	-	0.38 to 0.6	0.73	0.27 to 0.39
3000	-	0.37 to 0.59	-0.28	0.18

Notes: * - this sample was only tested for 10 periods of 100 hours each

Table 9.3: Net mass changes in CMSX-4 samples with silicon aluminide coating and with platinum aluminide coating RT-22, after oxidation tests at 950°C and 1050°C

From Table 9.3, it is seen that the one CMSX-4 sample having the silicon-aluminide coating, after 1000 hours cyclic oxidation testing at 950°C, had a similar net mass change after 1000 hours testing, to samples of CMSX-4 coated with RT-22, a platinum-aluminide coating. However, the cyclic oxidation test on the silicon aluminide coating could be expected to be more onerous than the single isothermal oxidation test on the RT-22 coated samples. Comparisons of the two coatings tested at 1050°C are more difficult to make, taking into account the cyclic versus isothermal testing conditions and the higher test temperature. The better performance of the RT-22 coating is apparent, but it has seen fewer cycles and the influence of cycle frequency on the extent of its oxidation is not assessed further here.

In the second comparison of coatings on CMSX-4, following oxidation testing, the results of several coatings oxidation tested at 1100°C [63], were compared with those of the novel silicon aluminide coating after oxidation testing at 1050°C. Both tests were cyclic, with weighing after an average of 54 hours for tests at 1100°C and, weighing after 100 hours for tests at 1050°C. The results of the second comparisons are shown in Table 9.3.

Item No.	Type of coating on CMSX-4	Avge coating depth (µm)	No. hours before zero-line crossed
1	Al-rich Fluoride-based pack coated at 900°C	26	120
2	Si-rich Fluoride-based pack coated at 900°C	15	150
3	Standard Aluminide coated at 900°C	8	65
4	Al-rich Fluoride-based pack coated at 1050°C	57	450
5	Si-rich Fluoride-based pack coated at 1050°C	51	140
6	Standard Aluminide coated at 1050°C	54	565
7	Al-rich Chloride-based pack coated at 1050°C	112	400
8	Si-rich Chloride-based pack coated at 1050°C	53	1422
9	*Single stage SiAl ; 60mins CVD at 1050°C*	*143*	*2750(920)*

Note: Items 1 to 8 were oxidation tested at 1100°C [63]
Item 9, novel coating, developed in this project, was oxidation tested at 1050°C; based on alumina scale growth [63] the predicted lifetime at 1100°C would be 33% of this value

Table 9.4: Results of oxidation testing on various CVD pack-coatings on CMSX-4

Results of cyclic oxidation testing of CVD pack coated CMSX-4 samples, shown in Table 9.3, provide a limited basis for comparison of the single-stage novel silicon aluminide pack coating with eight two-stage pack coated samples [19]. The difference in oxidation temperatures, of 1050°C for the novel coating and of 1100°C, would cause an increased oxidation rate in the latter, estimated from measured rates for alumina growth to be a factor of x3. Similarly, for Item 8 in Table 9.4, the cycles of the higher temperature tests, of 54 hours between tests, would equate to 26 cycles. This would compare with 100 hours between tests of the silicon-aluminide sample, equating to 27 cycles, giving very similar results..

9.4.2.5 Cyclic oxidation tests - summary

In summary, it may be concluded from the cyclic oxidation tests that the novel silicon aluminide coatings formed from 30 minutes and 60 minutes CVD, at 1050°C, had demonstrated viable rates of oxidation protection for IN738LC and CMSX-4, for long term industrial gas turbine service under aggressive operating conditions, such as those expected from firing on biomass. On all these samples, XRD measurements confirmed that coatings remained after the 3000 hours of oxidation testing at 1050°C. The CMSX-4 substrates had been significantly degraded by TPC phases which could impair their mechnical integrity and viable remanent life.

It was decided however, that only IN738LC and CMSX-4 samples with silicon-aluminide coatings formed from 60 minutes CVD soak periods would be subjected to corrosion tests at 700°C and 900°C.

10. Corrosion tests – novel silicon aluminide coatings

10.1 Description of corrosion tests on novel silicon aluminide coatings

Following the oxidation tests, the next stage in assessing the hot corrosion protection provided by the novel silicon-aluminide coatings was to subject them to two series of corrosion tests, when applied to IN738LC and CMSX-4. The first series were Type II low temperature hot corrosion (LTHC) tests at 700^{o}C. These would enable direct comparisons to be made of the hot corrosion protection provided by the novel, silicon-aluminide coatings, compared with LTHC tests carried out on commercial coatings, reported in Chapter 7 of this thesis. The second series were Type I high temperature hot corrosion (HTHC) tests at 900^{o}C, to explore the hot corrosion protection provided by the novel coatings, for high pressure stage gas turbine blades and vanes.

Both series of tests were carried out at atmospheric pressure, for five periods of 100 hours, with weighing (cold) and salt replenishment before and after each period. The same furnace, ancillary equipment and were used as those for the first two series of corrosion tests.

The two gas compositions used in these corrosion tests, each providing 50% of the total flow, were similar to those used in the first two series of corrosion tests, namely:

- 800ppm HCl, balance N_2;
- 500ppm SO_2, 39.7%O_2, balance N_2

The small difference in oxygen content of the gas used, compared with the 40% in the two earlier tests, was due to safety regulations being introduced in the interim period. The mass controller for each gas bottle was set to supply a mass flow of 25cc/min, giving a total mass flow along the common main of 50cc/min.

The combinations of sulphates of cadmium, lead, sodium and potassium, were the same as those for the corrosion tests on commercial coatings. Salt fluxes used for corrosion tests on commercial coatings were also adopted for the third and fourth series of corrosion tests; 1.5 µg/cm^2/h and 5.0 µg/cm^2/h.

All the novel, silicon-aluminide coatings were applied to IN738LC and CMSX-4 samples by 60mins CVD at 1050^{o}C, followed by respective post heat treatment. One complete set of substrates and coatings used the same, low activity powder pack composition as that for samples subjected to the cyclic oxidation tests. In addition, in order to explore the effect of increasing the silicon content on the hot corrosion protection provided by the novel coating, one sample of each superalloy was coated with a low activity powder pack containing double the content of silicon to that used in the original novel coatings. In this case, the alumina content was reduced by the same weight as the increase in silicon weight. This second powder pack was used in coating one sample of each substrate, for each corrosion test, but only for these samples on which the higher salt flux was applied.

The schedule of samples, salt fluxes and salt combinations, used in corrosion test series 3 and 4, is shown in Table 10.1. In the table, Pwdr 1 refers to the same pack composition used in the oxidation tests, Pwdr 2 contains the higher proportion of silicon.

IN738LC	Smpl No	CorrTst	Temp °C	Salt flux*	Salt combination
Pwdr 1	IN1/1	3	700	5.00	$CdSO_4(50)+(Na_2SO_4(80)+K_2SO_4(20))(50)$
	IN1/2	3	700	5.00	$PbSO_4(50)+(Na_2SO_4(80)+K_2SO_4(20))(50)$
	IN1/3	4	900	5.00	$CdSO_4(50)+(Na_2SO_4(80)+K_2SO_4(20))(50)$
	IN1/4	4	900	5.00	$PbSO_4(50)+(Na_2SO_4(80)+K_2SO_4(20))(50)$
	IN1/5	*Reference*	*sample*		
	IN1/6	3	700	1.50	$CdSO_4(50)+(Na_2SO_4(80)+K_2SO_4(20))(50)$
	IN1/7	3	700	1.50	$PbSO_4(50)+(Na_2SO_4(80)+K_2SO_4(20))(50)$
	IN1/8	4	900	1.50	$CdSO_4(50)+(Na_2SO_4(80)+K_2SO_4(20))(50)$
	IN1/9	4	900	1.50	$PbSO_4(50)+(Na_2SO_4(80)+K_2SO_4(20))(50)$
	IN1/10	*Reference*	*sample*		
Pwdr 2	IN2/1	3	700	5.00	$CdSO_4(50)+(Na_2SO_4(80)+K_2SO_4(20))(50)$
	IN2/2	3	700	5.00	$PbSO_4(50)+(Na_2SO_4(80)+K_2SO_4(20))(50)$
	IN2/3	4	900	5.00	$CdSO_4(50)+(Na_2SO_4(80)+K_2SO_4(20))(50)$
	IN2/4	4	900	5.00	$PbSO_4(50)+(Na_2SO_4(80)+K_2SO_4(20))(50)$
	IN2/5	*Reference*	*sample*		

CMSX-4	Smpl No	CorrTst	Temp °C	Salt flux*	Salt combination
Pwdr 1	CM1/1	3	700	5.00	$CdSO_4(50)+(Na_2SO_4(80)+K_2SO_4(20))(50)$
	CM1/2	3	700	5.00	$PbSO_4(50)+(Na_2SO_4(80)+K_2SO_4(20))(50)$
	CM1/3	4	900	5.00	$CdSO_4(50)+(Na_2SO_4(80)+K_2SO_4(20))(50)$
	CM1/4	4	900	5.00	$PbSO_4(50)+(Na_2SO_4(80)+K_2SO_4(20))(50)$
	CM1/5	*Reference*	*sample*		
	CM1/6	3	700	1.50	$CdSO_4(50)+(Na_2SO_4(80)+K_2SO_4(20))(50)$
	CM1/7	3	700	1.50	$PbSO_4(50)+(Na_2SO_4(80)+K_2SO_4(20))(50)$
	CM1.8	4	900	1.50	$CdSO_4(50)+(Na_2SO_4(80)+K_2SO_4(20))(50)$
	CM1.9	4	900	1.50	$PbSO_4(50)+(Na_2SO_4(80)+K_2SO_4(20))(50)$
	CM1/10	*Reference*	*sample*		
Pwdr 2	CM2/1	3	700	5.00	$CdSO_4(50)+(Na_2SO_4(80)+K_2SO_4(20))(50)$
	CM2/2	3	700	5.00	$PbSO_4(50)+(Na_2SO_4(80)+K_2SO_4(20))(50)$
	CM2/3	4	900	5.00	$CdSO_4(50)+(Na_2SO_4(80)+K_2SO_4(20))(50)$
	CM2/4	4	900	5.00	$PbSO_4(50)+(Na_2SO_4(80)+K_2SO_4(20))(50)$
	CM2/5	*Reference*	*sample*		

Note * : $\mu g/cm^2/h$

Table 10.1: Schedule of samples, salt combinations and salt fluxes for Corrosion Test Series 3 and 4

10.2 Corrosion test series 3: 500 hours at 700°C; results and evaluation

10.2.1 Mass change

10.2.1.1 Gross mass change

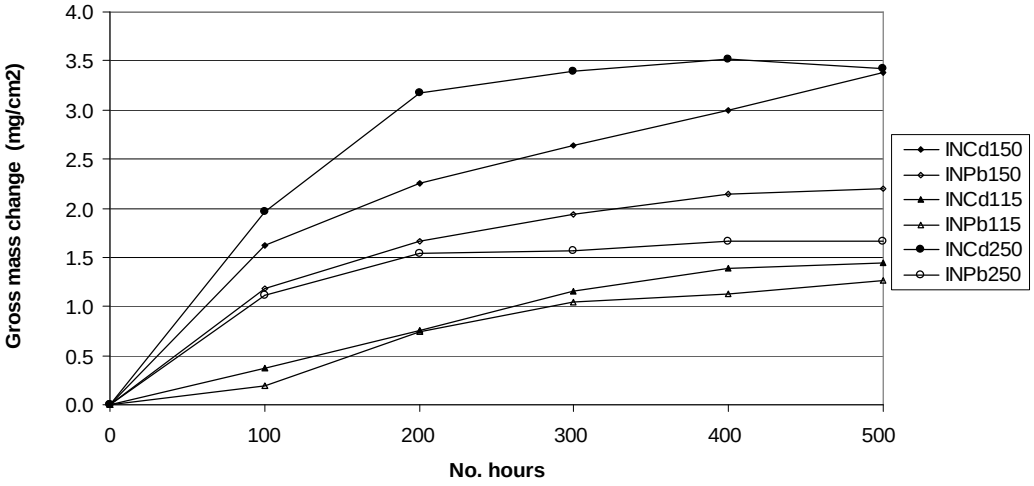

Key: INCd150; IN738LC, $CdSO_4$+(Na_2SO_4(80)+K_2SO_4(20)), salt flux 5.0 µg/cm^2/h, pwdr 1
INPb150; IN738LC, $PbSO_4$+(Na_2SO_4(80)+K_2SO_4(20)), salt flux 5.0 µg/cm^2/h, pwdr 1
INCd115; IN738LC, $CdSO_4$+(Na_2SO_4(80)+K_2SO_4(20)), salt flux 1.5 µg/cm^2/h, pwdr 1
INPb115; IN738LC, $PbSO_4$+(Na_2SO_4(80)+K_2SO_4(20)), salt flux 1.5 µg/cm^2/h, pwdr 1
INCd250; IN738LC, $CdSO_4$+(Na_2SO_4(80)+K_2SO_4(20)), salt flux 5.0 µg/cm^2/h, pwdr 2
INPb250; IN738LC, $PbSO_4$+(Na_2SO_4(80)+K_2SO_4(20)), salt flux 5.0 µg/cm^2/h, pwdr 2

Figure 10.1: IN738LC samples with silicon-aluminide coatings; gross mass changes after 500 hours corrosion testing at 700°C

In Figure 10.1, it will be seen that gross mass changes in IN738LC samples, having the lower salt flux and formed from the lower silicon content powder, are lower than those subjected to the higher salt fluxes during these corrosion tests. Both the Cd+alkali and Pb+alkali samples subject to the lower salt flux have gross mass changes of a similar value. On the lower silicon content powder samples, the Cd+alkali combination sample subject to the higher salt flux, gains significantly more gross mass than the sample with the equivalent Pb+alkali combination. Both Cd+alkali combinations subject to the higher salt flux, one with the higher silicon content coating and the other with the lower silicon content coating, gain more gross mass change than the equivalent samples with Pb+alkali combinations. After 500 hours corrosion testing at 700°C, these Cd+alkali combination samples exhibit similar gross mass changes, of about 3.4 mg/cm^2, whereas the gross mass changes of the equivalent Pb+alkali combination samples range from 1.7 mg/cm^2 to 2.2 mg/cm^2.

The gross mass change graphs for CMSX-4 samples, seen in Figure 10.2, exhibit similar differences in equivalent samples, to those for IN738LC. However, for CMSX-4, the gradients of both Cd+alkali combination samples having the higher salt fluxes, rise significantly.

After 500 hours corrosion testing at 700°C, their gross mass changes rang from 8.0 mg/cm^{2}to 10.5 mg/cm^2, compared with 3.4 mg/cm^2, for the equivalent IN738LC samples. Similarly, the lower salt flux samples of CMSX-4, after 500 hours corrosion testing, exhibit a range of gross mass changes from 2.0 mg/cm^2 to 3.1 mg/cm^2, compared with the range of 1.7 mg/cm^2 to 2.2 mg/cm^2 exhibited by the equivalent IN738LC samples.

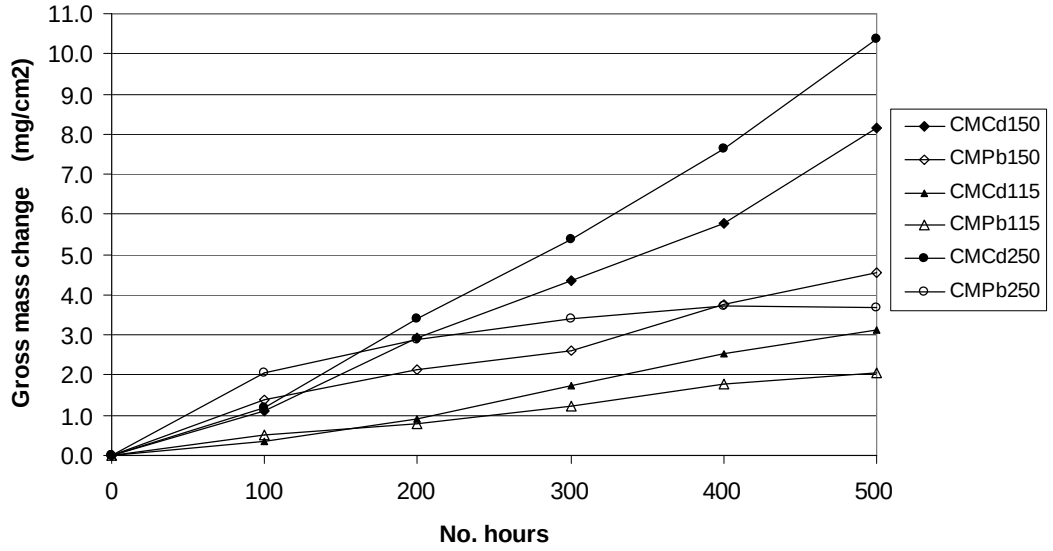

Key: CMCd150; CMSX-4, $CdSO_4$+(Na_2SO_4(80)+K_2SO_4(20)), salt flux 5.0 µg/cm^2/h, pwdr 1
CMPb150; CMSX-4, $PbSO_4$+(Na_2SO_4(80)+K_2SO_4(20)), salt flux 5.0 µg/cm^2/h, pwdr 1
CMCd115; CMSX-4, $CdSO_4$+(Na_2SO_4(80)+K_2SO_4(20)), salt flux 1.5 µg/cm^2/h, pwdr 1
CMPb115; CMSX-4, $PbSO_4$+(Na_2SO_4(80)+K_2SO_4(20)), salt flux 1.5 µg/cm^2/h, pwdr 1
CMCd250; CMSX-4, $CdSO_4$+(Na_2SO_4(80)+K_2SO_4(20)), salt flux 5.0 µg/cm^2/h, pwdr 2
CMPb250; CMSX-4, $PbSO_4$+(Na_2SO_4(80)+K_2SO_4(20)), salt flux 5.0 µg/cm^2/h, pwdr 2

Figure 10.2: CMSX-4 samples with silicon-aluminide coatings; gross mass changes after 500 hours corrosion testing at 700°C

10.2.1.2 Spall mass

There are significant differences in the spall masses of all IN&38LC samples compared with those of CMSX-4 samples, as seen in Figures 10.3 and 10.4. For IN738LC samples the higher silicon containing coatings spall at significantly higher rates than those with the lower silicon coatings. Figure 10.3 also shows that, for IN738LC, samples subjected to the higher salt fluxes have greater spall mass rates than those subject to lower salt fluxes. In the lower silicon coating samples, those with Pb+alkali combinations have marginally higher spall rates than their equivalent Cd+alkali samples. This pattern is reversed in the samples with the higher silicon coatings. For IN738LC samples, after 500 hours the lower silicon coated sample spall mass amounts to around 0.1 mg/cm^2, the values for samples with the higher silicon containing coatings are 0.4 and 0.83 mg/cm^2.

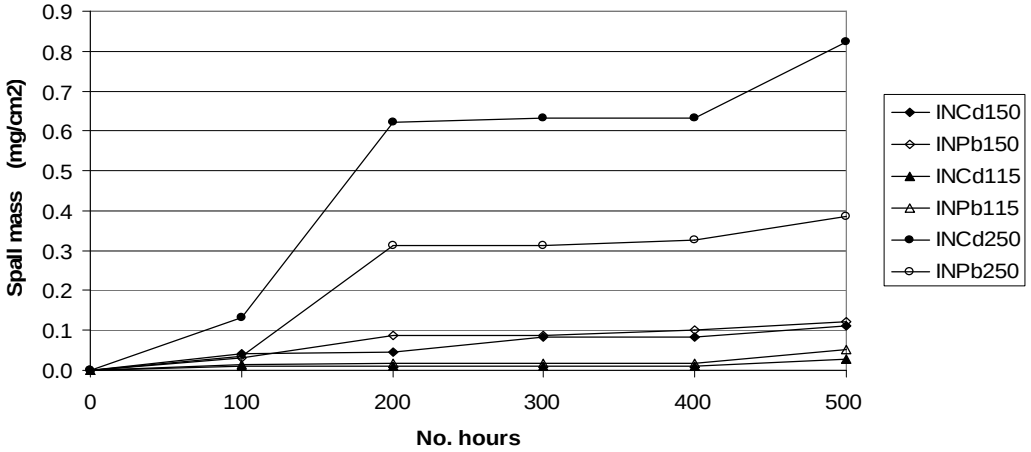

Key: INCd150; IN738LC, $CdSO_4$+(Na_2SO_4(80)+K_2SO_4(20)), salt flux 5.0 µg/cm^2/h, pwdr 1
INPb150; IN738LC, $PbSO_4$+(Na_2SO_4(80)+K_2SO_4(20)), salt flux 5.0 µg/cm^2/h, pwdr 1
INCd115; IN738LC, $CdSO_4$+(Na_2SO_4(80)+K_2SO_4(20)), salt flux 1.5 µg/cm^2/h, pwdr 1
INPb115; IN738LC, $PbSO_4$+(Na_2SO_4(80)+K_2SO_4(20)), salt flux 1.5 µg/cm^2/h, pwdr 1
INCd250; IN738LC, $CdSO_4$+(Na_2SO_4(80)+K_2SO_4(20)), salt flux 5.0 µg/cm^2/h, pwdr 2
INPb250; IN738LC, $PbSO_4$+(Na_2SO_4(80)+K_2SO_4(20)), salt flux 5.0 µg/cm^2/h, pwdr 2

Figure 10.3: IN738LC samples with silicon-aluminide coatings; spall mass after 500 hours corrosion testing at 700^{o}C

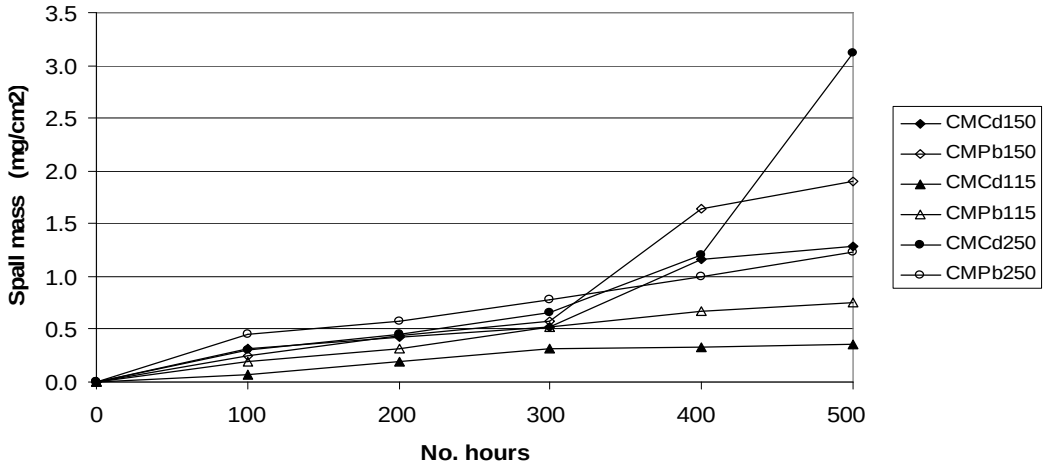

Key: CMCd150; CMSX-4, $CdSO_4$+(Na_2SO_4(80)+K_2SO_4(20)), salt flux 5.0 µg/cm^2/h, pwdr 1
CMPb150; CMSX-4, $PbSO_4$+(Na_2SO_4(80)+K_2SO_4(20)), salt flux 5.0 µg/cm^2/h, pwdr 1
CMCd115; CMSX-4, $CdSO_4$+(Na_2SO_4(80)+K_2SO_4(20)), salt flux 1.5 µg/cm^2/h, pwdr 1
CMPb115; CMSX-4, $PbSO_4$+(Na_2SO_4(80)+K_2SO_4(20)), salt flux 1.5 µg/cm^2/h, pwdr 1
CMCd250; CMSX-4, $CdSO_4$+(Na_2SO_4(80)+K_2SO_4(20)), salt flux 5.0 µg/cm^2/h, pwdr 2
CMPb250; CMSX-4, $PbSO_4$+(Na_2SO_4(80)+K_2SO_4(20)), salt flux 5.0 µg/cm^2/h, pwdr 2

Figure 10.4: CMSX-4 samples with silicon-aluminide coatings; spall mass after 500 hours corrosion testing at 700^{o}C

Spall rates of CMSX-4 samples are consistently higher than those of IN738LC, as comparisons of Figures 10.3 and 10.4 show. Low salt flux CMSX-4 samples have a spall mass, after 500 hours corrosion testing at 700°C, of 0.3 mg/cm^2 and 0.75 mg/cm^2. The equivalent IN738LC samples have spall rates below 0.1 mg/cm^2 after the same period. The samples of CMSX-4 with the higher silicon content coating have spall rates of 1.3 mg/cm^2 and 3.2 mg/cm^2 after 500 hours testing compared with 0.4 mg/cm^2 and 0.82 mg/cm^2 for the IN738LC samples, although, for both substrates, the Cd+alkali combination sample has a higher spall mass than that having the Pb+alkali combination.

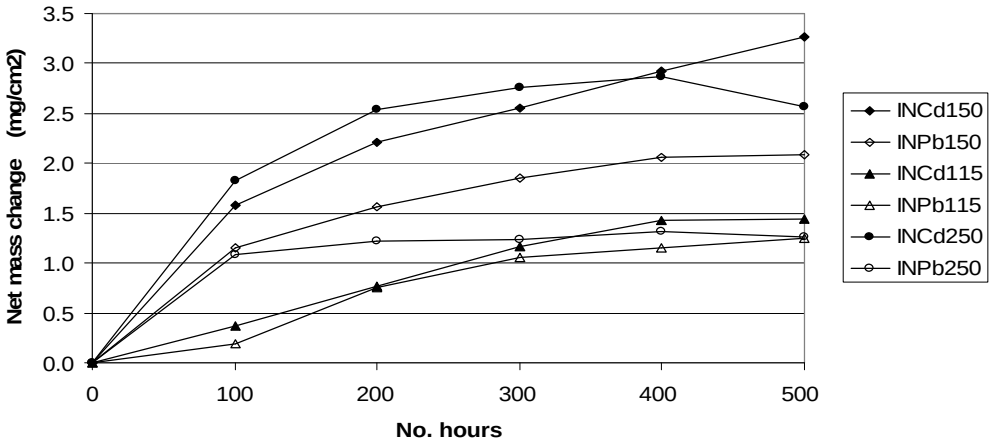

Key: INCd150; IN738LC, $CdSO_4$+(Na_2SO_4(80)+K_2SO_4(20)), salt flux 5.0 µg/cm^2/h, pwdr 1
INPb150; IN738LC, $PbSO_4$+(Na_2SO_4(80)+K_2SO_4(20)), salt flux 5.0 µg/cm^2/h, pwdr 1
INCd115; IN738LC, $CdSO_4$+(Na_2SO_4(80)+K_2SO_4(20)), salt flux 1.5 µg/cm^2/h, pwdr 1
INPb115; IN738LC, $PbSO_4$+(Na_2SO_4(80)+K_2SO_4(20)), salt flux 1.5 µg/cm^2/h, pwdr 1
INCd250; IN738LC, $CdSO_4$+(Na_2SO_4(80)+K_2SO_4(20)), salt flux 5.0 µg/cm^2/h, pwdr 2
INPb250; IN738LC, $PbSO_4$+(Na_2SO_4(80)+K_2SO_4(20)), salt flux 5.0 µg/cm^2/h, pwdr 2

Figure 10.5: IN738LC samples with silicon-aluminide coatings; net mass changes after 500 hours corrosion testing at 700°C

10.2.1.3 Net mass change

The net mass change graphs for IN738LC and CMSX-4, shown in Figures 10.5 and 10.6 respectively, reflect the same relative changes as those for gross mass change and spall rate, discussed above. The gradients of the higher silicon coating samples of both IN738LC substrates changed to a falling trend after 400 hours corrosion testing, as did the sample with higher silicon content coating, on CMSX-4. The gradients of all other samples of both substrates continued on rising though varying trends.

No net mass change curves had crossed, or even approached crossing, the zero-line. Although net mass changes of CMSX-4 samples, after 500 hours corrosion testing at 700°C, were significantly higher than those of IN738LC, both substrates carrying the novel silicon-aluminide coatings provided protection against Type II hot corrosion.

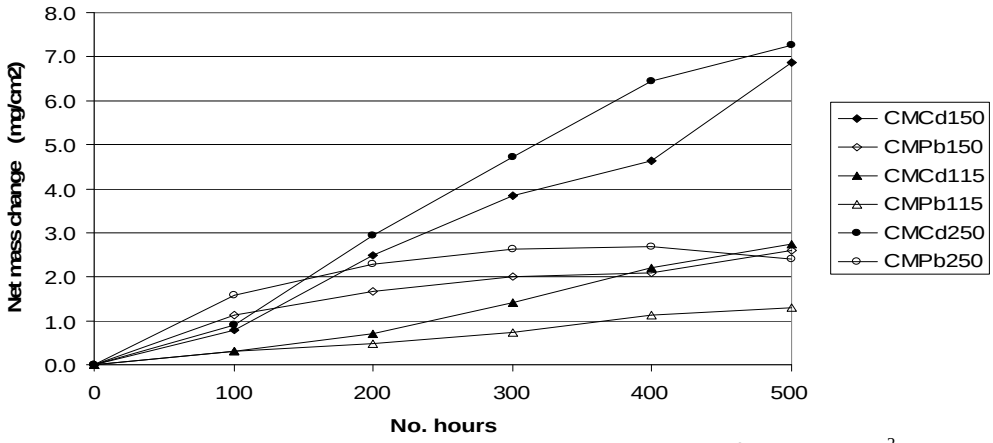

Key: CMCd150; CMSX-4, $CdSO_4+(Na_2SO_4(80)+K_2SO_4(20))$, salt flux 5.0 µg/cm^2/h, pwdr 1
CMPb150; CMSX-4, $PbSO_4+(Na_2SO_4(80)+K_2SO_4(20))$, salt flux 5.0 µg/cm^2/h, pwdr 1
CMCd115; CMSX-4, $CdSO_4+(Na_2SO_4(80)+K_2SO_4(20))$, salt flux 1.5 µg/cm^2/h, pwdr 1
CMPb115; CMSX-4, $PbSO_4+(Na_2SO_4(80)+K_2SO_4(20))$, salt flux 1.5 µg/cm^2/h, pwdr 1
CMCd250; CMSX-4, $CdSO_4+(Na_2SO_4(80)+K_2SO_4(20))$, salt flux 5.0 µg/cm^2/h, pwdr 2
CMPb250; CMSX-4, $PbSO_4+(Na_2SO_4(80)+K_2SO_4(20))$, salt flux 5.0 µg/cm^2/h, pwdr 2

Figure 10.6: CMSX-4 samples with silicon-aluminide coatings; net mass changes after 500 hours corrosion testing at 700^{o}C

10.2.2 Corrosion Test Series 3 - microstructural analyses

In Chapter 9, describing the two series of oxidation tests, the significant differences in depths of coatings, between the bottom and top sides of samples, was described. In this section, on the results of corrosion tests, the BSE images of both sides are shown for each sample, together with their post testing average coating depths.

Also included are maps of the significant elements relevant to the performance of coatings being developed to provide hot corrosion protection; aluminium, nickel, chromium, cobalt, silicon and oxygen. These element maps are complemented by EDX line scans to include these main elements and those alloying elements which, through outward diffusion, can influence coating and substrate performance.

Where significant content of these elements is indicated, comment will be made in the associated text, otherwise mention will be made of traces of such elements being present, and their location in the interdiffusion zone, coating or scale or deposit.

10.2.2.1 IN738LC with novel SIAl1 coating (sample IN1/1):
Salts; $CdSO_4(50) + (Na_2SO_4(80) + K_2SO_4(20))(50)$
Salt flux; 5.0 µg/cm^2/h

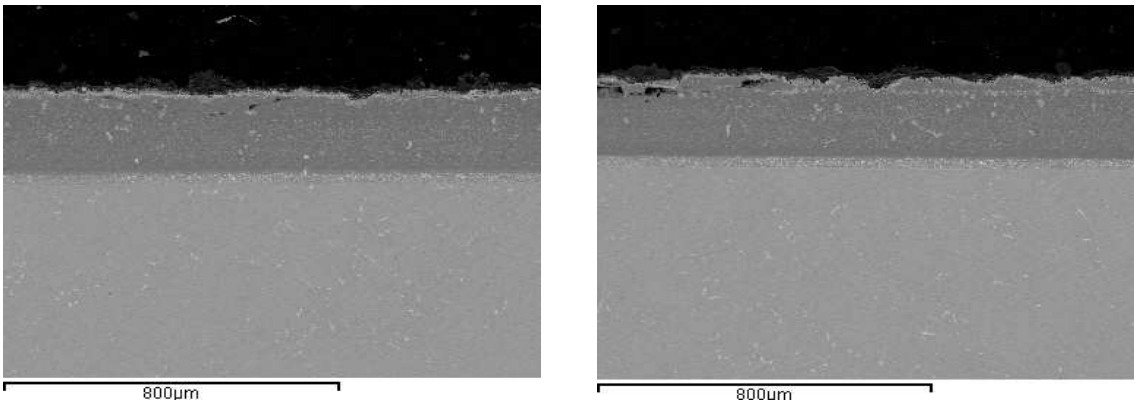

Bottom side average coating depth: 207µm
Ref sample bottom side coating depth: 235µm
Top side average coating depth: 194 µm
Ref sample top side coating depth: 197µm

Figure 10.7: IN738LC sample IN1/1; after 500 hours corrosion testing at 700°C – BSE images of both sides

The BSE maps in Figure 10.9 show a generally stable NiAl matrix proceeding from the interdiffusion zone through the coating to the outer deposit and scale layer, about 40µm from the outer surface. A deep layer, rich in outwardly diffused chromium and titanium occurs through the coating, with a central, narrow layer containing molybdenum and tungsten. Titanium and silicon particulates are distributed in the coating, the surface layer of which is rich in aluminium, silicon, chromium and titanium. Corrosion is comparatively evenly distributed along the coating. The maps, EDX results and mass change graph trends, in Figures 10.1, 10.3 and 10.5, indicate continuing slow growth of the protective scale.

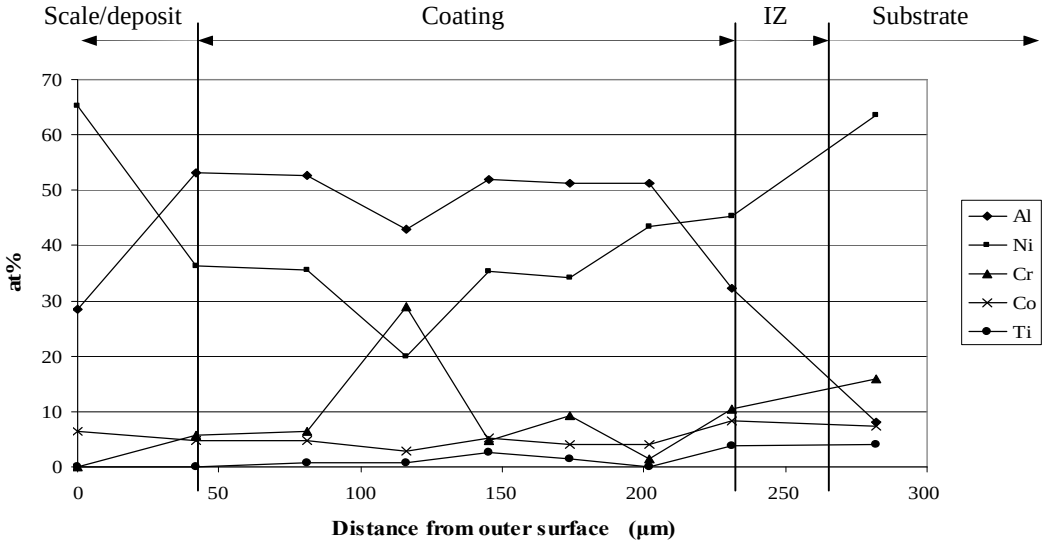

Figure 10.8: IN738LC sample IN1/1; after 500 hours corrosion testing at 700°C: main elements on EDX line in Figure 10.9

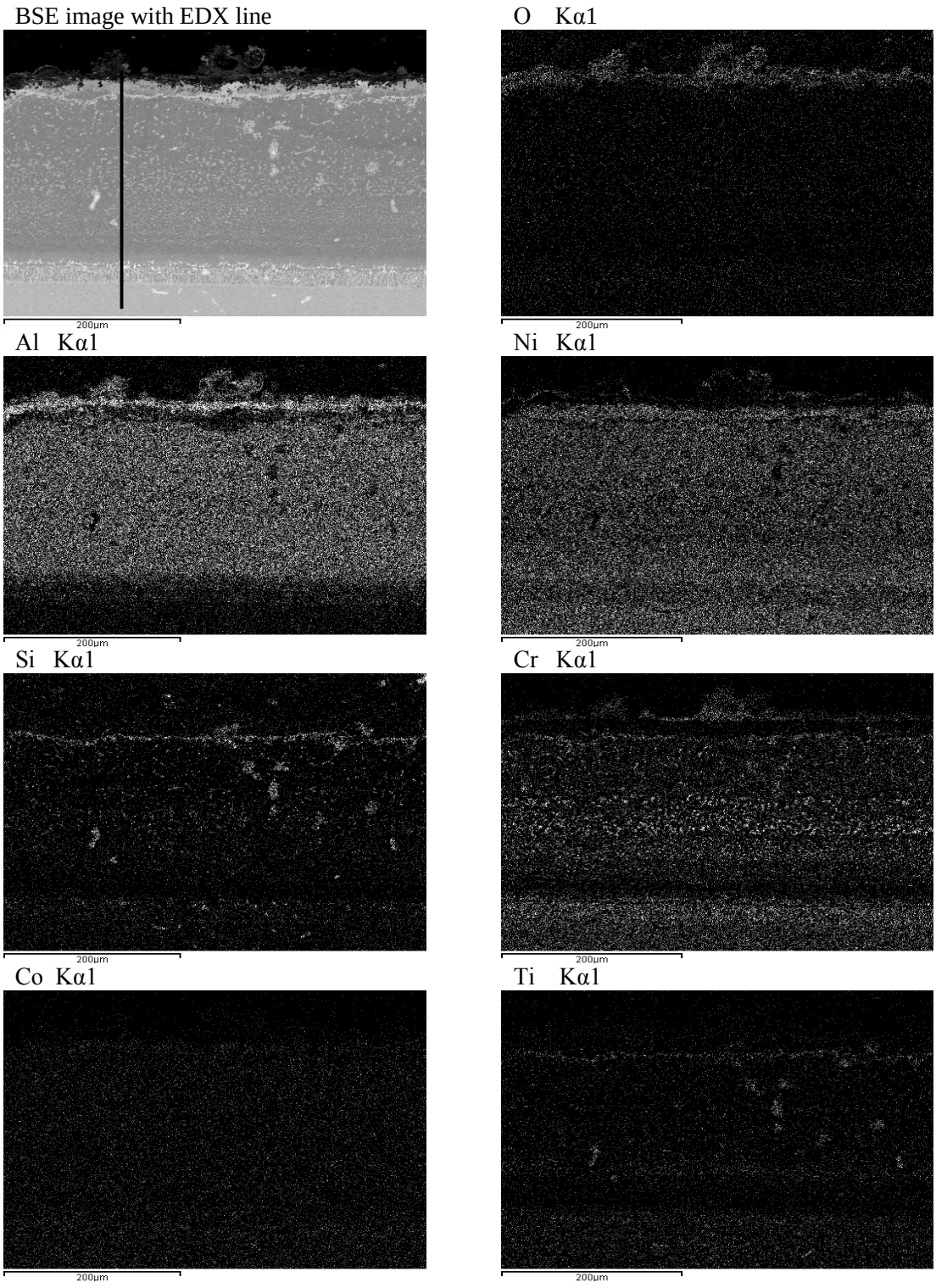

Figure 10.9: IN738LC sample IN1/1 after 500 hours corrosion testing at 700°C - element maps

10.2.2.2 IN738LC with novel silicon-aluminide (pwdr 1) coating (sample IN1/2):
Salts; $PbSO_4(50) + (Na_2SO_4(80) + K_2SO_4(20))(50)$
Salt flux; 5.0 $\mu g/cm^2/h$

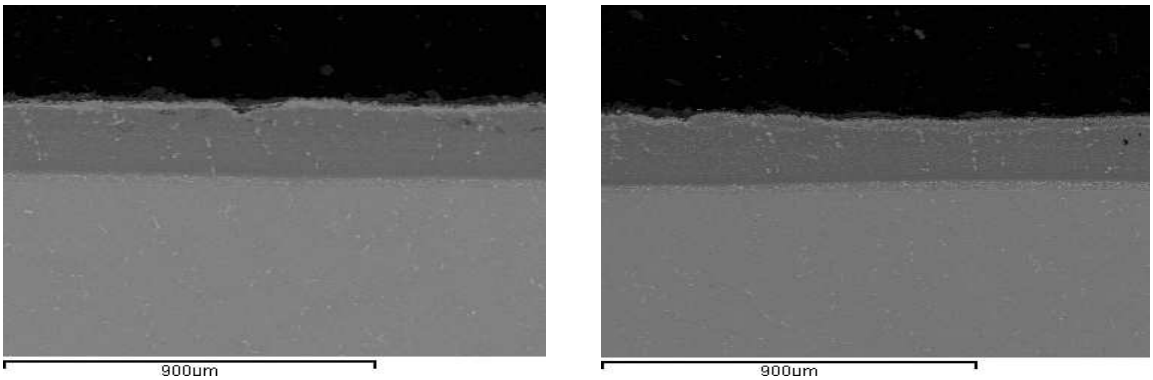

Bottom side average coating depth: 203 µm
Ref sample bottom side coating depth: 235 µm

Top side average coating depth: 194µm
Ref sample top side coating depth: 197µm

Figure 10.10: IN738LC sample IN1/2; after 500 hours corrosion testing at 700°C – BSE images of both sides

BSE maps for IN1/2, subjected to Pb+alkali salts, seen in Figures 10.10, 10.11 and 10.12, after 500 hours corrosion testing at 700°C, are similar to those exhibited by the previous sample, IN1/1 (Cd+alkali salts), subjected to the same salt flux. The average depths of sound coating are similar, the β-NiAl phase remains stable throughout the sound coating, albeit closer to the α-edge than for the Cd+alkali sample. Outward diffusion of refractory elements in IN1/2 is of a similar nature but of lower content than that of IN1/1. The maps, EDX results and trends in mass change graphs for sample IN1/2, also indicate the continuing slow growth of the protective scale.

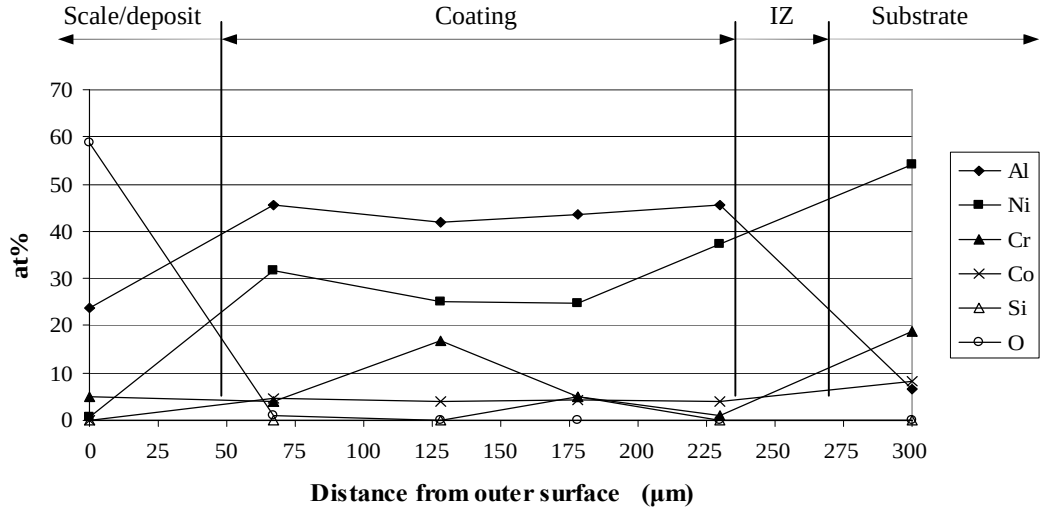

Figure 10.11: IN738LC sample IN1/2; after 500 hours corrosion testing at 700°C – main elements on EDX line in Figure 10.12

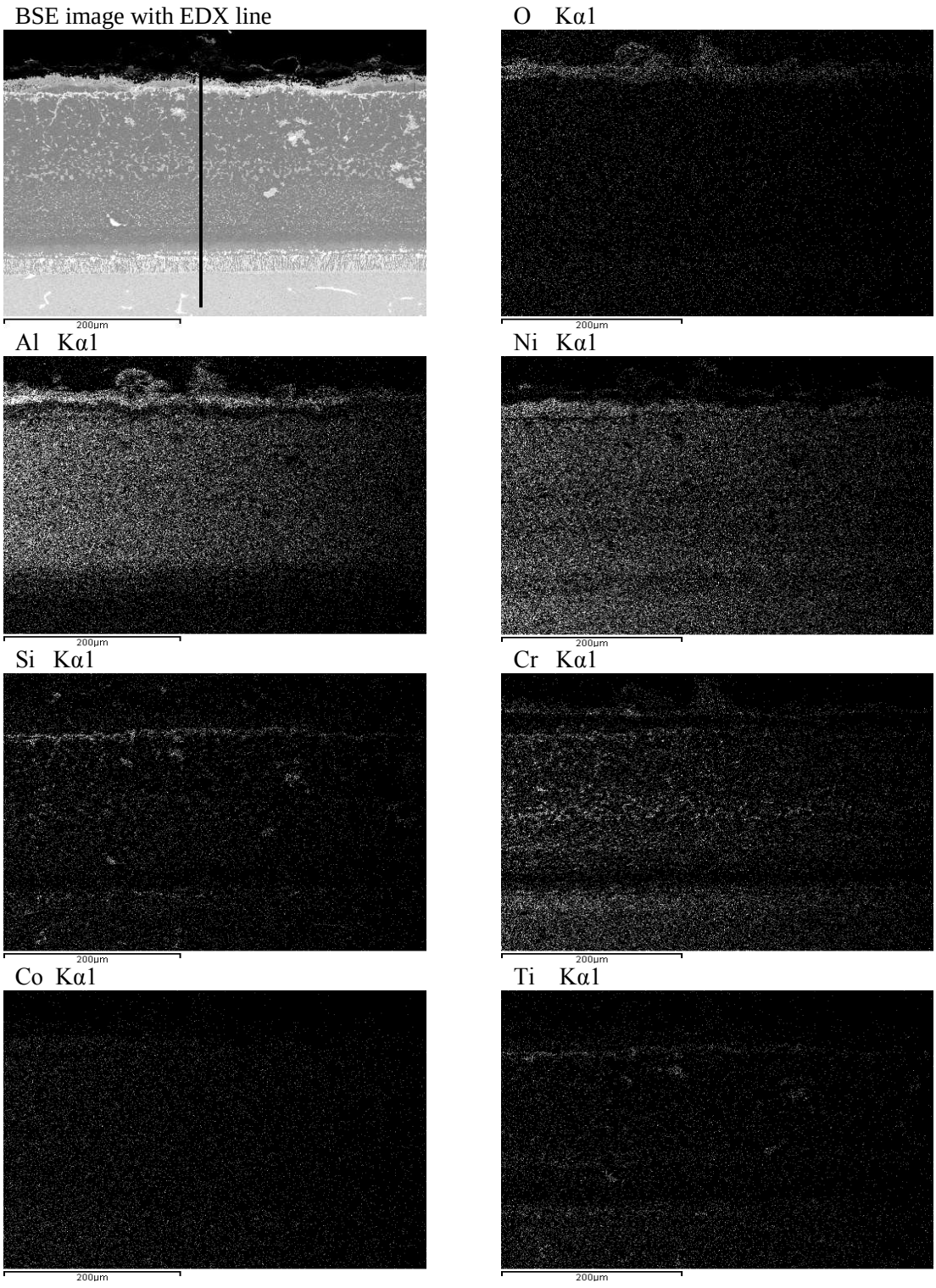

Figure 10.12: IN738LC sample IN1/2 after 500 hours corrosion testing at 700^{o}C
- element maps

10.2.2.3 IN738LC with novel silicon-aluminide (pwdr 1) coating (sample IN1/6):
Salts; $CdSO_4(50) + (Na_2SO_4(80) + K_2SO_4(20))(50)$
Salt flux; 1.5 µg/cm^2/h

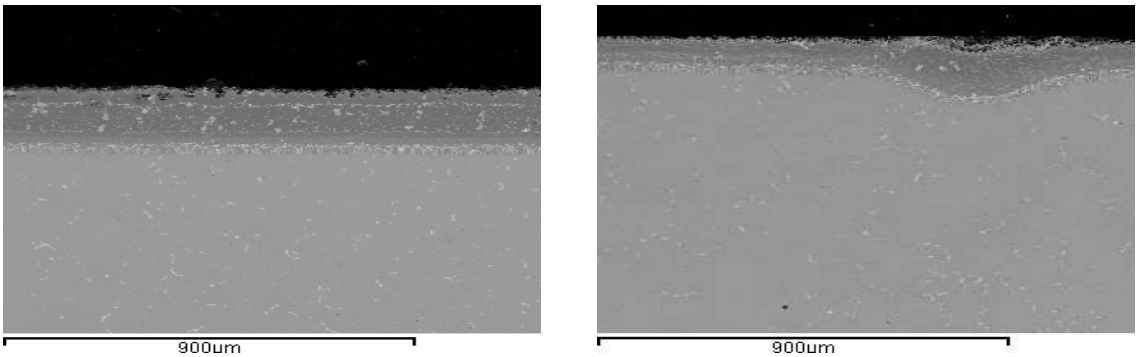

Bottom side average coating depth: 152µm
Ref sample bottom side coating depth: 90µm

Top side average coating depth: 111µm
Ref sample top sid coating depth: 51µm

Figure 10.13: IN738LC sample IN1/6; after 500 hours corrosion testing at 700°C – BSE images of both sides

The element maps for this sample in Figure 10.15 are similar to those for IN1/1, seen in Figure 10.9, but with the stable γ-NiAl phase. Outward diffusion of chromium peaks at 33 at%Cr compared with 29 at%Cr in IN1/1. As was to be expected, the lower salt flux of this sample resulted in lower mass change values compared with those having the higher salt flux, with minimal spallation. It can be forecast that the coating will continue to provide Type II hot corrosion protection for longer periods of testing. It should be noted that the reference sample in this case carried significantly less coating than those of IN1/1 and IN1/2, having been produced in a different CVD operation. The weight of SiAl1 coating applied to the reference sample, of 0.1g compares with an average coating weight of 0.14g for the other four samples which were corrosion tested.

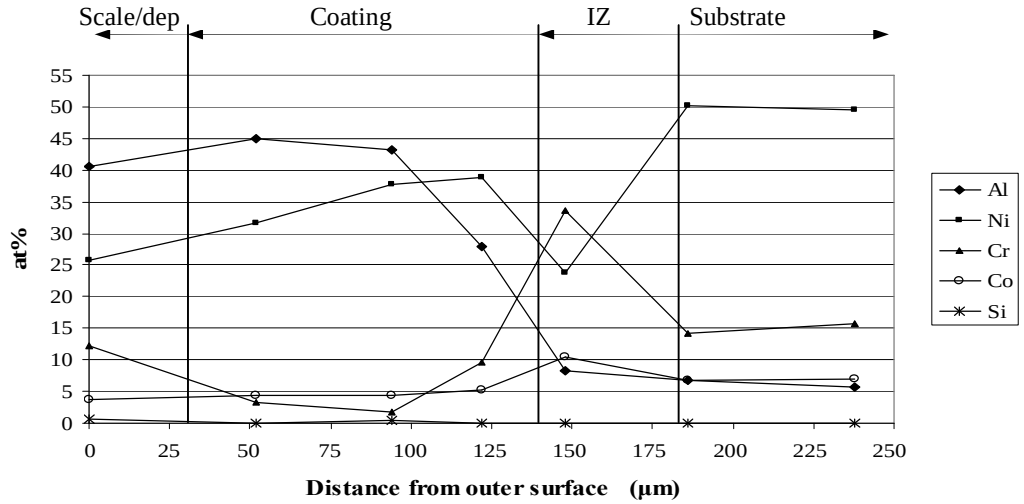

Figure 10.14: IN738LC sample IN1/6; after 500 hours corrosion testing at 700°C – main elements on EDX line in Figure 10.15

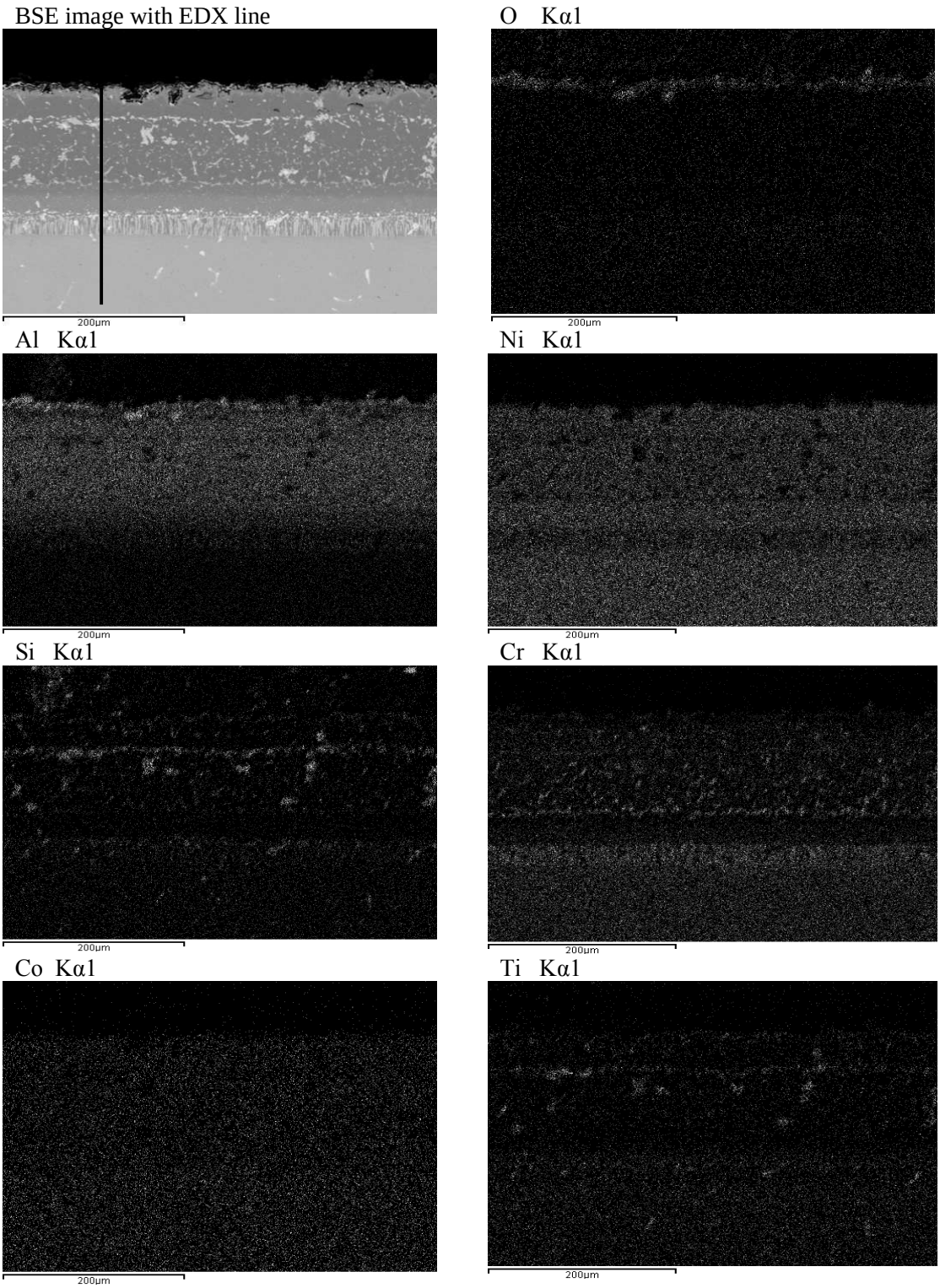

Figure 10.15: IN738LC sample IN1/6 after 500 hours corrosion testing at 700°C – element maps

10.2.2.4 IN738LC with novel silicon-aluminide (pwdr 1) coating (sample IN1/7): Salts; $PbSO_4$(50) + (Na_2SO_4(80) + K_2SO_4(20))(50), Salt flux; 1.5 µg/cm^2/h

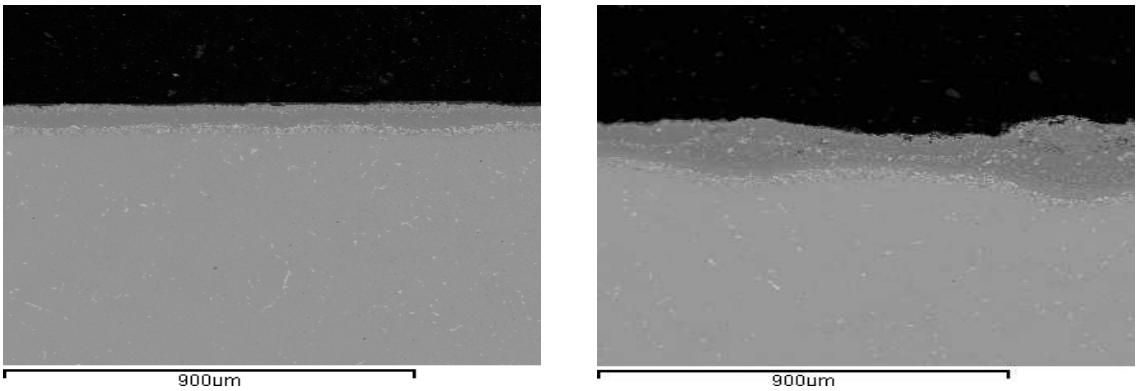

Bottom side average coating depth: 148µm
Ref sample bottom side coating depth: 90µm

Top side average coating depth: 79µm
Ref sample top side coating depth: 51µm

Figure 10.16: IN738LC sample IN1/7; after 500 hours corrosion testing at 700°C – BSE images of both sides

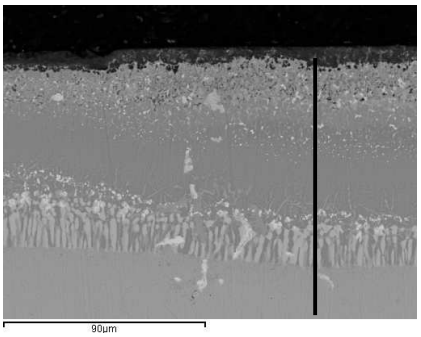

Figure 10.17: Sample IN1/7 – BSE image with EDX line

The β-NiAl phase of IN1/7 is stable through the coating but is towards the γ-edge when compared with that of the Cd+alkali sample subject to the same low salt flux (IN1/6), which is richer in aluminium. Outward chromium diffusion is of a similar content in both samples but occurs towards the surface in IN1/7, in the Cd+alkali sample, where it occurs centrally.

The SiAl coating provides similar levels of Type II hot corrosion protection for lower salt flux samples of both salt combinations tested.

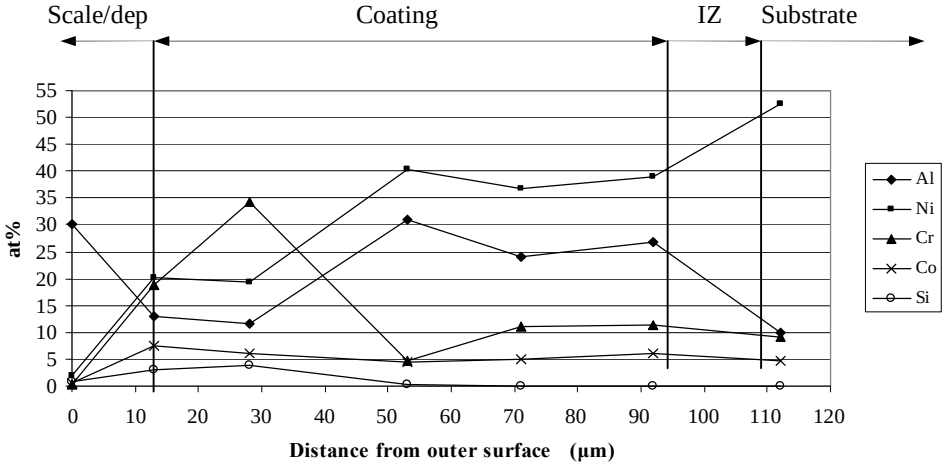

Figure 10.18: IN738LC sample IN1/7; after 500 hours corrosion testing at 700°C – main elements on EDX line in Figure 10.17

10.2.2.5 IN738LC with novel silicon-aluminide (pwdr 2) coating (sample IN2/1):
Salts; $CdSO_4(50) + (Na_2SO_4(80) + K_2SO_4(20))(50)$
Salt flux; 5.0 $\mu g/cm^2/h$

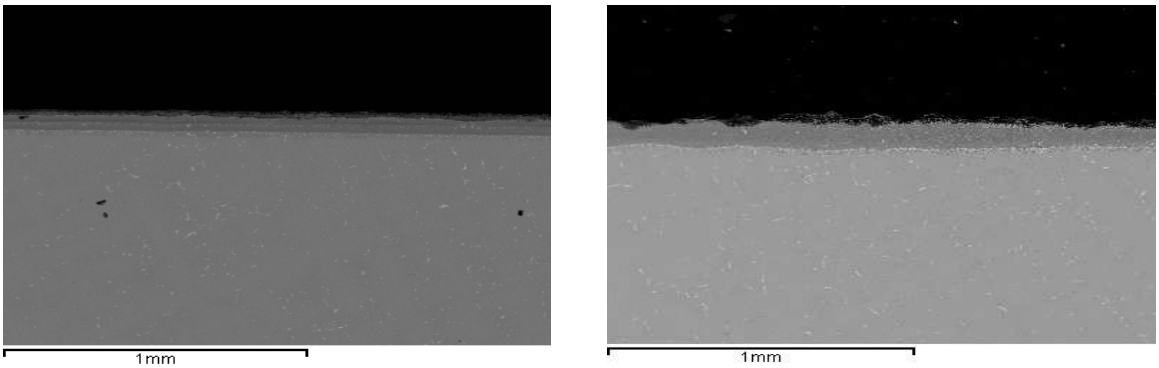

Bottom side average coating depth: 97µm
Ref sample bottom side coating depth: 97µm

Top side average coating depth: 67µm
Ref sample top side coating depth: 40µm

Figure 10.19: IN738LC sample IN2/1; after 500 hours corrosion testing at 700°C – BSE images of both sides

The maps in Figure 10.21 show the deep protective near-surface alumina and oxides of silicon, chromium, and nickel in the same layer. Outward diffusion of chromium has resulted in its depletion at the substrate/IZ interface, and a mid-coating layer rich in chromium and silicon. The β-NiAl matrix varies from the γ-edge at the IZ, towards the α-edge at the centre of the coating, reversing towards the γ direction, then becoming depleted in nickel and rich in aluminium in the outer layer. The effect of the higher silicon content of powder 2 in this sample, has been to reduce the aluminium content in the coating, compared with that from powder 1 in sample IN1/1, after the corrosion testing. However, this coating continues to provide Type II hot corrosion protection.

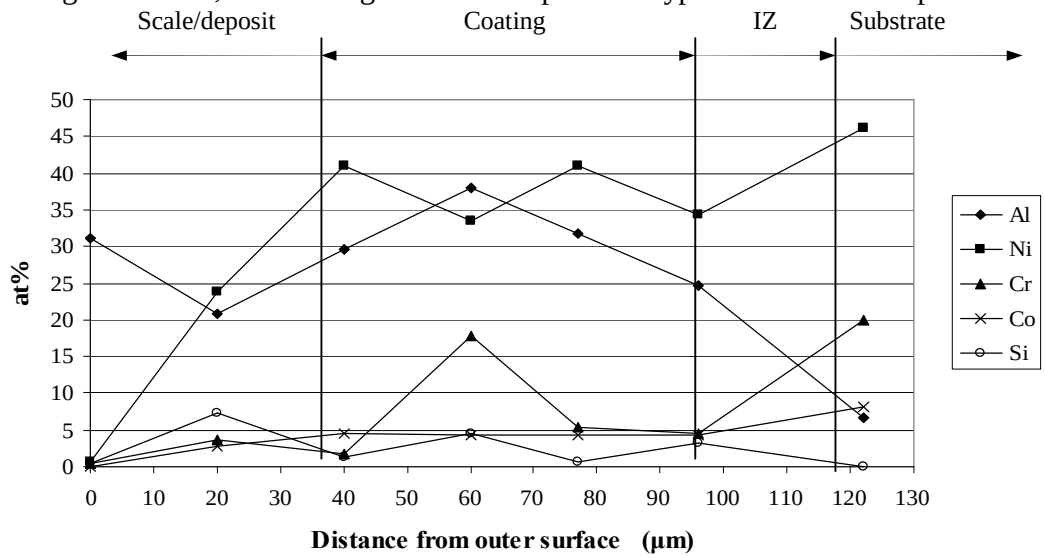

Figure 10.20: IN738LC sample IN2/1; after 500 hours corrosion testing at 700°C – main elements on EDX line in Figure 10.21

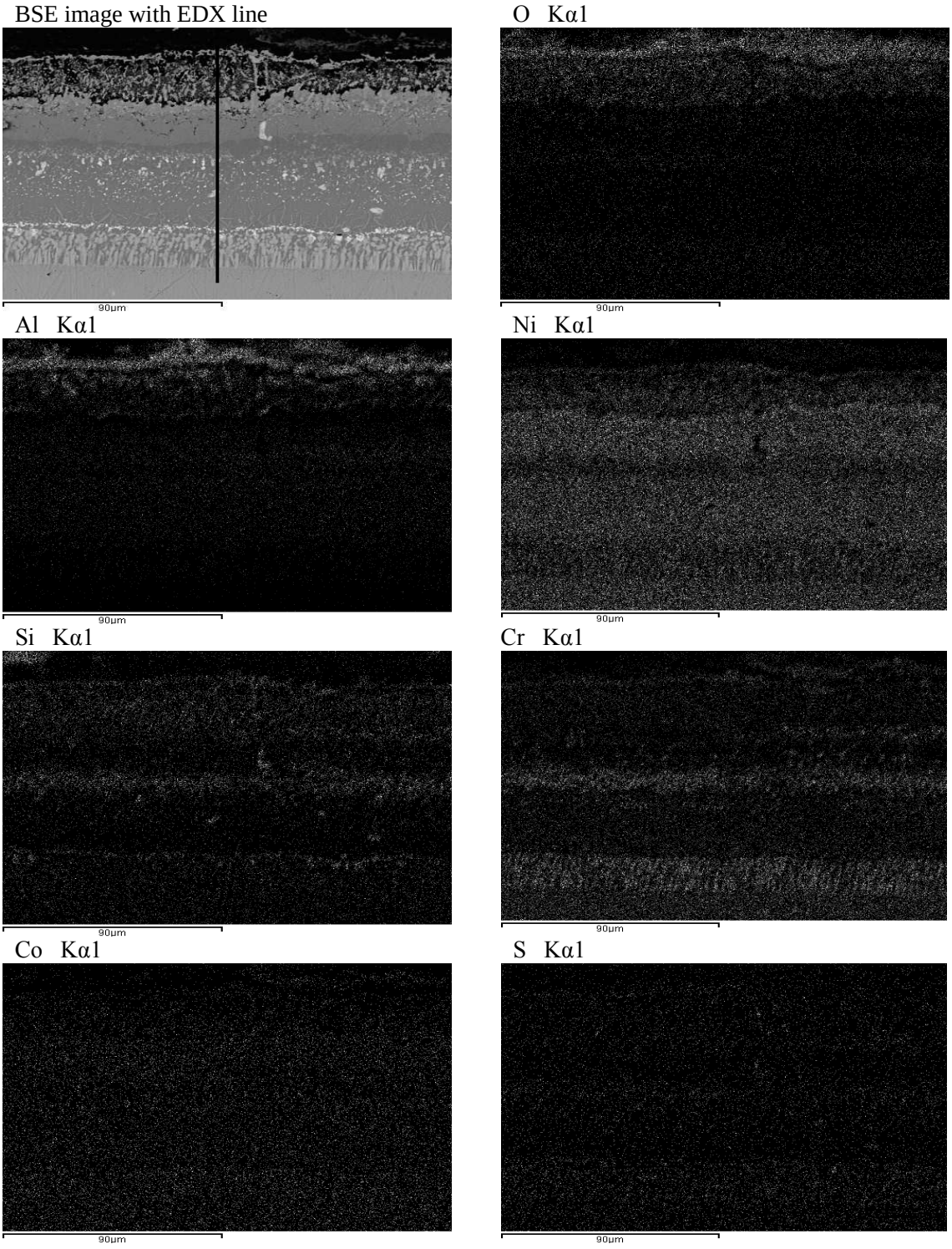

Figure 10.21: IN738LC sample IN2/1 after 500 hours corrosion testing at 700°C - element maps

10.2.2.6 IN738LC with novel silicon-aluminide (pwdr 2) coating (sample IN2/2):
Salts; $PbSO_4(50) + (Na_2SO_4(80) + K_2SO_4(20))(50)$
Salt flux; 5.0 µg/cm^2/h

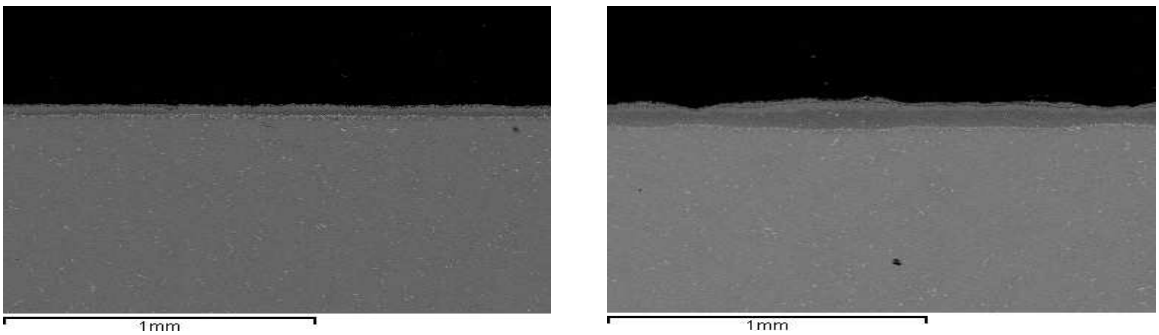

Bottom side average coating depth: 102µm
Ref sample bottom side coating depth: 97µm

Top side average coating depth: 100 µm
Ref coating top side coating depth: 40µm

Figure 10.22: IN738LC sample IN2/2; after 500 hours corrosion testing at 700°C – BSE images of both sides

The element maps in Figure 10.24 and EDX results show the deposit/scale to be rich in alumina. Above the IZ, a 30µm deep layer deficient in chromium occurs, after which it becomes chromium rich through into the deposit/scale. Silicon deficiency also occurs above the IZ but becomes increasingly distributed through the coating, peaking at 12 at%Si approximately 20µm from the coating to deposit/scale interface. Uniform outward diffusion of titanium occurs in the coating with an average content of 1.5 at%Ti, as do traces of molybdenum and tungsten. The results for IN2/1 and IN2/2 show that the SiAl2 coating provides similar Type II hot corrosion protection for IN738LC, when corrosion tested with Pb+alkali salts as it does for Cd+alkali salts.

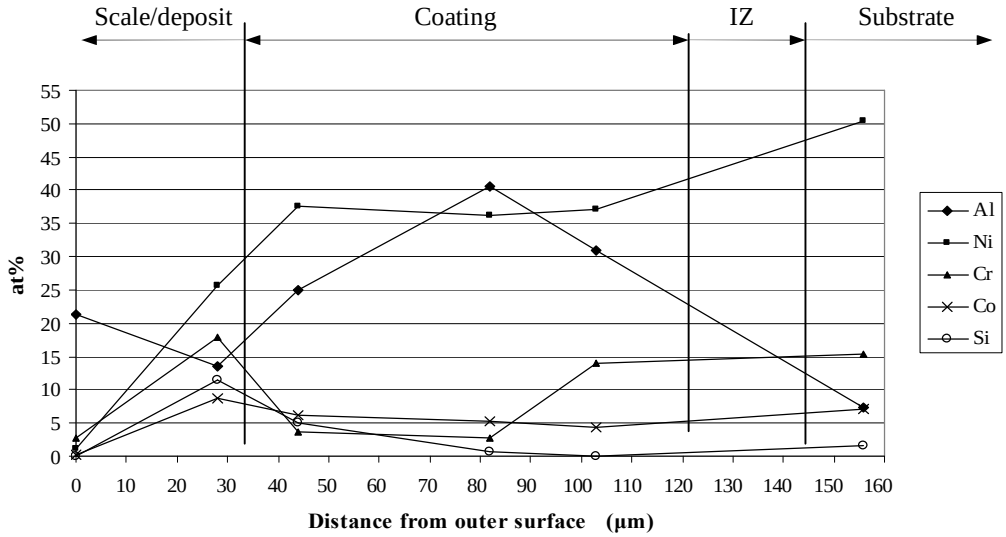

Figure 10.23: IN738LC sample IN2/2; after 500 hours corrosion testing at 700°C – main elements on EDX line in Figure 10.24

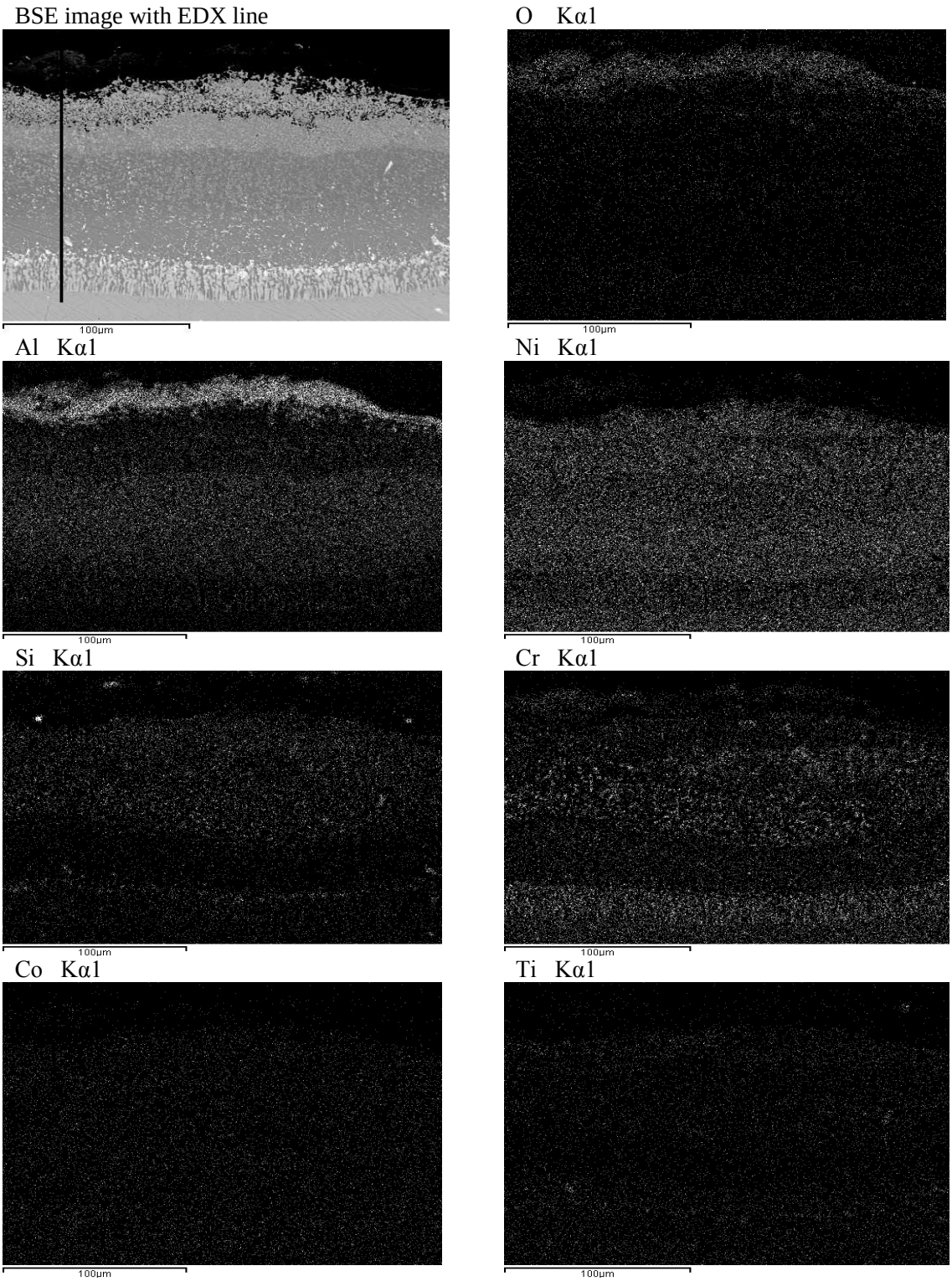

Figure 10.24: IN738LC sample IN2/2 after 500 hours corrosion testing at 700^{o}C - element maps

10.2.2.7 CMSX-4 with novel silicon-aluminide (pwdr 1) coating (sample CM1/1): Salt flux; 5.0 µg/cm^2/h
Salts; $CdSO_4$(50) + (Na_2SO_4(80) + K_2SO_4(20))(50)

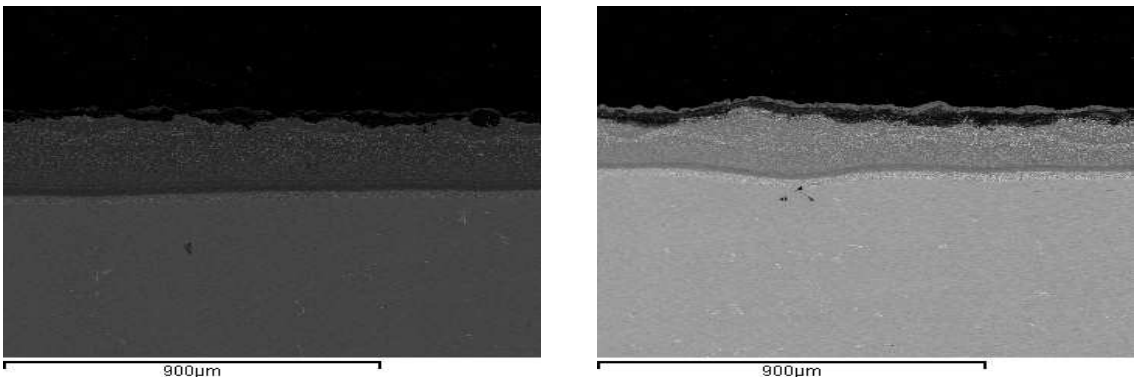

Bottom side average coating depth: 193µm
Ref sample bottom side coating depth: 250µm

Top side average coating depth: 146µm
Ref coating top side coating depth: 184 µm

Figure 10.25: CMSX-4 sample CM1/1; after 500 hours corrosion testing at 700°C – BSE images of both sides

Element maps in Figure 10.27 show the pitting in the coating surface, above which the deposit/scale occur in a layer, with a depth varying from 13µm to 42µm, the bottom of which is rich in oxides of sulphur and chromium. Outside this layer the deposit/scale are rich in oxides of aluminium, nickel and cobalt. Immediately above the IZ lies a layer, approximately 10µm deep, depleted in chromium and silicon, after which these elements become more uniformly distributed in the coating. EDX results indicate the trend towards γ-NiAl phase. Mid-way through the coating lies a 25µm layer rich in silicon, outwardly diffused titanium and tantalum and traces of molybdenum and tungsten. The EDX results also show that this coating has the potential to provide protective scale for a significant period.

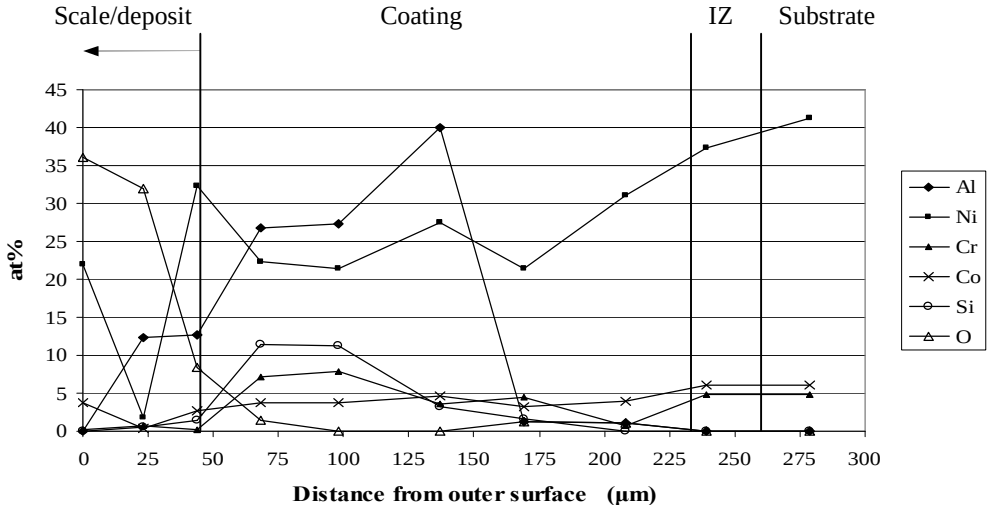

Figure 10.26: CMSX-4 sample CM1/1; after 500 hours corrosion testing at 700°C – main elements on EDX line in Figure 10.27

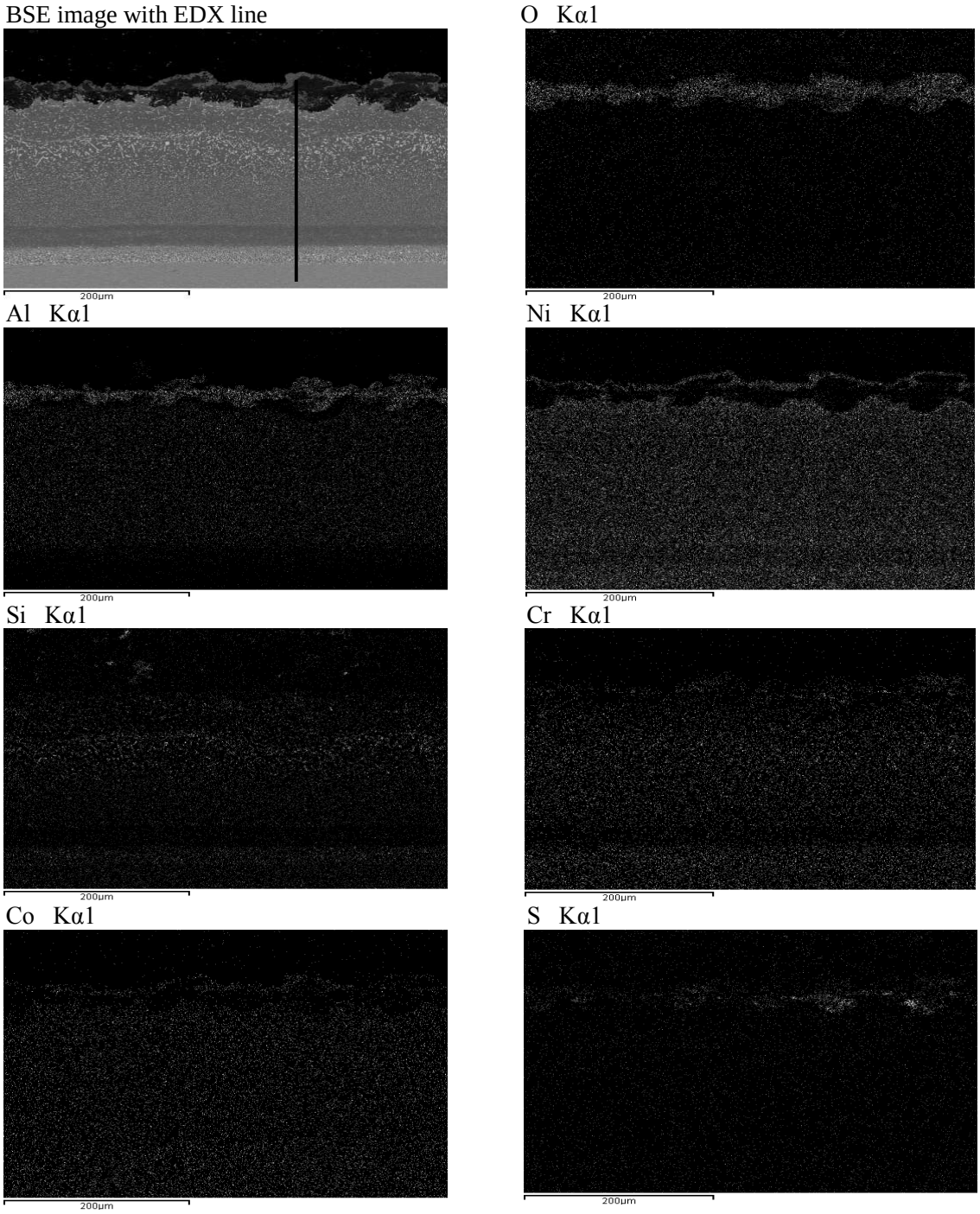

Figure 10.27: CMSX-4 sample CM1/1 after 500 hours corrosion testing at 700°C - element maps

10.2.2.8 CMSX-4 with novel silicon-aluminide (pwdr 1) coating (sample CM1/2): Salt flux; 5.0 µg/cm^2/h
Salts; $PbSO_4$(50) + (Na_2SO_4(80) + K_2SO_4(20))(50)

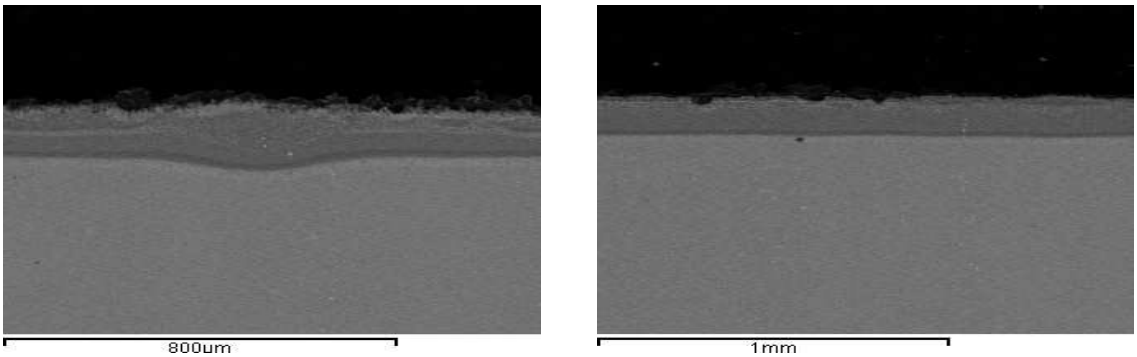

Bottom side average coating depth: 156µm
Ref sample bottom side coating depth: 250µm

Top side average coating depth: 126µm
Ref sample top side coating depth: 184µm

Figure 10.28: CMSX-4 sample CM1/2; after 500 hours corrosion testing at 700°C – BSE images of both sides

Compared with the previous sample (CM1/1), the Pb+alkali sample CM1/2 does not display heavy pitting at the coating surface. The maps in Figure 10.30 show the surface scale and salt deposit to be mainly rich in oxides, of aluminium and to lesser extents of sulphur, chromium and nickel. Below the degraded layers, there is a 78µm deep, stable matrix at the α-edge of the β-NiAl phase. Above the IZ/coating interface is a 16µm deep layer depleted in chromium and silicon, after which these elements become similarly distributed through to the start of coating degradation. The EDX results indicate that significant coating remains to maintain protective scale growth for a significant period.

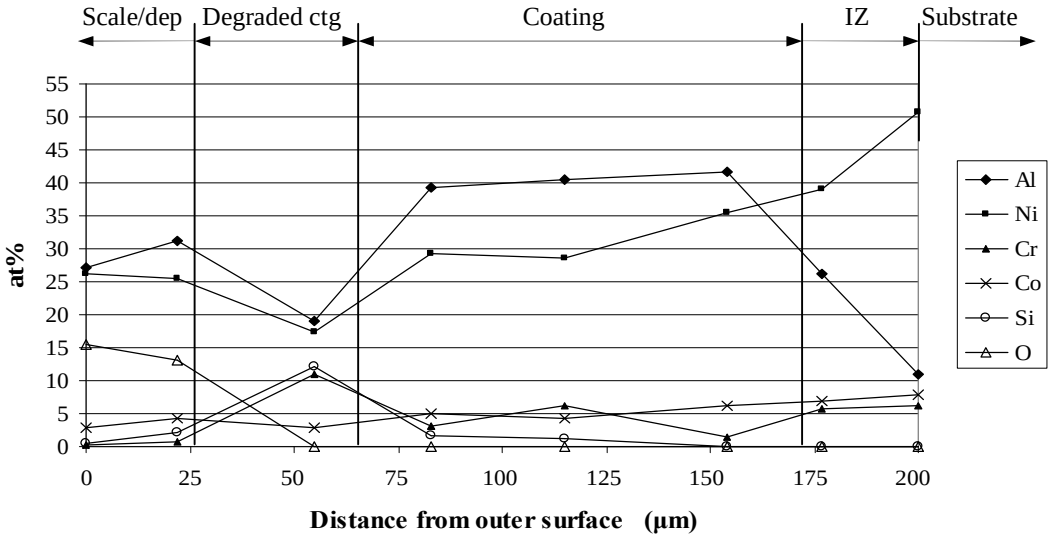

Figure 10.29: CMSX-4 sample CM1/2; after 500 hours corrosion testing at 700°C – main elements on EDX line in Figure 10.30

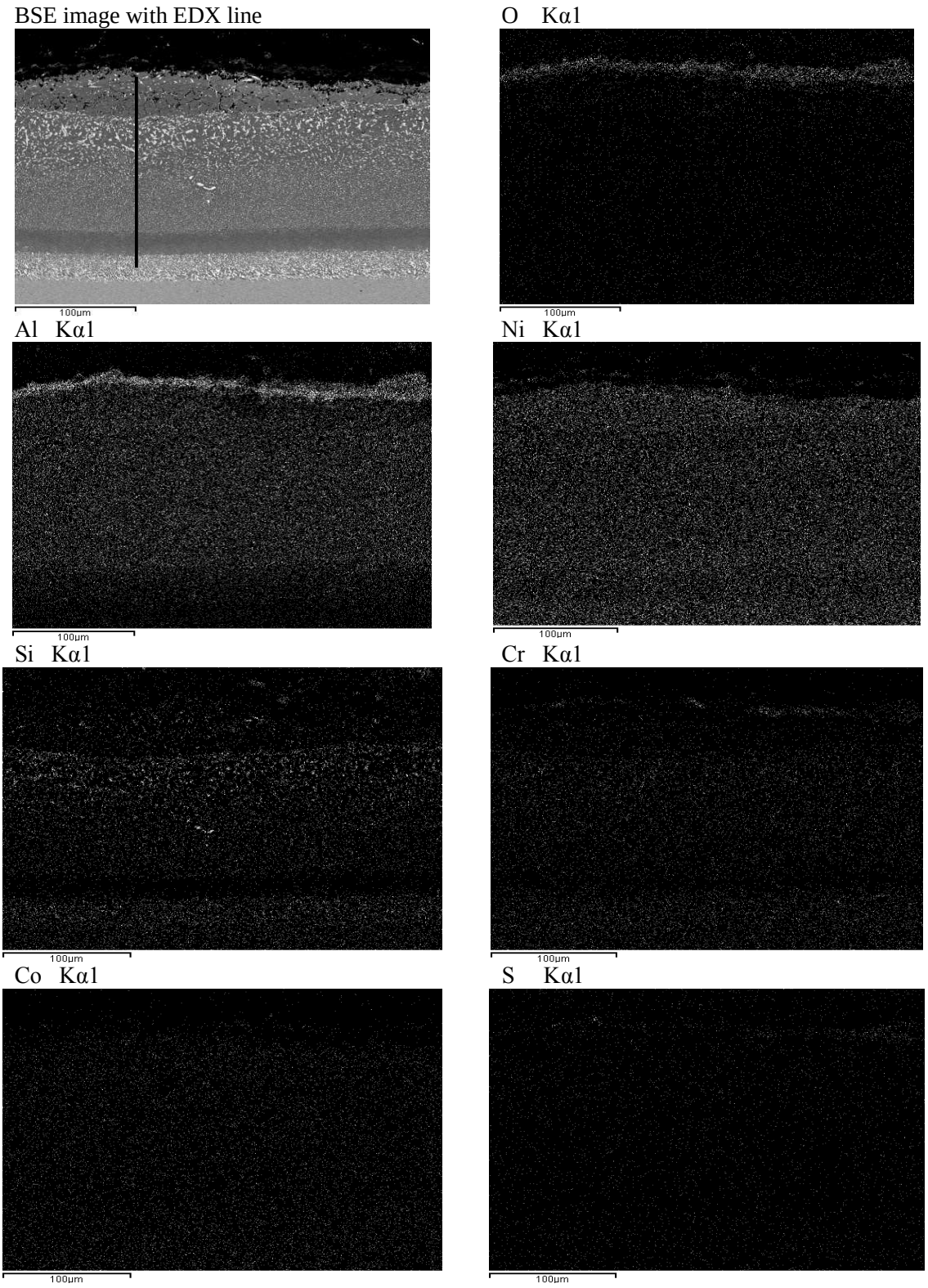

Figure 10.30: CMSX-4 sample CM1/2 after 500 hours corrosion testing at 700^{o}C - element maps

10.2.2.9 CMSX-4 with novel silicon-aluminide (pwdr 1) coating (sample CM1/6): Salt flux; 1.5 µg/cm^2/h
Salts; $CdSO_4$(50) + (Na_2SO_4(80) + K_2SO_4(20))(50)

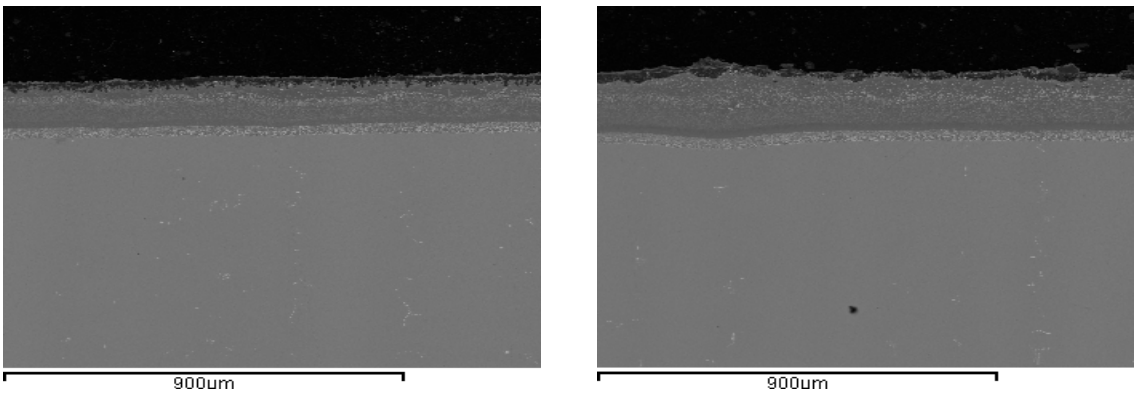

Bottom side average coating depth: 136µm
Ref sample bottom side coating depth: 203 µm

Top side average coating depth: 113µm
Ref sample top side coating depth: 188 µm

Figure 10.31: CMSX-4 sample CM1/6; after 500 hours corrosion testing at 700°C – BSE images of both sides

The element maps in Figure 10.33 show the three varying phase layers of the β-NiAl matrix in the coating, between the IZ and degraded layer. In all three layers the phases remain biased to the α-end of β-phase but alternately shift to a small extent towards the γ-end, but remain stable. These variations coincide with layers rich in silicon and chromium. EDX results show outward diffusion of titanium (3 at%Ti) and traces of molybdenum, tantalum and tungsten. Inward diffusion has resulted in the IZ being rich in silicon. After 500 hours corrosion testing at 700°C the coating has sufficient depth to grow protective scale for a significant period.

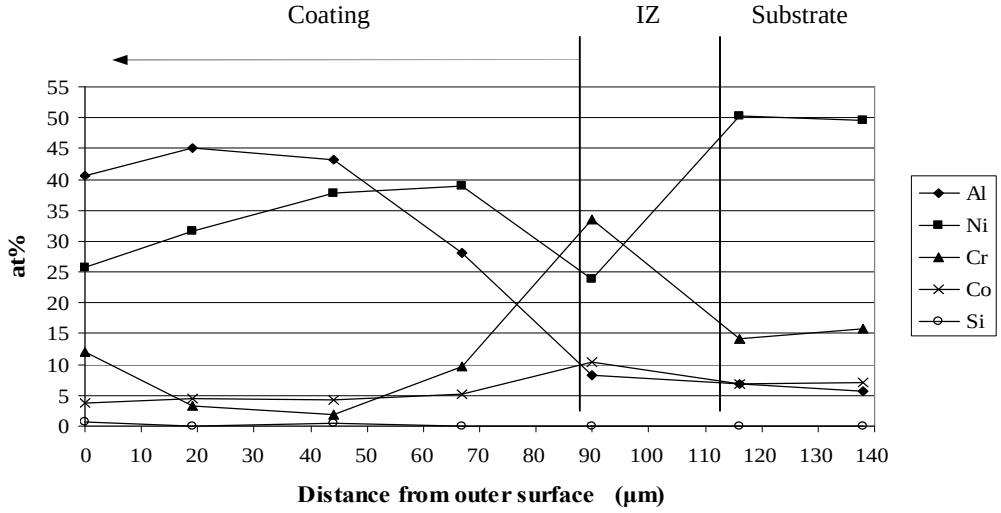

Figure 10.32: CMSX-4 sample CM1/6; after 500 hours corrosion testing at 700°C – main elements on EDX line in Figure 10.33

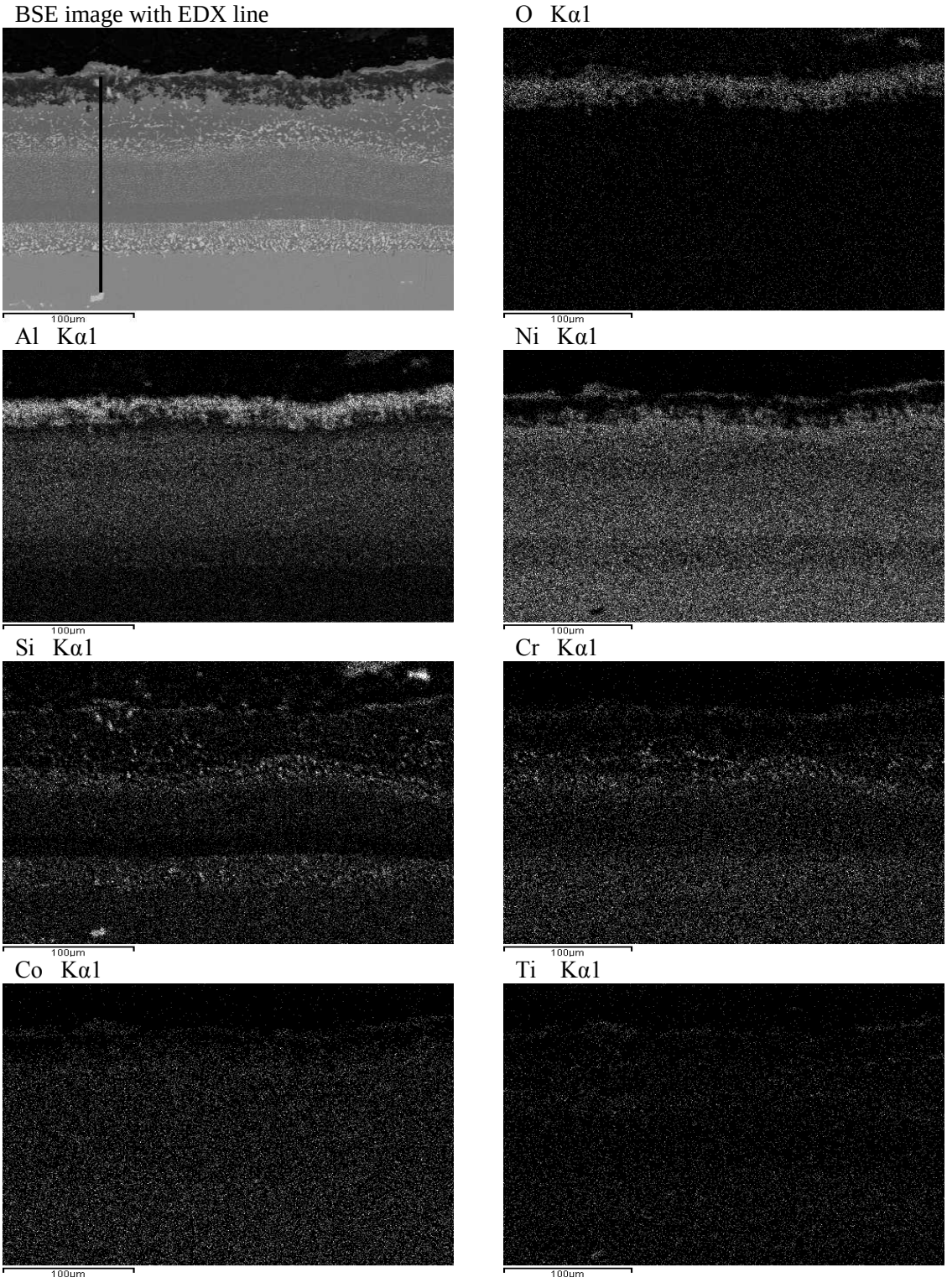

Figure 10.33: CMSX-4 sample CM1/6 after 500 hours corrosion testing at 700°C - element maps

10.2.2.10 CMSX-4 with novel silicon-aluminide (pwdr 1) coating (sample CM1/7): Salt flux; 1.5 µg/cm^2/h
Salts; $PbSO_4$(50) + (Na_2SO_4(80) + K_2SO_4(20))(50)

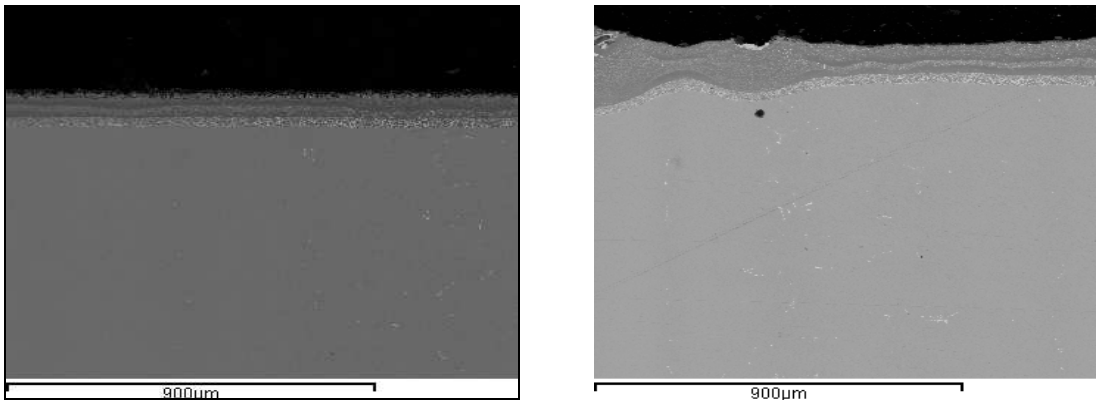

Bottom side average coating depth: 148µm
Ref sample bottom side coating depth: 203µm

Top side average coating depth: 112µm
Ref sample top side coating depth: 188µm

Figure 10.34: CMSX-4 sample CM1/7; after 500 hours corrosion testing at 700°C – BSE images of both sides

The element maps in Figure 10.36, and EDX results in Figure 10.35, show that, from the IZ/coating interface to the surface, the β-NiAl phase is stable, but tends towards the α-end. The scale contains oxides of aluminium, chromium and sulphur. There is uniform outward diffusion of titanium, tantalum, tungsten and rhenium, with traces of molybdenum. The remaining depth of stable β-NiAl, of around 60µm, will continue to provide hot corrosion protection for a significant period.

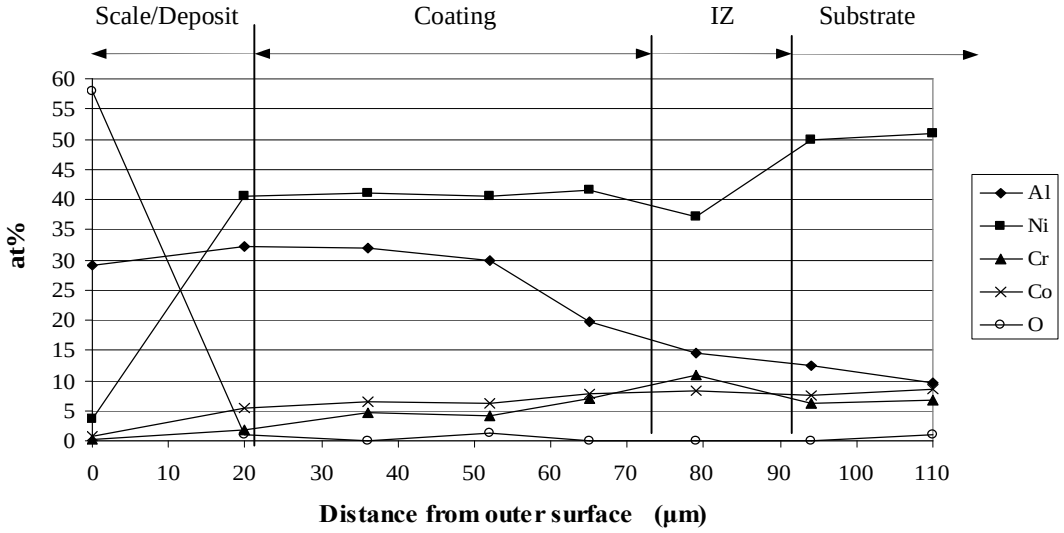

Figure10.35: CMSX-4 sample CM1/7; after 500 hours corrosion testing at 700°C – main elements on EDX line in Figure 10.36

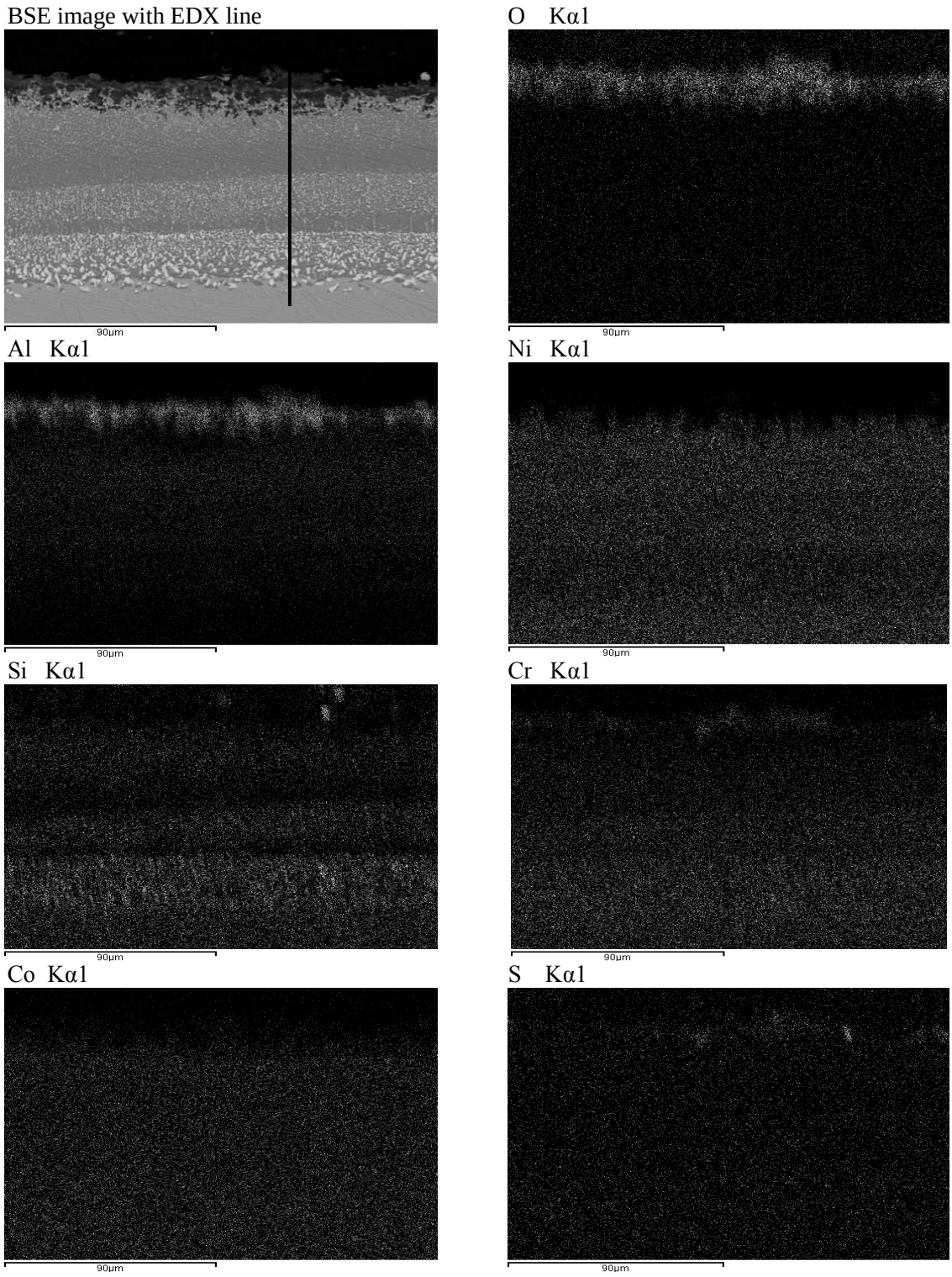

Figure 10.36: CMSX-4 sample CM1/7 after 500 hours corrosion testing at 700°C - element maps

10.2.2.11 CMSX-4 with novel silicon-aluminide (pwdr 2) coating (sample CM2/1): Salt flux; 5.0 µg/cm^2/h
Salts; $CdSO_4$(50) + (Na_2SO_4(80) + K_2SO_4(20))(50)

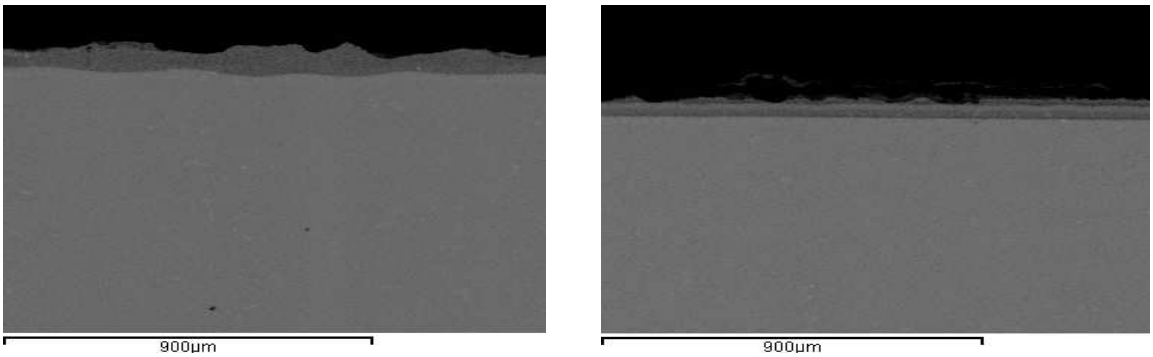

Bottom side average coating depth: 78µm
Ref sample bottom side coating depth: 97µm

Top side average coating depth: 53µm
Ref sample top side coating depth: 67µm

Figure 10.37: CMSX-4 sample CM2/1; after 500 hours corrosion testing at 700°C – BSE images of both sides

The element maps in Figure 10.39, supported by the EDX results in Figure 10.38 show that the β-NiAl phase proceeds from the γ-end towards the α-end, with the increasing aluminium content. In contrast with sample CM1/2 (Figure 10.30) for powder 1, there is no silicon and chromium depleted layer above the IZ, in CM2/1 produced from powder 2. The surface deposit/scale is rich in oxides of aluminium, silicon and chromium. Like previous corrosion tested CMSX-4 samples, silicon has diffused into the IZ, and outward diffusion of titanium, tantalum and tungsten has occurred.

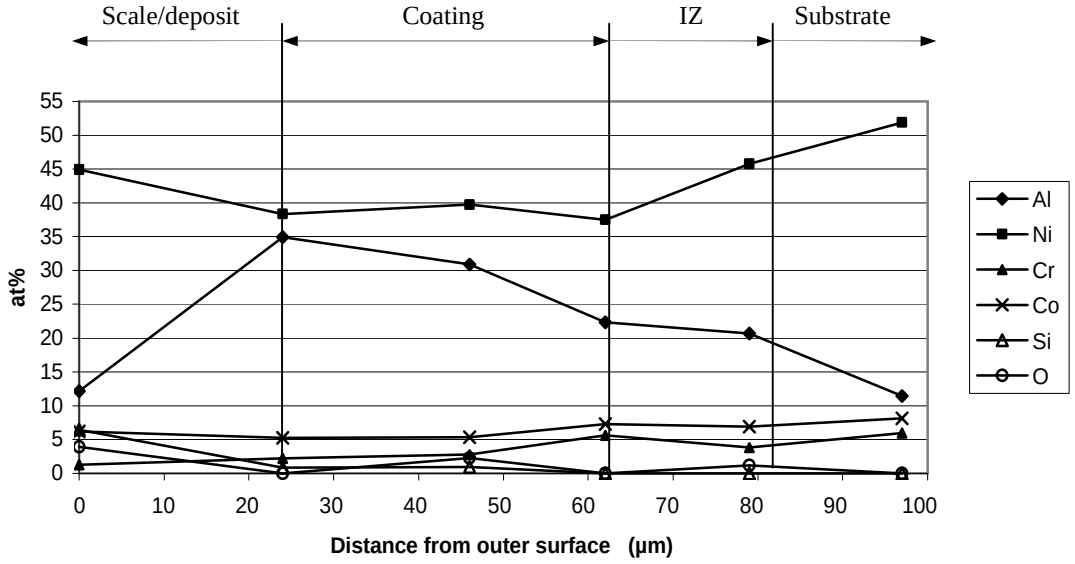

Figure 10.38: CMSX-4 sample CM2/1; after 500 hours corrosion testing at 700°C – main elements on EDX line in Figure 10.39

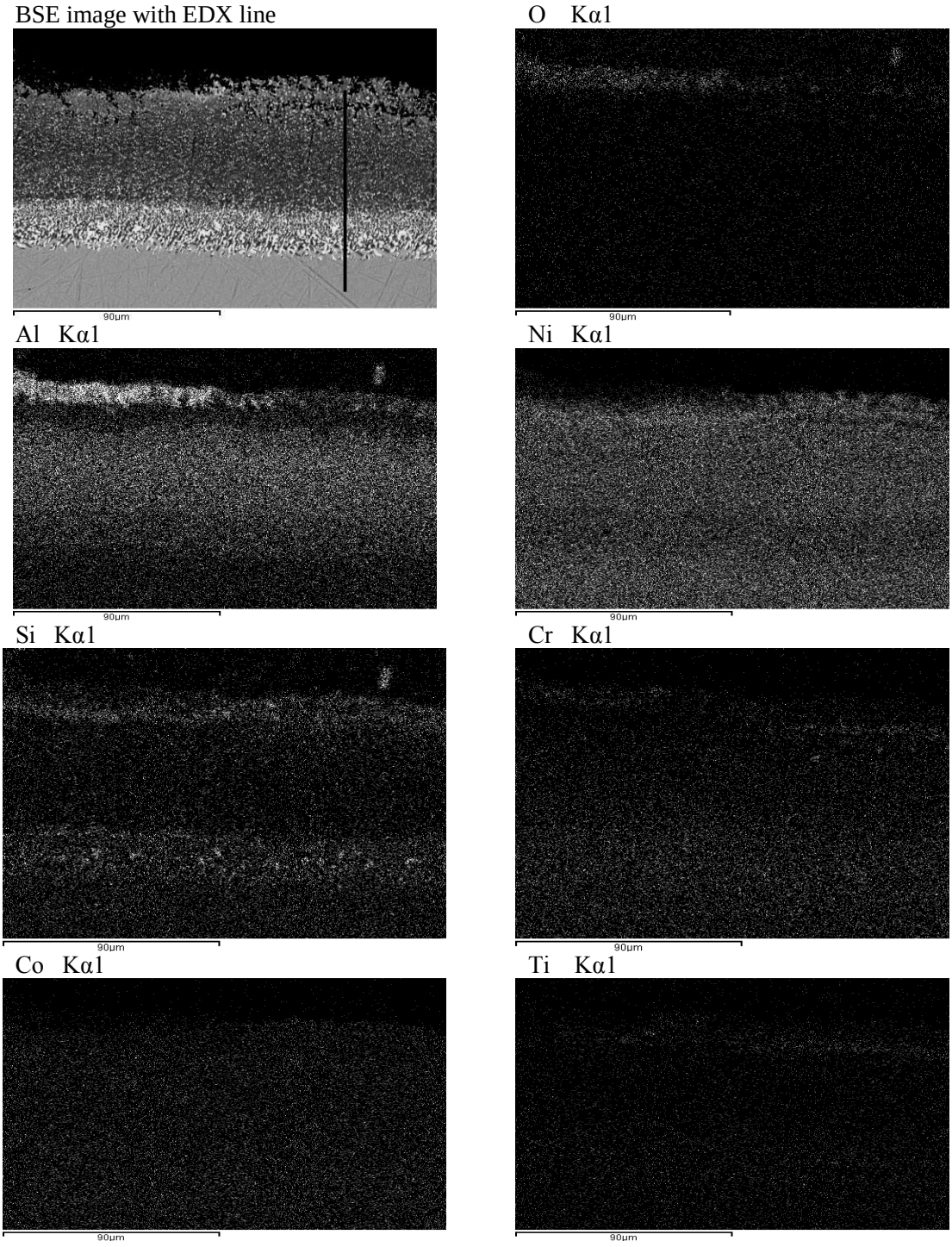

Figure 10.39: CMSX-4 sample CM2/1 after 500 hours corrosion testing at 700^{o}C - element maps

10.2.2.12 CMSX-4 with novel silicon aluminide (pwdr 2) coating (sample CM2/2): Salt flux; 5.0 µg/cm^2/h
Salts; $PbSO_4$(50) + (Na_2SO_4(80) + K_2SO_4(20))(50)

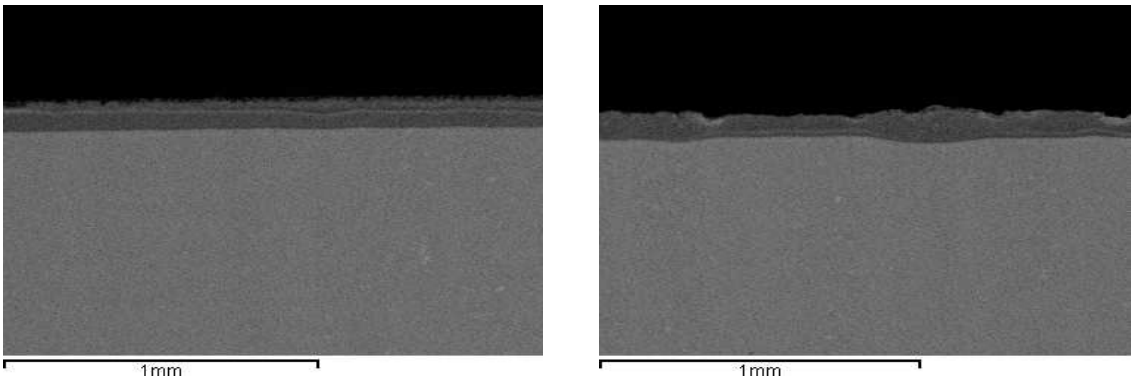

Bottom side average coating depth: 83µm
Ref sample bottom side coating depth: 97µm

Top side average coating depth: 78µm
Ref sample top side coating depth: 67µm

Figure 10.40: CMSX-4 sample CM2/2; after 500 hours corrosion testing at 700°C – BSE images of both sides

In this sample, the NiAl matrix starts, at the top surface of the IZ, at the α-edge of β-NiAl phase. After a depth of approximately 20µm, aluminium depletion causes it to move towards γ-edge. Over the next 40µm of depth, a minimum content of 11 at%Al occurs centrally, then peaks at 36 at%Al. The aluminium content then commences a downward trend to 14 at%Al at the base of the degraded coating. The maps in Figure 10.42 show the increasing content of oxides of chromium and silicon where depletion of aluminium occurs. Titanium and traces of tantalum and tungsten have outwardly diffused into the coating.

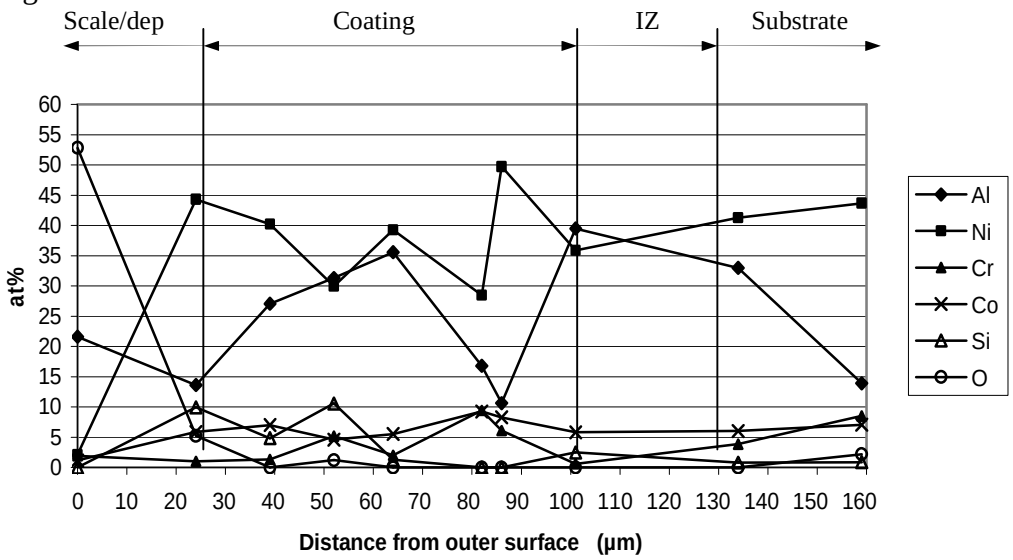

Figure 10.41: CMSX-4 sample CM2/2; after 500 hours corrosion testing at 700°C – main elements on EDX line in Figure 10.42

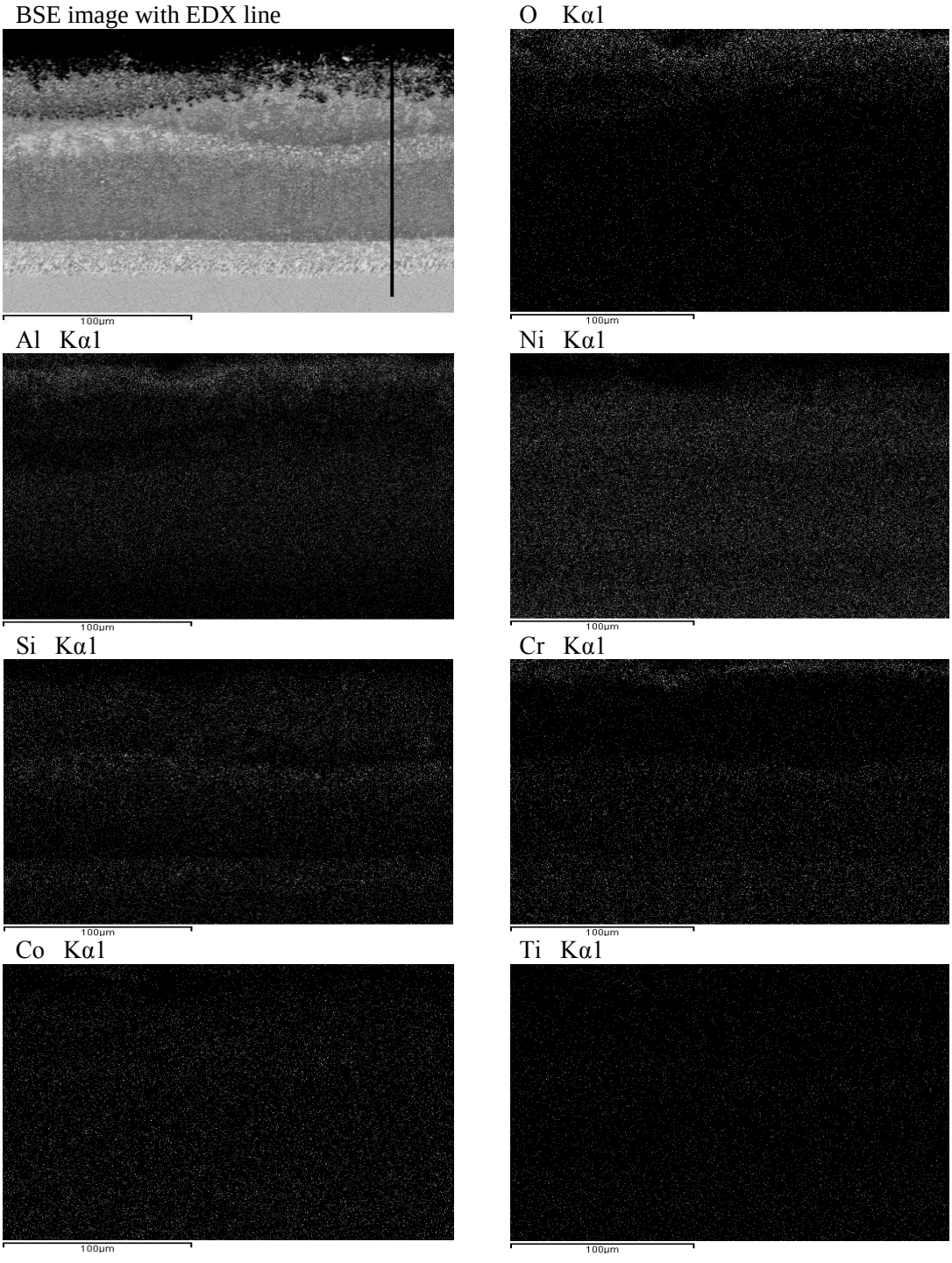

Figure 10.42: CMSX-4 sample CM2/2 after 500 hours corrosion testing at 700°C - element maps

10.2.3 Corrosion test series 3; 500 hours at 700°C, discussion and conclusions

The novel single-step silicon-aluminide coatings, after 500 hours corrosion testing at 700°C, continue to provide protection against Type II hot corrosion for IN738LC and CMSX-4. In each case, there continues to be sufficient aluminium, provided by the coating and chromium outwardly diffused from the substrate, to support protective scale growth. As shown by the mass changes over the testing period, there are differences in the rates of oxidation and sulphidation, between the coatings on the two substrates. The IN738LC mass changes follow parabolic curves of the incubation or oxidation stage after 300 hours testing, then generally level-off. The mass changes of both lower salt flux samples were of a similar order, lower than those for the four samples subjected to the higher salt flux. This was the case for CMSX-4 samples. However, the CMSX-4 mass changes indicated that the incubation stage continued for all samples except those subject to the higher salt flux of the Cd+alkali salt combination. These commenced propagation, the oxide reacting with the deposit, which was continuing at the same gradient after 500 hours corrosion testing. The spall mass changes also illustrate the differences in aluminium and chromium content between the two substrates, where the spalling rates for IN738LC samples are significantly lower than those for CMSX-4.

Results show that the higher silicon content of powder 2 did not provide any advantages compared with powder 1. Coatings formed from CVD using powder 2, on both substrates, produced similar mass changes to those formed from powder 1. The spall rates were significantly higher on the powder 2 coated IN738LC samples than the powder 1 samples. For CMSX-4, the higher salt flux Cd+alkali sample with powder 2 coating, the spalling rate of the powder 2 was highest, with the equivalent Pb+alkali sample spalling at a similar rate to those of the other higher salt flux samples. It is concluded that increasing the silicon content, which resulted in coatings of lesser depth and increased spalling rates, provided no advantage over powder 1 which had the lower silicon content.

To confirm the consistency of results obtained from mass changes, BSE microstructures and EDX line scans, XRD assessments were carried out on selected, exposed samples of CMSX-4 and IN738LC, in a similar manner to XRD examination of oxidation test samples, reported in section 9.4.2.3. The XRD diffractogram of both substrates, exposed samples and unexposed reference samples of IN738LC and CMSX-4 with the silicon-aluminide coatings, are shown in Figure 10.43. In this diffractogram, only one side is shown. From the list of samples shown with Figure 10.43, where coatings are identified as SiAl1 and SiAl2, the former refers to coating with the lower silicon content, the latter refers to the coating having the higher silicon content.

Table 10.2 lists the compounds identified in the peaks in Figure 10.43. The samples shown in Figure 10.43 are repeated in the diffractogram in Figure 10.44, but within the more limited 2-Theta-Scale of 42 to 46, which covers the range for the substrates, exposed and reference samples. To assist analysis of XRD results, individual graphs for exposed IN738LC and CMSX-4 samples, within the limited 2-Theta-Scale range, are set out in Figures 10.45 and 10.46. These graphs show plots for both sides of each sample which will confirm the differences in depths identified BSE microstructures.

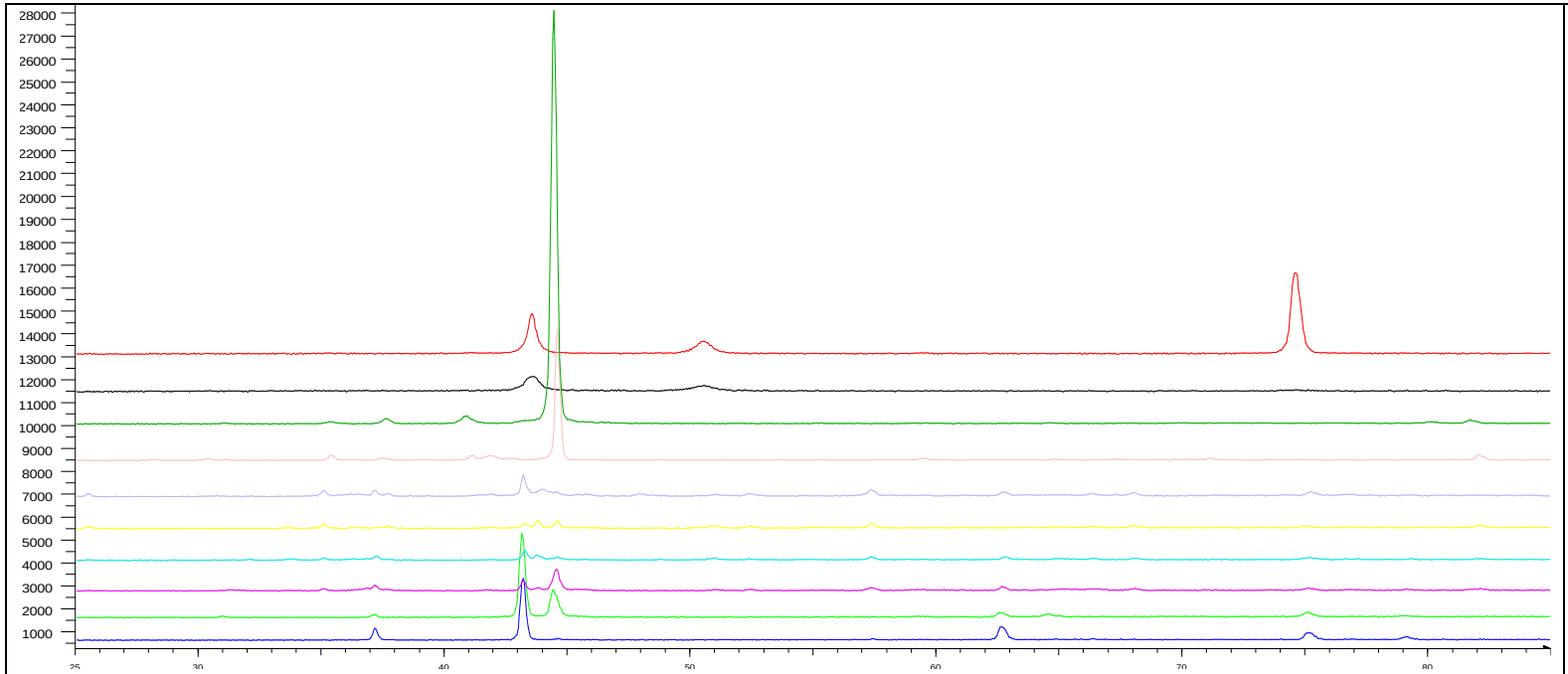

Y-axis units: 'Counts' Key: 1 - Unexposed IN738LC substrate
X-axis: 2-Theta-Scale 2 - Unexposed CMSX-4 substrate
3 - Unexposed CMSX-4 with SiAl1 coating reference sample
4 - Unexposed IN738LC with SiAl1 coating reference sample
5 - Exposed sample IN1-1; IN738LC with SiAl1 coating, exposed to Cd+alkali sulphates
6 - Exposed sample IN1-2; IN738LC with SiAl1 coating, exposed to Pb+alkali sulphates
7 - Exposed sample IN 2-1; IN738LC with SiAl2 coating, exposed to Cd+alkali sulphates
8 - Exposed sample CM1-2; CMSX-4 with SiAl1 coating, exposed to Pb+alkali sulphates
9 - Exposed sample CM2-1; CMSX-4 with SiAl2 coating, exposed to Cd+alkali sulphates
10 - Exposed sample CM1-1; CMSX-4 with SiAl1 coating, exposed to Cd+alkali sulphates

Figure 10.43: Corrosion test series 3; 500 hours at 700°C, XRD assessments of selected exposed samples

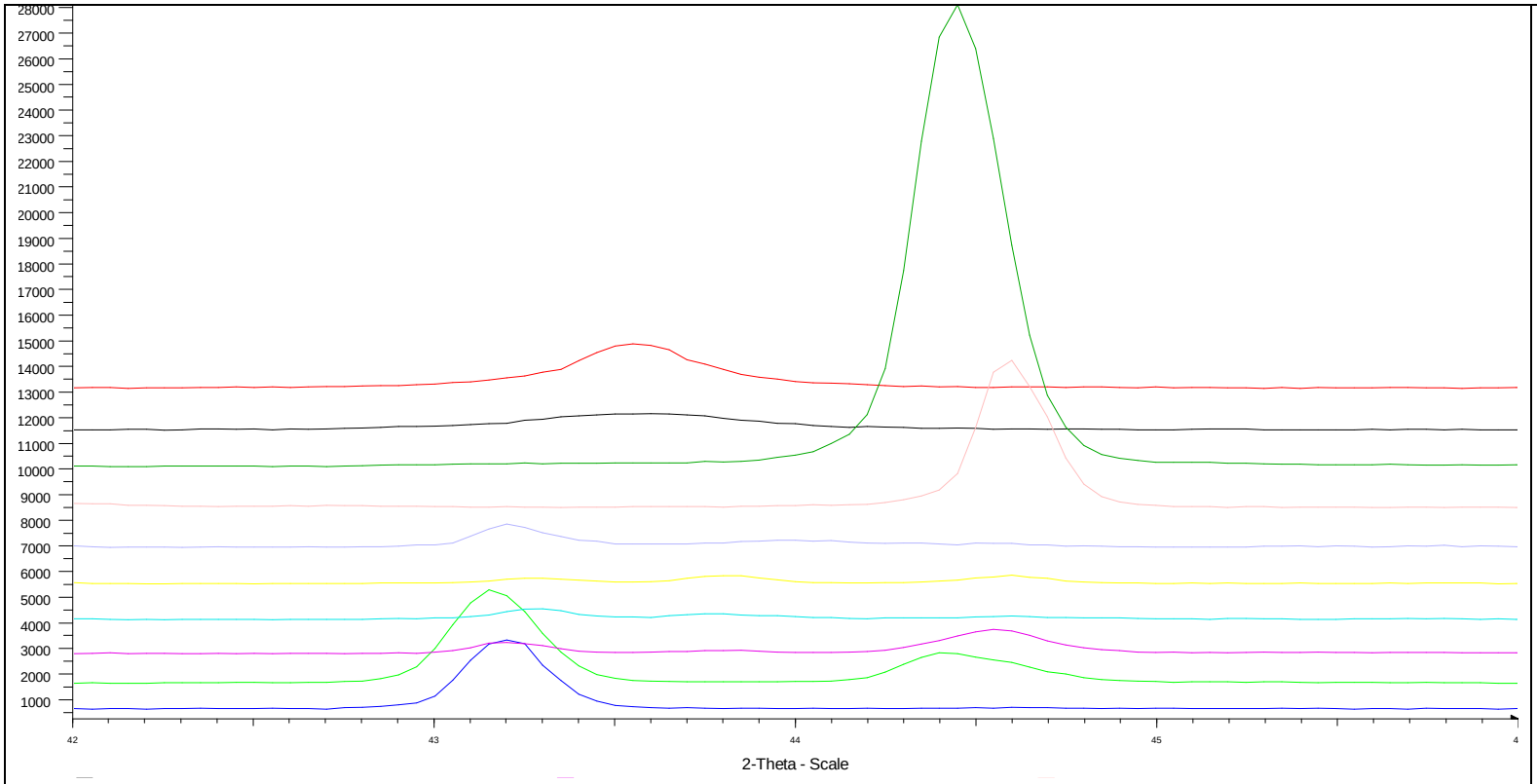

Y-axis units 'Counts'

Key:
1 - Unexposed IN738LC substrate
2 - Unexposed CMSX-4 substrate
3 - Unexposed CMSX-4 with SiAl1 coating reference sample
4 - Unexposed IN738LC with SiAl1 coating reference sample
5 - Exposed sample IN1-1; IN738LC with SiAl1 coating, exposed to Cd+alkali sulphates
6 - Exposed sample IN1-2; IN738LC with SiAl1 coating, exposed to Pb+alkali sulphates
7 - Exposed sample IN 2-1; IN738LC with SiAl2 coating, exposed to Cd+alkali sulphates
8 - Exposed sample CM1-2; CMSX-4 with SiAl1 coating, exposed to Pb+alkali sulphates
9 - Exposed sample CM2-1; CMSX-4 with SiAl2 coating, exposed to Cd+alkali sulphates
10 - Exposed sample CM1-1; CMSX-4 with SiAl1 coating, exposed to Cd+alkali sulphates

Figure 10.44: Corrosion test series 3: 500 hours at 700°C, XRD assessments of selected exposed samples

Peak 2-Theta-Scale position	**Compound**
37.0	Al_2O_3, NiO
43.3	$AlNi_2Ti$, Al_2O_3, NiO
44.4	NiAl, NiO, TiO_2
50.7	Ni_3Al, Co_3O_4
63.0	$AlNi_2Ti$, NiO
75.5	$AlNi_2Ti$, NiO
79.0	TiO_2

Table 10.2 : Corrosion test series 3; XRD analyses, compounds associated with peaks shown in XRD plots in Figure 10.43

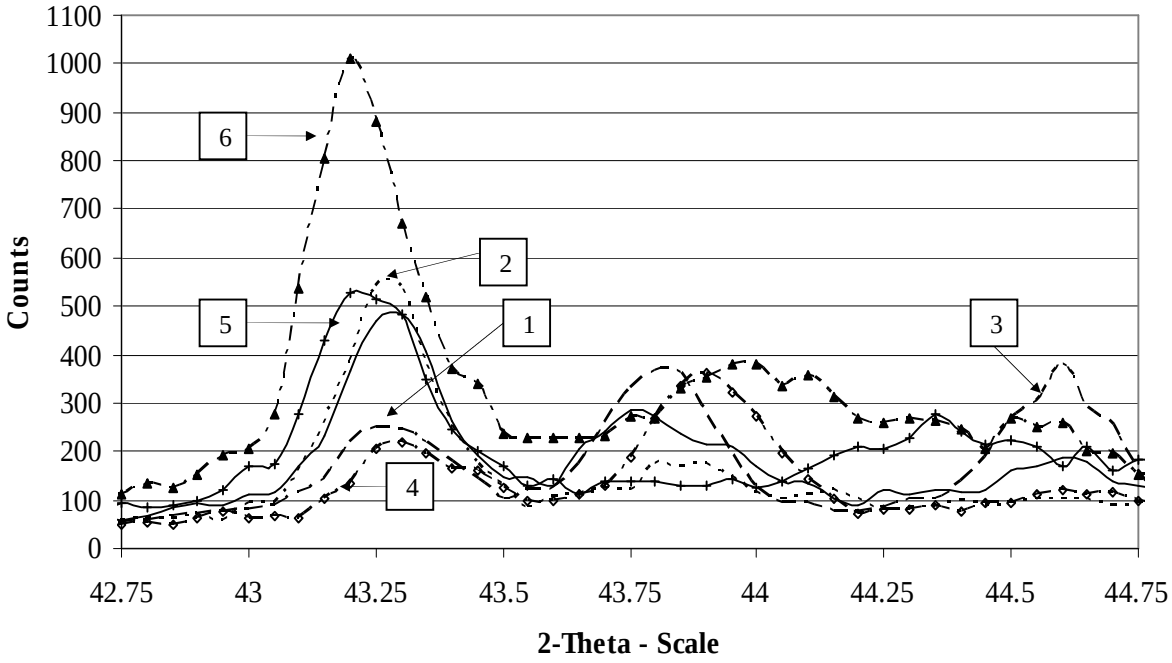

Key : 1 - IN1/1 side 1, IN738LC with SiAl1 coating, Cd+alkali
2 - IN1/1 side 2, IN738LC with SiAl1 coating, Cd+alkali
3 - IN1/2 side 1, IN738LC with SiAl1 coating, Pb+alkali
4 - IN1/2 side 2, IN738LC with SiAl1 coating, Pb+alkali
5 - IN2/1 side 1, IN738LC with SiAl2 coating, Cd+alkali
6 - IN2/1 side 2, IN738LC with SiAl2 coating, Cd+alkali

Figure 10.45: Corrosion test series 3; XRD plots of exposed IN738LC samples with silicon-aluminide coatings

XRD results for IN738LC show there to be residual coatings on all three samples assessed, with the Pb+alkali sample coating having more residual coating than that with the same SiAl1 coating, exposed to Cd+alkali. This confirms that the SiAl1 coating is more Type II hot corrosion protective against Pb+alkali than it is against Cd+alkali. The sample with SiAl2, higher content silicon, had the deepest residual coating, but was the most degraded of all. All sample coatings were significantly degraded, that with the SiAl2 coating being the most severely degraded. This confirms earlier assessments that showed SiAl2 coating did not provide superior Type II hot corrosion protection to that provided by SiAl1, for IN738LC. XRD results for exposed IN738LC samples showed differences in coating depths, between the bottom side compared with the top side. As was shown in earlier analyses, the residual coatings on the top sides were more severely degraded than the thicker residual coatings on the bottom sides.

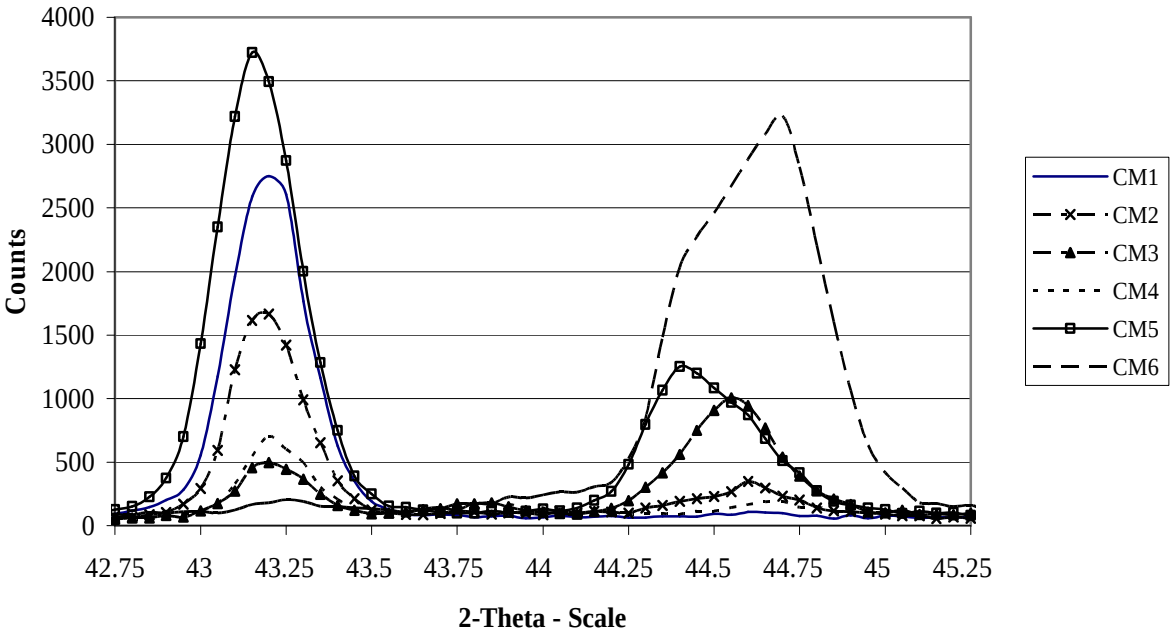

Key: CM1 - CM1/1 side 1, CMSX-4 with SiAl1 coating, Cd+alkali
CM2 - CM1/1 side 2, CMSX-4 with SiAl1 coating, Cd+alkali
CM3 - CM1/2 side 1, CMSX-4 with SiAl1 coating, Pb+alkali
CM4 - CM1/2 side 2, CMSX-4 with SiAl1 coating, Pb+alkali
CM5 - CM2/1 side 1, CMSX-4 with SiAl2 coating, Cd+alkali
CM6 - CM2/1 side 2, CMSX-4 with SiAl2 coating, Cd+alkali

Figure 10.46: Corrosion test series 3; XRD plots of exposed CMSX-4 samples with silicon-aluminide coatings

The XRD assessments of exposed CMSX-4 samples with the silicon-aluminide coatings, seen in Figure 10.46, exhibited wider differences in residual coating thicknesses and degradation, than those for IN738LC reported above. There were negligible residual coatings on the sample coated with SiAl1 which was exposed to Cd+alkali and what remained of the coating was severely degraded.

The SiAl1 coated CMSX-4 sample exposed to Pb+alkali contained more residual coatings which were less degraded, on both sides, than those on the Cd+alkali sample. These results indicated that the SiAl1 coating is more hot corrosion protective of CMSX-4 exposed to Pb+alkali than when exposed to Cd+alkali. The CMSX-4 sample with the SiAl2 coating has more residual coating on side 2, which is the least degraded of all exposed samples. However, side 1 has spalled heavily, confirming the spall mass rate seen in Figure 10.4. In summary, the XRD results show that for IN738LC, the SiAl1 coating is more Type II hot corrosion protective than SiAl2, whereas for CMSX-4, the SiAl2 coating is more protective. In general, residual coatings on exposed CMSX-4 samples were deeper, but more degraded than those on IN738LC.

The XRD plots also confirmed the microstructures in BSE maps and EDX results which showed the scale on remanent coatings to consist of Al_2O_3. Between this oxide and the β-NiAl coating is a layer of partly degraded γ'-phase NiAl coating.

The coatings on the two substrates exhibit differing levels of outward diffusion of alloying elements which are common to each substrate. Coatings in all IN738LC samples contain significantly higher chromium content than those in CMSX-4 samples, reflecting the chromium content of each substrate; 17.6 at%Cr in IN738LC and 7.7 at%Cr in CMSX-4, assisting the superior hot corrosion protection provided by the former. Outward diffusion of titanium occurs at similar levels in coatings on both substrates, despite the content in each substrate, 4.3 at%Ti in IN738LC and 1.2 at%Ti in CMSX-4, but more titanium rich particles are formed in coatings on IN738LC. Tungsten content in coatings of corrosion tested samples showed, in IN738LC (0.6 at%W), general trace levels with particles rich in tungsten randomly distributed, in CMSX-4 (2.1 at%W) more generally distributed levels varying from 2 at%W to 3 at%W. Generally, only trace levels of molybdenum occurred in coatings on both substrates, with occasional molybdenum rich particles (3 at%Mo) occurring in IN738LC, which were also rich in chromium and titanium. Of elements unique to one substrate; trace levels of niobium occurred randomly in IN738LC, and of rhenium in CMSX-4.

The corrosion test results identified the differences in Type II hot corrosion protection provided by the bottom and top coating depths of exposed samples. In each case the bottom side coatings had greater depth than those of the top side. The benefit of manufacturing coatings having coatings with both sides of similar depths, equal to those of the bottom sides, would be to provide greater Type II hot corrosion protection than those returned in these tests.

10.3 Corrosion test series 4: 500 hours at 900°C; results and evaluation

Photographs of samples after testing are shown in Figure 10.47. After parting, samples were mounted and their surfaces prepared, as described in Chapter 4. The corrosion test results were evaluated on the bases of mass change, microstructural analysis and XRD measurements.

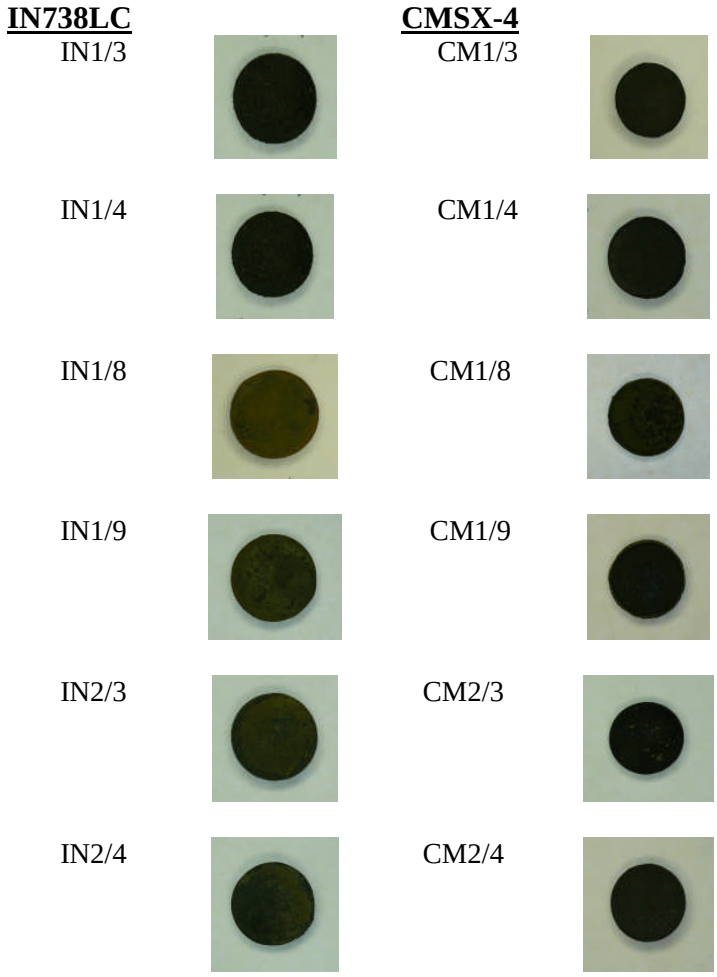

Figure 10.47: Corrosion test series 4; 500 hours at 900°C, post-test photographs of samples

10.3.1 Mass change

10.3.1.1 Gross mass change

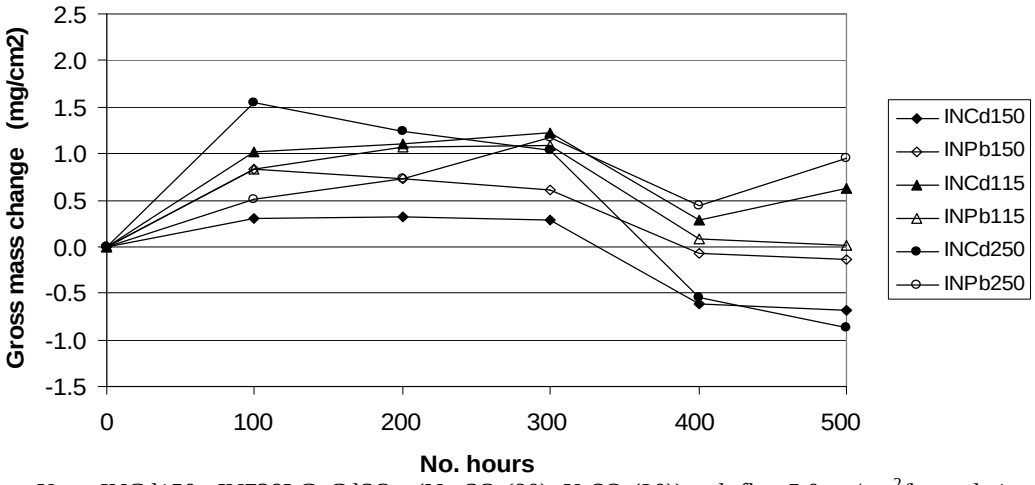

Key: INCd150; IN738LC, $CdSO_4$+(Na_2SO_4(80)+K_2SO_4(20)), salt flux 5.0 µg/cm^2/h, pwdr 1
INPb150; IN738LC, $PbSO_4$+(Na_2SO_4(80)+K_2SO_4(20)), salt flux 5.0 µg/cm^2/h, pwdr 1
INCd115; IN738LC, $CdSO_4$+(Na_2SO_4(80)+K_2SO_4(20)), salt flux 1.5 µg/cm^2/h, pwdr 1
INPb115; IN738LC, $PbSO_4$+(Na_2SO_4(80)+K_2SO_4(20)), salt flux 1.5 µg/cm^2/h, pwdr 1
INCd250; IN738LC, $CdSO_4$+(Na_2SO_4(80)+K_2SO_4(20)), salt flux 5.0 µg/cm^2/h, pwdr 2
INPb250; IN738LC, $PbSO_4$+(Na_2SO_4(80)+K_2SO_4(20)), salt flux 5.0 µg/cm^2/h, pwdr 2

Figure 10.48: IN738LC samples with silicon-aluminide coatings; gross mass changes after 500 hours corrosion testing at 900^{o}C

As noted in the gross mass change graphs for the LTHT corrosion tests, results for the equivalent samples in the fourth series of corrosion tests are not consistent with salt flux levels or whether the Cd+alkali or Pb+alkali composition is involved. For example, in Figure 10.48, for IN738LC, both lower salt flux samples (INCd115 and INPb115) exhibit higher gross mass changes than those having higher salt fluxes (INCd150 and INPb150). Similar inconsistencies, exhibited by the CMSX-4 samples seen in Figure 10.49, result from differencies in coating depths of the bottom and top sides of sample discs.

Gross mass changes, after 100 hours testing, range from 0.3 mg/cm^2 to 1.6 mg/cm^2 for IN738LC samples, and from 0.3 mg/cm^2 to 2.2 mg/cm^2 for CMSX-4 samples. Similar gross mass change rates of IN738LC continue until, after 300 hours they commence a downward trend to 400 hours, after which their gradients become shallower. Three samples cross the zero-line between 300 and 400 hours of testing, INCd150 after 330 hours, INCd250 after 360 hours and INPb150 after 390 hours. Only samples INPb250 and INCd115 have not crossed the zero-line after 500 hours. Similar patterns are shown by CMSX-4 samples in Figure 10.49, despite their greater range of gross mass changes than those of IN738LC.

After 300 hours corrosion testing at 900°C, gross mass changes of CMSX-4 samples rapidly fall to the extent that, after 400 hours, all but CMPb250 have crossed the zero-line.

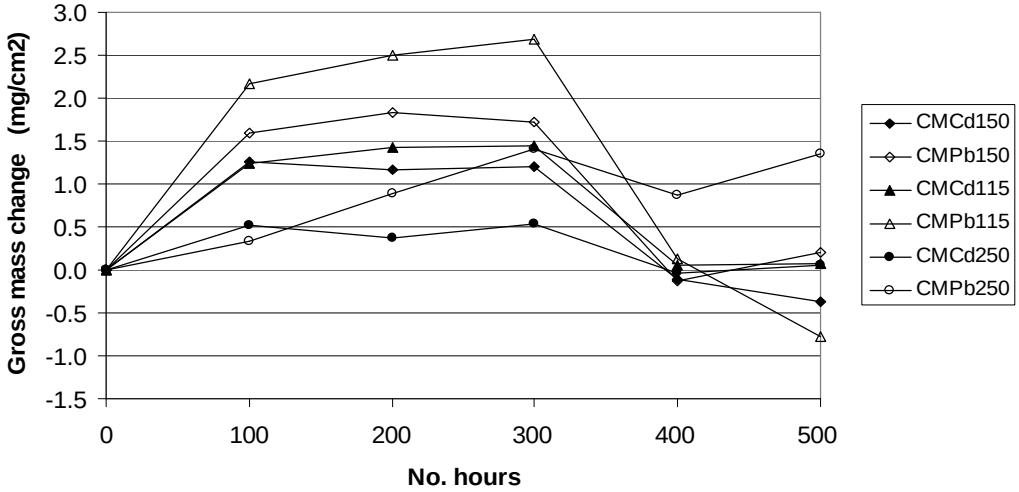

Key: CMCd150; CMSX-4, $CdSO_4$+(Na_2SO_4(80)+K_2SO_4(20)), salt flux 5.0 µg/cm^2/h, pwdr 1
CMPb150; CMSX-4, $PbSO_4$+(Na_2SO_4(80)+K_2SO_4(20)), salt flux 5.0 µg/cm^2/h, pwdr 1
CMCd115; CMSX-4, $CdSO_4$+(Na_2SO_4(80)+K_2SO_4(20)), salt flux 1.5 µg/cm^2/h, pwdr 1
CMPb115; CMSX-4, $PbSO_4$+(Na_2SO_4(80)+K_2SO_4(20)), salt flux 1.5 µg/cm^2/h, pwdr 1
CMCd250; CMSX-4, $CdSO_4$+(Na_2SO_4(80)+K_2SO_4(20)), salt flux 5.0 µg/cm^2/h, pwdr 2
CMPb250; CMSX-4, $PbSO_4$+(Na_2SO_4(80)+K_2SO_4(20)), salt flux 5.0 µg/cm^2/h, pwdr 2

Figure 10.49: CMSX-4 samples with silicon-aluminide coatings; gross mass changes after 500 hours corrosion testing at 900°C

10.3.1.2 Spall mass

As seen in Figures 10.50 and 10.51, spalling of scale on both substrates commences after 100 hours corrosion testing. After 200 hours, the spall rates of CMSX-4 samples were generally higher than those for IN738L, ranging from 0 mg/cm^2 to 0.62 mg/cm^2 for CMSX-4 based samples, compared with 0 mg/cm^2 to 0.23 mg/cm^2 for IN738LC samples. After 500 hours of corrosion testing at 900°C, the spall mass values ranged from 0.3 mg/cm^2 to 1.1 mg/cm^2 for CMSX-4 samples and from 0.3 mg/cm^2 to 0.58 mg/cm^2 for IN738LC samples. Generally, the spall mass is higher than gross mass gain showing that external scale spalling and evaporation have occurred, rather than signifying internal attack, if massed spall had been lower than gross mass change. After 400 hours, when the net mass changes had crossed the zero-line, the mass spalling gradients had become similar for all samples of the respective substrate.

10.3.1.3 Net mass change

Net mass change graphs for the two substrates, shown in Figures 10.52 and 10.53, indicate changes from the incubation stage occurring after 100 hours exposure.

Subsequently, the propagation stage of hot corrosion, plus evaporation and spalling culminated in net mass changes crossing the zero-line after 400 hours of corrosion testing at 900°C.

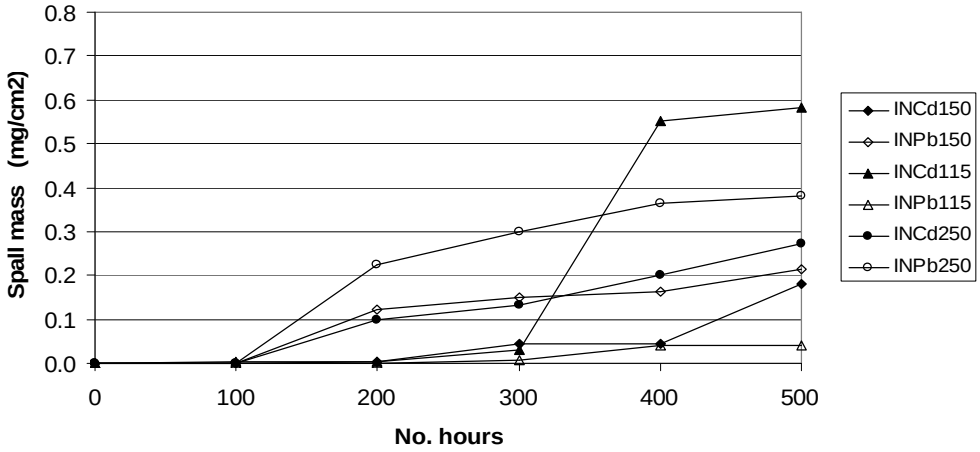

Key: INCd150; IN738LC, $CdSO_4$+(Na_2SO_4(80)+K_2SO_4(20)), salt flux 5.0 µg/cm^2/h, pwdr 1
INPb150; IN738LC, $PbSO_4$+(Na_2SO_4(80)+K_2SO_4(20)), salt flux 5.0 µg/cm^2/h, pwdr 1
INCd115; IN738LC, $CdSO_4$+(Na_2SO_4(80)+K_2SO_4(20)), salt flux 1.5 µg/cm^2/h, pwdr 1
INPb115; IN738LC, $PbSO_4$+(Na_2SO_4(80)+K_2SO_4(20)), salt flux 1.5 µg/cm^2/h, pwdr 1
INCd250; IN738LC, $CdSO_4$+(Na_2SO_4(80)+K_2SO_4(20)), salt flux 5.0 µg/cm^2/h, pwdr 2
INPb250; IN738LC, $PbSO_4$+(Na_2SO_4(80)+K_2SO_4(20)), salt flux 5.0 µg/cm^2/h, pwdr 2

Figure 10.50: IN738LC samples with silicon-aluminide coatings; spall mass after 500 hours corrosion testing at 900°C

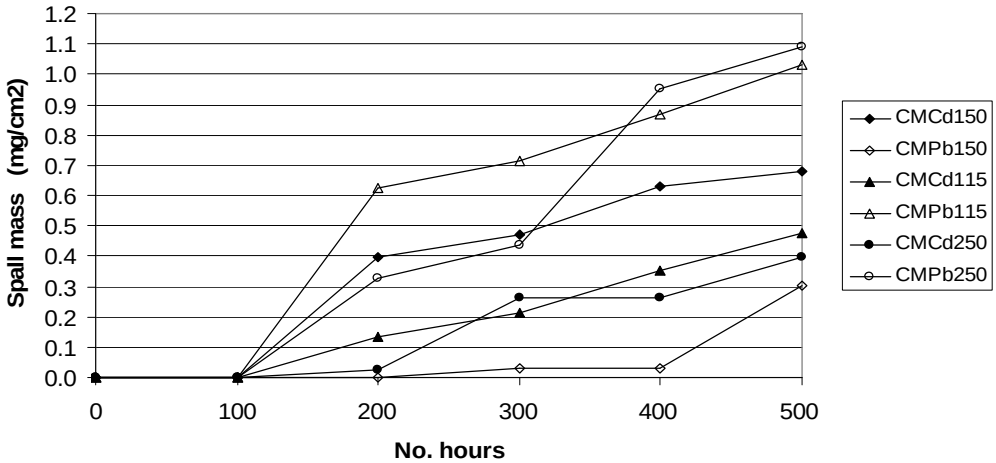

Key: CMCd150; CMSX-4, $CdSO_4$+(Na_2SO_4(80)+K_2SO_4(20)), salt flux 5.0 µg/cm^2/h, pwdr 1
CMPb150; CMSX-4, $PbSO_4$+(Na_2SO_4(80)+K_2SO_4(20)), salt flux 5.0 µg/cm^2/h, pwdr 1
CMCd115; CMSX-4, $CdSO_4$+(Na_2SO_4(80)+K_2SO_4(20)), salt flux 1.5 µg/cm^2/h, pwdr 1
CMPb115; CMSX-4, $PbSO_4$+(Na_2SO_4(80)+K_2SO_4(20)), salt flux 1.5 µg/cm^2/h, pwdr 1
CMCd250; CMSX-4, $CdSO_4$+(Na_2SO_4(80)+K_2SO_4(20)), salt flux 5.0 µg/cm^2/h, pwdr 2
CMPb250; CMSX-4, $PbSO_4$+(Na_2SO_4(80)+K_2SO_4(20)), salt flux 5.0 µg/cm^2/h, pwdr 2

Figure 10.51: CMSX-4 samples with silicon-aluminide coatings; spall mass after 500 hours corrosion testing at 900°C

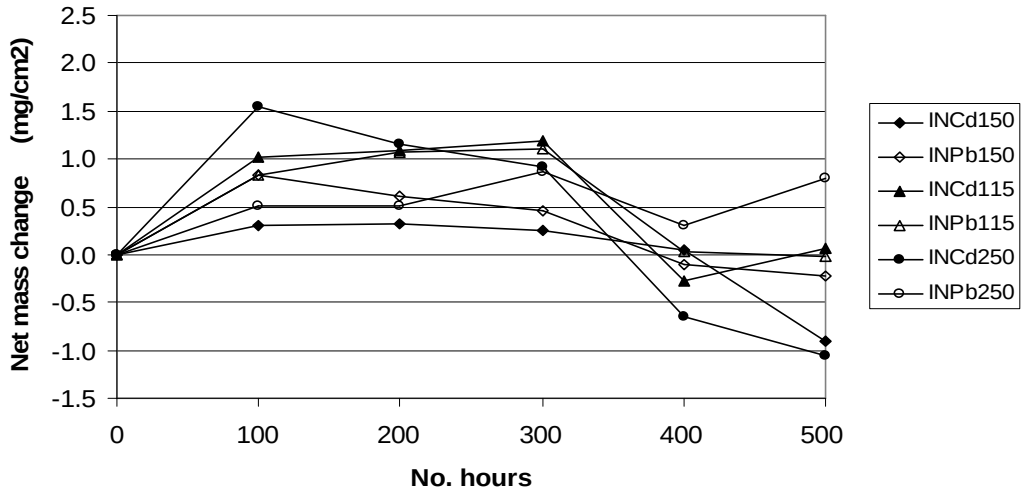

Key: INCd150; IN738LC, $CdSO_4$+(Na_2SO_4(80)+K_2SO_4(20)), salt flux 5.0 µg/cm^2/h, pwdr 1
INPb150; IN738LC, $PbSO_4$+(Na_2SO_4(80)+K_2SO_4(20)), salt flux 5.0 µg/cm^2/h, pwdr 1
INCd115; IN738LC, $CdSO_4$+(Na_2SO_4(80)+K_2SO_4(20)), salt flux 1.5 µg/cm^2/h, pwdr 1
INPb115; IN738LC, $PbSO_4$+(Na_2SO_4(80)+K_2SO_4(20)), salt flux 1.5 µg/cm^2/h, pwdr 1
INCd250; IN738LC, $CdSO_4$+(Na_2SO_4(80)+K_2SO_4(20)), salt flux 5.0 µg/cm^2/h, pwdr 2
INPb250; IN738LC, $PbSO_4$+(Na_2SO_4(80)+K_2SO_4(20)), salt flux 5.0 µg/cm^2/h, pwdr 2

Figure 10.52: IN738LC samples with silicon-aluminide coatings; net mass changes after 500 hours corrosion testing at 900^{o}C

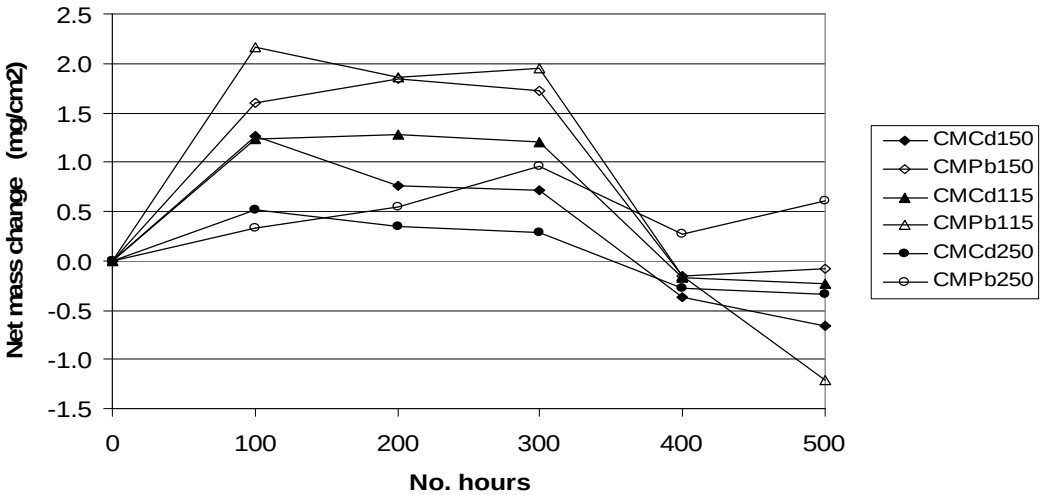

Key: CMCd150; CMSX-4, $CdSO_4$+(Na_2SO_4(80)+K_2SO_4(20)), salt flux 5.0 µg/cm^2/h, pwdr 1
CMPb150; CMSX-4, $PbSO_4$+(Na_2SO_4(80)+K_2SO_4(20)), salt flux 5.0 µg/cm^2/h, pwdr 1
CMCd115; CMSX-4, $CdSO_4$+(Na_2SO_4(80)+K_2SO_4(20)), salt flux 1.5 µg/cm^2/h, pwdr 1
CMPb115; CMSX-4, $PbSO_4$+(Na_2SO_4(80)+K_2SO_4(20)), salt flux 1.5 µg/cm^2/h, pwdr 1
CMCd250; CMSX-4, $CdSO_4$+(Na_2SO_4(80)+K_2SO_4(20)), salt flux 5.0 µg/cm^2/h, pwdr 2
CMPb250; CMSX-4, $PbSO_4$+(Na_2SO_4(80)+K_2SO_4(20)), salt flux 5.0 µg/cm^2/h, pwdr 2

Figure 10.53: CMSX-4 samples with silicon-aluminide coatings; net mass changes after 500 hours corrosion testing at 900^{o}C

10.3.2 Corrosion test series 4 – microstructural analyses

10.3.2.1 IN738LC with novel silicon-aluminide coating (powder 1), (sample IN1/3) with Cd+alkali salt composition, salt flux 5.0 µg/cm^2/h

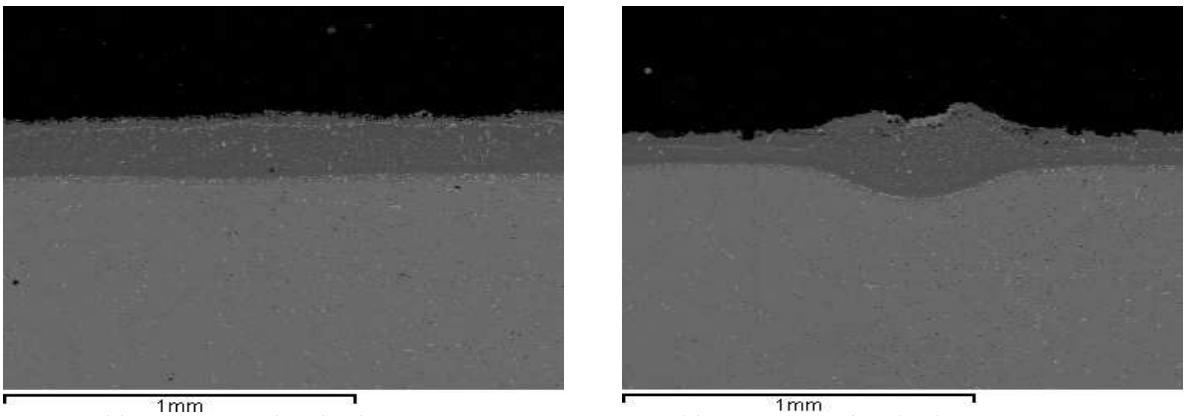

Bottom side average coating depth: 197µm
Ref sample bottom side coating depth: 235µm

Top side average coating depth: 118µm
Ref sample top side coating depth: 197µm

Figure 10.54: IN738LC sample IN1/3; after 500 hours corrosion testing at 900°C – BSE images of both sides

The element maps in Figure 10.54 show the β-NiAl matrix to be generally stable for a coating depth of 145µm, between the IZ and the degraded layer. The EDX results confirm that the scale/deposit layer is rich in oxides of aluminium and silicon. Outwardly diffused titanium and chromium occur and there are traces of molybdenum and tungsten. The net mass change graph in Figure 10.52 shows that the zero-line is crossed after 400 hours of corrosion testing. It is proposed that the top side coating, being of significantly less depth than that of the bottom side coating can not continue to produce the necessary protective scale.

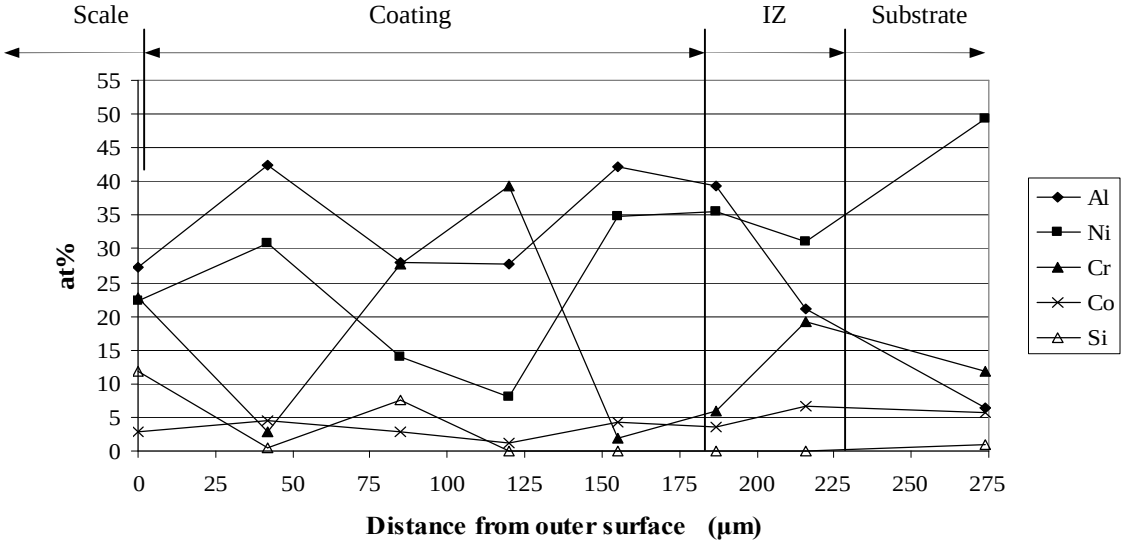

Figure 10.55: IN738LC sample IN1/3; after 500 hours corrosion testing at 900°C – main elements on EDX line in Figure 10.56

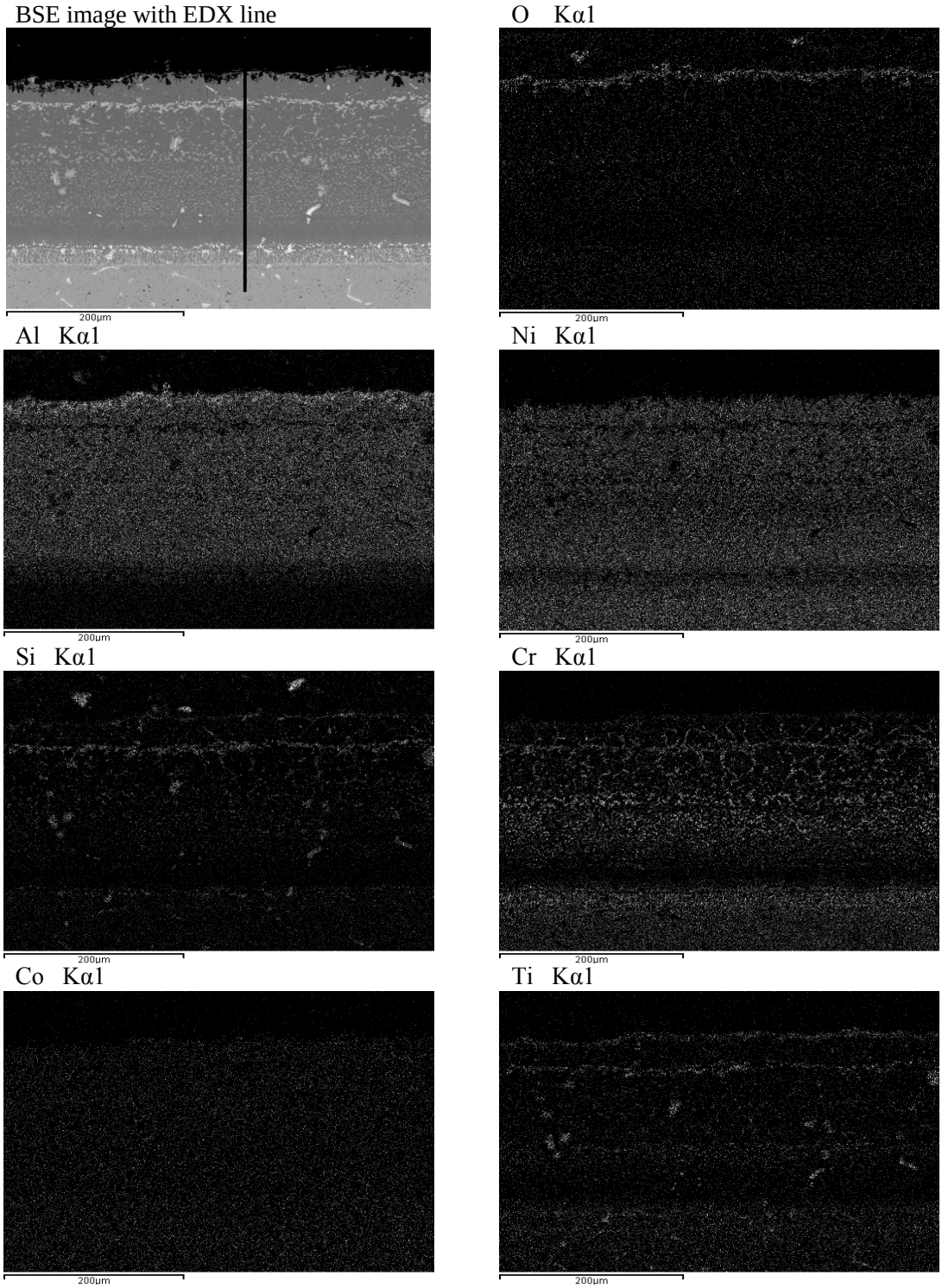

Figure 10.56: IN738LC sample IN1/3; after 500 hours corrosion testing at 900°C – element maps

10.3.2.2 IN738LC with novel silicon-aluminide coating (powder 1), (sample IN1/4) with Pb+alkali composition, salt flux 5.0 µg/cm^2/h

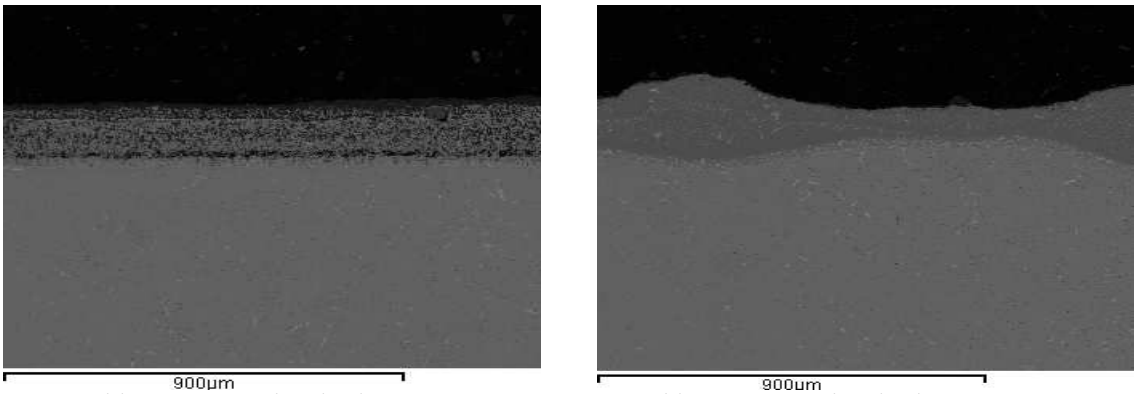

Bottom side average coating depth: 143µm
Ref sample bottom side coating depth: 235 µm

Top side average coating depth: 135µm
Ref sample top side coating depth: 197µm

Figure 10.57: IN738LC sample IN1/4; after 500 hours corrosion testing at 900°C – BSE images of both sides

It is clear, from the element maps in Figure 10.57 and EDX results in Figure 10.58 that the coating in this sample is degraded throughout its remaining depth. Alumina is present under the surface deposit/scale but the aluminium diminishes to average 12 at%Al down to the IZ. Outward diffusion of chromium is lower than for the Cd+alkali sample, averaging approximately 2 at%Cr in the coating, to a 20µm chromium depleted layer above the IZ. Nickel is heavily depleted through the coating. Only traces of titanium, molybdenum and tungsten have outwardly diffused into the coating.

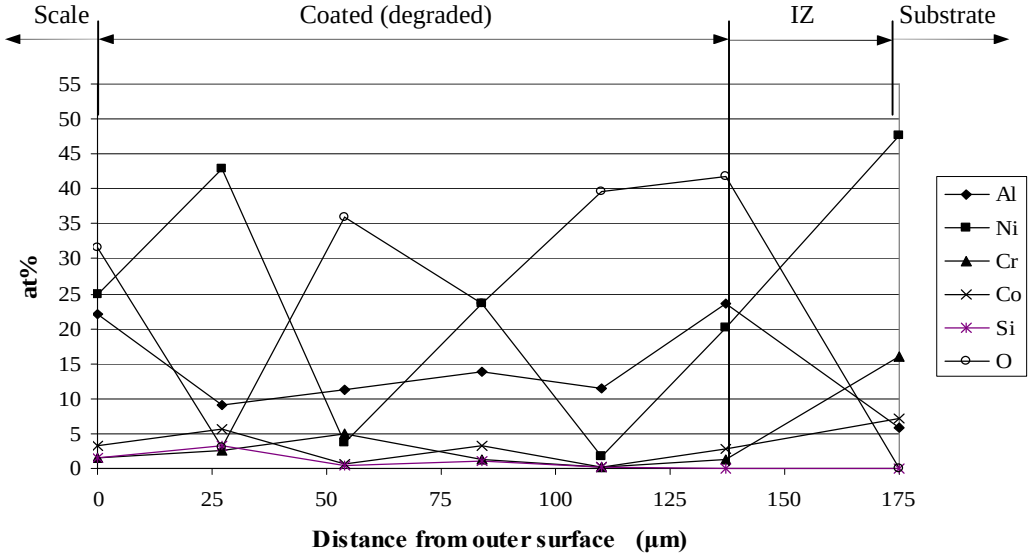

Figure 10.58: IN738LC sample IN1/4; after 500 hours corrosion testing at 900°C – main elements on EDX line in Figure 10.59

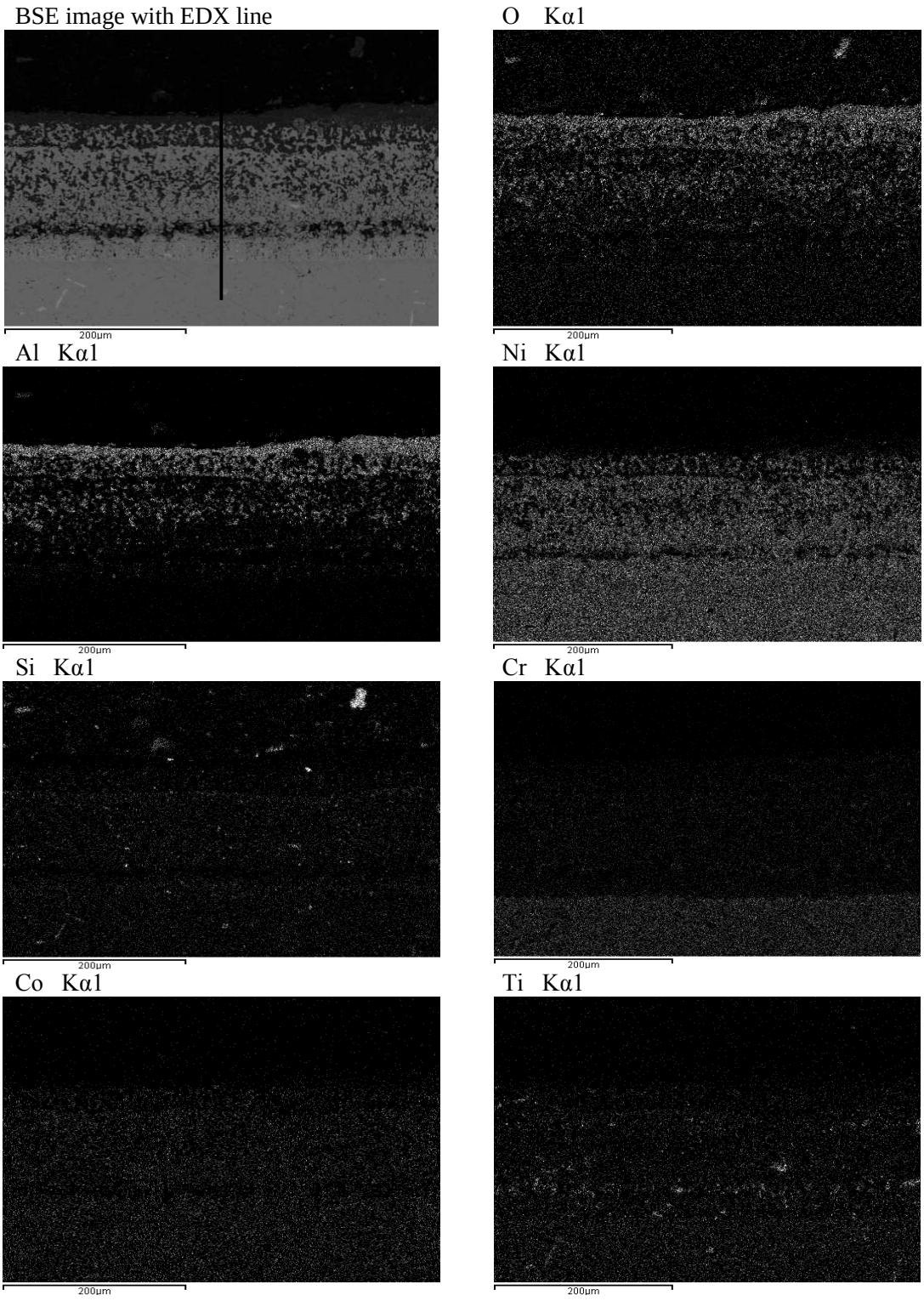

Figure 10.59: IN738LC sample IN1/4; after 500 hours corrosion testing at 900°C – element maps

10.3.2.3 IN738LC with novel silicon-aluminide coating (powder 1), (sample IN1/8) with Cd+alkali salt composition, salt flux 1.5 µg/cm^2/h

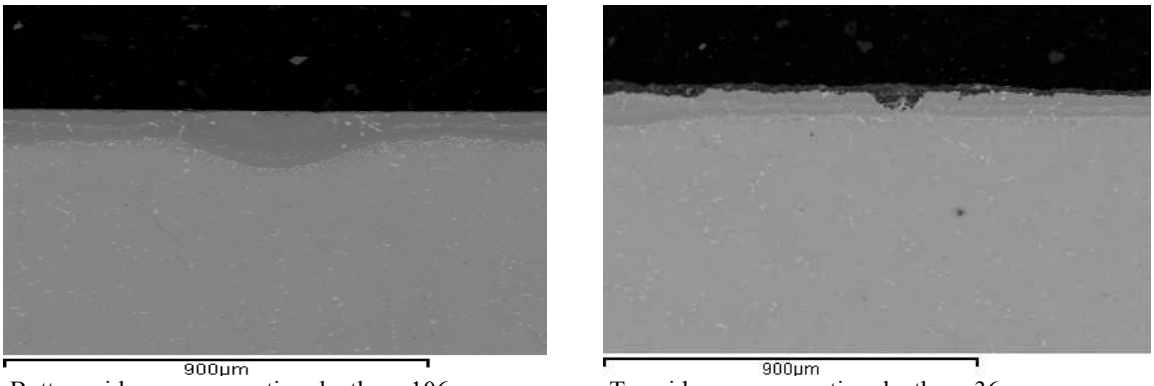

Bottom side average coating depth: 106µm
Ref sample bottom side coating depth: 90µm

Top side average coating depth: 36µm
Ref sample top side coating depth: 51 µm

Figure 10.60: IN738LC sample IN1/8; after 500 hours corrosion testing at 900°C – BSE images of both sides

The maps in Figure 10.62 and the average coating depths in Figure 10.60, show that the scale growth on the bottom side of the sample continues to provide hot corrosion protection. The top side coating of the sample shows local areas of coating failure seen in Figure 10.63), which would not show up on the various mass change graphs. The bottom side of the sample shows generally uniform corrosion, compared with that of the top side, with its sites of severe degradation (seen in Figure 10.63). EDX results for both sides show similar outward diffusion of chromium and distribution of silicon. Element maps (Figure 10.62) show that outward diffusion has created Cr-Si and Si-Ti rich precipitates in the coating.

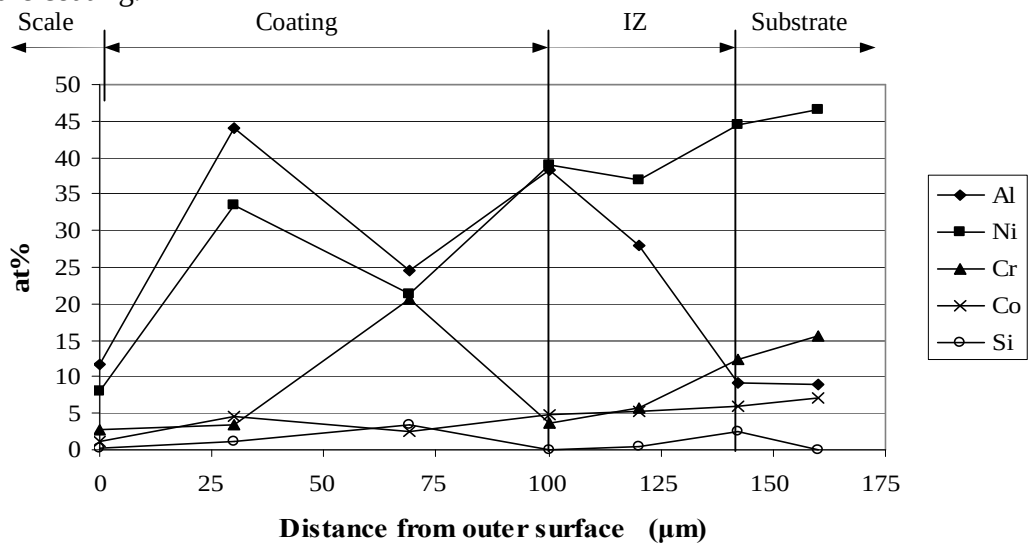

Figure 10.61: IN738LC sample IN1/8 (bottom side); after 500 hours corrosion testing at 900°C – main elements on EDX line in Figure 10.58

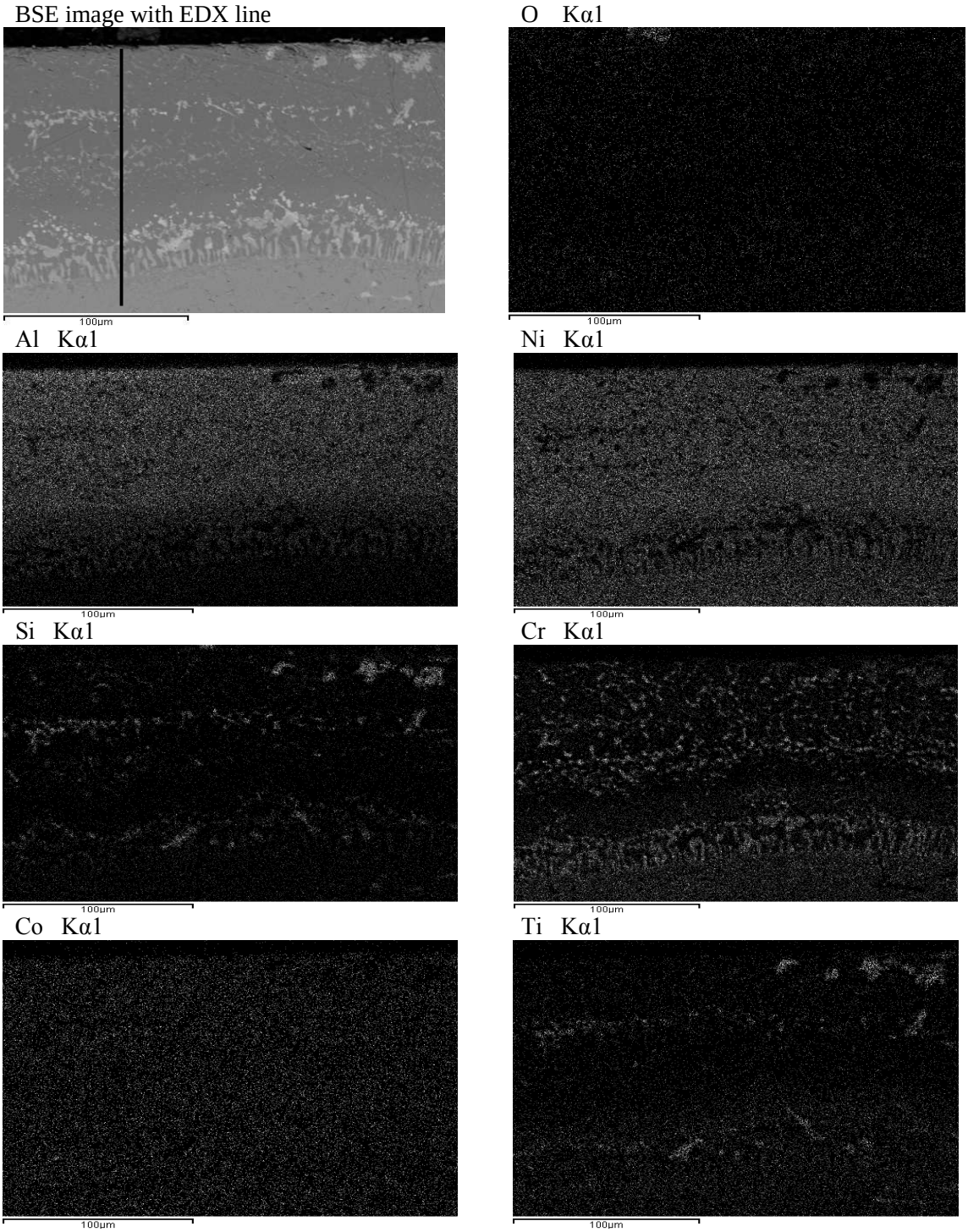

Figure 10.62: IN738LC sample IN1/8 (bottom side); after 500 hours corrosion testing at 900°C – element maps

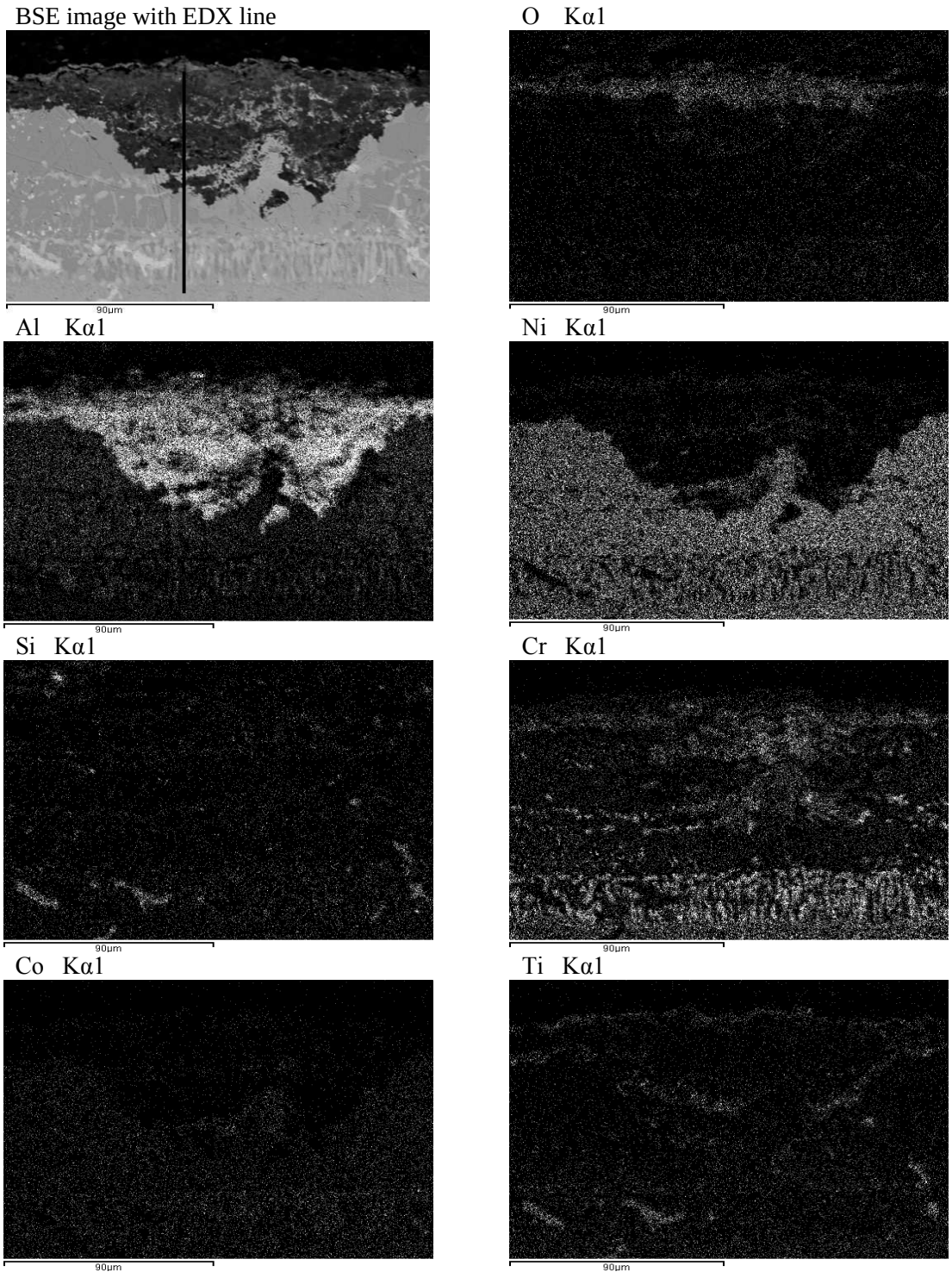

Figure 10.63: IN738LC sample IN1/8 (top side); after 500 hours corrosion testing at 900°C – element maps

EDX results of the top side degraded site indicate that the base of the deep pit is sulphur rich, with 1.7 at%S, coinciding with outwardly diffused titanium. The IZ is rich in chromium and, to a lesser extent silicon, molybdenum and tungsten. The depth of the degraded coating, seen in Figure 10.63, of about 65µm, is greater than the average top side coating depth of 36µm and points to the failure of the top side coating.

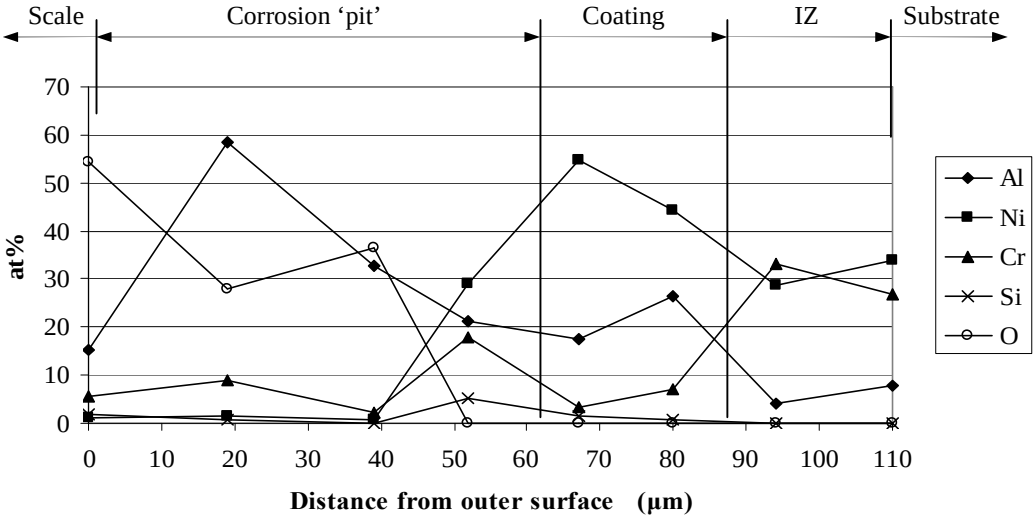

Figure 10.64: IN738LC sample IN1/8 (top side); after 500 hours corrosion testing at 900°C – main elements on EDX line in Figure 10.63

10.3.2.4 IN738LC with novel silicon-aluminide coating (powder 1), (sample IN1/9) with Pb+alkali salt composition, salt flux 1.5 µg/cm^2/h

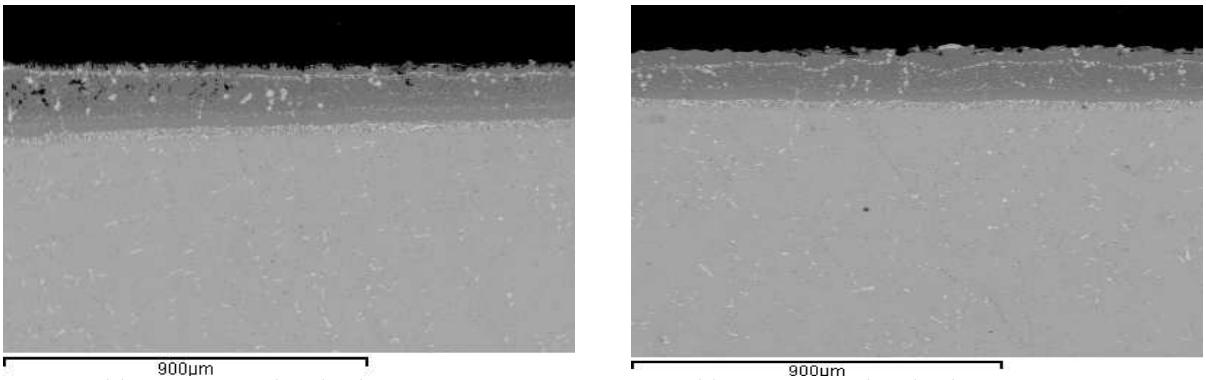

Bottom side average coating depth: 144µm
Ref sample bottom side coating depth: 90µm

Top side average coating depth: 89µm
Ref sample top side coating depth: 51µm

Figure 10.65: IN738LC sample IN1/9; after 500 hours corrosion testing at 900°C – BSE images of both sides

The pictures in Figur 10.65 and maps in Figur 10.67 show the coatings to be good and still Type I hot corrosion protective. EDX results, seen in Figure 10.66 show that, in the bottom side, rapid reduction of aluminium and nickel commenced 63µm from the surface. Aluminium content commenced an upward trend 30µm from the surface to reach 27 at%Al at the surface. The element maps in Figure 10.67 do not show the NiAl matrix changes. A 40µm layer deplete in chromium occurs above the IZ surface, further out most of the coating contains Si-Al and Si-Ti rich precipitates.. The depth of coating on the reference sample is not representative of that of the other four samples, including IN1/9, but shows that, on both sides, growth of degraded coating, deposit/scale is comparatively high.

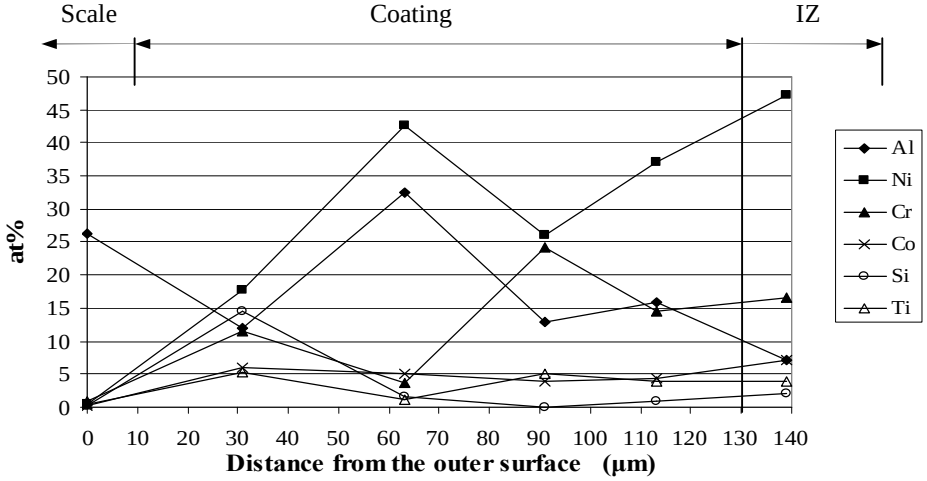

Figure 10.66: IN738LC sample IN1/9; after 500 hours corrosion testing at 900°C – main elements on EDX line in Figure 10.67

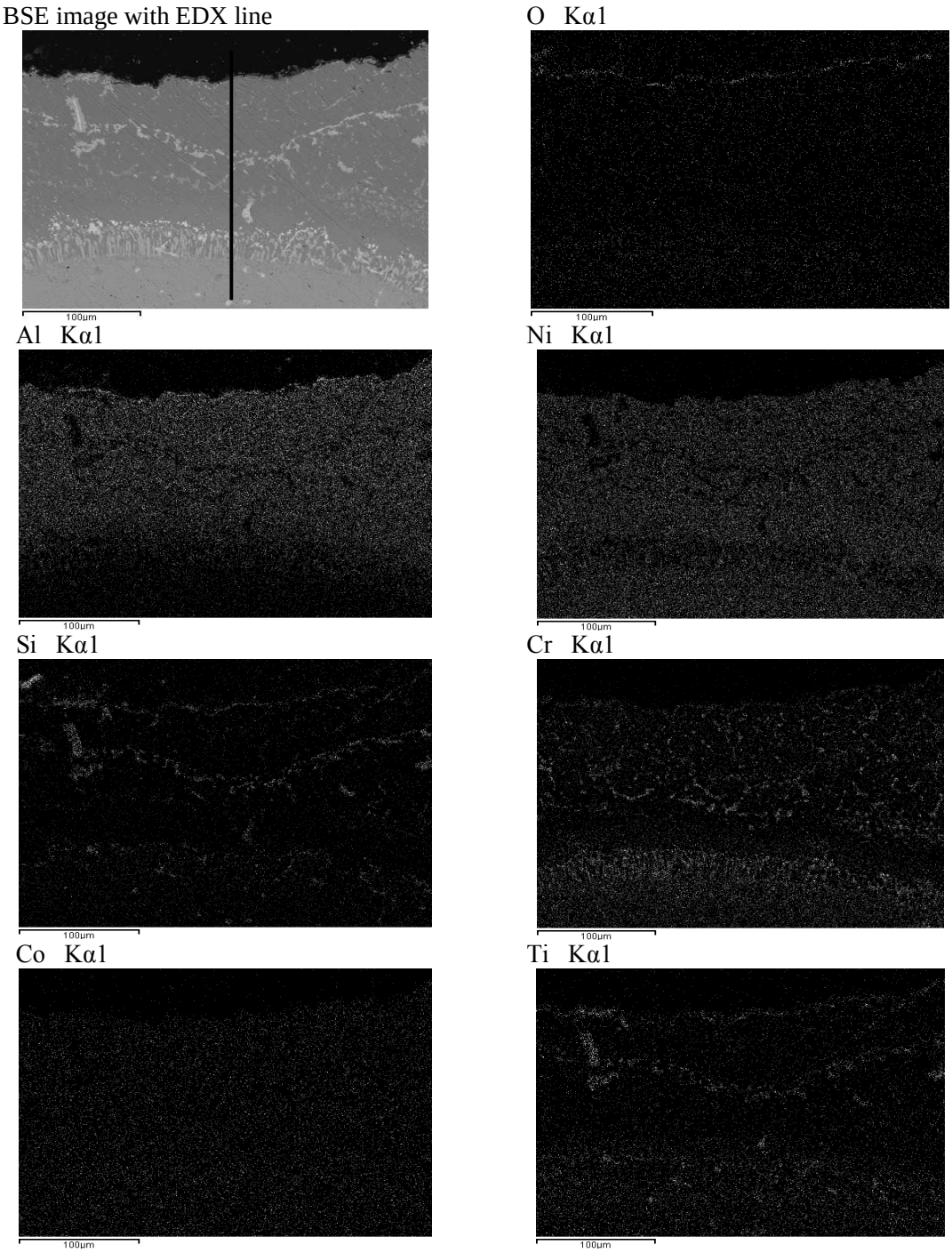

Figure 10.67: IN738LC sample IN1/9; after 500 hours corrosion testing at 900°C – element maps

10.3.2.5 IN738LC with novel silicon-aluminide coating (powder 2), (sample IN2/3) with Cd+alkali salt composition, salt flux 5.0 µg/cm^2/h

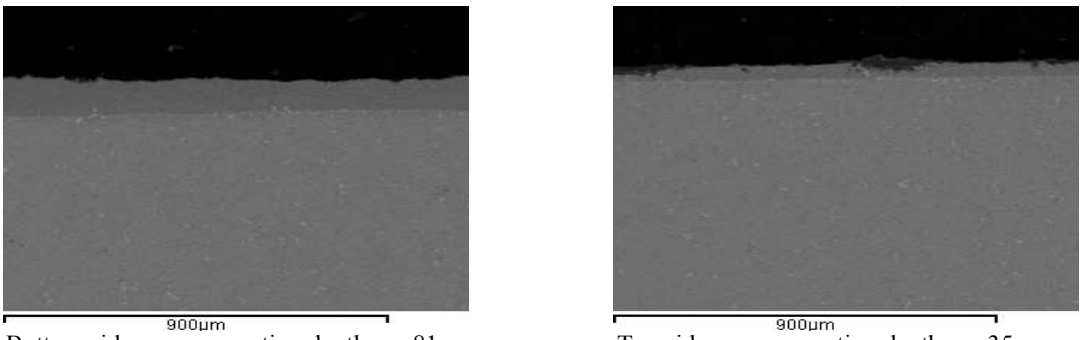

Bottom side average coating depth: 81µm
Ref sample bottom side coating depth: 97µm

Top side average coating depth: 35µm
Ref sample top side coating depth: 40µm

Figure 10.68: IN738LC sample IN2/3; after 500 hours corrosion testing at 900°C – BSE images of both sides

The element maps in Figure 10.70 show that the approximately 80µm deep residual, degraded coating has been further penetrated by pits containing oxides of aluminium, chromium and titanium, in some cases of 30µm depth. EDX results shown in Figure 10.69 confirm that the β-NiAl matrix remains stable from the IZ to approximately 30µm from the outer deposit/scale surface. The IZ is rich in chromium and, to a lesser extent silicon. Si-Ti rich precipitates occur in the IZ. The layers of deposit/scale are rich in oxides of aluminium, chromium, titanium and, to a lesser extent silicon. In the bottom side there remains sufficient coating to provide protective scale growth.

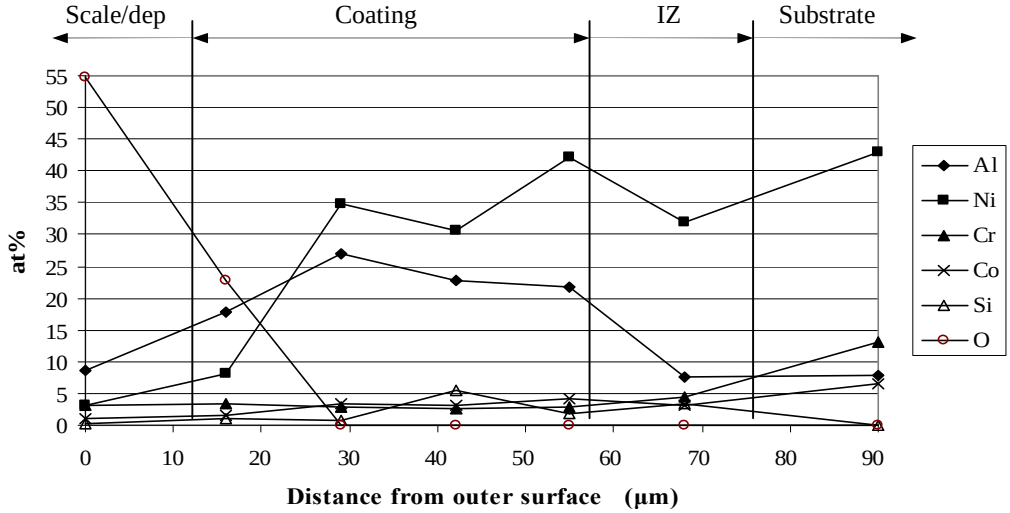

Figure 10.69: IN738LC sample IN2/3; after 500 hours corrosion testing at 900°C – main elements on EDX line in Figure 10.70

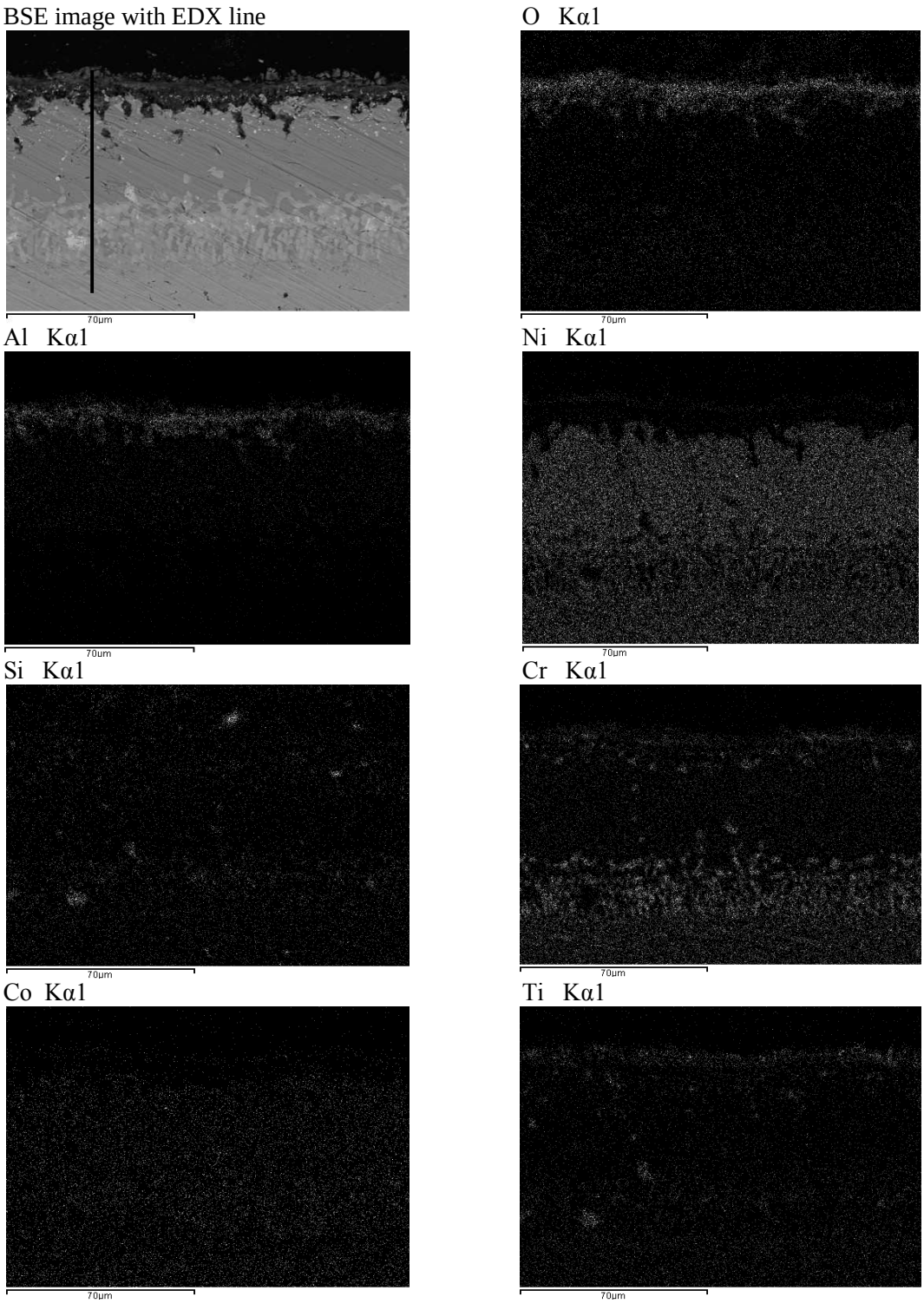

Figure 10.70: IN738LC sample IN2/3; after 500 hours corrosion testing at 900°C – element maps

10.3.2.6 IN738LC with novel silicon-aluminide coating (powder 2), (sample IN2/4) with Pb+alkali salt composition, salt flux 5.0 µg/cm^2/h

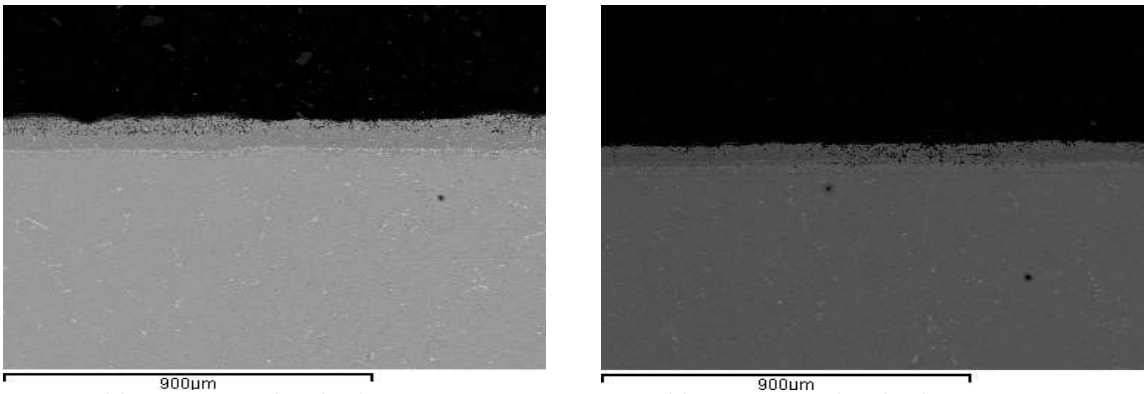

Bottom side average coating depth: 84µm
Ref sample bottom side coating depth: 97µm

Top side average coating depth: 51µm
Ref sample top side coating depth: 40µm

Figure 10.71: IN738LC sample IN2/4; after 500 hours corrosion testing at 900°C – BSE images of both sides

The element maps in Figure 10.73 and EDX results in Figure 10.72 show that the residual coating is heavily degraded down to the IZ, although the coating is not fully consumed. The deposit/scale layer is rich in oxides of aluminium, mainly Al_2O_3. Chromium precipitates underneath the scale deposit assist in continuing to provide hot corrosion protection. Due to the nature of the degradation, an EDX line scan in another area could show up variations in the microstructure.

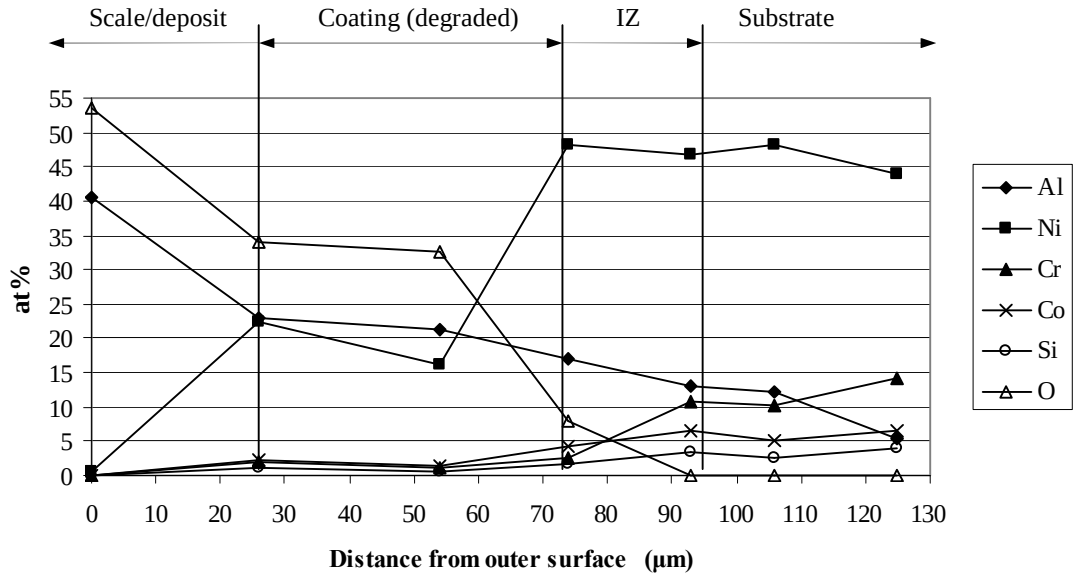

Figure 1072: IN738LC sample IN2/4; after 500 hours corrosion testing at 900°C – main elements on EDX line in Figure 10.73

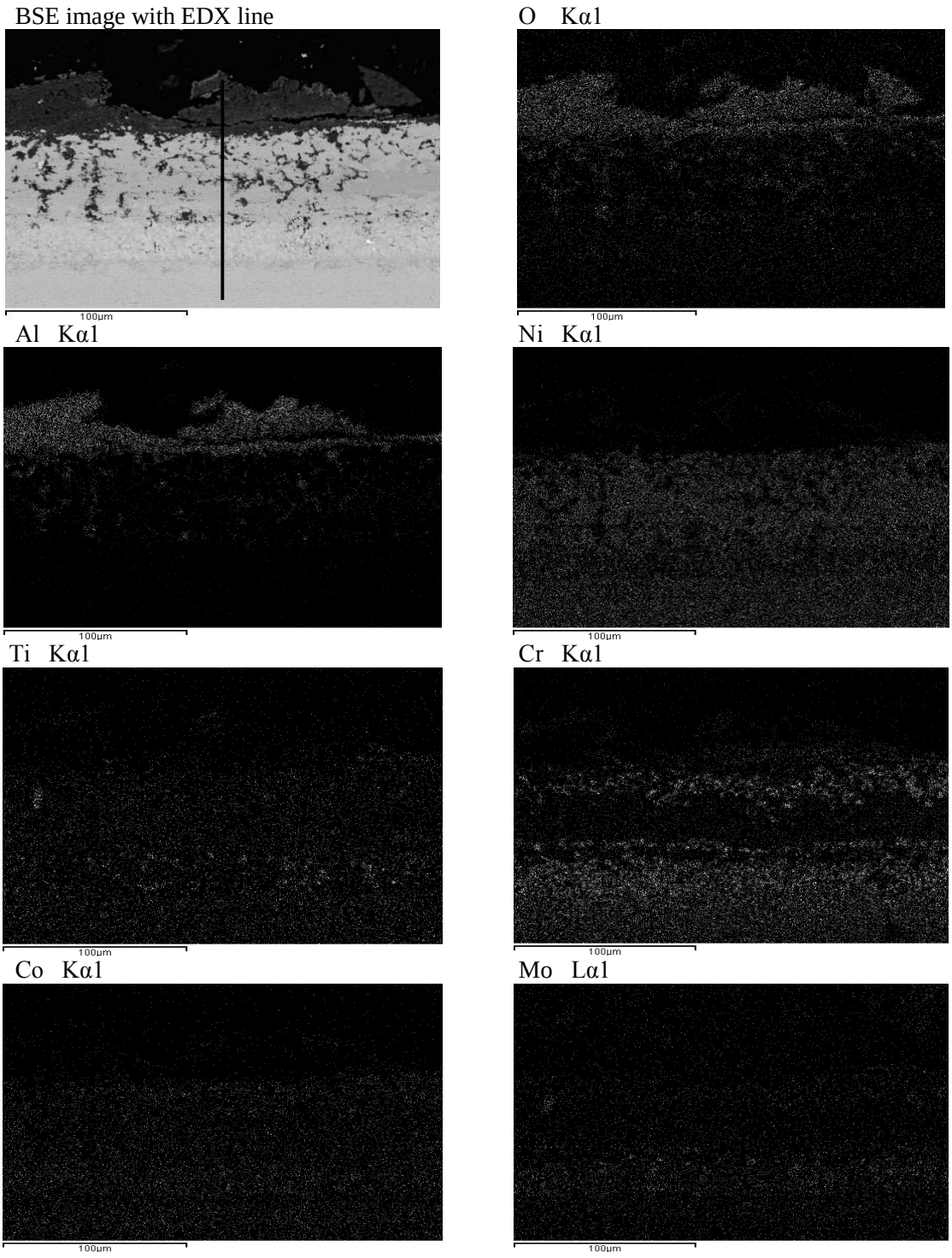

Figure 10.73: IN738LC sample IN2/4; after 500 hours corrosion testing at 900°C – element maps

10.3.2.7 CMSX-4 with novel silicon-aluminide coating (powder 1), (sample CM1/3) with Cd+alkali salt composition, salt flux 5.0 µg/cm^2/h

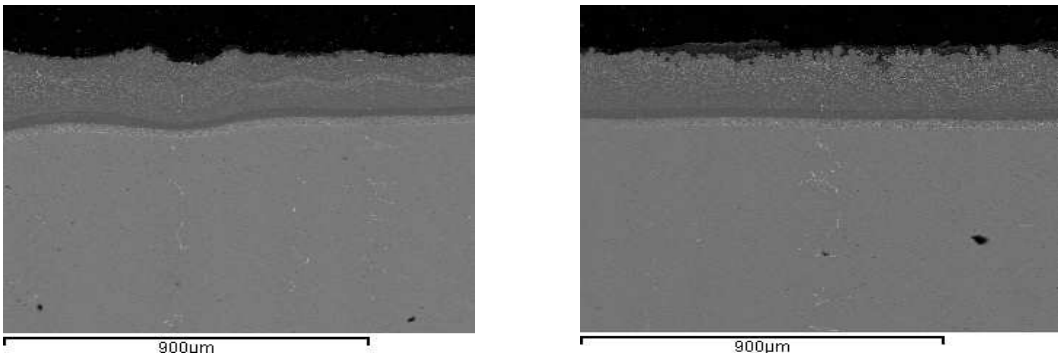

Bottom side average coating depth: 197µm
Ref sample bottom side coating depth: 250µm

Top side average coating depth: 171µm
Ref sample top side coating depth: 184µm

Figure 10.74: CMSX-4 sample CM1/3; after 500 hours corrosion testing at 900°C – BSE images of both sides

As seen in the element maps and EDX results in Figures 10.74 and 10.75, the bottom side coating of sample CM1/3 retains a stable β-NiAl matrix for an average depth of around 100µm. The top side of CM1/3, seen in Figure 10.74, shows surface scal and some internal degradation but the coating still looks to be Type I hot corrosion protective. Above the IZ is a layer, deplete in silicon and chromium, with a depth of 20µm. These two elements become distributed in the coating above this layer. There is a thin surface layer of aluminium oxide. Although not shown in the element maps, EDX results show outward diffusion of titanium, molybdenum, tantalum and rhenium, in three distinct layers, the most notable being in the zone rich in silicon and chromium, approximately 60µm from the surface.

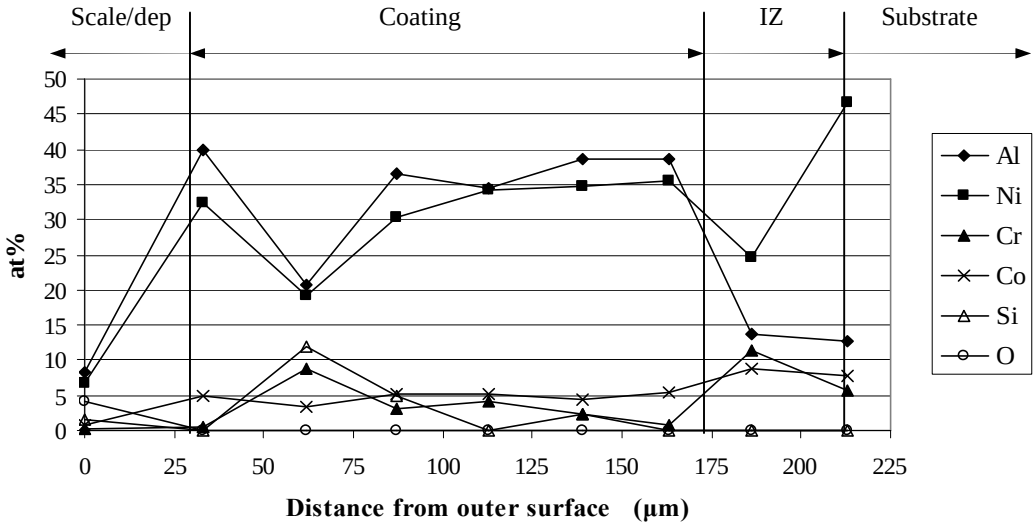

Figure 10.75: CMSX-4 sample CM1/3; after 500 hours corrosion testing at 900°C – main elements on EDX line in Figure 10.76

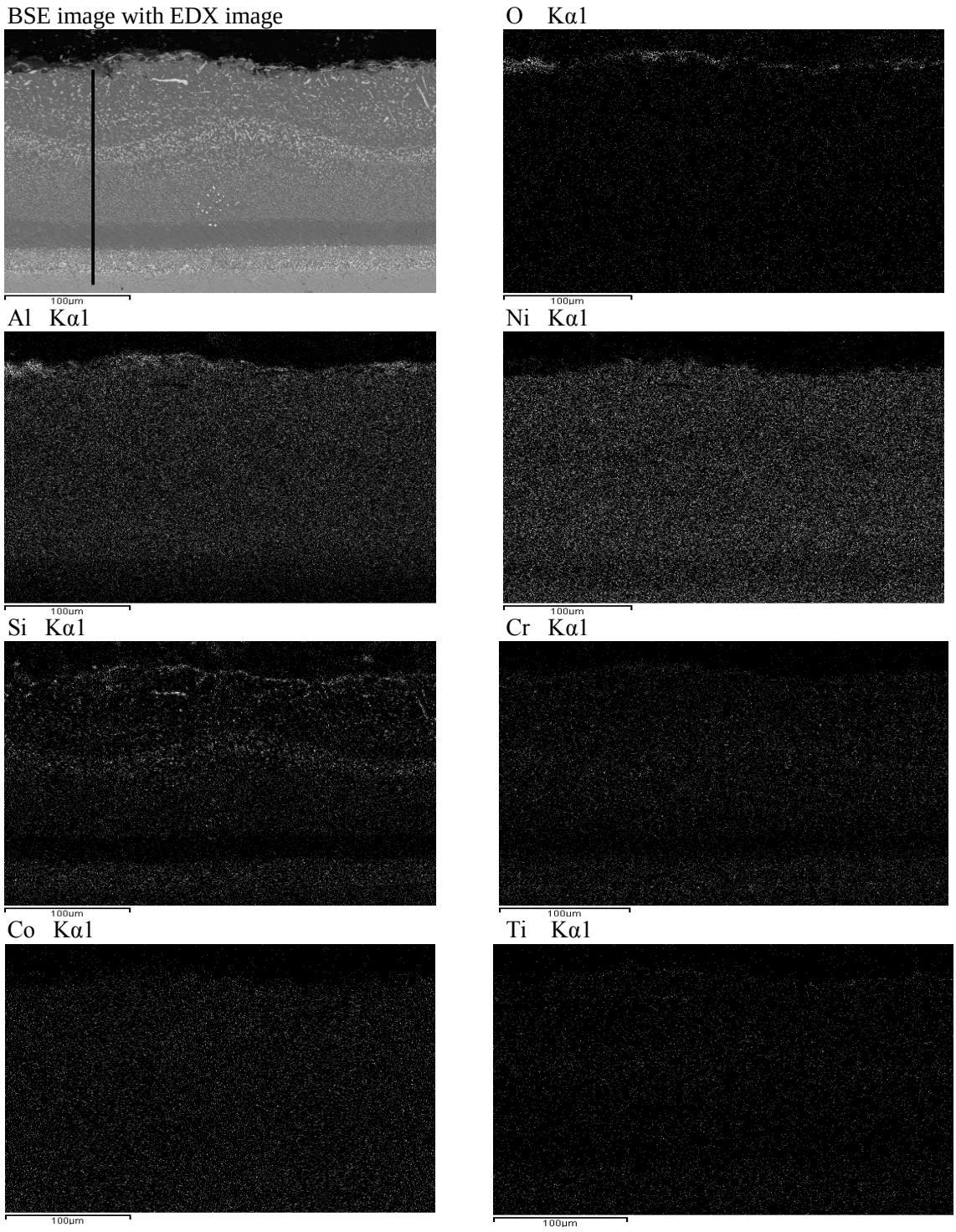

Figure 10.76: CMSX-4 sample CM1/3; after 500 hours corrosion testing at 900°C – element maps

10.3.2.8 CMSX-4 with novel silicon-aluminide coating (powder 1), (sample CM1/4) with Pb+alkali salt composition, salt flux 5.0 µg/cm^2/h

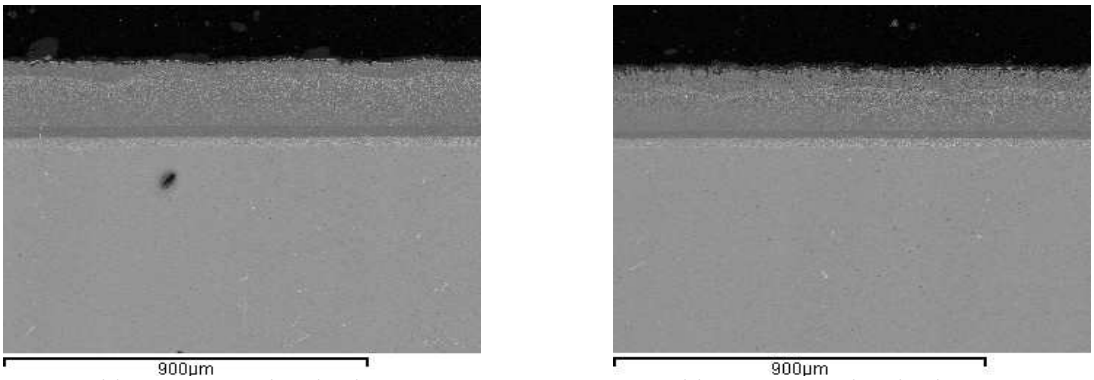

Bottom side average coating depth: 196µm
Ref sample bottom side coating depth: 250µm

Top side average coating depth: 175µm
Ref sample top side coating depth: 184µm

Figure 10.77: CMSX-4 sample CM1/4; after 500 hours corrosion testing at 900°C – BSE images of both sides

The element maps and EDX results in Figures 10.79 and 10.78, show that, after 500 hours corrosion testing at 900°C, the bottom side of sample CM1/4 retains a stable β-NiAl matrix coating 196µm deep. A combination of spalling and evaporation caused the net mass change to cross the zero-line, seen in Figure 10.45, after 390 hours corrosion testing. In common with the previous sample, above the IZ, there occurs a layer deficient in silicon and chromium, 22µm deep, after which the two elements are uniformly distributed in the coating. The deposit/scale layer is rich in aluminium oxide, but in contrast to the previous sample only traces of refractory elements have outwardly diffused into the coating.

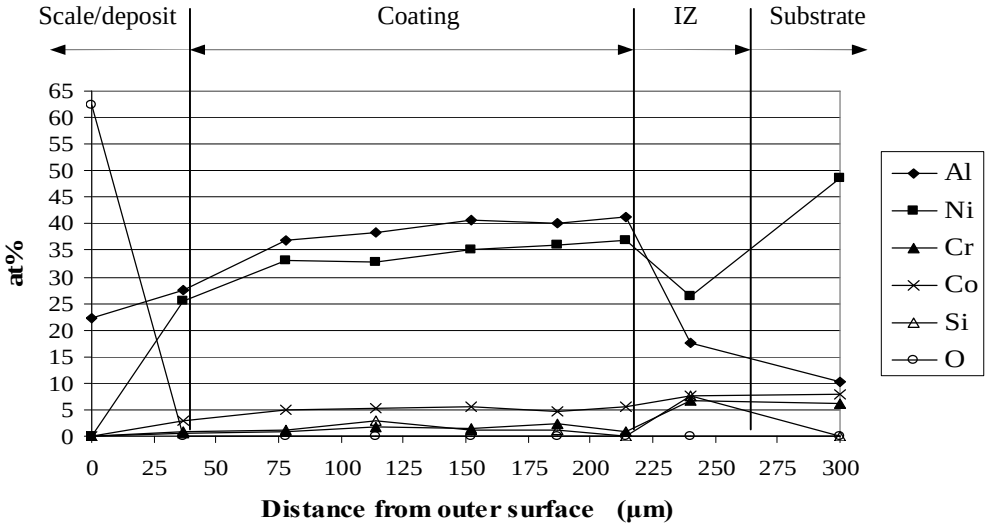

Figure 10.78: CMSX-4 sample CM1/4; after 500 hours corrosion testing at 900°C – main elements on EDX line in Figure 10.79

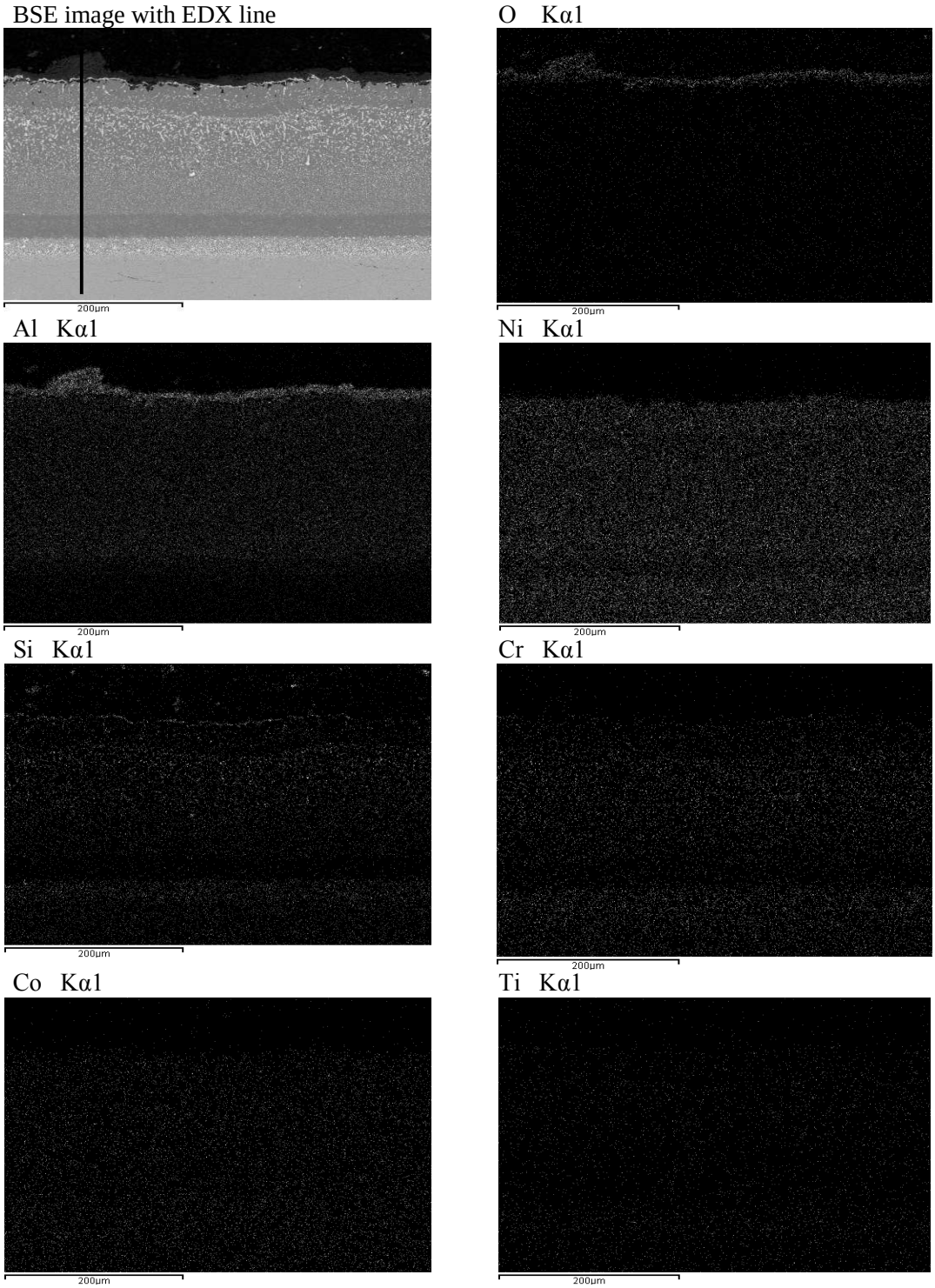

Figure 10.79: CMSX-4 sample CM1/4; after 500 hours corrosion testing at 900°C – element maps

10.3.2.9 CMSX-4 with novel silicon-aluminide coating (powder 1), (sample CM1/8) with Cd+alkali salt composition, salt flux 1.5 µg/cm^2/h

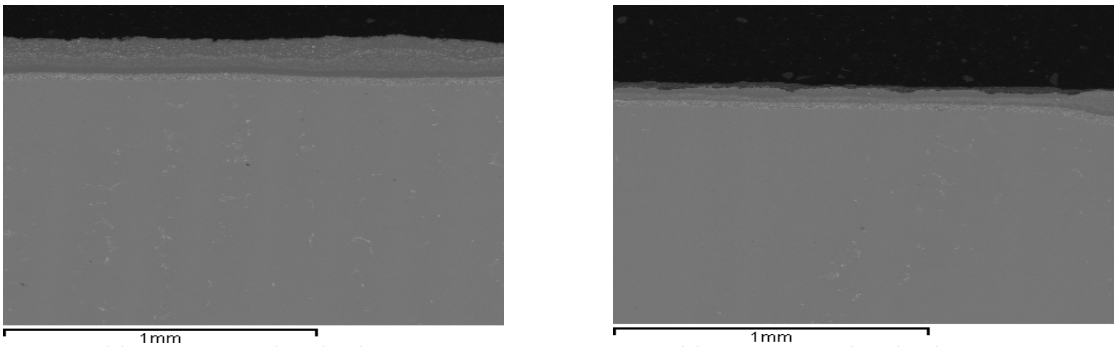

Bottom side average coating depth: 143µm
Ref sample bottom side coating depth: 203µm

Top side average coating depth: 54µm
Ref sample top side coating depth: 188µm

Figure 10.80: CMSX-4 sample CM1/8; after 500 hours corrosion testing at 900°C – BSE images of both sides

The element maps in Figure 10.82 and EDX results in Figure 10.81 show that, after 500 hours corrosion testing at 900°C, the bottom side of this sample retains a stable β-NiAl matrix for a depth of about 100µm above the IZ. This points to the degradation of this sample, after 390 hours corrosion testing, being caused by the inadequacy of the top side coating. The microstructure of this sample is very similar to that of CM1/3, which was subject to the higher salt flux of the Cd+alkali salt combination. The net mass change graph of sample CM1/8 seen in Figure 10.49, which was subjected to the lower salt flux, compared with CM1/3, shows that the zero-line was crossed after 390 hours testing, 30 hours longer than CM1/3. Despite lower spall mass results for the lower salt flux sample, the much larger reductions in coating depths, between the tested and reference samples, contrast with those for the higher salt flux sample.

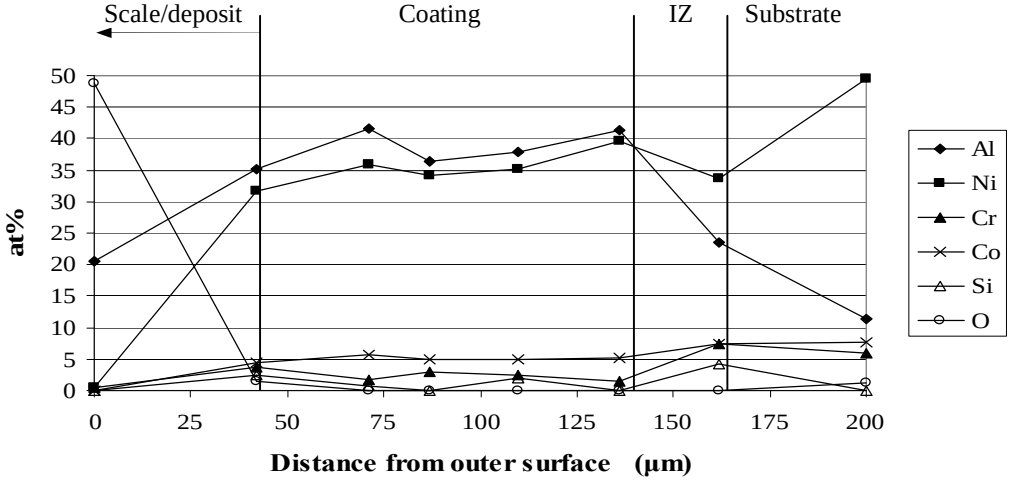

Figure 10.81: CMSX-4 sample CM1/8; after 500 hours corrosion testing at 900°C – main elements on EDX line in Figure 10.82

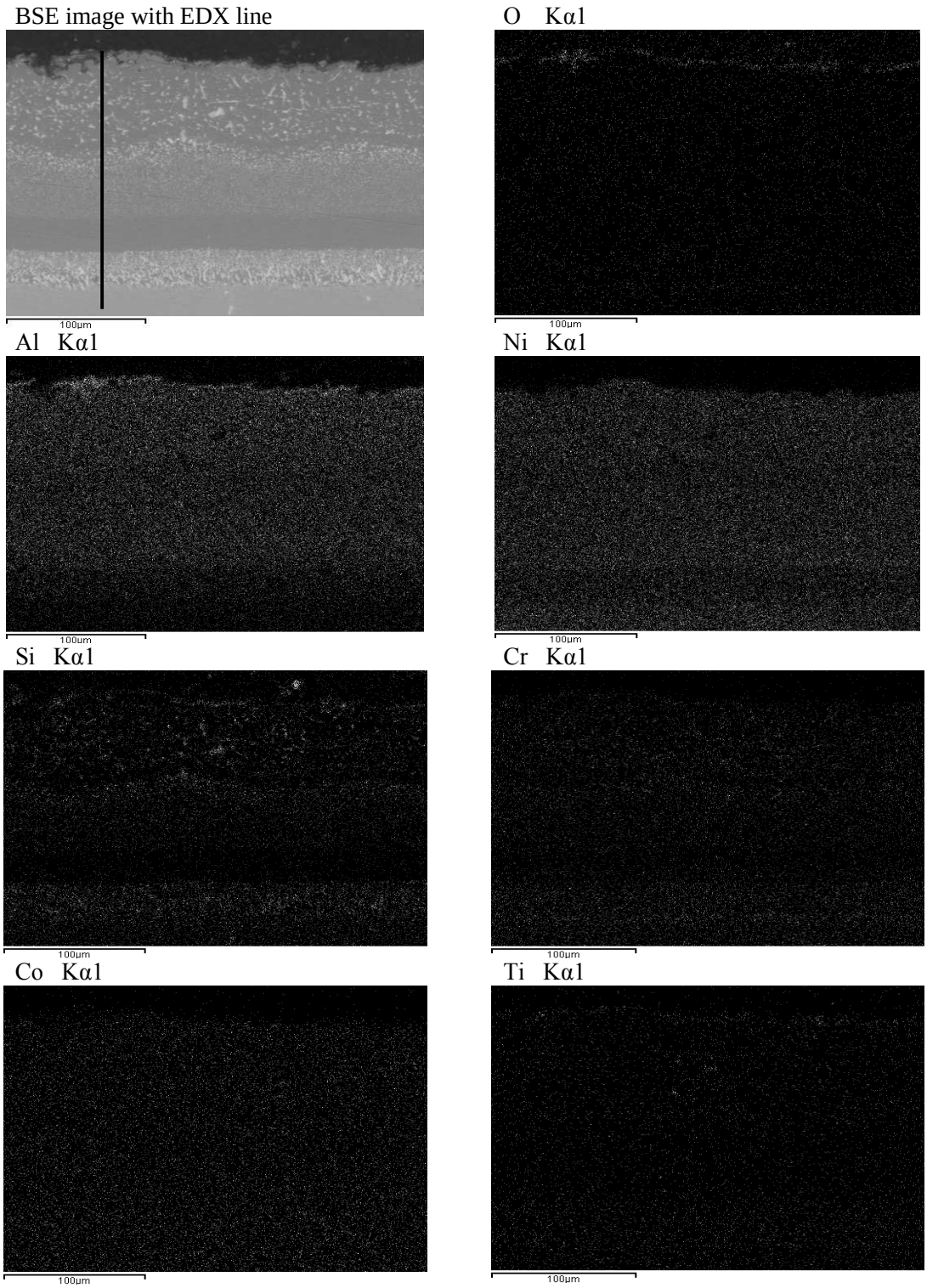

Figure 10.82: CMSX-4 sample CM1/4; after 500 hours corrosion testing at 900°C – element maps

10.3.2.10 CMSX-4 with novel silicon-aluminide coating (powder 1), (sample CM1/9) with Pb+alkali salt composition, salt flux 1.5 µg/cm^2/h

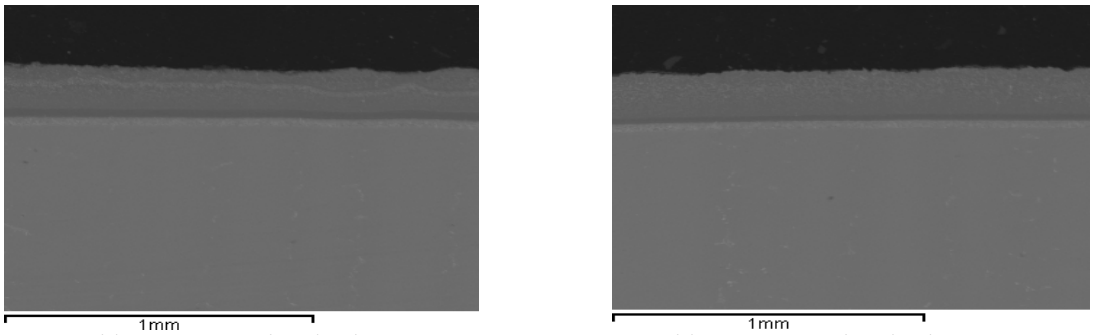

Bottom side average coating depth: 181µm
Ref sample bottom side coating depth: 203µm

Top side average coating depth: 176µm
Ref sample top side coating depth: 188 µm

Figure 10.83: CMSX-4 sample CM1/9; after 500 hours corrosion testing at 900°C – BSE images of both sides

As seen by the element maps in Figure 10.85 and EDX results in Figure 10.84 the β-NiAl matrix is maintained from the IZ to the surface which consists of a thin, aluminium oxide layer, containing 1.3 at%O. The microstructure is very similar to that of the Cd+alkali, lower salt flux sample, but with minimal degradation at the surface. The coating is more protective of the Pb+alkali salt combination on CMSX-4, compared with that for Cd+alkali. Only traces of alloying elements have outwardly diffused into the coating. Silicon distribution in the coating is more uniform in CM1/9 than in CM1/8, averaging 2.6 at%Si, compared with 1.5 at%Si for the latter. The coating looks good and will continue to provide Type I hot corrosion protection for the lower salt flux Pb+alkali for a significant period.

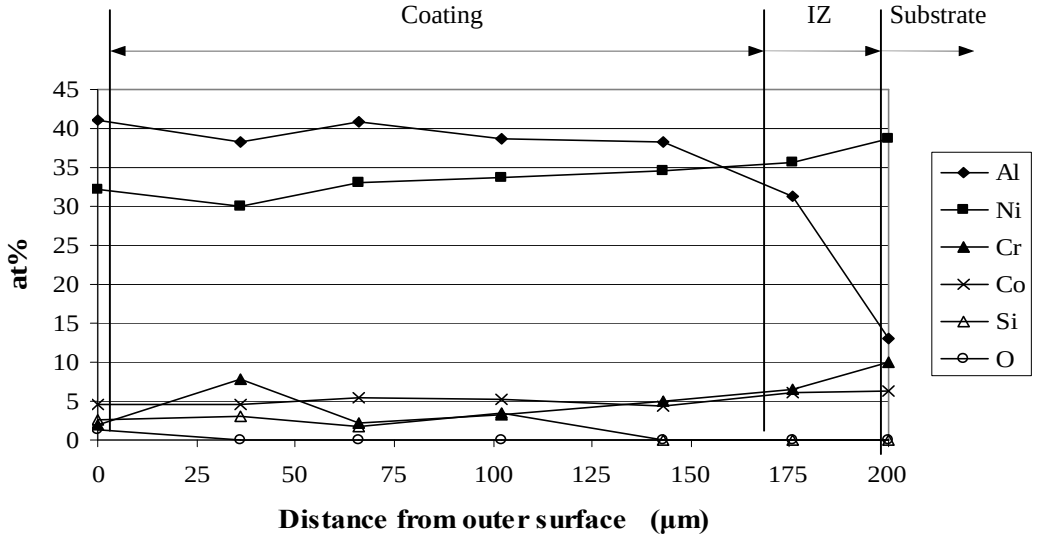

Figure 10.84: CMSX-4 sample CM1/9; after 500 hours corrosion testing at 900°C – main elements on EDX line in Figure 10.85

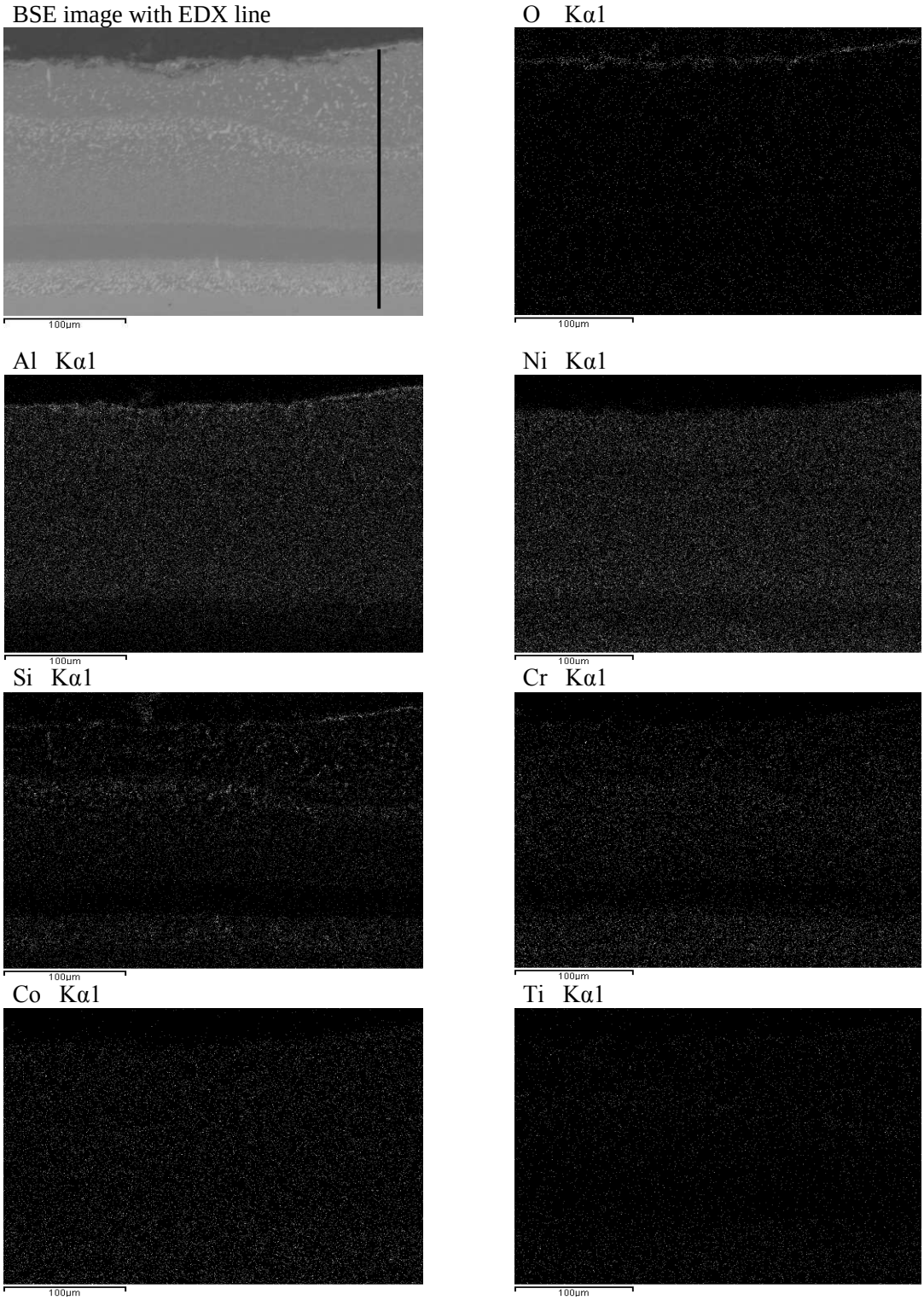

Figure 10.85: CMSX-4 sample CM1/9; after 500 hours corrosion testing at 900°C – element maps

10.3.2.11 CMSX-4 with novel silicon-aluminide coating (powder 2), (sample CM2/3) with Cd+alkali salt composition, salt flux 5.0 μg/cm^2/h

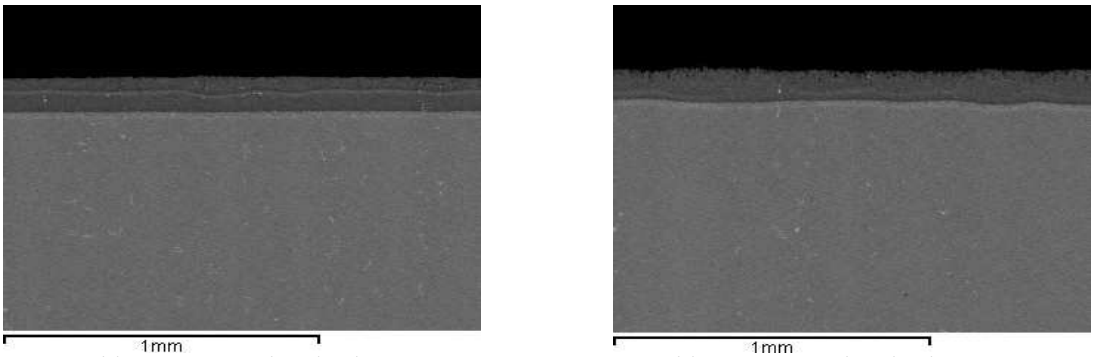

Bottom side average coating depth: 123μm
Ref sample bottom side coating depth: 97μm

Top side average coating depth: 106μm
Ref sample top side coating depth: 67μm

Figure 10.86: CMSX-4 sample CM2/3; after 500 hours corrosion testing at 900°C – BSE images of both sides

In Figure 10.87, the β-NiAl matrix of the bottom side coating of sample CM2/3 is seen to be stable for a depth of 60μm above the IZ. It continues the same phase, despite a reduction in aluminium content from 34 at%Al to 25 at%Al, over the remaining 75μm depth to the surface. Over the last 25μm of depth to the surface, the content remains steady at 25 at%Al, as it oxidises to Al_2O_3 along the surface. The element maps in Figure 10.88 show the coating to be rich in silicon (7 at%Si) and chromium (5 at%Cr) through the depth of stable coating. The feature of this coating, formed from the high silicon content powder is the increase in coating depths during corrosion testing, compared with those of the reference coating.

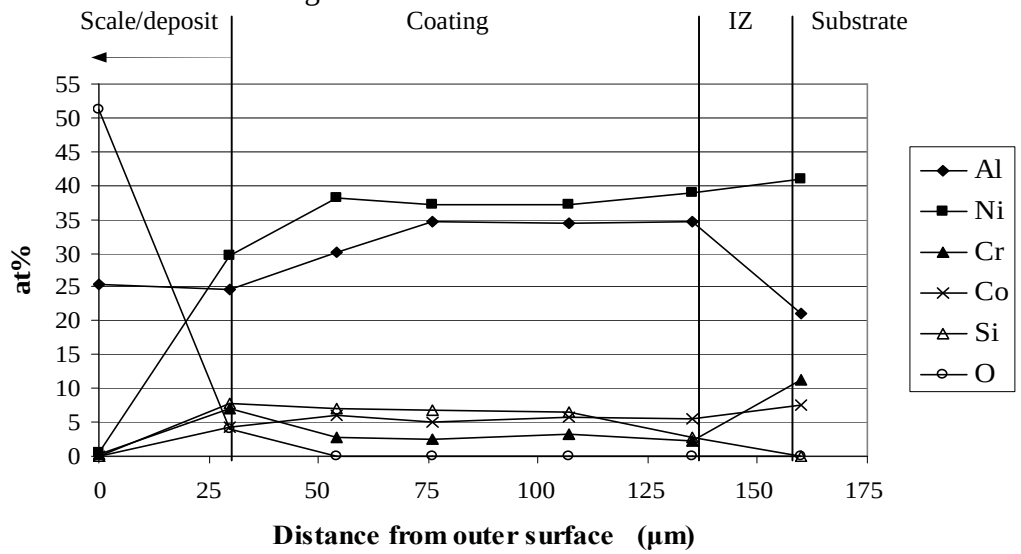

Figure 10.87: CMSX-4 sample CM2/3; after 500 hours corrosion testing at 900°C – main elements on EDX line in Figure 10.88

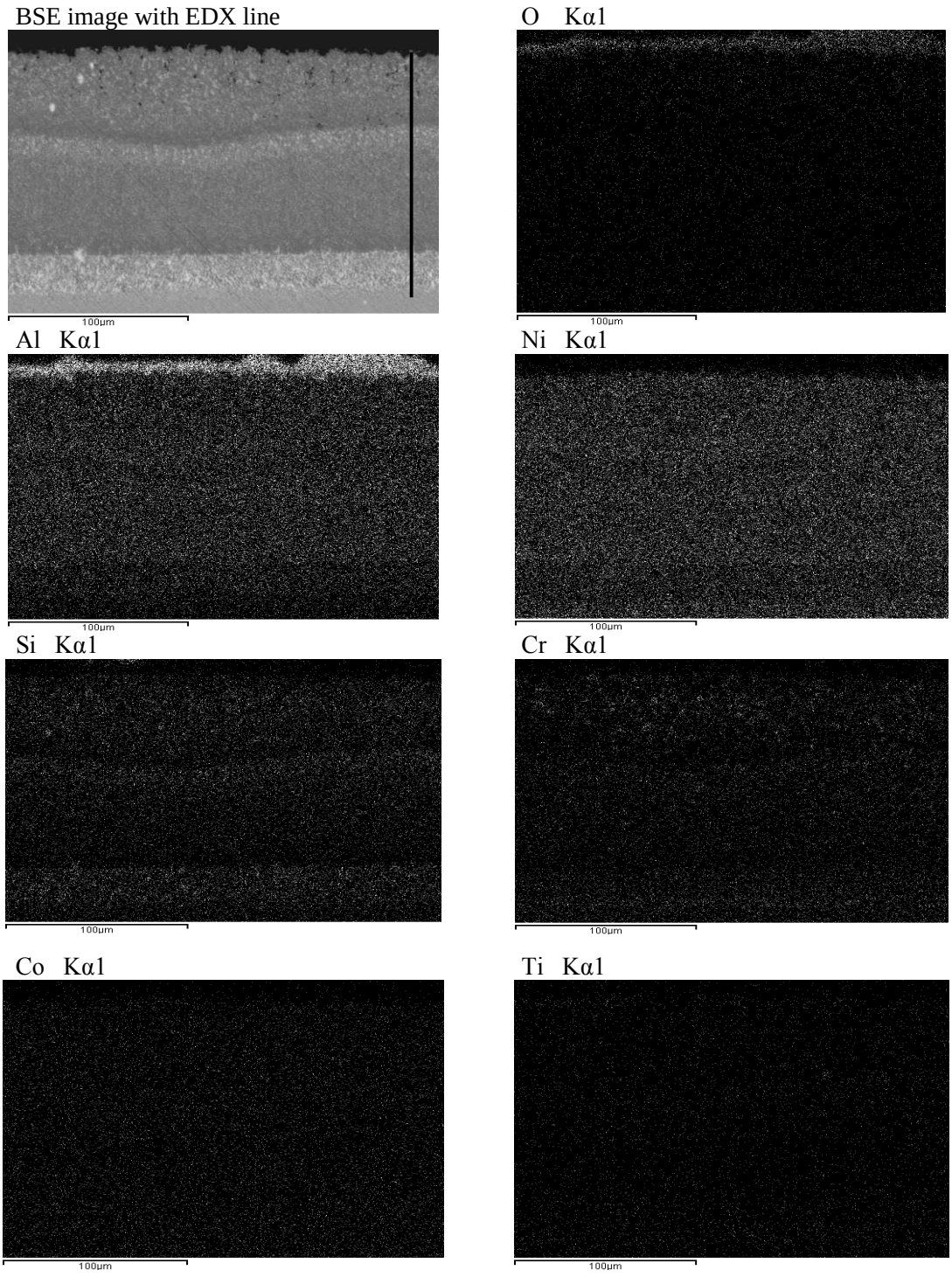

Figure 10.88: CMSX-4 sample CM2/3; after 500 hours corrosion testing at 900°C – element maps

10.3.2.12 CMSX-4 with novel silicon-aluminide coating (powder 2), (sample CM2/4) with Pb+alkali salt composition, salt flux 5.0 µg/cm^2/h

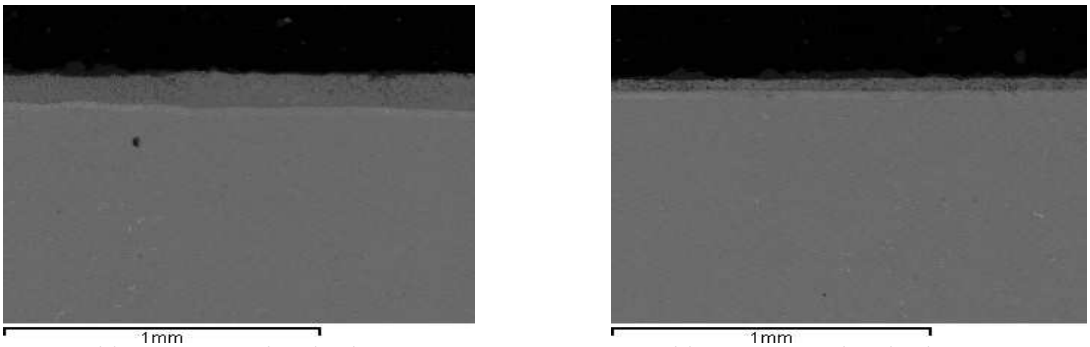

Bottom side average coating depth: 87µm
Ref sample bottom side coating depth: 97µm

Top side average coating depth: 31µm
Ref sample top side coating depth: 67µm

Figure 10.89: CMSX-4 sample CM2/4; after 500 hours corrosion testing at 900°C – BSE images of both sides

The element maps in Figure 10.91 show the remaining coating to be heavily degraded, in parts the depth of sound coating is only 14µm. Above the IZ, the β-NiAl matrix in the coating is 70µm deep before aluminium content falls from 26 at%Al to 13 at%Al at a depth of 40µm from the surface, before rising to 28 at%Al at the surface. This reflects as internal damage. Compared with the equivalent Cd+alkali sample (CM2/3) the spall mass for this sample is high, accounting for the high loss in depth of coating, when compared with the Cd+alkali sample. Despite this, there remains sound coating to continue to provide Type I hot corrosion resistance.

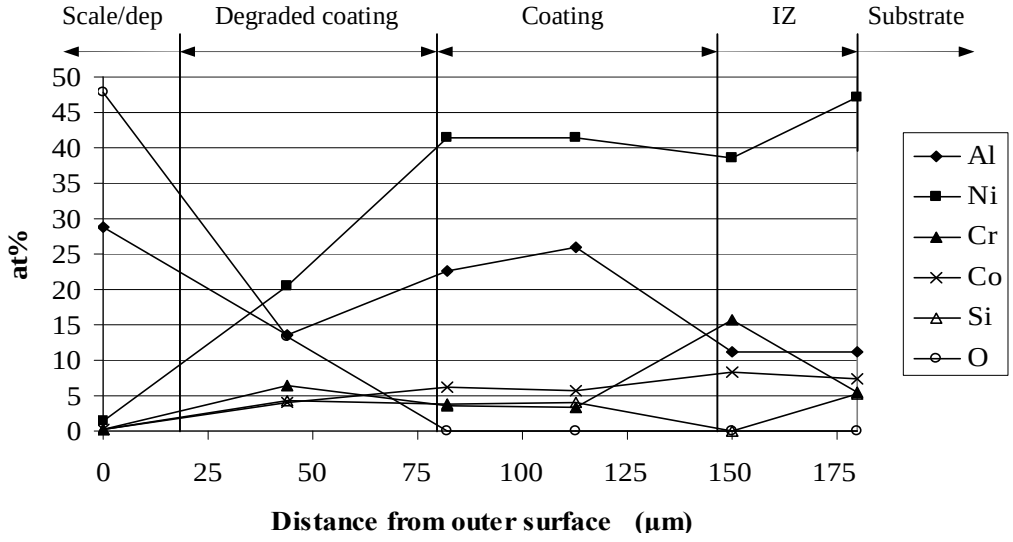

Figure 10.90: CMSX-4 sample CM2/4; after 500 hours corrosion testing at 900°C – main elements on EDX line in Figure 10.91

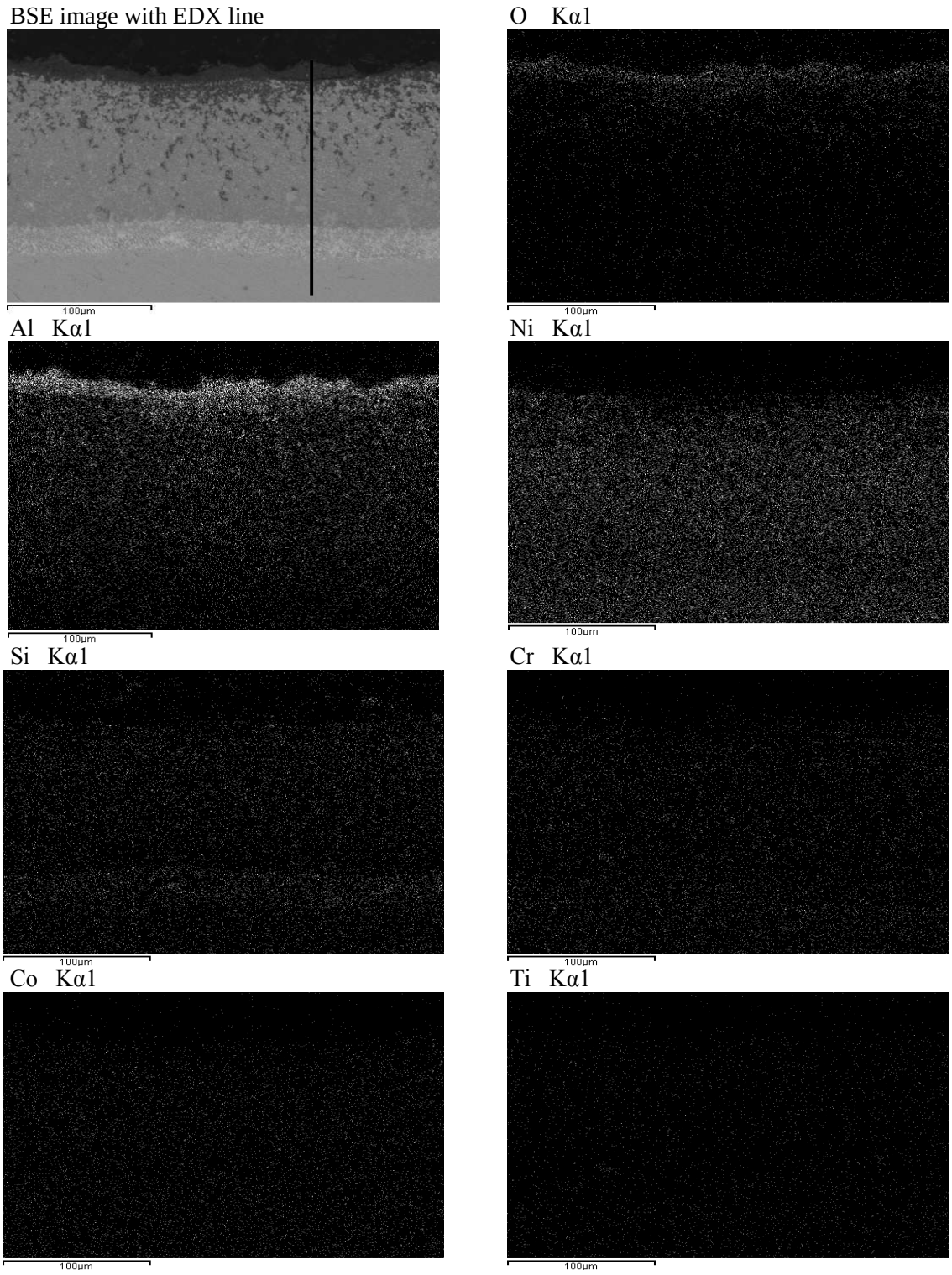

Figure 10.91: CMSX-4 sample CM2/4; after 500 hours corrosion testing at 900°C – element maps

10.3.3 Corrosion test series 4; 500 hours at 900°C, discussion and conclusions

All the corrosion tested novel single-step silicon aluminide coatings provide protection against Type I hot corrosion for at least 300 hours, after which propagation apparently accelerates. Mass change graphs show that generally, the incubation rates over the first 100 hours of testing are similar for all samples, but after this time spall rates are typically of a higher order for the CMSX-4 samples than those of IN738LC. Spalling and evaporation tend to distort the overall conclusions to be made from mass change results. Although net mass change crosses the zero-line in several samples, sound coatings remain in most cases, with degraded coatings remaining in the worst performing coatings.

In addition to mass change, BSE maps and EDX analyses, XRD assessments of selected samples were undertaken, to assist in analysing the Type I hot corrosion protection provided by the silicon-aluminide coatings. The diffractogram in Figure 10.92 shows the XRD plots for the exposed samples, together with the unexposed reference samples and uncoated, unexposed IN738LC and CMSX-4 samples. The Y-axis counts have been adjusted to enable differentiation of individual sample plots. The compounds associated with peaks in Figure 10.92 are shown in Table 10.3.

Peak 2-Theta-Scale position	**Compound**
26.0	$AlNi_2Ti$
35.5	Al_2O_3
37.5	$AlNi_2Ti$, Al_2O_3, NiO
43.5	$AlNi_2Ti$, Al_2O_3, NiO
44.5	$AlNi_2Ti$, Al_2O_3, NiO
50.7	Ni_3Al, Co_3O_4
53.5	$AlNi_2Ti$
57.5	Al_2O_3
75.0	$AlNi_2Ti$, Al_2O_3
82.0	TiO_2

Table 10.3 : Corrosion test series 4; XRD analyses, compounds associated with peaks shown in XRD plots in Figure 10.92

A diffractogram covering a limited 2-Theta – Scale, with the same samples as those in Figure 10.92, 'stepped' for clarity, is shown in Figure 10.93. Compared with similar plots for the Type II corrosion tests, seen in Figure 10.44, exposed samples in the Type I corrosion tests have more residual coatings which are less degraded. To enable better differentiation of these plots, XRD plots of the exposed samples have been presented, over a reduced 2-Theta-Scale, in Figure 10.94.

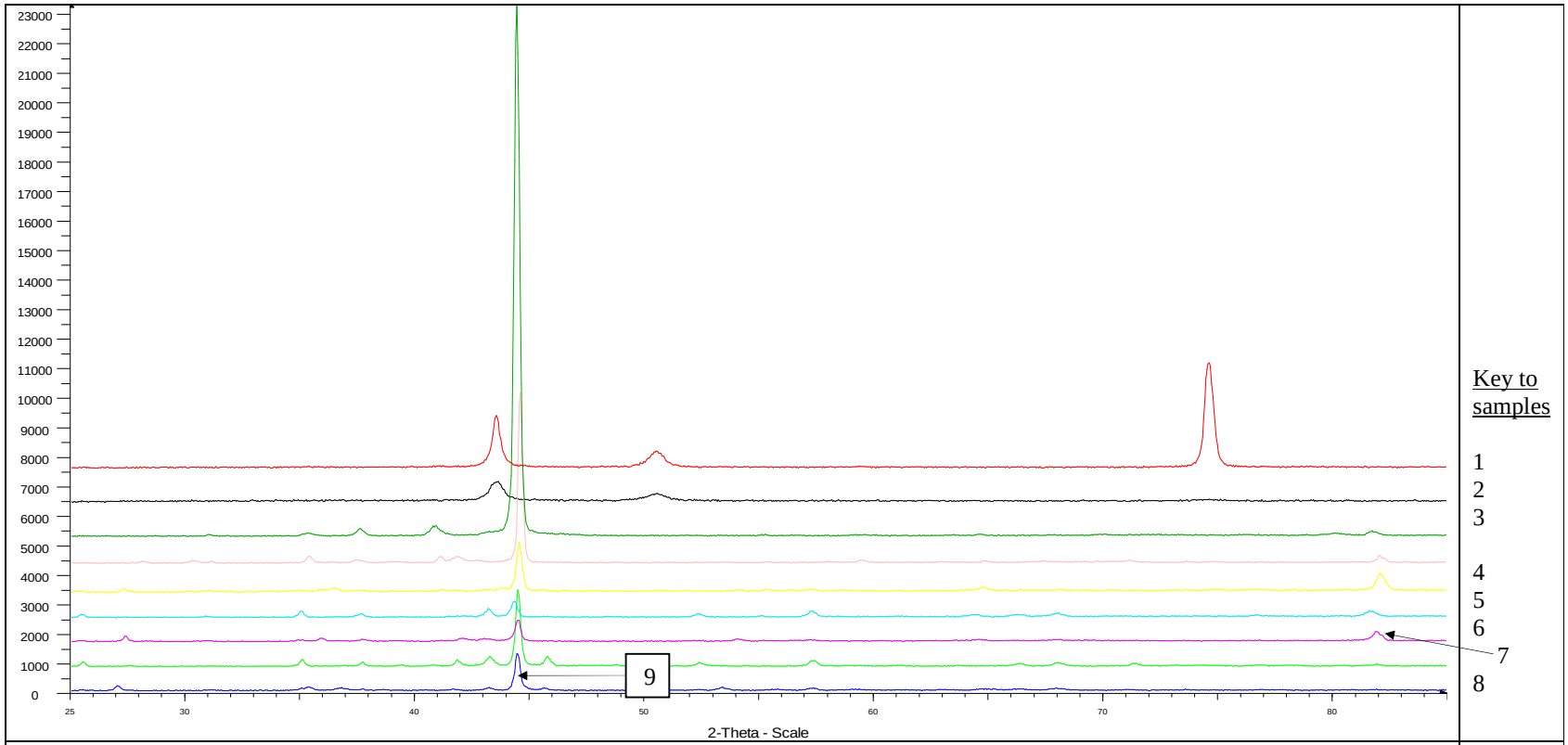

Y-axis units 'Counts'

Key;
1 – Unexposed IN738LC substrate
2 – Unexposed CMSX-4 substrate
3 – Unexposed IN738LC with SiAl1 coating reference sample
4 – Unexposed CMSX-4 with SiAl1 coating reference sample
5 – Exposed sample IN2-3, IN738LC with SiAl2 coating exposed to Cd+alkali sulphates
6 - Exposed sample IN1-4, IN738LC with SiAl1 coating exposed to Pb+alkali sulphates
7 – Exposed sample IN1-3, IN738LC with SiAl1 coating exposed to Cd+alkali sulphates
8 – Exposed sample CM2-3, CMSX-4 with SiAl2 coating exposed to Cd+alkali sulphates
9 - Exposed sample CM1-3, CMSX-4 with SiAl1 coating exposed to Cd+alkali sulphates

Figure 10.92 : Corrosion test series 4; 500 hours at 900°C, XRD assessment of selected exposed samples

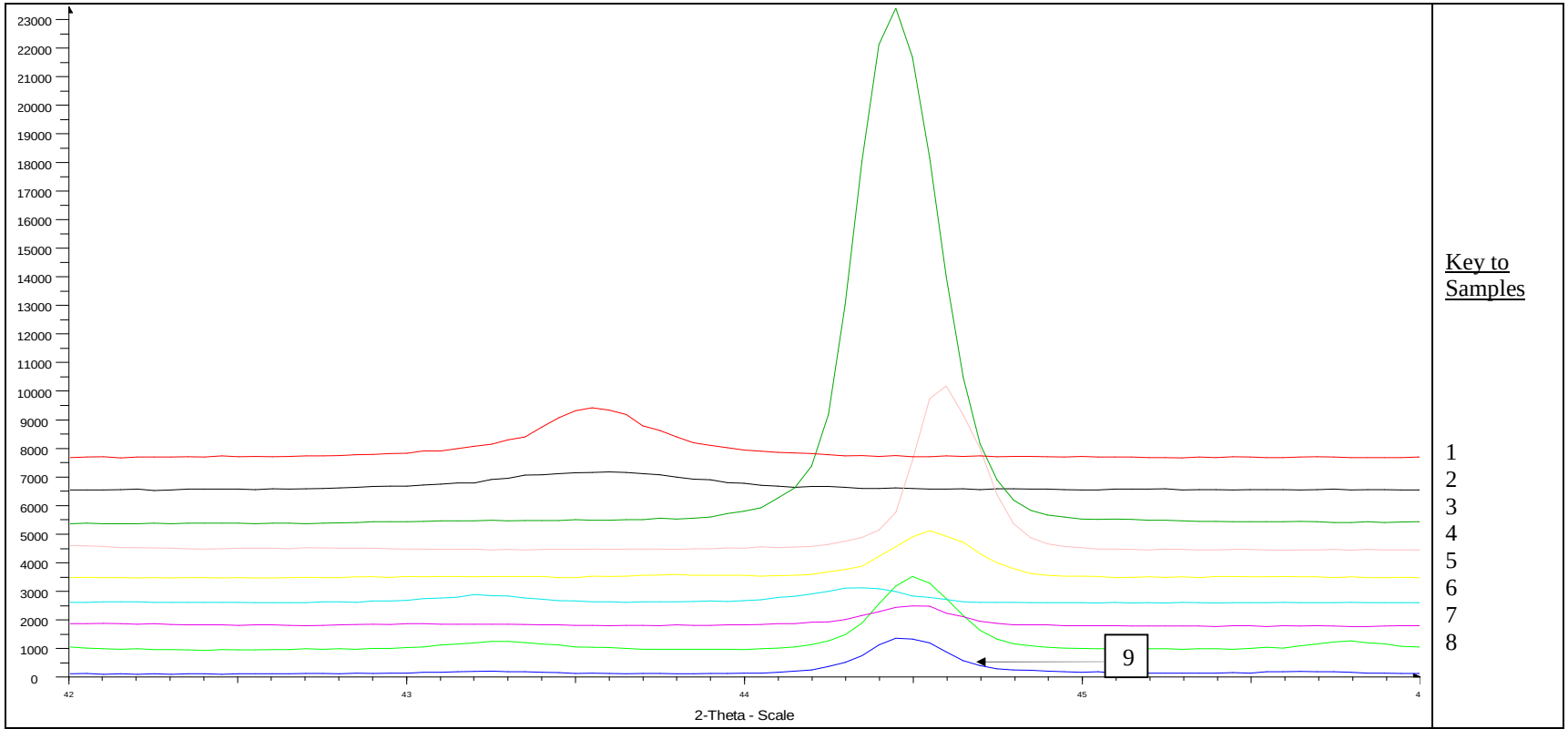

Y-axis units 'Counts'

Key;
1 – Unexposed IN738LC substrate
2 – Unexposed CMSX-4 substrate
3 – Unexposed IN738LC with SiAl1 coating reference sample
4 – Unexposed CMSX-4 with SiAl1 coating reference sample
5 – Exposed sample IN2-3, IN738LC with SiAl2 coating exposed to Cd+alkali sulphates
6 - Exposed sample IN1-4, IN738LC with SiAl1 coating exposed to Pb+alkali sulphates
7 – Exposed sample IN1-3, IN738LC with SiAl1 coating exposed to Cd+alkali sulphates
8 – Exposed sample CM2-3, CMSX-4 with SiAl2 coating exposed to Cd+alkali sulphates
9 - Exposed sample CM1-3, CMSX-4 with SiAl1 coating exposed to Cd+alkali sulphates

Figure 10.93 : Corrosion test series 4; 500 hours at 900°C, XRD assessments of samples over reduced 2-Theta-Scale

In Figure 10.94, plots are shown for one side only of each of the five samples, included for clarity. The microstructures exhibited earlier in this and earlier chapters clearly show there are differences between the coating thicknesses on the sides of samples and do not need to be repeated in this case.

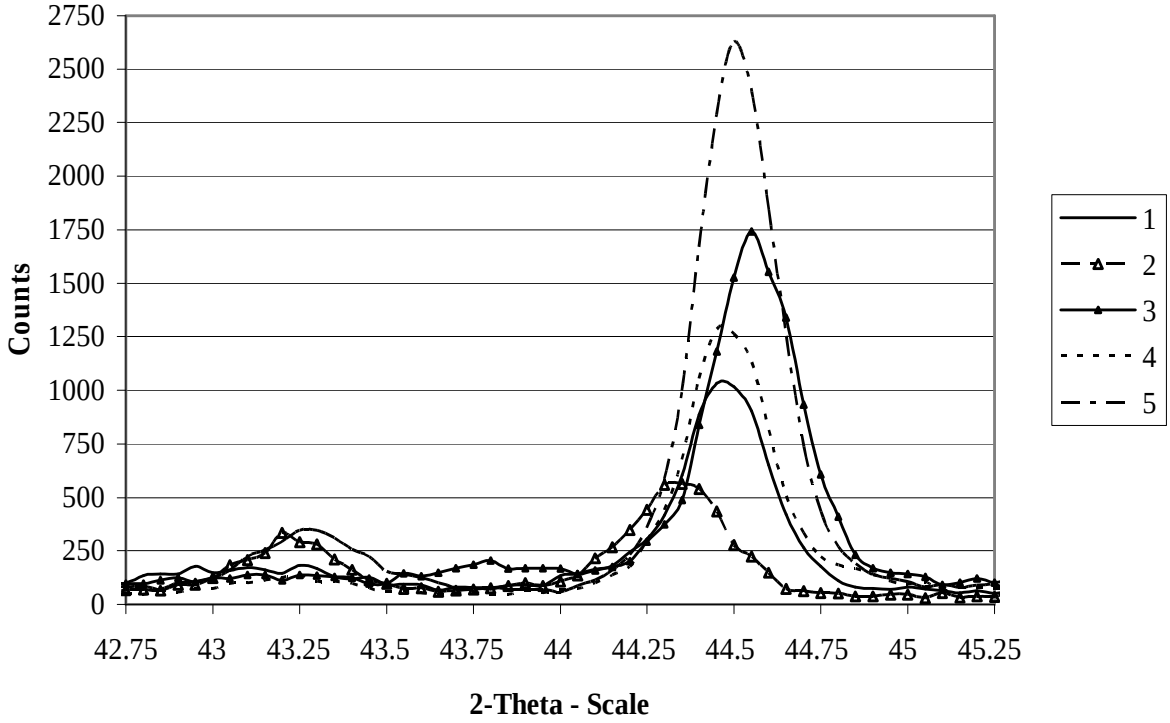

Key: 1 ; IN738LC with SiAl1 coating exposed to Cd+alkali sulphates
2 ; IN738LC with SiAl1 coating exposed to Pb+alkali sulphates
3 ; IN738LC with SiAl2 coating exposed to Cd+alkali sulphates
4 ; CMSX-4 with SiAl1 coating exposed to Cd+alkali sulphates
5 ; CMSX-4 with SiAl2 coating exposed to Cd+alkali sulphates

Figure 10.94: Corrosion test series 4; 500 hours at 900°C, XRD assessments of selected exposed samples

The XRD assessments show the SiAl1 coating on IN738LC is more Type I hot corrosion protective against Cd+alkali than against Pb+alkali. The SiAl1 coating on CMSX-4 is more Type I hot corrosion protective than when applied to IN738LC exposed to either Cd+alkali and Pb+alkali. The coating SiAl2 is more protective of both IN738LC and CMSX-4 when exposed to Type I hot corrosion. The comparatively high peaks show remanent coatings to be thicker and less degraded than when exposed to Type II hot corrosion conditions. In summary, the XRD assessments are consistent with mass change results, microstructures and EDX analyses in showing that SiAl1 and SiAl2 coatings provide high levels of Type I hot corrosion protection.

10.4 Assessment of the hot corrosion protection provided by novel single-step silicon-aluminide coatings

10.4.1 Effects of CVD furnace temperature ramping rates

As previously mentioned in assessing the corrosion test results, a factor affecting the performance of the novel silicon aluminide coatings is the variation in coating depths between the bottom and top sides of the samples. The reason for these variations has been explained earlier. Variations in coating depths have also occurred due to different CVD furnace ramping rates. In preparation for the Type I and Type II corrosion tests, three different operations were undertaken. The first CVD run produced the first batch of IN738LC and CMSX-4 samples using powder 1, the second CVD run used powder 2. A third CVD run was carried out, using powder 1, to produce more IN738LC sample discs for the corrosion tests, together with two turbine blades for coating trials, described later in section 12.

Differences in furnace and CVD chamber ramping rates are shown in Figure 10.95. Between the first and second CVD operations, furnace heating elements were repaired which produced faster temperature ramping for the second CVD run. Between the second and third CVD runs the furnace was refurbished and new controls fitted. The result was a significant reduction in the time for the chamber to reach 800°C, when powder pack vapourisation commences, and for it to reach 1050°C, the CVD soak temperature, at which the one hour soak period commences. The significant variation in CVD periods, seen in Figure 10.95, resulted in the variations in coating depths, shown in the microstructures for the corrosion tests.

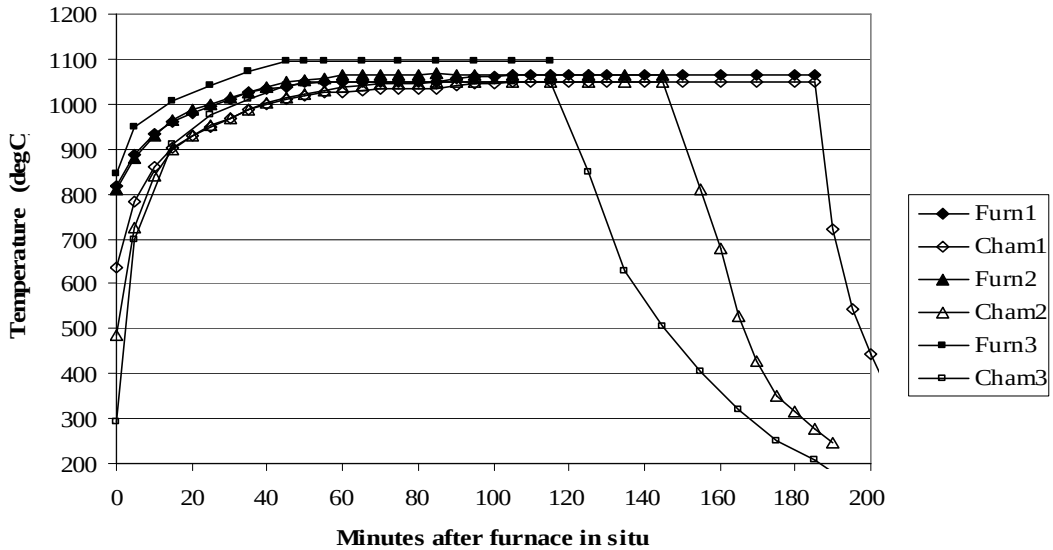

Furn1/Cham1 – to produce IN738LC & CMSX-4 samples with SiAl1 coatings (powder 1)
Furn2/Cham2 – to produce IN738LC & CMSX-4 samples with SiAl2 coatings (powder 2)
Furn3/Cham3 – to produce additional IN738LC samples with SiAl1 coatings (powder 1)

Figure 10.95: Furnace/chamber temperature ramping rates for CVD operations to produce novel coatings for Type I and Type II corrosion tests

10.4.2 Comparison of Type II hot corrosion protection provided by novel silicon-aluminide coatings with commercial coatings

The main means of assessing the performance of novel single-step aluminide coatings, to protect gas turbines burning biomass and waste-fuels from hot corrosion, is to compare the results of corrosion tests on these coatings with those on commercial coatings, applied to the same substrates, under the same conditions.

Results of the Type II corrosion tests on novel silicon-aluminide coatings are reported in section 10.2, and those for the commercial coatings, in section 7.4. Conditions for both Type II corrosion tests were similar: exposures for five periods of 100 hours at 700°C, with Cd+alkali and Pb+alkali salt combinations and salt fluxes of 1.5 $\mu g/cm^2/h$ and 5.0 $\mu g/cm^2/h$. Gases used in the tests included 400ppm HCl and 250ppm SO_2, typically produced from gasification of biomass and waste-fuels.

When comparing the hot corrosion protection provided by the novel silicon-aluminide and commercial coatings, the accuracy of the comparisons will be affected by the use of discs in tests of the former and cylindrical bobbins in tests of the latter. The superalloy samples used in the commercial coating corrosion tests were cylindrical bobbins, described in Chapter 4, whereas all samples used in corrosion tests on novel silicon aluminide coatings were thin discs. As explained in sections 10.2.3 and 10.2.4, during the CVD processes, the depths of coatings on bottom and top sides of discs varied. In addition, the sharp, perpendicular edges of the discs caused more uneven coating depths, compared with the round circumferential sides of bobbins. As a result, the commercial coatings, having more uniform coatings could be expected to provide better hot corrosion protection compared with the discs. Another factor relating to sample bobbins and discs, concerned the measurement of changes in sound metals. These differences are described more fully in Chapter 4. The net result is that the depths of changes in sound metal could be measured more accurately by image analyser than by measurements from SEM 'full sized' BSE images.

The changes in sound metal of commercial coatings and novel silicon-aluminide coatings are shown in Table 10.4 for IN738LC based samples and Table 10.5 for CMSX-4 based samples. The percentage change in sound metal parameter is included to allow a direct comparison to be made between coatings of different original depths.

Not that, for brevity the following abbreviations may be used:

(a) Substrates; IN refers to IN738LC, CM refers to CMSX-4,
(b) Commercial coatings; 29 refers to GT29+, 22 refers to RT-22,
S15 refers to Sermaloy1515,
(c) Novel silicon aluminide coatings; SiAl1, made from CVD powder 1,
SiAl2, made from CVD powder 2
(d) Salts applied; Cd refers to Cd+alkali or $CdSO_4(50)+(Na_2SO_4(80)+K_2SO_4(20))(50)$
Pb refers to Pb+alkali or $PbSO_4(50)+(Na_2SO_4(80)+K_2SO_4(20))(50)$
(e) Salt fluxes; H refers to high salt flux or 5.0 $\mu g/cm^2/h$,
L refers to low salt flux or 1.5 $\mu g/cm^2/h$

10.4.2.1 Commercial coatings and novel silicon aluminide coatings on IN738LC

Substrate + coating	Salt	Salt Flux μg\cm^2/h	Coating depth μm	Change in sound metal μm	Change in sound metal %
IN738LC+GT29+					
	Cd+alkali	1.5	115	-19	-16.5
	Cd+alkali	5.0	115	-24	-20.9
	Pb+alkali	1.5	115	-27	-23.5
	Pb+alkali	5.0	115	-52	-45.2
IN738LC+RT-22					
	Cd+alkali	1.5	102	-12	-11.8
	Cd+alkali	5.0	102	-24	-23.5
	Pb+alkali	1.5	102	-8	-7.8
	Pb+alkali	5.0	102	-24	-23.5
IN738LC+Serm1515					
	Cd+alkali	5.0	40	-20	-50.0
	Pb+alkali	5.0	40	-22	-55.0
IN738LC+SiAl1					
CVD3	Cd+alkali	1.5	87	-9	-10.3
CVD1	Cd+alkali	5.0	200	-16	-8.0
CVD3	Pb+alkali	1.5	78	-18	-23.1
CVD1	Pb+alkali	5.0	198	-18	-9.1
IN738LC+SiAl2					
CVD2	Cd+alkali	5.0	82	-8	-9.8
CVD2	Pb+alkali	5.0	85	-5	-5.9

Table 10.4: Commercial coatings and novel coatings on IN738LC; changes in sound metal after 500 hours corrosion testing at 700°C

The changes in sound metal of IN738LC samples, seen in Table 10.4, show that SiAl1, when produced from CVD1, and SiAl2, produced from CVD2, show less degradation after Type II corrosion testing than GT29+, a CoCrAlY overlay coating with a diffusion aluminide top layer, RT-22, a platinum-aluminide coating and Sermaloy1515, a triple layered silicon-aluminide coating. The novel silicon-aluminide coating SiAl1, produced from the shorter soak period of CVD3, provided similar levels of Type II hot corrosion protection as GT29+ and RT-22. However, the lower coating depths resulting from the shorter CVD3 are less Type II hot corrosion protective than those produced from CVD1, but of a similar order to those of GT29+ and RT-22. The Sermaloy1515 coating as tested is significantly less hot corrosion protective than all the other coatings tested, having lost half of the protective depth of coating for both Cd+alkali and Pb+alkali salt combinations. The platinum-aluminide RT-22 is more protective of Type II hot corrosion from Pb+alkali than GT29+, but both coatings are similar in the hot corrosion protection they provide against the higher salt flux Cd+alkali combination.

Of the novel coatings for IN738LC, SiAl1 is the most Type II hot corrosion protective, and there appears to be no benefit in increasing the silicon content as in SiAl2.

10.4.2.2 Commercial coatings and novel silicon-aluminide coatings on CMSX-4

Substrate+coating	Salt	Salt Flux μg\cm^2/h	Coating depth μm	Change in sound metal μm	Change in sound metal %
CMSX-4+Serm1515					
	Cd+alkali	1.5	40	-18	-45.0
	Cd+alkali	5.0	40	-33	-82.5
	Pb+alkali	1.5	40	-20	-50.0
	Pb+alkali	5.0	40	-50	-125.0
CMSX-4+SiAl1					
CVD3	Cd+alkali	1.5	113	-71	-56.8
CVD1	Cd+alkali	5.0	170	-42	-24.7
CVD3	Pb+alkali	1.5	84	-112	-57.1
CVD1	Pb+alkali	5.0	140	-77	-55.0
CMSX-4+SiAl2					
CVD2	Cd+alkali	5.0	66	-16	-24.2
CVD2	Pb+alkali	5.0	81	-4	-4.9

Table 10.5: Commercial coatings and novel silicon-aluminide coatings on CMSX-4, changes in sound metal after 500 hours corrosion testing at 700°C

The changes in sound metal of CMSX-4 samples, seen in Table 10.5, show that both SiAl1 and SiAl2 coatings are more Type II hot corrosion protective than Sermaloy 1515, except for the lower salt flux samples of the Cd+alkali and Pb+alkali salt combinations. However, the SiAl1 coated samples which were less protective, were those produced by CVD3 and therefore of less depth than those produced by CVD1. It is considered that if SiAl1 coatings on CMSX-4, produced by CVD1, were to be Type II hot corrosion tested under the same conditions, the novel coatings would be more hot corrosion protective than the Sermaloy 1515 coating as tested.

The Type II hot corrosion protection provided for CMSX-4 by SiAl2 is higher than by SiAl1 and significantly higher than that provided by Sermaloy 1515. The higher salt flux CMSX-4+Sermaloy 1515 sample was very severely degraded, by 82.5% in the case of the Cd+alkali sample, and to a depth of 10μm into the CMSX-4 substrate, for the Pb+alkali sample.

Of the novel coatings, for CMSX-4, both SiAl1 and SiAl2 were significantly more protective of Type II hot corrosion than Sermaloy 1515.

10.4.2.3 Comparisons of Type II hot corrosion protection provided by novel silicon-aluminide and commercial coatings - conclusions

The Type II hot corrosion tests, were carried out on coated samples of IN738LC and CMSX-4, as a direct means of comparing the hot corrosion protection provided by novel, single-step silicon-aluminide coatings with typical commercial coatings. The gas composition, salt combinations and salt fluxes used in the corrosion tests, represented the fuel-gases resulting from gasification of biomass and waste-fuels, for combustion in industrial gas turbines. The single-step novel silicon-aluminide coatings were developed in this project, the commercial coatings selected for comparison consisted of an overlay coating with additional diffusion aluminide outer layer (GT29+), a platinum-aluminide coating (RT-22) and a triple-layered silicon-aluminide (Sermaloy 1515). From the Type II hot corrosion test results the following conclusions can be made:

- BSE results showed that deep degradation of the Pt layers had occurred in RT-22 coatings of both higher salt flux samples of IN738LC substrates, and on CMSX-4 samples, Sermaloy 1515 failed on the higher salt flux Pb+alkali sample, no novel coatings failed;
- Based on the degradation depths of coatings after 500 hours corrosion testing at 700°C; both novel silicon-aluminide coatings provide more Type II hot corrosion protection than the commercial coatings although, for some salt combinations the protection from the lower silicon novel coating is of similar levels to those of GT29+ and RT-22;
- As the coating depths of the novel coatings were based on the average depth of both sides, compared with the accurate depths of the commercial coatings, it is concluded that, if depths of both sides of novel coatings could equal those of the bottom sides, the novel coatings would clearly be more protective than the commercial coatings tested in this project;
- Both novel silicon-aluminide coatings provide more Type II hot corrosion protection than the commercial coatings tested here, the higher silicon novel coating being more protective of CMSX-4 samples than those of IN738LC.

11. Novel silicon-aluminide coating – TBC bonding

11.1 Introduction

In previous sections, evaluations of hot corrosion protection provided by novel silicon-aluminide coatings, for gas turbines burning biomass and waste fuels, shows favourable comparisons with the performance of commercial coatings, making them a viable solution if higher coating quality can be achieved. By developing novel hot corrosion protective coatings for gas turbines burning these fuels the objective of this project has been met. However, it would be beneficial if the novel coating could also provide an effective bond coating for a TBC, by avoiding the need for an additional bonding coat, thus allowing the gas turbines to benefit from thermal barrier coating technology whist retaining its hot corrosion resistance.

This section reports on a trial to determine whether the novel, single-step silicon-aluminide coating could effectively bond a TBC by EB-PVD, as a single process. In addition, coating a low pressure (LP) turbine blade of IN738LC, would provide further information on the novel coating's properties, compared with those of the substrate discs used in developing and testing coatings in this project.

As the project was particularly concerned with industrial gas turbines, another feature in the TBC bonding trial was the incorporation of a thermoluminescent indicator in the TBC. By reacting to a laser light source, this could show the condition of the coating, on-line during gas turbine operation – the performance of this feature was not investigated further in this project.

11.2 Description of trial

The trial consisted of a number of stages; coating the part IN738LC LP blade with the novel silicon-aluminide coating, coating SiAl1, post CVD heat treatment then depositing the TBC by EB-PVD. To enable bonding evaluation the blade with TBC applied would then be sectioned and the blade sections mounted, ground and polished for evaluation, as explained in section 4.7.

11.2.1 Application of novel silicon-aluminide coating

The single-step, novel SiAl1 coating was applied by CVD using the same; low activity powder pack chemical mixture, CVD soak temperature of 1050^{o}C and one hour soak period, as for developing the hot corrosion resistant novel coatings, described in Chapter 8. Other than cleaning, blade surfaces remained as received prior to CVD operations. The blades were buried in the powder pack, with a minimum powder thickness of 10mm maintained around each blade.

11.2.2 Post CVD heat treatment

Following CVD, blades were tack welded to their Nimonic 75 carriers, cleaned and heat treated in the Cranfield vacuum furnace, using the standard programme for IN738LC of 2 hours at 1120^{o}C and 24 hours at 843^{o}C.

11.2.3 TBC materials and coating deposition

11.2.3.1 TBC ceramic material

The most common ceramic material which has the combination of suitable properties for a TBC is yttria partially stabilised zirconia (PYSZ). This provides low thermal conductivity and superior chemical stability. It also has a relatively high thermal expansion coefficient to minimise the coating to substrate mismatch [127]. Authors have shown that the TBCs providing the highest thermomechanical resistance are those where the yttria level is in the range 6-9 wt% [128,129]. Due to these qualities at temperatures up to 1500^{o}C, 8 wt% PYSZ TBCs have become the industrial standard to reduce the heat flux into hot-path components in gas turbines. Use of these TBCs enables a high thermal gradient across the coating without any increase in metal surface temperature, with the potential to allow an increase of up to 150^{o}C in turbine entry temperature or reduced cooling air mass, leading to a 0.25% efficiency gain [36].

The main thrust of this project is to develop hot corrosion protective coatings for industrial gas turbines fuelled by gasified biomass and waste-fuels. Depending on their purpose, industrial gas turbines operate at high or maximum continuous rating when in service, in contrast to gas turbines in aviation which mainly operate at reduced, cruise power except during take-off and landing stages. Major maintenance outages of power generating units are generally planned to take place during national statutory inspection periods, which allow major gas turbine maintenance to be carried out. A major strategy in power plant maintenance is condition monitoring, from data obtained on-line in real-time and by off load inspection, to enable residual life assessment to be made. The ability to use self-diagnostic TBCs will assist in maintenance planning and cost optimisation, by enabling replacements to be obtained in time for outages at lower premium periods, such as weekends. Laboratory tests have already demonstrated that EB-PVD TBCs can be deposited which incorporate laser-induced fluorescence and Choy et al obtained a patent for a thermal barrier coating with thermoluminescent indicator material embedded therein [130]. For these trials, the rare earth dopant dysprosium was added to the PYSZ refractory material, to deposit the TBC structure shown in Figure 11.1. Dysprosium has been shown to be a viable thermoluminescent addition that can be incorporated in an EB-PVD TBC

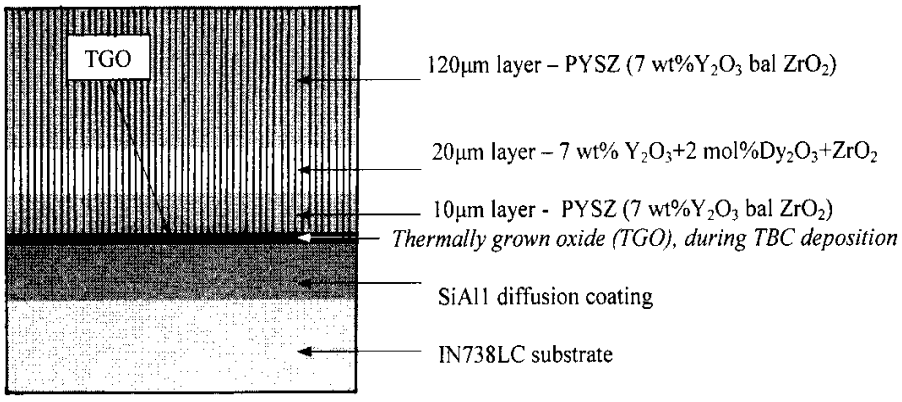

Figure 11.1: Diagrammatic section of IN738LC substrate coated with silicon-aluminide coating and TBC incorporating a thermoluminescent indicator

The ingot for the EB-PVD operation, consisted of discs of the materials for the TBC, placed in the order they were to be deposited and of the thicknesses required, to produce the depths of coating shown in Figure 11.1.

11.2.3.2 TBC deposition

Plasma-sprayed TBCs have been successful on annular surfaces of $1^{st}/2^{nd}$ stage blades/nozzles in large industrial gas turbines. However, for coatings having higher levels of strain compliance, erosion resistance, or surface finish, required in 1^{st} and 2^{nd} stage blades/vanes for aero-engines and in some smaller industrial gas turbines, EB-PVD is commonly used. EB-PVD deposited TBCs have a columnar microstructure, as seen in Figure 2.33, which provide high levels of strain compliance. The columnar microstructure results from the atomistic nature of the deposition process. The nucleation and growth of the coating is controlled by condensation from the vapour phase [128]. Other benefits provided by EB-PVD over plasma-sprayed TBCs are improved adhesion, surface finish and erosion resistance, properties which make them appropriate for coating turbine aerofoils. The EB-PVD process equipment at Cranfield, described in section 4.6, was used for these trials. The rate of deposition was 2µm per minute, taking 75 minutes to deposit the 150 µm TBC. Conditions during the EB-PVD process for this trial are shown in Table 11.1 and explained in section 4.6.

Cumulative Time	**Pressure**	**Temp**	**Gas Flow**	**EB gun voltage**	**EB gun current**	**Lower chamber pressure**
mins	mBar	^{o}C	scc/min	kV	amp	mbar
0	$7.06x10^{-3}$	958	50	10	0.30	$1.2x10^{-4}$
1	$1.25x10^{-2}$	1004	50	10	0.58	$1.3x10^{-4}$
3	$1.06x10^{-2}$	1005	50	10	0.56	$1.1x10^{-4}$
12	$1.15x10^{-2}$	1007	70	10	0.56	$1.3x10^{-4}$
22	$1.03x10^{-2}$	997	70	10	0.52	$1.3x10^{-4}$
31	$1.05x10^{-2}$	1002	70	10	0.52	$1.3x10^{-4}$
40	$1.25x10^{-2}$	1003	80	10	0.52	. $1.4x10^{-4}$
51	$1.22x10^{-2}$	1003	80	10	0.52	$1.3x10^{-4}$
60	$1.22x10^{-2}$	1005	80	10	0.52	$1.3x10^{-4}$
68	$1.38x10^{-2}$	1004	80	10	0.52	$1.4x10^{-4}$
74	$1.25x10^{-2}$	1002	80	10	0.52	$1.3x10^{-4}$
75	$1.25x10^{-2}$	1003	80	10	0.52	$1.3x10^{-4}$

Table 11.1: Conditions during the EB-PVD deposition of TBC on to silicon-aluminide coating on IN738LC LP turbine blades

In Figure 11.2, (c) and (d) show the blade after EB-PVD but before sections were cut for evaluating the TBC. Prior to the EB-PVD stage, four sections had been cut off for use in evaluating the silicon-aluminide coating, hence the TBC along the top of the blade was directly deposited onto IN738LC, resulting in an inadequate bonding. The resulting, inadequated bonding of the TBC on this uncoated surface can be seen on these pictures.

(a) Blade after SiAl CVD; before heat treatment

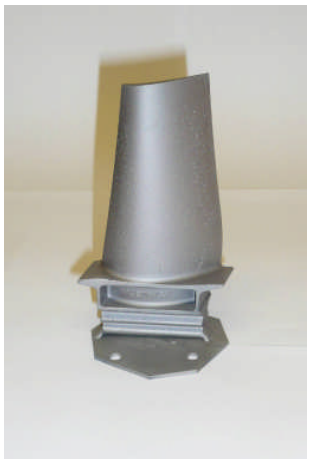

(b) Mounted blade after heat treatment

(c) Blade SiAl 1 with TBC - side 1

(d) Blade SiAl 1 with TBC - side 2

(e) Blade SiAl 2 with TBC - side 1

(f) Blade SiAl 2 with TBC - side 2

Figure 11.2: LP turbine blade after silicon-aluminide coating CVD, post heat treatment and surface clean, and with TBC

11.3 TBC bonding trial results and evaluation

11.3.1 Weights of coatings deposited

Column	1	2	3	4	5	6	7	8
Blade no.	Wt before CVD	Wt after CVD	Wt of coating deposited	%age wt coating deposited	Wt before EB-PVD	Wt After EB-PVD	Wt of TBC deposited	%age wt TBC deposited
Al -1	263.25	264.41	1.16	0.44	293.84	300.88	7.04	2.40
Al -2	264.73	265.83	1.10	0.42	301.59	308.70	7.11	2.35
SiAl1	266.47	268.90	2.43	0.91	286.40	294.67	8.27	2.88
SiAl2	267.56	270.08	2.52	0.94	303.69	314.11	10.42	3.43

Weights: (g)

Table 11.2: Weights of coatings and TBCs deposited

Table 11.2 shows weights of TBCs and diffusion coatings deposited on four similar IN738LC LP blades; with aluminide and silicon modified aluminide coatings produced using the same CVD equipment, soak temperatures and one hour soak periods, and the same EB-PVD equipment and conditions. The weights of blades Al-1 and Al-2 are included for comparisons; evaluation of their thermoluminescence performance is not available here. CVD deposition was carried out on blades with their fir-tree roots, after which both SiAl blades were mounted on Nimonic 75 carriers for heat treatment and EB-PVD operations, hence the differences between weights in columns 2 and 5. Sections were cut from blade SiAl 1, before and after EB-PVD, for the evaluations reported in this trial.

11.3.2 Silicon-aluminide coating evaluation

For CVD operations the blades were positioned with their convex surfaces facing downwards, lying on the powder pack on the tray bottom, as shown diagrammatically in Figure 11.3. It can be seen from the diagram that there are variations in pack depths at different positions around the blade profile which will account for variations in coating depths shown in Figures 11.4 and 11.5.

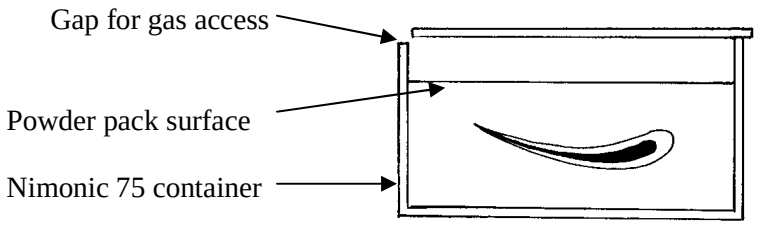

Figure 11.3: Diagram showing position of blade in powder pack for CVD

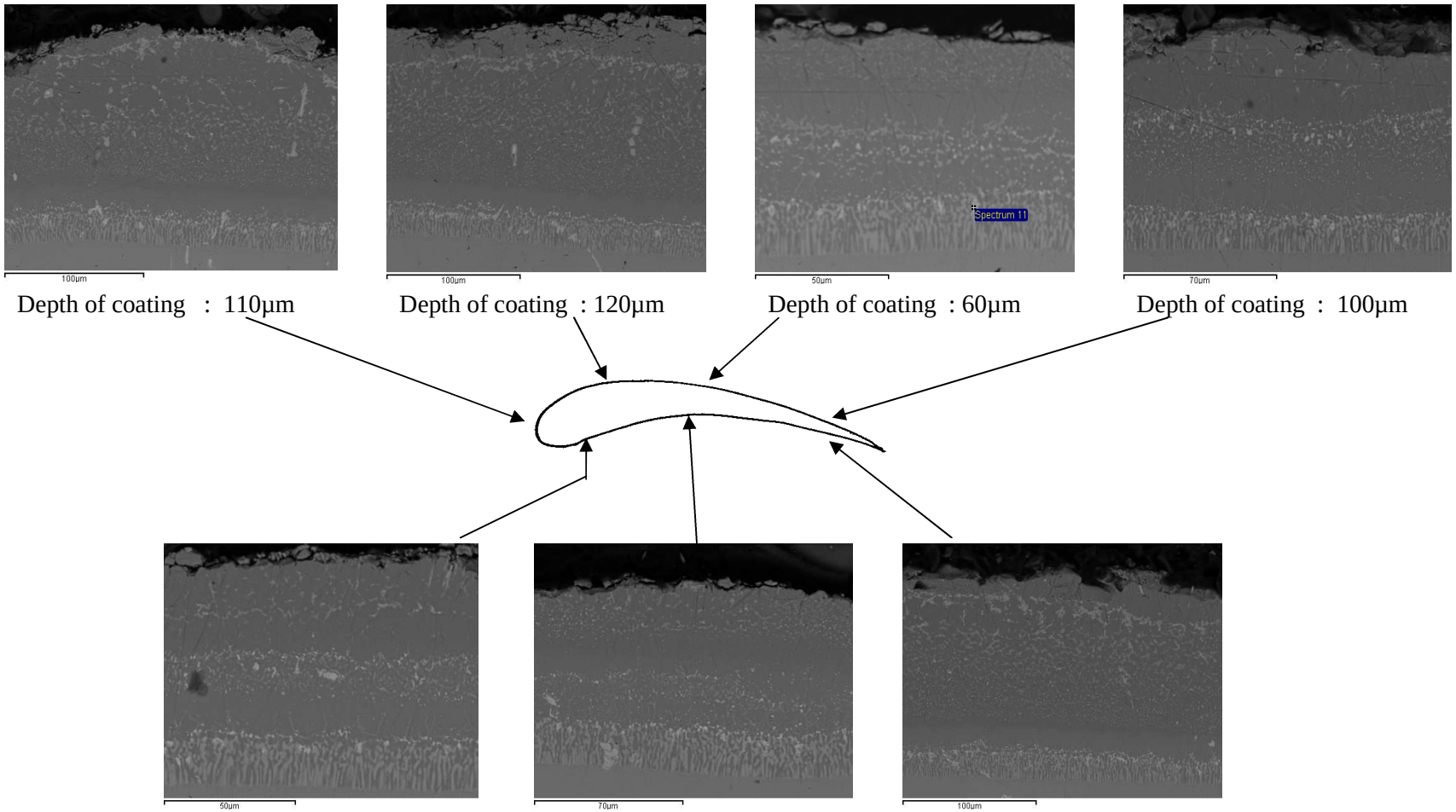

Figure 11.4: BSE images of the top of four sections through IN738LC LP blade with SiAl1 coating

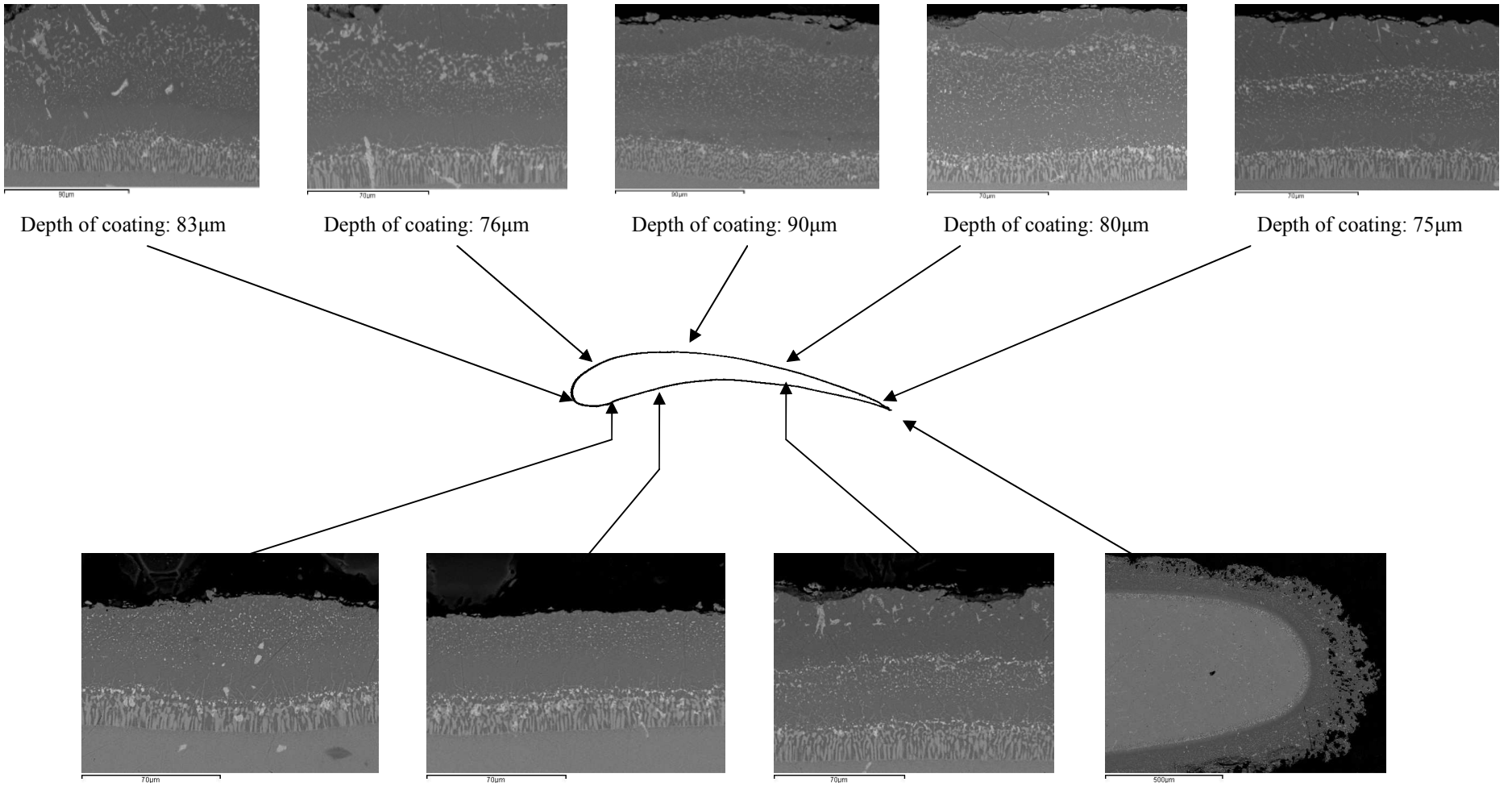

Notes: (i) depths rounded to nearest 5µm, depths measured to top of interdiffusion zone,
(ii) images are to different scales

Figure 11.5: BSE images of the bottom of four sections through IN738LC LP blade with SiAl1 coating

11.3.3 TBC coating and bonding evaluation

11.3.3.1 TBC – coating morphology

As shown in Figure 11.6, the TBC columnar structure is uniform. This uniformity continues around the blade profile, as seen in the BSE images at sites around the blade peripheries of the top section, in Figures 11.7 and in the bottom section, in Figure 11.8. TBC depths are generally uniform around the convex, outer profile of the blade, of the order of 175µm, higher up the blade, and varying between 150µm and 160µm lower down the blade. On the inner, concave surface of the top section, seen in Figure 11.7, the TBC depth is 150µm which increases uniformly to 180µm in the vicinity of the trailing edge. However, lower down the blade, as seen in Figure 11.8, the depth of the TBC along the inner surface of the TBC is 130µm.

The columnar structures at sites around the blade profile, seen in the BSE images in Figures 11.7 and 11.8, are perpendicular to the SiAl1 coating and TBC interface around the outer, convex blade profile. On the concave, inner profile, under the blade leading edge, the columns are slightly skewed, as seen in Figure 11.6(b). This degree of skewing is similar at different blade heights above the base. Where columnar perpendicularity is critical to the strain tolerance and erosion resistance of the TBC, then a means of profile following during the EB-PVD process could correct the skew.

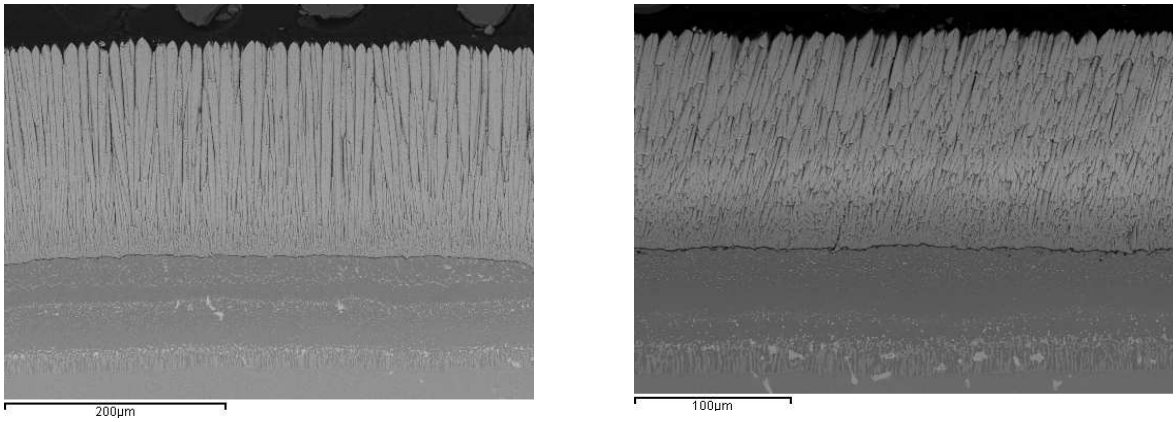

(a) perpendicular columns (b) skewed columns

Figure 11.6: IN738LC turbine blade with TBC applied by EB-PVD – BSE images of peripheral sites with perpendicular and skewed columnar structures

In Figure 11.6(b), the location of the thermoluminescent indicator is readily apparent whereas it is not so pronounced in (a). This variation is apparent in other images in Figures 11.7 and 11.8, most likely due to fine differences in adjusting contrast during SEM evaluation. Element maps shown in Figure 11.9 confirm the overall, consistent morphology of both TBC and SiAl coatings. The zirconium and yttrium maps show good uniformity and both exhibit a ‘shadow’ coinciding with the position of the dysprosium layer. The dysprosium map does not clearly define the 20µm depth of this layer. This may be due to the diffusion effects as the EB-PVD process proceeds through the different layers of the segmented ingot, or illustrate limitations in the SEM/EDX analysis systems.

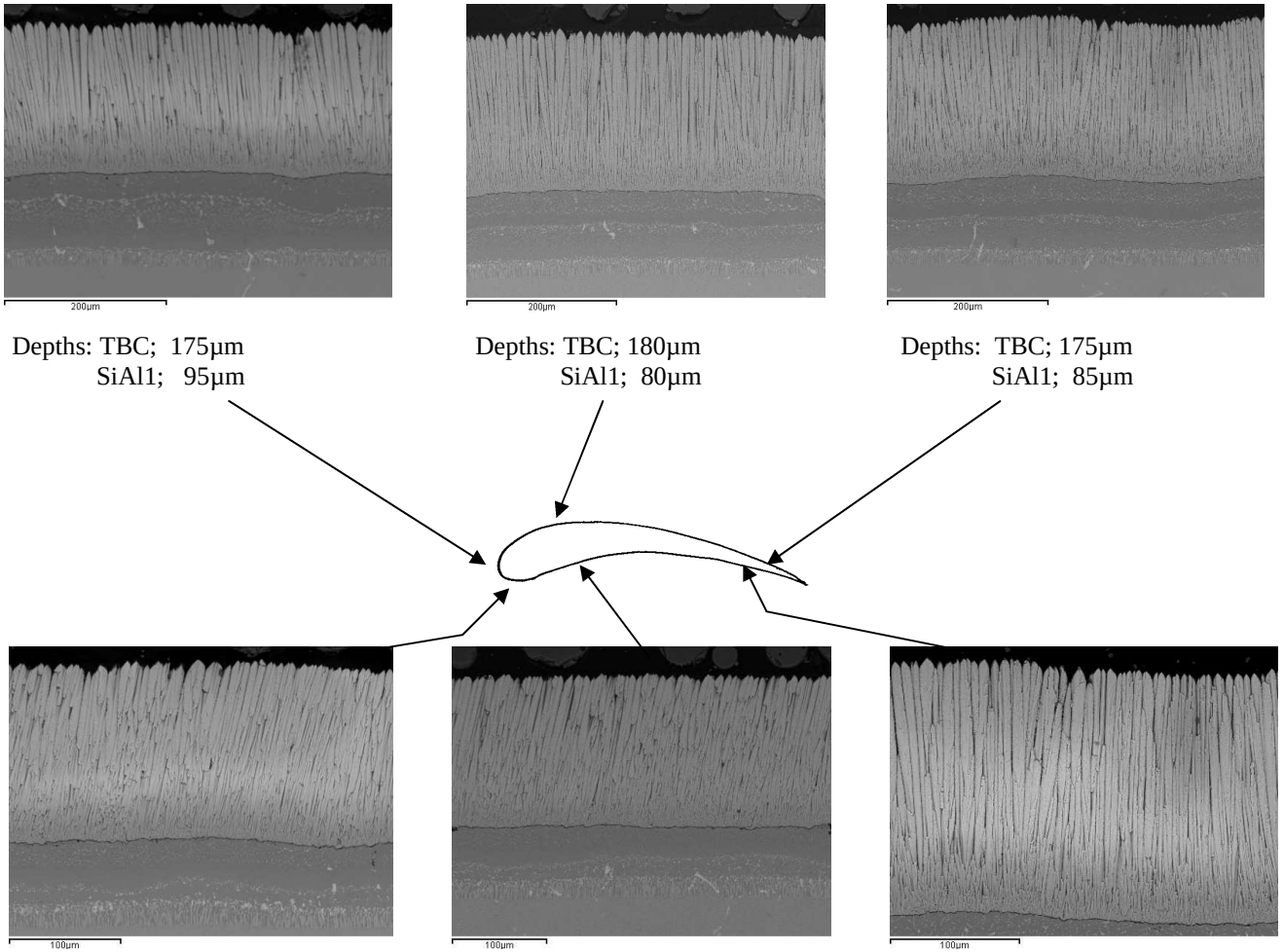

Figure 11.7: BSE images of the top of four sections through IN738LC LP blade with SiAl1 coating and TBC

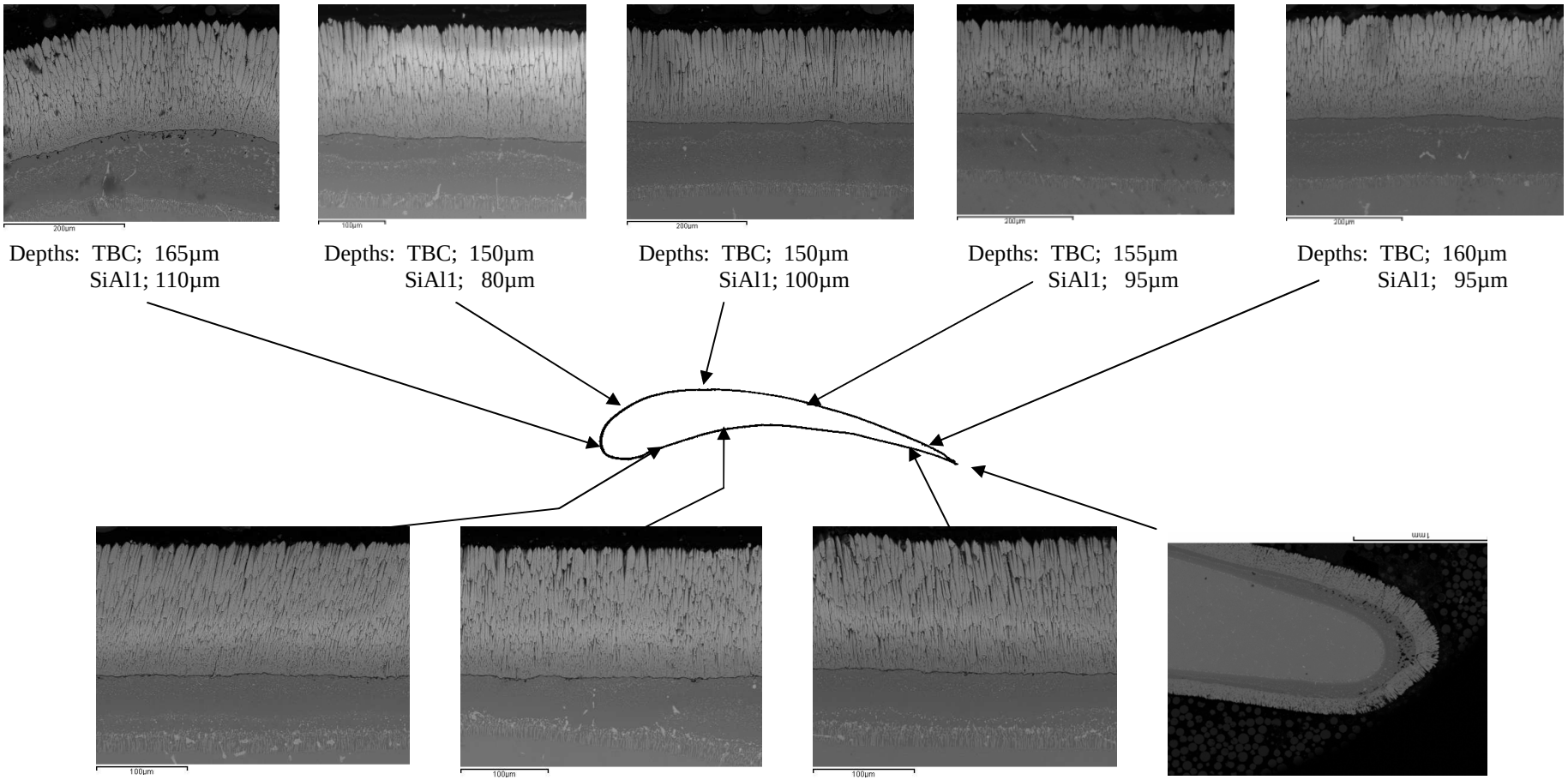

Notes: (i) depths rounded to nearest 5µm, depths measured to top of interdiffusion zone,
(ii) images are to different scales

Figure 11.8: BSE images of the bottom of four sections through IN738LC LP blade with SiAl1 coating and TBC

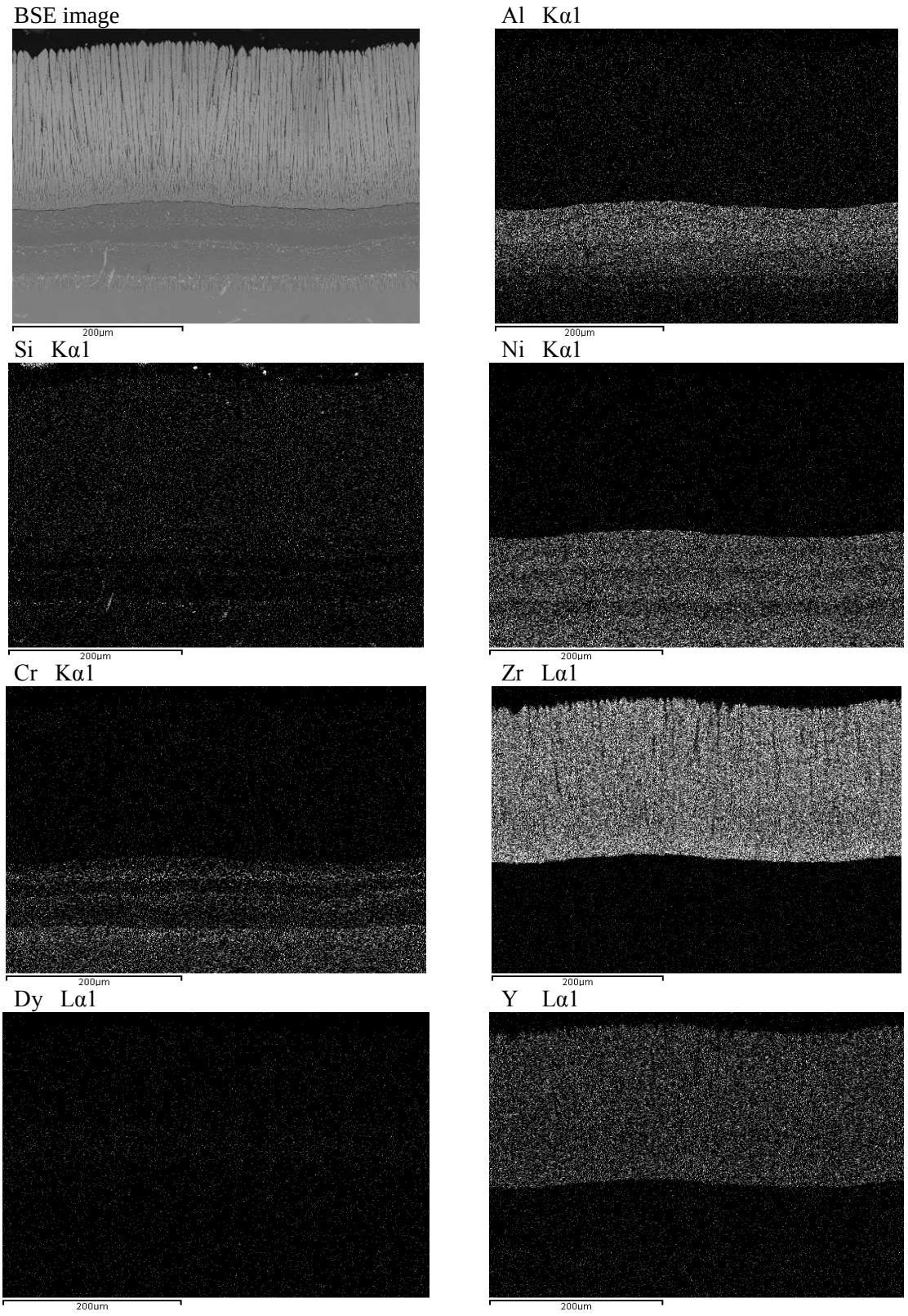

Figure 11.9: IN738LC blade with SiAl1 coating and TBC – element maps

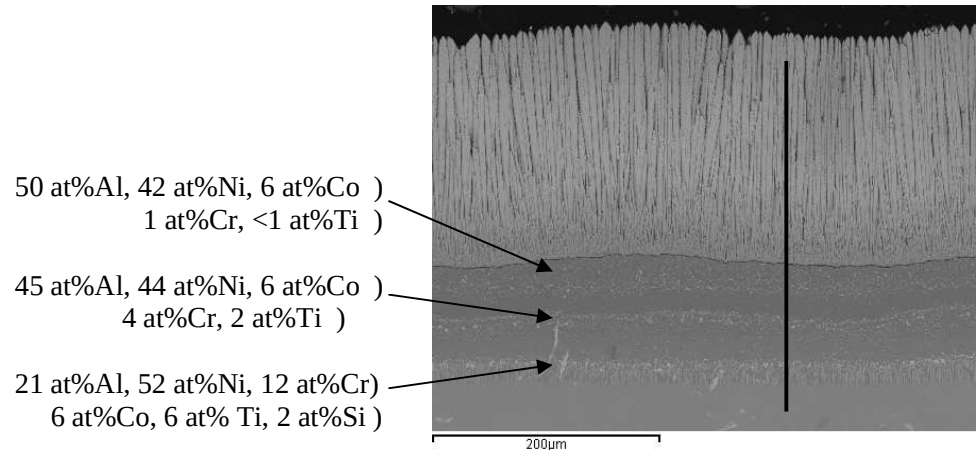

Figure 11.10: IN738LC blade with SiAl1 coating and TBC – elements in SiAl1 coating and line of EDX scan through both coatings

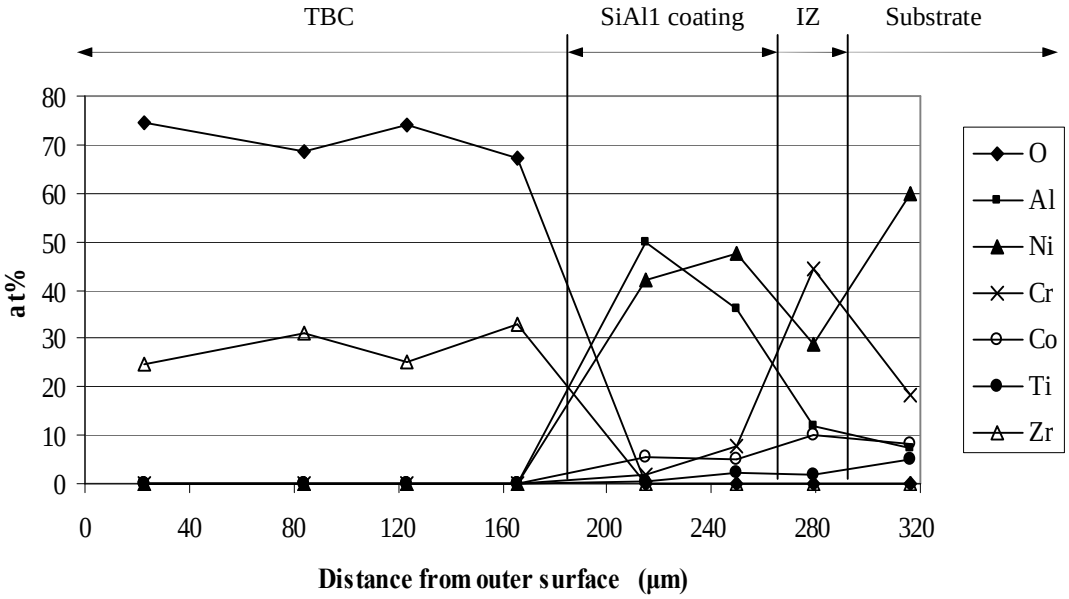

Note: IZ; interdiffusion zone

Figure 11.11: IN738LC blade with SiAl1 coating and TBC – main elements along EDX scan line shown in Figure 11.10

The elements seen in Figure 11.10 show the NiAl matrix through the silicon-aluminide coating and, in the same coating, outward diffusion at reducing rates, of titanium, chromium and cobalt. These trends are confirmed by the elements shown along the EDX line in Figure 11.11. The BSE image shown in Figure 11.12 illustrates the structure of the TBC and clearly shows the dysprosium layer.

In the element maps of the TBC, seen in Figure 11.13, the distribution of dysprosium is less definitive, but there is some indication of its denser layer towards the TBC/SiAl1 coating interface.

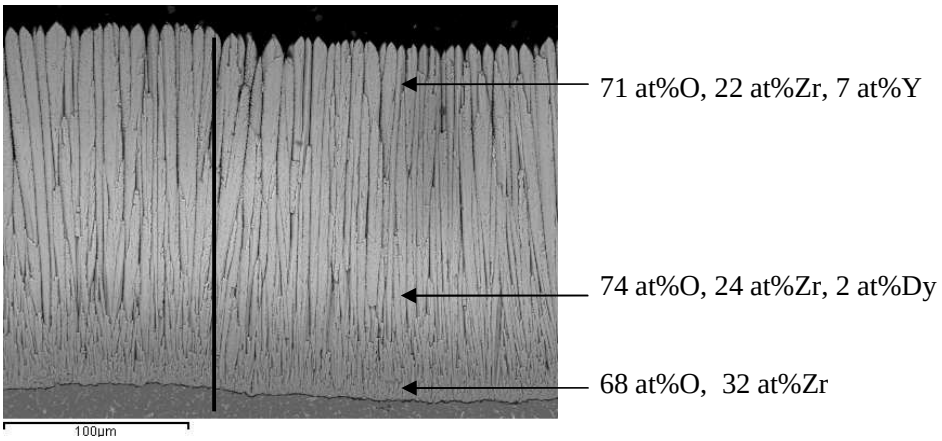

BSE image with EDX line

Figure 11.12: IN738LC blade with SiAl1 coating and TBC with thermoluminescent dopant – element spectra and EDX line in the TBC

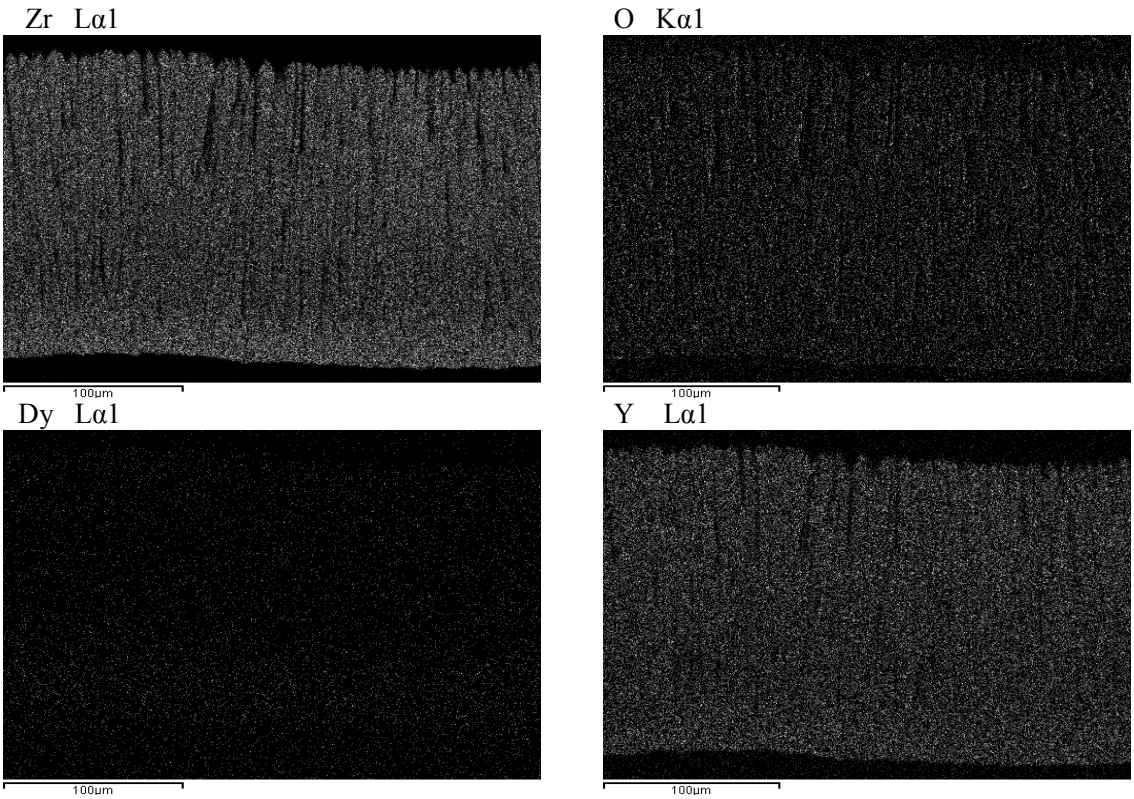

Figure 11.13: IN738LC blade with SiAl1 coating and TBC with thermoluminescent dopant – maps of TBC elements

11.3.3.2 Effectiveness of TBC bonding onto silicon-aluminide coating

Bond coat oxidation has been identified as a major factor which influences the durability of a TBC system. In this regard, Nicholls has explained that EB-PVD coatings tend to fail at the alumina-scale /bond-coat interface unless there is substantial surface rumpling to provide horizontal constraint, at which point failure may transfer to the interface between the ceramic and thermally grown oxide (TGO) [127]. The failure at this interface results from progressive reduction in adhesion as microcracks form and grow. This points to oxidation of the bond coat being a major driver in the failure of EB-PVD TBCs. The oxide growth rate is reasonably constant for all alumina-formers if α-alumina is formed at the ceramic/bond-coat interface, but the critical issue is to what extent, during service, the TGO can resist spallation caused by defect formation, microcrack growth and adhesion loss. In service, the critical issues are the ease of void formation at the bond-coat to TBC interface, how readily less-protective oxides form under/above the alumina scale and how easily debonding occurs at the bond-coat to TBC interface. Over recent years, to overcome these problems, improvements in surface treatment have included diffusion of platinum into single-crystal substrate surfaces, to prevent or delay these degradation processes, resulting in stronger bond-coat systems that provide high creep strength to resist 'rumpling' [127].

The objective in relation to TBC bonding in this section, is to evaluate whether the novel silicon-aluminide coating developed in this project, to protect against hot corrosion in gas turbines burning biomass and waste-fuels, will provide effective TBC bonding without involving any additions to prevent surface defects occurring, to improve TBC adhesion.

Evaluation of the bonding effectiveness of the coating here is limited to examining the microstructure in the region of the SiAl1 coating and TBC interface, including the TGO. Cyclic oxidation testing of the IN738LC blade with SiAl1 coating and TBC does not form part of this project. Figure 11.14 shows a BSE image of the interface region, at x3500 magnification. The image includes element analyses at specific sites in the region.

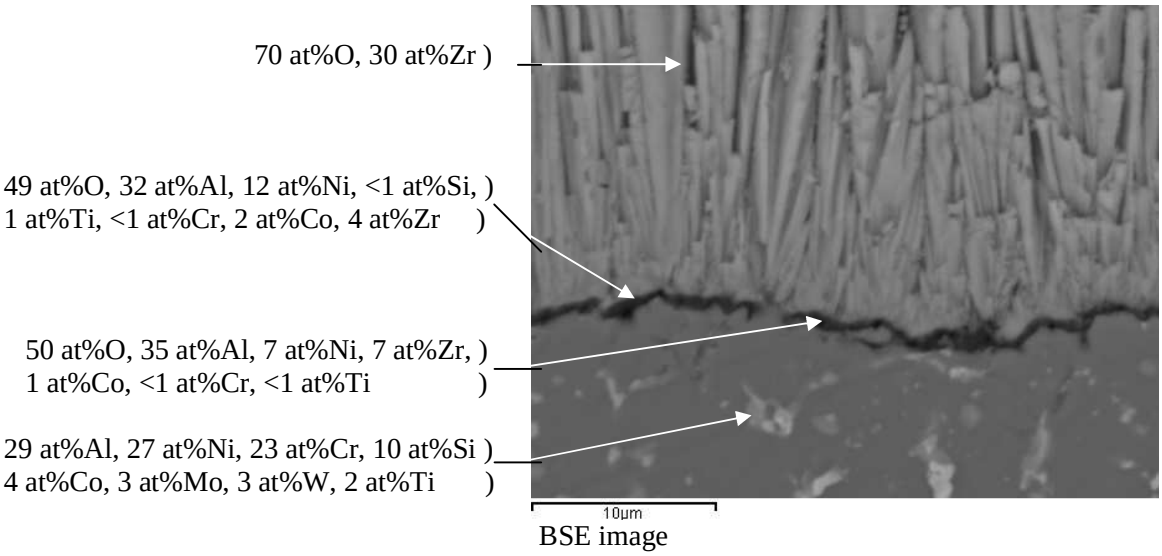

Figure 11.14: BSE image of the TGO interface between the TBC and SiAl coating

TGO sites in Figure 11.14 are predominantly alumina which will provide effective bonding. The site in the SiAl1 coating shows particles, rich in chromium, silicon, cobalt, molybdenum, tungsten and titanium occur which are.randomly distributed. The SiAl1 matrix mainly comprises β-phase NiAl. Another benefit of the silicon-aluminide coating is that silicon forms stable silicide phases with elements which are deleterious to the TGO, such as titanium, tantalum, tungsten, molybdenum and chromium, thus preventing their outward diffusion and contamination of the TGO [98]. No voids are apparent in the BSE maps. The schematic diagram in Figure 11.15 shows the TGO and elements within the region of interfaces with the TBC and SiAl hot corrosion protective coating.

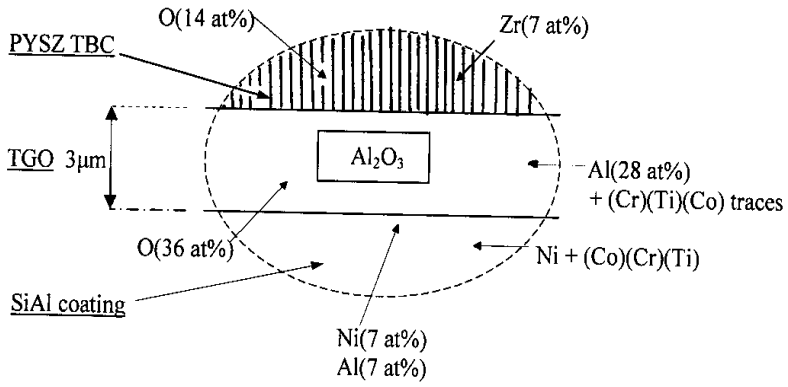

Figure 11.15: Schematic diagram of the TGO region of the TBC and SiAl coating, seen in Figure 11.14

11.4 TBC trial - conclusions

From evaluation of the results of this TBC trial it is concluded that the novel silicon-aluminide diffusion coating developed in this project provides:

- a hot corrosion resistant coating of adequate depth and uniformity on an IN738LC turbine blade;
- effective bonding of a PYSZ TBC applied onto an IN738LC turbine blade by EB-PVD, without requiring additional bonding treatment being needed.

12. Summary of the research completed

12.1 Project strategy and research activities

The objective of this research programme was to develop coatings to provide hot corrosion protection for gas turbines burning biomass and waste-fuels. To achieve this objective required original research and laboratory work in the following areas:

- To identify the contaminants contained in fuel gases produced by the gasification of biomass and waste fuels, which had the potential, when combusted in the gas turbine, to initiate hot corrosion in gas path components;
- To carry out corrosion tests on superalloys and typical commercial hot corrosion protective coatings used in gas turbines, to confirm whether or not hot corrosion would be initiated by the identified contaminants;
- To develop novel coatings, to provide hot corrosion protection for gas turbines fuelled by the gases containing the contaminants which had initiated hot corrosion in commercial coatings, during the previous corrosion tests;
- To carry out cyclic oxidation tests and types I and II corrosion tests on the developed novel coatings to evaluate their hot corrosion resistance and to compare them with results of previous corrosion tests on commercial coatings;
- To assess the effectiveness of novel coatings to bond EB-PVD TBCs without additional bonding processes being necessary, a desirable feature in hot corrosion resistant coatings developed for use on turbine blades and vanes.

A minimal cost approach was adopted in developing the novel coatings to protect against hot corrosion. This aimed at minimising the number of processes, and lowest CVD soak temperatures and soak periods, required to produce effective coatings. The measure for assessing the levels of hot corrosion protection provided by the novel coatings was that they should be comparable to those provided by commercial coatings developed for gas turbines burning fossil fuels. This chapter reviews the results of this research in the context of the project objectives.

12.2 Hot corrosion in gas turbines fuelled by biomass and waste fuels

The IGCC plant and operating parameters selected for this project was similar to that installed in the Varnamo Maintenance-IGCC Demonstration Plant in Sweden. This plant, designed to generate 6 MW of electricity and 9 MW of heat for district heating, had proved the IGCC concept, burning wood fuel in an air-blown, pressurised circulating-bed gasifier (Figures 2.1, 2.3). The main results of this demonstration/development programme showed that high pressure gasification technology works, gas produced can be burnt in a gas turbine under stable conditions, that gas filtration is efficient and reliable and, that the technology is capable of gasifying “difficult fuels” [8,9].

In this project, similar operating parameters were assumed with the exception of a higher gas cleaning temperature (500°C compared with 400°C), with a view to optimising cycle efficiency.

The first research activity identified the contaminants in gases produced by the gasification of biomass and waste fuels which, after gas cleaning at 500°C, could be carried through for combustion in the gas turbine(s) of the IGCC power generating units. The potential of these contaminant species to form molten surface deposits on gas turbine high temperature components and thereby initiate hot corrosion, was investigated using the MTDATA software to make multiphase and multi-species thermodynamic assessments. These were based on the assumptions:

- gas could contain vapour phase contaminant trace species,
- trace species could pass through to gas turbine after gas cleaning,
- trace species could condense to form molten deposits after combustion

From these assessments, cadmium and lead species were identified as having the potential to initiate hot corrosion (see Chapter 5 for results and detailed discussion). The next research activity was to carry out corrosion tests, involving these species, to establish whether they would initiate hot corrosion in superalloys and commercial coatings. The first series of Type II hot corrosion tests were carried out on three superalloys of differing properties; the more hot corrosion resistant IN738LC and IN939 and the strongest but less hot corrosion resistant CMSX-4. Five salt combinations were applied in the 5x100 hour tests:

- $CdSO_4$
- $CdSO_4(50) + (Na_2SO_4(80)+K_2SO_4(20))(50)$ – referred to as Cd+alkali
- $(Na_2SO_4(80)+K_2SO_4(20))$
- $PbSO_4$
- $(PbSO_4(50) + (Na_2SO_4(80)+K_2SO_4(20))(50)$ – referred to as Pb+alkali

High salt fluxes were applied (see Chapter 6 for results and detailed discussion). In summary, at 700°C, of the five salt combinations applied in the tests, when applied individually, $CdSO_4$ and $PbSO_4$ initiated negligible levels of hot corrosion on the superalloys. $(Na_2SO_4(80)+K_2SO_4(20))$ initiated the heaviest hot corrosion. Cd+alkali caused damage to CMSX-4 but not to IN738LC or IN939. Pb+alkali caused significant hot corrosion in all the superalloys, with CMSX-4 being the worst. IN939 was more corrosion protective than IN738LC, for alkali containing samples, reflecting their respective chromium contents. However, Figure 12.1, which plots chromium content against depth of corrosion, is not significant for samples subject to $CdSO_4$ and $PbSO_4$ alone, pointing to differences in their impact on the melting point of the deposit. From this it is possible to speculate that cadmium for Cd+alkali and lead for Pb+alkali are beneficial in reducing corrosion. This would require further research. Overall, the tests showed that $CdSO_4$ initiated the least hot corrosion in IN738LC and IN939, whereas $PbSO_4$ caused the least corrosion on CMSX-4. In all tests, there was little spallation.

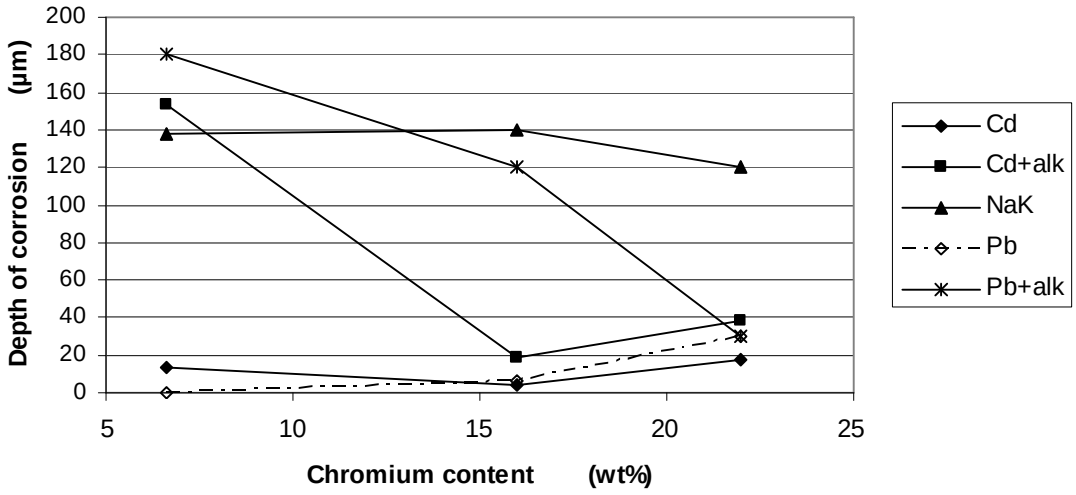

Figure 12.1: Type II corrosion tests on superalloys, depths of corrosion plotted against chromium content

The Type II hot corrosion tests on the commercial coatings GT29+, RT-22 and Sermaloy 1515, when applied to IN738LC and CMSX-4 were completed (see Chapter 7 for results and detailed discussion). The implication is that Cd+alkali is less corrosive than Pb+alkali on chromia formers, whereas Cd+alkali and Pb+alkali are very similar on alumina formers. In summary these tests showed that the Cd+alkali deposits were more aggressive than the Pb+alkali deposits and that GT29+ and RT-22 were more corrosion resistant than Sermaloy 1515. See 12.4.2 for more detailed discussion.

Both series of corrosion tests confirmed that the species identified, together with other alkali species contained in biomass and waste fuels, when combusted in typical gasifier gases, did initiate Type II hot corrosion.

12.3 Development of single-step silicon modified aluminide coatings

(see Chapter 8 for results and detailed discussion)

The direction of novel coating development was initially determined by the requirement that internal cooling air passages of blades and guide vanes should be coated. CVD has the potential ability to coat all surfaces of a component and was the practical route to achieve this. The most common and inexpensive coating, used by gas turbine manufacturers to enhance hot corrosion protection, based on aluminide diffusion, was adopted in this project. To improve on the limited thickness of aluminide coatings that can be achieved in practice, alternative methods of modifying aluminide coatings, by using platinum, chromium and silicon, were considered. Given the need to coat internal cooling passages as well as external surfaces, platinum was ruled out and chromium modification did not provide adequate cyclic oxidation protection. Silicon modified aluminide coatings were therefore adopted for developing novel, hot corrosion protective coatings in this project.

Two routes for manufacturing silicon-aluminide coatings were considered; two-step siliconising followed by aluminising or a single-step silicon-aluminising process. Previous research at Cranfield had showed no overall superiority of either process, but on the bases of the single-step process offering good hot corrosion protection and lower risk and cost, this was selected for coating development. The Cranfield CVD equipment was used for novel coating development, with superalloy samples buried in low activity powder packs containing alumina, aluminium, silicon and the activator aluminium fluoride. In order to avoid any cracking caused by excess silicon, the powder contained <10 at%Si, the proportions decided after MTDATA assessments. In all trials, IN738LC and CMSX-4 samples were coated.

The first four aluminising CVD trials had the same soak temperature of 1050°C, and soak periods of one-, two-, four- and eight-hours duration. After CVD, half samples were examined without heat treatment, the other half being heat treated prior to examination. It was concluded from the aluminising trials that microstructures were similar and stable for IN738LC and CMSX-4, irrespective of CVD soak time. Average depths of coatings on IN738LC, ranged from 46μm for the one hour CVD process, to 62μm for eight hours CVD. For CMSX-4 samples, depths ranged from 53μm for the one hour CVD run to 94μm, for the eight hours CVD run. The silicon-aluminising trials commenced with one hour CVD soak periods, at soak temperatures of 800°C, 850°C and 1050°C, to explore whether adequate coatings would be produced at lower process cost. The lower temperatures produced coatings of inadequate depth and stability, which led to the next series of trial CVDs, all at 1050°C, but with soak periods of fifteen minutes and thirty minutes. The silicon-aluminising trials showed that the coatings expected to offer the best hot corrosion protection, for both IN738LC and CMSX-4, were those produced at a CVD soak temperature of 1050°C. Each of the three coatings had stable aluminium-rich β-phase NiAl of sufficient depth to maintain protection and extend the initiation stage of hot corrosion. Enhanced hot corrosion resistance could also be expected from the outward diffusion of chromium and cobalt, from the substrates into these coatings.

Based on these trials the three silicon-aluminised coatings, produced by CVD at 1050°C, were selected to evaluate the protection they provide, when compared with that provided by commercial coatings.

12.4 Novel silicon-aluminide coating performance

12.4.1 Oxidation protection (see Chapter 9 for results and detailed discussion)

The performance of novel silicon-aluminide coatings was evaluated by testing their resistance to cyclic oxidation and to both type I and type II hot corrosion. Post-testing evaluation consisted of mass change measurements, changes in sound metal and assessing the morphology of residual coatings. Two series of cyclic oxidation tests were carried out, consisting of 100 hours exposure, with weighing at laboratory temperature before and after each exposure period. In the first series, at 950°C, after 1000 hours of oxidation testing, gradients of mass changes were similar for IN738LC and CMSX-4 substrates, irrespective of CVD soak periods.

Spall mass of coated samples of CMSX-4 were significantly higher than those for samples of IN738LC, but was not influenced by CVD soak periods. As the coatings had not degraded significantly after 1000 hours of cyclic oxidation testing at 950°C, the second series, at 1050°C, was started. Over the first 100 hours of testing, the gross mass changes of all the coated IN738LC samples ranged from 0.4 mg/cm^2 to 1.2 mg/cm^2, but did not vary in proportion to CVD soak periods. During the testing periods from 100 hours to 1000 hours, the increasing mass changes of all IN738LC samples followed similar kinetics. Similarly, for CMSX-4 samples, during the initial 100 hours, the gross mass changes ranged from 0.4 mg/cm^2 to 1.6 mg/cm^2. However, during the oxidation testing from 100 hours to 900 hours, the gross mass changes of CMSX-4 samples with the coatings formed from 15 minutes- and 30 minutes- CVD, degraded at higher rates than others coated by 60 minutes CVD. At this point the curve of the second IN738LC sample coated from 60 minutes-CVD remained parabolic from 100 hours to 1000 hours.

After 1000 hours of oxidation testing, the worst performer of each CVD coating period was selected for continuing cyclic oxidation testing at 1050°C, to failure. The samples of IN738LC and CMSX-4 coated from 15 minutes- and 30 minutes-CVD failed, shown by the net mass crossing the zero-line, at intervals from 700 hours (CMSX-4, 15 minutes CVD), 950 hours (IN738LC, 30 minutes CVD, 1700 hours (IN738LC, 15 minutes CVD) and 2050 hours (CMSX-4, 30 minutes CVD). Of the two samples formed from 60 minutes CVD, the CMSX-4 sample failed after 2850 hours, whereas the IN738LC sample had not failed after 3000 hours, the point at which testing was stopped. Examinations of microstructures showed that, in all cases, the depths of coatings on the top sides of samples were significantly less than those of the bottom sides. These differences resulted from the top sides of samples being exposed to gas entry and exit (during vacuum raising), whereas the bottom side was not. Improved oxidation resistance would be achieved if the depth of the top side could equal that of the bottom. The inadequacies in powder pack CVD could be overcome by gas phase CVD.

XRD analyses identified remanent coatings in samples formed from 30 minutes CVD, confirming that although heavy spalling had occurred, the coatings were not completely degraded. Deeper remanent coatings were present on the samples formed from 60 minutes CVD. Cyclic oxidation tests also showed that IN738LC with the silicon-aluminised coating formed from 60 minutes CVD at 1050°C was more oxidation resistant than CMSX-4 with the same coating. CMSX-4 samples had also been significantly degraded by TCP phases which would impair their mechanical integrity and viable remanent life.

12.4.2 Type II hot corrosion protection (see Chapter 10 for results and detailed discussion)

The next stage in evaluating performance of the novel, single-step silicon-aluminide coatings was to subject the coatings formed from 60 minutes CVD, considered to be viable after cyclic oxidation tests, to Type II and Type I corrosion tests.

The low temperature hot corrosion (LTHC) tests were carried out at 700°C, comprising five periods of 100 hours exposure, with the same; substrates, gas composition, salt solutions and salt fluxes, as those used in the corrosion tests on commercial coatings, reported in Chapter 7.

These enabled direct comparisons to be made between the performances of the novel silicon-aluminide coatings and commercial coatings. The only differences between the two series of corrosion tests was the use of discs of superalloys in the later tests, compared with the cylindrical form used in the tests on commercial coatings. Coatings on the cylindrical samples would be of uniform depth, whereas, as mentioned above, coating depths on the top and bottom sides of discs varied, as did depths at the edges. In both series of corrosion tests on novel coatings, a second novel, single-step silicon-aluminide coating was included, to provide more information on the merits of additional silicon. The second coating was produced by CVD, with one hour soak period and soak temperature of 1050°C, but with an increased silicon content and commensurate reduction in alumina.

After 500 hours corrosion testing at 700°C the novel silicon-aluminide coatings continued to provide protection against Type II hot corrosion for IN738LC and CMSX-4. Although there were differences in oxidation and sulphidation rates between the substrates, there continued to be sufficient aluminium in the coatings and chromium outwardly diffused from the substrates, to support growth of the protective scale. The exception to this situation was the higher salt flux Cd+alkali salt combination on CMSX-4, where propagation had commenced after 500 hours of testing. Spalling rates for IN738LC were significantly lower than those for CMSX-4. The spalling rates for the higher silicon containing novel coatings were greater than those of the lower content silicon coatings. As the higher silicon content novel coatings were of lesser depth and spalled more, they provided no advantage over the lower silicon containing coatings. Both novel silicon-aluminide coatings were more resistant to Type II hot corrosion for Pb+alkali species than for Cd+alkali species. This was in contrast to the commercial coatings which were more resistant to Type II corrosion for the Cd+alkali species. The Type II hot corrosion tests showed that, on coated IN738LC, both novel silicon-aluminide coatings were less degraded than the commercial coatings; GT29+, a CoCrAlY overlay coating having a diffusion aluminide top layer, RT-22, a platinum aluminide coating and Sermaloy 1515, a triple layered silicon aluminide coating. For CMSX-4, the two novel, silicon-aluminide coatings are more Type II hot corrosion protective than Sermaloy 1515 except in the low salt flux samples of both salt combinations, where the lower silicon novel coating provides similar levels to those of GT29+ and RT-22. Although both novel silicon-aluminide coatings provide more protection to type II hot corrosion than the commercial coatings tested, the higher silicon novel coating was more protective of CMSX-4 samples than those of IN738LC.

Comparisons of Type II hot corrosion resistance of the novel coatings and commercial coatings which are discussed above, are shown visually in the following series of bar-charts. These are included to assist comparison of the hot corrosion resistance provided by the novel coatings to that provided by typical hot corrosion protective commercial coatings, a major objective in the development of novel coatings in this project.

The bar charts for the commercial coatings in Figures; 12.2, 12.3, 12.4 and 12.5 are based on the loss of sound metal results (seen in Chapter 7). These were measured by image analysis (IA) of the cylindrical samples supplied for the corrosion tests and described in sections 4.3.1 and 4.3.4. Bar charts for the novel coating samples are based on similar criteria measured from SEM analyses of the bottom sides of the disc samples and averaged for each substrate.

In all the bar charts, the basic structure of each coating is shown in the reference sample, eg the platinum-aluminide outer layer of RT-22 is defined. The graphs show the reference untested sample for each group on the right hand side, eg the outer aluminide diffusion layer of GT29+ is defined, then the remainder is CoCrAlY overlay. In tested samples the corrosion bar at the top shows the depth of attack through the sample. The bottom bar shows the superalloy.

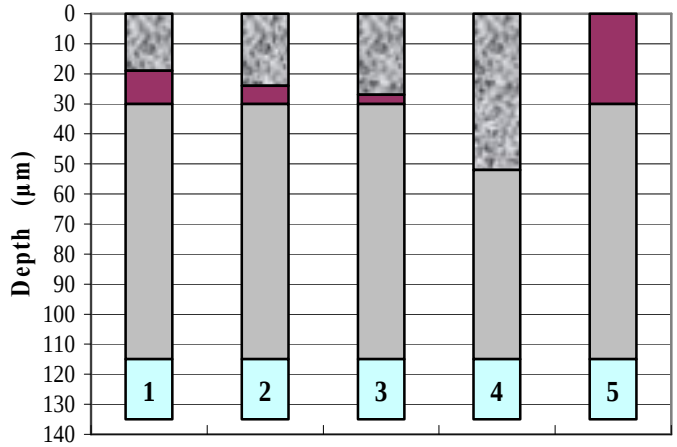

Shading key: - Corrosion - Al diff layer - CoCrAlY - IN738LC

Sample key: 1; Cd+alkali. salt flux, 1.5 µg/cm^2/h
2; Cd+alkali, salt flux, 5.0 µg/cm^2/h
3; Pb+alkali, salt flux, 1.5 µg/cm^2/h
4; Pb+alkali, salt flux, 5.0 µg/cm^2/h
5; Reference sample of GT29+ coating on IN738LC

Figure 12.2: Type II corrosion tests on commercial coatings; GT29+ coating on IN738LC, comparisons with untested reference sample

It can be seen for GT29+ samples that the outer aluminide diffusion layer provides good hot corrosion protection. However, when this layer is fully degraded, the rate of corrosion in the overlay section is more rapid. Similarly, although the platinum rich outer layer of RT-22 is highly protective, in both high salt flux samples, over 70% of this layer has been degraded. When fully degraded, the rate of hot corrosion in the aluminide diffusion section can be expected to increase. This increase may be less than that in GT29+ however, as the aluminide diffusion section of RT-22 contains some platinum.

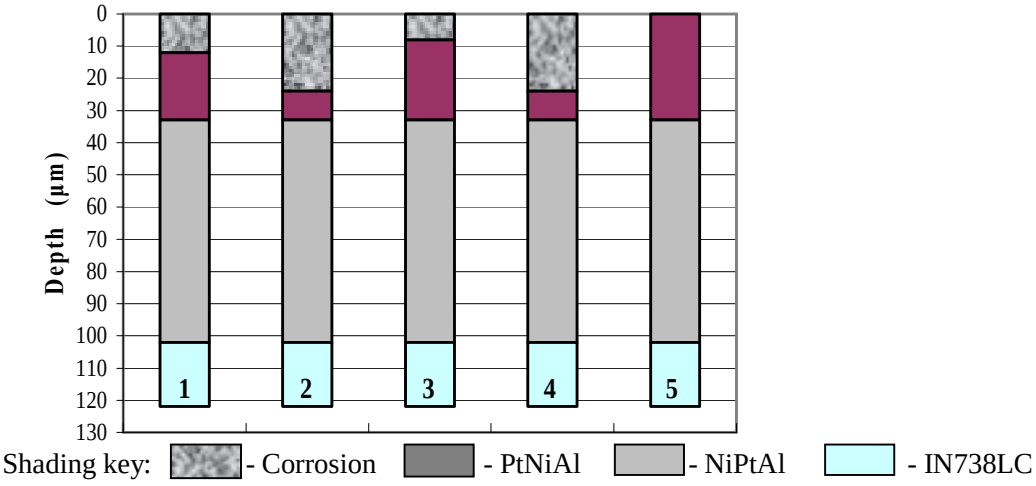

Sample key: 1; Cd+alkali. salt flux, 1.5 µg/cm^2/h
2; Cd+alkali, salt flux, 5.0 µg/cm^2/h
3; Pb+alkali, salt flux, 1.5 µg/cm^2/h
4; Pb+alkali, salt flux, 5.0 µg/cm^2/h
5; Reference sample of RT-22 coating on IN738LC

Figure 12.3: Type II corrosion tests on commercial coatings; RT-22 coating on IN738LC, comparisons with untested reference sample

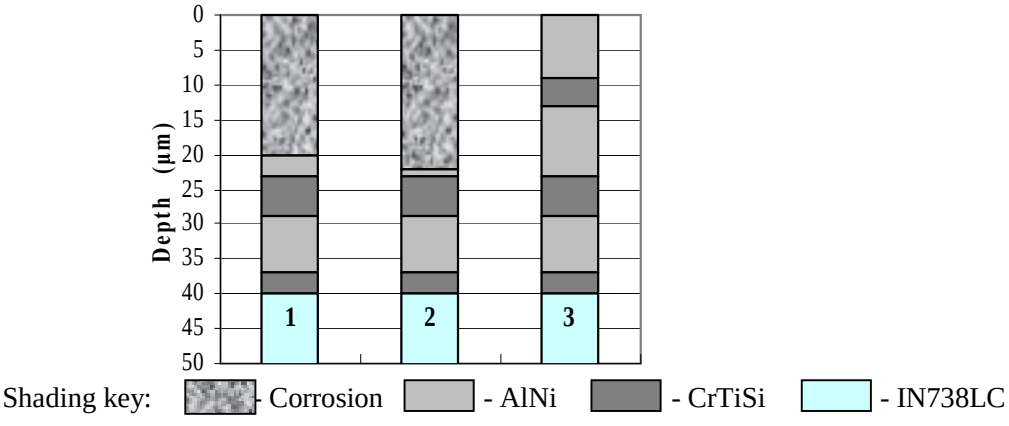

Sample key: 1; Cd+alkali. salt flux, 5.0 µg/cm^2/h
2; Pb+alkali, salt flux, 5.0 µg/cm^2/h
3; Reference sample of Sermaloy 1515 coating on IN738LC

Figure 12.4: Type II corrosion tests on commercial coatings; Sermaloy 1515 coating on IN738LC, comparisons with untested reference sample

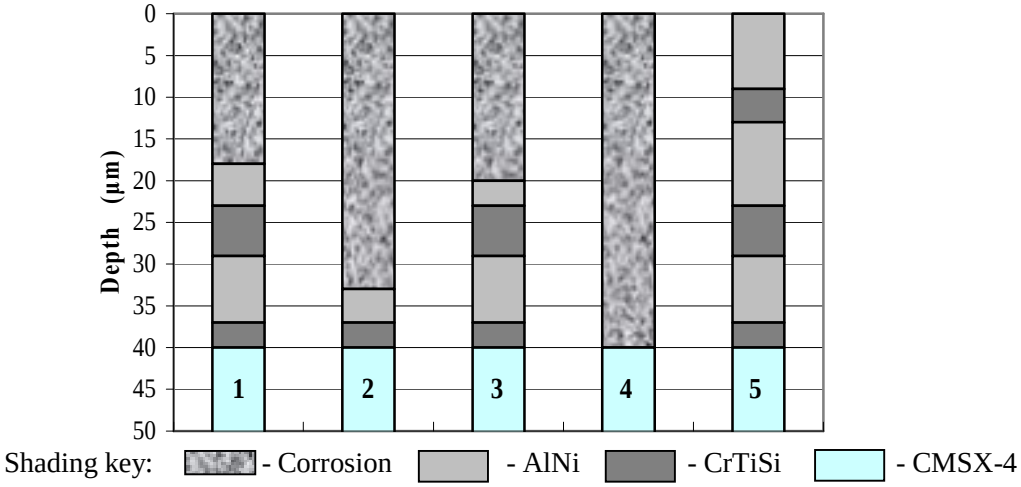

Sample key: 1; Cd+alkali. salt flux, 1.5 µg/cm^2/h
2; Cd+alkali, salt flux, 5.0 µg/cm^2/h
3; Pb+alkali, salt flux, 1.5 µg/cm^2/h
4; Pb+alkali, salt flux, 5.0 µg/cm^2/h
5; Reference sample of Sermaloy 1515 coating on CMSX-4

Figure 12.5: Type II corrosion tests on commercial coatings; Sermaloy 1515 coating on CMSX-4, comparisons with untested reference sample

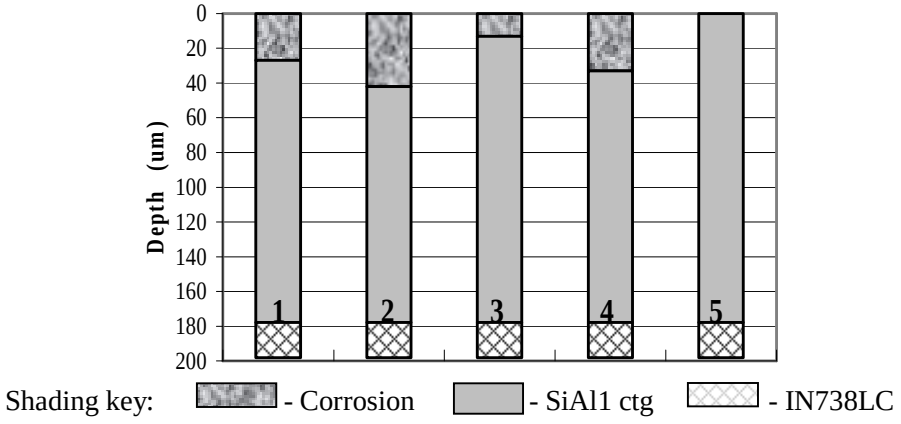

Sample key: 1; Cd+alkali. salt flux, 1.5 µg/cm^2/h
2; Cd+alkali, salt flux, 5.0 µg/cm^2/h
3; Pb+alkali, salt flux, 1.5 µg/cm^2/h
4; Pb+alkali, salt flux, 5.0 µg/cm^2/h
5; Reference sample of novel coating SiAl1 on IN738LC

Figure 12.6: Type II corrosion tests of novel coating SiAl1 on IN738LC, comparisons with untested reference sample

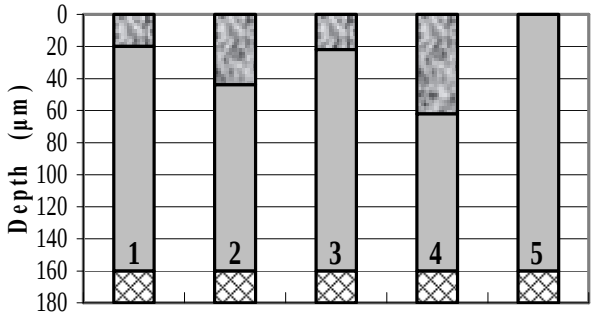

Shading key: - Corrosion - SiAl1 ctg - CMSX-4

Sample key: 1; Cd+alkali. salt flux, 1.5 µg/cm^2/h
2; Cd+alkali, salt flux, 5.0 µg/cm^2/h
3; Pb+alkali, salt flux, 1.5 µg/cm^2/h
4; Pb+alkali, salt flux, 5.0 µg/cm^2/h
5; Reference sample of novel coating SiAl1 on CMSX-4

Figure 12.7: Type II corrosion tests of novel coating SiAl1 on CMSX-4, comparisons with untested reference sample

In Figures 12.6 and 12.7 the greater depths of the novel coatings are apparent, with deep un-degraded sections remaining to provide hot corrosion protection. These enable the novel coatings to offer similar or better hot corrosion protection than the, as tested, commercial coatings. Bar charts showing the percentages of the coatings degraded on IN738LC in the high salt flux Cd+alkali and Pb+alkali tests, on the commercial coatings and the novel SiAl1 coatings, are shown as examples in Figures 12.8 and 12.9.

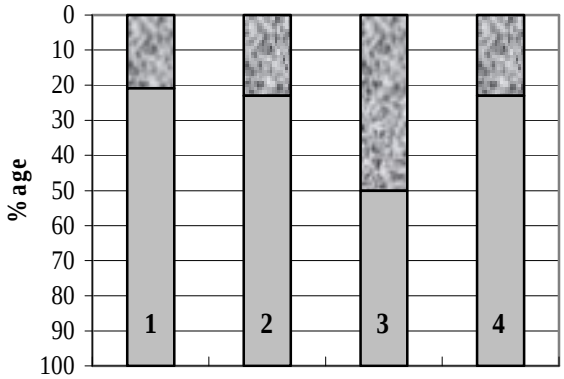

Shading key: - Corrosion - Coating

Coating key: 1; GT29+, 2; RT-22, 3; Sermaloy 1515, 4; SiAl1

Figure 12.8: Type II corrosion tests; percentage corrosion of commercial and novel coatings on IN738LC, subject to Cd+alkali with salt flux of 5.0 µg/cm^2/h

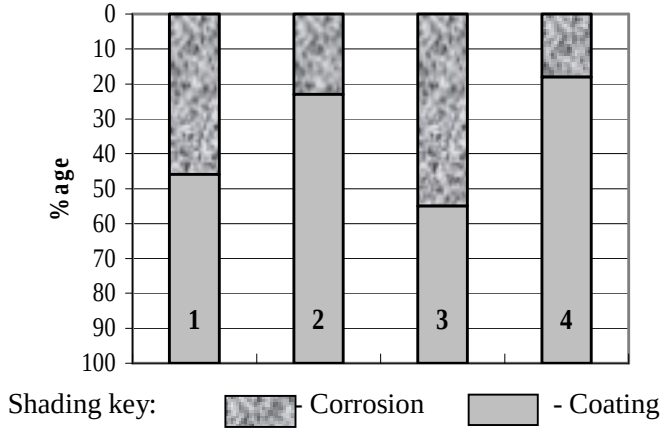

Figure 12.9: Type II corrosion tests; percentage corrosion of commercial and novel coatings, on IN738LC, subject to Pb+alkali with salt flux of 5.0 μg/cm^2/h

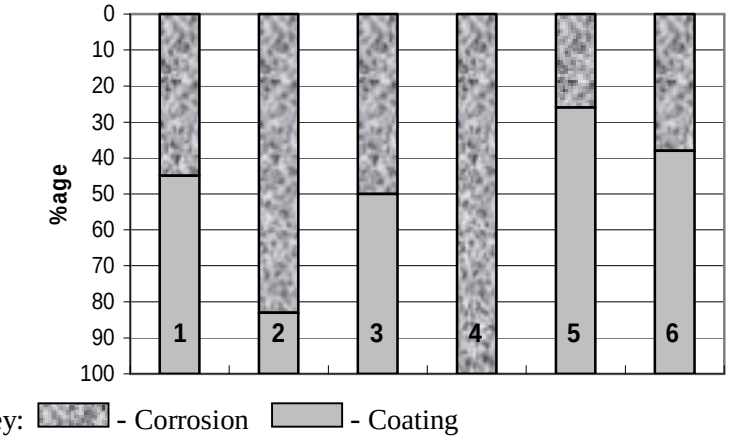

Sample key: 1; Coating Sermaloy 1515, Cd+alkali. salt flux, 1.5 μg/cm^2/h
2; Coating Sermaloy 1515 Cd+alkali, salt flux, 5.0 μg/cm^2/h
3; Coating Sermaloy 1515, Pb+alkali, salt flux, 1.5 μg/cm^2/h
4; Coating Sermaloy 1515, Pb+alkali, salt flux, 5.0 μg/cm^2/h
5; Coating SiAl1, Cd+alkali, salt flux, 5.0 μg/cm^2/h
6; Coating SiAl1, Pb+alkali, salt flux, 5.0 μg/cm^2/h

Figure 12.10: Type II corrosion tests; percentage corrosion of Sermaloy 1515 and novel coating SiAl1 on CMSX-4

The bar charts in Figure 12.10 compare the depths of corrosion on the coating Sermaloy 1515 (as tested) and novel coating SiAl1, when applied to CMSX-4, and show the superior Type II hot corrosion resistance of the novel coating. These bar charts confirm that, for IN738LC, for Cd+alkali, the novel coating SiAl1, provides comparable corrosion resistance as GT29+ and RT-22 coatings but is superior to Sermaloy 1515. However, for Pb+alkali tests, SiAl1 is more protective than any of the commercial coatings tested.

Although there is potential for producing commercial coatings of greater depths, when compared with the single-step silicon-aluminide novel coatings, higher production costs will be incurred. General comparisons of all the bar charts show that the novel coatings provide as good as, or better hot corrosion protection than commercial coatings (as tested) for IN738LC and higher levels of protection for CMSX-4 coated with Sermaloy 1515 (as tested).

12.4.3 Type I hot corrosion protection (see Chapter 10 for results and detailed discussion)

All the novel, silicon-aluminide coatings provided protection against Type I hot corrosion after 500 hours. For both substrates, the higher silicon novel coating provided greater Type I hot corrosion resistance for the Pb+alkali salt combination than for the Cd+alkali combination. The silicon content of the novel coatings has no influence on Type I hot corrosion protection for either low or high salt flux Cd+alkali samples, or for low salt flux Pb+alkali samples. As was seen from the oxidation and type II hot corrosion tests, after 500 hours at 900°C, there were deeper remanent coatings on the bottom sides of samples than those on the top sides. However, in the Type I tests, both IN738LC sample coatings, with lower and higher silicon novel coatings, and subjected to the higher salt fluxes of Pb+alkali, had been heavily degraded. Remanent coatings, following Type I hot corrosion testing for 500 hours, were less degraded than those after Type II hot corrosion testing. This was the case in tests of two-step silicon-aluminide coating tests on CMSX-4 carried out at Cranfield [63]. Outward diffusion of titanium, tungsten and molybdenum were similar in content and distribution, to those resulting from the oxidation and type II hot corrosion tests, reported in 10.2.3.

12.5 **Single-step silicon-aluminide coating – EB-PVD TBC bonding**
(see Chapter 11 for results and detailed discussion)

The final research activity of the project proved that the novel, single-step silicon-aluminide coating could bond a TBC, applied by EB-PVD to IN738LC, without any further bonding process being necessary. This was important because the columnar structure produced by EB-PVD is necessary to counter the high stresses in TBCs on turbine blades. Having EB-PVD TBC bonding capability is an advantage for the novel silicon-aluminide coatings developed in this project, complementing their role in providing hot corrosion protection for turbine blades and vanes. Evaluating the effectiveness of bonding provided by the novel coating was limited here to a metallographic investigation of the TGO region. This showed that the bondcoat developed a stable thin alumina scale during manufacture. Cyclic testing will be necessary, to prove the capability of the TBC bond with the novel coating, under service conditions.

Another feature of this activity was the incorporation of a thermoluminescent layer in the TBC. In this case, the layer will fluoresce under ultra-violet light to show, on-line the state of the TBC, providing a useful maintenance aid for an industrial gas turbine.

13. Conclusions

- Cd+alkali and Pb+alkali species in gases produced by gasification of biomass and waste fuels, following hot gas cleaning, initiated hot corrosion in superalloys and typical commercial, corrosion-protective coatings, when corrosion tested under simulated gas turbine operating conditions. Silicon-aluminide diffusion coatings were most resistant to this form of attack;

- A single-step silicon-aluminising process was developed which was successfully tested in cyclic oxidation, Type I and Type II hot corrosion. The key parameters, with a fluoride-based, low activity powder pack, were CVD temperature and deposition time, to control silicon content and coating depth;

- The results of silicon aluminising CVD trials, with differing CVD soak periods and soak temperatures, of 800°C, 850°C and 1050°C, showed that the optimum coating depth and stable microstructure resulted from a CVD soak period of one hour at a soak temperature of 1050°C;

- Variations in the depths, between the top and bottom sides of samples with silicon-aluminide coatings, were caused by the top sides being open to gas during the CVD operations, whereas the bottom sides had no gas exposure. The top side coating, having less depth, reduced the overall oxidation and hot corrosion resistance provided by these coatings. These variations can be improved, by redesign of CVD powder pack trays, or by adopting gas phase CVD, to equalise the top coating depth with that of the deeper, more protective bottom side;

- The novel, single-step, low activity silicon-aluminide coating, developed in this project, provided good resistance to Type I and Type II hot corrosion, initiated by species in the gases produced from the gasification of biomass and waste fuels;

- Type II hot corrosion tests showed that IN738LC samples, with the novel coating, were less degraded than three commercial coatings; an overlay coating with diffusion aluminide top layer, a platinum-aluminide coating and a triple layered silicon-aluminide coating. For CMSX-4, the novel silicon-aluminide coatings were more protective than the triple layered silicon-aluminide coating and were comparable with the overlay coating with diffusion aluminide top layer and the platinum-aluminide coating. The novel coatings on IN738LC samples were seen to follow parabolic curves of the incubation, or oxidation, stage to 300 hours testing, after which the trends became more linear with similar gradients through to the completion of 500 hours testing. This was the case for CMSX-4 samples, except those subject to the higher salt flux of the Cd+alkali salt combination, which commenced the propagation stage after 100 hours of corrosion testing and continued at similar gradients to the completion of tests. In all samples tested, the remanent novel coatings had retained a stable structure and their integrity to the interdiffusion zone/coating interface;

- Under the more onerous Type I corrosion testing conditions, the mass changes of novel coatings were comparatively low on samples of both substrates, showing that there was little coating damage on average. Over the 500 hours of testing, although the coating structures had been changed by exposure, and exhibited surface damage and localised sites of internal corrosion, they continued to provide protection against Type I hot corrosion. The extent of degradation was not noticeably dependent on salt flux and was similar for Cd+alkali and Pb+alkali salt combinations;

- In Type I and Type II hot corrosion tests, samples coated with the novel silicon-aluminide coating having the higher content of silicon, showed no improvement in hot corrosion resistance, to that of samples coated with the lower silicon content, but had higher spalling rates. The latter disadvantage and higher cost of production, point to the lower silicon content coating being the better prospect for further development;

- In cyclic oxidation tests at 1050°C, the novel silicon-aluminide coatings produced by 60 minutes CVD at 1050°C were more protective than coatings produced by shorter CVD soak periods at the same CVD soak temperature, on IN738LC and CMSX-4 samples. The coatings achieved cyclic lives of 2850 hours on CMSX-4 samples and in excess of the 3000 hours test duration on IN738LC samples;

- Evaluation of EB-PVD TBC bonding trials, on an IN738LC turbine blade coated with the novel, single-step silicon-aluminide coating, showed that the latter had grown a thin, stable alumina based TGO, effectively bonding the TBC. The TBC, mainly PYSZ but containing a layer of dysprosium based thermoluminescent dopant, was distributed uniformly around the blade surface.

14. Further Work

- In this study, identification of potentially damaging contaminants contained in gases produced by gasification of biomass and waste fuels, assumed a hot gas cleaning temperature of 500°C, during the thermodynamic assessments. Subsequent corrosion tests confirmed that hot corrosion was initiated by the species identified. Further work would investigate whether other hot cleaning techniques or direct water cleaning, could significantly reduce the potential contaminants in gases, from these fuels.

- As the development and production of second generation fuels from biomass and waste fuels proceeds, further work would be required to identify the content of trace species produced from such fuels, which may also be harmful in gas turbines. Measurements on operational plants would be particularly valuable and enable models to be validated

- Further work would be required to develop single-step silicon modified aluminising technology, to produce higher quality coatings, with consistently similar depths and composition, on blades, including coating of internal cooling passages. This work would include CVD tray design and the application of true gas phase CVD and should also explore hot corrosion protection during cyclic operations at higher temperatures.

- As the CVD silicon modified aluminising technology is improved, further work should investigate the extent that the addition of reactive elements, hafnium and yttrium, together with addition of platinum, could further enhance hot corrosion resistance of the basic single-step low activity silicon modified aluminising process.

- Further work should involve accurate identification of the refractory element silicides, either by TEM or X-ray analysis of extracted precipitates. This work could lead to development of diffusion barriers to prevent or reduce interdiffusion of silicon and also of substrate strengthening metals, to avoid interdiffusion and microstructural degradation at high operating temperatures, with the commensurate reduction in substrate mechanical strength.

- As development of single-step silicon aluminide coating proceeds and coating quality improves, further work should test their thermo-mechanical fatigue integrity under cyclic operating conditions, and to compare their performance with commercial coatings;

- Further work should aim to optimise the EB-PVD TBC thicknesses around turbine blades having single-step silicon modified aluminide coatings. Further tests should investigate the quality of TBC bonding provided by these coatings. Subsequently, further work should investigate the hot corrosion protection provided by the silicon modified aluminide bonded TBC coatings, by cyclic oxidation and corrosion testing.

- Further work could incorporate methods of monitoring in-service parameters in EB-PVD TBCs with single-step silicon aluminide coatings, using thermochromic dopants, and to develop methods for monitoring such thermochromic signals on operating turbine components.

References

[1] Grubb M., Vrolijk C., Brack D., The Kyoto Protocol, A Guide and Assessment, Royal Institute of International Affairs, London, 1999, ISBN 1 85383 581 1.

[2] UK Energy Review, A Performance and Innovation Unit Report, produced by the Cabinet Office, London 2002.

[3] Sustainable biofuels; prospects and challenges 2010 and beyond. *The Royal Society*, Policy Document 01/08, January 2008, ISBN 978 0 85403 662 2.

[4] Thornley P. Increasing biomass power generation in the UK. *Energy Policy 34* (2006) 2087-2099.

[5] Boyle G., Renewable Energy Power for a Sustainable Future, *Open University,* Oxford Press, 2000.

[6] Johansson T.B., Kelly H., Reddy A.K.N., Williams R.H., Renewable Energy: Sources for Fuels and Electricity, Island Press, Washington D.C., U.S.A., 1992.

[7] Kilgallon P.J., Simms N.J., Oakey J.E., Fate of Trace Contamination from Biomass Fuels in Gasification Systems, Cranfield University, 2004.

[8] Oakey J.E., Simms N.J., Kilgallon P.J., Gas turbines: Gas Cleaning Requirement for Biomass-Fired Systems, Materials Research, Vol.7, No.1, 17-25, 2004.

[9] Williams R.H., Larson E.D., Biomass Gasifier Gas Turbine Power Generating Technology, Biomass & Bioenergy, Vol.10. Nos 2-3, pp149-166, Elsevier, 1996.

[10] Williams R.H., Larson E.D., Advanced gasification-based biomass power generation, *Renewable Energy: Sources for Fuels and Electricity,* Chapter 17, pp. 729-786, Island Press, Washington D.C., 1993.

[11] Demirbas A., Combustion Characteristics of Different Biomass Fuels, *Progress in Energy and Combustion Science* 30 (20040, PP. 220-229, Elsevier, 2003.

[12} Salo K., Kotka Ecopower IGCC-Project, the Attempt to Transfer the Biocycle Project to Finland, *Biomass and Bioenergy,* Vol. 15, No.3, pp. 225-228.

[13] Stevens D.J., Hot Gas Conditioning: Recent Progress with Larger-Scale Biomass Gasification Systems, National Renewable Energy Laboratory, Golden, Colorado, U.S.A., 2001.

[14] Demirbas A., Biomass Co-Firing for Boilers Associated with Environmental Impacts, *Energy Sources,* 27: 1385-1396, 2005.

[15] Jeffrey D.W., Soil-Plant Relationships: an Ecological Approach, Croom Helm, London, 1986, ISBN 0-7099-1498-8.

[16] Pilavachi P.A., Mini- and micro-gas turbines for combined heat and power, *Applied Thermal Engineering* 22 (2002) 2003-2014.

[17] Efficiency in Electricity Generation, Report produced by EURELECTRIC, VGB, Ref. 2003 – 030 – 0548, Brussels, 2003.

[18] Bradley E.F., Superalloy, A Technical Guide, ASM International, U.S.A., 1988.

[19] Encinas-Oropesa A., A Study of Hot Corrosion of Single Crystal Superalloys and Platinum-Aluminide Coatings, PhD thesis, Cranfield University, 2005.

[20] Ross E.W., Sims C.T., Nickel-Based Alloys, in *Superalloys II. High Temperature Materials for Aerospace and Industrial Power,* J. Wiley, New York, pp. 97-134, 1987.

[21] Nalin L., Degradation of Environmental Protection Coatings for Gas Turbine Materials, MPhil thesis, Cranfield University, 2008.

[22] Donachie M.J., Donachie S.J., Superalloys, a Technical Guide, Second Edition, ASM International, 2002.

[23] Giggins C.S. and Pettit F.S., Oxidation of Ni-Cr-Al Alloys between 1000^{o}C and 1200^{o}C, *Journal of the Electrochemical Society,* Vol. 118, pp. 1782-1790, 1971.

[24] Smialek J.L. and Meier G.H., High Temperature Oxidation, in *Superalloys II. High Temperature Materials for Aerospace and Industrial Power.* J.Wiley, New York, pp. 293-326.

[25] Kofstad P., Oxidation mechanisms for Pure Metal in Single Oxidant Gases, in Rapp R.A. *High Temperature Corrosion* at San Diego, California; National Association of Corrosion Engineers, Houston Texas, pp. 123-138, 1981.

[26] Wagner C., Diffusion and High Temperature Oxidation of Metals, in *Atom Movements,* The American Society for Metals, pp. 153, 1951.

[27] Wagner C., Equations for Transport in Solid State Chemistry, *Progress in Solid State Chemistry*, Vol. 10 part 1, pp. 3-16, 1975.

[28] Richardson F.D. and Jeffes H.E., The Thermodynamics of Substances of Interest in Iron and Steel Making. III Sulphides, *Journal of the Iron and Steel Institute,* pp. 165-175, 1952.

[29] Ellingham J.H.T., Reducibility of Oxides and Sulphates in Metallurgical Processes, *Journal of the Society of Chemical Industry,* Vol. 63, No. 125, pp.125-133, 1944.

[30] Kofstad P., *High Temperature Corrosion*, Elsevier Applied Science, London & New York, 1988.

[31] Kofstad P., H*igh Temperature Oxidation of Metals*, Wiley, New York, 1966.

[32] Kubaschewsli O. and Hopkins B.E., *Oxidation of Metals and Alloys* (Edition 2), Butterworth, London, 1967.

[33] Evans U.R., *The Corrosion and Oxidation of Metals*, Edward Arnold Ltd., London, 1961.

[34] Birks N. and Meier G.H., *Introduction to High Temperature Oxidation of Metals*, Edward Arnold, 1983.

[35] Manning J.R., Theory of Diffusion, paper to Seminar of the American Society for Metals, D*iffusion*, Seminar October 14/15, pp. 1-25, 1973.

[36] Nicholls J.R., Designing Oxidation-resistant coatings, *Journal of Minerals, metals and Materials Society*. 2000; 52: pp. 28-35.

[37] Chester G.W., *Diffusion in Duplex Ni-Cr/Ni-Al Overlay Coatings.* Cranfield University; 1988.

[38] Smeggil J.G., Bornstein N.S. Study of interdiffusion effects on oxidation/ corrosion resistant coatings for advanced single crystal superalloys. High Temperature Protective Coatings: Atlanta, Georgia. AIME; 1983.

[39] Cooper S.P., Strang A. High temperature stability of pack aluminide coatings on IN738LC. Proceedings of the Conference on High Temperature Alloys for Gas Turbines: Liege, Belgium. London: D. Reidel Publ.; 1982.

[40] Steinmetz P., Roques B., Dupre B., Duret C., Morbioli R. Hot corrosion of aluminide coatings on nickel base superalloys. High Temperature Protective Coatings: Atlanta, Georgia. AIME; 1983.

[41] Phillips M.A., Gleeson B. Beneficial effects of rhenium additions on the cyclic-oxidation behaviour of beta-NiAl+alpha-Cr alloys. *Oxidation of Metals.* 1998; 50:399-429.

[42] Pichoir R. Influence of the mode of formationon the oxidation and corrosion behaviour of NiAl type protective coatings. Materials and Coatings to Resist High Temperature Corrosion.: London: Applied Science Publishers Ltd; 1977.

[43] Rickerby K., Bell S.R., Wing R.G., inventors; Chromalloy United Kingdom Ltd, Rolls-Royce plc, assignees. *Method of Applying a Thermal Barrier Coating to a Superalloy and a Thermal Barrier Coating.* US 5,667,663. 1997.

[44] Jones R.E. *Bondcoat Developments for Thermal Barrier Coatings.* Sheffield Hallam University; 1999.

[45] Stringer J., Hot Corrosion of High Temperature Alloys, *Annual Review Material Science,* Vol. 9, pp.447-509.

[46] Pettit F.S. and Giggins C.S., Hot Corrosion, in *Superalloys II*, J.Wiley, U.S.A., pp. 327-357, 1987.

[47] Johnson D.M., Whittle D.P. and Stringer J., Mechanism of Na_2SO_4 – Induced Accelerated Oxidation, *Corrosion Science,* Vol. 15, pp. 721-739, 1975.

[48] Bornstein N.S. and DeCrescente M.A., The Role of Sodium in the Accelerated Oxidation Phenomenon Termed Sulfidation, *Metallurgical Transactions,* Vol. 2, pp. 2875-2883, 1971.

[49] Bornstein N.S. and DeCrescente M.A., The Relationship between Compounds of Sodium and Sulfur and Sulfidation, *Transactions of the Metallurgical Society of AIME,* Vol. 245, pp. 1947-1952, 1969.

[50] Goebel J.A., Pettit F.S. and Goward G.W., Mechanism for the Hot Corrosion of Nickel-Base Alloys, *Metallurgical Transactions,* Vol. 4, pp. 261-278, 1973.

[51] Hot Corrosion Degradations of Metals. A Unified Theory Final Scientific Report, Pratt & Whitney Aircraft Group, Florida, U.S.A., 1979.

[52] Roth R.S., Negas T. and Cook L.P., *Phase Diagrams for Ceramists*, Vol IV. Completed at the National Bureau of Standards, The American Ceramic Society, U.S.A., 1981.

[53] Simms N.J., Smith P.J., Encinas-Oropesa A., Ryder S., Nicholls J.R. and Oakey J.E., Development of Type II Hot Corrosion in Solid Fuel Fired Gas Turbine, in *Life Time Modelling of High Temperature Corrosion Processes. Proceedings of an EFC Workshop 2001*, Vol.34, pp. 247-260, Maney Publishing, London, 2001.

[54] Kilgallon P., Simms N.J. and Oakey J.E., Fate of Trace Contaminants From Biomass Fuels in Gasification Systems, in Lecomte-Beckers J. et al. *Materials for Advanced Power Engineering 2002. Proceedings of the 7th Liege Conference Part II,* Vol.21 Forschungszentrum Julich GmbH, pp. 161-169.

[55] Simms N.J., Encinas-Oropesa A., Kilgallon P. and Oakey J.E., Performance of Gas Turbine Materials in "Dirty Fuel" Environments, in Lecomte-Beckers J. et al. *Materials for Advanced Power Engineering 2002. Proceedings of the 7th Liege Conference Part II,* Vol.21 Forschungszentrum Julich GmbH, pp. 923-932.

[56] Giggins C.S. and Pettit F.S., Corrosion of Metals and Alloys in Mixed Gas Environments at Elevated Temperatures, *Oxidation of Metals,* Vol. 14, pp. 361-413. 1980.

[57] Goebel J.A. and Pettit F.S., Na_2SO_4 – Induced Accelerated Oxidation (Hot Corrosion) of Nickel, *Metallurgical Transactions,* Vol.1, pp. 1943-1954, 1970.

[58] Conde J.F.C., Erdos E. and Rahmel A., Mechanisms of Hot Corrosion. High Temperature Alloys for Gas turbines 1982: Liege, Belgium. London: D. Reidel Publishing Company; 1982;pp. 99-148.

[59] Khanna A.S. and Jha S.K., Degradation of Materials Under Hot Corrosion Conditions, *Transactions of the Indian Institute of Metals*, Vol. 51, No. 5, pp. 279-290, 1998.

[60] Duret-Thual C., Morbioli R. and Steinmetz P. *A Guide to the Control of High Temperature Corrosion and Protection of Gas Turbine Materials*., Commission of the European Communities, Belgium, 1986.

[61] Gleeson B., Cheung W.H., Da Costa W., Young D.J., The hot corrosion behaviour of novel co-deposited chromium-modified aluminide coatings. *Oxidation of Metals.* 1992; 38: pp.407-424.

[62] Rapp R.A. and Goto K.S., The Hot Corrosion of Metals by Molten Salts, in Braunstein J. and Selman J.R. *Molten Salts*, The Electrochemical Society, NJ, pp. 159-177, 1981.

[63] Long K., Aluminide-based coatings for turbine blade internal cooling passages, PhD thesis, Cranfield University, 2004.

[64] Morrow III H., Sponseller D.L., Kalns E. The effects of molybdenum and aluminium on the hot corrosion (sulfidation) behaviour of experimental nickel-base superalloys. *Metallurgical Transactions.* 1974; 5 pp.673-683.

[65] Beltran A, and Shores A., Hot Corrosion, in *The Superalloys,* J.Wiley, New York, pp317, 1972.

[66] Luthra K.L., Shores D.A., Mechanism of Na_2SO_4 induced corrosion at 600-900^{o}C. *Journal of the Electrochemical Society*. 1980; 127 pp.2202-2210.

[67] Luthra K.L., Wood J.H., High chromium cobalt-base coatings for low temperature hot corrosion. *Thin Solid Films.* 1984; 119, pp.271-280.

[68] Goward G.W., Low-Temperature Hot Corrosion in Gas Turbines: a Review of Causes and Coatings Therefore, *Journal of Engineering for Gas Turbines and Power,* Vol. 108, pp. 421-425, 1986.

[69] Simms N.J., Oakey J.E. and Nicholls J.R., Development and Application of a Methodology for the Measurement of Corrosion and Erosion Damage in Laboratory, Burner Rig and Plant Environments, *Materials at High Temperatures,* Vol. 17, No. 2, pp. 355-362, 2000.

[70] Rapp R.A. Chemistry and Electrochemistry of the Hot Corrosion of Metals. *Corrosion*. 1986; 42: pp. 568-577.

[71] Berry D., Meelu M.C., McMordie B.G., Kircher T.A. Enhancing performance of silicon- modified slurry aluminides on turbine components operating in marine environments (Paper No.95-GT-359). Proceedings of the International Gas Turbine and Aeroengine Congress and Exposition: Houston, TX, U.S.A. New York, U.S.A.: ASME; 1995.

[72] Misra A.K. Mechanism of Na_2SO_4- induced corrosion of molybdenum containing nickel-base superalloys at high temperatures II. Corrosion in $O_2 + SO_2$ atmospheres. *Journal of the Electrochemical Society*. 133: pp. 1038-1042. 1986.

[73] Fullagar K.P.L., Broomfield R.W., Hulands M., Harris K., Erickson G.L., Sikkenga S.L. Aero-engine test experience with CMSX-4® alloy single crystal turbine blades. *Journal of Engineering for Gas Turbines and Power.* 1996; 118, pp. 380-388.

[74] Matsugi K., Kawakami M., Murata Y., Moringa M., Yukawa N., Takayanagi T. Alloying effects on chromium and rhenium on the hot corrosion resistance of nickel-based single crystal superalloys coated with a Na_2SO_4-NaCl salt (Japanese). *Journal of the Iron and Steel Institute of Japan.* 1992; 78 pp.821-828.

[75] Kobayashi T., Koizumi Y., Nakazawa S., Yamagata T., Harada H. Design of a high rhenium containing single crystal superalloy with balanced intermediate and high temperature creep strengths. Advances in Turbine Materials, Design and Manufacturing: Newcastle-upon-Tyne, UK. London, UK: Institute of Materials; 1997.

[76] Erickson G.L. A new. 3rd-generation, single-crystal, casting superalloy. *Journal of Minerals, Metals and Materials Society.* 1995; 47 pp.36-39.

[77] Conde J.F.G., McCreathC.G. The control of hot corrosion in marine gas turbines. *Transactions of the ASME.* 1981; 103 pp.188-197.

[78] Hurst R.C., Johnson J.B., Davies M. and Hancock P. Sulphate and Chloride Attack of Nickel-Based Alloys and Mild Steels, in Hart A.B. and Cutler A.J.B. *Depositions and Corrosion in Gas Turbines*, John Wiley & Sons, New York pp. 143-157. 1973.

[79] Hossain M.K., Saunders S.R.J. A microstructural study of the influence of NaCl vapour on the oxidation of a Ni-Cr-Al alloy at 850^{o}C. *Oxidation of Metals.* 1978; 12 pp. 1-22.

[80] Shores A., Luthra K.L. and McKee D.W., The Effect of Small Concentrations of NaCl on Hot Corrosion, in D.L. Hildenbrand and D.D. Cubicciotti, *Proceedings of the Symposium on High Temperature Metal Halide Chemistry.* The Electrochemical Society, Princeton, N.J., pp. 538-554, 1978.

[81] Hancock P., The Role of Halides in Gas Temperature Hot Corrosion, in D.L. Hildenbrand and D.D. Cubicciotti, *Proceedings off the Symposium on High Temperature Metal Halide Chemistry.* The Electrochemical Society, Princeton, N.J., pp. 538-554, 1978.

[82] Malik A.U., Asrar N., AHMAD s. AND Siddiqi N.A., Hot Corrosion Behaviour of Some Industrially Important Nickel-Base Alloys in Presence of Na_2SO_4 and NaCl, Z. *Metallkde,* Vol. 79 No. 5, pp. 285, 1988.

[83] Sharma R.N. and Prakash S., Hot Corrosion of a Nickel Base Superalloy in Varying Salt Atmosphere Between 700^{o}C-950^{o}C. *Transactions of the Metal Finishers Association of India,* Vol. 5, No. 1, pp. 47-54, 1996.

[84] Bourhis Y. and John C.St., Na_2SO_4 and NaCl-Induced Hot Corrosion of Six Nickel-Based Superalloys, *Oxidation of Metals,* Vol. 9, No. 6, pp. 507-527. 1975.

[85] Conde J.F.G., Wareham B.A., Hancock P., Hurst R.C., Clelland J.C. Inhibition of hot corrosion. 4th UK/US Conference on Gas Turbine Materials in a Marine Environment: MD, U.S.A. 1979.

[86] McKee D.W., Shores D.A., Luthra K.L. The effect of SO_2 and NaCl on high temperature hot corrosion. *Journal of the Electrochemical Society.* 1978;125: pp. 411-419.

[87] Sun X.F., Guan H.R., Pang Y., Jiang X.X., Hu Z.Q. Microstructure and hot corrosion behaviour of Pt-Al coatings on IN738 nickel-base superalloy. Proceedings of the 6th Liege Conference on Materials for Advanced Power Engineering: Liege, Belgium. Julich, Germany: Forschungszentrum Julich GmbH; 1998.

[88] Halstead W.D., Hart A.B. The Role of Chloride in Corrosion by Flue Gas Deposits. *Report of the Meeting Held on 26-27 November 1969 at Sudbury House. Job No. VF 474:* Central Electricity Generating Board; 1970.

[89] Stringer J., Nagarajan V. and Whittle D.P. The Role of Chlorides in the Hot Corrosion of Cobalt-Base Alloys, in D.L. Hildenbrand and D.D. Cubicciotti, *Proceedings of the Symposium on High Temperature Metal Halide Chemistry.* The Electrochemical Society, Princeton, N.J., pp. 509-520, 1978.

[90] Giggins C.S. and Pettit F.S., Hot Corrosion Degradation of Metals and Alloys – A Unified Theory. PWA Report N. FR-11545, U.S.A., 1976.

[91] Sourmail T., Coatings for Turbine Blades, Cambridge University, 2003.

[92] Nicholls J.R., Review of Coatings for Gas Turbines, Cranfield University, 2000.

[93] Levine S.R. and Caves R.M., Thermodynamics and kinetics of pack-aluminide coating formation on IN100, *Journal of the Electrochemical Society*. 1974, 121:1051.

[94] Pichoir R., Aluminide coatings on nickel or cobalt-base superalloys, in High Temperature Alloys for Gas Turbines, D.Coutsouradis et al. eds., Applied Science Publishers Ltd., London, p191, 1978.

[95] Hancock P. and Nicholls J.R., Fundamental and Engineering Aspects of Coatings for Diesels and Gas Turbines. *NATO Workshops into Advanced Coatings for Diesels and Gas Turbines*. 1994, pp. 31-58.

[96] Nicholls J.R., Smart Coatings - A Bright Future, *Materials World,* 4(1), pp.19-21, 1996.

[97] Nicholls J.R., Wing R.G. Advances in Coating Systems for Utility Gas Turbines. Cost 2002 – Materials for Advanced Power Engineering.

[98] Nicholls J.R., Advances in Coating Design for High-performance Gas Turbines, *MRS Bulletin*, Sept.2003.

[99] Sims C.T. and Hagel W.H. The Superalloys. Vital High Temperature Gas Turbine Materials for Aerospace and Industrial Power, U.S.A., pp.595, 1972.

[100] Nicholls J.R., Simms N.J., Chan W.Y. and Evans H.E., Smart overlay coatings – concept and practice. *Surface and Coatings Technology* 149, pp.236-244, 2002.

[101] Nicholls J.R., Smart Coatings – A Bright Future, *Materials World* 4 (1), pp.19-21, 1996.

[102] Nicholls J.R., Simms N.J., Neseyif S., Evans H.E., Ponton C., Taylor M. Hot corrosion of smart overlay coatings, in McNallan M., Opila E., Maruyama T., Narita T. (Eds.), High Temperature Corrosion and Materials Chemistry, *Electrochemical Society Proceedings*, 99-38, pp. 270-281, 2000.

[103] Restall J.E., Gill B.J., Hayman C., Archer N.J., A process for protecting gas turbine blade cooling passages against degradation. Superalloys: Silversprings, PA, U.S.A. American Society for Metals, 1980.

[104] Restall J.E. and Wood M.I., Alternative processes and treatments. *Material Science and Technology.* 1986;2:225-231.

[105] Goward G.W. and Boone D.H., Mechanisms of Formation of Diffusion Aluminide Coatings on Nickel_Base Superalloys. *Oxidation of Metals,* Vol. 3, No. 5, pp. 475-495, 1971.

[106] Swadzba L., The Influence of Silicon on the Structure and Properties of Diffusion Aluminide Coatings on Nickel Base Superalloys. *Materials Science Forum,* Vols. 163-165, pp. 619-626, 1994.

[107] Khajavi M.R., Shariat M.H. and Pasha A., Aluminide Coatings for Nickel Based Superalloys, *Surface Engineering*, Vol. 20, No. 4, pp. 261-265, 2004.

[108] Squillace A., Bonetti R., Archer N.J., Yeatman J.A., The control of the composition and structure of aluminide layers formed by vapour aluminising. *Surface and Coatings Technology*, 120-121, pp. 118-123, 1999.

[109] MTDATA Handbook, Documentation for NPL Databank for Mtallurgical Thermochemistry, National Physical Laboratory, Teddington, ISSN 0959-2423, 1994.

[110] Warnes B.M., Near D.L., Punola D.C. and Basta W.C., inventors; Howmet Research Corp., assignee, Active Element Modified Platinum Aluminide Diffusion Coating Method, US 5,989,733. 1999.

[111] Warnes B.M., Reactive element modified chemical vapour deposition low activity platinum aluminide coatings, *Surface and Coatings Technology*, 2001; 146-147: pp. 7-12.

[112] Nash P., Singleton, and Murray J.L. (1991), *ASM Handbook, Vol.3, Alloy Phase Diagrams*, pp. 2.49, ASM International, 2006, ISBN: 0-87170-5.

[113] Munro T.C. and Gleeson B., The Deposition and Oxidation Resistance of Aluminide Coatings on γ-TiAl, *Materials Science Forum*, Vols. 251-254 (1997), pp. 753-760.

[114] Netherlands Energy Research Centre (ECN), PHYLLIS Database web site, http://www.ecn.nl/phyllis.

[115] Reed G.P., Control of trace elements in gasification, PhD Thesis for University of London, 1998.

[116] Janssen M.M.P., Rieck G.D., Reaction Diffusion and Kirkendall-Effect in the Nickel-Aluminium System. *Transactions of the Metallurgical Socity of the AIME.* 1967; 239: pp. 1372-1385.

[117] Bradshaw A., Simms N.J., Nicholls J.R., Passage of trace metal contaminants through hot gas paths of gas turbines burning biomass and waste-fuels, *Fuel 87* (2008), pp. 3529-3536.

[118] Desai V.H., Short- and Long-term Hot Corrosion Behaviour of Gas Turbine Superalloys, ASM Materials Solutions Conference, Columbus, USA., 2004.

[119] Aoki S., Trend and Key Technologies for Gas Turbine Combined Cycle Power Generation in a Globally Competitive Market and Environmental Regulations, Proc. 2000 International Joint Power Generation Conference, Miami Beach, Florida, July 23-26, 2000.

[120] Pampana M.S., Study of Oxidation and IPAP Nitriding Characteristics of Supralloy IN738LC, LSU ME Graduate Student Conference, USA, 2004.

[121] Cox M., Wickins M., Kuang J.P., Harding R.A., and Campbell J., Effect of top and bottom filling on reliability of investment castings in Al, Fe and Ni based alloys, *Materials Science and Technology*, Nov/Dec 2000, Vol. 16, 1446.

[122] Lee K.N., Barrett C.A. and Smith J., Long-term CyClic Oxidation Behaviour of Uncoated and Coated Re 108 and In939 at 980°C and 870°C, NASA TM 209072, 1999.

[123] Henderson M.B., Arrell D., Heobel., Larsson R. and Marchant G., Nickel-Based Superalloy Welding Practices for Industrial Gas Turbine Applications. Alstom Energy Technology Cntre, Whetstone, UK, 2001.

[124] Giggins C.S. and Pettit F.S., Hot Corrosion, The Superalloys High Temperature Materials for Aerospace and Industrial Power, ISBN 0-471-01147-9, pp. 327, U.S.A., 1987.

[125] Brandon D. and Kaplan W.D., Microstructural Characterisation of Materials, John Wiley & Sons, London, 1999, ISBN 0-471-98756-5.

[126] West A., Basic Solid State Chemistry, Second Edition, John Wiley & Sons, London, 1999, ISBN 0-471-98502-3.

[127] Nicholls J.R., Lawson K.J., Rickerby D.S. and Morrell P., Advanced Processing of TBC's for Reduced Thermal Conductivity, Pub., AGARD-R-823, April 1998.

[128] Nicholls J.R., Lawson K.J., Johnstone A. and Rickerby D.S., Low Thermal Conductivity EB-PVD Thermal Barrier Coatings, *Materials Science Forum*, Vols. 369-372 (2001) pp. 595-606.

[129] Nicholls J.R., Lawson K.J., Johnstone A. and Rickerby D.S., Methods to reduce the thermal conductivity of EB-PVD TBCs, *Surface and Coating Technology*, 151-152 (2002) 383-391.

[130] Levin E.M., Robbins C.R. and McMurdie H.F., Phase Diagrams for Ceramists, American Cramics Society, 1964.

Appendix

Papers published:

1. Bradshaw A., Simms N.J., Nicholls J.R., Passage of trace metal contaminants through hot gas paths of gas turbines burning biomass and waste-fuels, *Fuel*, 87 (2008) 3529-3536.